Editorial

As part of the continuing exercise to involve more of our active scientists in the publication of the Academy's journals, many Editorial Boards including that of the **Journal of Astrophysics and Astronomy** have been reconstituted. At the request of the President of the Academy I have agreed to assume the Editorship of this journal in addition to my responsibilities as the Editor of Publications of the Academy. D. C. V. Mallik will continue as the Associate Editor for JAA.

On behalf of the President and the Fellowship of the Academy I wish to take this opportunity to thank the outgoing members of the Editorial Board for all their help and efforts to sustain this journal, as well as to improve it. Special thanks are due to J. C. Bhattacharyya for shouldering the responsibility as the Editor for four years. I would also like to welcome the new members and look forward to their active involvement in improving the quality of the journal, its circulation, and in ensuring that the journal conforms to the highest international standards.

Another important decision that has been taken for reasons of practicality is to shift the Editorial Office from the Indian Institute of Astrophysics (where it was located ever since the journal was started in 1980) to the Academy Office on the campus of the Raman Research Institute. I wish to record the Academy's deep gratitude to Ms. Sandra Rajiva who not only served as the Editorial Secretary but took charge of much of the work connected with the printing of the journal all these years.

G. Srinivasan
Raman Research Institute
Bangalore

Address for correspondence
Indian Academy of Sciences,
C V. Raman Avenue,
P.B. No. 8005,
Bangalore 560080.

J. Astrophys. Astr. (1992) **13**, 3–52

Evolution of Massive Binary Stars in the LMC and its Implications for Radio Pulsar Population

N. Rathnasree & A. Ray *Theoretical Astrophysics Group, Tata Institute of Fundamental Research, Bombay 400005*

Received 1991 May 28; accepted 1992 January 13

Abstract. The Hertzsprung-Russell diagram of the Large Magellanic Cloud compiled recently by Fitzpatrick & Garmany (1990) shows that there are a number of supergiant stars immediately redward of the main sequence although theoretical models of massive stars with normal hydrogen abundance predict that the region $4.5 \leqslant \log T_{\rm eff} \leqslant 4.3$ should be un-populated ("gap"). Supergiants having surface enrichment of helium acquired for example from a previous phase of accretion from a binary companion, however, evolve in a way so that the evolved models and observed data are consistent – an observation first made by Tuchman & Wheeler (1990). We compare the available optical data on OB supergiants with computed evolutionary tracks of massive stars of metallicity relevant to the LMC with and without helium-enriched envelopes and conclude that a large fraction (≈ 60 per cent) of supergiant stars may occur in binaries. As these less evolved binaries will later evolve into massive X-ray binaries, the observed number and orbital period distribution of the latter can constrain the evolutionary scenarios of the supergiant binaries. The distributions of post main sequence binaries and closely related systems like WR + O stars are bimodal–consisting of close and wide binaries in which the latter type is numerically dominating. When the primary star explodes as a supernova leaving behind a neutron star, the system receives a kick and in some cases can lead to runaway O-stars. We calculate the expected space velocity distribution for these systems. After the second supernova explosion, the binaries in most cases, will be disrupted leading to two runaway neutron stars. In between the two explosions, the first born neutron star's spin evolution will be affected by accretion of mass from the companion star. We determine the steady-state spin and radio luminosity distributions of single pulsars born from the massive stars under some simple assumptions. Due to their great distance, only the brightest radio pulsars may be detected in a flux-limited survey of the LMC. A small but significant number of observable single radio pulsars arising out of the disrupted massive binaries may appear in the short spin period range. Most pulsars will have a low velocity of ejection and therefore may cluster around the OB associations in the LMC.

Key words: stellar evolution—binary stars—Large Magellanic Cloud—radio pulsar population

1. Introduction

A luminosity limited complete survey of supergiant stars can provide important observational tests of the theory of evolution of massive stars. Stars in the Large Magellanic Cloud (LMC) are all essentially at the same distance from us. Their relatively well known distance and reddening corrections make this stellar population homogeneous and ideal for comparison with theoretical computations of massive stellar evolution. A recent survey of the LMC supergiants by Fitzpatrick & Garmany (1990) (hereafter FG) has shown a number of features in the Colour-Magnitude (Hertzsprung-Russell) diagram that were not discernible among the galactic supergiants. Notable among these is that the region immediately redwards of the main sequence in the H-R diagram is well-populated by supergiants although theoretical models of massive stars with a canonical hydrogen abundance, $X \simeq 0.7$, predict that the region ($4.5 \leqslant \log T_{\rm eff} \leqslant 4.3$) should be un-populated. 'Standard' theory therefore leads to a predicted 'gap' in this region (Tuchman & Wheeler 1990, hereafter TW).

Tuchman and Wheeler, however, suggested that these stars are or were members of binary systems which acquired an outer helium-enriched layer through accretion that substantially increased the probability of finding these stars in the "gap". The hypothesis of duplicity of supergiant stars is compatible with the observations of five blue LMC stars by Kudritzki *et al.* (1989) where the use of non-LTE model atmosphere analysis indicates that all five are helium enriched ($Y_s \leqslant 0.5$). All these blue stars appear in the temperature range mentioned above. In addition, there are indications of helium and barium enrichment in the envelope of SN1987A (Arnett *et al.* 1989). This is again consistent with the hypothesis that the progenitor Sanduleak – 69°202 may have been left in a helium-enriched stage.

Helium-enriched massive stars in binaries may also be candidate progenitor systems for supernovae of Type Ib. These SNe show no evidence of hydrogen but have strong helium lines near the maximum of the light curve (see *e.g.* Filippenko 1991). When the original primary explodes as a hydrogen-stripped core (resulting in the Type Ib SN), in most cases the collapsed core (*e.g.* a neutron star) is retained in the binary orbit. Depending upon the initial orbital separation, some of these systems could be X-ray active objects when the helium-enriched secondary evolves and expands. Hence some of the massive X-ray binaries in the LMC have companions that can show evidence of helium enrichment. Likewise some of the seemingly single Blue Supergiant Stars (BSG) in this region of the HR-diagram of the LMC could show weak X-ray activity. TW have suggested that the peculiar Blue Supergiants could be yet another clue that SN Ib events occur in binary systems (Wheeler & Levreault 1985). Alternatively, immediately before the supernova explosion of the primary, the binary may in many cases reveal itself as a Wolf-Rayet (WR + O) system since the exposed core of the primary star would be like a WR star. Observational data· about such systems in LMC also exist (Moffat 1989; Moffat, Niemela & Marraco 1990) and can be useful towards constraining the results derived from the binary hypothesis.

The first supernova explosion (whether a Type II or Type Ib) is expected to leave behind a neutron star which at a later stage may be detectable as a radio pulsar. The binary is disrupted if more than half the total mass of the system immediately prior to the explosion is ejected (Boersma 1961). Blaauw (1961) has suggested that the origin of "run-away" OB stars in our Galaxy was in supernova exlosions in binaries where the secondary (OB star) was released and got a high velocity kick ($v \leqslant 50$ km/s) due

to the primary's explosion. If the binary survives the first supernova, then the second supernova explosion of the erstwhile secondary will unbind the system if the mass of the companion of the neutron star exceeds $M_2 \geqslant 16M_{\odot}$ (van der Heuvel 1987). Under most circumstances, the second explosion will lead to two runaway neutron stars one of which will have a spin-up history. The peculiar velocities of these pulsars and their spin distribution can then reveal substantial information about their progenitor systems. The characteristics of the progenitor systems in the LMC, a sub-class of which are the massive X-ray binaries can in turn reveal information about the helium-enriched massive stars in binaries we referred to earlier. A luminosity-limited survey of radio pulsars in the LMC will also be free of the many distance-related selection effects that affect the study of Galactic pulsars and can therefore shed some light on the evolution of pulsars and their progenitor population.

In this paper we first report in Section 2 the calculation of the steady state population of such stars in the immediate Blue Supergiant region. We compute models of massive stars with a metallicity relevant to LMC with a stellar evolution code. We compare the observed distribution of stars in the H-R diagram (FG) with an ensemble of two sets of stellar models in which one set has helium-enriched outer layers while the other has a normal helium and hydrogen abundance (X_S = 0.75, Y_S = 0.24). This comparison indicates that approximately 60 per cent of the supergiant stars are likely to have their surface enriched by helium and that at least this fraction of the massive stars probably occur in binary systems. We then make an overall study of the production of evolved high mass binaries from the population of un-evolved massive binaries in the LMC. In this context in Section 3, we consider the orbital evolution of massive binaries taking the effects of mass exchange and mass loss (where relevant) into account. We use the observational data available so far on the LMC massive X-ray binaries and Wolf-Rayet + O star binaries to characterize the orbital period and mass-ratio distribution of the BSG binaries. The former may have progeny/progenitor relationships with the peculiar BSG binaries hypothesized by TW. In Section 4 we investigate the properties of single pulsars released after the second supernova explosion disrupts the binary. We make predictions about the pulsar velocities and spatial distribution, and give the expected spin and radio luminosity distributions. These can be compared with future flux-limited radio surveys of the LMC. Our analysis is carried out for a particular mass ratio in the peculiar BSG – neutron star binary stage primarily because we are interested in progenitor · systems of *single* pulsars in the LMC and also because the relevant data from the H-R diagram is most easily compared for this case. Finally discussion and conclusions form Section 5. Preliminary results from Sections 2 and 3 have been reported elsewhere (Ray & Rathnasree 1991).

2. Evolution of massive stars with helium enrichment and their implied duplicity fraction

Compared to the sample of stars in our own galaxy where the uncertainties in the distance and reddening of *individual* stars lead to a scatter in the colour-magnitude diagram, the homogeneous sample of stars in the Large Magellanic Cloud (LMC) can induce mostly an overall shift in the distribution in the Hertzsprung-Russell diagram due to the common uncertainty in the distance to LMC. Thus the comparison of the observed colour-magnitude diagram to their theoretical or numerical counter-

part becomes more meaningful. In this section we report computed stellar models incorporating surface enrichment of helium and obtain a theoretically determined distribution of stars in the BSG region using a combination of stellar models with and without helium-enriched envelopes. These we compare with the colour-magnitude diagram of FG and derive the implied fraction of enriched stars among massive post main sequence stars. For a population of stars in a steady state the distribution in a given surface temperature and magnitude bin is proportional to the time that stars in an appropriate main sequence mass range spend in that bin. We have obtained evolutionary models for a 20 $M_\odot$ star incorporating helium enrichment in varying amounts of envelope mass to determine the evolutionary timescales in various surface temperature bins. The number counts of stars in the BSG region of the HR-diagram of FG have been obtained from the region $-8 \leqslant M_v \leqslant -7$ – the region populated by Blue Supergiants with main sequence masses in the range $15\,M_\odot \leqslant M_{\rm ZAMS} \leqslant 25M_\odot$. We used a stellar evolution code originally written by Icko Iben that was subsequently modified by us. Updated nuclear reaction rates (Caughlan & Fowler 1988) and stellar mass loss rates, according to de Jager, Nieuwenhuijzen & van der Hucht (1988) have been incorporated in the code. In the present work, we use a mass loss rate three times that of the de Jager, Nieuwenhuijzen & van der Hucht (1988) formula. This is consistent with the estimated mass loss rate for the BSG progenitor of SN 1987A by Trumper *et al.* (1991) based on ROSAT observations. These observations

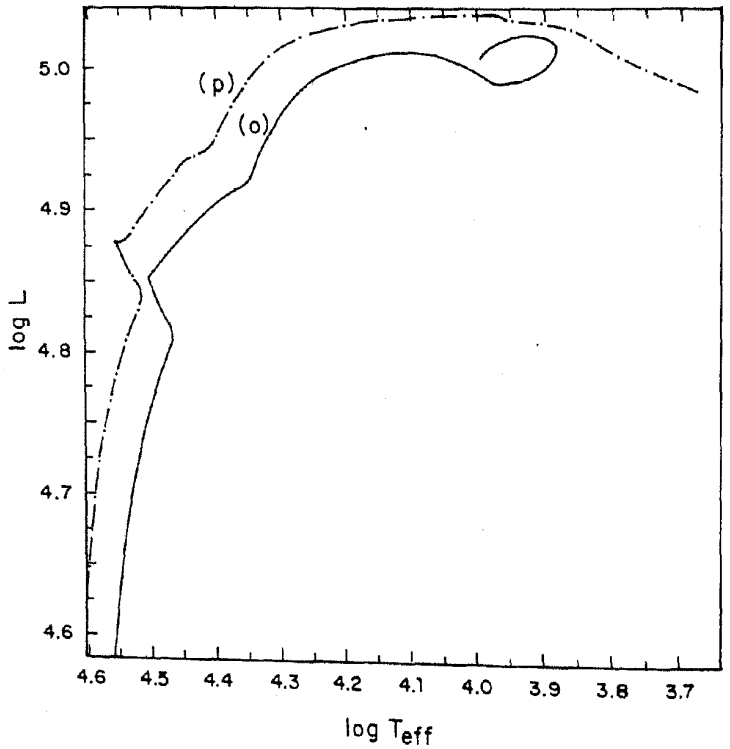

Figure 1. L–$T_{\rm eff}$ diagrams for helium enriched stars (marked p) with $Y_{\rm s}$ = 0.5 down to 1.4 $M_\odot$ below the surface and with normal hydrogen abundance (X = 0.7) marked o. The reported curves are for a 20 $M_\odot$ star with $Z=Z_\odot/2$ incorporation the relative abundances of elements from Dufour (1984). Mass loss rate used in these figures is a factor 3 times that given by de Jager *et al.*

indicate a mass loss rate approximately 3 to 6 times larger than the Galactic value for stars in the LMC in the direction of SN1987A from the derived upper limit on the density of the circumstellar material in that region (Trümper *et al.* 1991).

Fig. 1 shows the theoretically determined HR-diagram for two models one of which is evolved with an ordinary hydrogen-rich envelope while the other is evolved with a helium-enriched envelope. A metallicity of Z = 0.01 has been used in obtaining these models. The model marked 'p' is evolved close to the end of the main sequence with an ordinary hydrogen rich envelope similar to the model marked 'o'. At this point, the outer 1.4 $M_{\odot}$ of the envelope is enriched to a helium abundance Y = 0.5. This has the effect of increasing the surface temperature and the luminosity of this model compared to model 'o'. In the following sub-section we will discuss a quantitative measure of the evolutionary rates in the post main-sequence region introduced by TW and discuss the implications for the stellar models with helium enrichment *vis-a-vis* the observations.

2.1 *Relative Populations of Supergiants in Different Regions of the H-R Diagram*

Tuchman & Wheeler (1990) have defined a normalized 'duration function' as,

$$D(L, T_{\rm eff}) = \frac{1}{t_{\rm br}} \frac{{\rm d}t}{{\rm d}\log T_{\rm eff}} \tag{1}$$

where $t_{\rm br}$ is the total time spent by a star, in crossing the HR-diagram from blue to red in the post main-sequence region for a given luminosity interval. This function has been plotted in Fig. 1 of Ray & Rathnasree (1991) where $t_{\rm br}$ used was as defined by Tuchman & Wheeler (1990) *i.e.*

$$t_{\rm br}(L) \approx \frac{1.5 \times 10^{11}}{L/L_{\odot}} {\rm yr.} \tag{2}$$

In the present work the duration functions (shown in Figs 2 and 3) have been determined using the calculated value of $t_{\rm br}$ for the corresponding models *i.e.*

$$t_{\rm br} = \int_{T_{\rm eff} = 35{,}000}^{T_{\rm eff} = 5{,}000} \frac{{\rm d}t}{{\rm d}\log T_{\rm eff}} {\rm d}\log T_{\rm eff}. \tag{3}$$

The duration function calculated from the equilibrium stellar envelope model for a 20 $M_{\odot}$ star with normal helium abundance is neglible in the immediate post main sequence region (TW 1990). Here, however, the observed stellar density function is high. The latter is defined as:

$$N(L, T_{\rm eff}) = \frac{1}{N_{\rm tot}} \frac{{\rm d}n(L, T_{\rm eff})}{{\rm d}\log T_{\rm eff}}. \tag{4}$$

This discrepancy has led to a hypothesis by TW that stars seen in the post main sequence region are primarily those having anomalously helium-enriched envelopes ($Y_{\rm s} \gtrsim 0.5$). We have calculated the duration functions from numerically evolved models of 20 $M_{\odot}$ stars with metallicity appropriate to LMC (Z = 0.01) with (a) an envelope of ordinary helium abundance ($Y_{\rm s}$ = 0.24) and (b) with an envelope of enriched helium abundance (with the outer 1.4 $M_{\odot}$ of the envelope enriched to

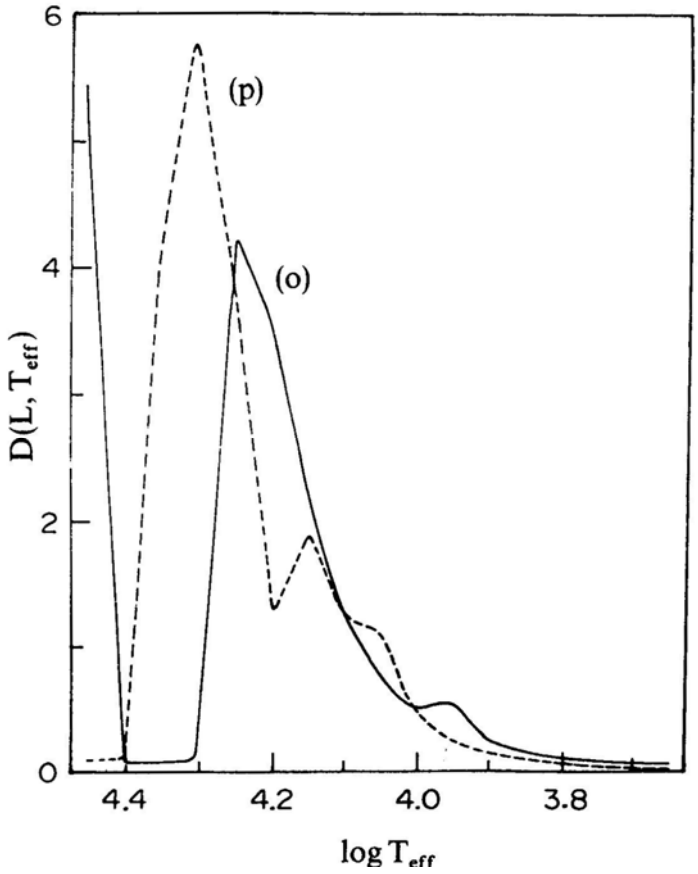

Figure 2. Duration function $D(L, T_{\rm eff})$ for the stellar models ‘p’ and ‘o’ for the same set of parameters as in Fig. 1.

$Y_{\rm s}$ = 0.5). These are plotted in Figs 2 and 3 where the cases (a) and (b) are marked 'o' and 'p' respectively. Fig. 2 is constructed from evolutionary runs where individual heavy element abundances are simply scaled (by a factor 0.5) with respect to the solar values. In Fig. 3 we use models having relative abundances determined from observations of LMC (Dufour 1989).

The post main sequence peak in the computed duration functions for the models having normal surface helium abundance occurs redwards of log $T_{\rm eff}$ = 20,000°K, whereas the peak moves into the "gap" region for models with enriched surface helium. The first peak in the duration function near log $T_{\rm eff}$ = 4.45 for models with normal surface helium abundance occurs on account of the fact that in these models this point is reached immediately after the hydrogen shell ignition whereas in the enriched models the shell ignition occurs at higher $T_{\rm eff}$. Therefore, populating the post main sequence region of the HR-diagram with a mixed ensemble of stars with and without helium enriched envelopes narrows considerably the log $T_{\rm eff}$ region where a gap in the stellar density is expected but does not entirely bridge this gap. Nevertheless, the number count of stars in the post main sequence region given the quoted uncertainties (of $M_{\rm v}$ and $T_{\rm eff}$) in FG and the theoretical calculations agree if there exist a substantial

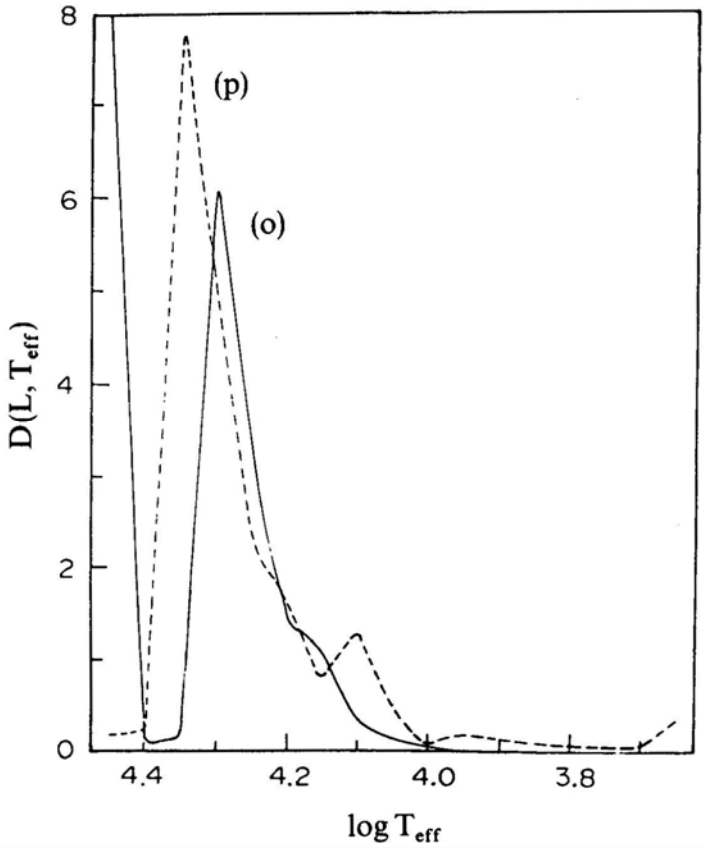

Figure 3. Duration functions calculated for stellar models incorporating the relative abundance of heavy elements in the LMC according to Dufour (1984) and for the same set of parameters as in Fig. 1.

fraction of helium-enriched stars among the Blue Supergiants in the LMC. Several evolutionary runs were completed for Y_s= 0.5 and M_s=0.5, 0.75, 1.0 and 1.4$M_\odot$. The effect of helium enrichment is to shift the post main sequence peak in the duration function bluewards with the magnitude of the shift increasing with the value of M_s. The model with Y_s = 0.5 for M_s = 1.4 $M_\odot$ illustrated in Figs 2 and 3 has the maximum shift of the peak towards higher temperature. Work is under progress to calculate a number of stellar models with different extents of helium enrichment, mass loss rates, different relative ratios of individual heavy elements at constant Z *etc* to match not only the immediate post main sequence behaviour but also to reproduce the many qualitative features of stellar evolution seen in the data of Fitzpatrick & Garmany (1990).

2.2 *Calculation of the Duplicity Fraction*

Since the helium-enriched stars in binaries and the single stars traverse the post main sequence regions with different speeds the observed numbers can be used to calculate

the fraction of binaries. If N is the total number of BSG stars in the temperature interval $4.5 \geqslant \log T_{\rm eff} \geqslant 3.7$ and the relevant magnitude interval and f is the fraction of helium-enriched stars among them, then the number of stars N^i observed in the i-th temperature bin is:

$$N^i = N_p^i + N_0^i = Nf\frac{\tau_p^i}{\tau_p^{\rm tot}} + N(1-f)\frac{\tau_0^i}{\tau_0^{\rm tot}}. \tag{5}$$

Here, $\tau_{p(o)}^{\rm tot}$ is the total time that a He-enriched (or normal) star spends in the BSG region. The number counts of stars (from FG) in the two bins i ($4.5 \geqslant \log T_{\rm eff} \geqslant 4.4$) and j($4.4 \geqslant \log T_{\rm eff} \geqslant 4.3$) in the magnitude interval $-8 \geqslant M_{\rm v} \geqslant -7$ and the corresponding pair of Equations (5) give a solution for $f = 0.6$ when the computed timescales for a $20M_{\rm O}$ star are used. That is 60 per cent of all stars traversing this post main sequence region (*i.e.* OB Supergiants) have to be helium enriched. This number should be considered a lower limit on the actual duplicity fraction since this, is the required fraction of stars which should have been *processed* in binaries. The other 40 per cent could be either single stars or members of binary systems which have not undergone helium enrichment. The same fraction/is obtained if the number counts of BSG stars up to the blue boundary of the Hertzsprung gap ($\log T_{\rm eff} = 3.7$) in eight bins (of 0.1 dex width in $\log T_{\rm eff}$) are used for a least square fit to the theoretically determined steady-state population of normal and helium-enriched stars determined from Equation (5). Here, the total number of stars and the duplicity factor are used as constraints. Even though the binary fraction in the post main sequence band seems quite substantial, it is not excessive when such fractions are considered in the context of WR + OB (Moffat 1989) or O-stars (van den Heuvel 1984). Thus from a number count of stars reported in the bins i and j one expects approximately 90 stars in these bins currently observable as parts of binaries as a consequence of Tuchman and Wheeler's hypothesis.

The occurrence of such a large number of stars in binary systems may have evolutionary consequences and observational implications which we shall now investigate. In particular if a large number of stars in the BSG region are present in close binary systems with compact companions, then the presence of a large number of high luminosity X-ray sources corresponding to later evolutionary stages of these stars is also implied. The presence of a substantial fraction of WR stars in short orbital period systems which could be easily detected is also expected. Existing observations of massive X-ray binaries and WR + OB systems thus constrains the relative fractions of the binary systems in the short and wide orbital period ranges. We investigate the implications of these observations for the distributions in orbital periods of the initial binary systems in the following section.

3. Evolution of binary supergiants and their relation to observed MXRBs and WR + binaries in the LMC

3.1 *Classification of Massive Binary Stars and their Response to Mass Transfer*

The initially more massive companions (the primaries) of the peculiar BSG stars would transfer mass either by Roche-lobe overflow (RLO) or through a stellar wind. In close binary systems, the stages of tidal mass exchange are defined by the phase

of nuclear evolution of the Roche-lobe filling component. Given a mass ratio this also defines the initial orbital period of the binary (see for example, Webbink 1979). Following Webbink (1979), mass transfer from the primary to the secondary during shell hydrogen burning of the former is denoted Case B^1 (the superscript 1 referring to the first stage mass transfer from the primary). A second letter, *e.g.* B or C with superscript 2 following the first denotes the second stage when the secondary transfers mass to the compact remnant of the exploded primary. Similary, mass transfer during shell helium burning of the primary is called here to be Case C^1 although Webbink uses a more general definition in calling both core and shell helium burning as Case C. We use an additional notation Case D^1 in which the orbit is so wide that a primary of a given mass and an initial mass-ratio is unable to fill the Roche-lobe even in its most extended state during nuclear evolution. The ranges of the radii of the primary star at the start of the mass transfer for the above cases, *i.e.*, at the shell hydrogen burning stage (BSG), the shell helium burning stage (RSG) and at the carbon ignition stage (tip of the RSG branch) have all been obtained as a function of the ZAMS mass of the primary star by extrapolating from the evolutionary models of Brunish & Truran (1982) for main sequence masses 15, 30 and 40 $M_\odot$ with Z = 0.01. These models ignite helium at the centre shortly following the shell hydrogen ignition. Thus, the start of Case B^1 mass transfer here has been assumed to occur close to central helium ignition when log $T_{\rm eff} \approx 4.3$ for all the models under consideration. Case C^1 mass transfer is assumed to start when log $T_{\rm eff} \approx 3.6$ *i.e.*, when the stellar model just reaches equilibrium on the Hayashi track following shell helium ignition. These ranges of radii are given below.

$$\frac{R_{1i}}{R_\odot} \leqslant 1.1\left(\frac{M_{1i}}{M_\odot}\right)^{0.96} \qquad \textit{Case A}$$

$$1.1\left(\frac{M_{1i}}{M_\odot}\right)^{0.96} < \frac{R_{1i}}{R_\odot} \leqslant 37\left(\frac{M_{1i}}{M_\odot}\right)^{0.95} \qquad \textit{Case B}$$

$$37\left(\frac{M_{1i}}{M_\odot}\right)^{0.95} < \frac{R_{1i}}{R_\odot} \leqslant 76\left(\frac{M_{1i}}{M_\odot}\right)^{0.88} \qquad \textit{Case C} \qquad (6)$$

The masses of the primary in the above relations correspond to the ZAMS masses. Fig. 4 shows the mass radius diagram illustrating the regions occupied by binary systems undergoing these cases of mass transfer.

An equivalent classification scheme which relates the nuclear burning stage and the structure of the primary together with the mass ratio of the binary at the start of mass transfer to the characteristics of the mass transfer process has been discussed by Webbink (1979). Binary systems undergoing Case B^1 mass transfer and with widely disparate mass ratio soon evolve into a contact configuration and undergo Mode I interaction outlined by Webbink. This tendency to evolve into contact increases markedly for extreme mass ratios, both because of the greater orbital shrinkage during mass reversal (in conservative mass transfer), and because of the great difference in thermal time scales between components. Case B^1 systems with nearly equal mass components undergo Mode II interaction with the Roche-lobe filling component having a radiative envelope. The primary star in this case is able to pass through the mass-ratio reversal phase without greatly exceeding its tidal radius at any time because of its ability to contract sufficiently rapidly in response to mass loss to accommodate

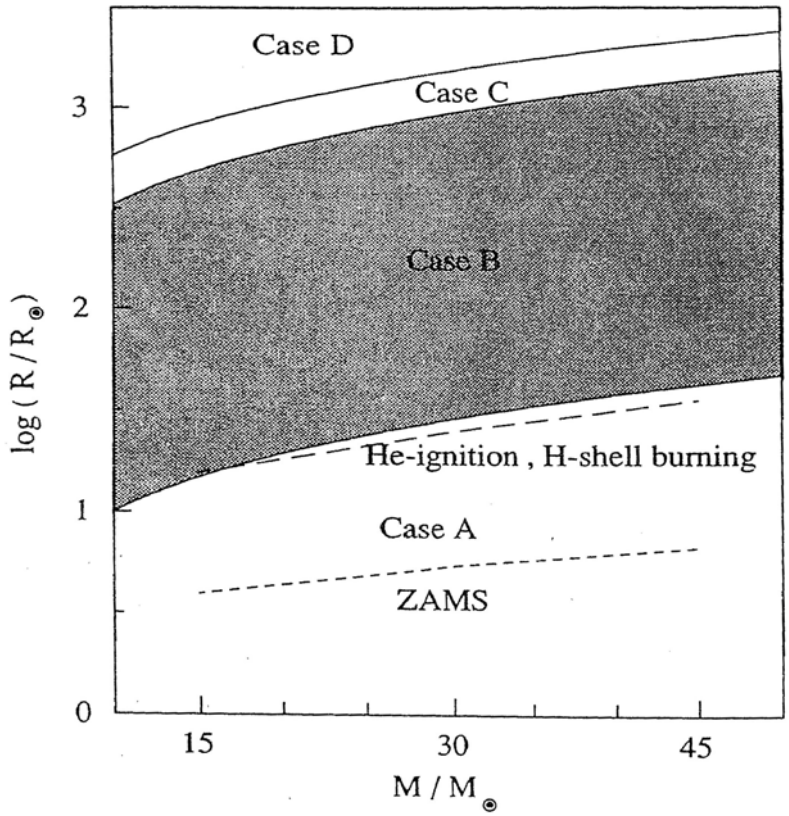

Figure 4. The ranges of radii for a given mass corresponding to the different cases of mass transfer obtained from the evolutionary models of Brunish & Truran (1982) (see text).

its shrinking tidal limit. The underlying reason for this is the star's stability against convection. These stars, however, develop convective envelopes as they evolve towards central helium exhaustion. Thus Case C^1 systems with the primary having a convective envelope, in general undergo Mode III interaction. This mass transfer is unstable and leads towards a common envelope situation in Case C^1 systems which have widely disparate component masses. On the other hand, in Case C^1 systems with nearly equal component masses the runaway mass transfer is avoided with the onset of mass reversal, beyond which mass transfer leads to a stable orbit expansion. The two classification schemes outlined above for the evolution of binary systems with mass transfer are equivalent and for notational convenience we will use the former classification henceforth.

3.2 *The Dividing Line in Mass Ratio and Channels of Evolution*

The evolutionary path taken by a binary depends on the initial separation and the initial mass ratio $q_i = M_2/M_1$ and is also affected by the envelope structure of the

mass losing star as discussed above. The discussion following in this and the next subsection (3.3) illustrates how and under what conditions a given primordial binary evolves through any particular channel. The relevant formulae for the calculation of conservative evolution of orbits for systems ($q_i \geqslant 0.4$) are given in Appendix A whereas those for orbit evolution for systems with $q_i < 0.4$ are given in Appendix B. We focus attention on those systems where the secondary star has a mass of 20 $M_\odot$ as mentioned earlier so that the mass ranges and the orbital period ranges quoted below are only for such systems. Much of the discussion in the text of these two sub-sections is to be considered along with Figs 5–12.

Case B^1B^2: In systems with $q_{in} \leqslant 0.4$ where the primary star has undergone a Case B^1 mass transfer there is a continued orbit shrinkage on account of conservative mass transfer from a more massive primary star to a relatively low mass secondary (Appendix A). The mass transfer related swelling of the secondary in turn soon brings it into Roche-lobe contact leading to a common envelope situation. The evolution during this stage is calculated under the assumption that total energy of the binary system is conserved during the common envelope evolution (Appendix B). The Roche-lobe overflow of the secondary following mass transfer is certainly true for close binary systems where the radius of the primary star is close to the lower limit required for Case B^1 mass transfer. However, for substantially wider systems undergoing Case B^1 mass transfer the secondary star while still burning hydrogen in its core at the time when mass ratio reversal takes place (the "reflection point") may still not fill its Roche-lobe. This is possible even though the secondary may have swollen up beyond its main sequence radius due to accretion of mass from the primary (*e.g,* Mode I of Webbink's classification). We therefore place an upper limit on the initial orbital separation of binary systems evolving in this channel from the requirement that the radius of the secondary expands by a factor of two over its thermal equilibrium radius at the 'reflection point' as it accretes matter from the primary over timescales shorter than its thermal timescale. This has been shown to be the case in mass accreting stars by Shu & Lubow (1981). The calculation of the subsequent orbit evolution and the limits on the primary masses arising from the requirement of having a secondary at 20 $M_\odot$ following the mass transfer are summarized in Appendix B. The required range of masses for the primary star in this case are $M_{1i} \approx 28$ — 36 $M_\odot$ (see Appendix BIII). Following the explosion of the primary star, a binary system with a neutron star and a post main sequence star with $M \approx 20\ M_\odot$ that is in Roche-lobe contact results. The secondary star, thus would also undergo a Case B^2 mass transfer. Mass transfer timescales for a RLO secondary in a post main-sequence stage are expected to be short and the envelope of the secondary would be lost from the system over $\approx 10^4$ years. The X-ray luminosity of these systems at this stage is expected to be substantial and close to the Eddington luminosity and should thus be easily detected. The X-ray active lifetimes of the binary systems depend on the evolutionary timescales for the secondary star in the post main sequence region and are summarized in Appendix D for systems evolving in this evolutionary channel as well as for the other evolutionary channels to be described below. Case B^1B^2 binaries are so close that the mass transfer from the secondary is expected to continue even after the loss of its hydrogen envelope and might perhaps lead to a complete merger of the two binary components. This is because the orbital separation after spiral-in and loss of hydrogen envelope is so small that the helium core of the primary star at the He main sequence stage is expected to overflow its Roche-lobe.

Case B^1 S^2: In systems with $q_i > 0.4$, *i.e.* with $M_{1i} \approx 12 - 18 M_\odot$ where the primary undergoes a Case B^1 mass transfer, the secondary star will not fill its Roche lobe at the time of the explosion of the primary but will do so at a later stage of evolution. The upper limit on the orbital period for given component masses of the binary system is thus obtained from the requirement that the secondary star should fill its Roche lobe as it evolves to the maximum possible radius for its mass (after accreting mass from the primary). The orbit evolution is conservative during mass transfer from the primary, and is described in Appendix A. The primary mass can be determined for a given q_i from the assumption of conservative mass transfer as described in Appendix A. These systems should be visible for $\approx 3 \times 10^5$ years as (high luminosity) transient X-ray sources driven by the stellar wind from the secondary (see Appendix D). They will appear like Be star X-ray binaries. The X-ray luminosity driven by wind-fed mass transfer from the secondary to the compact remnant of the primary is determined by the evolutionary stage of the secondary as well as the orbital dimensions at this stage (see Appendix C). The post RLO mass transfer from the secondary is assumed to lead to a common envelope and consequent spiral-in of the components on account of the disparate component masses at this stage. For some of the close systems evolving in this channel, this spiral-in is expected to continue after the loss of the hydrogen envelope of the secondary. For somewhat wider systems this situation and the subsequent merger of the binary components is avoided if after spiral-in following mass transfer from the secondary the helium core of the secondary underfills its Roche-lobe. To calculate the boundary of the complete spiral-in for this channel in the $q_i - P_i$ plane, we have used the He-core radius by extrapolating to the relevant mass the models computed by Habets (1985) of He main sequence stars. The helium core radius-mass relation can be obtained by fitting with the models of Habets as,

$$(R_{\rm He}/R_\odot) = 0.65 (M_{\rm He}/M_\odot)^{0.22}. \tag{7}$$

Case C^1B^2: In systems with $q_i \leqslant 0.4$ and $M_{1i} \geqslant 50 M_\odot$, where the primary undergoes a Case C^1 mass transfer, there is a runaway mass transfer immediately following the Roche lobe overflow of the primary star and the secondary star spirals in through the envelope of the primary which is lost in this process. The orbit of the system shrinks considerably so that the secondary star, when it evolves, undergoes a Case B^2 mass transfer. These systems should be high luminosity X-ray sources for $\approx 10^4$ years (see Appendix D). The secondary star receives negligible amount of mass during the evolution of the primary and thus its initial mass is assumed $\approx 20 M_\odot$. The primary mass is thus determined for a given q_i which is less than 0.4. The orbit evolution is assumed non-conservative during the spiral-in process (Appendix B). Since the primary star in this evolutionary channel is quite massive, it would lose a considerable amount of matter even while on the main sequence. To account for this, we have obtained the mass of the primary star at the Terminal Age Main-Sequence as a function of its ZAMS mass by extrapolating from our evolutionary models of masses 10, 15, 20 and 25 $M_\odot$ with Z = 0.01 computed with a mass loss rate three times that of the de Jager formula. In addition, the massive WR star which is left after the loss of the hydrogen envelope of the primary in turn is expected to lose some mass in a strong stellar wind. The amount of mass lost during this stage has been obtained by assuming a mass loss rate for the WR star as a function of its mass from Langer (1989) and assuming a WR lifetime of $\simeq 10^5$ years. As the secondary star

fills its Roche-lobe following the first supernova explosion in these binary systems, a rapid shrinking of the orbit due to the formation of a common envelope is expected to occur. As in the case of systems in the B^1 S^2 channel, the shorter orbital period systems are assumed to lead to mergers, while the wider systems would lead to two runaway neutron stars following the explosion of the secondary. Again the merger *vs* non-merger boundary is calculated by the condition that at the end of the second stage spiral-in the helium core of the secondary (WR) star does or does not fill its Roche-lobe.

Case C^1D^2: In systems with $q_i \geqslant 0.4$ *i.e.* with $M_{1i} \approx 12 - 18 M_\odot$ (see Appendix A, part II), where the primary star undergoes a Case C^1 mass transfer, the secondary star does not fill its Roche lobe at any stage of its evolution. The orbit evolution during mass transfer from the primary is assumed conservative (Appendix A) while the orbit evolution during the mass transfer from the secondary in the form of a stellar wind is calculated as in Appendix B (Subsection 3). These systems should be then visible for $\approx 3 \times 10^5$ years as low luminosity transient X-ray sources ($L_x \approx 10^{33} -$ ergs^{-1}) driven by the stellar wind from the primary (Appendices C and D).

Case D^1 D^2: In systems where the primary does not fill its Roche lobe at any stage of its evolution the secondary star with an initial mass less than the primary mass would not fill its Roche lobe at any stage of its evolution. These systems are not X-ray active for a majority of their lifetime but may show some X-ray activity powered by stellar wind if and when the secondary star evolves to the RSG stage. The terminal masses of the primary after its main sequence and WR phase have been calculated in the same away as in the C^1 B^2 channel.

We now describe the various stages in the evolution of the binary systems belonging to each of these evolutionary channels in detail in the following subsection.

3.3 *Evolution of Binary Supergiants and their Relation to MXRBs*

We identify the stages through which the binary evolves and denote them by upper case letters for the ease of later discussion. For example the various evolutionary stages with masses of the components and orbital separation are shown in Fig. 9 for the evolutionary channel B^1 B^2 where the initial masses of the components are 28.6 $M_\odot$ and 11.4$M_\odot$.

The stage at which the primary begins to transfer mass to the companion either by Roche-lobe overflow (or by strong stellar wind from a wide orbit) is denoted as *stage I.* Fig. 5 shows the positions of binary systems belonging to various evolutionary channels in the $q_i - P_i$ plane at this stage. The un-populated regions in this figure are occupied either by binary systems in which the primary undergoes a Case A^1 mass transfer, or by systems where the mass of the secondary after accreting matter from the primary is different from 20 $M_\odot$. The lower and upper boundaries of regions populated by binaries in the different evolutionary channels have been obtained from considerations of the evolutionary state of the primary at the start of mass transfer and that of the secondary following mass accretion, as discussed in the earlier subsection. The narrow hatched regions in Figs 5–8 show the orbital period and initial mass ratio ranges in the evolutionary channels C^1B^2 and B^1S^2 which are expected to evolve towards merger of the two components following the mass transfer

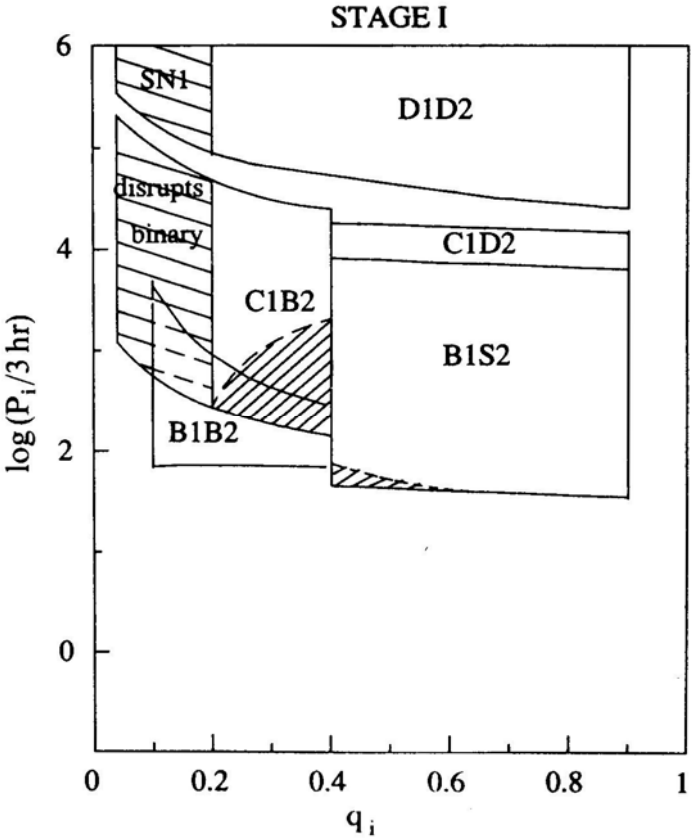

Figure 5. Populated regions in the initial orbital period P_i and q_i plane at *stage I* shown for binary systems evolving through various evolutionary channels. The widely hatched regions indicate the range in q_i where following the SN explosion of the primary the binary would be disrupted. The narrowly hatched regions are populated by binary systems which undergo complete merger following mass transfer from the secondary. In addition all the systems in the B^1B^2 channel undergo complete merger after Stage SN1. Note that both sets of hatched regions where there is overlap between C^1B^2 and B^1B^2 are relevant for systems in C^1B^2 channel only.

from the secondary. In addition all the binary systems in the evolutionary channel B^1B^2 are expected to lead to mergers. The wide hatched regions in Figs 5 and 6 shows the regions populated by systems in the C^1B^2 and D^1D^2 evolutionary channels where the first supernova explosion is expected to disrupt the binary system, if the massive primary were to leave a neutron star remnant of $1.4M_{\odot}$.

By the time primary has transferred (or lost) the entire envelope and is left with its helium core $M_{He}^{(1)}$, the binary is in *stage WR1*. The system may be observable as a WR + O system at this stage since the exposed helium core of the primary may appear as a WR star. Fig. 6 shows the regions in the initial mass ratio and the orbital period (*at stage WR1*) plane populated by binary systems. The binaries starting out from the various regions in Fig. 5 migrate to the corresponding regions in Fig. 6 following the mass transfer from the primary. Binary systems in the B^1B^2 and C^1B^2 evolutionary channels evolve towards considerably shorter orbital periods due to

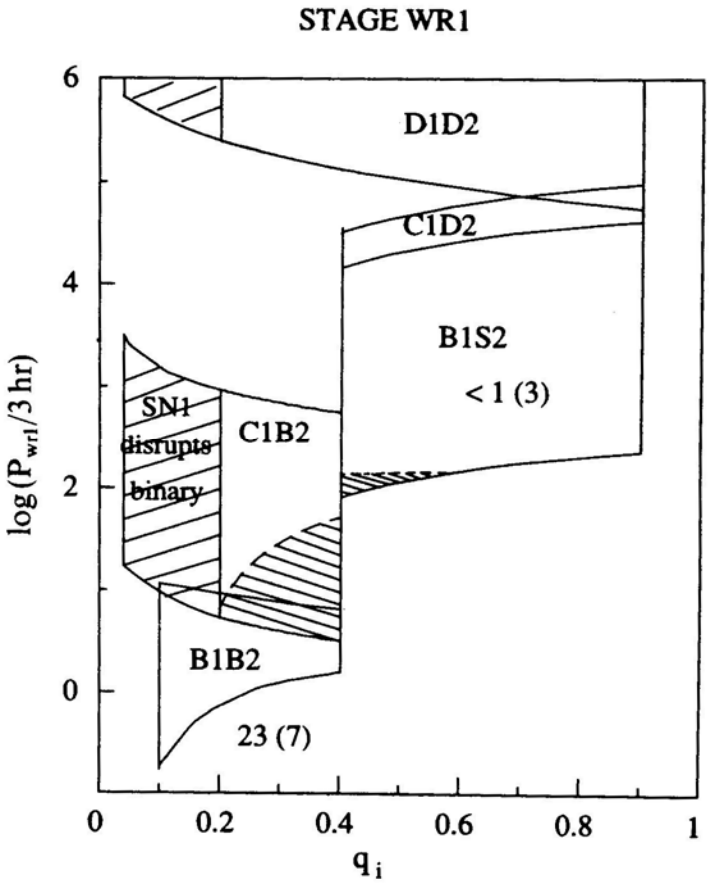

Figure 6. Populated regions for binary systems at *stage WR1* in the q_i–P_{Wr1} plane. The hatched regions have the same significance as in Fig. 3. The numbers by the side of the regions shown give the predicted number of systems and the numbers inside brackets give the actual number of systems interpreted from observations of the LMC that have these orbital characteristics. The numbers quoted below B^1B^2 pertain to a sum of the B^1B^2 and the C^1B^2 channels.

spiral-in in a common envelope following mass transfer while the systems in the other evolutionary channels evolve to slightly wider orbits from *stage I* to *stage WR1*. The numbers placed near the shorter and the intermediate orbital period systems in Fig. 6 show the expected number of such WR + OB systems obtained from a consideration of the orbital period distribution of MXRBs in the LMC as well as the timescales of evolution of the binary systems in the relevant evolutionary stages. The analysis leading to this distribution is explained in Subsection 3.4. The numbers in brackets in Fig. 6 show the number of actually observed WR + O systems in the LMC for the corresponding orbital period ranges.

When the helium star explodes in a supernova explosion the binary will not be disrupted if the mass lost is less than half the total mass of the system before explosion. The system after explosion would, however, be somewhat wider than the pre-supernova binary due to sudden mass loss; this post explosion stage is denoted *stage SN* 1. It is at this stage that the secondary star (which does not yet fill the

Roche lobe) may appear and linger in the post main sequence colour temperature region $4.48 \leqslant \log T_{\rm eff} \leqslant 4.3$ provided that it has accreted enough nuclear processed helium enriched material from the erstwhile primary. For all our calculations in this paper we take the mass of the secondary at this stage to be $20M_{\odot}$ so that the star would appear in the magnitude interval $-8 \geqslant M_{\rm v} \geqslant -7$ in the H-R diagram. In the next stage when the secondary evolves to fill its Roche lobe (for relatively close binaries) and transfers matter onto the neutron star, the system should appear as a higher luminosity X-ray source. It would be a weaker X-ray source if the neutron star is powered by wind from the secondary star. This stage now is called *stage X*. In some of the shorter orbital period binary systems (*i.e.* systems evolving through the evolutionary channels $B^1\ B^2$, and $B^1\ S^2$ and $C^1\ B^2$) the binary would be significantly X-ray active even during *stage SN1*. Some relatively wide B^1S^2 and C^1B^2 systems may stop terminal orbital decay after the hydrogen envelopes of the secondary are lost through common envelope if their helium core does not fill the corresponding Roche-lobes at the time of complete envelope ejection. Fig. 7 shows the corresponding orbital period ranges of the binary systems at this stage. The numbers in brackets show the observed number of MXRBs in these orbital ranges (discussed in Subsection 3.4).

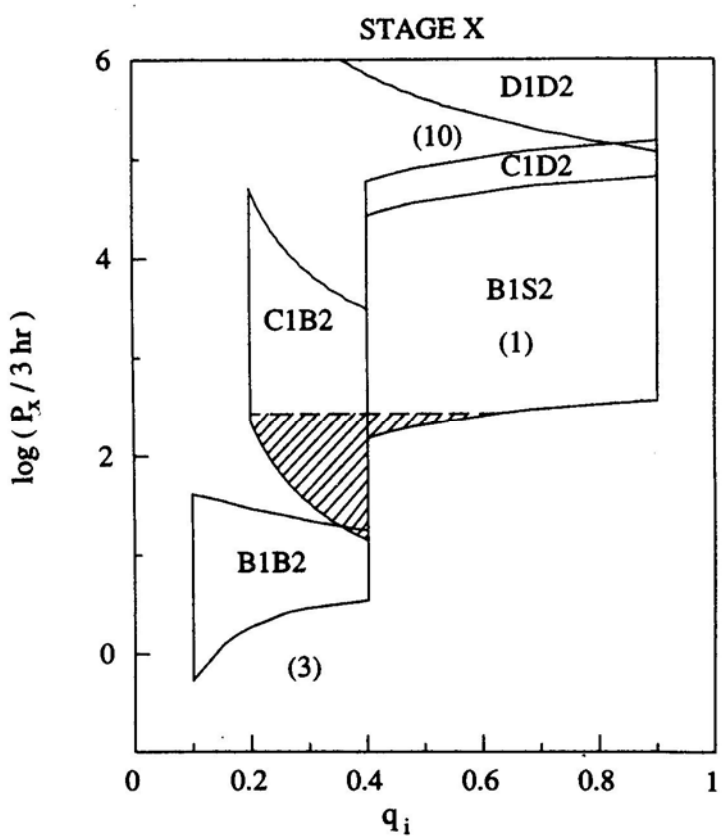

Figure 7. Shown are the orbital period ranges at *stage* X for systems in different evolutionary channels for given q_i. The mass of the compact star is $1.4M_{\odot}$. The narrow hatched regions have the same significance as in Figs 5 and 6. The numbers shown give the observed number of X-ray sources (possibly) associated with these orbital period ranges.

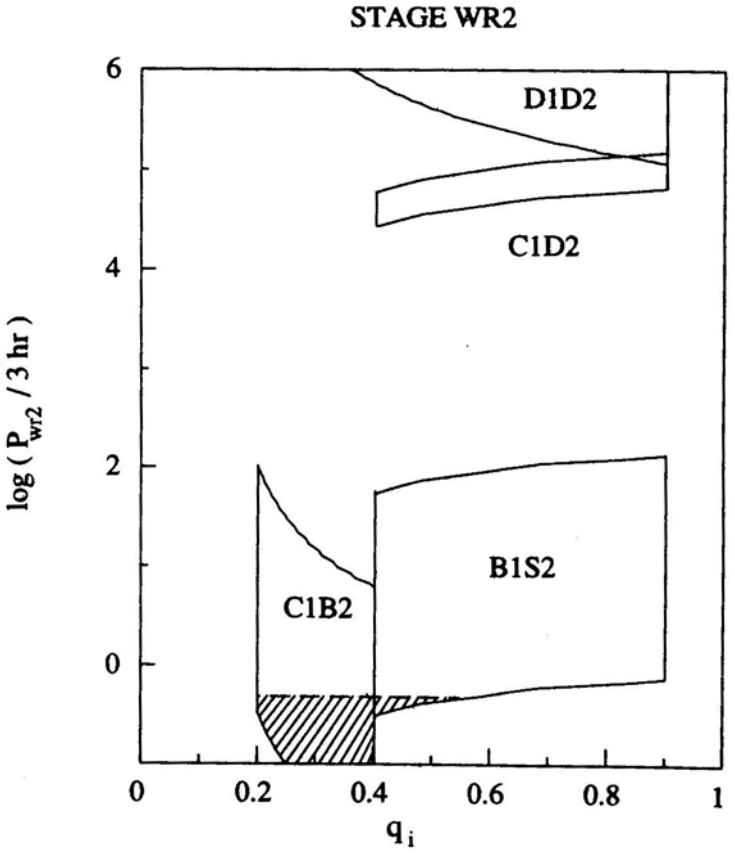

Figure 8. Same as in Fig. 7 for binary systems in *stage WR2*. The B^1B^2 systems at this stage have become so compact that their orbital periods are less than the lowest shown ordinate.

Finally when the extended star is left behind with its helium rich core of mass $M_{He}^{(2)}$ denuded of the envelope (lost from the system) we have a second stage WR star: a $WR^{(2)}$ orbiting the neutron star. We call this *stage WR2*. Fig. 8 shows the orbital period ranges for the binary systems at this stage. By this stage a distinct gap in the orbital distribution becomes apparent. This arises due to the fact that systems in the C^1D^2 and D^1 D^2 evolutionary channels evolve towards longer orbital periods during mass transfer from the primary as well as the secondary, while the binary systems in the other evolutionary channels go through a common envelope evolution at least once during their lifetimes and hence evolve towards considerably shorter orbital periods. In some channels of evolution (in rather close binaries) this and the subsequent stage may be absent altogether as a spiral-in all the way towards the centre of the extended star's core by the neutron star may lead to a complete merger (see Thorne & Zytkow 1977) in such cases. Nevertheless, if *stage WR2* exists as a stable intermediate stage then subsequently two (runaway) neutron stars will result when the helium core explodes in a second supernova. Appendices A and B describe in detail the evolution of the binary systems in different evolutionary channels through the various stages of evolution discussed above.

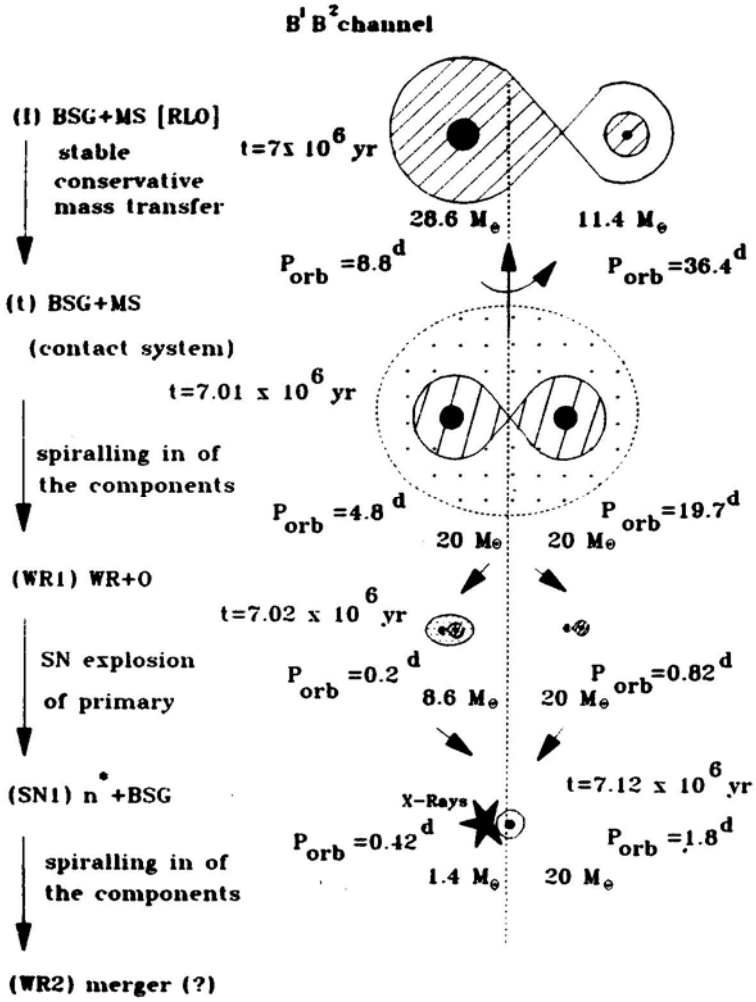

Figure 9. Orbit evolution from *stage I* to *stage* WR2 for a system evolving in the B^1 B^2 channel with initial masses of the binary components 28.6 $M_\odot$ and 11.4$M_\odot$. The approximate age of the system at each evolutionary stage and the orbital period ranges corresponding to the lower and upper boundaries (see Figs 5-8) in this evolutionary channel (for q_i = 0.4 systems) are indicated on two sides of the figure. (Note in stage WR1 even in the wider system at P_{orb} = 0.82d the secondary on its main sequence does not quite fit inside its Roche-lobe and therefore could lead to a spiral-in from this stage until the stage when the helium star explodes).

Figs 9–12 describe the binary evolution for some of the evolutionary channels mentioned in the previous subsection. These figures show the orbital dimensions and the Roche-lobe configuration of these binary systems at the different evolutionary stages. Fig. 9 for example, shows the orbital periods at different evolutionary stages for binary systems with q_t = 0.4 in the B_1B_2 evolutionary channel. The orbital periods shown on the left in this figure correspond to those for binary systems starting out at the lower boundary of the $q_i - P_i$ region occupied by B^1B^2 systems in Fig. 5 while those shown on the right correspond to the systems on the upper boundary of this

region. This convention is followed in all of the Figs 9-12. Between the evolutionary stages I and WR1 discussed earlier, an additional stage is shown in this figure which has been labeled 't'. Prior to this stage the mass transfer is conservative and results in a shrinkage of the orbit and an increase in the secondary star's mass till the masses become equal. If conservative mass transfer proceeds beyond this stage, an expansion of the orbit would occur since the secondary is the more massive star beyond this point (Appendix A). However, this is avoided in the case of these systems since the secondary star is in Roche-lobe contact by this stage, resulting in a common envelope. The subsequent spiral-in and non-conservative evolution is likely to lead to a merged system in a short time for the closer systems shown on the left, whereas the merger is delayed till after the secondary evolves away from the main sequence for the wider systems shown on the right.

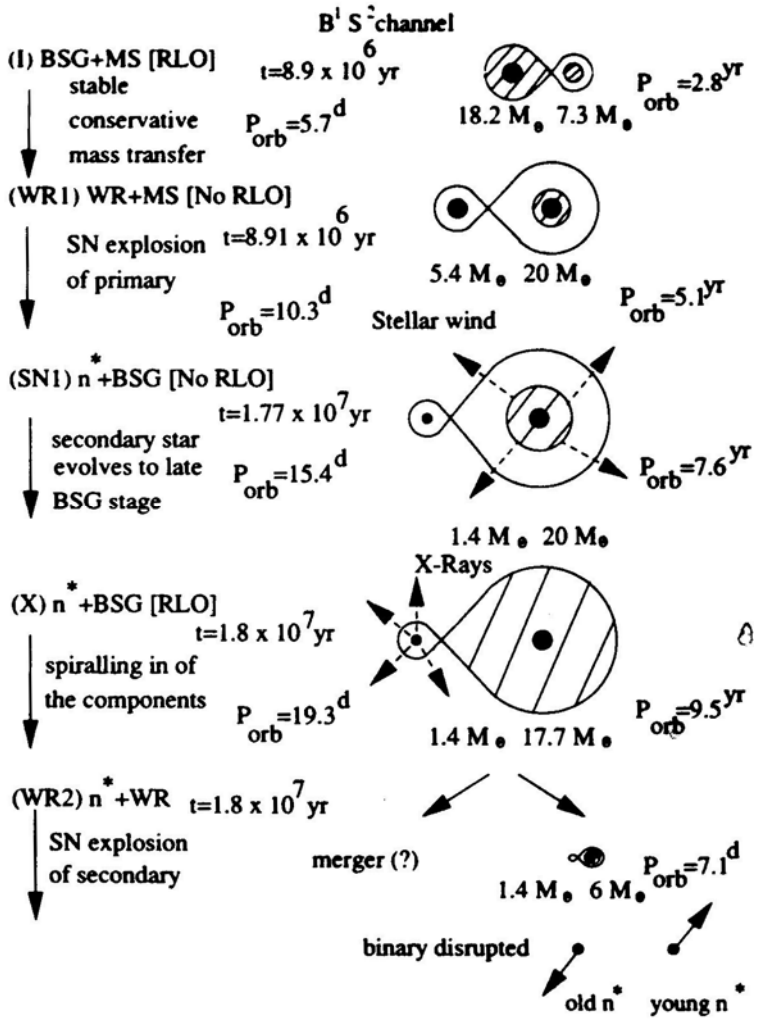

Figure 10. Orbit evolution for *stages I to WR2* for the B^1S^2 channel with initial masses of the binary components 18.2 $M_\odot$ and 7.3 $M_\odot$. Note that in the last stage (WR2) the non-merger system (at P_{orb} = 7.1^d) is not drawn on the same scale as the rest of the diagram. This system should be relatively far more compact than shown.

Figs 10 and 11 show the evolution and the orbital ranges for binary systems with q_i=0.4 in the B^1S^2 and C^1B^2 evolutionary channels respectively. The evolution between stage I and WR1 is completely conservative in Fig. 10 (B^1S^2 channel) while it is completely non-conservative leading to a spiral-in of the components in Fig.11 (C^1B^2 channel). An additional stage 1_0 is shown in Fig. 11 corresponding to the main sequence stage of the $50M_\odot$ primary star when it underfills its Roche-lobe. Following the explosion of the primary, the secondary star underfills its Roche-lobe while on the main sequence but comes into Roche-lobe contact at later evolutionary stages. Some amount of mass is lost while on the main sequence by the 20 $M_\odot$ secondary star, which has been obtained from our evolutionary models. The shorter orbital period systems lead to mergers following the RLO of the secondary while the wider systems shown on the right evolve into highly compact binary systems contaning

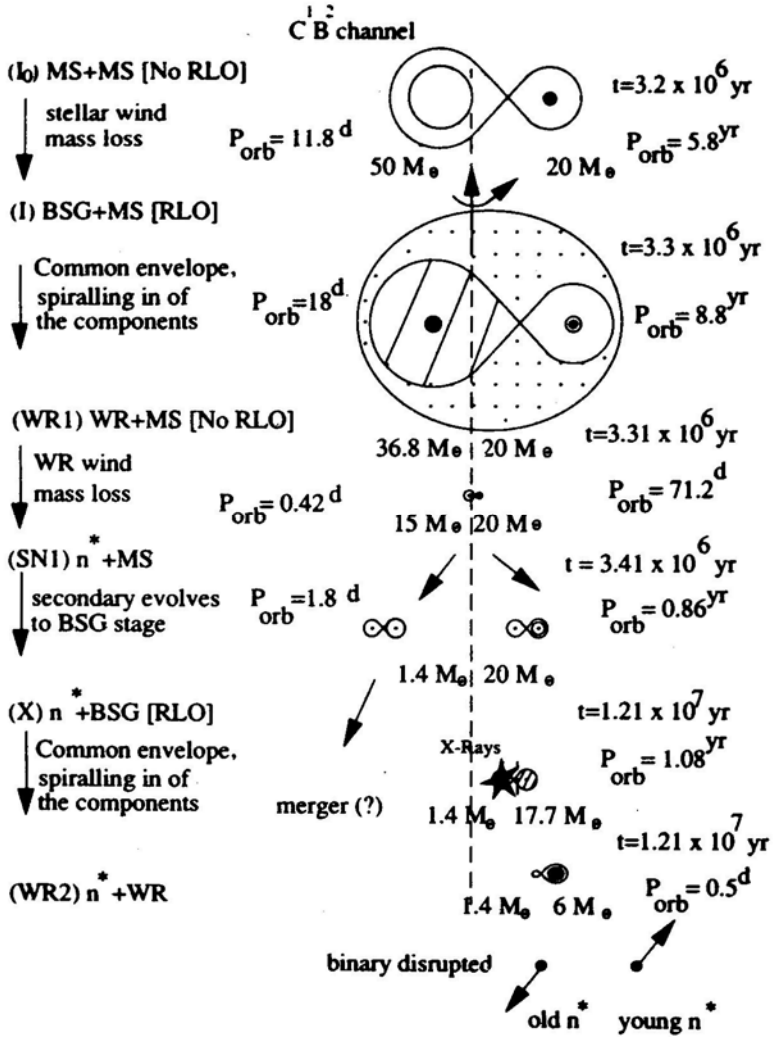

Figure 11. Orbit evolution for the C^1 B^2 channel with the component masses 50 $M_\odot$ and 20 $M_\odot$. At stage 1, the mass of the primary is reduced to 36.8 $M_\odot$ due to stellar wind. Again the system shown in stage WR2 is not drawn to the same relative scale.

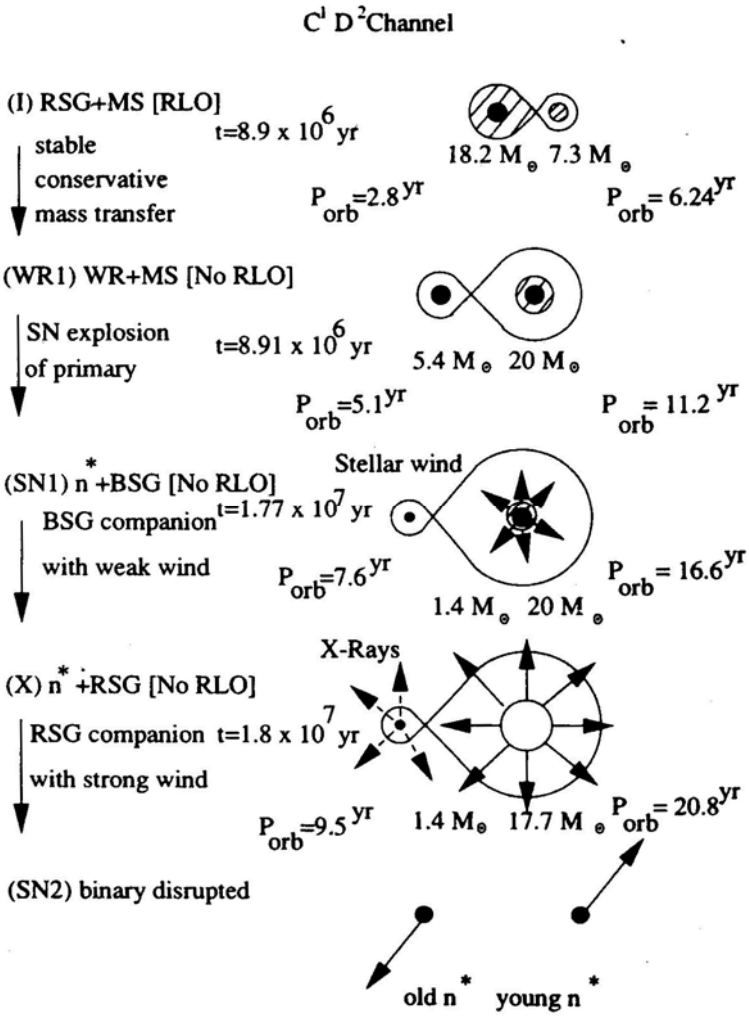

Figure 12. Orbit evolution for the C^1D^2 channel with the component masses 18.2 $M_\odot$ and 7.3$M_\odot$.

a neutron star and the helium core of the secondary. Ultimately these binaries disrupt upon the second supernova explosion, giving two high velocity runaway pulsars. Fig. 12 shows the evolution of q_i=0.4 systems in the C^1D^2 evolutionary channel. There is no qualitative difference in the evolution of binary systems at the two boundaries of this evolutionary channel. The secondary star underfills its Roche-lobe throughout its lifetime and the binary ultimately is disrupted giving rise to low velocity runaway pulsars as will be discussed in Section 4.

In Section 3.5 we compare the orbital periods of the observed MXRBs and WR + O systems in the LMC and compare with the orbital period ranges obtained for binary systems in each of the evolutionary channels when they pass through Stages WR1, SN1 and X. We summarize the available observational data on the massive X-ray Binaries in the LMC through the Einstein survey and also the characteristics of the WR + O binary systems in the LMC observed via optical searches.

3.4 *Observational Results on Binary Systems in the LMC*

3.4.1 *Observed massive X-ray binaries*

Soft X-ray survey (Long, Helfand & Grabelsky 1981; Cowley *et al.* 1984) of the LMC and a comprehensive re-analysis of the Einstein X-ray data (Wang *et al.* 1990) confirm the presence of five massive (Population I) X-ray binaries in the LMC. Two of the sources (CAL 8 and CAL 37) in the earlier survey do not appear in the re-analysis of Wang *et al.* due to "higher criteria for source acceptance and more strictly selected data base". Long Helfand & Grabelsky conclude that out of the 49 or so unidentified sources, there are some 10 sources which are LMC members. The data of Wang *et al.* indicate the presence of 35 unidentified point sources. From an analysis of the expected integral flux distribution for these sources which lies well within the expected distribution for background sources they conclude that most of the unidentified X-ray sources in their catalogue are background objects. In the present analysis we have assumed the number of less luminous point sources associated with the LMC to be 10. Among the low luminosity point objects, these are relatively strong sources.

The orbital parameters and the X-ray luminosities for the five confirmed MXRBs in the LMC are shown in Table 1. The last entry in this table indicates the possible evolutionary classification through which these systems could have evolved as explained in Section 3.3. Of the four confirmed massive X-ray binary sources two have O or OB companions (LMC X-4: O7III-V; LMC X-l: OB). The former has an orbital period 1.4^d and a companion mass between 11.5–18.5 $M_\odot$ (Nagase 1989) whereas LMC X-l has an orbital period in the range 3.9 to 4.2^d with a 14 $M_\odot$ companion. In addition, X 0538–668 is a high luminosity transient source ($\approx 1.2 \times 10^{39} s^{-1}$) with a wide $P_{orb} = 16.7^d$ and a companion mass in the range of 7–11$M_\odot$, and is possibly similar to a Be-star binary in a wide, elliptical orbit. CAL 9 which is most likely to be associated with the LMC appears in the region of OB stars with broad variable He II line emission and has a periodicity of 6.9 days. The two systems LMC X-l and LMC X-4 have orbital periods consistent with evolutionary channel B^1B^2 while the transient source is consistent with the B^1S^2 channel. The ten less luminous point X-rays sources (between 10^{35} to $l0^{36}$ $ergs^{-1}$) (Long., Helfand & Grabelsky (1981) referred to above

Table 1. Massive X-ray binaries in the LMC.

Source	P_{orb} (days)	Companion spectral type	M_{opt} ($M_\odot$)	L_X ergs/sec	Reference	Evolutionary channel
LMC X–1	3.9–4.2	O7	14	2.0×10^{38}	1	$B^1B^2, C^1B^2(m)$[a]
LMC X–3	1.7	B3V	4–8	4.0×10^{38}	1	$B^1B^2, C^1B^2(m)$
LMC X–4	1.4	O7III–V	11.5–18.5	4.0×10^{38}	3	$B^1B^2, C^1B^2(m)$
A0538–66	16.7	B2IVe	13–15	1.2×10^{39}	1,2	B^1S^2
CAL–9	6.9	OB		4.0×10^{35}	1,2	$B^1B^2, C^1B^2(m)$

1) Ilovaisky (1983) and references therein.
2) Tutukov & Cherepaschuk (1985) and references therein.
3) Nagase (1989).
[a] C^1B^2 (m) refers to systems in C^1B^2 channel which undergo eventual mergers.

are consistent with wind-fed wide binaries containing compact objects. One of the five confirmed massive X-ray binaries in the LMC X-3 has a relatively low mass companion (5–8 $M_\odot$ and of a spectral type B III-IV). This system has been excluded from the data set considered here as it is unlikely that the optical companion would have traversed the HR diagram in the region $-8 \leqslant M_v \leqslant -7$. The orbital elements of the other confirmed MXRBs in LMC have been used in the present analysis, to determine the parameters of the evolutionary scenarios as explained in Section 3.3.

3.4.2 *Observed WR + O systems*

Just prior to the first SN explosion the exposed core of the primary will appear like a WR star with an O or an early B-type companion. These are close cousins of the binary systems postulated to have undergone surface helium enrichment and can therefore have a related distribution of orbital periods. The observed data on the WR + O binaries (Moffat *et al.* 1989; Moffat, Niemela & Marraco 1990) are summarized in Table 2.

The binary search among WR stars in the LMC has so far been sensitive to shorter orbital periods. The binary frequency among WNL stars (which constitute 25 per cent of the total WR population in LMC) is likely to be representative of the entire WR population as all massive WR stars probably pass through the WNL stage. Of the 25 WNL stars, 75 per cent are WN6,7 types amongst which the binary frequency is $\sim$ 56 per cent. The total number of WR stars in the LMC being approximately 100 (Breysacher 1981, 1986), the expected number of binaries based on the binary frequency among WNL stars is approximately 42.

Table 2 shows 10 systems of which one (R140a of spectral type WC5 + WN6) strictly speaking, is not a WR + O binary system although it is quite probably a multiple system with companions of other spectral types as in HD36402. All the other systems shown have companions with spectral type earlier than Bl. It is thus likely that the main sequence mass of these stars was larger than 15 $M_\odot$ and they could hence have evolved through the H-R diagram in the region $-8 \leqslant M_v \leqslant -7$.

Table 2. Observed WR + O systems in the LMC.

System	P_{orb} (days)	Companion spectral type	Reference	Evolutionary channel
HD 36521	1.91674	WC4 + O6V–III	1	$B^1B^2, C^1B^2(m)$[a]
HD 36402	3.03269	WC4(+ O?) + O8I	3	$B^1B^2, C^1B^2(m)$
HD 36063	1.9075		2	$B^1B^2, C^1B^2(m)$
Sk–69°104	14.926	WC6 + O5–6V–III	3	B^1S^2
R 130	4.3092 ± .004	WN6 + B1Ia	2	$B^1B^2, C^1B^2(m)$
FD 21	12.29	WC5 + O6	1	B^1S^2
R 136	4.377 ± .003	WN6 + O3–4	2	$B^1B^2, C^1B^2(m)$
R 140a	2.7596 ± .001	WC5 + WN6	1	$B^1B^2, C^1B^2(m)$
E 269828	3.0032	WN7	1	$B^1B^2, C^1B^2(m)$
R 145	25.17	WN7	1	B^1S^2

1 Moffat *et al.* 1986.
2 Moffat 1989.
3 Moffat, Niemela & Marraco 1990.
[a] $C^1B^2(m)$ refers to systems in C^1B^2 channel which undergo eventual mergers.

3.5 *Comparison of Observational Data with Predicted Distribution of Evolved Massive Binaries*

3.5.1 *MXRBs in LMC*

In Section 2 we argued on the basis of the H-R diagram that currently there are some 90 helium enriched stars (which are secondaries in binary systems) in the post main sequence BSG region of the relevant magnitude interval. These binaries could be of varying orbital separations and could have arisen out of the different channels of evolution referred to above. A priori, the distribution of the total number of post main sequence binaries (in bins i and j) in the different evolutionary channels is unknown. But from the observed data (see Section 3.4.1) on the orbital period distribution of MXRBs in the LMC and their X-ray luminosities, the different sources can be classified in generic evolutionary sequences and limits can be placed on the approximate number of the very wide binary systems. The expected fraction of binary systems evolving through each of the channels determined through the initial orbit separation and mass ratio is then calculated from a comparison of the observed number of X-ray sources in these channels.

Figs 5–12 showing the evolution of binary systems in the different evolutionary channels indicate that the systems of B^1B^2, B^1S^2 and C^1B^2 evolutionary channels go through a high X-ray luminosity phase when the secondary star evolves through the BSG stage. Since the total number of such luminous massive X-ray binaries in the LMC is small, we expect the contribution to the BSG region from stars which belong to these evolutionary channels to be also small. From the orbital period calculations outlined in Appendices A and B we obtain the orbital ranges during the X-ray active stage for systems in all the evolutionary channels. Thus, systems in B^1B^2 and C^1B^2 channels could have orbital periods ranging from $\leqslant 1$ day to few tens of days depending on whether the primary star undergoes an early Case B (or Case C) or a late Case B type of mass transfer. Similarly early Case B mass transfer systems in B^1S^2 channel could have orbital periods as low as $\approx$ 15 days while the maximum orbital period achievable with, late Case B mass transfer in this evolutionary channel is $\approx$ 10 years during *Stage* X. Orbital periods of $\approx$ 10–100 years are obtained during *Stage* X for systems evolving through C^1D^2 channel while for D^1D^2 systems the orbital periods during this stage are > 100 years. Thus the strong X-ray sources like LMC-X1 etc having orbital periods close to 1 day could have evolved through either B^1B^2 or the C^1C^2 channels, while the wide Be X-ray binary with orbital period of 16.5 days could have been a late Case B^1B^2 or an early Case B^1S^2 type of a system. The total number of systems in the close orbital period ranges (*i.e.*, of orbital periods less than a few tens of days) cannot, however, be greater than the total number of observed luminous MXRBs in the LMC.

Let us define by $f_{B^1B^2}$, $f_{B^1S^2}$, $f_{C^1B^2}$, $f_{C^1B^2}$, and $f_{D^1D^2}$, the fraction of binary systems which have evolved through the corresponding channel and let N_{tot} to their total number in the entire post main sequence region ($4.48 \leqslant \log T_{eff} \leqslant 3.7$). If t_x is the relevant X-ray lifetime for a given channel, then out of a total number of systems $N_{tot}\ f_c$ only a fraction(t_x / t_{tot}) will be visible in the relevant part of the q-P diagram at any given time. For each of the evolutionary channels the number $N_{tot}\ f_c(t_x/t_{tot})$ of binary systems with their secondary star in the BSG region cannot be greater than the observed X-ray sources which have orbital periods and luminosities in the range

predicted for these systems. For example, the observed number of high luminosity steady X-ray sources in the LMC (LMC X-l, LMC X-4, CAL 9; ignoring for the moment LMC X-3 which is most likely an accreting black hole binary) implies that:

$$N_{\rm tot}(f_{\rm B^1B^2}+f_{\rm C^1B^2})\left(\frac{t_{\rm x}}{t_{\rm tot}}\right)_{\rm B^1B^2,C^1B^2}\leqslant 3. \tag{8}$$

The timescale of this mass transfer is determined by the rate of mass loss during RLO (Savonije 1983) and is approximately 1.2×10^4 years. The X-ray active life time in the channel $B^1\ S^2$, $t_{\rm x^-tr} \simeq 3.3 \times 10^5$ yr from evolutionary calculations (see Appendix D). The number of B^1B^2 systems (at least those where the primary undergoes an early Case B mass transfer) appearing in the BSG region is again limited by the observed number of luminous X-ray sources at intermediate orbital periods. Hence,

$$N_{\rm tot}f_{\rm B^1S^2}\left(\frac{t_{\rm t-tr}}{t_{\rm tot}}\right)_{\rm B^1B^2}\leqslant 1. \tag{9}$$

In addition, taking the upper limit of the number of weak X-ray sources (expected to be powered by wind from secondaries) to be 10 (see Wang *et al.* 1990, Long *et al.* 1983) we obtain:

$$N_{\rm tot}f_{\rm C^1D^2}\left(\frac{t_{\rm x-tr}}{t_{\rm tot}}\right)_{\rm C^1D^2}\approx 10. \tag{10}$$

Since the orbital period distribution for B^1S^2 and C^1D^2 is continuous (as can be seen from Figs 5 and 6) we have taken B^1S^2 systems as those which have high X-ray luminosity ($L_{\rm x} \leqslant 10^{35}$ ergss^{-1}) through wind type mass transfer from the secondary star while the C^1D^2 systems have low X-ray luminosity ($L_{\rm x} \approx 10^{33} - 10^{35}$ergss^{-1}) when the secondary star is in the BSG stage. Finally since we have

$$(f_{\rm C^1B^2}+f_{\rm B^1B^2})+f_{\rm B^1S^2}+f_{\rm C^1D^2}+f_{\rm D^1D^2}=1, \tag{11}$$

the calculated values of these fractions from the above four equations turn out to be:

$$f_{\rm B^2}=f_{\rm B^1B^2}+f_{\rm C^1B^2}=1.5\times10^{-2};\ f_{\rm B^1S^2}=5\times10^{-3};\ f_{\rm C^1D^2}=0.14 \text{ and } f_{\rm D^1D^2}=0.84. \tag{12}$$

The ratios of timescales for the different channels are calculated in Appendix D. The normalization to 90 binary systems expected to be present in the post main sequence region as a consequence of the hypothesis of Tuchman and Wheeler requires that a large number of binary systems be present in the wide binary channel. These would not show appreciable X-ray activity for most of their lifetimes.

3.5.2 *WR + 0 systems in the LMC*

An observational signature of the presence of the large number of binaries with the secondary star in the post main sequence region would be the existence of WR + O systems which are precursors to such post main sequence binary systems. The expected number of such systems can be obtained from the relevant lifetimes in the main-sequence and the post main sequence stages and the number of BSG binaries in the post main sequence region. Observation of WR + O systems and X-ray binaries in the LMC can be used to constrain the possible evolutionary scenarios for the post main sequence binary systems. The expected distribution of these systems

in orbital period and the mass ratio is shown in Fig. 5 by the numbers in brackets shown by the side of the populated regions. We use the WolfRayet lifetime ($\approx 10^5$ years) of the primary star from the calculation of Maeder (1981) in calculating these expected values. The orbital periods and spectral types of the WR + O systems observed so far in the LMC are given in Table 2.

The predicted number of short period WR + O binaries evolving through the channels B^1B^2 and C^1B^2 is $\approx$ 23. This is obtained by the method mentioned above. The number of observed WR + O binaries so far is 10 (the binary search among WR stars in the LMC is not complete). As argued in Section 3.2 the expected WR + O binaries is $\approx$ 42. Thus the predicted number (23) of short orbital period WR + O binaries in which the secondary star later evolves through the magnitude and surface temperature bin being considered here, gives the maximum contribution to the total expected number of WR + O binaries in the LMC. However according to Abbot & Conti (1987), a helium star becomes a WR star only if its mass is larger than 8–10 $M_\odot$. The existence of such a lower limit implies that WR + OB binaries are only a subsection of the population of helium star + OB binaries. If the M_{He} mass limit is as high as this, then only some of the He star + O star binaries (*e.g.* in B^1B^2 or C^1B^2 channels) may ultimately show up as WR + OB binaries. Therefore it may not be surprising that the *observed* number of WR + OB binaries in the LMC is *lower* than the numbers predicted here for He star + OB binaries.

The contribution to the expected sample of WR + O binaries from those systems where the secondary star does not evolve through the magnitude and surface temperature band being considered here can be argued to be small. This contribution would come from (1) those systems where the secondary star has a mass larger than 25 $M_\odot$ The number of high mass systems would be small due to the steep IMF (α_1 = 1.5 according to Humphreys & Blaha 1989) and (2) those systems where the secondary star has a mass less than 15$M_\odot$. The spectral type of the companion star in the latter systems would be later than Bl in the post main sequence region as can be seen from the evolutionary models of Maeder (1990). These systems can thus be eliminated from the observed sample by restricting to those systems which have optical companions of spectral type earlier than Bl. In fact the observed sample contains no system with an optical companion of spectral type later than Bl.

3.6 *Runaway OB Stars and Possible Neutron Star Companions in Evolved Binaries*

In the Milky Way galaxy the fraction of high velocity objects among early type stars is substantial (~ 20–30 per cent among O-stars; ~ 2 per cent among early B-stars; Stone 1979). These runaway stars were suggested to originate in binaries where a supernova explosion occurred giving the remnant system (or the companion) a systemic high velocity (Zwicky 1957; Blaauw 1961). By the same argument massive X-ray binaries could also acquire runaway characteristics under some circumstances (Sutantyo 1982; van den Heuvel 1985). Van den Heuvel (1985) has argued that the MXRBs as a group belong to the runaway OB stars rather than to the group of OB stars with low peculiar velocities by comparing the $|z|$ distribution of galactic MXRBs and runaway stars as well as due to the general lack of association of the MXRBs within the boundaries of known OB associations (see also van Oijen 1989).

Furthermore, on the basis of evolutionary considerations it is expected that most of the Galactic post supernova binary systems have low amplitude of radial velocity variation of the O-star ($\leqslant$13km/s) and hence the binary nature of these would be undetectable even in most complete surveys of radial-velocity variations (van den Heuvel 1985). This is because of the considerable line-widths and large, erratic velocity variations observed in many O-type stars which mask the low-amplitude radial velocity variation due to binary nature. For example, only 2 out of 14 post-SN O-type binaries in the sample taken by van den Heuvel (1985) would have expected radial velocity variation in excess of 20km/s. The standard MXRBs (which are a highly selected sample among OB-star binaries with neutron star companions, in terms of short orbital periods that favour high X-ray luminosity and radial velocity variation) thus turn out to be the tip of an iceberg of binaries, making up no more than ~ 14 per cent of the total.

We have calculated both radial velocity amplitude as well as centre of mass velocity after the first SN explosion immediately after stage SN1. The latter is given by (Stone 1982):

$$v_{\mathrm{CM}} = \left(\frac{2\pi G}{P_0}\right)^{1/3} \frac{M_{2\mathrm{f}}}{(M_1^{\mathrm{He}} + M_{2\mathrm{f}})^{2/3}} \left(\frac{M_1^{\mathrm{He}} - M_{\mathrm{n}^*}}{M_{2\mathrm{f}} + M_{\mathrm{n}^*}}\right). \tag{13}$$

From these calculations it emerges that $\approx$ 2 per cent of the binary systems would have runaway velocities in the range 50-700 km/s, $\approx$ 0.5 per cent of systems have velocities in the range 10–40 km/s while a vast majority of systems receive smaller than 10 km/s velocity from the first explosion in the binary system. Thus only the systems evolving through the B^1B^2, C^1B^2 and some of those from B^1S^2 will have considerable peculiar space velocities and be classified as "runaway" stars. Even in the Galactic case, however, runaway OB stars are far from the majority. As in the case of our Galaxy where it is difficult to detect spectroscopically most of the O-star binaries with neutron star companions (since only the short P_{orb} standard MXRBs would be normally detectable because of favourable selection effects) this is more so in the case of the LMC as the predicted number of short P_{orb} systems are even smaller. Some of the wide binary systems which form the majority may be like the ζ-Aurigae type binaries which will produce smaller runaway velocities (of their early type components) when the more massive (red giant) primaries in them explode in an SN.

We have discussed in the current Section 3 the implications of the presence, in the BSG region of the HR-diagram of the LMC, of a large number of stars which are the secondaries in binary systems. We have so far confined ourselves to the stages in the evolution of the binary systems prior to the SN-explosion of the secondary star. Following this second explosion the binary in most cases would be disrupted. This is certainly true for massive binary systems with secondary mass in the range 15–25 $M_\odot$. Two runaway neutron stars appear following the disruption of the binary system. The first born neutron star among these would have gone through a prior mass accretion and the consequent spin evolution phase before the disruption of the binary. We discuss in the following section, the expected distribution of the spin period, pulsed radio luminosity and the space velocities of pulsars which could arise from the binary secnarios presented in this section.

4. Statistics of pulsars arising from binary systems

Comparison of the results of pulsar satistics in the LMC obtained from given evolutionary models with a complete sample of detectable pulsars would offer a better testing ground for ideas about pulsar evolution and their origin, *e.g.* their evolution from binary systems. This is because a flux-limited sample of pulsars -from the LMC would not suffer from the distance-related selection effects which a Galactic pulsar sample is plagued with. However, the total number of pulsars which is detected at a given flux level is smaller compared to the Galaxy. There are essentially two analytical approaches of treating pulsar spin statistics. Phinney & Blandford (1981) used the pulsar continuity equation,

$$\frac{\partial f(P,\dot{P})}{\partial t}+\frac{\partial}{\partial P}(f(p,\dot{P})\dot{P})+\frac{\partial}{\partial \dot{P}}(f'P,\dot{P})\ddot{P})=S(P,\dot{P}) \tag{14}$$

where $S(P,\dot{P})$ is the source function of the *observable* pulsars, i.e.. the difference between the number becoming newly observable and the number becoming un-observable per unit time in a given bin of P and $\dot{P}$. $f(P, \dot{P})$ is the observed distribution function of pulsars and is related to the observed number of pulsars of given P and $\dot{P}$ at a particular time. One can also start with an *a priori* initial birth rate in terms of number density in spin period P_o and the initial magnetic field B_o for a sample of pulsars. Using a model of pulsar spin and magnetic field evolution it is possible to obtain the number distribution of pulsars in terms of the desired pulsar property (*i.e.* spin period, characteristic age etc.). This approach has been used by several authors notably Narayan & Ostriker (1990), Chevalier & Emmering (1986, 1989), Sang & Chanmugam (1990). These two approaches are in fact equivalent. In Section 4.1 we calculate the pulsar spin period distribution expected in LMC when the single pulsar population arises from two classes of pulsars, *viz* those which have been *processed* in binary systems due to accretion (considered in the earlier sections) and those which are remnants of single or the younger remnants of the disrupting binary. This approach has also been used to determine the expected pulsar radio luminosity distribution. We summarize the observational situation regarding LMC pulsars in Section 4.3 and in Section 4.4 we discuss the expected distribution of pulsar space velocities resulting from the disrupting binaries.

Given the intrinsic source function $D(P_0, B_0)$ in the initial spin period P_0 and the initial magnetic field B_0, we have

$$S \propto D(P_0,B_0)dP_0dB_0d\tau \tag{15}$$

as the probability that a pulsar was born with a period in the range P_0 to $P_0+ dP_0$, an initial magnetic field in the range B_0 to $B_0 + dB_0$, and that it has an age in the range τ to $\tau + d\tau$ (Chevalier & Emmering 1986). We assume that pulsars slow down due to magnetic dipole radiation and that the magnetic field of the neutron star decays exponentially with a time constant τ_B (see however a discussion at the end of Section 4.2 for situations with no field decay). The pulsar spin period at any time τ is then given by,

$$P(\tau)=[P_0^2+CB_0^2\tau_B(1-\exp(-2\tau/\tau_B))]^{1/2}. \tag{16}$$

Here $P(\tau)$ $\dot{P}(\tau)$ $CB(\tau)^2$ = CB_o^2 $\exp(2-2\tau/\tau_B)$ and $C = 9.84 \times 10^{-40}$ assuming the moment of inertia and radius of the neutron star to be 10^{45} g cm^2 and 10^6 cm

respectively. Integrating the probability distribution of Equation (15) one obtains,

$$N(<P) = \int_0^{\tau_B} \int_{B_{0\min}}^{B_{0\max}} \int_{P_{0\min}}^{P_{0H}} D(P_0, B_0) d\tau dB_0 dP_0 \tag{17}$$

as the probability of observing a pulsar with spin period less than a given period P, if the integral is performed over all possible combinations of the initial spin period, field strength and current age which give a pulsar with spin period less than P. This constraint can be imposed by choosing the upper-limit of the initial spin period such that,

$$P_{0H} = [P^2 - CB_0^2 \tau_B (1 - \exp(-2\tau/\tau_B))]^{(1/2)}. \tag{18}$$

The upper limit τ_D in expression (16) is the age of pulsars at which they become so faint (due to spin and/or field decay) that they become unobservable. The distribution of pulsar spin period can then be obtained by suitably differentiating Equation (17). In the following subsection we use this approach to obtain the spin period and the pulsed luminosity distribution of radio pulsars in the LMC.

4.1 *Pulsar Spin and Luminosity Distribution*

In determining the spin period distribution for the Galactic pulsars, it is usual to define the probability distribution function not only in terms of the period, period derivative and age of the pulsar but also in terms of its galactic co-ordinates. This probability function is then integrated over these co-ordinates within a limiting distance r_L where a pulsar with radio luminosity LR is visible only out to a limiting distance $r_L = (L_R / 4\pi F_L)^{1/2}$ (Chevalier & Emmering 1986). This is necessary for the determination of the Galactic pulsar statistics to account for the distance-related selection effects which arise in the observed sample of pulsars but is not needed for the LMC sample of pulsars since all these pulsars can be assumed to be virtually at the same distance. However, while obtaining the number distribution of pulsars one has to remove all those pulsars from the sample which will not be detectable here due to the flux limitations of a given survey. This is achieved by placing a lower limit on the field strength of sample pulsars such that the pulsar luminosity is above the limit required for detectability from the LMC. This point will be discussed in detail later in this section. The number of pulsars observable with periods between P and $P + dP$ is then:

$$n(P) = GP \int_{B_{\min}}^{B_{\max}} dB \int_1^{u_D} \frac{du}{[P^2 - CB^2 \tau_B (u^2 - 1)]^{1/2}} \mathcal{D}(P, B, u) \tag{19}$$

where $u = \exp(\tau/\tau_B)$ and G is an undetermined constant which is determined by an overall normalization to a given number of observable pulsars. $\mathcal{D}(P, B, u)$ is the intrinsic source function $D(P_0, B_0)$ redefined in terms of the current variables P, $\dot{P}$ and the age τ. Thus given a source function and suitable limits $B_{\max}$ and $B_{\min}$ (later determined from radio flux limits), one can obtain the present spin period distribution of pulsars.

In integrating Equation (19) the choice of u_D is dictated by the requirement that for all P, B *and* u, the following condition is met:

$$[P^2 - CB^2 \tau_B (u^2 - 1)]^{1/2} \geqslant P_{0\min}. \tag{20}$$

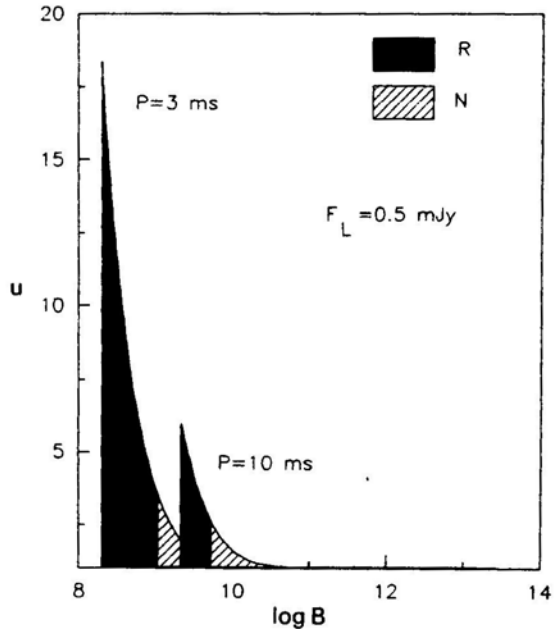

Figure 13(a). Shown are the regions of integration (of Equation 19 in the text) in the u-log B plane for the normal and the reprocessed pulsars at spin periods of 3 and 10 ms. The region of integration for the reprocessed pulsars are only the dark regions while that for the normal pulsars shown by the hatched area also extends fully into the dark regions to the left.

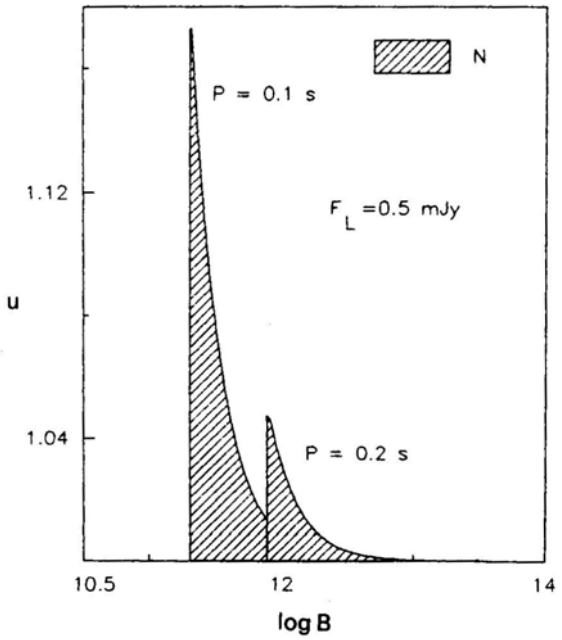

Figure 13(b). Same as Fig. 13(a) for pulsar spin periods of 0.1 and 0.2 s. The reprocessed pulsars are not visible at these periods due to flux limitations (see text) and hence are not shown here.

Here P_{0min} is the minimum possible period a pulsar could be born with (taken to be ≈ 1 millisec). For a given spin period and field strength of a radio pulsar, the above condition gives the maximum possible age which is considerably larger for pulsars with small P and *B* as opposed to that for the pulsars with long *P–B.* This can be seen clearly from Figs 13 (a) and (b), showing the region of integration of Equation (19) in the *u* — *B* plane at different pulsar periods for the normal and reprocessed pulsars. For example $\tau_{max} \approx 7 \times 10^7$ years for a pulsar with *P* = 3ms and *B* = $10^8 G$ while $\tau_{max} \approx 9.6 \times 10^6$ years for a pulsar with *P* = 1 s and *B* = 10^{12} G.

To calculate properties of single pulsar distribution we take a source function $D(P_0 , B_0)$ that has contributions from a mixed sample of pulsars consisting of (a) those which are born from the first SN explosion in binaries whose initial spins are determined by mass accretion and (b) those pulsars which are born in single SN explosions or in the second SN explosion that disrupts the binary. The source function for the former class of pulsars has been assumed to be of the form

$$D_1(P_0, B_0) = q_1 \delta(P_0 - AB_0^{\Gamma}) B_0^{\delta}, \tag{21}$$

i.e. these pulsars are assumed to be "born" (the birth referring to the disruption of the binary system with the second supernova explosion) with a spin period $P_s = AB^{\Gamma}$ on the equilibrium spin-up line. For the standard neutron star parameters the Eddington rate of accretion gives $A = 4.4 \times 10^{-11}$ and $\Gamma = 6/7$. The power law dependence of the intrinsic source function on the initial magnetic field of neutron star arises from the assumption of the exponential field decay and the assumption that the number of binary stars in the LMC should scale with the secondary star mass as $M_2^{-\alpha 1}$ where α_1 is the IMF index. This is also the number of systems where the neutron star born from the explosion of the primary star would have a magnetic field αB_{0exp} (— $T(M_2)/\tau_B$) where B_0 is the initial field strength and $T(M_2)$ is the total lifetime of the secondary star after the explosion of the primary. In the case of substantial difference in the initial masses of the two components of the binary system, $T(M_2)$ is nearly the total lifetime of the secondary. The value of the index δ is related to the lifetimes for two stellar models evolved with helium enrichment (which in the presentcase we havetaken to be 10 and $20 M_{\odot}$), and the IMF index for the LMC. The parameter δ can then be obtained as,

$$\delta = -\alpha_1 \tau_B \frac{\ln(M_2/M_1)}{(T_1 - T_2)} \tag{22}$$

where the masses *M* and the lifetimes *T* refer to the two stellar models mentioned above. If one takes the evolutionary model of pulsar magnetic fields that allow no decay for magnetic fields, then δ has to be treated as an independent parameter. For the parameters we have chosen (discussed towards the end of this subsection) we obtain $\delta = -1.2$.

The source function D_2 (P_0,B_0) for the second class of pulsars, *i.e.* those born in single SN explosions or in the second SN disrupting the binary is assumed to have an equal probability for all bins in P_o and B_o within the limits P_{0min} P_{0max} *and* B_{0mix}, B_{0max}. The value of $B_{min}$is chosen such that any pulsar with amagnetic field strength below $B_{min} = B_{min}(P)$ falls below the detectability limit for a given survey with a flux limit F_L at a particular radio frequency. This is done by assuming that the pulsar luminosity can be obtained as a function of the spin period and its derivative as given by Proszynski & Przybycien (1984):

$$L(P, \dot{P}) = \alpha P^{\alpha} \dot{P}^{\beta}. \tag{23}$$

Thus the requirement that all the pulsars in the sample being presented here have a luminosity greater than $F_L d^2$ in mJy kpc^2 where F_L is the flux limit at 400 MHz for a given survey and d is the distance to the LMC gives,

$$B_{\min}(P) = \left[\frac{F_L d^2}{aC^{\beta} P^{\alpha-\beta}}\right]^{(1/2\beta)} = q_D P^{((\beta-\alpha)/2\beta)} \tag{24}$$

which is the same for the two classes of pulsars. The upper limit on the observed field strength for the pulsars of class (a) is determined by the equilibrium spin-up line, since no reprocessed pulsar can be found above this line in the pulsar P–B diagram *i.e.* $B_{\max} = [P/A]^{1/\Gamma}$ while the maximum possible observed field strength in the case of pulsars in category (b) is assumed to be independent of P. The resulting expressions for the spin period distributions for the two classes of pulsars are,

$$N_1(P)]_{P_1}^{P_2} = N_1(P_2) - N_1(P_1) = G_1\left[\frac{P^{(\delta+\Gamma+1)/\Gamma}}{A^{(\delta-\Gamma+1)/\Gamma}((\delta+\Gamma+1)/\Gamma)} - \frac{q_D^{\delta-\Gamma+1} P^{2\delta-2\Gamma+4}}{2\delta-2\Gamma+4}\right]_{P_1}^{P_2} \tag{25}$$

and

$$N_2(P)]_{P_1}^{P_2} = G_2 P^2 \int_{P/(C\tau_B)^{1/2} B_{\max}}^{1/(C\tau_B)^{1/2} q_D P} \frac{\tan^{-1} x}{x} dx\Bigg]_{P_1}^{P_2} + G_2 \int_{P_1}^{P_2} P\left[\tan^{-1}\left(\frac{1}{(C\tau_B)^{1/2} q_D P}\right) + \tan^{-1}\left(\frac{P}{(C\tau_B)^{1/2} B_{\max}}\right)\right] dP \tag{26}$$

where $N_1(P)$ and N_2 (P) are the distribution functions for the pulsars in classes (a) and (b) respectively, for $P_1 \leqslant P \leqslant P_2$. The fraction of pulsars from category (a) in the intrinsic sample of pulsars in the LMC is taken to be half the fraction of binaries determined in section 2, since only one of the components of the binary is reprocessed. As will be discussed later, the observable fraction of the reprocessed pulsars is different from this fraction (half) due to the differences in the maximum possible life-times for the normal and the reprocessed pulsars as well as due to the fact that the reprocessed pulsars appearing within certain region of P and B in general are selected against due to their low radio luminosity. Given the total number of pulsars currently present in the LMC the constants G_1 and G_2 can be determined. McConnell *et al.* (1991) have estimated the number of pulsars in the LMC to be $\approx$ 9500. This estimate is based on the number of pulsars in the solar neighbourhood (of area 1 kpc^2 of the Galactic plane) containing some 70 pulsars and the ratio of the LMC and the solar neighbourhood masses. It also accounts for the fact that the number of massive stars per unit total mass in the LMC is about twice that of the solar neighbourhood. While obtaining the values of the constants G_1 and G_2 using the above number of total pulsars in the LMC, Equation (19) is integrated over all possible values of the magnetic fields of pulsars. After determining these constants, the actual distributions are obtained by restricting the region of integration of Equation (19) to the magnetic fields lying above $B_{\min}$ as explained earlier so that the pulsars which could not be detectable from the LMC in a survey with a given flux limit are eliminated from the sample being presented.

In Figs 14(a) and (b) we have shown the predicted spin period distribution from the two classes of pulsars for the following choice of parameters: (i) the IMF index

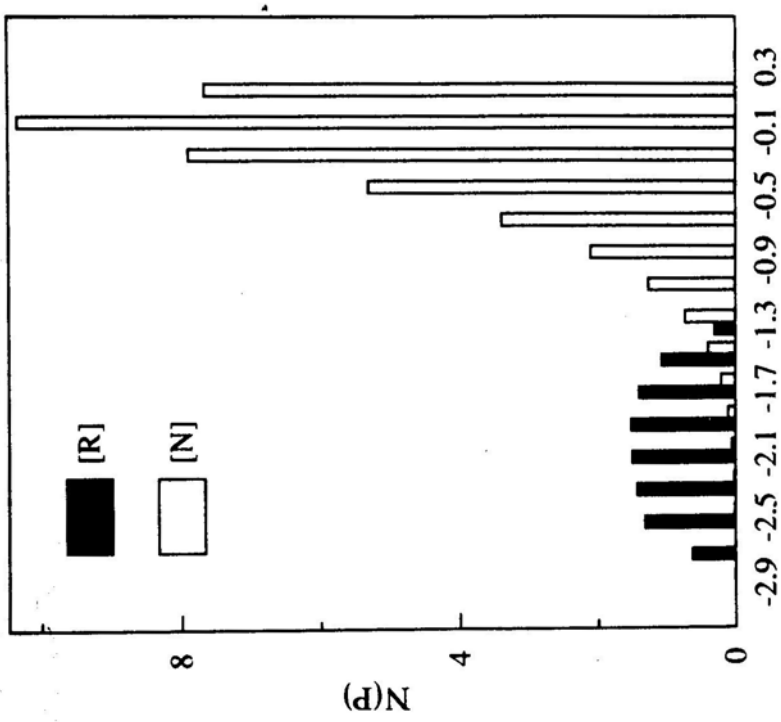

Figure 14(b). The spin period distribution (same as in Fig. 14a) calculated for a flux limit of 0.5 mJy.

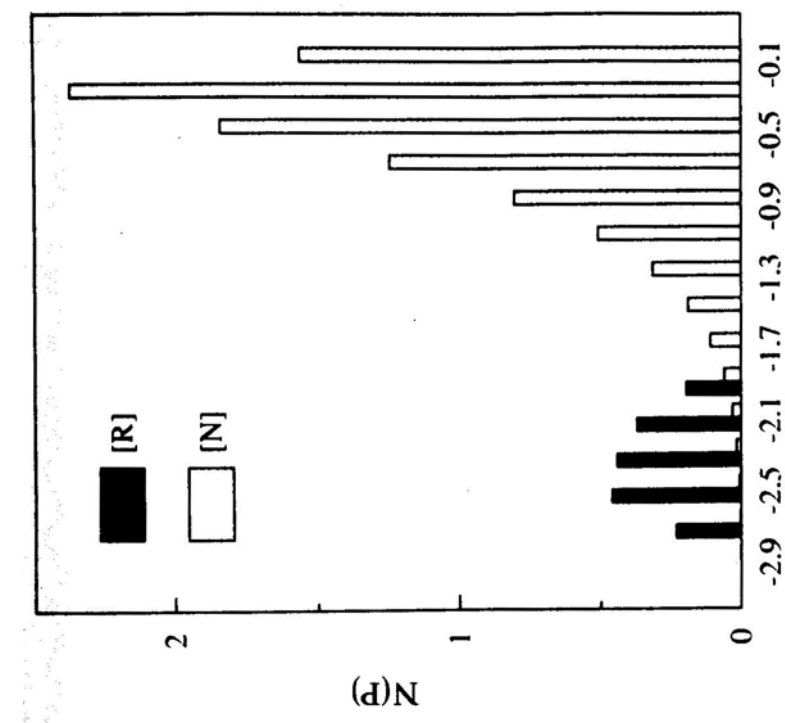

Figure 14(a). The predicted spin period distribution for the reprocessed pulsars (marked R) and the normal pulsars (marked N) which include those that have not been spin evolved in binaries. The assumed flux limit for a radio pulsar survey of the LMC is 1·0 mJy in this figure.

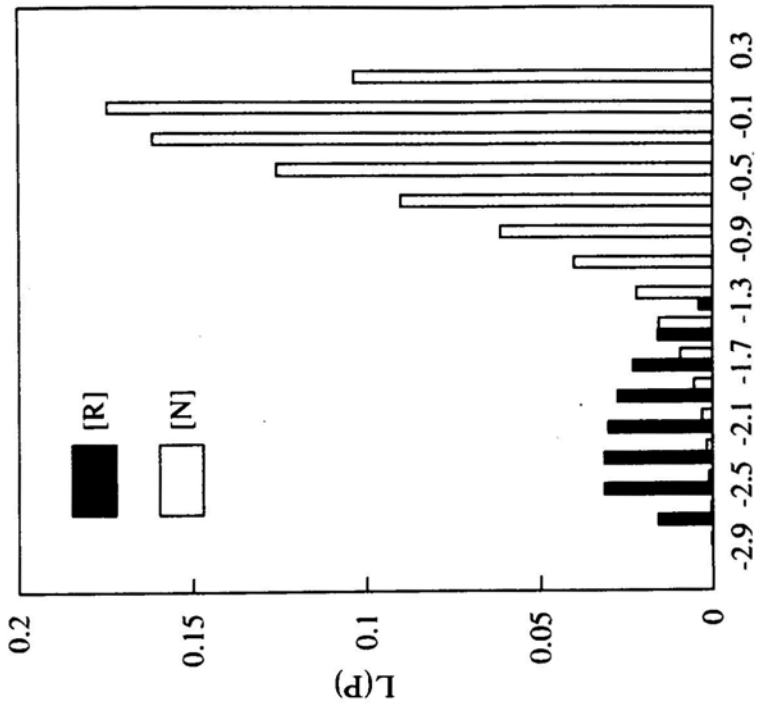

Figure 15(b). Pulsed radio luminosity distribution calculated for a flux limit of 0.5 mJy.

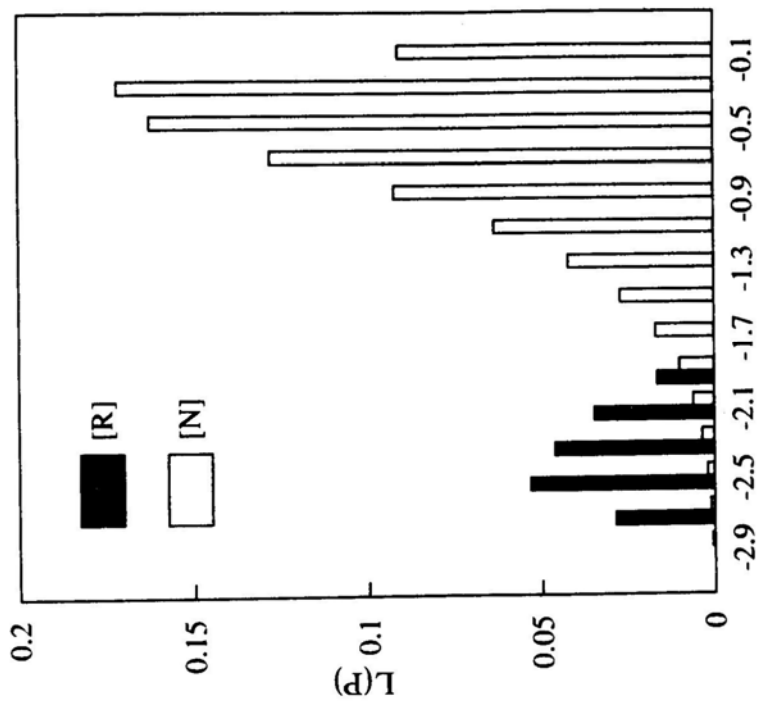

Figure 15(a). Predicted distribution of pulsed radio luminosity with respect to the spin period for categories R and N of pulsars calculated for a flux limit of 1.0 mJy.

for the LMC $\alpha_1 = 1.5$ (Humphreys & Blaha 1989), (ii) a binary fraction of 0.6 in the Blue Supergiant region of the HR-diagram of the LMC, (iii) the timescale for the decay of the magnetic field of the pulsars $\tau_B = 2 \times 10^7$ years (Narayan & Ostriker 1990), (iv) the maximum possiblefieldstrengthfor the class (b)pulsars – $B_{max} = 10^{13}$ G and (v) the constants of the radio luminosity model as $\alpha = -1.04$, $ß = 0.35$ and $a = 10^{7\,52}$ (*e.g* Chevalier & Emmering 1989; Prozynski & Przybycien 1984). Fig. 14(a) assumes that all radio pulsars down to 1 mJy level at 400 MHz will be detectable while Fig. 14b is for a flux limit of 0.5 mJy.

The above procedure can also be used in obtaining the expected distribution of the pulsed luminosity from the sample of pulsars in the LMC, in various bins of the spin period. The resulting distribution of the pulsed radio luminosity with respect to the spin period is shown in Figs 15 (a) and (b) which have been obtained for an identical set of parameters as in Fig. 14.

4.2 *The Distribution of Pulsar Spin in a FluxLimited Survey*

A distinct feature of the pulsar spin period and the pulsed luminosity distributions is their bimodality. In these distributions the peaks at short periods arise from the reprocessed pulsars. It can be seen from Figs 14(a) and (b) that the observable *reprocessed* pulsars are a very small fraction of the total number of observable pulsars from the LMC. This fraction f'_b which is 0.15 in Fig. 14(a) and is 0.18 in Fig. 14(b) is different from the fraction of first born pulsars $f_b = f/2$ (where $f = 0.6$ is the duplicity fraction discussed in Section 3). This is due to the fact that a larger fraction of the reprocessed pulsars are below the detection limit for a survey of a given flux limit since they are generally less luminous than the normal pulsars. In fact, the region in the P–B plane where reprocessed pulsars from the LMC are detectable is highly restricted as can be seen from Fig. 17. This region in the *P–B* plane is shown by the hatched area in Fig. 17 which lies between the two lines defined by the equilibrium spinup line and the line below which any pulsar in the LMC would not be detectable at a given flux level and for a luminosity model assumed in Equation (23). This line is parallel to (and displaced to the left of) the Taylor & Stinebring (1976) "death-line" defined for the Galactic pulsars, to the right of which the pulsars intrinsically turn off. On the shorter period side this region is restricted by the minimum possible field strength that these pulsars could be born with. The minimum possible initial field strength for the normal pulsars along with the maximum possible lifetime of the secondary star (sufficiently massive to disrupt the binary during its SN explosion) defines the corresponding lower limit of the initial field strength for the reprocessed pulsars, *i.e*.,

$$B^{\mathrm{R}}_{0\,\mathrm{min}} = B^{\mathrm{N}}_{0\,\mathrm{min}} \exp(-t(M_2)/\tau_B). \tag{27}$$

Here $M_2 = 15 M_\odot$. Thus the region populated by observable pulsars in the $P_{\mathrm{spin}} - B$ diagram is more restricted in the case of the LMC pulsars than in the case of the Galactic pulsars since the former have to be intrinsically more luminous at a given flux level due to the larger distance. The extent of this region depends also on the range of initial field strength that the class (a) pulsars are born with. The distribution functions shown in Figs 14 and 15 are for an initial strength range $B_{0\mathrm{min}} = 1 \times 10^9$ to $B_{0\mathrm{max}} = 4 \times 10^{13}$ and initial spin period range $P_{0\mathrm{min}} = 1$ ms to $P_{0\mathrm{max}} = 4$s.

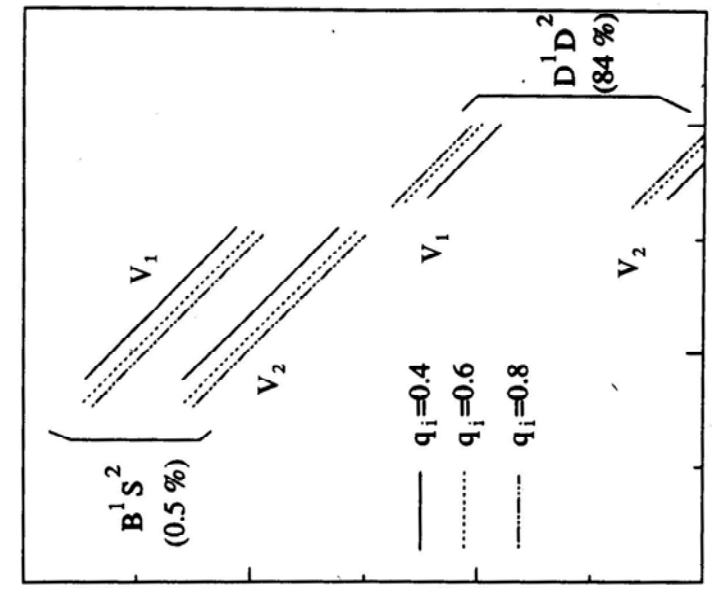

Figure 16(a). Predicted velocities of pulsars following the distribution of the binary shown as a function of the initial orbit separation at different values of the initial mass ratio for the pulsars born from binary systems in the B^1S^2 and D^1D^2 evolutionary channels. The velocities corresponding to the first born pulsars (V_1) and the second born pulsar (V_2) are indicated. The numbers in brackets indicate the relative percentages of pulsars in these velocity ranges.

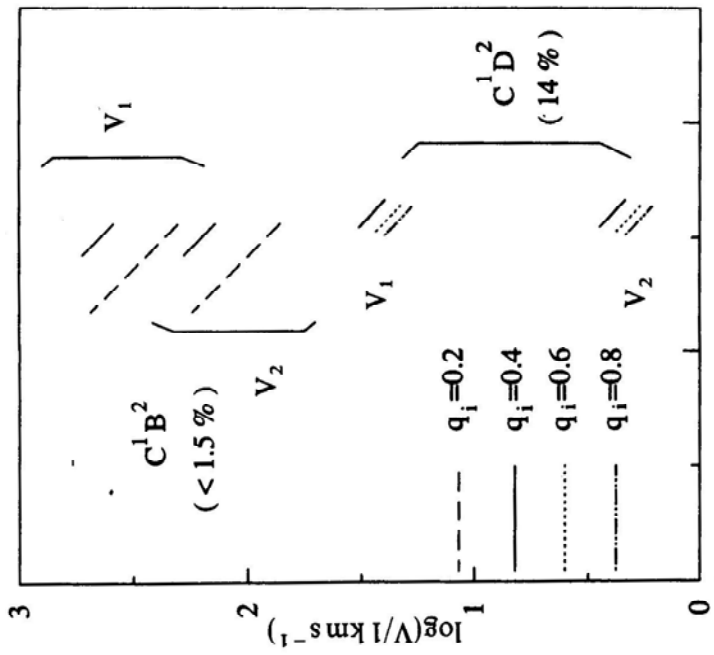

Figure 16(b). Same as Fig. 16(a) for pulsars born from binary systems in the C^1B^2 and C^1D^2 evolutionary channels. The relative percentages of pulsar falling in each velocity range shown here and in the previous figure are normalized with respect to the total number of pulsars arising out of binary systems.

The relative height of the peak arising from the reprocessed pulsars in Figs 14 and 15 in comparison to the peak at longer period is sensitive to the chosen value of the field decay timescale τ_B. The figures shown are calculated for $\tau_B = 2\times 10^7$ years. Choosing a value of $\tau_B = 5 \times 10^6$ makes this peak quite small. This arises from a linear dependence of δ on τ_B, The larger the value of τ_B, more negative is δ. This makes the probability of class (b) pulsars large at lower P_0 because of the equilibrium spin period relationship, thus making the peak at lower periods more prominent. There is, however, some evidence from the data on Galactic pulsars that τ_B is longer than 5 x 10^6 years and close to 2×10^7 years (Narayan & Ostriker 1990). But arguments against field decay in single pulsars also exist in the literature (Sang & Chanmugam 1990), although some field decay induced by accretion for neutron stars in binary systems is considered possible. Our results for the spin period and the pulsed luminosity distributions shown in Figs 14 and 15 would be qualitatively unchanged even if the magnetic fields of single pulsars do not decay. (In this case, however, we have to take the index δ appearing in Equation (21) as a parameter).

4.3 *LMC Pulsar Observations*

Very recently a search for radio pulsars in the LMC and SMC has been completed at 610 MHz using the 64-m Parkes radio telescope (McConnel *et al.* 1991). The sensitivity limit of this survey is equivalent to a limit $S_{400} \approx 1.4$ mJy for a search conducted at 400 MHz. This has discovered two pulsars 0529–669 and 0456–698 with dispersion measures that suggest that they lie in the LMC. Of these, the first was reported earlier (McCulloch *et al* 1983). A third pulsar 0502–665 was found in the direction of the LMC but is probably not associated with it and may be a foreground object belonging to the Galactic pulsar population because of its relatively similar DM sin |b| (b is the galactic latitude). Another pulsar 0540–69 with 50ms period was detected in the LMC at X-rays by the Einstein Observatory (Seward, Harnden & Helfand 1984) and at optical wavelengths (Middleditch & Pennypacker 1985). Recently radio pulsations with high DM ($\approx$ 140 pccm^{-3}) and low flux density has also been reported from 0540–693 (Manchester 1991). First and second derivatives of the pulse frequency for this pulsar have also been measured (Nagase *et al* 1990) which inidicate that the pulsar has a large spin-down rate (and a correspondingly large magnetic dipole field or momemt). The pulse period, its derivatives as well as the detection of an optical synchroton nebula surrounding the pulsar (Chanan, Helfand & Reynolds 1984) makes the PSR 0540–69 and its SN remnant very similar to the Crab pulsar and SNR. The two LMC pulsars' spins (and magnetic fields) are plotted in Fig. 17. The radio pulsars 0529–669 and 0456–698 have periods of 0.976 and 0.320 seconds with mean fluxes of 1.8 and 1.0 mJy at 645 MHz respectively. All three pulsars have positions that fall within identified regions of Supergiant shells and close to regions of high UV flux (McConnell *et al.* 1991) which are associated with hot, massive O and B stars.

4.4 *Velocity Distribution of Pulsars*

A closer connection between the evolution of binary supergiants and single pulsars can be discerned by looking at the velocity distribution of pulsars if a substantial

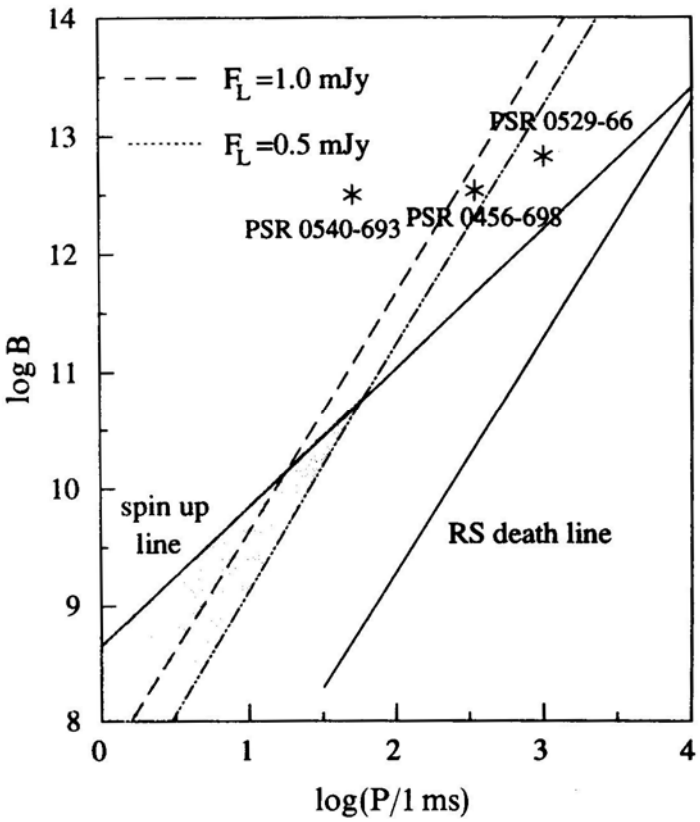

Figure 17. Regions (shaded) in the log B-log P_{spin} plane where reprocessed pulsars would be bright enough to be detectable in a radio pulsar survey of the LMC at limiting fluxes of 0.5 mly and 1.0 may (at 400 MHz). Three pulsars detected so far in the LMC are indicated.

fraction of these are born from binary systems. The determination of the velocity distribution of single pulsars from the LMC is not likely in the near future with the current detection techniques. A global distribution of pulsars in the LMC and their relative separation from the regions of their birth-sites could, however, give some indication of the actual velocity distribution. We use the orbital period distribution of binary systems prior to the explosion of the secondary star obtained in Section 3 to determine the expected distribution of pulsar velocities in the LMC.

When the secondary (which in our calculation was assumed to have a mass of 20 $M_{\odot}$ at the post main sequence phase) ultimately explodes, the binary is disrupted leading to two run-away neutron stars. We have calculated the expected distribution of the space velocities of pulsars whose progenitors have evolved through the evolutionary channels B^1S^2, C^1B^2, C^1D^2 and D^1D^2 under the assumption that these systems had circular orbits prior to the explosion of the secondary star. It has been assumed that these runaway velocities are solely due to the orbital velocities of the two binary components and the effects of either asymmetric supernova explosions or the impact of the supernova ejecta from the explosion of the secondary star on the compact companion are negligble.

In the present calculation the pulsars which might arise from the binary systems

in the B^1 B^2 channel have been ignored since in this case the final evolution resulting in a common envelope configuration seems to lead to a merger of the two binary components. The final outcome of such an evolution is uncertain. Likewise we have excluded the shorter period systems from the B^1B^2 and C^1B^2 channels which are likely to be merger systems following mass transfer from the secondary star in these systems *i.e.*, all the systems falling within the hatched areas marked as mergers are excluded from the pulsar velocity calculations. For some of these excluded systems it is possible to have very high velocity pulsars if the second supernova in the binary systems occurs before the complete merger of the binary components (*e.g.* before even the carbon core starts filling its Roche-lobe after the helium envelope is ejected). We have, however, ignored this possibility in view of the uncertainties involved in the final evolution of such systems.

Tracing the orbital evolution from this stage back to the stage at the start of mass transfer from the primary star according to the evolutionary paths for each of the channels as mentioned in Appendices A and B (see also Figs 5–12) one can determine the space velocities of the two pulsars released from the second supernova explosion in a binary system as a function of the initial mass of the primary star and the initial orbital separation. The space velocity V_2 for the pulsar (in km/s) born from the SN explosion of the secondary *i.e.* the younger pulsar released from the binary system can be expressed (for the three evolutionary channels mentioned above) as,

$$V_{B^1S^2} = \frac{438 M_{n^*} N_1 (M_{1wr1} M_{2wr1})[M_{1wr2} + 2M^e_{2x}/r_L(q_x)^{1/2}]}{[[M_{n^*} + M_{2wr2}](M_{1wr2} M_{2wr2})]^{1/2}[M_{1sn1} + M_{2sn1}](M_{1i} M_{2i}) a_i^{1/2}}$$

$$N_1 = [[M_{2wr2} + M^e_{2x}][M_{1x} + M_{2x}][2(M_{1sn1} + M_{2sn1}) - (M_{1wr1} + M_{2wr1})]]^{1/2} \quad (28)$$

$$V_{C^1B^2} = \frac{438 M_{n^*} N_2 [M_{1wr2} + 2M^e_{2x}/r_L(q_x)]^{1/2}}{[[M_{1wr1} + M_{2wr1}](M_{1wr1} M_{2wr1})]^{1/2}[M_{1sn1} + M_{2sn1}] a_i^{1/2}}$$

$$N_2 = \frac{[N_3[M_{1wr1'} + M_{2wr1'}][M_{1wr1} + M^e_{1i}][M_{2wr1} + 2M^e_{1i}/r_L(q_i)]]^{1/2}}{[[M_{1wr2} + M_{2wr2}](M_{1wr2} + M_{2wr2})]^{1/2}}$$

$$N_3 = [[2(M_{1sn1} + M_{2sn1}) - (M_{1wr1'} + M_{2wr1'})][M_{2wr2} + M^e_{2x}][M_{1x} + M_{2x}]]^{1/2} \quad (29)$$

$$V_{C^1D^2} = \frac{438 M_{n^*}[M_{1x} + M_{2x}]^{1/2} M_{1wr1} M_{2wr1}(2(M_{1sn1} + M_{2sn1}) - (M_{1o} + M_{2o}))^{1/2}}{(M_{1wr2} + M_{2wr2})(M_{1sn1} + M_{2f})(M_{1i} M_{2i}) a_i^{1/2}} \quad (30)$$

and

$$V_{D^1D^2} = \frac{438 M_{n^*}[(M_{1o} + M_{2o})[M_{1x} + M_{2x}][2(M_{1sn1} + M_{2f}) - (M_{1o} + M_{2o})]]^{1/2}}{(M_{1wr2} + M_{2wr2})(M_{1sn1} + M_{2f})(M_{1i} + M_{2i})^{1/2} a_i^{1/2}} \quad (31)$$

Here the subscripts on the masses refer to the various stages of evolution as mentioned in 3.1 and $M_{n_\star} = M_{sn1}$ refers to the mass of the neutron star born from the upernova explosion of the primary star and is equal to 1.4 $M_\odot$. The masses and the separation a_i in the above expression are in solar units. The velocity of the first born pulsar following the second explosion is then given by,

(32)

where χ is the fraction of the total mass of the binary which is lost in the second explosion, and V_1 and V_2 are the velocities of the first born and second born pulsars respectively. (Equations (28–31) give the V_2 for the different channels).

Figs 16(a) and (b) show the expected pulsar velocities for the first born and the second born pulsars as a function of the initial separation. The ranges of orbital separation corresponding to the different evolutionary channels and the velocities of the two runaway pulsars are shown in these figures. Also shown enclosed in square brackets are the relative percentages of pulsars in each of the evolutionary channels. Thus, although the velocity distribution of the released pulsars is expected to be bimodal with peaks at large and small velocities, the former type of pulsars is very small in number compared to the low velocity pulsars. The velocities of the first and second born pulsars also differ considerably, which is expected for symmetric explosion and when the amount of mass ejected during the SN explosion of the primary star is large as can be seen from the Equation (32) above. However, this difference is less marked for the pulsars arising from binary systems in the evolutionary channels B^1B^2 and C^1B^2. The secondary star in these systems loses most of its envelope mass at some stage of its evolution through RLO (which is lost from the system) and is thus less massive prior to its explosion as compared to the secondary star in the wider systems of C^1D^2 and D^1D^2 evolutionary channels. For pulsar ages $\approx 10^7$ years and with the expected low velocity of ejection from the binary system, the majority of pulsars would be found clustered around their birth-places *i.e.* the OB-associations in the LMC. Also a majority of the intermediate velocity pulsars ($V \approx 10 - 30$ km/s) will be the first born pulsars and therefore of a spun-up variety i.e., with short spin periods.

5. Discussion and conclusions

As already mentioned, a number of stars in the LMC have photospheres enriched with helium. Such stars have properties that reconcile the theoretically computed evolution of massive stars with the observed population of Blue Supergiant stars in the LMC. As the primordial helium abundance ($Y_5 = 0.24$) is considerably less than what is expected or indicated for the surface of the helium enriched stars ($Y_5 > 0.5$) it has been suggested that the helium enriched layers have been acquired by accretion from an evolved binary companion. Therefore these stars which appear as peculiar *BSG* stars should be examined for evidence of duplicity. While some of the close binaries may reveal themselves as double-lined spectroscopic binaries, the results of Section 3 suggest that their number is likely to be small and for most of these the evidence has to be indirect.

Study of helium-enriched massive stars may also be of interest in relation to Type Ib supernovae in the LMC. Uomoto (1986) suggested that SN Ib might be more massive cousins of observed hydrogen-deficient binaries in which a helium supergiant is dumping matter on to a hot main sequence companion (Drilling 1986). This model is particularly attractive because helium is seen in abundance in this type of SNe although potential problems of this model may exist in terms of the distance of the SN Ib from the HIT regions and the relative rarity of the hydrogen-deficient binaries in our Galaxy (see Filippenko 1991 and references therein.) The lifetime and number estimates of the progenitor systems (see Section 3.5) would together imply a Type

Ib SN rate in LMC of approximately 1 per thousand years. As indirect evidence of the binary nature of the peculiar BSG stars possibly bound to neutron stars, spectroscopic evidence of their surface enrichment with intermediate mass and iron group element resulting from Type Ib SNe may be sought.

The observed number count of stars in the post main sequence region of the H–R diagram of the LMC, together with computed duration functions, implies that at least ≈ 60 per cent of the Blue Supergiants are likely to be parts of binary systems. This binary fraction among the BSGs is not excessive when compared with the binary fraction among the WR + O systems (Moffat 1989), and Galactic O-stars. Furthermore, if consistency with observed X-ray binary systems with known orbital period is imposed, a large fraction of these supergiant binaries is required to be in wide binary systems. Recently the Hubble Space Telescope has discovered a large number of massive stars in the 30 Doradus region of the LMC, all of which are confined within a linear dimension of roughly one parsec. This region was previously suspected to contain a single star. Many of these newly discovered stars could be dynamically bound to each other. Our prediction of a large number of wide binary progenitor systems based on an independent line of argument is consistent with this discovery. The presence of a large fraction of wide binary systems is also consistent with the analysis of Bailes (1989) who concludes that a large fraction of the Galactic pulsars should arise from wide (with orbital periods > 100 days) binary systems to obtain consistency with the Galactic pulsar velocity distribution.

The bimodal nature of the orbital period distribution of the relatively unevolved binaries, together with the relatively few systems in the short orbital period ranges imply that the relative number of high velocity runaway O-stars (with unseen neutron star companions) compared to the total sample of O-stars is quite small in the LMC. In addition, following Blaauw's (1985) study in the context of local Galactic birthrates of pulsars and local rate of formation/death of massive stars, similar estimates for the LMC may also be useful to constrain the mass range of pulsar progenitors. In the Galaxy there are binary pulsars like PSR 1913 + 16, 1534+12, 1820 – 11 and 2303 + 46 which have massive companions (*e.g.* neutron stars) and are likely to have evolved from massive close binary stars. Only in very rare cases like these would the progenitor systems remain bound after the second supernova explosion in which the younger neutron star is born. In most cases the binary would disrupt leading to two runaway stars. Thus the velocity distribution of the pulsars born from binaries in the LMC would trace out the orbital distribution of the progenitor systems. In this paper we have determined the general nature of this distribution.

The requirement of placing the secondary star in the magnitude band being considered here restricts its mass close to 20 $M_{\odot}$ in our analysis. Therefore, when the secondary star evolves and explodes as a supernova, since more than half the total mass of the systems is likely to be lost in the explosion, the binary would give rise to two runaway pulsars. The distribution of pulsars in their space velocities is shown in Figs 16(a) and (b), and it can be seen that the bimodal distribution in orbital periods of the progenitor systems is reflected in the bimodal distribution in space velocities of the resulting pulsars. The high velocities are ≈ 150–500 km/sec and the low velocity peak is at ≈ 1–30 km/sec. The larger peak occurs at lower velocities. With velocities of this order, in their entire lifetime (≈ 10^7–10^8 years) the pulsars would travel ≈ 100–900pc from the site of their birth. These are the massive star formation regions associated with O–B star clusters that are largely localized and

contiguous and have dimensions of the order of ≈ 1kpc. Thus most of the pulsars born out of binary systems evolving through the magnitude and surface temperature bin considered above are expected to be localized in narrow regions in the LMC. In fact the pulsars discovered in the most recent radio survey of LMC (McConnell *et al.* 1991) all have these characteristics. In this context it is of interest to note the situation regarding the binary origin of pulsar velocities in the Milky-Way galaxy. Blaauw (1985) has pointed out that among the early B-type stars in the nearest O–B associations, only 18 per cent are well established single line spectroscopic binaries with determined orbits. The semi-amplitudes of the velocity variations of their primaries are in the range in the 14 to 131 km/s with a median value of 50 km/s. For the remaining 82 per cent, there are limits on the semi-amplitudes of the primary velocities which are successively smaller. Thus, Blaauw concludes that only a small fraction of binaries are close enough to give high velocity pulsars ($\geqslant$100 km/s) after the explosion of either of the two components.

The spin of the first born neutron star at the time of disruption will be affected by mass transfer from the companion before the latter explodes in the second SN. Given a birthrate of the reprocessed pulsars (interpreted from IMF considerations of the secondary) we have estimated the steady-state spin and pulsed radio luminosity distributions in the LMC. Since only the brightest radio pulsars will be seen in the LMC, the observable reprocessed pulsars (the first born neutron stars) would be restricted to short spin periods. Since most neutron stars will be released as single pulsars in the second SN explosion of the massive binary, this class of binaries could be an important source of observable single short period pulsars in the LMC, especially because the companions in low mass binary pulsars can be gotten rid of only under rather specialised circumstances (Kluzniak *et al.* 1988).

We thank Prof. Icko Iben for his stellar evolution code which was used in this work and Prof. A.F.J. Moffat for sending us his reprints. NRS wishes to thank Dr. Patrick Das Gupta for useful discussions. AR wishes to thank several participants of the Santa Barbara Workshop on Neutron stars in Binary systems in June 1991, especially Drs. Rachel Dewey, Edward van den Heuvel, Craig Wheeler and Martin van Kerkwijk for useful discussions. We also thank two anonymous referees for their helpful criticisms and for pointing out references that are relevant here. This research was particularly supported by U.S. N.S.F. grant No: INT87-15411-A01-TIFR and is part of the 8th Five Year Plan Project 8P-45 at TIFR.

Appendix A

1. *Binary evolution under conservative mass transfer: Systems with* $q_i > 0.4$.

First we consider the evolution under mass transfer from the more massive primary star. Systems with $q_i > 0.4$ having Case B^1 as well as Case C^1 type of mass transfer are stable and assumed to be completely conservative at this stage (*i.e.*, during the stage of mass transfer from the primary to the secondary star – stage I to stage WR1). The orbit evolution during this state is governed by (Savonije 1983),

$$\frac{\dot{a}}{a} = -2\left(1 - \frac{M_1}{M_2}\right)\frac{\dot{M}_1}{M_1}. \tag{A1}$$

Here a is the orbital separation, M1 the mass of the (mass transferring) primary and M_2 is the mass of the secondary. The orbital separation at stage WR1 can be obtained as a function of the orbital separation at stage I by integrating the above equation. The final orbital period $P_{\rm wrl}$ after conservative mass exchange where the entire envelope of the primary is transferred to the secondary is related to the initial period P_i by (Paczynski 1971)

$$P_{\rm wr1} = \left[\frac{q_i}{f(1+q_i-f)}\right]^3 P_i.$$

Here $f = M_{1\rm i}^{\rm He}/M_{1\rm i}$. The initial separation a_i determines whether the system undergoes a Case B^1 or Case C^1 type of mass transfer. The ranges of the radii of the primary star at the start of the mass transfer for the different cases of evolution have been obtained as a function of the ZAMS mass of the primary star by extrapolating from the evolutionary models of Brunish & Truran (1982) for main sequence masses 15, 30 and 40 $M_\odot$ and with Z = 0.01 and are quoted in the beginning of Section 3.1. The Roche-lobe radius $R_{1\rm c}$ of the primary is related to the initial separation a_i at the start of the mass transfer by the equation (see *e.g.* Savonije 1983):

$$a_i = (0.38 + 0.2\log(M_{1i}/M_{2i}))^{-1} R_{1\rm c}. \tag{A2}$$

The orbit evolution from stage WR1 to SN1 is governed by the amount of mass lost during the supernova explosion of the primary star. For a symmetric explosion and neglecting the impact of the supernova ejecta on the secondary star, the equations governing the orbit evolution are (Flannery & van den Heuvel 1975),

$$a_{\rm sn1} = \frac{\mu_f}{(2\mu_f - 1)} a_{\rm wr1} \tag{A3}$$

where,

$$\mu_f = \frac{(M_1^{\rm sn1} + M_2^{\rm sn1})}{(M_1^{\rm wr1} + M_2^{\rm wr1})}. \tag{A4}$$

The conservative orbit evolution in such systems is identical up to this stage (stage SN1), for both Case B^1 as well as Case C^1. The Roche-lobe radius of the secondary at stage SN1 can then be obtained from $a_{\rm snl}$. The initial orbital separation a_i, can be related to the initial radius of the primary and hence to its mass as argued earlier.

Next we consider the orbit evolution during mass transfer from the secondary. For given masses $M_{1\rm i}$ and $M_{2\rm snl}$ and for a given $q_i > 0.4$ the Roche-lobe radius of the secondary at a stage after the SN explosion of the primary star can be determined and the stage of evolution (if any) when the secondary star will fill its Roche lobe can be determined. In the case of systems (with $q_i > 0.4$) undergoing Case B^1 type of mass transfer, it turns out that, the secondary star would fill its Roche lobe at some later stage in its evolution whereas for systems in Case C^1 channels the secondary star does not fill its Roche lobe at any stage of its evolution. The orbit evolution from this stage onwards is hence different for the two systems. Systems in the B^1S^2 channel go through a common envelope evolution arising out of (RLO) mass transfer from a massive supergiant component to a neutron star. There is a rapid shrinking of the orbit due to the large disparity in the masses of the two components and the neutron star is soon engulfed by the envelope of the secondary star, which is subsequently ejected. The evolution of the orbit during this stage is similar to the

common envelope evolution of the close systems with q_i < 0.4 as described in Appendix B (see also Equations B1 and B2). Systems falling in the evolutionary channel C^1D^2 are evolved with mass loss from the system during mass transfer from the secondary. Up till the stage just prior to the SN explosion of the secondary star they are governed by Equation (B3), (in Appendix B) just as in the case of wind-fed (non-conservative) mass transfer from the primary star.

2. *Calculation of the allowed mass ranges.*

We make the following assumptions regarding the mass transfer process and the resultant masses of the binary components at various stages in order to track the binary evolution during different stages of evolution:

(1) At stage WR1 the primary is left with the helium core. This would be the mass of the WR star evolved from the primary star. The mass of the helium core can be related to the initial mass of the primary star from a least-square fit of the helium core masses of 15, 30 and 40 $M_\odot$ stars (Brunisli & Truran, 1982). From this fit, $M_{1\mathrm{wr1}} = f(M_{1i}) = cM_{1i}$ where c= 0.25 for Case B and c = 0.3 for Case C. In our calculation we take this factor c to be 0.3 uniformly. Here M_{1i} and $M_{1\mathrm{wrl}}$ are the main sequence mass and the mass of the helium core left after the loss of the envelope.

(2) $M_{1\mathrm{sn1}}$–the mass of the neutron star left after the explosion of the WR star is taken to be 1.4$M_\odot$.

(3) In the conservative case since all the mass leaving the primary is accreted by the secondary,

$$M_{2i} = M_{2\mathrm{wr1}} - (M_{1i} - f(M_{1i})) \approx M_{2\mathrm{sn1}} - (M_{1i} - f(M_{1i})) \tag{A5}$$

assuming the secondary mass remains unchanged during the primary explosion phase.

From the assumption of conservative evolution in Case B and C and the assumptions (1)–(3) mentioned above, the allowed ranges of initial masses for the primary star can be constrained for a given mass of the secondary star at a stage after the explosion of the primary. Starting with initial masses M_{1i} and M_{2i} for the two stars, the masses after the end of the first stage of mass transfer are, cM_{1i} and $(M_{2i} + (1 - c)M_{1i})$ respectively, where c is as defined in assumption. (1) above. Assuming that the secondary star mass remains unchanged during the supernova explosion of the primary star,

$$M_{2\mathrm{sn1}} = M_{2i} + (1 - c)M_{1i}. \tag{A6}$$

Thus for a given q_i one can determine the required initial mass for the primary as,

$$M_{1i} = \frac{M_{2\mathrm{sn1}}}{(1 + q_i - c)}. \tag{A7}$$

The upper limit on M_{1i} comes by putting q_i= 0.4 (since for values of q_i below this, we assume that conservative evolution does not take place) and the lower limit, by having the initial secondary mass comparable to the primary mass. This one obtains,

$$\frac{M_{2\mathrm{sn1}}}{(2 - c)} < M_{1\mathrm{i}} < \frac{M_{2\mathrm{sin1}}}{(1.4 - c)}. \tag{A8}$$

In all the calculations of Section 3, $M_{2\mathrm{sn1}}$ was taken to be 20 $M_\odot$.

Appendix B

1. *Orbit evolution with mass loss from the system.*

First we consider the evolution of close systems with $q_i < 0.4$. Close binary systems with $q_i < 0.4$ where the primary star fills its Roche-lobe in either a Case B^1 or a Case C^1 type of contact evolve via RLO of the primary in such a way that at some stage of mass transfer there is a common envelope formation and subsequent spiraling in of the two components. The envelope of the mass losing star is ejected during this spiral-in phase. The orbit evolution during the spiral-in is assumed here to be governed by the requirement that the final energy in the orbit equals the difference between the initial energy of the orbit and the binding energy of the envelope of the mass losing star:

$$-\frac{GM_1M_2}{2a_i}+E^{(1)}_{\text{binding}}=-\frac{GM_{1\text{core}}M_2}{2a_f}. \tag{Bl}$$

For Case C^1 systems with $q_i < 0.4$ the orbit shrinks during the mass transfer and there is an increase in the radius of the secondary star due to mass accretion. Soon the system comes into a contact configuration which leads to the common envelope situation. For Case B^1 systems with $q_i < 0.4$, however, this is somewhat delayed and the mass transfer is completely stable and conservative till the stage of contact (stage 't') is achieved. The orbit evolution during this phase is thus governed by Equation Al, as in the case of systems with $q_i > 0.4$. This leads to the orbital separation at the end of spiral-in (Webbink 1984)

$$a_{\text{wr1}}=a_{\text{t}}\left(\frac{M_{1\text{wr1}}M_{2\text{wr1}}}{M_{1\text{wr1}}+M^{\text{e}}_{1\text{t}}}\right)[M_{2\text{wr1}}+2M^{\text{e}}_{1\text{t}}/r_{\text{L}}(q_{\text{t}})]^{-1}. \tag{B2}$$

Here a_{wrl} refers to the orbital separation after the loss of the envelope mass at the start of mass transfer and $r_{\text{L}}(q_{\text{t}})$ is the ratio of the Roche-lobe radius of the primary to the orbital separation at the pre-contact stage. In principle, the final orbit dimension should also be determined by the effects due to the structure of the common envelope (and its effect on the binding energy of the envelope). In addition, the spiral-in may stop at an intermediate point and may not lead to a complete ejection of the envelope. However, due to the uncertain physics involved, we ignore these effects and use the form of Equation (B2) as stated.

For primary star undergoing a Case C^1 evolution a common envelope evolution arises in systems with $q_i < 0.4$ immediately following the RLO of the primary star owing to the convective envelope of the primary star. In such situations there is no prior stage of stable mass transfer and the orbit evolution is just governed by Equation (B2) with the subscript 't' replaced by 'i', since the spiral-in starts during stage 'i' itself.

The calculated orbital parameters for the two classes of systems discussed above (*i.e.* systems evolving through channels B^1B^2 and C^1B^2) indicate that these systems evolve into close binary systems where the secondary star would undergo a Case B^2 type of mass transfer. The subsequent orbital evolution of these systems is analogous to the evolution of systems in the B^1S^2 evolutionary channel beyond this point and is governed by Equation (Bl) etc.

2. *Orbit evolution for wide systems without Roche-lobe overflow.*

In very wide binary systems where the primary star does not fill its Roche-lobe at any stage of its evolution, as far as the orbit evolution is concerned it is assumed to be completely non-conservative, *i.e.* with small amount of mass lost by the primary being accreted by the secondary star. In this case the orbit evolution is governed by (Savonije 1983):

$$\frac{\dot{a}}{a} = -\frac{\dot{M}_1}{(M_1 + M_2)} \tag{B3}$$

where as before M_1 is the mass losing star. The orbit evolution from stage I to stage WR 1, *i.e.* the stage just before the SN explosion of the primary star can be determined by integrating the above equation. The orbit evolution during the explosion of the primary star is determined, as in the case of all other systems from Equation (A3). The Roche-lobe radius of the secondary star determined at a stage after the SN explosion of the primary star indicates that in such systems the secondary star too does not fill its Roche-lobe at any stage of its evolution. The orbit evolution during the stage of mass transfer from the secondary star is thus also governed by Equation (33)

3. *Allowed mass ranges for the primary star.*

For systems evolving through the B^1 B^2 channel, for a given q_i, restrictions can be placed on the masses of the two stars at various stages of evolution such that the orbit evolution *is* completely determined. Under the assumptions that (1) the masses of the two stars are equal at the stage of contact and are equal to 20 $M_\odot$ and (2) the mass transfer is completely conservative before the system comes into contact, the primary mass M_1at the initial stage is related to q_i as,

$$M_{1i} = \frac{40}{1 + q_i} M_\odot. \tag{B4}$$

For systems evolving through the evolutionary channels C^1B^2 and D^1D^2 since the mass is lost from the system from the outset, the secondary star would have to start out with a ZAMS mass of roughly $20M_\odot$ and, to be observed in the given region of interest in the LMC HR-diagram, have a thin layer of helium-enriched matter accreted from the primary's wind. Thus for a given the corresponding ZAMS mass of the primary star is determined in all the cases and the orbit evolution can be uniquely specified within the assumptions stated above.

Appendix C

1. *X-ray luminosity through wind-fed mass transfer.*

The secondary star in binary systems evolving through all the channels mentioned in Section 3 is out of Roche lobe contact immediately following the supernova explosion of the primary. The X-ray luminosity of the system powered by wind from the secondary star to the neutron star is:

$$L_X = \frac{GM_{1f}}{R_{1f}} \dot{M}_X \tag{C1}$$

where $\dot{M}_x$ is the mass accretion rate onto the neutron star. This is related to the stellar wind loss rate of the secondary star by (Henrichs 1983):

$$\frac{\dot{M}_X}{M_{2f}} = \frac{1}{(1+M_{2f}/M_{1f})^2}\left(\frac{v_{\rm orb}}{v_{\rm w}}\right)^4 \frac{1}{(1+\psi(v_{\rm orb}/v_{\rm w})^2)^{3/2}} \qquad \text{(C2)}$$

where $v_{\rm orb}$ is the orbital velocity of the binary system at this stage and $v_{\rm w}$ is the velocity of the stellar wind ejected from the secondary star and ψ is a parameter of the order of unity or less. A value of 2–3 × 10^3 km/s (White 1984) for the wind velocity of the secondary star in the immediate post main sequence region results in negligible X-ray luminosity from the system for any but the closest binary systems (with orbital periods less than a few tens of days). However, White argues that the wind velocities of OB stars in binary systems are likely to be smaller compared to the, corresponding wind velocities from single stars, based on the observations of some Galactic massive X-ray binaries (4U1538–52, Cen X-3 and GX301–2) where the massive star is underfilling its Roche lobe. Smaller wind velocities for the OB-star companions in these systems are required to obtain a better correspondence with their observed X-ray luminosities. In addition, the massive X-ray binary GX301–2 having observed outbursts with a period of 41.5 days and a given ratio of the maximum to minimum X-ray flux during this cycle also require a low wind velocity powering the X-ray emission. The wind velocities in binary systems could be lower either due to the disruption of the wind as the OB star comes close to its critical Roche-lobe, or, due to the ionization of the elements whose line transitions are responsible for the acceleration of the wind by the X-rays. In addition the wind velocities in supergiant stars decrease as the star evolves further into the BSG stage (Kudritzki *et al.* 1988). Thus a value of ≈ 100–300 km/sec used for the wind velocity from the secondary star as it evolves further into the BSG stage, consistent with the stellar wind velocities observed in late B type supergiants (Kudritzki *et al.* 1989) results in weak X-ray emission ($L_{\rm x} \approx 10^{33} - 10^{35}$) ergss^{-1} from binary systems with orbital periods of few years. In such a case, the observed 10 less luminous point sources in the LMC could possibly be systems evolving through the evolutionary channel C^1D^2.

Appendix D

1. *Evolutionary timescales during different evolutionary stages.*

To determine the fraction of binary systems evolving through the various evolutionary channels, a knowledge of the fraction of the total Blue-Supergiant ($3.7 \leqslant \log T_{\rm eff} \leqslant 4.5$) lifetime that is spent in the immediate post main sequence region ($4.3 \leqslant \log T_{\rm eff} \leqslant 4.5$) as well as the X-ray lifetime of the binary systems in the corresponding evolutionary channels are required. The nuclear lifetimes of a 20 $M_\odot$ star are obtained from the evolutionary models incorporating surface helium enrichment. In the case of close binary systems evolving in the evolutionary channels $B^1\,B^2$, $C^1\,B^2$ and $B^1\,S^2$ the actual lifetime in these stages is less than that of nuclear evolution. This is because the secondary fills its Roche-lobe at some stage while it evolves through this region. Immediately following the Roche-lobe contact of the secondary star, there is a rapid loss of its envelope in a common envelope.

For systems in evolutionary channels $B^1\,B^2$ and $C^1\,B^2$, the secondary star while still on the main sequence would underfill its Roche-lobe following the SN explosion of the primary star. The secondary star fills its Roche-lobe as soon as it evolves away

from the main sequence (into the "gap" region). During this stage it appears as a high luminosity X-ray source in the BSG region. Thus,

$$\left(\frac{t_{\mathrm{X}}}{t_{\mathrm{BSG}}}\right) B^1 B^2,\ C^1 B^2 = 1. \tag{Dl}$$

For systems in the evolutionary channel $B^{\mathrm{l}}\ S^2$ the orbit following the supernova explosion of the primary star is relatively wide and the secondary star does not fill its Roche-lobe at this stage or during the immediate post main sequence stage. Its lifetime in the "gap" region is hence dictated by the nuclear timescale of the enriched model and is $\approx 3.2 \times 10^5$ years. During this stage, however, the system would appear as a fairly high luminosity transient X-ray source driven by the stellar wind of the supergiant secondary. From the orbital separation at this stage it can be seen that the secondary star 'is likely to fill its Roche-lobe with further nuclear evolution in the BSG stage. Following this there is again a common envelope evolution and rapid loss of the secondary's envelope terminating the BSG phase. Its BSG lifetime is a sum of nuclear evolution timescale in the "gap" region and the shorter lifetime in the mass transfer stage ($\approx 1.2 \times 10^4$ years). At the end of this phase, the secondary will no longer appear as a blue supergiant. Thus,

$$\left(\frac{t_{\mathrm{X-tr}}}{t_{\mathrm{BSG}}}\right) B^1 S^2 = \frac{3.2 \times 10^5}{3.3 \times 10^5} = 0.96. \tag{D2}$$

For wider binary systems evolving through channels $C^{\mathrm{l}}D^2$ and D^1D^2 the secondary star does not fill its Roche-lobe at any stage of its evolution and hence its lifetime in the "gap" region as well as in the entire BSG region is governed by the nuclear evolution timescales. Systems evolving through the C^1D^2 channel are weakly X-ray active when the secondary star is evolving through the post main sequence region with $L_{\mathrm{x}} \approx 10^{33} - 10^{35}$ ergs/s. The X-ray lifetime during this stage is $\approx 3.2 \times 10^5$ years, dictated by the nuclear evolution timescales through this region. As the secondary star evolves further into the BSG region, it loses some mass in the form of a stellar wind and the system expands. The X-ray luminosity at this stage then goes below the detection limits of the Long, Helfand & Grabelsky (1981) survey and is thus not considered X-ray active during this stage lasting $\approx 5.95 \times 10^5$ years. Thus,

$$\left(\frac{t_{\mathrm{gap}}}{t_{\mathrm{BSG}}}\right) C^1 D^2, D^1 D^2 = \frac{3.2 \times 10^5}{9.15 \times 10^5} = 0.35. \tag{D3}$$

By using the fractional lifetimes in various regions of the HR-diagram and the X-ray stages as obtained above into the Equations (8–10) from Section 3.5.1 the relative fractions of binary systems evolving through the various channels have been obtained. In the above analysis, the BSG lifetimes are different for the different channels since we assume that the BSG phase for the secondary is terminated when its entire envelope is lost, which happens at different phases of evolution in the different channels.

References

Abbot, D. C, Conti, P. S. 1987, *A. Rev. Astr. Astrophys.*, **25**, 113

Arnett, W. D., Bahcall, J. N., Kirshner, R. P., Woosley, S. E. 1989, *A. Rev. Astr. Astrophys.*, **27,** 629.

Bailes, M. 1989, *Astrophys. J.,* **342,** 917.
Blaauw, A. 1961, *Bull. astr. Inst. Netherl.,* **15,** 265.
Blaauw, A. 1985, in *Birth and Evolution of Massive Stars and Stellar Groups,* Eds W. Boland, & H. van Woerden, D. Reidel, Dordrecht, p. 211.
Boersma, J. 1961, *Bull. astr. Inst. Netherl.,* **15,** 291.
Breysacher, K. 1981, *Astr. Astrophys. Suppl.,* **43,** 203.
Breysacher, K. 1986, *Astr. Astrophys.,* **160,** 185.
Brunish, W. M., Truran, J. W. 1982, *Astrophys. J. Suppl.,* **49,** 447.
Caughlan, G. R., Fowler, W. A. 1988, *Atomic Data and Nuclear Data Tables,* **40,** 283.
Chanaa, G. A., Helfand, D. J., Reynolds, S. P. 1984, *Astrophys. J.,* **287,** L23.
Chevalier, R. A., Emmering, R. T. 1986, *Astrophys. J.,* **304,** 140.
Chevalier, R. A., Emmering, R. T. 1989, *Astrophys. J.,* **345,** 931.
Cowley, A. P., Crampton, D., Hutchings, J. B., Helfand, D. J., Hamilton, T. T., Thorstensen, J. R. Charles, P. A. 1984, *Astrophys. J.,* **286,** 196.
de Jager, C, Nieuwenhuijzen, H., van der Hucht, K. A. 1988, *Astr. Astrophys. Suppl. Ser.,* **72,**259.
Drilling, J. 1986, in *IAU Symp. 87:* Hydrogen Deficient Stars and Related Objects, Eds K. Hunger, D. Schönberner & N. Kameshwara Rao, D. Reidel, Dordrecht, p. 9.
Dufour, R. 1984, in *I A U Symp. 108:* Structure and Evolution of the Large Magellanic *Clouds*, Eds S. van den Bergh & K. S. de Boer, D. Reidel, Dordrecht, p. 353.
Filippenko, A. 1991, in *Supernovae and Stellar Evolution*, Eds A. Ray & T. Velusamy, World Scientific, Singapore, in press.
Fitzpatrick, E. L. Garmany, C. D. 1990, *Astrophys. J.,* **363,** 119 (FG).
Flannery, B. P., van den Heuvel, E. P. J. 1975, *Astr. Astrophys.,* **39,** 61.
Habets, G. M. H. J. 1985, *PhD Thesis.* Univ. Amsterdam.
Henrichs, H. F. 1983, in *Accretion Driven Stellar X-ray Sources,* Eds W. H. Lewin, & E. P. J. van den Heuvel, Cambridge Univ. Press, p. 393.
Humphreys, R. M., Blaha, C. 1989, *Astr. J.,* **98,** 1598.
Ilovaisky, S. A. 1983, in *Interacting Binaries,* Eds P. P. Eggleton & J. E. Pringle, *NATO Advanced Study Institute,* p. 205.
Kluzniak, W., Rudermann, M., Shaham, J., Tavani, M. 1988, *Nature,* **334,** 225.
Kudritzki, R. P., Gabler, A., Gabler, R., Groth, H. G., Pauldrach, A. W. A., Puls, J. 1989, in *IAU Coll. 113: The Physics of Luminous Blue Variables,* Eds K. Davidsen, A. F. J. Moffat & H. J. G. L. M. Lamers, Kluwer, Dordrecht, p. 67.
Langer, N. 1989, *Astr. Astrophys.,* **210,** 93.
Long, K. S., Helfand, D. J., Grabelsky, D. A. 1981, *Astrophys. J.,* **248,** 925.
Maeder, A. 1981, *Astr. Astrophys.,* **102,** 401.
Manchester, R. N. Taylor, J. H., Durdin, J. M., Large, M. I., Little, A. G. 1978, *Mon. Not. R. astr. Soc,* **185,** 409.
McConnell, D., McCulloch, P. M., Hamilton, P. A., Abies, J. G., Hall, P. J., Jacka, C. E., Hunt, A. J. 1991, *Mon. Not. astr. Soc,* **249,** 654.
Moffat, A. F. J. 1989, *Astrophys. J.,* **347,** 373.
Moffat, A. F. J., Niemela, V. S., Marraco, H. G. 1990, *Astrophys. J.,* **348,** 232.
Moffat, A. F. J., Vogt, N., Paquin, G., Lamontagne, R., Barrera, L. 1986, *Astr. J.,* **91,** 1386.
McCulloch, P. M., Hamilton, P. A., Abies, J. G., Hunt, A. J. 1983, *Nature,* **303,** 307.
Middleditch, J., Pennypacker, C. R. 1985, *Nature,* **313,** 659.
Nagase, F. 1989, *Pub. astr. Soc. Japan,* **41,** 1.
Nagase, F., Deeter, J., Lewis, W., Dotani, T., Makino, F., Mitsuda, K. 1990, *Astrophys. J.,* **351,** L13.
Narayan, R., Ostriker, J. P. 1990, *Astrophys. J.,* **352,** 222.
Paczynski, B. 1971, *A. Rev. Astr. Astrophys.,* **9**, 183.
Phinney, E. S., Blandford, R. D. 1981, *Mon. Not. R. astr. Soc,* **194,** 137.
Proszynski, M., Przybycien, D. 1984, in *Proc NRAO Workshop: Millisecond Pulsars,* Eds S. P. Reynolds & D. R. Stinebring, NRAO, p. 151.
Ray, A., Rathnasree, N. 1991, *Mon. Not. R. astr. Soc,* **250,** 453.
Sang, Y., Chanmugam, G. 1990, *Astrophys. J.,* **363,** 597.
Savonije, G. J. 1983, in *Accretion Driven Stellar X-ray Sources,* Eds W. H. G. Lewin & E. P. J. van den Heuvel, Cambridge Univ. Press, p. 343.

Seward, F. D., Harnden, F. R., Jr., Helfand, D. J. 1984, *Astrophys. J.,* **287,** L19.
Shu, F. H., Lubow, S. H. 1981, *A. Rev. Astr. Astrophys.,* **19,** 277.
Stone, R. 1979, *Astrophys. J.,* **232,** 520.
Stone, R. 1982, *Astr on. J.,* **87**, 90.
TayJor, J. H., Stinebring, D. R. 1986, *A. Rev. Astrophys.*, **24,** 285.
Thome, K. S., Zytkow, A. 1977, *Astrophys. J.,* **212,** 832.
Trümper, J, Hasinger, G., Aschenbach, B., Brauninger, H., Briel, U. G., Burkert, W., Fink, H., Pfeffermann, E.,Pietsch, W.,Predehl, P.,Schmitt,J.H. M. M., Voges,W.,Zimmermann, U., Beuermann, K. 1991, *Nature,* **349,** 597.
Tuchman, Y., Wheeler, J. C. 1990, *Astrophys. J.,* **363,** 255 (TW).
Tutukov, A. V.,Cherepaschuk, A. M. 1985, *Sov. Astr.,* **29,** 654.
Uomoto, A. 1986, *Astrophys. J.,* **310,** L35.
van den Heuvel, E. P. J. 1983, in *Accretion Driven Stellar X-ray Sources,* Eds W. H. G. Lewin & E. P. J. van den Heuvel, Cambridge Univ. Press, p. 303.
van den Heuvel, E. P. J. 1985, in *Birth and Evolution of Massive Stars and Stellar Groups* Eds W. Boland & H. van Woerden, D. Reidel, Dordrecht, p. 107.
van den Heuvel, E. P. J. 1987, in *JAU Symp. 125: The birth and Evolution of Neutron Stars,* Eds D. Helfand & J. Haung, D. Reidel, Dordrecht, p. 393.
van Oijen, J. G. J. 1989, *Astr. Astrophys.,* **217,** 115.
Wang, Q., Hamilton, T., Helfand, D. J., Wu, X. 1991, *Astrophys. J.,* in press.
Webbink, R. 1979, in *IAU Coll. 53: White Dwarfs and Variable Degenerate Stars,* Eds H. M. van Horn & V. Weidemann, Univ. Rochester, p. 426.
Webbink, R. 1984, *Astrophys. J.,* **277,** 355.
Wheeler, J. C, Levreault, R. 1985, *Astrophys. J.* **294,** L17.
White, N. E. 1983, in *Interacting Binaries,* Eds P. P. Eggleton, & J. E. Pringle, D. Reidel, Dordrecht, p. 249.
Zwicky, F. 1957, in *Morphological Astronomy,* Springer-Verlag, Berlin, p. 258.

J. Astrophys. Astr. (1992) **13**, 53–59

Gamma-Ray Emission from Pulsars

V. B. Bhatia, S. Mishra & N. Panchapakesan *Department of Physics and Astrophysics, University of Delhi, Delhi 110007*

Received 1991 August 22; accepted 1991 December 21

Abstract. We have attempted to devise a scheme by which it may be possible to identify pulsars which are likely to be γ–ray pulsars. We apply this test to a representative population of pulsars and identify the likely candidates for γ emission . We also discuss some individual cases including the Crab and Vela pulsars.

Key words: pulsars, γ–rays

1. Introduction

Emission of radiation from pulsars is a very complex phenomenon. Several models have been proposed to explain this phenomenon, but none are entirely satisfactory. One of the more successful models is the one due to Ruderman & Sutherland (1975). The main feature of this model is the development of polar 'gaps' across which there exist potential differences of the order of 10^{12} V. The self-consistent height of the gap is such that a charged particle traversing the gap picks up enough energy from the potential difference across the gap that it can end up producing an avalanche of electron-positron ($e^- - e^+$) pairs which short the electric field and thereby close the gap. In the Ruderman-Sutherland (RS) scheme the $e^- - e^+$ plasma is essential as it initiates processes which ultimately produce radio emission. In recent years the work of Jones (1985) has cast some doubt on the validity of the RS model. Nevertheless, at present this model is perhaps our best hope of understanding a host of phenomena associated with pulsars.

It has been suggested recently that extremely strong magnetic fields present near the surface of a neutron star do not allow high energy photons to create free $e^- - e^+$ pairs, but convert them instead into bound $e^- - e^+$ pairs, or positronia (Shabad & Usov 1982, 1985; Herold, Ruder & Wunner 1985). The effect of this trapping of photons on the RS model was investigated by us (Bhatia, Chopra & Panchapakesan 1987,1988). We showed that the trapping was energy-dependent and that the photons of low as well as high energy escaped this fate. These photons were available for the production of radio emission. We also showed that the self consistent height of the gap becomes somewhat larger if trapping is taken into account and this actually improves agreement of the RS model with the observations.

In this paper we investigate, within the framework of the RS model, a scheme by which it may be possible to find out whether a given pulsar will be a γ-ray pulsar or not. An alternative model of emission of γ-rays is due to Cheng, Ho & Ruderman (1986) involving the outer gaps in the magneto spheres of pulsars. We also calculate the yield

of γ-rays from pulsars which are likely to emit them. Our calculation takes into account the conversion of photons into positronia by the strong magnetic fields of pulsars. Similar calculations performed by Zhao *et al.* (1989) are flawed on two counts. Firstly, the possibility of photon capture is not taken into account. Secondly, the radius of curvature of the magnetic field near the neutron star surface is taken so large (~ 10^8 cm for a 1-sec pulsar) that it will prevent the formation of gaps, without which there is no RS model. Actually, the radius of curvature adopted by Zhao *et al.* is valid only at large distances from the star (Equation (58) of RS paper). On the other hand, the expression adopted for the critical photon energy above which a photon is absorbed and creates a pair, is true only near the surface of the star. This inconsistency reduces the value of the calculations of Zhao *et al.* Nevertheless, there are some useful ideas in their work, such as the cascading of photons into $e^- - e^+$ pairs.

In Section 2 we discuss briefly the process of conversion of photons into positronia and derive the criterion that a pulsar must satisfy if it is to emit γ-rays. In Section 3 we apply this criterion to a sample population of pulsars and discuss some special cases such as the Crab and the Vela pulsars and millisecond pulsars in binary systems.

2. Criterion for the emission of γ-rays

In our earlier papers we derived the expression for the self-consistent gap height taking into account the conversion of photons into positronia. It is well known that in the presence of a magnetic field both energy and momentum conservation can be satisfied for the conversion of a photon into an $e - e^+$ pair. If the magnetic field be considered along the z-direction, then the momentum conservation relation may be written as

$$k_\perp = (eB/c)(y^- - y^+) \tag{1}$$

where $k_\perp$ is the momentum of the photon perpendicular to B and y^- and y^+ are the y-coordinates of the Landau orbits of e^- and e^+. Equation (1) also holds for the conversion of the photon into a bound $e^- - e^+$ pair if the Coulomb interaction between the pair particles can be considered as perturbation. Since the photon energy is proportional to $k_\perp$ and the positronium energy depends mildly on $k_\perp$, there is a possibility of the dispersion relations, *i.e.*, (ω, $k_\perp$) curves, of the two intersecting and therefore the two having a quantum state with the same energy. However, vacuum polarization correction keeps the two states separated, and this separation is well marked for the ground state of the positronium (Herold, Ruder & Wunner 1985; Shabad & Usov 1985). The gap between the two states is given by

$$\Delta k = \alpha mc^2[\ln\{B^2/(4\alpha^2 B_c^2)\}]^{1/2}(B/B_c)^{1/2}\exp(-B_c/B), \tag{2}$$

assuming $B \ll B_c$, where B_c is the so called critical magnetic field ($B_c = m^2c^3/eh \sim 4.4 \times 10^{13}$ G). In the above equation α is the fine-structure constant. Since the energy of the positronium at the cross-over point, the point where the two dispersion curves crossed (now the degeneracy having been removed by vaccum polarization), is less than the energy of the photon by the amount Δk, the reconversion of the positronium into two or more photons is prohibited. The conversion of a photon into a bound pair takes a time $h/\Delta k$. During this time the photon, travelling straight while the lines of force of the magnetic field curl away, gains in momentum perpendicular to the magnetic field. If the energy gained by the photon is larger than Δk, then the photon

does not get converted into a positronium and will continue as a photon. Thus, the condition for the photon to avoid conversion becomes

$$(\hbar/\Delta k)(\hbar\omega c/\rho) > \Delta k$$

or

$$\omega > (\rho/c\hbar^2)(\Delta k)^2, \tag{3}$$

where ρ is the radius of curvature of the magnetic field and ω is the frequency of the photon. Since the photons are due to curvature radiation, it'is customary to identify ω with the characteristic frequency of curvature radiation, namely,

$$\omega \sim \omega_c = (3/2)(\gamma^3 c/\rho), \tag{4}$$

where γ is the energy in units of mc^2 of the charged particle acquired in travelling a distance *d:*

$$\gamma = e\Omega B d^2/mc^3, \tag{5}$$

where $\Omega = 2\pi/P$, P being the period of the pulsar in sec. Following RS theory, we identify d with the gap height for self-consistency. Then, from Equations (2)–(5) we get the expression for the gap height in the presence of the photon $\Rightarrow$ positronium conversion. It is given by

$$d > (2/3)^{1/6}(P/2\pi)^{1/2}(c^2\rho^2\hbar/m)^{1/6}[2\ln(B/2\alpha B_c)]^{1/6} \times (\alpha B_c/B)^{1/3}\exp(-B_c/3B) \tag{6}$$

where B now is the surface magnetic field of the pulsar. It has been argued by RS that in the neighbourhood of the star the magnetic field is likely to be a mixture of dipole and higher multipole fields and a reasonable value of ρ is 10^6cm. It may be noticed that d has a weak dependence on ρ and therefore a small factor multiplying 10^6 will have not much effect on d. The surface magnetic field of a pulsar is given by the well known expression:

$$B_{12} = 1.01(P\dot{P}_{15})^{1/2}G, \tag{7}$$

where $B_{12} = B/10^{12}$ and $\dot{P}_{15} = \dot{P}/10^{-15}$. After traversing the gap height d, the charged particle (electron or positron) will acquire energy with a typical Lorentz factor given by Equation (5). As these particles move along the magnetic field lines, they emit curvature radiation with photon frequency typically centred at ω_C given by Equation (4). In terms of P and $\dot{P}$, the energy of the curvature photon becomes

$$E_c = 2.61 \times 10^5(P\dot{P}_{15})^{1/2}\ln(2.461 P\dot{P}_{15}) \times \exp[-87.32/(P\dot{P}_{15})^{1/2}]\text{erg}. \tag{8}$$

If this energy exceeds a critical energy E_a given by

$$E_a = 1.5 \times 10^{-2}(P/\dot{P}_{15})^{1/2}(r/R)\text{erg}, \tag{9}$$

then according to Hardee (1977) the photon will be absorbed at a distance r from the centre of the star of radius R at the magnetic axis and will be transformed into a $e^- - e^+$ pair. This expression holds near the surface of the star, therefore $(r/R) \sim 1$. If $E_c \gg E_a$, then the pair particles will also acquire sufficient energy to radiate γ- photons. Zhao *et al.* have estimated that if $E_c > 20E_a$, then it is possible for γ photons to escape the star and make the pulsar a γ–ray pulsar. Thus, for a pulsar to be a potential

γ-emitter the condition $E_c > nE_a (n \sim 20)$ should be satisfied. In the $P - \dot{P}$ plane this criterion takes the form

$$(1.7 \times 10^6/n)\dot{P}_{15} \ln (2.461 P\dot{P}_{15}) \exp[-87.32/(P\dot{P}_{15})^{1/2}] = 1, \quad (10)$$

where we have used Equations (8) and (9)

3. Results and discussion

The usefulness of Equation (10) is obvious. One can check whether a given pulsar is expected to be a γ-pulsar or not. We plot its observed P against observed $\dot{P}$. If this point lies above the curve of Equation (10), the pulsar is expected to be a γ-emitter. This curve is shown in Figure 1 and is labelled as curve 1. In this figure we have also shown a number of pulsars with $B > 3 \times 10^{12}$G, the lower limit of the field for conversion of photons into positronia (Bhatia, Chopra & Panchapakesan 1987), taken from the data collected by Manchester & Taylor (1981). The pulsars which lie above the curve are the likely candidates for γ-ray pulsars. The γ-luminosity of these pulsars can be estimated from the expression (Ruderman & Sutherland 1975; Harding 1981),

$$L_\gamma = \dot{N}\gamma mc^2, \quad (11)$$

where γ is given by Equation (5) and N is the net charged particle flux from the polar cap given by

$$\dot{N} = \pi R_p^2 B/(eP)$$

Table 1. List of pulsars likely to be γ-ray pulsars.

Designation (PSR)	P (sec)	$\dot{P}_{15}$	B_{12}	Predicted γ-luminosity ($h\nu > 1$ MeV) erg sec^{-1}
1831 − 03	0.686	41.5	5.39	1.2×10^{32}
0959 − 54	1.436	51.66	8.70	5.1×10^{32}
1524 − 39	2.417	19.07	6.85	4×10^{32}
1558 − 50	0.864	69.57	7.83	8.3×10^{32}
1727 − 47	0.829	163.67	11.76	8.5×10^{33}
1822 − 09	0.768	52.32	6.40	3.2×10^{32}
1846 − 06	1.451	45.7	8.22	3.9×10^{32}
1916 + 14	1.180	211.4	15.95	3.8×10^{33}
1844 − 04	0.597	51.9	5.62	2.2×10^{32}
1845 − 19	4.308	23.31	10.12	8.6×10^{30}
2002 + 31	2.111	74.57	12.67	2.3×10^{32}
1802 − 23	0.112	110	3.53	1.7×10^{32}
1509 − 58	0.150	1490	15.09	6.5×10^{36}
0531 + 21	0.033	422.4	7.37	1.5×10^{35}*
0833 − 45	0.089	124.7	6.57	1.0×10^{34}*

PSR 1802 – 23 reported by Raubenheimer *et al.* (1986) as emitting high energy γ-rays. PSR 1509-58 observed by Nel *et al.* (1990) at Tev γ-rays with the observed luminosity of 4.7×10^{34} erg sec^{-1}.

*Estimated luminosities of Crab and Vela pulsars with revised magnetic fields (see text).

following the RS theory. Here $R_p = (2/3)^{3/4} R(\Omega R/c)^{1/2}$ is the radius of the polar cap. These luminosities are shown in Table 1. It is worth noting that all the pulsars in Table 1 (which are the ones likely to be γ-ray pulsars) have surface magnetic fields $> 5 \times 10^{12}$G. This is perhaps as well because the minimum strength of the magnetic field for the conversion of a photon into positronium is $\sim 3 \times 10^{12}$G. In this connection it is interesting to note that the pulsars suggested by Zhao *et al.* as possible γ-emitters are not found to be so if we apply the above criterion as they all lie below the curve in Fig. 1. These pulsars are PSR 1951 + 32, PSR 1356–60, PSR 1754–24 and PSR 0740–28. As a matter of fact, none of these have been confirmed as γ–emitters, lending weight to the argument advanced by us.

The Crab and Vela pulsars are also shown in Fig. 1. Both these lie below the curve. Since both these are established γ-emitters, this seems anomalous. The magnetic fields for these pulsars quoted in the literature, $\sim 2 - 3 \times 10^{12}$G, are rather weak. However, it must be remembered that the magnetic fields of pulsars are found from P and $\dot{P}$ by

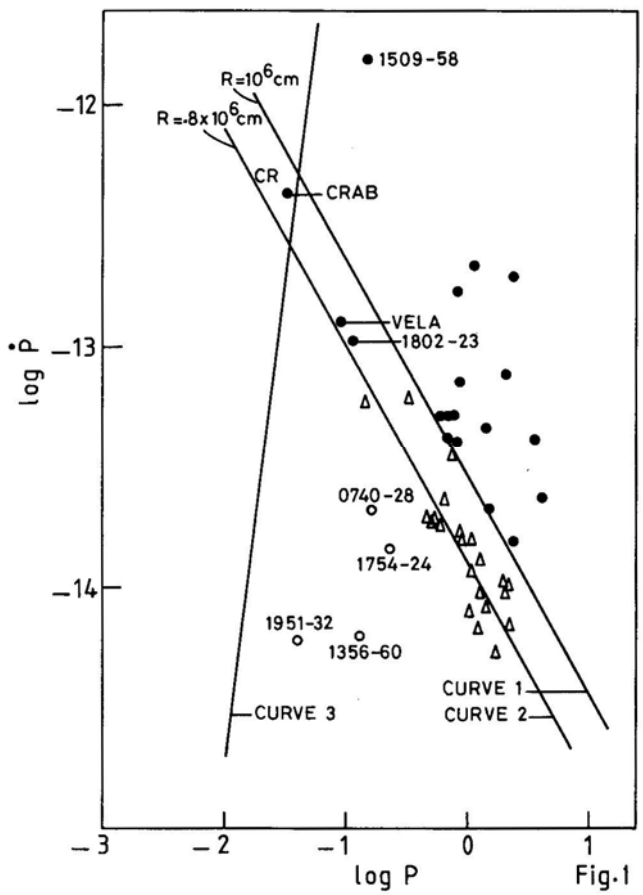

Figure 1. Curve obtained from Equation (10) in the $P - \dot{P}$ plane. The labelling of curves, 1, 2 or 3, is explained in the text. ● – likely emitters of γ-rays, Δ – not likely to emit γ-rays, o – pulsars suggested by Zhao *et al.* as possible emitters of γ-rays but not confirmed so far and unlikely to emit γ-rays if we apply our criterion.

using the following expression derived on the basis of classical dipole radiation,

$$B^2 = [3Ic^3/(8\pi^2 R^6)](P\dot{P}) \tag{12}$$

where I is the moment of inertia of the star. It is customary to adopt $R = 10^6$ cm and $I = 10^{45}$ gm-cm^2 for all stars. But all the stars do not have this precise radius. The various equations of state of the neutron star matter give the radius in the range 7–15 km (see Table 2 in Cutler, Lindblom & Splinter 1990). If we take the radius on the lower side of the range, say, 7 km, and calculate the magnetic fields of the Crab and Vela pulsars, we find them increased by a factor of about two. The point to be emphasized is that the magnetic fields of pulsars estimated by Equation (12) may be uncertain to within a factor of two. If we redraw the curve of Equation (10) with the magnetic field enhanced by a factor of two (the curve is labelled as 2) then we find that both the Crab and the Vela pulsars lie above the curve and their case is no longer anomalous. In fact, the estimated luminosities of these pulsars with the revised magnetic fields are of the same order of magnitude as observed (see Table 1). However, the position of the pulsars mentioned above and suggested by Zhao *et al.* as possible γ-ray emitters does not improve even with respect to the modified curve. It may be pointed out that we have argued elsewhere also (Bhatia, Chopra & Panchapakesan 1987) that the magnetic fields of the Crab and the Vela pulsars may have been underestimated by a factor of 2.

In Fig. 1 we have also drawn the curve one would get from the RS theory in case the conversion of photons into positronia is not operational, that is the magnetic fields are weak. For this curve (labelled as curve 3) we have adopted $\rho = 10^6$ cm (and $n = 20$) to make it consistent with the RS scheme unlike Zhao *et al.* who take $\rho \sim 10^8$ cm. The pulsars likely to emit γ-rays should lie to the left of this curve. In our sample there is hardly any such pulsar, although there could be such cases. So, one could conclude that for a pulsar to be γ-ray emitter it must generally lie above the curve I or it must lie on the left of the curve 3. With the ongoing search for γ-ray pulsars with instruments of decreasing thresholds this prediction is open to verification.

The millisecond pulsars found in binary systems are spun-up pulsars. Here the pulsar is resurrected from a run-down neutron star by accreting matter from its companion. The resulting contraction of the star gives rise to a millisecond period neutron star. These pulsars differ from the usual pulsars as far as the strength of the magnetic field is concerned. The magnetic field of the spun-up pulsars is $\sim 10^8$ G compared to $\sim 10^{12}$ G for the usual pulsars. This low magnetic field does not allow the formation of polar gaps in the manner suggested by the RS theory. Hence the mechanism discussed above for γ-ray emission appears to be inadequate to explain the γ-emission of spun-up pulsars. One will have to seek some other explanation, such as that involving outer gaps (Cheng, Ho & Ruderman 1986).

References

Bhatia, V. B., Chopra, N., Panchapakesan, N. 1987, *Astrophys. Sp. Sci.,* **129,** 271.
Bhatia, V. B., Chopra, N., Panchapakesan, N. 1988, *Astrophys. Sp. Sci.,* **150,** 181.
Cheng, K. S., Ho, C., Ruderman, M. 1986, *Astrophys. J.,* **300,** 495.
Cutler, C., Lindblom, L., Splinter, R. J. 1990, *Astrophys. J.,* **363,** 603.
Hardee, P. E. 1977, *Astrophys. J.,* **216,** 873.
Harding, A. K. 1981, *Astrophys. J.,* **245,** 267.
Herold, H., Ruder, H., Wunner, G. 1985, *Phys. Rev. Lett.,* **54,** 1452.

Jones, P. B. 1985, *Mon. Not. R. ast. Soc,* **216,** 503.
Manchester, R.N.,Taylor, J.H.1981, *Astr.J.,* **86,** 1953.
Nel, H. I., De Jager, O. C, Raubenheimer, B. C, North, A. R., Brink, C. 1990, *Astrophys. J*., **361,** 181.
Raubenheimer, B. C, North, A. R., De Jager, O. C, Van Urk, G., Van Tonder, A. J. 1986, *Astrophys. J.,***307**,L43.
Ruderman, M. A., Sutherland, P. G. 1975, *Astrophys. J.,* **196,** 51.
Shabad, A. E., Usov, V. V. 1982, *Nature,* **295,** 215.
Shabad, A. E., Usov, V. V. 1985, *Astrophys. Sp. Sci.,* **117,** 309.
Zhao, Y., Lu, T., Huang, K., Lu, J., Peng, Q. 1989, *Astr. Astrophys.,* **223,** 147.

J. Astrophys. Astr. (1992) **13,** 61–107

Effects of Rotation on the Colours and Line Indices of Stars 5. The ZRMS and the ZRZAMS

Annamma Mathew* & R. Rajamohan *Indian Institute of Astrophysics, Bangalore 560034*

Received 1991 August 14; accepted 1992 January 15

Abstract. The observed *uvby* and H_β indices of member stars of the Hyades and Praesepe clusters have been analysed in detail for rotation effects. The Alpha Persei, Pleiades and the Centaurus subgroup of the Scorpio–Centaurus association have been reanalysed using the observed indices instead of the extinction-corrected indices used earlier. The observed rotation effects from the analysis of these cluster data are found to be in excellent agreement with the theoretical predictions of Collins & Sonneborn (1977). We have also analysed the β, c and $(u - b)$ values of the member stars of NGC 1976, 2264, 2287, 2422, 4755,1C 2391, IC 2602 and IC 4665 for rotation effects. The results are found to be consistent with the theoretical predictions.

The observed slopes of the rotation effects were used to determine the zero rotation main sequence values of the intermediate band photometric indices for selected clusters. We also corrected the observed indices for each star in each cluster using the theoretical predictions of Collins and Sonneborn and derived the ZRMS values for each cluster. The agreement between the two determinations is found to be good. The various ZRMS curves were utilised to derive the ZRZAMS values. A preliminary calibration of the absolute visual magnitudes as a function of β valid for ZRZAMS has also been derived. The ZRMS values of the intermediate band photometric indices for different clusters and the ZRZAMS values are listed as a function of β.

Key words: stars, rotation—stars, colours—star clusters, individual

1. Introduction

The idea that axial rotation could be determined from the measurements of the widths of spectral lines was first put forward by Captain W. de Abney (1877). Since then many efforts have been made to determine the rotational velocities of various types and groups of stars (see *e.g.* reviews by Huang & Struve 1960; Slettebak 1970; Plavec 1970; Abt 1970). Simultaneously attempts were also made to estimate the changes in the structure of the stars due to rotation and the observable effects such changes would produce (see *e.g.* reviews by Roxburgh 1970; Kraft 1969; Collins 1970).

* on leave from Assumption College, Changanacherry, Kerala.

Broadly, the main results can be summarized as follows. The early type B, A and F main sequence stars rotate fairly fast while stars later than F5 are in general, very slow rotators. Amongst the early-type stars, those that are in binaries are slow rotators on an average than similar single stars, mainly due to the synchronization of rotational and orbital periods. The chemically peculiar (CP) stars of the upper main sequence are in general slow rotators. The differences between field and cluster stars and between cluster and cluster in the observed rotational velocity distribution are caused by differences in binary and CP star frequencies and by the differences in their ages. Even though there seems to be a consensus as far as these results are concerned, the situation regarding the predicted changes in the structure of these stars and their effects on the observable parameters is quite different.

In fact, the results of the analysis of observations by different authors have led to conflicting results on the possible effects of steller rotation on the observable parameters (see *e.g.* the review by Collins 1970). As of today, all existing calibrations of various parameters and the estimates of ages of stars from colour magnitude diagrams have all been done completely disregarding the (predicted) effects due to rotation.

The earliest effort in this field seems to be that of Sweet & Roy (1953) who showed that rotation modifies the luminosity of a star and that it could be as large as one magnitude relative to its non-rotating counterpart. Since then Roxburgh, Griffith & Sweet (1965) Roxburgh & Strittmatter (1965, 1966) Hardorp & Strittmatter (1968) and Collins (1963, 1965), Collins & Harrington (1966) Collins & Sonneborn (1977) and Collins & Smith (1985) have considered in detail the expected rotation effects on the various observable parameters of stars.

In general, such predicted effects in colours and the absolute magnitudes of stars and other observable parameters such as the equivalent widths of the lines are not large excepting in case of extreme rotational velocities. Attempts to verify such predicted effects were made successfully by Strittmatter (1966) in the Praesepe cluster. Strittmatter measured the difference in the observed M_v and the M_v defined by non-rotators at a fixed $(B - V)$. These deviations ΔM_v were found as expected to be proportional to $(V\sin i)^2$ based on Roxburgh & Strittmatter's (1966) work. These results, however, were questioned by Dickens, Kraft & Krzeminski (1968) who found that more accurate data do not show the expected relationship between $(U - B)$ colours and $V\sin i$.

Kraft & Wrubel (1965) attributed the large spread in c_1, $(b–y)$ diagram in Hyades to rotation effects. Strömgren (1967) pointed out that no rotation effects are discernible in the intermediate band indices while Crawford & Barnes (1974) found that the c_1 index was affected by as much as 0.035 magnitudes per 100 km s^{-1} of $V\sin i$ in A stars of α-Persei while the values of B-stars showed no such effects. Hartwick & Hesser (1974) found evidence for rotation effects in the c_1 and β indices of field A and F type stars while Rajamohan (1978) found similar evidence for B and A stars of the α-Persei cluster and the Scorpio-Centaurus association.

Similarly Guthrie (1963) found that rotation effects are indeed discernible in H_β line strengths at a given $(U - B)$ index. The theoretical predictions by Collins & Harrington (1966) are in good agreement with Guthrie's findings. However, Crawford & Manders (1966) and Petrie (1964) found no evidence for effects of rotation on H_β and H_γ line strengths respectively. Warren (1976) discussed the proposed rotation effects in some detail, for B-stars in Orion, and showed that no systematic effects are present for

$V\sin i$ less than 250kms^{-1}. Gray & Garrison (1987, 1988, 1989) from a refined MK classification of A and F type field stars, showed that indeed rotation effects can be clearly established in the intermediate band indices c_1 and β.

No consistent picture had emerged as on 1987 when we took up this work to investigate systematically the effects of rotation on the colours and line indices of stars. We decided to reinvestigate this problem in galactic clusters and determine empirically the effects of rotation on the colours and line indices of stars.

Our attempt since 1987 was to first establish that the effects of rotation on colours are not subtle but are easily discernible provided we choose a sample of single main sequence stars at the same stage of evolution. In Papers 1, 2 and 4 of this series (Rajamohan & Mathew 1988, Mathew & Rajamohan 1990a,b) it was shown that rotation effects in *uvby* H_β and *UBV* colours can be firmly established for B and A stars of Alpha Persei, Pleiades clusters and the Scorpio-Centaurus association. These relative effects were basically established from the observed position of single main sequence stars in a plane defined by a combination of any two of the photometric indices. The Pleiades and Scorpio-Centaurus data were analysed using the indices corrected for interstellar extinction and the data for α-Persei cluster was analysed using the observed as well as the dereddened indices. However, Gray & Garrison (1989) pointed out that the dereddening procedures and the system calibration, especially for the A-stars are themselves affected by rotation. We, have therefore carried out our analysis of a number of clusters using the observed indices. The results which include extensive analysis of the Hyades and Praesepe are given in Section 3. In Section 4, the zero rotation main sequence (ZRMS) values of selected clusters derived are given. The results in Section 4 for various clusters are combined to derive the zero rotation zero age main sequence (ZRZAMS) values of the narrow band photometric indices and is given in Section 5. A preliminary calibration of the absolute magnitudes on the ZRZAMS is also given in this section. A summary of the results is given in the final section.

2. Data and analysis

We clarify a few details of the procedures adopted as this paper summarises the results obtained with our present approach to determine the rotation effects on intermediate band photometric indices. Each star cluster was analysed independently as the member stars are assumed to have formed coevally. This was done to avoid any zero point errors in the photometry of star clusters by different observers and to avoid systematic differences that may exist between clusters due to the differences in the distribution of their rotational velocities. All known double-lined binaries and visual binaries with Δm less than 2.0 magnitudes were excluded from analysis. Am and Ap stars that are single in general were included. However, they were found to deviate in the analysis of the $(u - b)$ index and hence were excluded from the analysis for that index.

The errors in photometry are of the order of ±0.01 magnitudes. The errors in $V\sin i$ generally quoted are of the order of 10 per cent. However, according to Collins the errors in $V\sin i$ derived by conventional methods for stars rotating close to break-up speeds can be as large as 40 per cent. In general, such stars will be classified as *Be* and they have not been included in the analysis.

In principle it is difficult to determine rotation effects on colours as theory predicts

that almost all observable parameters of the stars are affected by rotation and the magnitude of this effect depends for each star on its mass m, true rotational velocity V and i the inclination of the rotation axis to the line of sight. Thus, two objects of differing masses can have identical colour indices due to their differences in V and i (see *e.g.* Collins & Smith 1985).

Another problem is the role of interstellar extinction as both rotation and extinction lead to reddened indices. The determination of the extinction values will be uncertain especially when both effects are comparable and the individual extinction values for each star will be highly uncertain if rotation effects are not allowed for. Also as pointed out by Gray & Garrison (1989), the system calibration and dereddening procedures especially for A-stars are themselves affected by rotation which then would cast some doubt in the determination of colour excess due to extinction. Thus in order to derive the intrinsic parameters for a calibration of indices, we need to correct for extinction and rotation but the calibration procedures depend on an assumed relationship that has not taken rotation into account. Also only V sin i is observable whereas to calibrate we need to know the individual values of V and i. Also quantities such as the mass of the star, which are unaffected by rotation are unkown. Theory also predicts that rotation effects vary as a function of mass and each index varies differently (Collins & Sonneborn 1977; Collins & Smith 1985).

Our approach to this complicated problem was the following. The effect of rotation is to displace the main sequence of a cluster of coeval stars from its non-rotating counterpart and broaden it by about twice the displacement (Collins & Smith 1985). The maximum shift of a single star depends on the maximum rotational velocity that the star can rotate with; this corresponds to the balance between the centrifugal force and gravity at the equator. The distribution of the stars in the band between its zero rotation main sequence (ZRMS) and the critical velocity main sequence (CVMS) depends on the spread in the true rotational velocities of the stars. This spread is not sensitive to i. (Collins & Sonneborn 1977; Collins & Smith 1985).

Therefore one can expect, for a Maxwellian distribution in V and i, the spread to be dependent on the observed (projected) rotational velocity Vsin i as only few objects will be at the tail end of such a distribution. If the spread in the distribution of V is not large as suggested by Rajamohan (1978), the observed main sequence is not expected to show a large spread caused by differences in the observed rotational velocities of the member stars. Even though the effects of the rotation of stars are nonlinear in V and Vsin i, such nonlinearities are important only for rotating close to their break-up speeds ($\omega = 1.0$). Only early B-stars rotate close to their break-up speeds and such objects can be generally recognised by the emission phenomenon associated with them. The maximum observed rotational velocities for others correspond to $\omega \leqslant 0.9$ (Rajamohan 1978). Hence if Be stars are excluded, then the rest of the objects can be expected to show a deviation from the ZRMS which will depend, linearly on the average observed rotational velocities of stars (Collins & Harrington 1966; Mathew & Rajamohan 1990). But the position of the ZRMS is unknown. Hence the following procedure was adopted.

We eliminated in each cluster, known Be stars, SB2's and VB's with Am < 2.0 magnitudes. Only stars of luminosity classes IV and V were considered. In a colour-colour plot, we assume that these apparently single stars will define an average sequence parallel to the ZRMS. A single intrinsic line that defines this mean relationship also

defines the average shift of the main sequence for the mean observed rotational velocities of the cluster members. The advantage of this method is that while we use all stars in a cluster to get a statistically significant sample, the intrinsic differences in the angular momentum distribution at different masses will not affect the results significantly. Errors in photometry and $V\sin i$ determinations cannot completely account for the residual scatter in all these correlation diagrams.

B and A type main sequence members were analysed separately. For each cluster, two indices were plotted against each other and a second order polynomial fit was derived. The observed minus computed (O – C) residuals in each index were determined and plotted against $V \sin i$. A least square fit was derived to determine the rotation effects. The rotation effects determined are relative as both indices are affected by rotation. In general we plotted all other indices against the β index to determine the rotation effects. For selected clusters, the rotation effects were analysed in all possible planes defined by any two of the intermediate band photometric indices.

A list of clusters with available *uvby*, β and $V \sin i$ data was provided by Dr. J. Mermilliod of the University of Lausanne, Switzerland. We analysed the data of most of these clusters in which a statistically significant sample of single main sequence members with known $V \sin i$ values were present. The references to the cluster data utilised in this study are given in Table 1. A final summary of the results of all the clusters analysed is given in Table 2 and the results for all the indices for a few selected clusters are given in Tables 3, 4 and 5.

3. Results

Detailed analysis of the α-Persei cluster, the Pleiades cluster and the Scorpio-Centaurus association have already been published (Rajamohan & Mathew 1988; Mathew & Rajamohan 1990a). For the α-Persei cluster, the analysis was done using observed as well as dereddened indices. However, the other two clusters were analysed after correcting the indices of each star for interstellar extinction. There is some uncertainty in the use of dereddened indices especially for A-stars (Gray & Garrison 1989). Hence we have used observed indices in the analysis even though for clusters analysed by both procedures, the differences were only marginal. One tends to get slightly larger effects if the indices are not corrected for extinction especially in the $(u - b)$ index for B stars.

The slopes of the rotation effects determined in the (β, c) plane and the (β, $u - b$) plane for all the clusters studied are given in Table 2. The symbol Δ is used to denote the residual in a given index in a given plane. For example, in the (β, c) plane, $\Delta\beta$ is defined as the difference between β observed and the calculated β value for its observed c value. Similarly, Δc is defined as the difference between c observed and the calculated c value for its observed β. The calculated values were determined from a second-order polynomial fit to the observed values of β and c.

As in Paper 2 (Mathew & Rajamohan 1990a), the slopes of rotation effects were derived from the theoretical predictions of Collins & Sonneborn (1977). In order to compare the predictions from theoretical models of Collins & Sonneborn (1977), we have analysed the theoretical u, v, b, y and H_β indices in a similar way as we did for the cluster data. For this we have arranged the stars into three groups: B0 to B3, B5

to B9 and A3 to F0. For each group at a given value of i and different values of ω, a second-order polynomial fit was determined for each of the various pairs of colour indices like β versus c_1 β versus $(u - b)$ *etc* and the deviations $\Delta\beta$, Δc, Δ $(u–b)$, $\Delta(b– y)$ etc were determined. This was done for i = 30°, 45°, 60° and 90°. The slopes of the relation between V sin i and the colour excess derived for different values of i are given in Tables 3–5 along with the observed rotation effects in α–Persei, Pleiades, Hyades, Praesepe and the members of the lower and upper Centaurus subgroup of the Scorpio-Centaurus association. The choice of this subgroup is given as an example

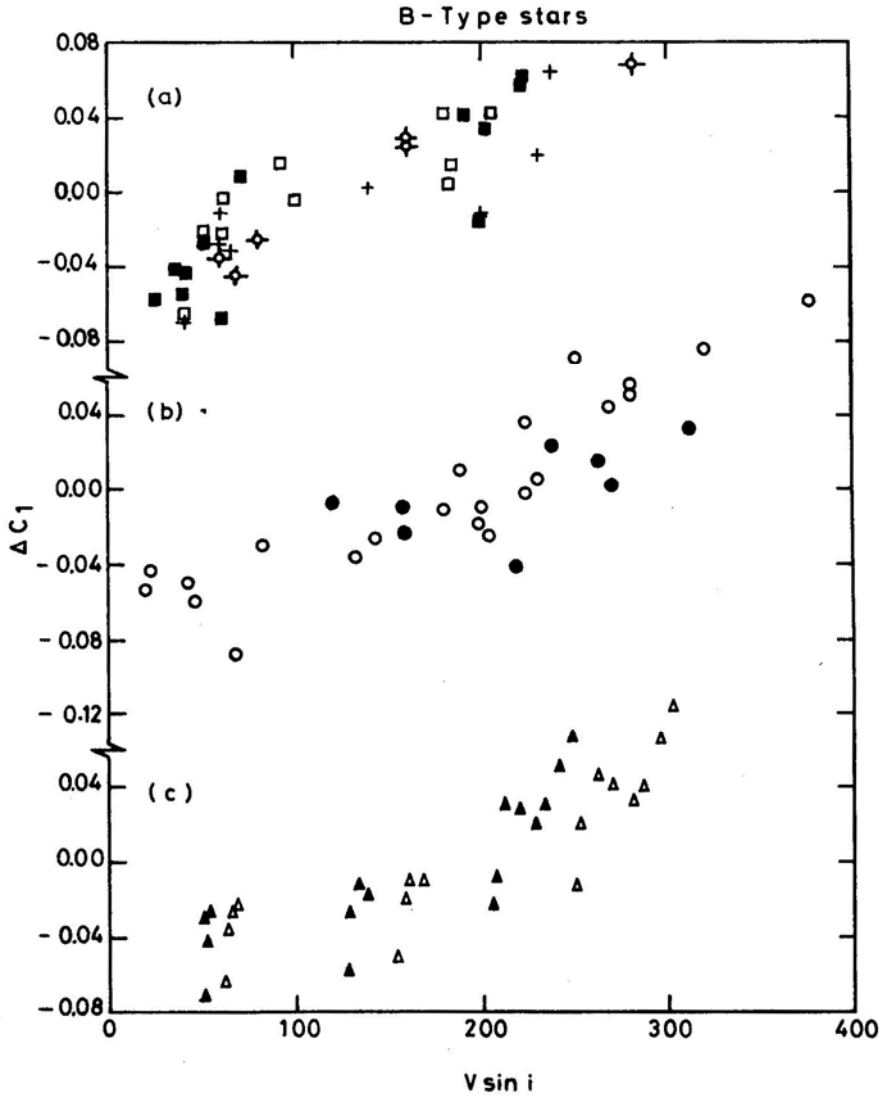

Figure1. Residuals in c_1 derived from the observed mean relationship in the (β,c_1) plane for B-stars are plotted against Vsin i for (a) IC 2391 (squares), IC 4665 (filled squares), NGC 2264 (circles with cross bars) and NGC 2422 (plus); (b) Pleiades (filled circles) and α-Persei (open circles); (c)Residuals derived from the oretical predictions by Collins & Sonneborn (1977) for B5–B9stars for i =45°(filled triangles) and i = 60°(open triangles) are shown for comparison.

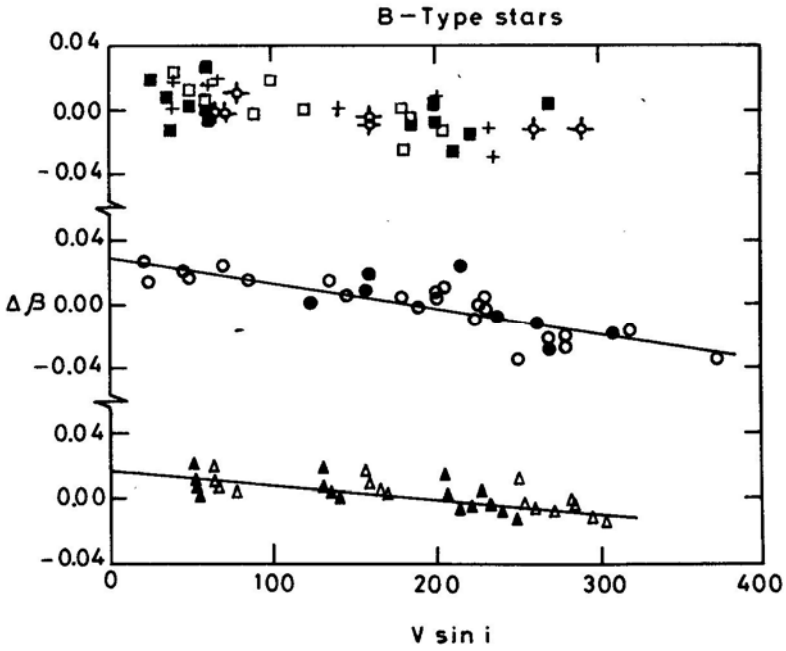

Figure 2. The residuals $\Delta\beta$ derived for B-stars from the (β, c) relationship is plotted against Vsin i. Symbols have the same meaning as in Fig. 1.

as it represents a least reddened sample of pure B2 and B3 main sequence stars. The B5 to B9 range is represented by the α-Persei Bstars while Hyades and Praesepe represent the A3-F2 type domain. The A3 to F2 domain is also represented by the α-Persei and Pleiades clusters.

These results for the B-stars are shown in Figs 1–3. In Figs 1 and 2 the residuals in c_1 and β derived from the (β, c) relationship are plotted against V sin i. The results for the B-stars in α-Persei, Pleiades, IC 2391, IC 4665, NGC 2264 and NGC 2422 have been plotted. We have shown for comparison the theoretically expected relationship for the B5-B9 mass range derived from the calculations of Collins & Sonneborn (1977) for representative i value of 45° and 60°.

Fig. 3 is similar to Fig. 1. The residuals in ($u - b$) derived from the (β, $u - b$) relationship have been plotted. The ($b - y$) results derived from the (β, $b - y$) plane are shown in Fig 4.

Results for the A-stars are shown in Figs 5–9. The deviations in c_1 and β derived from the (β, c) plane have been plotted against V sin i for α-Persei, Pleiades, IC 4665, IC 4756, NGC 2516, Coma, Hyades and Praesepe in Figs 5 and 6. The results from the theoretical predictions for the A3-F2 mass range are also shown for comparison. Similarly $\Delta(u - b)$ from (β, $u–b$) relation, $\Delta(b - y)$ from (c_1, $b - y$) relation and Δm_1 from (c_1 ,m_1) relation have been plotted against V sin i in Figs 7–9 respectively.

It can be easily noticed from Tables 2–5 and Figs 1–9 that the observations are in excellent agreement with the theoretical predictions of Collins & Sonneborn (1977).

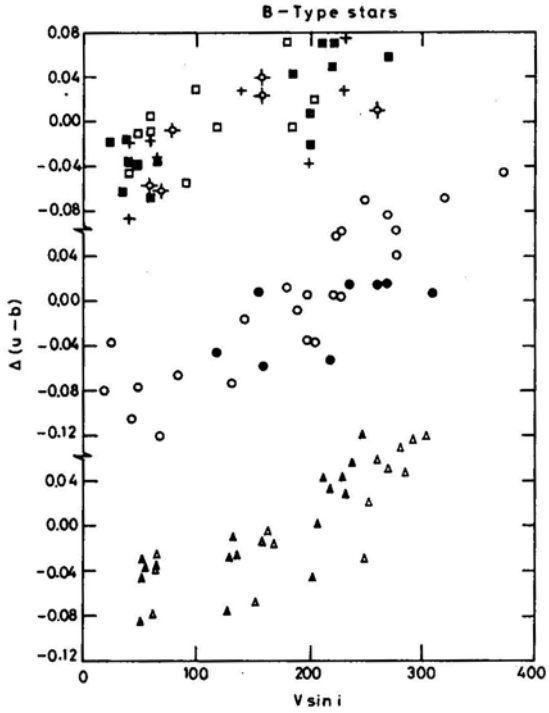

Figure 3. Δ (*u–b)* versus *Visin i* derived for Bstars from the (*β, u–b*) relation. Symbols have same meaning as in Fig. 1.

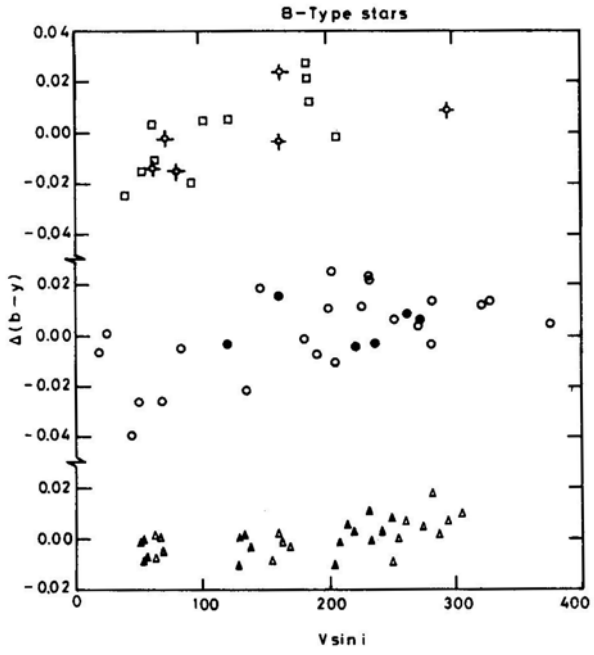

Figure 4. The residuals Δ (*b–y*) for B-stars from the (*β,b—y*) relation is plotted against *V*sin i. Symbols have the same meaning as in Fig. 1.

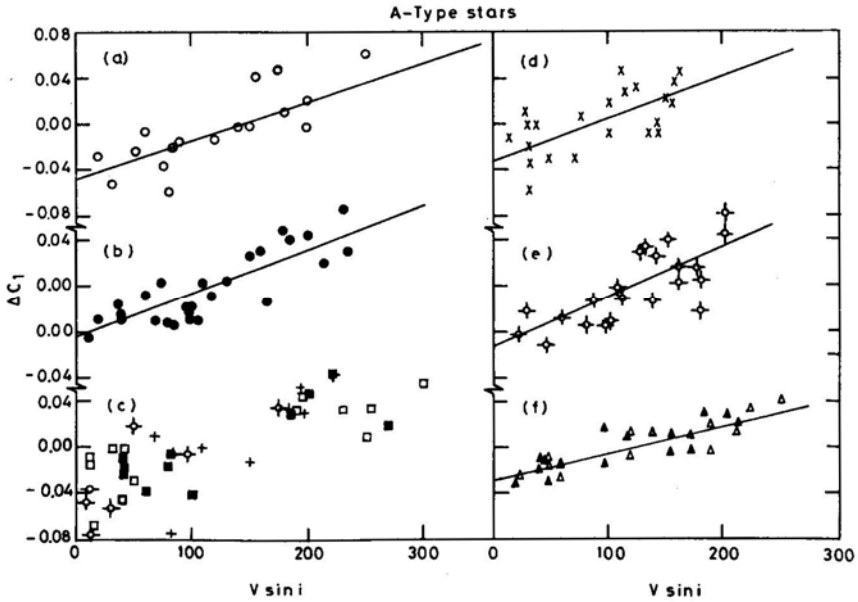

Figure 5. Δc_1 versus $V\sin i$ diagram derived from the (β,c_1) plane for A stars in various clusters (a) O α-Persei (b) ● Pleiades (c) ■ IC 4665. ✣ Coma, + 1C 4756, □ NGC 2516 (d) ×Hyades (e) ✣ Praesepe (f) ▲ $i = 45°$ and $\Delta i = 60°$ derived from theoretical predictions.

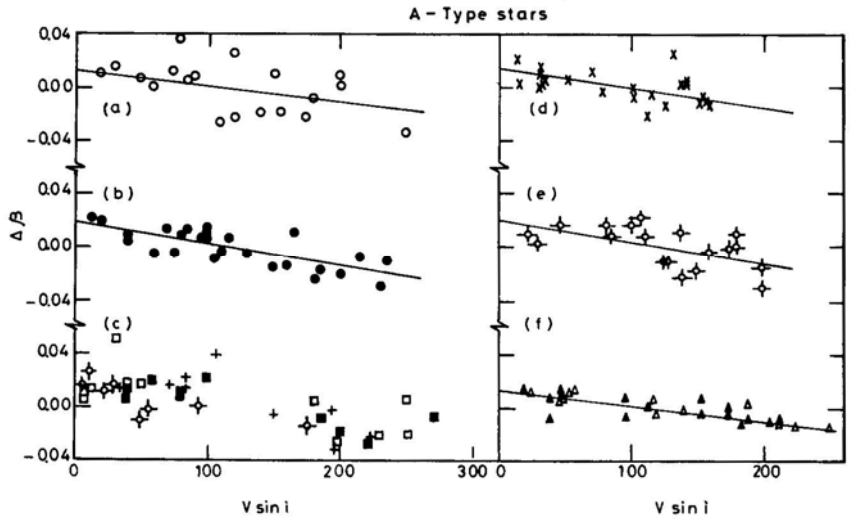

Figure 6. The $\Delta\beta$ versus $V\sin i$ diagram derived from (β,c_1) plane for A-stars in various clusters. Symbols have the same meaning as in Fig. 5.

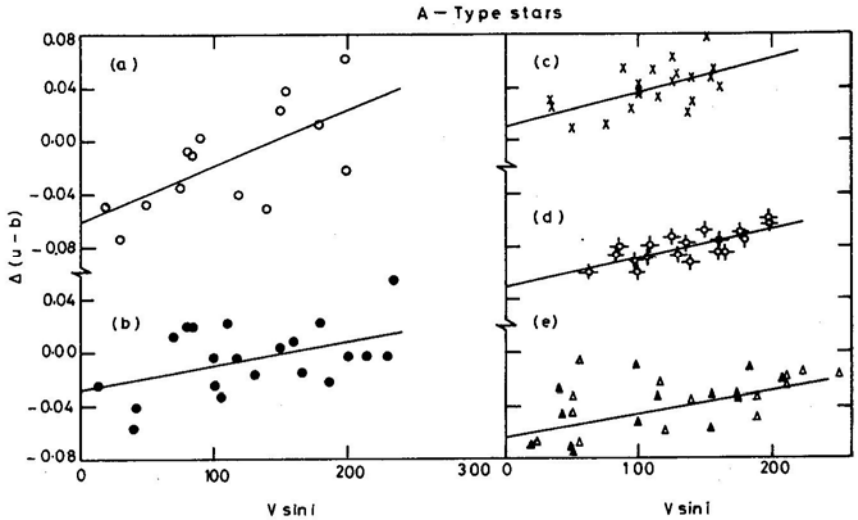

Figure 7. Δ ($u - b$) Vsin i diagram derived from the (β, $u - b$) relationship for (a) α-Persei (b) Pleiades (c) Hyades (d) Praesepe and (e) theoretical predictions for i = 45° and i = 60°.

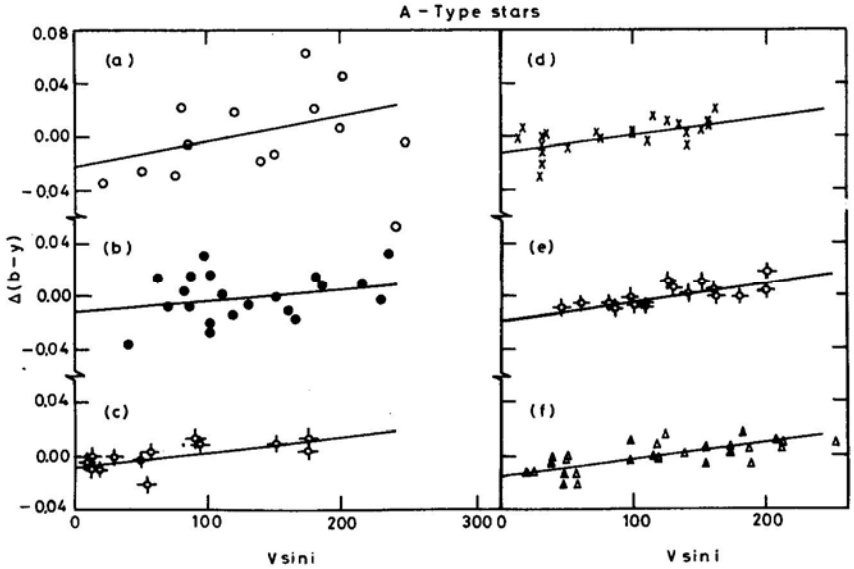

Figure 8. Δ ($b - y$) versus Vsin i diagram from (c_1b–y) plane for A stars in various clusters. Symbols have the same meaning as in Fig. 5.

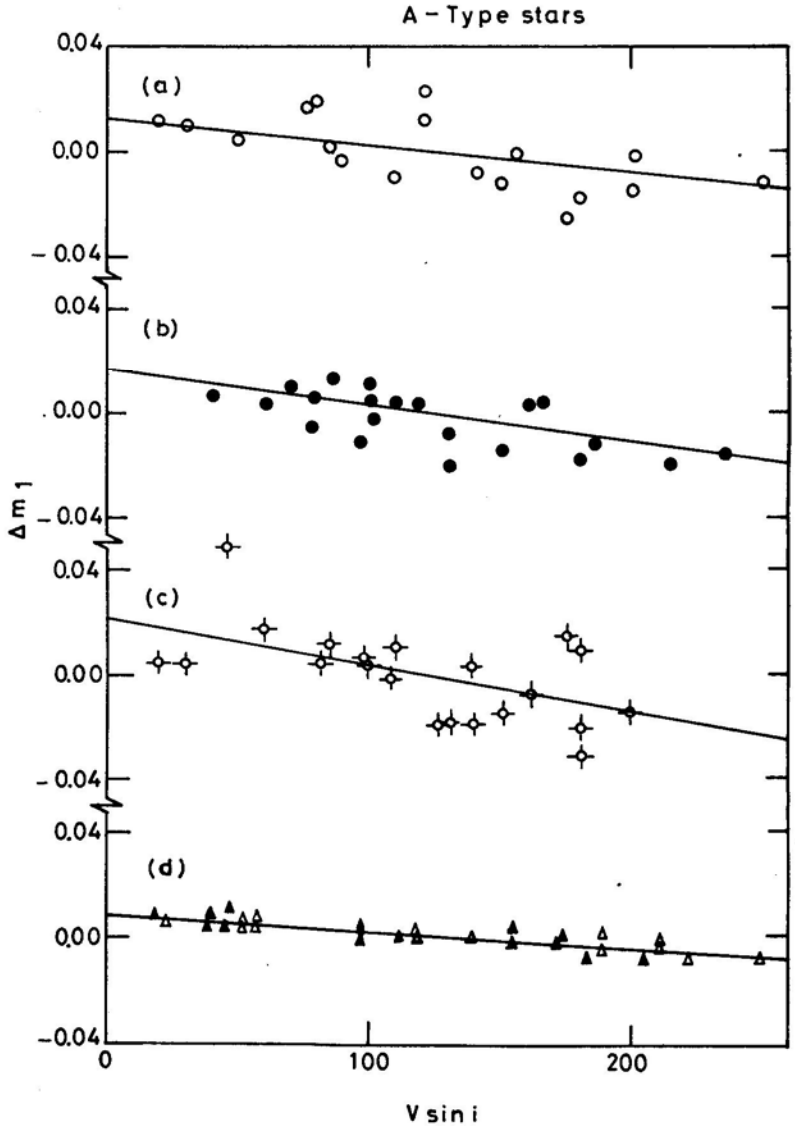

Figure 9. Δm_1 versus $V\sin i$ diagram derived from the (c_1, m_1) relationship for (a) α Persei (b) Pleiades (c) Praesepe and (d) theoretical predictions for $i = 45°$ and 60°.

Table 1. References to cluster data.

Cluster	Data	Reference	Cluster	Data	Reference
α-Persei (mel 020)	$uvbyH_\beta$	Crawford & Barnes (1974)	Coma	$uvbyH_\beta$	Crawford & Barnes (1969)
	UBV	Mitchell (1960)		UBV	Johnson & Kunckles (1955)
	$V\sin i$	Kraft (1967)		$V\sin i$	Kraft (1965)
	ST	Morgan Hiltner & Garrison (1971)		ST	Mendoza (1963)
Pleiades (mel 022)	$uvbyH_\beta$	Crawford & Perry (1976)	Cep OB3	$uvbyH_\beta$	Crawford & Barnes (1970)
	UBV	Johnson & Mitchell (1958)		UBV	Blaauw, Hiltner & Johnson (1959)
	$V\sin i$	Anderson, Stoeckly & Kraft (1966)		$V\sin i$	Garmany (1973)
	ST	Mendoza (1956)			
Hyades (mel 025)	$uvbyH_\beta$	Crawford & Perry (1966)	NGC 1039	$uvbyH_\beta$	Canterna & Perry (1979)
	UBV	Johnson & Knuckles (1955)		$V\sin i$	Ianna (1970)
	$V\sin i$	Kraft (1965)		ST	Ianna (1970) Abt & Levato (1977)
	ST	Morgan & Hiltner (1965)			
Praesepe (NGC 2632)	$uvbyH_\beta$	Crawford & Barnes (1969)	NGC 1976	$uvbyH_\beta$	Warren & Hesser (1977)
	UBV	Johnson (1952)		$V\sin i$	Abt, Muncaster & Thompson (1970)
	$V\sin i$	Mc Gee, Khogali, Baum & Kraft (1967)			Mc Namara & Larson (1961)
	ST	Bidelman (1956)		ST	Abt & Levato (1977)
Sco-Cen	$uvbyH_\beta$	Glaspey (1971)	NGC 2264	$uvbyH_\beta$	Strom, Strom & Yost (1971)
	UBV	Moreno & Moreno (1968)		$V\sin i$	Vogel & Kuhi (1981)
	$V\sin i$	Rajamohan (1976) Slettebak (1968) Uesugi & Fukuda (1982)		ST	Yong (1978)
	ST	Garrison (1967)			
NGC 2287	$uvbyH_\beta$	Nissen (1988) Eggen (1974, 1981)	IC 2391	$uvbyH_\beta$	Perry & Hill (1969)
	$V\sin i$	Levato & Garcia (1984)		$V\sin i$	Levato (1974)
	ST	Hartoog (1976)		ST	Perry & Bond (1969)
NGC 2422	$uvbyH_\beta$	Shobbrook (1984)	IC 2602	$uvbyH_\beta$	Hill & Perry (1969)
	UBV	Hoag *et al* (1961) Smyth & Nandy (1962)		UBV	Braes (1962)
				$V\sin i$	Levato (1975)
	$V\sin i$	Dworetsky (1975)			
NGC 2516	$uvbyH_\beta$	Snowden (1975)	IC 4665	$uvbyH_\beta$	Crawford & Barnes (1972)
	$V\sin i$	Abt & Clements (1969)		UBV	Hogg & Kron (1955)
	ST	Abt & Morgan (1969) Hartoog (1976)		$V\sin i$	Abt & Chaffee (1967)

Table 1. Continued

Cluster	Data	Reference	Cluster	Data	Reference
NGC 4755	$uvbyH_\beta$	Shobbrook (1984)	IC 4756	$uvbyH_\beta$	Schmidt (1978)
	UBV	Perry, Franklin, Landolt & Crawford (1976)		$V \sin i$	Schmidt & Forbes (1984)
	$V \sin i$	Balona (1975)		ST	Herzog, Sanders & Seggewiss (1975)
	ST	Feast (1963) Schild (1970)			
NGC 6475	$uvbyH_\beta$	Snowden (1976)			
	$V \sin i$	Abt & Jewsbury (1969)			

Table 2. Observed reddening due to rotation for 100 kms^{-1} of $V \sin i$.

	from (β, c_1)		from $(\beta, u-b)$	
Cluster	$\Delta\beta$	Δc_1	$\Delta\beta$	$\Delta(u-b)$
Hyades	−.015	.037	−.022	.026
	±.002	±.006	±.005	±.006
Praesepe	−.015	.037	−.028	.022
	±.003	±.006	±.004	±.004
Pleiades	−.017	.039	−.015	.018
A stars	±.002	±.004	±.007	±.006
α-Persei	−.014	.030	.012	.043
A stars	±.004	±.006	± 006	±.008
α-Persei	−.015	.045	−.013	.062
B stars	±.001	±.003	±.001	±.005
IC 4665	−.016	.033		
A stars	±.003	±.006		
IC 4665	−.013	.043	−.010	.045
B stars	±.002	±.007	±.002	±.005
NGC 2264	−.008	.038	−.007	.052
	±.001	±.006	±.001	±.001
IC 2391	−.016	.038	−.019	.066
	±.003	±.007	±003	±016
IC 2602	−.013	.036	−.012	.057
	±.004	±.011	±.004	±.015
NGC 2422	−.013	.032	−.013	.036
	±.003	±.008	±.004	±.011
NGC 4755	−.011	.032	−.008	.031
	±.002	±.005	±.002	±.007
Scorpio-	−.007	.028	−.006	.033
Centaurus	±.001	±.003	±.001	±.004
NGC 2287	−.006	.020	−.026	.064
	±.004	±.024	±.007	±.016
NGC 1976	−.007	.032	−.002	.013
	±.003	±.011	±.002	±.011

Table 3. Theoretical reddening due to rotation for 100 km s^{-1} of $V \sin i$ for B0 to B3 stars.

	from (β, c_1)		from $(\beta, b-y)$		from $(\beta, u-b)$		from (β, m_1)		from $(c_1, b-y)$	
i	$\Delta\beta$	Δc_1	$\Delta\beta$	$\Delta(b-y)$	$\Delta\beta$	$\Delta(u-b)$	$\Delta\beta$	Δm_1	Δc_1	$\Delta(b-y)$
30	−.004	.021	−.004	.004	−.004	.027	.003	−.001	−.001	.001
	±.000	±.002	±.000	±.000	±.000	±.003	±.001	±.000	±.001	±.000
45	−.003	.016	−.004	.003	−.003	.022	.002	−.001	−.004	.001
	±.000	±.002	±.000	±.000	±.000	±.003	±.001	±.000	±.001	±.000
60	−.003	.016	−.004	.003	−.003	.021	.001	.000	−.003	.001
	±.000	±.002	±.000	±.000	±.000	±.002	±.000	±.000	±.001	±.000
90	−.003	.015	−.003	.003	−.003	.021	.001	−.000	−.002	.001
	±.000	±.002	±.000	±.000	±.000	±.002	±.000	±.000	±.001	±.000
	Observed reddening due to rotation for 100 km s^{-1} of $v \sin i$ for B0, B3 stars.									
Upper-Cen + Lower-Cen B2, B3 stars	−.005	.017	−.004	.000	−.006	.028	−.002	.001	−.002	−.001
	±.002	±.006	±.003	±.002	±.001	±.006	±.003	±.001	±.009	±.001

Theoretical reddening due to rotation for 100 km s^{-1} of $V \sin i$ for B0, B3 stars.

	from $(c_1, u-b)$		from (c_1, m_1)		from $(b-y, u-b)$		from $(b-y, m_1)$		from $(u-b, m_1)$	
i	Δc_1	$\Delta(u-b)$	Δc_1	Δm_1	$\Delta(b-y)$	$\Delta(u-b)$	$\Delta(b-y)$	Δm_1	$\Delta(u-b)$	Δm_1
30	.001	−.001	.038	−.001	.001	−.004	.006	−.001	.050	−.001
	±.000	±.001	±.005	±.000	±.000	±.001	±.001	±.000	±.007	±.000
45	.001	−.001	.028	−.001	.001	−.004	.005	−.001	.038	−.001
	±.000	±.001	±.003	±.000	±.000	±.001	±.001	±.000	±.004	±.000
60	.000	.000	.020	.001	.001	−.004	.004	−.001	.027	−.001
	±.000	±.000	±.003	±.000	±.000	±.001	±.001	±.000	±.004	±.000
90	.000	.000	.018	−.001	.001	−.004	.003	−.001	.025	−.001
	±.000	±.000	±.003	±.000	±.000	±.000	±.000	±.001	±.004	±.000
	Observed reddening due to rotation for 100 km s^{-1} of $V \sin i$ for B2, B3 stars.									
Upper-Cen	.000	−.000	.010	−.001	−.002	−.001	−.002	.000	.006	−.001
Lower-Cen	±.003	±.004	±.013	±.001	±.001	±.011	±.003	±.002	±.017	±.001
B2, B3 stars										

Table 4. Theoretical reddening due to rotation for 100 km s^{-1} of $V \sin i$ for B5 to B9 stars.

	from (β, c_1)		from $(\beta, b-y)$		from $(\beta, u-b)$		from (β, m_1)		from $(c_1, b-y)$	
i	$\Delta\beta$	Δc_1	$\Delta\beta$	$\Delta(b-y)$	$\Delta\beta$	$\Delta(u-b)$	$\Delta\beta$	Δm_1	Δc_1	$\Delta(b-y)$
30	−.014	.058	−.010	.006	−.012	.066	.007	−.001	.006	.000
	±.002	±.007	±.003	±.002	±.002	±.009	±.001	±.000	±.005	±.002
45	−.011	.046	−.009	.005	−.010	.054	.006	−.001	.000	.000
	±.001	±.005	±.002	±.001	±.002	±.007	±.001	±.000	±.004	±.001
60	−.010	.041	−.008	.005	−.009	.049	.005	−.001	.001	.000
	±.001	±.004	±.002	±.001	±.001	±.006	±.001	±.000	±.003	±.001
90	−.009	.038	−.007	.005	−.008	.047	.002	−.000	.000	.000
	±.001	±.004	±.002	±.001	±.001	±.005	±.000	±.000	±.003	±.001
	Observed reddening due to rotation for 100 km s^{-1} of $V \sin i$ for α-Persei B stars.									
α-Persei	−.015	.045	−.017	.010	−.013	.062	.007	−.002	−.013	.002
B stars	±.001	±.003	±.005	±.002	±.001	±.005	±.005	±.002	±.015	±.002

Theoretical reddening due to rotation for 100 km s^{-1} of $V \sin i$ for B5 and B9 stars.

	from $(c_1, u-b)$		from (c_1, m_1)		from $(b-y, u-b)$		from $(b-y, m_1)$		from $(u-b, m_1)$	
i	Δc_1	$\Delta(u-b)$	Δc_1	Δm_1	$\Delta(b-y)$	$\Delta(u-b)$	$\Delta(b-y)$	Δm_1	$\Delta(u-b)$	Δm_1
30	.007	−.009	.087	−.004	.000	−.010	.009	−.004	.106	−.004
	±.002	±.003	±.009	±.001	±.001	±.006	±.002	±.001	±.013	±.001
45	.005	−.006	.070	−.003	.001	−.006	.008	−.003	.085	−.003
	±.002	±.003	±.006	±.001	±.001	±.005	±.001	±.001	±.008	±.001
60	.003	−.004	.050	−.002	.000	−.004	.005	−002	.060	−·002
	±.001	±.002	±.006	±.000	±.001	±.004	±.001	±.001	±.008	±.000
90	.003	−.004	.047	−.002	.000	−.004	.005	−.002	.057	−.002
	±.001	±.002	±.005	±.000	±.000	±.003	±.001	±.001	±.007	±.000
	Observed reddening due to rotation for 100 km s^{-1} of $V \sin i$ for B stars.									
α-Persei	.005	−.009	.072	−.007	.003	−.024	.012	−.006	.096	−.006
B stars	+.002	±.004	±.015	±.001	±.002	±.019	±.004	±.002	±.022	±.001

Table 5. Theoretical reddening due to rotation for 100 km s^{-1} of $V \sin i$ for A3 to F0 stars.

	from (β, c_1)		from $(\beta, b-y)$		from $(\beta, u-b)$		from (β, m_1)		from $(c_1, b-y)$	
i	$\Delta\beta$	Δc_1	$\Delta\beta$	$\Delta(b-y)$	$\Delta\beta$	$\Delta(u-b)$	$\Delta\beta$	Δm_1	Δc_1	$\Delta(b-y)$
30	−016	.035	.003	.003	−.003	.033	.009	−.004	.041	.020
	±.002	±.004	±.002	±.002	±.007	±.006	±.002	±.001	±.006	±.003
45	−.012	.027	.000	.000	−.022	.022	.005	−.002	.026	.013
	±.001	±.003	±.001	±.001	±.005	±.005	±.001	±.000	±.005	±.002
60	−.011	.022	−.002	−.001	−.018	.017	.003	−.001	.019	.009
	±.001	±.003	±.001	±.001	±.004	±.004	±.001	±.000	±.004	±.002
90	−.008	.016	−.002	−.002	−.011	.010	.002	−.001	.012	.006
	±.001	±.003	±.001	±.001	±.004	±.003	±.001	±.000	±.003	±.002
	Observed reddening due to rotation for 100 km s^{-1} of $V \sin i$ for A-type stars.									
α-Persei	−.014	.030	−.013	.007	.012	.043	.068	−.016	.065	.019
	±.004	±.006	±.005	±.005	±.014	±.008	±.006	±.002	±.012	±.006
Pleiades	−.017	.039	−.012	−.013	−.015	.018	.041	−.011	.023	.008
	±.002	±.004	±.004	±.004	±.007	±.006	±.002	±.002	±.010	±.005
Hyades	−.015	.037	−.004	−.003	−.022	.026	.003	−.002	.028	.013
	±.002	±.006	±.003	±.003	±.005	±.006	±.003	±.002	±.006	±.003
Praesepe	−.015	.037	−.018	−.017	−.028	.022	.003	−.004	.035	.015
	±.003	±.006	±.002	±.002	±.004	±.004	±.003	±.002	±.005	±.002

Table 5. Continued.

	from $(c_1, u-b)$		from (c_1, m_1)		from $(b-y, u-b)$		from $(b-y, m_1)$		from $(u-b, m_1)$	
i	Δc_1	$\Delta(u-b)$	Δc_1	Δm_1	$\Delta(b-y)$	$\Delta(u-b)$	$\Delta(b-y)$	Δm_1	$\Delta(u-b)$	Δm_1
30	−.038	.017	.055	−.011	.036	.035	−.006	−.003	.042	−.018
	±.013	±.005	±.007	±.001	±.009	±.007	±.003	±.001	±.007	±.003
45	−.021	.010	.037	−.008	.022	.021	−.005	−.002	.027	−.012
	±.009	±.004	±.005	±.001	±.007	±.005	±.002	±.001	±.005	±.002
60	−.015	.007	.028	−.006	.017	.015	−.004	−.002	.020	−.009
	±.007	±.003	±.004	±.001	±.005	±.004	±.002	±.001	±.004	±.002
90	−.007	.003	.021	−.005	.010	.008	−.004	−.002	.012	−.006
	±.007	±.003	±.004	±.001	±.005	±.004	±.002	±.001	±.004	±.002
	Observed reddening due to rotation for 100 km s^{-1} for A-type stars.									
α-Persei	.038	.018	.145	−.010	−.013	.050	−.040	−.007	.065	−.006
	±.020	±.009	±.016	±.003	±.012	±.012	±.007	±.002	±.013	±.003
Pleiades	.059	−.014	.125	−.014	−.021	−.004	−.048	−.013	.029	−.008
	±.018	±.009	±.011	±.002	±.012	±.011	±.005	±.002	±.010	±.003
Hyades	.021	−.009	.017	−.007	−.016	−.029	.004	−.025	.021	−.014
	±.041	±.005	±.025	±.003	±.006	±.008	±.013	±.003	±.007	±.003
Praesepe	.066	−.030	.025	−.013	−.016	.000	−.011	−.016	−.002	−.003
	±.014	±.006	±.023	±.003	±.005	±.005	±.008	±.004	±.008	±.003

4. Zero rotation main sequence (ZRMS) of selected star clusters

As the distance scale of the Universe is literally based on the observations of the nearby Hyades cluster, we first discuss the determination of the Hyades ZRMS. The observed colour indices are of course free of interstellar extinction for this cluster. We took two approaches to the determination of ZRMS values for each clusters.

4.1 *ZRMS from Observed Slopes of Rotation Effects*

In this approach, the observed rotation effects in different planes listed in Tables 2–5 were utilised to derive the ZRMS values as a function of β. This table does not reflect the true effects due to rotation as the slopes determined are relative. In these determinations two photometric quantities, say X versus Y are plotted and a polynomial fit is derived. The residuals ΔX in X at the observed value of Y and ΔY in Y at the observed value of X are plotted against V sin i to determine the rotation effects. The observed effects are therefore relative and the true effects cannot be determined unless one of the quantities X or Y is independent of rotation, such as the mass of the star.

However, we can use the slope of the relationship between ΔX and V sin i or ΔY and V sin i to determine where the nonrotating sequence actually lies. This can be done by shifting the observed points either in X or Y by an amount corresponding to its observed V sin i value. Even though the shifted value for each star does not correspond to the appropriate ZRMS value for its mass, the locus of the shifted positions of all stars would define the ZRMS in that plane. This method should work as long as the relationship between X and Y is not highly nonlinear and also that ΔX and ΔY are not highly nonlinear with V sin i. The analysis of B and A stars independently should partially take care of such nonlinearity in the relationship between different quantities. Also for ω up to 0.9 ($V \leqslant 250 \mathrm{kms}^{-1}$), the residuals can be expected to be linear (see Fig. 17 of Collins & Harrington 1966 and Fig. 5 of Collins & Smith 1985).

This was the logic followed for deriving the ZRMS values of different indices for each cluster from observationally determined slopes.

4.2 *ZRMS from Theoretical Predictions*

As the analysis of observations are in excellent agreement with theoretical predictions of Collins & Sonneborn (1977) one can in principle utilize the predicted effects to correct the observed data for each star to derive its ZRMS value. However, the value of i, the inclination between the rotation axis and the line of sight remains unknown. But we can derive the average ZRMS curve statistically based on the assumption that i is close to 60°.

Collins & Sonneborn (1977) list the effects as a function of mass for various values of V and i. They have also given the other indices like $(b - y)_0$ *etc.* as a function of mass. Collins & Smith (1985) have also listed the Zero Rotation Zero Age values as a function of mass for the A-stars. As the values in the latter paper appear to be more consistent with observations, we have combined the two tables appropriately to derive the theoretical values of $(b–y)_0$ m_0 and c_0 as a function of mass.

The calculations of rotation effects by Collins & Sonneborn (1977) for the mass range 14.5.$M_\odot$ to 1.5 $M_\odot$ for ω = 0.2 and ω = 0.9 and i = 60° were used to produce a table of average corrections in β, c_1,$(b-y)$, $(u-b)$ and m_1 for 100 km s^{-1} of V sin i. This is given in Table 6. The results from Collins & Smith (1985) were appropriately combined with those of Collins & Sonneborn (1977) to get the corresponding values of $(b-y)_0$ *etc* for the entire mass range. The table for rotation corrections in different indices were listed as a function of $(b-y)_0$ as the masses of stars are unknown. For A-stars the observed $(b-y)_0$ value was used to get the first set of corrections in $(b-y)$, $(c_1\ u-b)$, m_l and β. The corrected $(b-y)$ was used to derive a second set of corrections in $(b-y)$, c_1 *etc.* The average of these two sets was used to correct each and every star for its observed value of V sin i For B-stars, we followed the same procedure using the observed $(u-b)_0$ index instead of the $(b-y)_0$ index.

4.3 *ZRMS of Hyades*

4.3.1 *ZRMS values of β and c_1*

The observed rotation effects listed in Table 5 were used to correct, β and c_1 in the (β,c_1) plane. We denote these corrected indices as β_{ZR} and c_{1ZR} respectively.

As mentioned in the previous section we plot β_{zr} versus c_1 and $c1ZR$ versus β. The locus of these two plots should coincide. These are shown in Fig. 10(a). A least-square fit to the data points in the figure was derived to detemine the $(\beta_{ZR},\ c_{1ZR})$ relationship for Hyades. We list these ZRMS values (at equal intervals of β) in Table 7. β is chosen as an independent parameter following Crawford as it is free of instersteller extinction. The range in β for which the ZRMS values are listed corresponds to the observed range of β in Hyades.

Similarly, following Method lb, we use the theoretical corrections listed in Table 6 to correct the individual stars in β and c_0 . The corrected position and the least-square fit to the data points are shown in Fig. 10(b). The derived ZRMS values are given separately in Table 7.

The observed values of β and c_1 for all stars together with the ZRMS given in Table 7 are shown in Fig. 10(c). The Am stars are shown as filled circles, the apparent normal single stars are plotted as open circles and the SB2's and VB's with Δm < 2.0 mag as crosses.

4.3.2 *ZRMS values of* $(b-y)$

From Tables 4 and 5 we see that in the $(\beta,\ b–y)$ plane, rotation effects are negligible, while in the $(c_1\ b-y)$ plane they are discernible. The first set of $(b-y)_{ZR}$ values was derived from a least-square fit between β and $(b-y)$. A second set was derived by correcting for rotation effects in the $(c_1\ b-y)$ plane following procedures already described in the case of β, c_1 . Now the $(b-y)_{ZR}$ values that correspond to β_{ZR} and c_{ZR} listed in Columns 1 and 4 of Table 7 were calculated. The $(b-y)_{ZR}$ values from both these methods were found to agree very well. The average of the two values is listed in Column 2 of Table 7.

The same values derived by using Method lb are listed in Column 7 of Table 7. The observed positions of stars together with the ZRMS derived from observed slopes in the $(\beta,\ b-y)$ plane are shown in Fig 11 (a).

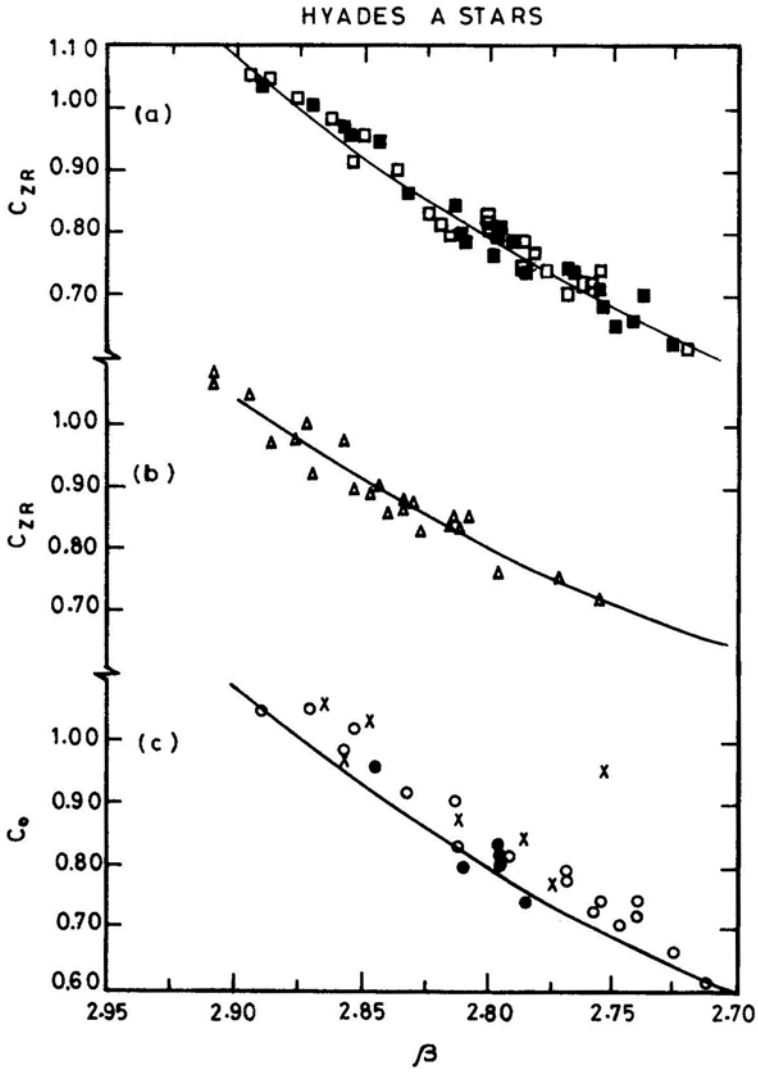

Figure 10. The ZRMS of Hyades cluster in the spectral type range A3-F0.
(a) Corrected positions of stars in the (c_1, β) plane. Each star has been plotted twice; the observed c_1 value versus β corrected for rotation effect and the c_1 value corrected for rotation versus the observed β value have been plotted. The locus defined by the leasts-quare fit to the data points which defines the zero rotation values from observed slopes of rotation effects is shown by a continuous line, (b) The c_0 and β index independently corrected for rotation effects for each star is shown. The least-square fit is shown by the continuous line which defines the zero rotation values determined from theoretically derived slopes for i = 60° from the work of Collins & Sonneborn (1977), (c) The observed position of all stars have been plotted in the c_0, β plane. The continuous line is the ZRMS determined from (a).

4.3.3 *ZRMS values of* (u– b)

Following procedures set up for c_1 and (b – y), the $(u - b)_{ZR}$ values derived from observed effects (Method la) are listed in Column 5 of Table 7 and those derived from theoretical expectations (Method lb) are listed in Column 10 of Table 7.

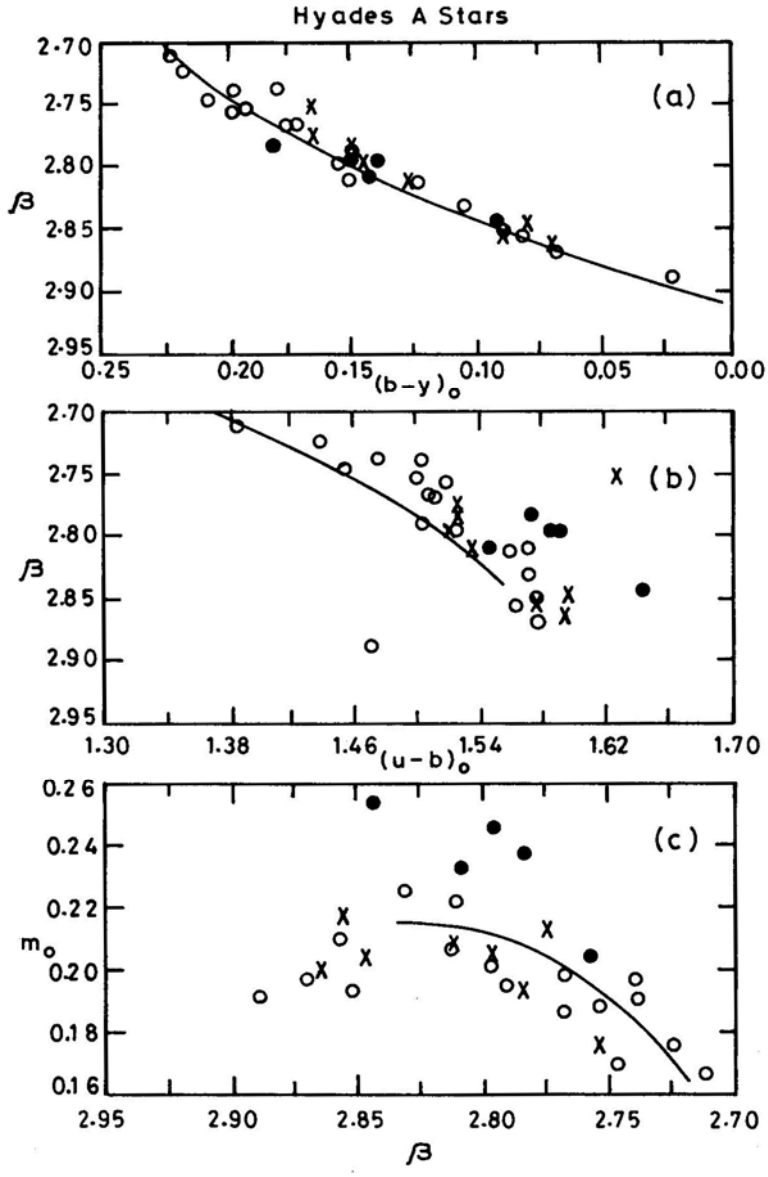

Figure 11. Same as Fig. 10 (a) The observed (*ß, b – y*) values of Hyades stars are plotted. The ZRMS locus determined from observed slopes of rotation effects is shown as a continuous line, (b) & (c): Same as (a) in the (*ß, u – b*) and *ß, m*$_1$ planes.

The (*ß, u – b*) ZRMS curve together with the observed (*ß,u – b*) values of the Hyades members is shown in Fig. 11 (b).

4.3.4 *ZRMS values of* m_1

The ZRMS values of m_1 were calculated from the observed rotation effects in the (*ß*, m_1) plane and (c_1 m_1) plane. The average value of m_{1ZR} thus derived was compared

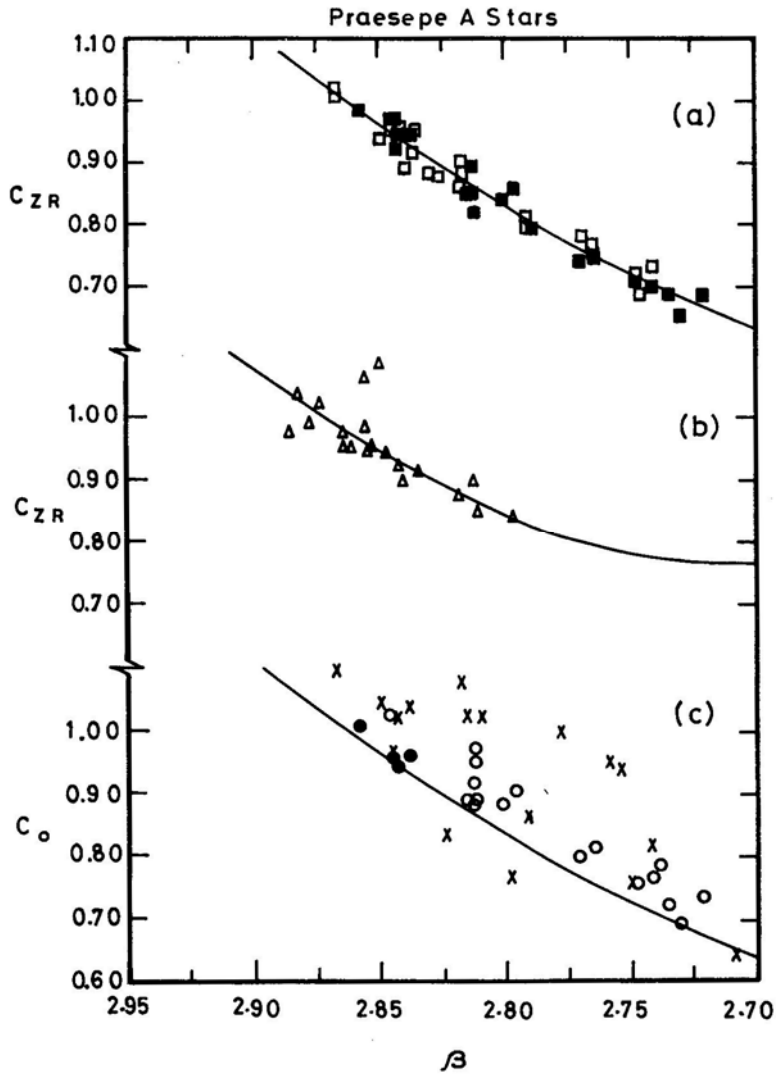

Figure 12. Same as Fig. 10 for the Praesepe cluster. (a) ZRMS values of (β, c_1) of Praesepe stars and the ZRMS curves from observed slopes of rotation effects. (b) ZRMS values of members and ZRMS curves from theoretical slopes of rotation effects. (c) Observed position of stars and the ZRMS curve from observed slopes of rotation effects.

With the m_{1zr} calculated from c_{1zr}, $(b–y)_{zR}$ and $(u–b)_{zR}$ derived in earlier sections. We find that for mid-values of β in Table 7 the two agree, while at the two end of the β range, the differences are of the order of 0.02 magnitudes.

We also calculate m_1 using Method 1b and find that it agrees very well with m_1 calculated from $(b–y)$, $(c_1, u – b)$.

The observed values of β, m_1 and the observed (β_{zR}, m_{1zR}) relation for Hyades are shown in Fig. 11(c).

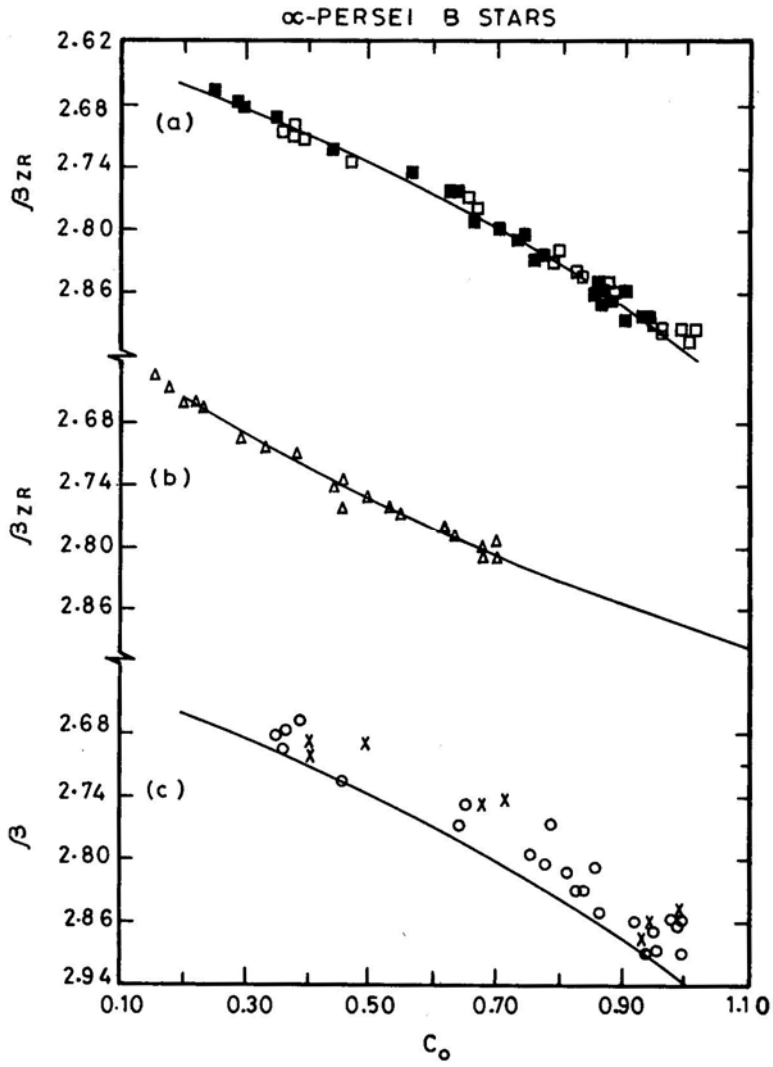

Figure 13. Same as Figs 10 and 12 for α–Persei B stars.

4.4 *ZRMS of Praesepe*

Procedures exactly similar to those followed for Hyades were used to determine the ZRMS of Praesepe. No interstellar extinction corrections are needed for this cluster either. The ZRMS derived from observed rotation effects (Method 1a) is listed in Table 8. The ZRM Svalues derived from predicted effects from theory (Method 1b) are also listed in Table 8 (Columns 6 to 10). The ZRMS values derived from theory seem to give consistently larger values for all indices (at a give β) for the late A-stars.

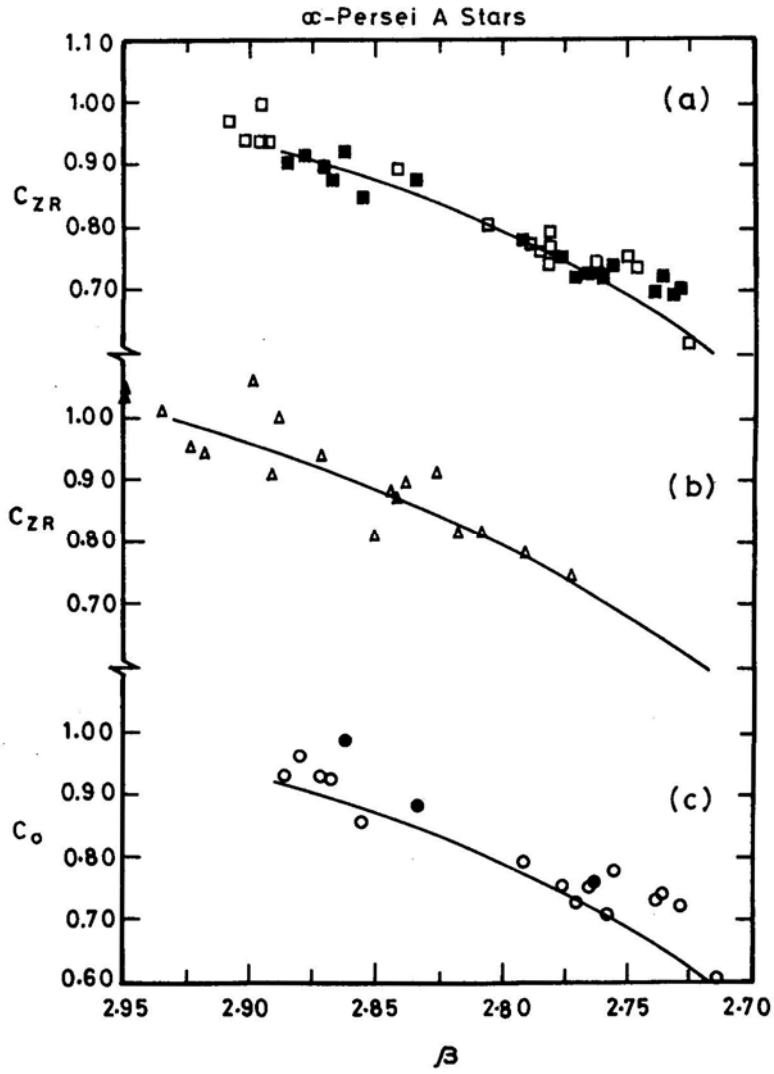

Figure 14. Same as Figs 10 and 12 for α-Persei A stars.

The different diagrams similar to that for Hyades, in the (β, c_1) plane are displayed in Fig. 12.

4.5 *ZRMS Values of α-Persei and Pleiades*

The B stars and A stars were treated separately for determining rotation effects. The methods followed are exactly similar to those for Hyades and Praesepe and we derived the ZRMS value from observed effects (Method 1a) for B stars and A stars for the A Stars independently. The ZRMS values for the B stars in α-Persei are listed in Table 9 and for the A stars in Table 10. We have taken care always to check for the self-consistency of the m_1 values derived.

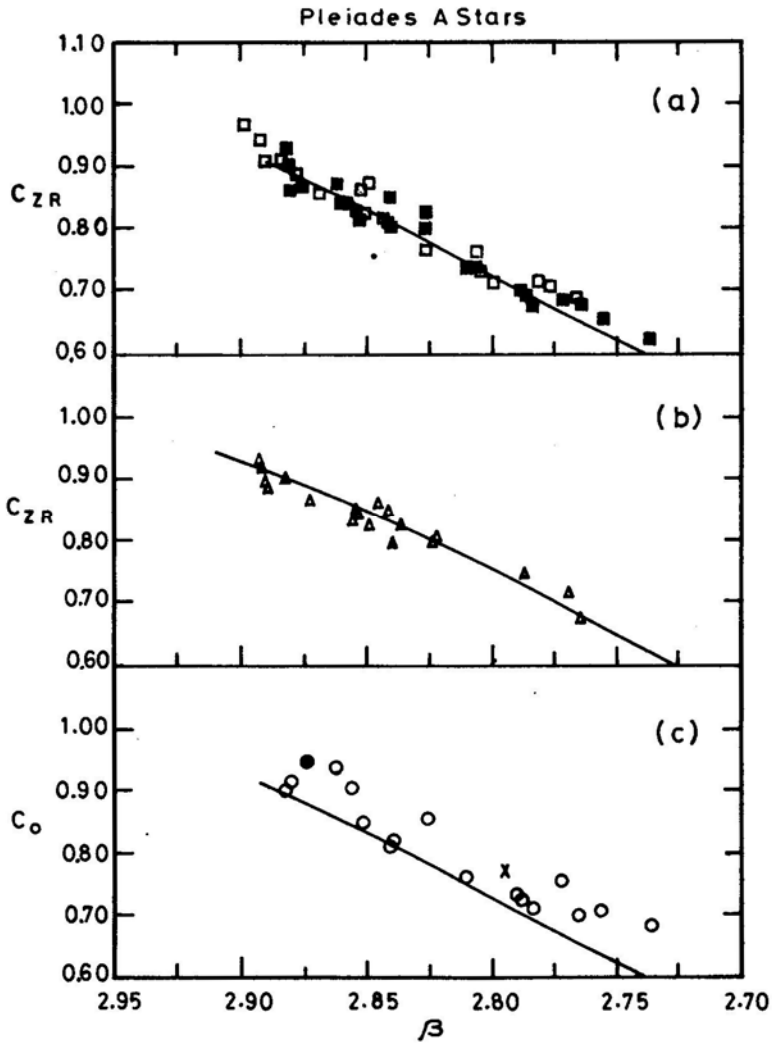

Figure. 15. Same as Figs 10 and 12 for Pleiades A stars.

The ZRMS values derived from predicted effects (Method lb) are listed in Table 9 for B stars and in Table 10 for A stars. The ZRMS values derived from both the methods are found to agree very well with each other.

The ZRMS values are corrected for the average observed intersteiler reddening. Extinction corrections are discussed in Section 5 where we discuss the derivation of the Zero Rotation Zero Age Main Sequence (ZRZAMS). In Figs 13 and 14 the different diagrams similar to those for Hyades in the (β, c_1) plane are shown respectively for the B and A stars in α-Persei.

Procedures similar to those for α-Persei were followed for the A-stars in Pleiades and the dereddened ZRMS values derived from observations (Method la) and theory (Method lb) are listed in Table 11. Diagrams similar to those of α-Persei are displayed in Fig. 15 for Pleiades A-stars. The theoretical ZRMS for the B stars in Pleiades are

Table 6. Average change in indices per 100 km s^{-1} of $V\sin i$ ($\omega = 0$; $i = 60°$).

$M/M_\odot$	$(u-b)$	$(b-y)$	$\delta(b-y)$	δM_v	$\delta(u-b)$	δc	δm_1	$\delta\beta$
14.5	−.200	−.150	.007	0.17	.044	.028	.001	.004
11.0	.030	−.118	.008	−.010	.068	.050	.001	.006
8.3	.210	−.098	.009	−.018	.087	.067	.001	.009
6.3	.390	−.078	.010	−.031	.115	.092	.002	.010
4.9	.620	−.059	.012	−.043	.154	.126	.003	.016
3.9	.810	−.045	.013	−.031	.181	.145	.005	.024
3.3	.959	−.034	.017	.009	.191	.144	.007	.029
2.8	1.228	−.015	.026	.106	.178	.115	.006	.022
2.5	1.358	.005	.045	.270	.145	.024	−.006	−.015
2.3	1.433	.026	.050	.311	.057	−.019	−.012	−.031
2.1	1.445	.082	.056	.332	.019	−.055	−.018	−.044
1.9	1.402	.152	.073	.400	−.030	−.118	−.029	−.070
1.8	1.375	.177	.084	.313	−.093	−.181	−.040	−.090
1.7	1.345	.208	.086	.227	−.114	−.203	−.042	−.088
1.5	1.308	.259	.076	.242	−.121	−.206	−.033	−.082

Table 7. Hyades.

β	$(b-y)_0$	m_0	c_0	$(u-b)_0$	M_v	$(b-y)_0$	m_0	c_0	$(u-b)_0$
	Observational ZRMS					Theoretical ZRMS			
2.680	.236	.154	.552	1.332	5.518	.235	.099	.619	1.287
2.690	.231	.160	.569	1.351	5.595	.230	.111	.629	1.311
2.700	.226	.166	.586	1.370	5.659	.224	.123	.640	1.334
2.710	.221	.171	.603	1.387	5.710	.218	.134	.652	1.356
2.720	.215	.177	.622	1.406	5.748	.212	.144	.665	1.377
2.730	.208	.181	.641	1.419	5.773	.205	.154	.678	1.396
2.740	.201	.186	.661	1.435	5.785	.197	.164	.692	1.414
2.750	.194	.190	.682	1.450	5.784	.189	.172	.708	1.430
2.760	.186	.194	.703	1.463	5.770	.181	.180	.724	1.445
2.770	.177	.198	.726	1.476	5.744	.172	.187	.741	1.459
2.780	.168	.201	.749	1.487	5.704	.163	.193	.759	1.472
2.790	.159	.204	.772	1.498	5.651	.153	.200	.777	1.483
2.800	.149	.207	.797	1.509	5.586	.143	.204	.797	1.492
2.810	.138	.209	.822	1.516	5.508	.132	.210	.817	1.501
2.820	.127	.211	.848	1.524	5.416	.121	.214	.839	1.508
2.830	.115	.212	.875	1.529	5.312	.109	.217	.861	1.513
2.840	.103	.214	.902	1.536	5.195	.097	.220	.884	1.518
2.850	.090	.215	.930	1.540	5.065	.084	.222	.908	1.521
2.860	.077	.210	.959	1.533	4.922	.071	.223	.933	1.522
2.870	.062	.215	.989	1.543	4.766	.057	.225	.959	1.523
2.880	.048	.214	1.019	1.543	4.597	.043	.226	.985	1.522
2.890	.033	.213	1.050	1.542	4.415	.029	.224	1.013	1.519
2.900	.016	.212	1.082	1.538	4.221	.014	.223	1.041	1.515

Table 8. Praesepe.

β	$(b-y)_0$	m_0	c_0	$(u-b)_0$	M_v	$(b-y)_0$	m_0	c_0	$(u-b)_0$
	Observational ZRMS					Theoretical ZRMS			
2.680	.253	.148	.605	1.408	2.156	.261	−.018	.752	1.238
2.690	.245	.154	.619	1.418	2.287	.250	.013	.751	1.277
2.700	.236	.161	.633	1.428	2.400	.240	.041	.751	1.313
2.710	.227	.167	.649	1.438	2.494	.230	.067	.753	1.346
2.720	.218	.173	.665	1.448	2.570	.219	.091	.756	1.376
2.730	.208	.179	.683	1.457	2.628	.208	.113	.761	1.404
2.740	.199	.183	.701	1.466	2.667	.198	.133	.767	1.429
2.750	.189	.189	.720	1.475	2.688	.186	.152	.775	1.451
2.760	.179	.193	.740	1.484	2.690	.175	.167	.785	1.470
2.770	.170	.196	.761	1.493	2.674	.164	.182	.795	1.487
2.780	.161	.198	.782	1.501	2.639	.152	.194	.808	1.501
2.790	.151	.201	.805	1.509	2.587	.141	.204	.820	1.512
2.800	.141	.203	.828	1.517	2.515	.129	.212	.837	1.520
2.810	.131	.204	.853	1.524	2.425	.117	.218	.854	1.525
2.820	.122	.205	.878	1.532	2.317	.105	.223	.873	1.528
2.830	.113	.204	.904	1.539	2.191	.093	.225	.893	1.528
2.840	.103	.204	.931	1.546	2.046	.080	.225	.914	1.525
2.850	.095	.202	.959	1.553	1.882	.068	.223	.937	1.519
2.860	.086	.199	.988	1.559	1.701	.055	.219	.962	1.510
2.870	.077	.196	1.018	1.565	1.500	.042	.214	.988	1.499
2.880	.069	.192	1.048	1.571	1.282	.029	.206	1.016	1.485
2.890	.061	.187	1.080	1.577	1.045	.016	.195	1.045	1.468
2.900	.054	.181	1.112	1.583	0.789	.003	.184	1.075	1.449

listed in Table 12. The ZRMS from observations (Method la) was not calculated as Pleiades, contains only a few single main sequence B-type stars.

4.6 *ZRMS of the Scorpio-Centaurus Association and 1C 4665*

As the Upper Scorpius sub-group is known to have highly variable reddening due to interstellar extinction, we decided to consider only the two other subgroups of this association for the derivation of the ZRMS values. The Lower Centaurus and Upper Centaurus subgroups consist mainly of B2 and B3 main sequence stars which gave us the opportunity of deriving accurate rotational effects for this mass range.

The ZRMS values derived from observations and theory (Methods la and lb) for these two subgroups are listed in Table 13. The extinction for this subgroup appears to be extremely small (Glaspey 1971) and therefore needs no correction.

The (dereddened) ZRMS values derived for B-stars of 1C 4665 from observed slopes and theory are given in Table 14.

Table 9. α-Persei B stars.

β	$(b-y)_0$	m_0	c_0	$(u-b)_0$	M_v	$(b-y)_0$	m_0	c_0	$(u-b)_0$
	Observational ZRMS					Theoretical ZRMS			
2.660	−.090	.092	.192	.232	−.919	−.077	.092	.198	.228
2.670	−.089	.092	.233	.277	−.636	−.072	.092	.223	.262
2.680	−.087	.094	.273	.323	−.374	−.069	.093	.250	.297
2.690	−.087	.096	.312	.368	−.134	−.065	.094	.277	.334
2.700	−.085	.097	.350	.414	.086	−.061	.094	.306	.372
2.710	−.081	.099	.388	.459	.284	−.058	.096	.335	.412
2.720	−.079	.101	.424	.505	.460	−.054	.098	.366	.454
2.730	−.076	.103	.461	.550	.616	−.051	.100	.398	.497
2.740	−.071	.105	.496	.596	.750	−.048	.104	.431	.542
2.750	−.068	.107	.530	.641	.863	−.045	.107	.464	.588
2.760	−.064	.110	.564	.687	.954	−.043	.111	.499	.636
2.770	−.060	.111	.597	.732	1.024	−.040	.116	.535	.686
2.780	−.056	.114	.629	.777	1.073	−.037	.120	.572	.737
2.790	−.050	.117	.661	.823	1.101	−.035	.125	.610	.789
2.800	−.045	.119	.692	.868	1.107	−.033	.130	.649	.843
2.810	−.040	.122	.722	.914	1.092	−.031	.136	.689	.899
2.820	−.033	.125	.751	.959	1.056	−.029	.142	.730	.956
2.830	−.027	.127	.779	1.004		−.027	.148	.772	1.015
2.840	−.020	.132	.807	1.050		−.026	.156	.815	1.075
2.850	−.015	.134	.834	1.095		−.024	.163	.859	1.137
2.860	−.006	.138	.860	1.140		−.023	.171	.905	1.201
2.870	−.001	.141	.886	1.185		−.022	.180	.951	1.266
2.880	−.009	.145	.911	1.231		−.021	.188	.998	1.333
2.890	−.018	.149	.935	1.276		−.020	.197	1.047	1.401
2.900	−.027	.152	.958	1.321		−.019	.206	1.096	1.471
2.910	−.035	.156	.980	1.366		−.019	.217	1.146	1.542
2.920	−.045	.160	1.002	1.412					

Table 10. α-Persei A stars.

β	$(b-y)_0$	m_0	c_0	$(u-b)_0$	M_v	$(b-y)_0$	m_0	c_0	$(u-b)_0$
	Observational ZRMS					Theoretical ZRMS			
2.650	.298	.151	.387	1.285	3.720	.304	.143	.389	1.283
2.660	.288	.150	.423	1.298	3.627	.291	.149	.421	1.301
2.670	.278	.149	.457	1.311	3.537	.278	.155	.453	1.319
2.680	.268	.149	.490	1.324	3.449	.266	.160	.484	1.336
2.690	.258	.149	.522	1.336	3.363	.254	.165	.514	1.353
2.700	.248	.150	.553	1.348	3.280	.242	.170	.544	1.368
2.710	.239	.150	.583	1.360	3.199	.230	.175	.572	1.383
2.720	.229	.151	.611	1.371	3.120	.219	.180	.600	1.397
2.730	.219	.152	.639	1.381	3.044	.208	.183	.627	1.410
2.740	.210	.153	.665	1.391	2.970	.197	.188	.653	1.423

Table 10. Continued.

β	$(b-y)_0$	m_0	c_0	$(u-b)_0$	M_v	$(b-y)_0$	m_0	c_0	$(u-b)_0$
	Observational ZRMS					Theoretical ZRMS			
2.750	.200	.156	.690	1.401	2.898	.186	.191	.679	1.434
2.760	.191	.157	.714	1.410	2.829	.176	.195	.703	1.445
2.770	.182	.159	.737	1.419	2.762	.166	.198	.727	1.455
2.780	.172	.163	.758	1.427	2.697	.156	.201	.750	1.464
2.790	.163	.165	.779	1.435	2.635	.146	.205	.772	1.473
2.800	.154	.168	.798	1.442	2.575	.137	.207	.793	1.481
2.810	.145	.172	.816	1.449	2.517	.128	.210	.813	1.488
2.820	.136	.175	.833	1.455	2.462	.119	.212	.833	1.494
2.830	.127	.179	.849	1.461	2.407	.111	.213	.852	1.499
2.840	.118	.184	.864	1.467	2.357	.102	.215	.870	1.504
2.850	.110	.188	.877	1.472	2.310	.094	.216	.887	1.507
2.860	.101	.193	.890	1.477	2.265	.086	.217	.904	1.510
2.870	.092	.198	.901	1.481	2.221	.079	.217	.919	1.512
2.880	.084	.203	.911	1.485	2.180	.072	.218	.934	1.514
2.890	.075	.209	.920	1.488	2.141	.065	.218	.948	1.515

Table 11. Pleiades A stars.

β	$(b-y)_0$	m_0	c_0	$(u-b)_0$	M_v	$(b-y)_0$	m_0	c_0	$(u-b)_0$
	Observational ZRMS					Theoretical ZRMS			
2.680	.253	.172	.467	1.318	3.824	.225	.149	.484	1.231
2.690	.244	.175	.490	1.329	3.687	.218	.158	.508	1.261
2.700	.235	.177	.512	1.337	3.555	.211	.167	.532	1.289
2.710	.226	.180	.534	1.347	3.429	.205	.174	.556	1.315
2.720	.217	.183	.556	1.357	3.308	.198	.182	.579	1.339
2.730	.208	.186	.578	1.367	3.192	.191	.189	.601	1.361
2.740	.199	.189	.600	1.377	3.081	.184	.195	.624	1.381
2.750	.190	.191	.621	1.384	2.976	.176	.200	.646	1.399
2.760	.180	.194	.643	1.392	2.876	.169	.204	.667	1.414
2.770	.171	.197	.664	1.401	2.781	.162	.208	.688	1.427
2.780	.162	.200	.685	1.410	2.691	.154	.211	.709	1.439
2.790	.152	.203	.706	1.417	2.607	.147	.212	.730	1.448
2.800	.142	.206	.727	1.424	2.528	.139	.214	.749	1.455
2.810	.133	.209	.748	1.433	2.455	.131	.214	.769	1.459
2.820	.123	.213	.768	1.441	2.386	.123	.214	.788	1.462
2.830	.113	.216	.789	1.448	2.323	.115	.213	.807	1.463
2.840	.103	.219	.809	1.454	2.265	.107	.211	.825	1.461
2.850	.093	.222	.829	1.460	2.213	.099	.208	.843	1.457
2.860	.082	.225	.849	1.464	2.166	.090	.205	.861	1.451
2.870	.072	.229	.869	1.472	2.124	.082	.200	.878	1.443
2.880	.062	.232	.888	1.477	2.087	.073	.196	.894	1.433
2.890	.051	.235	.908	1.481	2.056	.064	.191	.911	1.421

Table 12. Pleiades B stars.

β	M_v	$(b-y)_0$	m_0	c_0	$(u-b)_0$
		Theoretical ZRMS			
2·640	−1.046	−.111	.103	.258	.242
2.650	−.876	−.107	.101	.276	.265
2.660	−.711	−.103	.100	.294	.289
2.670	−.550	−.099	.101	.312	.315
2.680	−.394	−.095	.101	.332	.343
2.690	−.243	−.091	.101	.351	.371
2.700	−.096	−.087	.102	.372	.401
2.710	.046	−.083	.102	.393	.432
2.720	.184	−.079	.105	.414	.465
2.730	.317	−.076	.107	.436	.499
2.740	.445	−.072	.110	.458	.534
2.750	.569	−.068	.113	.481	.571
2.760	.688	−.064	.116	.504	.608
2.770	.803	−.061	.121	.528	.648
2.780	.913	−.057	.125	.552	.688
2.790	1.019	−.053	.129	.577	.730
2.800	1.120	−.050	.135	.603	.773
2.810	1.216	−.046	.140	.629	.818
2.820	1.308	−.043	.147	.655	.864
2.830	1.395	−.039	.153	.682	.911
2.840	1.478	−.036	.160	.710	.959
2.850	1.556	−.032	.167	.738	1.009
2.860	1.629	−.029	.176	.766	1.060
2.870	1.698	−.025	.184	.795	1.113
2.880	1.762	−.022	.193	.825	1.167
2.890	1.822	−.019	.202	.855	1.222
2.900	1.877	−.015	.212	.885	1.278
2.910	1.928	−.012	.222	.916	1.336

Table 13. Lower-Cen + Upper-Cen B2, B3 stars.

β	$(b-y)_0$	m_0	c_0	$(u-b)_0$	M_v	$(b-y)_0$	m_0	c_0	$(u-b)_0$
	Observational ZRMS					Theoretical ZRMS			
2.600	−.118	.065	−.020	−.125	−3.040	−.122	.081	−.029	−.111
2.610	−.114	.069	.014	−.077	−2.882	−.118	.084	.005	−.063
2.620	−.109	.070	.048	−.029	−2.706	−.115	.088	.037	−.017
2.630	−.105	.073	.081	.018	−2.512	−.111	.091	.067	.027
2.640	−.101	.077	.114	.066	−2.301	−.107	.095	.094	.070
2.650	−.097	.080	.147	.113	−2.071	−.103	.099	.120	.112
2.660	−.093	.084	.179	.160	−1.824	−.099	.104	.143	.152
2.670	−.089	.087	.211	.207	−1.560	−.095	.107	.165	.190
2.680	−.085	.091	.242	.253	−1.277	−.092	.113	.184	.227
2.690	−.082	.095	.273	.300	−.977	−.088	.119	.201	.263
2.700	−.078	.099	.304	.346	−.660	−.084	.125	.216	.297
2.710	−.075	.104	.334	.392	−.324	−.080	.131	.228	.329

Table 14. IC 4665 B starts.

β	$(b-y)_0$	m_0	c_0	$(u-b)_0$	M_v	$(b-y)_0$	m_0	c_0	$(u-b)_0$
	Observational ZRMS					Theoretical ZRMS			
2.680	−.050	.075	.251	.302	−.768	−.050	.076	.309	.361
2.690	−.057	.079	.287	.332	−.736	−.057	.080	.341	.387
2.700	−.063	.083	.323	.365	−.697	−.063	.083	.374	.414
2.710	−.069	.089	.358	.399	−.651	−.069	.088	.406	.444
2.720	−.072	.093	.392	.434	−.598	−.072	.091	.439	.477
2.730	−.075	.097	.426	.472	−.538	−.075	.095	.471	.511
2.740	−.077	.102	.460	.511	−.471	−.077	.100	.503	.549
2.750	−.077	.106	.493	.552	−.397	−.077	.104	.535	.588
2.760	−.076	.110	.526	.595	−.315	−.076	.108	.566	.630
2.770	−.074	.114	.558	.639	−.227	−.074	.112	.598	.674
2.780	−.070	.118	.590	.686	−.132	−.070	.116	.630	.721
2.790	−.065	.120	.622	.733	−.029	−.065	.120	.661	.770
2.800	−.060	.124	.653	.783	.080	−.060	.125	.692	.822
2.810	−.052	.128	.683	.835	.196	−.052	.128	.723	.875
2.820	−.044	.130	.714	.888	.320	−.044	.133	.754	.932
2.830	−.035	.134	.744	.943	.450	−.035	.138	.785	.990
2.840	−.024	.136	.773	.999	.588	−.024	.142	.816	1.051
2.850	−.012	.139	.802	1.058	.732	−.012	.147	.846	1.115
2.860	.001	.142	.830	1.118	.884	−.001	.152	.876	1.181
2.870	.016	.144	.858	1.179	1.042	.016	.155	.907	1.249
2.880	.032	.146	.886	1.243	1.208	.032	.159	.937	1.319
2.890	.049	.148	.913	1.308	1.381	.049	.164	.967	1.392
2.900	.067	.150	.940	1.375	1.560	.067	.178	.997	1.486

5. ZRZAMS

5.1 *Interstellar Reddening*

As both rotation and interstellar extinction redden the stars, we decided to check the $E(b-y)$ values given in the literature for various clusters.

For the Astars, β and $(b-y)$ are linearly related as both are functions of the effective temperature. Crawford (1977) finds a slight dependence of this relationship on δc_1 and δm_1 terms. The δc_1 term refers to reddening due to evolution and δm_1 the difference in line-blanketing with respect to Hyades values. The largest correction involved due to blanketing differences is of the order of 0.02 magnitudes only. The δc_1 term would be zero for unevolved members.

Rotation does not produce a shift away from the $(\beta, b-y)$ relation whereas extinction would shift the entire sequence, along the $(b-y)$ axis only. Hence mean extinction values derived from A-stars in the $(\beta, b-y)$ plane should be independent of rotation effects.

We plotted the ZRMS values of β and $(b-y)$ for various clusters and estimated their relative shift along the $(b-y)$axis with respect to the Hyades relation. The $E(b-y)$ values derived by us for a few selected clusters were compared with the values quoted in the original papers. The agreement between the two estimates was found to be good excepting for α-Persei where we find our estimate to be smaller by

about 0.03 magnitudes. For all the clusters the $E(b - y)$ taken from literature was used for extinction corrections excepting for α-Persei for which we use a value of 0.045 instead of the value 0.07 given by Crawford and Barnes (1974). In Table 15, we list the $E(b - y)$ values and the distance moduli to various clusters taken from the original literature that is listed in Table 1.

5.2 *Absolute Magnitudes*

The distance moduli of the clusters used for deriving the ZRZAMS are also listed in Table 15. These have been taken from the references listed in Table 1. The absolute magnitudes and dereddened colours for all stars were derived using the following relationship (Strömgren 1966).

$$E(b-y) = 0.70\,E(B-V)$$
$$E(m_1) = -0.18\,E(b-y)$$
$$E(c_1) = 0.20\,E(b-y)$$
$$E(u-b) = 1.84\,E(b-y)$$
$$A_v = 4.57\,E(b-y).$$

The ZRMS values listed in Section 4 have all been corrected for average extinction using the above relationship.

5.3 *ZRZAMS: From Observed Slopes of Rotation Effects*

The ZRMS values of various indices as a function of β derived for different clusters were all superposed to derive the mean ZRZAMS for B and A stars separately. In Fig. 16 we show in the (β, c) plane the ZRMS curves for B stars of α-Persei, Upper Centaurus and IC 4665. A similar diagram for the A stars is shown in Fig. 17 where the values for stars in α-Persei, Pleiades, Hyades and Praesepe are plotted. ZRMS

Table 15. $E(b–y)$ & distance modulus for clusters.

Cluster	$E(b-y)$ literature	$m-M$	Cluster	$E(b-y)$ literature	$m-M$
Hyades		3.2	NGC 2422	0.06	8.01
Praesepe	< 0.01	6.1	Coma	—	4.5
α-Persei	0.07	6.1	IC 2602	0.021	5.94
Pleiades	0.04	5.54	Cep OB3	0.6	9.3
Upper-Cen		6.0	NGC 2287	0.018	9.10
IC 4665	0.14	7.5	NGC 6475	0.067	7.02
NGC 2516	0.088	8.01	NGC 2244	0.34	10.96
IC 4756	0.161	8.05	h & χ-Persei	0.41	11.8
NGC 2264	0.057	9.5	NGC 4755	0.28	11.4
IC 2391	0.000	5.90			

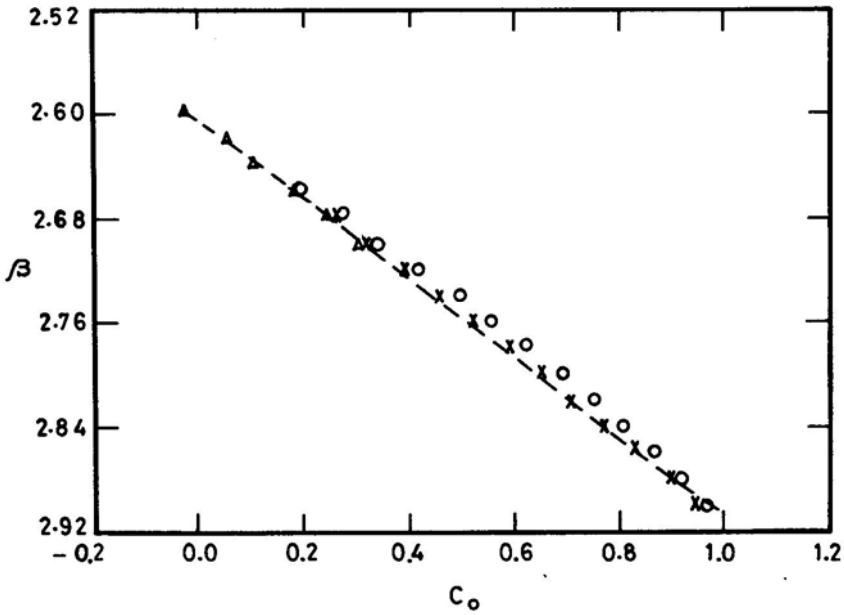

Figure 16. The ZRMS curves in the (β, c_0) plane determined from observed rotational effects for α-Persei B stars, Lower and Upper Centaurus B2, B3 stars IC 4665 B-stars are shown. The adoped ZRZAMS values of c_0 as a functions of β are shown by a dotted line.

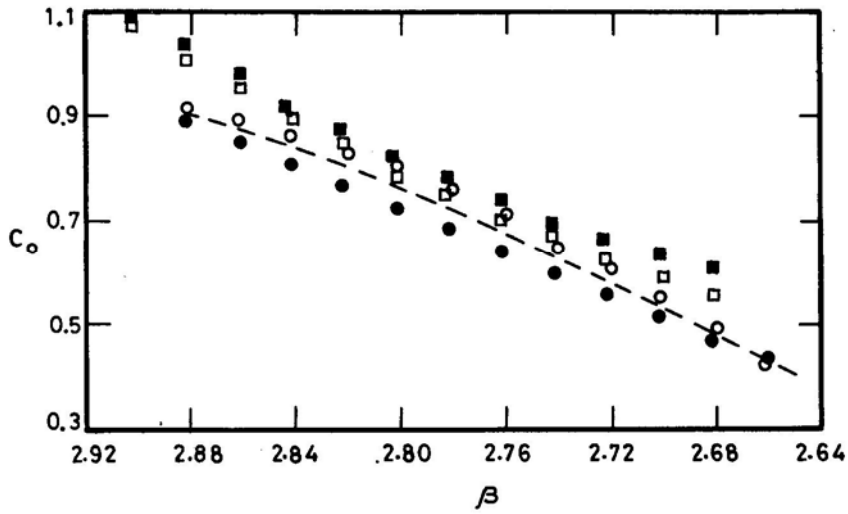

Figure 17. Same as Fig. 16 for A-stars. The ZRMS from observed slopes of rotation effects of α-Persei, Pleiades, Hyades and Praesepe are plotted. The adopted ZRZAMS curve is shown by a dotted line.

values for the B and A stars are plotted in the (β, $b - y$), and (β, $u–b$) planes respectively in Figs 18 and 19. Preliminary ZRZAMS values derived from this set of clusters are listed in Tables 16 and 17 for B and A stars respectively. We expect

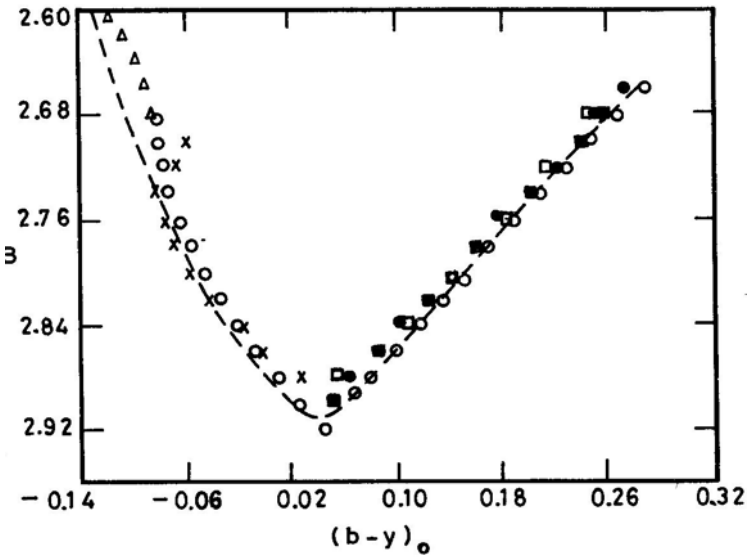

Figure 18. The ZRMS (observational) in the (β, $b - y$) plane for A and B-type stars of all clusters plotted in Figs 16 and 17 is shown. The adopted ZRZAMS values of ($b - y$) as a functions of β are shown by the dotted line.

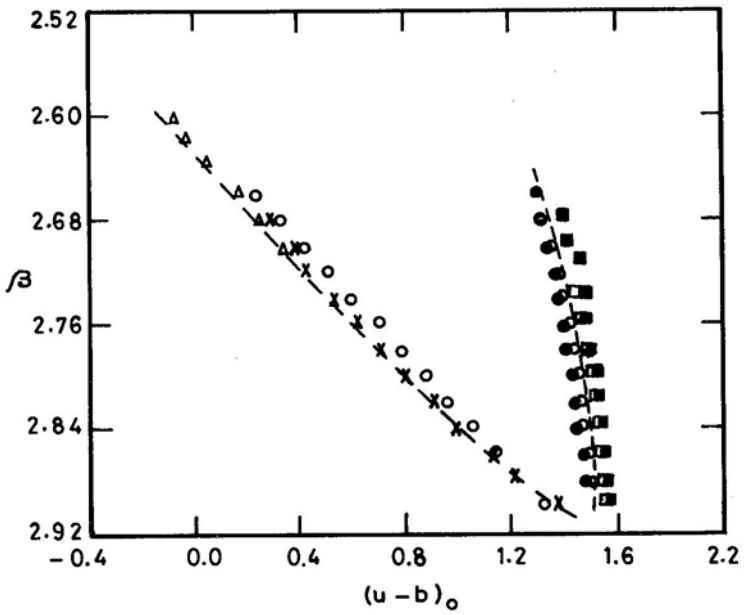

Figure 19. Same as Fig. 18 in the (β, $u - b$) plane.

that this would be highly representative of the true values from mid-B to late A and early F star ranges. The B2, B3 type stars are represented only by the Lower Centaurus and Upper Centaurus group.

5.4 *ZRZAMS: From Theoretical Corrections*

ZRZAMS from theoretical corrections also was derived by superposing the theoretical ZRMS curves for various clusters. In addition to α-Persei, Pleiades, Hyades, Praesepe, Upper Centaurus and IC 4665, we have used Cep OB3, Coma, IC 2602, IC 2391, IC 4756, NGC 2264, NGC 2516 and NGC 4755 to check the derived ZRZAMS by

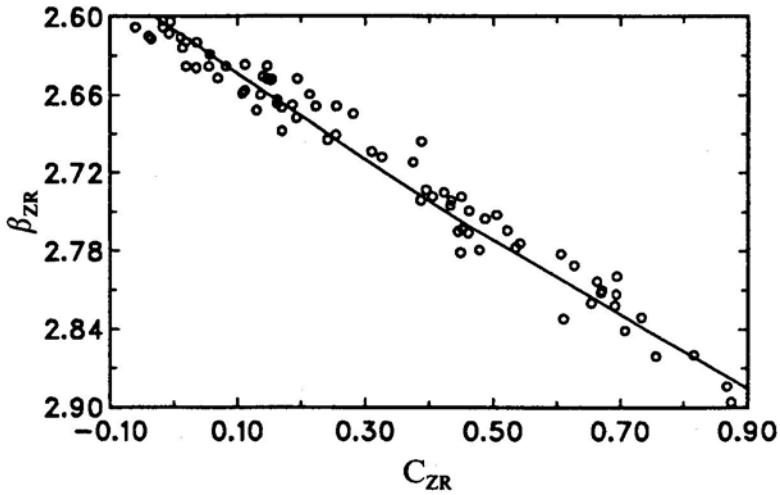

Figure 20. The theoretically corrected values of β *and* c_0 for B-stars in various cluster stars with $V \sin i \geqslant 100$ kms^{-1} have been plotted. The adopted ZRZAMS theoretical curve is shown as a line.

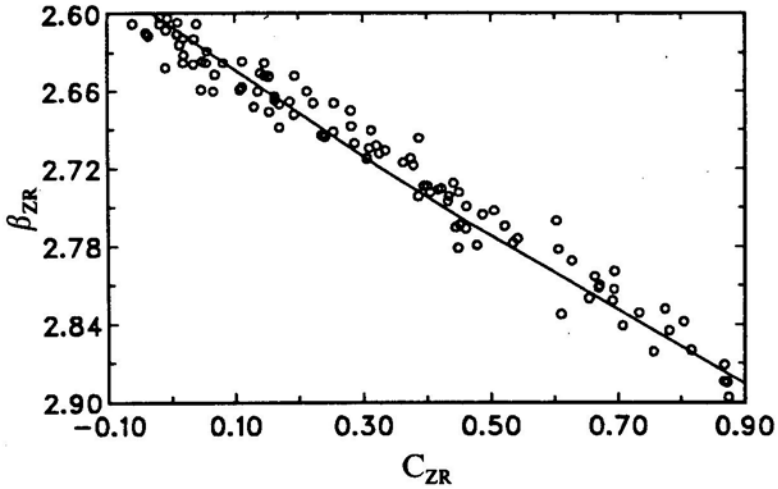

Figure 21. Same as Fig. 20 Stars with all $V \sin I$ values have been plotted.

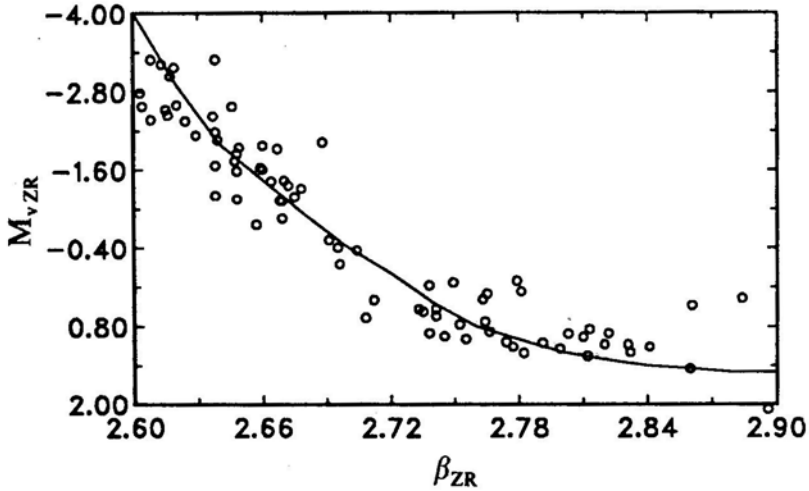

Figure 22. The theoretically corrected values of M_v, and β for B stars, with $V\sin i \geqslant 100$ km s^{-1}, in various clusters have been plotted. The adopted ZRZAMS curve (theoretical) is shown as a line.

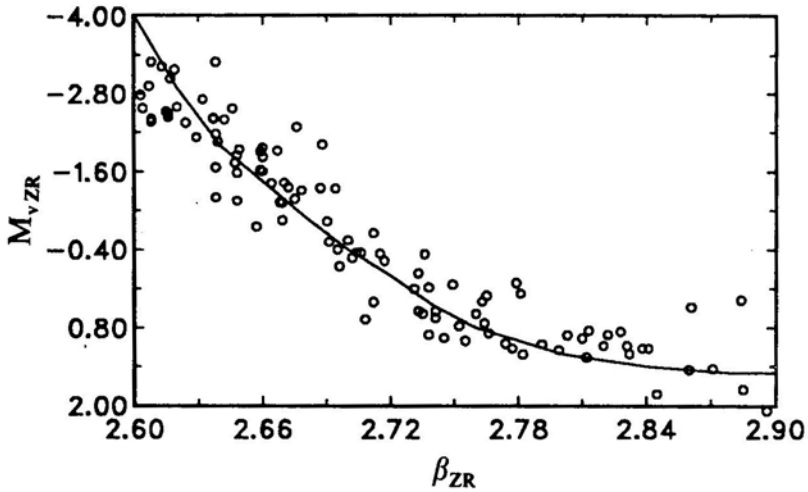

Figure 23. Same as Fig. 22. Stars with all $V\sin i$ values have been plotted.

correcting the indices using the theoretical predictions of Collins & Sonneborn for $i = 60°$.

Because we are assuming a value of $i = 60°$ for all stars, we are likely to leave uncorrected, all such stars which are rotating fast but seen pole-on. For example, in an M_v, versus c_0, plane for B-stars, these will be more than half a magnitude above the non-rotators at a given c_0. These objects would add to the scatter that would be introduced by the inclusion of visual and double-lined spectroscopic binaries.

We checked the derived ZRZAMS values using stars that have V sin i values greater than or equal to 100 km s^{-1}. We compared these determinations with those derived by using all stars without any discrimination. Fig. 20 shows, for fast rotating

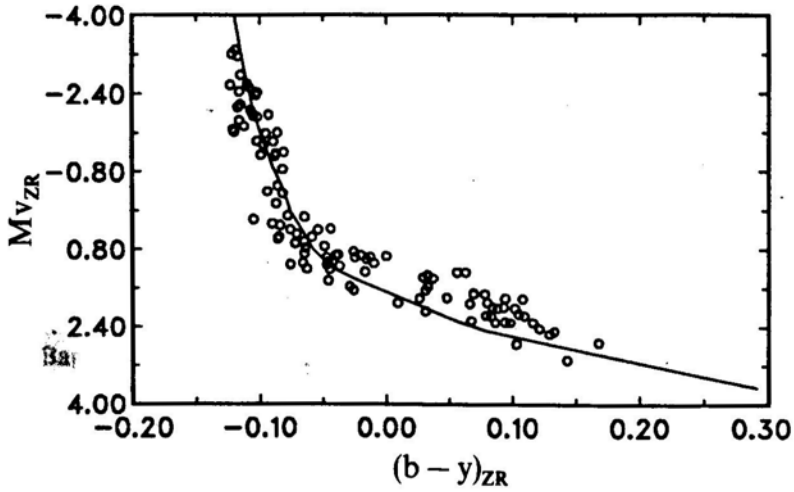

Figure 24. The theoretically corrected values of M_v and $(b - y)$ for B and A stars, with $V\sin i \geqslant 100\text{kms}^{-1}$, in various clusters have been plotted. The adopted ZRZAMS (theoretical) curve is also shown.

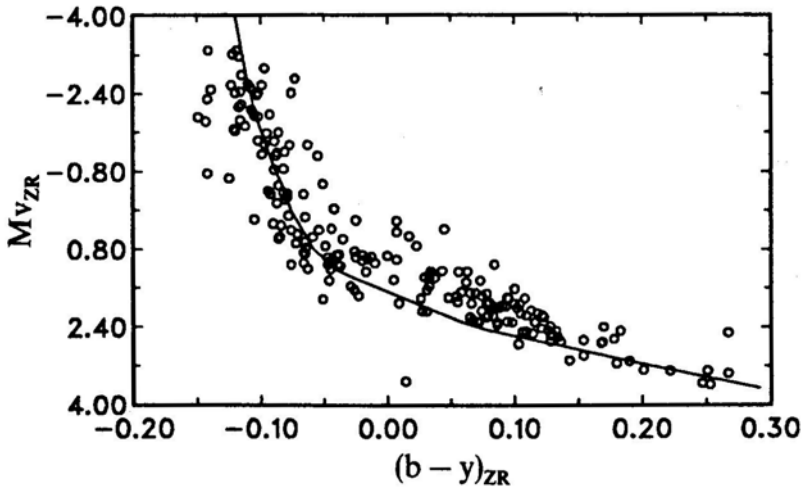

Figure 25. Same as Fig. 24. Stars with all $V\sin I$ values have been plotted.

($V \sin i \geqslant 100\text{kms}^{-1}$) B stars, the plot of β_{ZR} and c_{ZR} values corrected for rotation. The theoretical ZRZAMS curve is also shown. The relationship appears extremely smooth as expected. In Fig. 21 stars of all $V \sin i$ values are plotted. α-Persei, Pleiades, Upper and lower Centaurus, Cep OB 3,1C 4665,1C 2602,1C 2391, NGC 2264 and NGC 4755 have been included. Similar diagrams in the (M_v, β) and (M_v , $b - y$) planes are shown in Figs 22–27. Fig. 26 is a plot of β_{ZR}, $(b - y)_{ZR}$ for stars of all $V \sin i$ values and $(c_{ZR}, u - b)_{ZR}$, for fast rotators is plotted in Fig. 27.

Similarly from a superposition of various clusters containing A-stars the ZRZAMS values were determined. The following clusters were used; α-Persei, Pleiades, Hyades, Praesepe, IC 4665 and Coma. The theoretical ZRZAMS values are also listed in

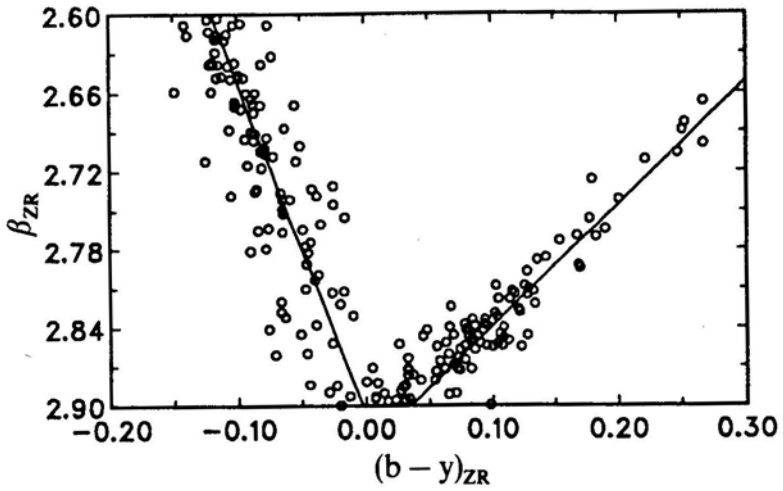

Figure 26. The theoretically corrected values of β and $(b - y)$ for B and A stars in various clusters have been plotted. The adoped ZRZAMS (theoretical) values are shown by lines.

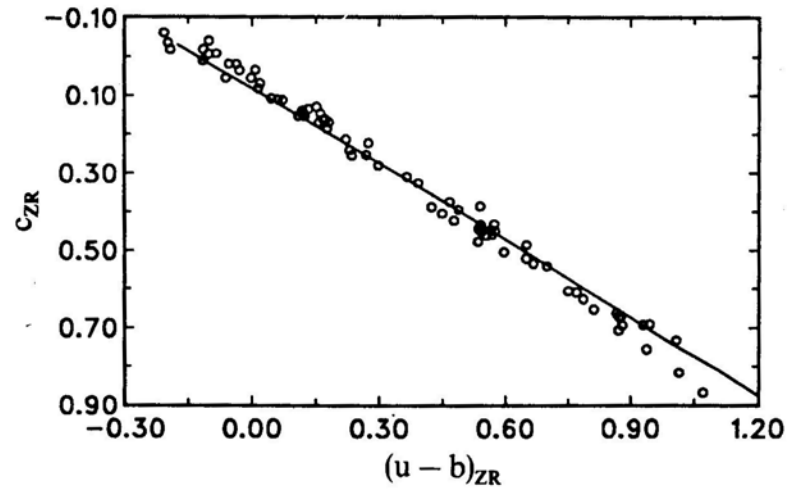

Figure 27. The theoretically corrected c_0 and $(u - b)_0$ values for cluster B-stars with $V\sin I \geqslant 100\text{kms}^{-}$ have been plotted. The adopted ZRZAMS values (theoretical) are shown by a line.

Tables 16 and 17 for B and A stars respectively. Adopted ZRZAMS values are the averages of the observational and theoretical ZRZAMS values and are listed in Tables 18 and 19 for B and A-type stars respectively.

A comparison of our adopted ZRZAMS values is made with the zero age main sequence values derived by Crawford (1975, 1978, 1979). Crawford has listed the ZAMS values derived from the locus of the blue envelope of B and A stars. We can easily anticipate that such a blue envelope should also represent the zero rotation zero age main sequence and hence must agree with our values derived by correcting for rotation effects. In Figs 28–30 we have compared these two independent determine-

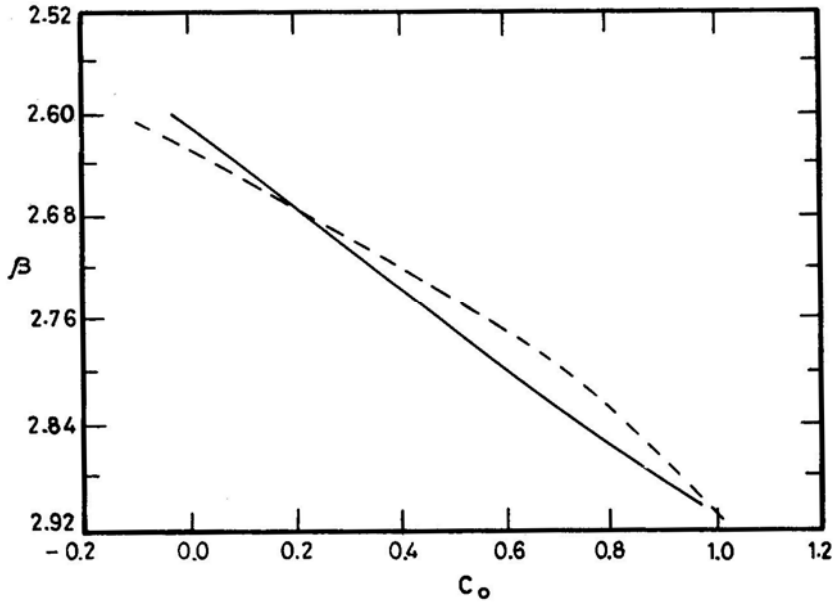

Figure 28. The ZRZAMS values for B stars derived in this study are compared with the values derived by Crawford (1978, 1979) from the lower envelope of field and cluster stars (dotted line), in the β, c_0 plane.

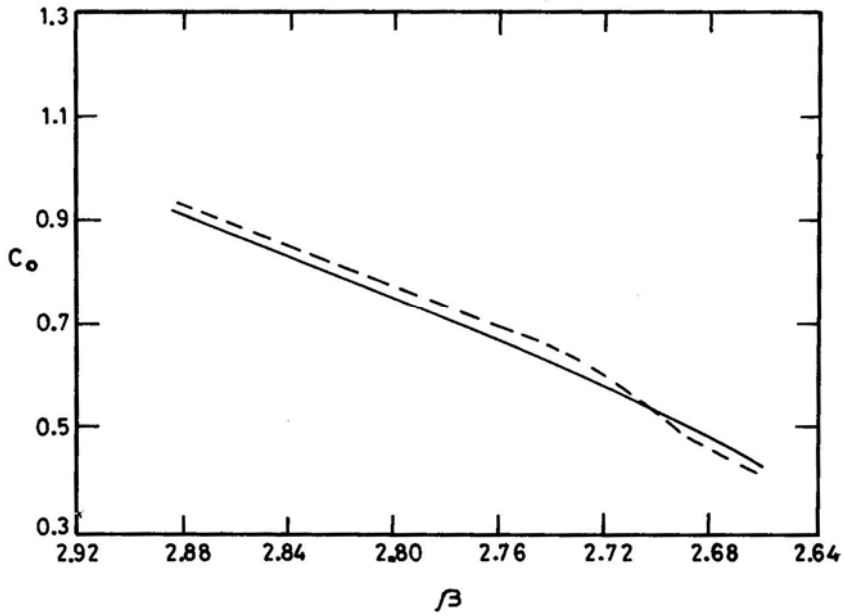

Figure 29. Same as Fig. 28 for A-type stars.

ations. The agreement is excellent and supports the fact that rotation affects all the observed parameters and our procedures in determining the ZRZAMS values should be valid.

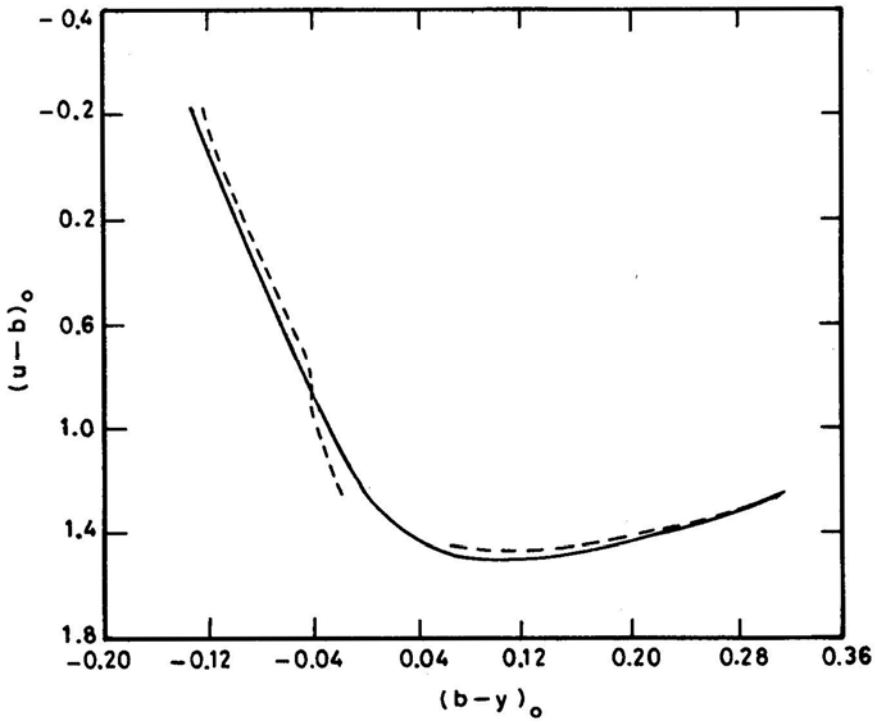

Figure 30. same as Figs 28 and 29 in the ($u - b$, $b - y$) plane for B and A-type stars.

Table 16. B-type stars.

β	$(b-y)_0$	m_0	c_0	$(u-b)_0$	M_v	$(b-y)_0$	m_0	c_0	$(u-b)_0$
	Observational ZRMS					Theoretical ZRMS			
2.60	−.130	0.067	−0.020	−0.146	−4.00	−0.120	0.047	−0.030	−0.175
2.62	−.125	0.073	0.046	−0.058	−2.90	−0.112	0.056	0.030	−0.082
2.64	−.118	0.079	0.111	−0.033	−2.00	−0.104	0.065	0.090	0.012
2.66	−.110	0.084	0.177	0.125	−1.45	−0.097	0.074	0.150	0.104
2.68	−.102	0.090	0.243	0.219	−0.90	−0.090	0.083	0.210	0.196
2.70	−.094	0.096	0.308	0.312	−0.40	−0.081	0.092	0.270	0.292
2.72	−.087	0.102	0.374	0.404	0.00	−0.073	0.101	0.330	0.386
2.74	−.080	0.108	0.440	0.496	0.45	−0.066	0.110	0.395	0.483
2.76	−.071	0.114	0.506	0.592	0.80	−0.058	0.119	0.460	0.582
2.78	−.062	0.120	0.571	0.687	1.00	−0.050	0.128	0.530	0.686
2.80	−.057	0.128	0.637	0.791	1.20	−0.042	0.136	0.600	0.788
2.82	−.040	0.137	0.702	0.896	1.30	−0.034	0.145	0.670	0.892
2.84	−.028	0.146	0.768	1.004	1.40	−0.026	0.154	0.740	0.996
2.86	−.014	0.155	0.834	1.116	1.50	−0.019	0.163	0.810	1.108
2.88	.002	0.166	0.900	1.236	1.75	−0.011	0.172	0.880	1.202
2.90	.020	0.176	0.966	1.358	1.80	−0.003	0.183	0.950	1.310

Table 17. A-type stars.

β	$(b-y)_0$	m_0	c_0	$(u-b)_0$	M_v	$(b-y)_0$	m_0	c_0	$(u-b)_0$
	Observational ZRZAMS					Theoretical ZRZAMS			
2.64						0.312	0.133	0.405	1.295
2.66	0.281	0.157	0.422	1.298	3.66	0.291	0.144	0.448	1.318
2.68	0.262	0.164	0.478	1.330	3.54	0.270	0.155	0.491	1.341
2.70	0.242	0.172	0.532	1.360	3.42	0.249	0.166	0.533	1.363
2.72	0.223	0.179	0.583	1.387	3.30	0.228	0.176	0.577	1.385
2.74	0.205	0.186	0.632	1.414	3.18	0.206	0.186	0.620	1.404
2.76	0.186	0.194	0.678	1.438	3.06	0.185	0.196	0.662	1.424
2.78	0.168	0.199	0.721	1.455	2.94	0.163	0.203	0.705	1.437
2.80	0.151	0.205	0.762	1.474	2.82	0.142	0.209	0.748	1.450
2.82	0.133	0.211	0.800	1.488	2.70	0.120	0.214	0.791	1.459
2.84	0.115	0.215	0.836	1.496	2.58	0.099	0.218	0.834	1.468
2.86	0.096	0.219	0.870	1.500	2.46	0.078	0.221	0.877	1.475
2.88	0.078	0.222	0.900	1.500	2.28	0.057	0.222	0.920	1.478
2.90		0.225				0.036	0.221	0.970	1.484

Table 18. Adopted ZRZAMS for Btype stars.

β	M_v	$(b-y)_0$	m_0	c_0	$(u-b)_0$
2.60	−4.00	−0.125	0.057	−0.025	−0.161
2.62	−2.90	−0.119	0.065	0.038	−0.070
2.64	−2.00	−0.111	0.072	0.100	0.023
2.66	−1.45	−0.104	0.079	0.164	0.115
2.68	−0.90	−0.096	0.087	0.226	0.208
2.70	−0.40	−0.088	0.094	0.289	0.302
2.72	0.00	−0.082	0.102	0.352	0.392
2.74	0.45	−0.073	0.109	0.417	0.490
2.76	0.80	−0.065	0.117	0.483	0.587
2.78	1.00	−0.056	0.124	0.550	0.687
2.80	1.20	−0.050	0.132	0.618	0.790
2.82	1.30	−0.037	0.141	0.686	0.894
2.84	1.40	−0.027	0.150	0.754	1.000
2.86	1.50	−0.017	0.159	0.822	1.112
2.88	1.75	−0.005	0.169	0.890	1.219
2.90	1.80	0.009	0.180	0.958	1.334

Table 19. Adopted ZRZAMS for A-type stars.

β	M_v	$(b-y)_0$	m_0	c_0	$(u-b)_0$
2.66	3.66	0.286	0.150	0.435	1.308
2.68	3.54	0.266	0.160	0.484	1.336
2.70	3.42	0.246	0.169	0.532	1.362
2.72	3.30	0.226	0.178	0.580	1.386
2.74	3.18	0.206	0.186	0.626	1.409
2.76	3.06	0.186	0.195	0.670	1.431
2.78	2.94	0.166	0.201	0.713	1.446
2.80	2.82	0.148	0.207	0.755	1.462
2.82	2.70	0.127	0.212	0.795	1.469
2.84	2.58	0.107	0.216	0.835	1.482
2.86	2.46	0.087	0.220	0.874	1.488
2.88	2.28	0.068	0.222	0.910	1.489

6. Discussion

We have established firmly the rotation effects in the intermediate band photometric indices for various mass ranges by analysing a large number of dusters for which sufficient data are available. This was possible because the method we followed took care of most of the complications that would have otherwise been introduced by causes other than rotation. In principle, this method is similar to the one followed by Strittmatter (1966) in his analysis of the Praesepe cluster. Stritttmatter measured ΔV at a given $(B - V)$ value, where ΔV was defined as the difference between the observed and assumed zero rotation main sequence value of the V-magnitude. But we did not wish to make any assumption on the ZRMS values, instead we decided to derive it after determining the rotation effects. This is where we departed in the data analysis from the earlier workers in the field. For example, Crawford & Barnes (1974) measured the deviations in c_1 from a preliminary calibration of ZAMS, In the α-Persei cluster, they found the deviation in c_1 for A-stars to show rotation effect while the B-star data appeared to be unaffected by rotation. Instead of assuming ZRMS or ZAMS values, we derived for each cluster a mean main sequence from which the deviations were measured. Our approach clearly demonstrates the rotation effects for both B and A-stars (Rajamohan & Mathew 1988, Mathew & Rajamohan 1990a, b). Likewise Warren's (1976) analysis of Orion association failed to reveal the rotation effects for $V \sin i$ values less than 250 km s^{-1}. Although the analysis of field stars by Hartwick & Hesser (1974) and by Gray & Garrison (1988, 1989, 1990 demonstrates the rotation effects on β and c_1, the spread is large as they have not taken into account the reddening by other causes. The causes for the conflicting results of earlier analysis of observational data can be traced to an assumption of an assumed calibration that does not take rotation into account together with the effects of evolution which causes a large spread when objects of different ages are pooled together. The smallness of the rotation effects for moderate rotational velocities, and the fact that rotation effects are a function of mass m, true rotational velocity V and the inclination i of the rotation axis to the line of sight (whereas only $V \sin i$ is observable) introduces further uncertainties in any analysis of data.

Our analysis has established not only the reality of rotation effects on observable parameters but also that the agreement is near perfect with the theoretical calculations, especially of Collins and his co-workers.

The analysis of B2, B3 stars of Upper and Lower Centaurus, the B5 to B9 stars of α-Persei, and IC 4665, the A3-F2 stars of α-Persei, Pleiades, Hyades and Praesepe clearly demonstrates this agreement with the predicted values by Collins & Sonneborn (1977). The A0-A2 type stars have not been analysed. This is a spectral domain in which almost all indices are a function of both the effective temperature and gravity. Further, the procedures we adopted are not suitable for this spectral type range. At these types both β and c reach a maximum value and the rotation effect on $(u - b)$ starts reducing here after reaching a maximum around B9—while the effect on $(b - y)$ starts becoming more pronounced.

A basic assumption which underlies all our calculations is that the rotation effects are linear. This is not true for values of $\omega > 0.9$. The early B-stars, where the Be phenomenon is known to be pronounced, appear to rotate with $\omega > 0.9$ when they arrive on the main sequence (Rajamohan 1978). The ZRMS and ZRZAMS values in this paper would be slightly uncertain in the B0–B3 range. We have also not

determined directly the rotation effects on M_v from observations. As theory and observations agreed for all other indices, we have used the theoretical predictions to derive ZRZAMS values of M_v as a function of β. The agreement with Crawford's (1978) determination of the β, M_v values for the blue envelope of B-stars tends to confirm the theoretical predictions of Collins and Sonneborn. However, having determined ZRZAMS values after first establishing the rotation effects,, it should now be possible to use all the unevolved members of the galactic clusters to establish firmly the rotation effects on M_v.

7. Summary and conclusions

Effects of rotation on the intermediate band indices *uvby* and H_β are firmly established empirically from published data for many clusters. The observed positions of single main sequence stars and single-lined spectroscopic binaries in a given plane defined by any two of the indices were used to establish the relative displacements due to rotation.

As interstellar extinction also reddens the stars, the Alpha Persei Cluster was analysed using both observed and dereddened indices. It was found that for Alpha Persei, where non-uniformity of extinction is not large, both reddened and dereddened indices lead to similar results. However, as suggested by Gray and Garrison, we used the observed indices for other clusters as dereddening procedures for A-stars are based on an assumed calibration which may be in error due to rotational reddening.

Evolutionary effects will introduce a scatter if the cluster members are not coeval. This is evident from our results for the Scorpio-Centaurus association. Here the Upper Scorpius members which are younger than the Lower Centaurus and Upper Centaurus subgroups were found to be separated in all diagrams of colour excess due to reddening versus $V \sin i$ diagrams (Mathew & Rajamohan 1990a). Also the scatter for Upper Scorpius was large where the interstellar extinction is highly non-uniform. The Upper Centaurus and Lower Centaurus groups which are unreddened, consisting mostly of B2 and B3 type-stars show the reddening effect due to rotation in perfect agreement with theoretical predictions by Collins & Sonneborn (1977) for stars in the similar mass range.

As the predicted effects are a function of the mass, we analysed all clusters grouping them into three ranges corresponding to the spectral type ranges B0-B3, B5-B9 and A3-F0. The predicted indices for these ranges by Collins and Sonneborn were analysed the same way as was done for our observational data.

In our analysis of the theoretically derived indices we did not assume any distribution in v or i. Instead, for each value of i (30°, 45°, 60° and 90°) we took sixteen values corresponding to ω = 0.2, 0.5, 0.8 and 0.9 for the mass range corresponding to the spectral types from B0–B3, B5–B9 and A3–F0 and derived the rotation effects in different planes (such as β, c_1, β, $(u–b)$ etc.). We found that the rotation effects determined from observed data points for clusters, very closely matched the predictions for the various mass ranges. We have established very firmly that not only rotation effects can be discerned from observations but also that the agreement is excellent with theoretical predictions of Collins & Sonneborn (1977) for rigidly rotating stars.

The observed rotation effects, together with theoretical predictions were used to derive ZRMS for various clusters. The sequences were combined to derive preliminary ZRZAMS values of the various indices.

Acknowledgements

All computations for this work was carried out with the Mighty Frame Computer located at the IIA campus. We are thankful to A. V. Raveendran and B. A. Varghese for the help they have rendered at the computer. One of us (Annamma Mathew) is thankful to the University Grants Commission, New Delhi for their grant under the Faculty Improvement Programme with which this work was carried out.

References

Abney, W. de W. 1877, *Mon Not. R. astr. Soc,* **37**, 278.
Abt, H. A. 1970, in *IAU Coll. 4:* Steller Rotation, Ed. A. Slettebak, D. Reidel, Dordrecht, p. 193.
Abt, H. A., Chaffee, F. H. 1967, *Astrophys. J.,* **148**, 459.
Abt, H. A., Clements, A. E. Doose, L. R., Harris, D. H. 1969, *Astr. J.,* **74**, 1153.
Abt, H. A., Jewsbury, C. P. 1969, *Astrophys. J.,* **156**, 983.
Abt, H. A., Levato,.H. 1977, *Publ. astr. Soc. Pacific,* **89**, 648.
Abt, H. A., Morgan, W. W. 1969, *Astr. J.,* **74**, 813.
Anderson, C. M., Stoeckly, R., Kraft, R. P. 1966, *Astrophys. J.,* **143**, 299.
Balona, L. A. 1975, *Mem. R. astr. Soc,* **78**, 51.
Bidelman, W. P. 1956, *Publ. astr. Soc. Pacific,* **68**, 318.
Blaauw, A., Hiltner, W. A., Johnson, H. L. 1959, *Astrophys. J.*, **130**, 69; (Erratum) *Astrophys. J.,* 131, 527.
Braes, L. L. E., 1962, *Bull astro. Inst. Netherl,* **16**, 297.
Canteriia, R., Perry, C. L., 1979, *Publ. astr. Soc. Pacific,* **91**, 263.
Collins, G. W. IL 1963, *Astrophys. J.,* **138**, 1136.
Collins, G. W. II. 1965, *Astrophys. J.,* **142**, 265.
Collins, G. W. II. 1970, in *IAU Coli. 4: Stellar Rotation,* Ed. A. Slettebak, D. Reidel, Dordrecht, p. 85.
Collins, G. W. Π, Harrington, J. P. 1966, *Astrophys. J.,* **146**, 152.
Collins, G. W. II, Smith, R. C. 1985, *Mon. Not. R. astr. Soc,* **213**, 519.
Collins, G. W. II, Sonneborn, G. H. 1977, *Astrophys. J. Suppl.,* **34**, 41.
Crawford, D. L. 1978, *Astr. J.,* **83**, 48.
Crawford, D. L., 1979, *Astr. J.,* **84**, 1858.
Crawford, D. L., Barnes, J. V. 1969, *Astr. J.,* **74**, 818.
Crawford, D. L., Barnes, J. V. 1969, *Astr. J.,* **74**, 407.
Crawford, D. L, Barnes, J. V. 1970, *Astr. J.,* **75**, 952.
Crawford, D. L., Barnes, J. V. 1972, *Astr. J.,* **77**, .862.
Crawford, D. L, Barnes. J. V. 1974, *Astr. J.,* **79**, 687.
Crawford, D. L., Mander, J. 1966, *Astr. J.,* **71**, 114.
Crawford, D. L., Perry, C. L. 1966, *Astr. J.,* **71**, 206.
Crawford, D. L.$_5$ Perry, C. L. 1976, *Astr. J.,* **81**, 419.
Dickens, R., Kraft, R., Krzeminski, W. 1968, *Astr. J.,* **73**, 6.
Dworetsky, M. 1975, *Astr. J.,* **80**, 131.
Eggen, O. J. 1974, *Astrophys. J.,* **188**, 59.
Eggen, O. J. 1981, *Astrophys. J.,* **246**, 817.
Feast, M W. 1963, *Mon. Not. R. astr. Soc,* **126**, 11.
Garmany, C D. 1973, *Astr. J.,* **78**, 185.
Garrison, R. F. 1967, *Astrophys. J.,* **147**, 1003.
Glaspey, J. W. 1971, *Astr. J.,* **76**, 1041.
Gray, R. O., Garrison, R. F. 1987, *Astrophys. J. Suppl,* **65**, 581.
Gray, R. O., Garrison, R. F. 1989, *Astrophys. J. Suppl,* **69**, 301.
Gray, R. O., Garrison, R. F. 1989, *Astrophys. J. Suppl,* **70**, 623.
Guthrie, B. N. G. 1963, *Publ R. Obs. Edinburgh,* **3**, 84.
Hardorp, J., Strittmatter, P. 1968a, *Astrophys. J.,* **151**, 203.
Hartoog, M. R. 1976, *Astrophys. J.,* **205**, 807.
Hartwick, F.'D. A., Hesser, I E. 1974, *Astrophys.* **192**, 391

Herzog, A. D., Sanders, W. L., Seggewiss, W. 1975, *Astr. Astrophys. Suppl.,* **19,** 211.
Hill, G., Perry, C. L. 1969, *Astr. J.,* **74,** 1011.
Hoag, A. A., Johnson, H. L., Iriate, B., Hallam, K., Sharpless, S. 1961, *Publ. US Naval Obs.,* **17,** 347.
Hogg, A. R., Kron, G. E. 1955, *Astr. J.,* **60**, 365.
Huang, S. S., Starve, O. 1960, Stellar Atmosphere, Ed. J. L. Greenstein, Univ. Chicago Press, p. 321.
Ianna, P. A. 1970, *Publ. astr. Soc. Pacific,* **82**, 825.
Johnson, H. L. 1952, *Astrophys. J.,* **116**, 640.
Johnson, H. L., Knuckles, C. F. 1955, *Astrophys. J.,* **122**, 209.
Johnson, H. L., Mitchell, R. I. 1958, *Astrophys. J.,* **128**, 31.
Kraft, R. P. 1965, *Astrophys. J.,* **142**, 681.
Kraft, R. P. 1967, *Astrophys. J.,* **148**, 129.
Kraft, R. P. 1969, *Struve Memo. Vol.,* p. 385.
Kraft, R. P., Wrubel, M. 1965, *Astrophys. J.,* **142**, 703.
Levato, H. 1974, *Publ. Astr. Soc. Pacific,* **86**, 940.
Levato, H. 1975, *Astrophys. J.,* **195**, 825.
Levato, $H._5$ Garcia, B. 1984, *Astrophys. Lett.,* **24**, 161.
Maeder, A. 1970, *Astr. Astrophys.,* **10**, 354.
Mathew, A., Rajamohan, R. 1990a, *J. Astrophys. Astr.,* **11**, 167 (Paper 2).
Mathew, A., Rajamohan, R. 1990b, *Bull. astr. Soc. India,* **18**, 329.
Me Gee, J. D., Khogali, A, Baum, W. A., Kraft, R. P. 1967, *Mon. Not. R. astr. Soc,* **137**, 303.
Mendoza, E. E. 1956, *Astrophys. J.,* **123**, 54.
Mendoza, E. E. 1963, *Bol. Obs. Tonantzintla Tacubaya,* **3**, 137.
Mitchell, R. I. 1960, *Astrophys. J.,* **132**, 68.
Moreno, A., Moreno, H. 1968, *Astrophys. J. Suppl.,* **15**, 459.
Morgan, W. W., Hiltner, W. A. 1965, *Astrophys. J. Suppl,* **141**, 177.
Morgan, W. W., Hiltner, W. A., Garrison, R. F. 1971, *Astr. J.* **76**, 242.
Nissen, P. E. 1988, *Astr. Astrophys.,* **199**, 146.
Perry, C. L., Bond, H. E. 1969, *Publ. astr. Soc. Pacific,* **81**, 629.
Perry, C. L., Franklin, C. B. Jr., Landolt. A. U., Crawford, D. L. 1976, *Astr. J.,* **81**, 632.
Perry, C L, Hill, G. 1969, *Astr. J.,* **74**, 899.
Petrie, R. M. 1964, *Publ. Dom. Astrophys. Obs.,* **12**, 317.
Plavec, M. 1970, in *IAU Coll. 4: Stellar Rotation,* Ed. A. Slettebak, D. Reidel, Dordrecht, p. 133.
Rajamohan, R. 1976, *Pramana,* **7**, 160.
Rajamohan, R. 1978, *Mon. Not. R. astr. Soc,* **184**, 743.
Rajamohan, R., Mathew, A. 1988, *J. Astrophys. Astr.,* **9,** 107.
Roxburgh, I. W. 1970, in *IAU Coll. 4: Stellar Rotation,* Ed. A. Slettebak, D. Reidel, Dordrecht, p. 318.
Roxburgh, I. W., Griffith, J., Sweet, P. 1965, Z. *Astrophys.,* **61**, 203.
Roxburgh, I. W., Strittmatter, P. A. 1965, Z. *Astrophys.,* **63**, 15.
Schild, R. E. 1970, *Astrophys. J.,* **161**, 855.
Schmidt, E. G. 1978, *Pub. astr. Soc. Pacific,* **90,** 157.
Schmidt, E. G., Forbes, D. 1984, *Mon. Not. R. Astr. Soc,* **208**, 83.
Shobbrook, R. R. 1984, *Mon. Not. R. astr. Soc,* **206**, 273.
Shobbrook, R. R. 1984, *Mon. Not. R. astr. Soc,* **211**, 659.
Slettebak, A. 1968, *Astrophys. J.,* **151**, 1043.
Slettebak, A. 1970, in *IAU Coll. 4:* Stellar Rotation, Ed. A. Slettebak, D. Reidel, Dordrecht, p. 3.
Smyth, M. J., Nandy, K. 1962, *Publ. R. Obs., Edinburgh,* **3**, No. 2, 23.
Snowden, M. S. 1975, *Publ. astr. Soc. Pacific,* **87**, 721.
Snowden, M. S. 1976, *Publ. astr. Soc. Pacific,* **88**, 174.
Strittmatter, P. A. 1966, *Astrophys. J.,* **144**, 430.
Strom, K. M., Strom, S. E., Yost, J. 1971, *Astrophys. J.,* **165**, 479.
Strömgren, B. 1966, *A. Rev. Astr. Astrophys.,* **4,** 433.
Strömgren, B. 1967, *Magnetic and Related Stars,* Ed. R. C. Cameron, Mono Book Corporation, Baltimore, p. 461.
Uesugi, A., Fukuda, I. 1982, *Revised Catalogue of Stellar Rotational Velocities,* Univ. Japan.
Vogel, S. N., Kuhi, L. V. 1981, *Astrophys. J.,* **245**, 960.
Warren, W. H. 1976, *Mon. Not. R. astr. Soc,* **174**, 111.
Young, A. 1978, *Publ. astr. Soc. Pacific,* **90,** 144.

J. Astrophys. Astr. (1992) **13**, 109–128

Effects of Rotation on the Colours and Line Indices of Stars 6. The Reality of the Blue Straggler Phenomenon

Jacqueline D'Souza, Annamma Mathew* & R. Rajamohan *Indian Institute of Astrophysics, Bangalore 560034*

Received 1991 August 20; accepted 1992 January 15

Abstract. The effect of rotation on the observed colours of stars has been considered as a possible cause for the blue straggler phenomenon in clusters listed by Mermilliod (1982). It appears that this phenomenon is definitely not real in the case of the late B and early A spectral type blue stragglers that are intrinsic slow rotators. Among clusters containing the early B type blue stragglers it is found that the anomalous position of the stragglers in NGC 6633, NGC 6475 and NGC 2516 cannot be accounted for by rotation effects alone.

Key words: stars, rotation—stars, colours—star clusters, individual—stars, blue stragglers

1. Introduction

Blue stragglers are stars that occupy a position in a cluster colour magnitude diagram above and to the left of the cluster main sequence. They appear bluer than the presumed cluster turn off, obviously contradicting the assumption that all cluster members are coeval. Various theories have been put forward to explain their anomalous position with respect to the cluster main sequence.

Williams (1964a) in his delayed formation theory suggested that these objects were formed later than other cluster members and that the assumption that cluster members are coeval is erroneous. This theory is not favoured any longer since there is no independent observational evidence especially in old open clusters for ongoing star formation such as the occurrence of T-Tauri stars, emission or reflection nebulae and differential reddening due to clumps of dusty gas (Wheeler 1979a).

Williams (1964b) proposed the theory of accretion in which a main sequence star accretes matter from high density regions and moves along the main sequence to become a bluer star. The interaction of the interstellar matter already present in the cluster with the mass ejected by supergiant members is supposed to produce such regions. For this mechanism to be operative such clusters must be fairly old while blue stragglers seem to occur in clusters of all ages.

Mass transfer in close binaries proposed by McCrea (1964) and quasi homogenous evolution proposed by Wheeler (1979b) are more viable but the evidence in support of them is not conclusive. While some blue stragglers do show radial velocity

*on leave from Assumption College, Changanacherry, Kerala.

variations, an equal number have constant radial velocity indicating that duplicity is not a necessary condition for their existence.

Maeder (1987) hypothesized extra-mixing by rotationally induced turbulent diffusion in OBN stars giving rise to nearly homogeneous evolution. This suggestion is analogous to the extensive mixing hypothesis proposed by Wheeler. Another mechanism that may lead to homogenous evolution is extensive core overshooting as suggested by Stothers & Chin (1979). Stellar coalescence suggested by Leonard (1989) attributes the formation of blue stragglers to binary –binary collisions in globular clusters. A blue straggler formed from the above mechanism must not be a slow rotator as the merger of binaries should produce a rapidly rotating star. Blue stragglers on the other hand have a wide range of observed $V \sin i$ values.

Mermilliod (1982) compiled a list of blue stragglers in clusters younger than the Hyades which show a large spread in properties indicating that no unique model would be able to explain all the observations.

Mermilliod (1982) has shown that there are no observable differences between the blue stragglers and corresponding normal main sequence stars, except for the distribution in their rotational velocities. He also found that the blue stragglers cannot be identified spectroscopically and can only be discovered from their position in the colour-magnitude diagram.

An interesting feature that has emerged out of the work on blue stragglers (Pendl & Seggewiss 1975; Mermilliod 1982) is that more than half of them belong to the class of chemically peculiar (CP) stars of spectral types B7 and later. This group, in general consists of slow rotators. The blue stragglers earlier than B5, in general, have a range in their observed rotational velocities and some of them are also Be stars. This marked characteristics in the rotational velocity distribution of the blue stragglers and the fact that even in the old galactic cluster M 67 (Mathys 1991) they are all slow rotators have led us to investigate the possibility of rotation effects on colours of cluster stars as a primary cause for their observed positions. We have already established in a series of papers (Rajamohan & Mathew 1988; Mathew Rajamohan 1990 a, b; 1991) that such rotation effects are discernible in the observed data of star clusters and also that the effects are fully consistent with the theoretical prediction of Collins & Sonneborn (1977).

The blue stragglers that fall in the early A-type domain the intrinsic slow rotators – are discussed in Section 2, and the B-type stragglers with a wide range in rotational characteristics are discussed in Section 3. A summary of the results is given in Section 4.

2. The A-type blue stragglers

The early B type stars in a cluster have maximum observed rotational velocities close to their break-up speeds, while the maximum observed rotational velocity for stars in the spectral range B5-FO is close to $\omega = 0.9$ (Rajamohan 1978; Kawaler 1987). The effect of rotation on the main sequence of a cluster, is to displace it from its non-rotating counterpart and broaden it by about twice the displacement (Collins & Smith 1985). The maximum displacement that a main sequence star would suffer, depends directly on the maximum rotational velocity that it can have; this corresponds to the balance between centrifugal force and gravity at the equator. The observed

distribution of main sequence stars in a cluster between the zero rotation main sequence curve and the main sequence curve for $\omega = 1.0$ therefore, depends on the spread in the true rotational velocities of the stars. Also the observed dispersion along the main sequence would be a function of mass as the effects on different indices peak in different mass ranges.

The maximum effects predicted for the $(u - b)$ index are for stars in the B7–A0 spectral range (Collins & Sonneborn 1979). The presence of a slow rotator in any cluster where the turn-up occurs for stars in the above spectral range, would make the slow rotator appear bluer than other normally rotating main sequence stars. Since the effects of rotation and evolution both act in the same direction, this observed colour difference would make the stars on the main sequence appear more evolved than the blue straggler itself. We have in the following analyses, taken this differential reddening effect due to rotation into account in judging how blue the blue stragglers really are, and how much really are the nearby cluster members evolved.

Table 1 gives the theoretically predicted changes for inclinations $i = 0°$ and $i = 90°$ in the various photometric indices for a non-rotator and a star of the same spectral type rotating with $\omega = 0.9$. This table was derived from the work of Collins and Sonneborn (1977). They have listed the values of $(b - y)$, c, m, β, M_v and $(u - b)$ for various values of i ranging from 0° to 90° and fractional velocities $\omega = 0.0$, 0.5, 0.8, 0.9 and 1.0. These values have been tabulated for the mass range that corresponds to the main sequence stars in the spectral type domain B0 to A7. Table 1 shows that the effects of rotation on the colour indices are almost independent of i in the B0 to A2 spectral domain.

Table 2, lists the blue stragglers belonging to the class of slow rotators taken from a list compiled by Mermilliod (1982). Column 2 lists the clusters to which the blue straggler belongs, Column 3 its HD number, Column 4 its spectral type and Column 5 its observed V sin i value. The last column contains remarks, if any, on the binary nature, membership probability, radial velocity variations etc. of the blue stragglers under consideration. The V sin i values of the stragglers in NGC 6633 and NGC 6281 have been taken from Abt (1985). The spectral type, V sin i values and other remarks for the clusters in the table are as given by Mermilliod.

Mermilliod's listing contains a few more clusters. We have considered only those for which intermediate and narrow-band photometric data along with V sin i values for the blue straggler were readily available. The membership probability of star no. 161 (HD 170563) in NGC 6633 (Abt 1985) and star no. 9 (HD 153947) in NGC 6281, (Feinstein & Forte 1974) is low.

From Table 1, it can be seen that rotation effects on the $(u - b)$ index are larger than on $(b - y)$ in the B7–A0 spectral range. In a given cluster the members in these spectral ranges, rotating with an average velocity typical of their spectral class should suffer a large change in both the $(u - b)$ and $(b - y)$ indices due to rotation and be pushed away from the zero rotation main sequence. This rotational reddening in $(u - b)$ is especially large for this spectral range. Most of the blue stragglers listed in Table 2, being peculiar, are intrinsic slow rotators (Abt 1979) and have anomalously low observed V sin i for their spectral type. They fall in the above mentioned spectral range where rotation effects on the $(u - b)$ index reach a maximum.

A plot in the M_v versus $(b - y)$ or M_v versus $(u - b)$ plane of any of these clusters containing an intrinsic slow rotator in the B9–A0 spectral range would, therefore, show the slow rotators in a position that is blue when compared to other stars in

the same spectral range rotating with an average velocity of the order of 150 kms^{-1}. The slow rotator would thus appear as a blue straggler, the effect being more pronounced in the M_v versus $(u - b)$ plane since rotation affects the $(\mu - b)$ index considerably.

Figs 1 to 5 show the clusters listed in Table 2 plotted in the (M_v, $b - y$); (M_v, $u - b$), and $(u - b)$, $(b - y)$ planes. The observed $(b - y)$ index of each of the

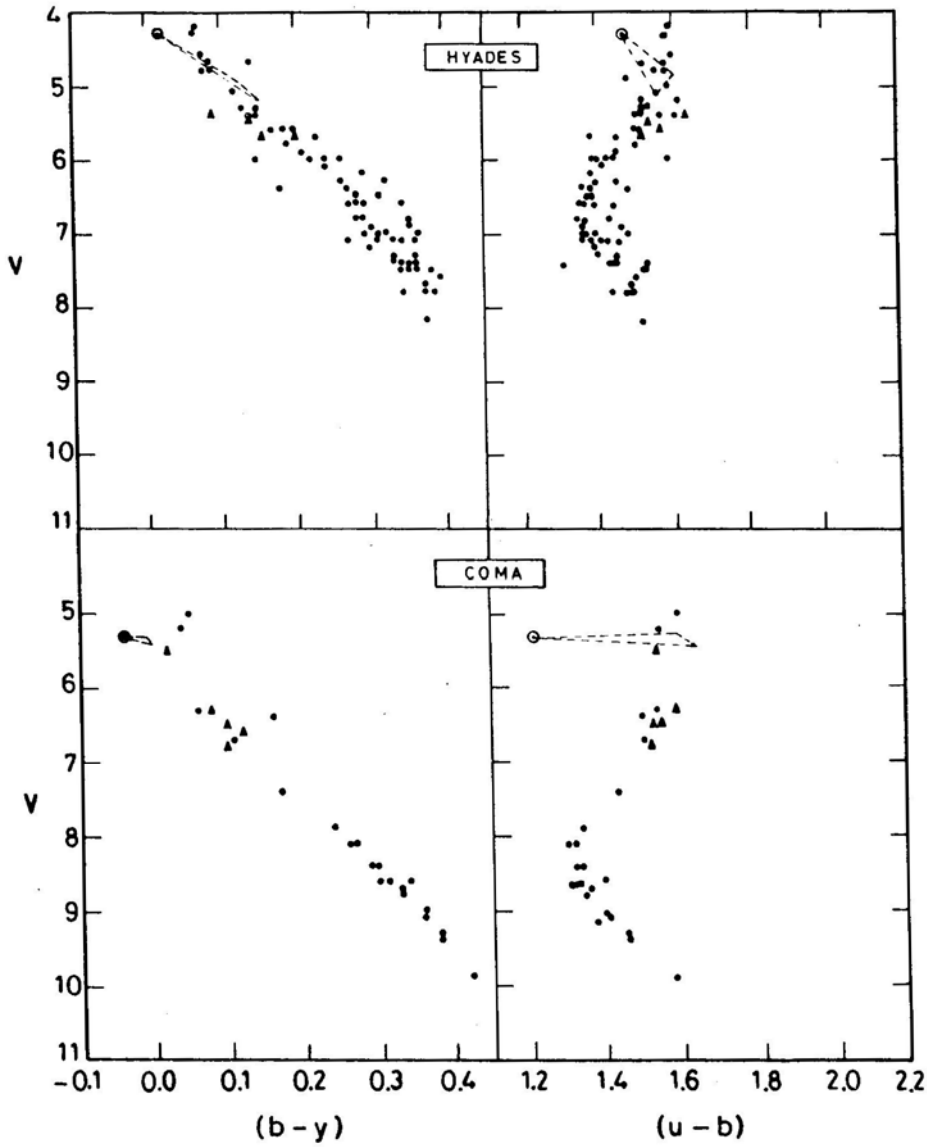

Figure 1 (a). Hyades and Coma in the V versus $(b - y)$ and V versus $(u - b)$ planes. The filled circles represent the cluster members and the filled triangles the Ap and Am stars in the cluster. The blue straggler is denoted by a dot inside an open circle. The triangle with one apex as the blue straggler represents the correction for ω =0.9 for angles of inclination i = 0 and i = 90.

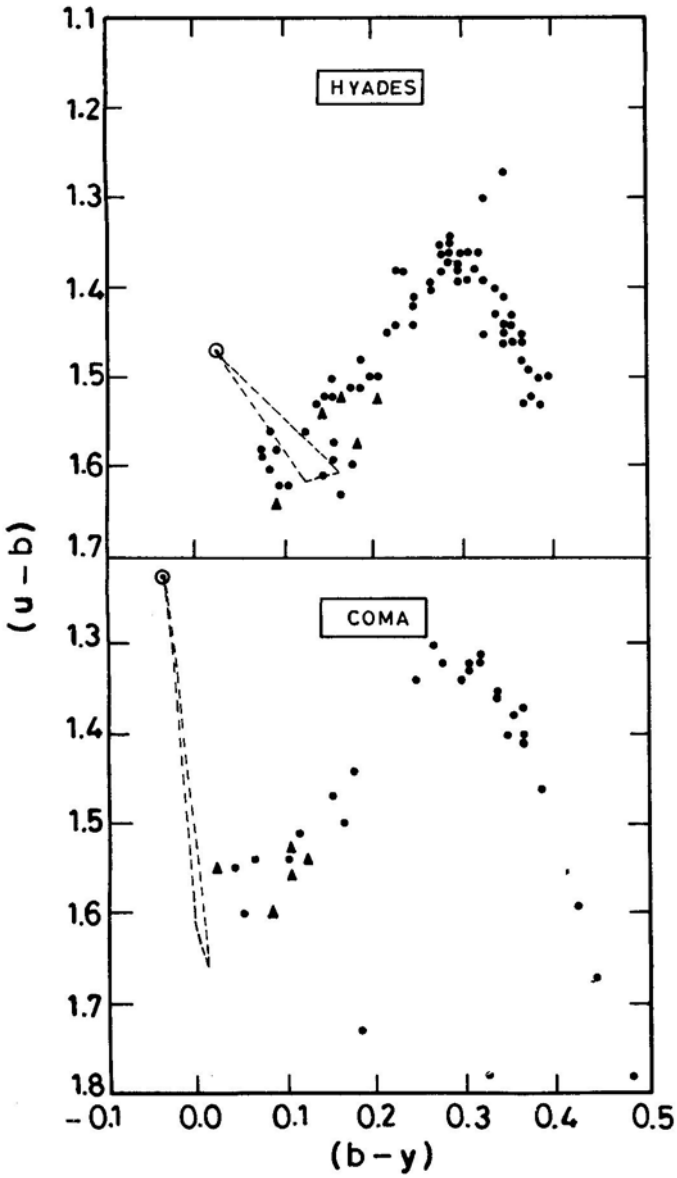

Figure 1 (b). Hyades and Coma clusters in the ($u - b$) versus ($b - y$) plane. Symbols are the same as in Fig. 1 (a).

blue stragglers in the clusters was corrected for interstellar reddening using the average $E(b - y)$ given for each of these clusters in the original papers giving photometric data. References to the cluster data along with the $E(b - y)$ value used are given in Table 3. The rotational correction for $\omega = 0.9$ at the observed $(b - y)_0$ was taken for $i = 0°$ and $i = 90^0$ from Table 1. We have indicated by means of a triangle in each of these figures the change in position of the blue straggler if it were to be rotating with velocity ranging anywhere from zero to a maximum velocity corresponding to $\omega = 0.9$. Rotation effects in the ($u - b$, $b - y$) plane push the stars along the

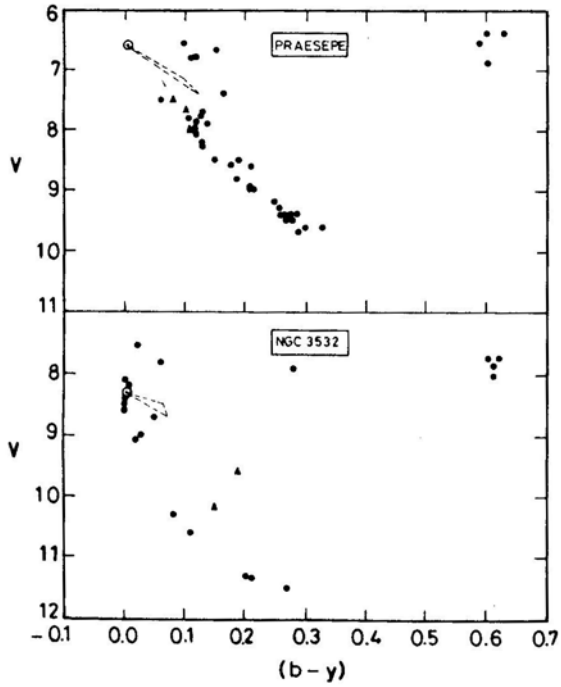

Figure 2(a). Praesepe and NGC 3532 in the V versus $(b - y)$ plane. Symbols are the same as in Fig. 1 (a).

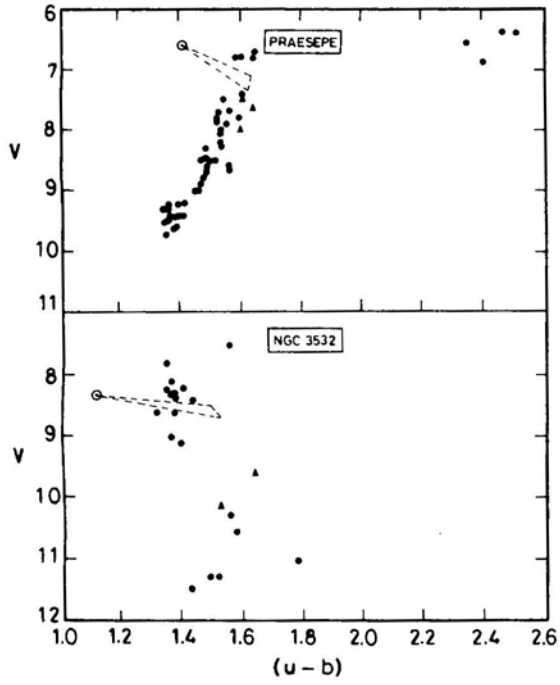

Figure 2(b). Praesepe and NGC 3532 in the V versus $(u - b)$ plane. Symbols are the same as in Fig. l(a).

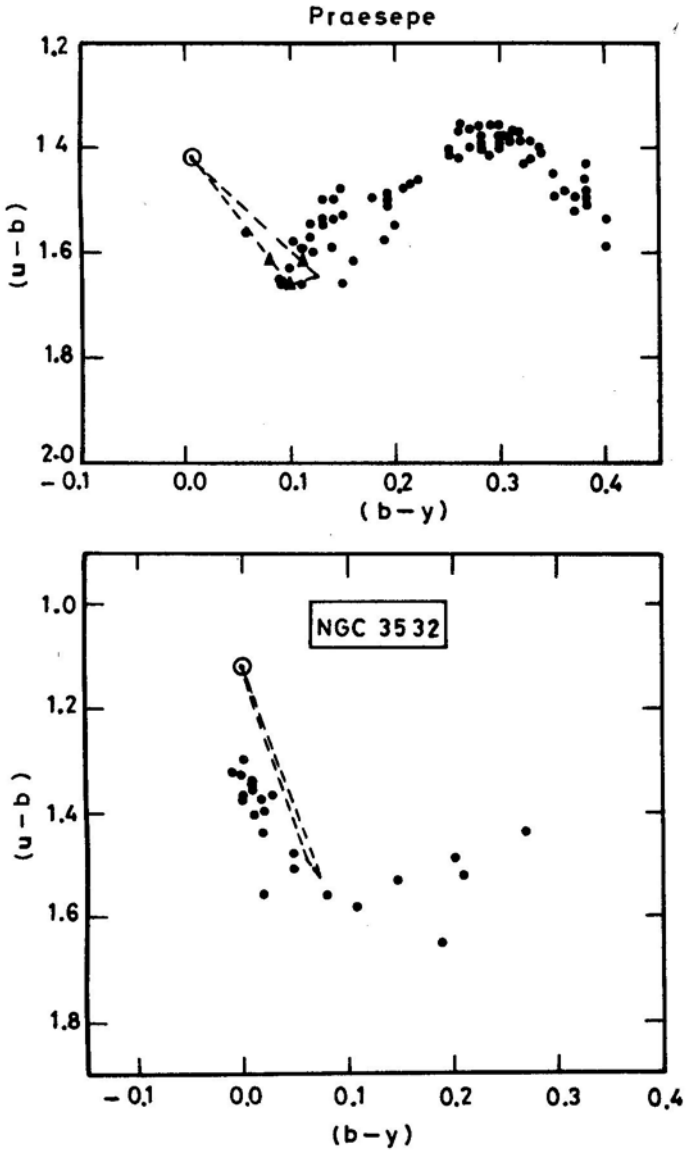

Figure 2(c). Praesepe and NGC 3532 in the ($u - b$) versus ($b - y$) plane. Symbols are the same as in Fig. l (a).

main sequence curve. For the B0 to A2 stars the ($u - b$) index is affected by a larger extent than the ($b - y$) index. A slow rotator in this plane would therefore, maintain its position on the curve, whereas the other normally rotating stars would be pushed downwards. This would cause a large gap between the slow rotators and the others. Correction of the blue straggler in this plane causes a significant reduction in this gap as shown in Fig. l (b) for Hyades and Coma and in Fig. 2 (c) for Praesepe and NGC 3532. An exception to these results is the cluster NGC 6633. The blue stragglers in this cluster are discussed in the next section.

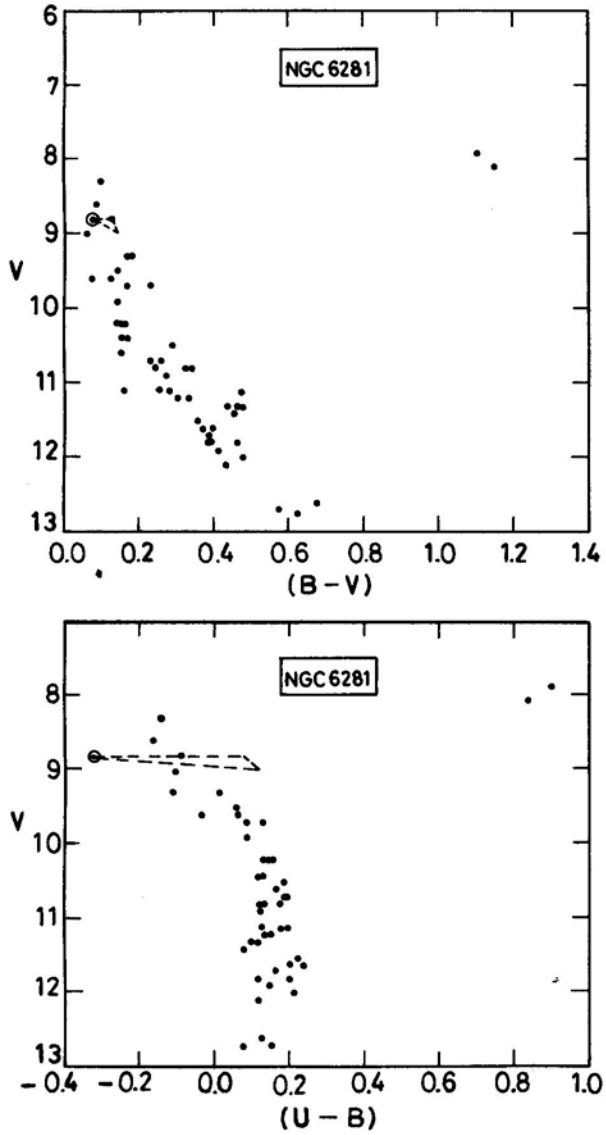

Figure 3. NGC 6281 in the V versus $(B - V)$ and V versus $(U - B)$ planes. Symbols are the same as in Fig. 1(a).

NGC 2281 has been analysed using *UBV* data since narrow-band data for this cluster is not available. Similarly, for NGC 6281 broad-band indices have been plotted as narrow band data for the blue straggler in this cluster is not available. The corrections applied to the blue stragglers in these cases would be underestimated since larger effects due to rotation on the broadband colours are predicted (Collins & Smith 1985). The analysis of rotation effects on the broad-band *UBV* colours of the α-Persei and Pleiades cluster (Mathew & Rajamohan 1991) show that the effects are of the order of 0.05 mag. per 100 km s^{-1} in $(U - B)$.

The cluster colour–colour and colour–magnitude diagrams show clearly that the

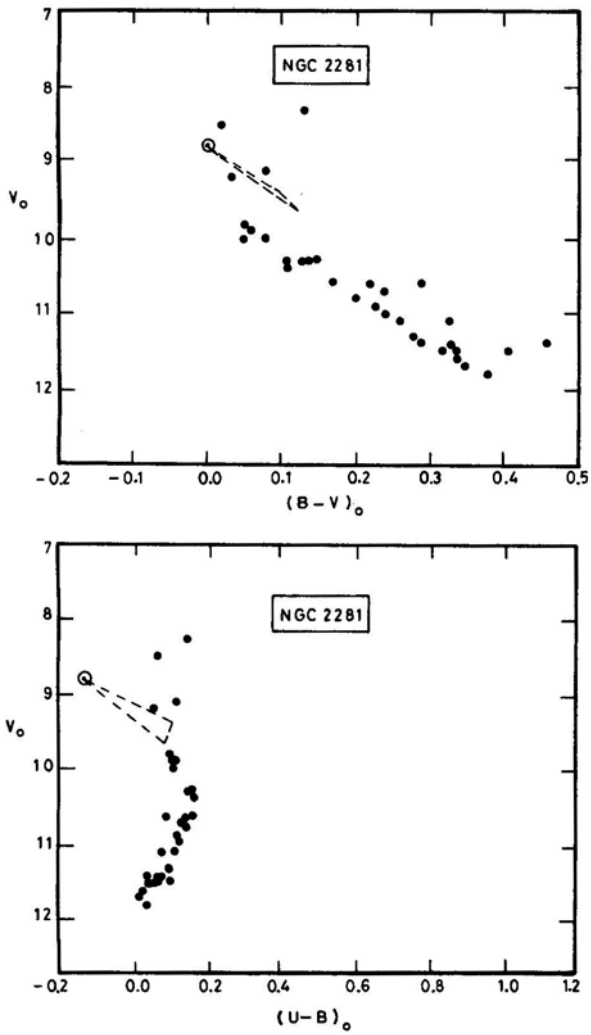

Figure 4. NGC 2281 in the V_0 versus $(B - V)_0$ and V_0 versus $(U - B)_0$ planes. Symbols are the same as in Fig. 1 (a).

anomalous position of all the blue stragglers listed in Table 2, with the exception of the blue stragglers in NGC 6633, can be explained purely by differences in the rotational velocities between the straggler and its nearest main sequence neighbours. The fact that blue stragglers in the *B* and early *A* spectral type domain appear bluer because of their low rotation seems to have been noted by Strittmatter & Sargent (1965) more than 25 years ago! They corrected the metallic-line stars in the Hyades, Praesepe and Coma clusters for blanketting effects and found that they lie to the left of the main sequence. They suggested that this was because they were slow rotators and that other stars of similar masses have been shifted to the red due to rotation.

We would also like to draw attention here to the blue stragglers in IC 4756, IC 4651, NGC 752 and M67. The stragglers studied by Pendl & Seggewiss (1975) in IC 4756 are all spectroscopically peculiar and these authors were the first to suggest

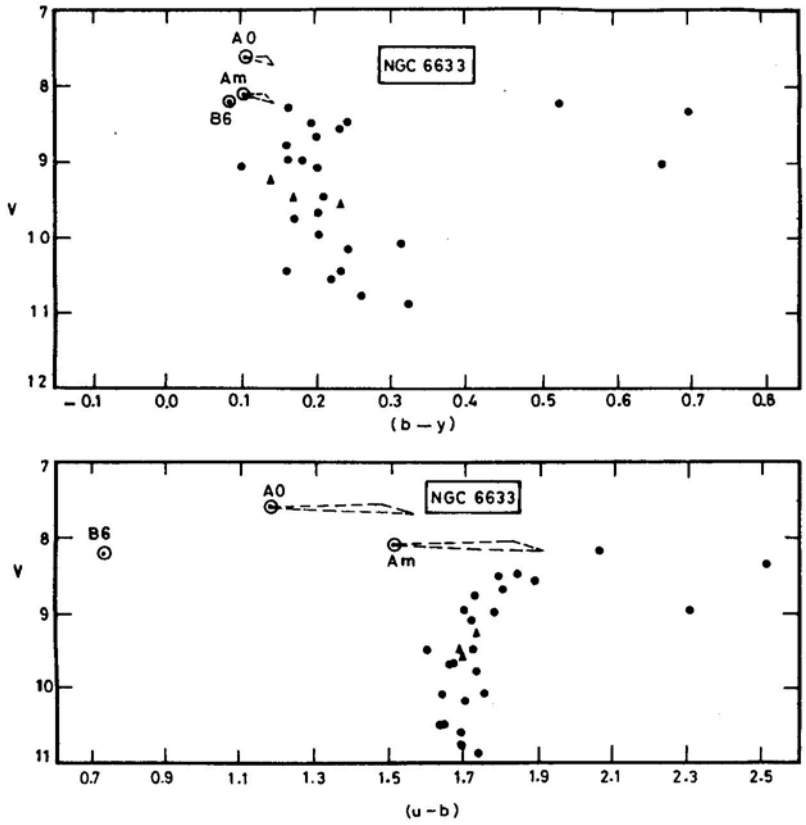

Figure 5. NGC 6633 in the V versus $(b - y)$ and V versus $(u - b)$ planes. Symbols are the same as in Fig. 1(a).

Table 1. Change in the indices from $\omega = 0.0$ to $\omega = 0.90$.

$M/M_\odot$	Sp. Type	ΔM_v		$\Delta(b-y)$		$\Delta(u-b)$		Δc_1	
		$i=0$	$i=90$	$i=0$	$i=90$	$i=0$	$i=90$	$i=0$	$i=90$
14.5	B0	0.07	0.23	0.025	0.029	0.149	0.158	0.097	0.098
11.0	B1	−0.01	0.15	0.027	0.031	0.208	0.085	0.152	0.156
8.3	B2	−0.05	0.12	0.028	0.033	0.247	0.265	0.185	0.193
6.3	B3	−0.07	0.10	0.028	0.034	0.291	0.314	0.229	0.242
4.9	B5	−0.09	0.09	0.029	0.035	0.347	0.379	0.281	0.300
3.9	B7	−0.06	0.12	0.032	0.039	0.391	0.430	0.311	0.336
2.8	B9	0.23	0.43	0.056	0.068	0.374	0.401	0.246	0.247
3.3	B8	0.03	0.21	0.039	0.047	0.401	0.442	0.303	0.324
2.5	A0	0.55	0.32	0.091	0.117	0.237	0.217	0.077	0.025
2.3	A1	0.64	0.93	0.104	0.137	0.152	0.114	−0.004	−0.082
2.1	A2	0.68	0.97	0.115	0.153	0.086	0.026	−0.078	−0.172
1.9	A3	0.72	1.01	0.129	0.174	−0.009	−0.086	−0.173	−0.290
1.8	A5	0.45	0.74	0.119	0.173	−0.107	−0.189	−0.239	−0.367
1.7	A7	0.31	0.59	0.120	0.179	−0.146	−0.217	−0.274	−0.403

Table 2. List of the *A*-type blue stragglers.

S. no.	Cluster	Star no. HD(E)	Spectral type	$V \sin i$	Remarks
1.	Hyades	27962	AIVm	< 30	Constant Vr, D 1″.4, 3^m.3
2.	Coma	108662	AOp (Sr, Cr)	15	Constant Vr, α CVn type var.
3.	Praesepe	73666	AIV	10	Constant Vr
4.	NGC 3532	96213	AOIV		D 0″.4, 0^m.5
5.	NGC 6281	153947	AOp(Si)	~ 30	Probable non member
6.	NGC 6633	169959	AOIII	< 40	
		170563	Am		Probable non member
7.	NGC 2281	49010	Ap		

Table 3. References to cluster data for the A-type stragglers.

S. no.	Cluster	Data	Reference
1.	Coma	*uvby*	Crawford & Barnes (1969)
2.	Hyades	*uvby*	Crawford & Perry (1966)
3.	Praesepe	*uvby*	Crawford & Barnes (1969)
4.	NGC 2281	*UBV*	Pesch (1961)
5.	NGC 3532	*ubvy*	Eggen (1981)
6.	NGC 6281	*UBV*	Feinstein & Forte (1974)
7.	NGC 6633	*uvby*	Schmidt (1976)

strongly that the two phenomena appear to be related. What is actually common to the two phenomena is slow rotation. Slow rotation is indirectly responsible for these objects to appear bluer and it is well known that almost all chemically peculiar stars on the upper main sequence are slow rotators.

In M 67 Mathys (1991) finds that all the blue stragglers are slow rotators and the blue straggler phenomenon seems to be related to the Am phenomenon even though only two of the eleven stragglers are known Am stars (Pesch 1967). As noted by Pendl & Seggewiss (1975) the blue stragglers have not been studied carefully to recognise Ap, Am characteristics and it would not be surprising if a large fraction of the M 67 stragglers turn out to be Ap stars of the Hg–Mn type. A comparison of IC 4651 and M 67 in the M_v versus $(B - V)$ plane also indicates that the stragglers in IC 4651 could possibly be explained in terms of rotation effects if they were to be intrinsic slow rotators. The position of the blue straggler in NGC 752 however does indicate that it cannot be explained by rotation effects alone.

3. The B-type blue stragglers

A listing of the blue stragglers in the B0–B6 spectral range is given in Table 4. The third coloum gives the HD number of the blue straggler, followed by its spectral type and observed $V \sin i$ values in Columns 4 and 5 respectively. The last column is similar to that in Table 2 and gives details regarding duplicity etc. The nine clusters listed in Table 4 along with the above data have been taken from Mermilliod's (1982) listing of blue stragglers. Unlike the A-type stragglers discussed in Section 2, the B-type

stragglers have a random V sin i distribution. Out of the nine clusters listed in the table, NGC 6633 and NGC 6475 stragglers have low observed V sin i's. The rotational velocities of the stragglers in NGC 6025 and NGC 2439 are not available. Out of the remaining five clusters, four contain emission-line objects, indicating rotation at a velocity close to their break-up speeds, while the blue straggler in IC 2602 has a V sin i typical of stars belonging to the spectral type B0.

The effect of rotation, in general, on the early B type (B0–B3) stars, is small in comparison with the effect on the late B type (B5–B9) stars. The reddening due to rotation in the $(u - b)_0$ and c_0 indices in particular shows a steep increase in the B5–B9 spectral range relative to the early B type stars. The blue stragglers that are fast rotators, except for Alcyone in Pleiades fall in the B0–B3 mass domain where the rotation effects are not pronounced. It is therefore possible that in a few of these clusters, differential rotational reddening, may cause the stars that are of slightly lower mass than the straggler, to appear redder and therefore more evolved.

To check that the above effect may be a possible cause for some of the stars to be designated blue stragglers we attempted to correct the brightest cluster stars on the main sequence for the effects of rotation. We do find that the bright main sequence stars close to the stragglers are indeed fast rotators and fall in the spectral type range where the rotational effects on their colours are large.

To correct each star for rotation effects, we need to know the individual values of V and i. We have assumed a value of $i = 45°$ to get an approximate estimate of the velocity V with which the star is rotating from the observed V sin i value. Table 5 contains the average corrections for 100 km s^{-1} of rotation that have to be applied in the M_v, $(u - b)_0$ and M_v, $(b - y)_0$ plane calculated from the work of Collins & Sonneborn (1977). These corrections have been listed as a function of $(u - b)_0$ since masses of the stars are unknown. The ZRZAMS values of $(u - b)_0$ as a function of mass is taken from Mathew & Rajamohan (1991). The observed $(u - b)_0$ for each star was used to get the first set of corrections in $(u - b)_0$ and M_v. These corrected indices were then used to derive the second set of corrections in M_v, and $(u - b)_0$. The average of these two sets was used to correct the stars in the M_v, range 0.0 to – 2.0 magnitude for which rotation velocity data are available. Some of the stars in this magnitude range have low observed V sin i (< 50 km s^{-1}). These appear considerably displaced from the ZRMS and are probably fast rotators seen pole-on. The velocities obtained from the V sin i values in these cases are obviously underestimated leaving these star uncorrected.

Six of the nine clusters listed in Table 4 are shown in the M_v versus $(u - b)_0$ plane in Figs 6 to 11. Table 6 gives the references to the cluster data along with the distance modulus and $E(b - y)$ value used. The straggler in NGC 2287 is considered a non-member by Mermilliod (1982), as it lies outside the cluster radius and its membership based on available radial velocities is difficult to assess. Intermediate-band photometric indices are not available for NGC 2439. The stragglers in the remaining seven clusters are discussed below in relation to the rotational reddening effects as a possible cause contributing to their erroneous designation as blue stragglers. More detailed discussion on other properties of these stragglers have been listed by Mermilliod (1982).

(a) *HD 93030 in IC 2602:* This bright southern object has been found by Walborn (1979) to be a short period binary (P = 1.7788 days) with a relatively low mass companion. Mass transfer phenomenon is supposed to account both for its spectral

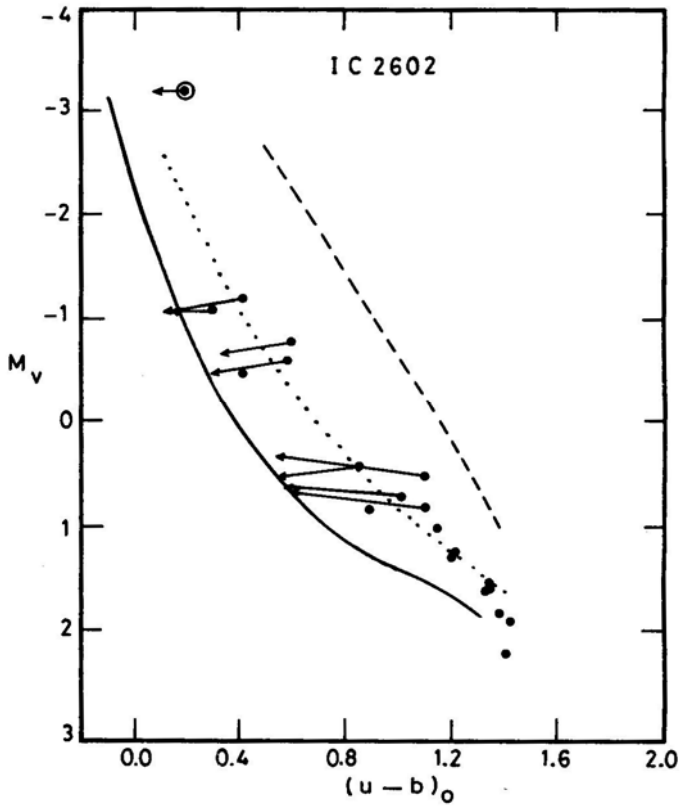

Figure 6. IC 2602 in the M_v versus $(u - b)_0$ plane. The blue straggler is denoted by a dot inside an open circle. The continuous line represents the zero rotation main sequence used by us. The theoretical sequence for ω = 0.9 and 1.0 are denoted by the dotted and broken lines respectively. The arrow heads indicate the position of the stars, when corrected for rotation

peculiarity and observed location in the HR diagram. The upper main sequence of the IC 2602 stars is shown in Fig. 6. Also shown, are the zero rotation zero age main sequence (ZRZAMS) from Mathew & Rajamohan (1991), the zero age main sequence (ZAMS) for ω = 0.9 and the ZAMS for ω = 1.0. The reddening effects predicted by Collins & Sonneborn (1977) for ω = 0.9 and 1.0 were appropriately combined with the adopted ZRZAMS to derive the two ZAMS curves. The arrow heads indicate the position which the stars indicated would occupy if they were to be non-rotators. The rotationl velocities for these stars were taken from Levato (1975) and were corrected using Table 5. It can be noticed that the majority of the stars scatter around the ZAMS for ω = 0.9 and would lie along the ZRZAMS if rotational reddening can be properly taken into account. The position of the blue straggler shows it is slightly evolved and cannot be considered anomalous.

(b) *HD 60855 in NGC 2422*: The upper main sequence of the stars in NGC 2422 is shown in Fig. 7. Rotational reddening corrections for the brightest members are indicated by arrows. Rotational velocities were taken from Dworetsky (1975). These corrections are a lower estimate if these stars have fractional velocities greater than ω = 0.9. The reddening effect due to rotation is highly nonlinear for ω > 0.9 (Collins &

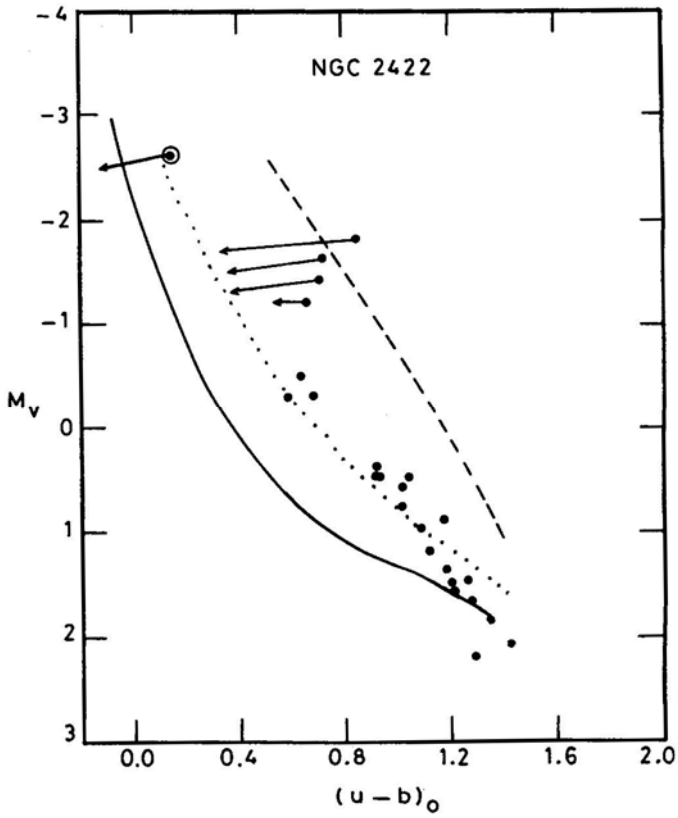

Figure 7. NGC 2422 in the M_v versus $(u - b)_0$ plane. Symbols are the same as in Fig. 6,

Sonneborn 1977; Collins & Smith 1985). On the other hand, if the stars on the upper main sequence are evolved, then they would be rotating with less than 0.9, as an increase in the radius would diminish the rotational velocity of the star. Our corrections in this case would be slightly overestimated. However, an ultraviolet excess of 0.15 magnitudes is not unusual for Be stars (Mermilliod 1982; Feinstein 1968). Therefore HD 60855 should be considered only as a probable blue straggler until detailed evolutionary tracks that take rotation into account become available.

(c) *HD 2S630 in Pleiades:* The Pleiades data are plotted in Fig. 8, and the observed position of the stars appear to be consistent with the fact that they are fast rotators. (Anderson, Stoeckly & Kraft 1966). The rotation corrections applied to the bright stars indicate that the age has to be revised downwards by a larger amount than that estimated by Maeder (1970). Remarks similar to the ones made in connection with NGC 2422 regarding the estimates for these corrections also apply to Pleiades. Given the uncertainties in the position of the bright members, HD 23630 should not be considered a blue straggler.

(d) *HD 143448 in NGC 6025:* The data for this cluster is plotted in Fig. 9 which seems to indicate that the majority of the stars are fast rotators. No rotational velocity data is available for this cluster. The cluster appears similar to that of NGC 2422 and the same remarks as before apply to this cluster.

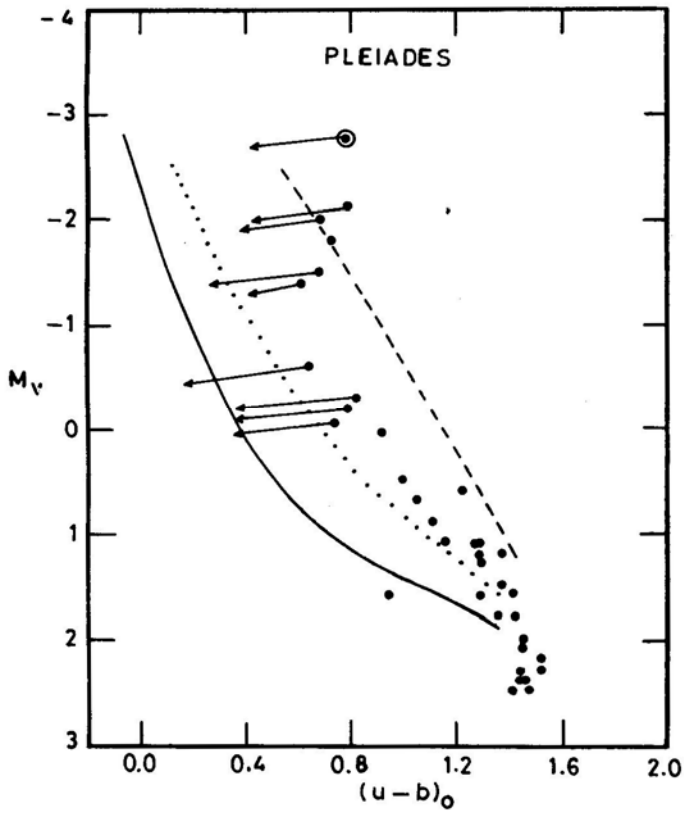

Figure 8. The Pleiades cluster in the M_v versus $(u - b)_0$ plane. Symbols are the same as in Fig. 6.

(e) *HD 66194 in NGC 2516:* The data for this cluster is plotted in Fig. 10. The large scatter of the stars in the $M_{v,}$ $(u - b)_0$ plane appears to be directly correlated to the large spread in their rotational velocities. The V sin i values were taken from Abt *et al.* (1989). The slowly rotating peculiar stars in this cluster are found closer to the ZRZAMS. This fact has already been noted by Eggen (1972) and Snowden (1975). Both of them call the CP stars in this cluster as stragglers! We find that a large number of slow rotators lie well above the main sequence indicating that they are probably fast rotators seen pole-on. For a few of the bright members, rotational velocities are not available. The age estimates for this cluster by Eggen (1972) and Snowden (1975) must be considered highly uncertain due to the large observed spread in the rotational velocity distribution for this cluster. However, the position in the colour-magnitude diagram of one of the evolved giants in this cluster indicates that HD 66194 should be considered as a blue straggler, as the giant appears to have evolved from a star less massive than the blue straggler itself.

(f) *ED 162374 and HD 162586 in NGC 6475:* The data for this cluster is plotted in Fig. 11. As both are slow rotators we can consider what would be their position if their rotational velocities were to be high as we have done for the A-type stragglers. If HD 162586 is an intrinsic slow rotator, a fact which we cannot prove, then it cannot be considered as a blue straggler, HD 162374 appears to be a definite blue straggler

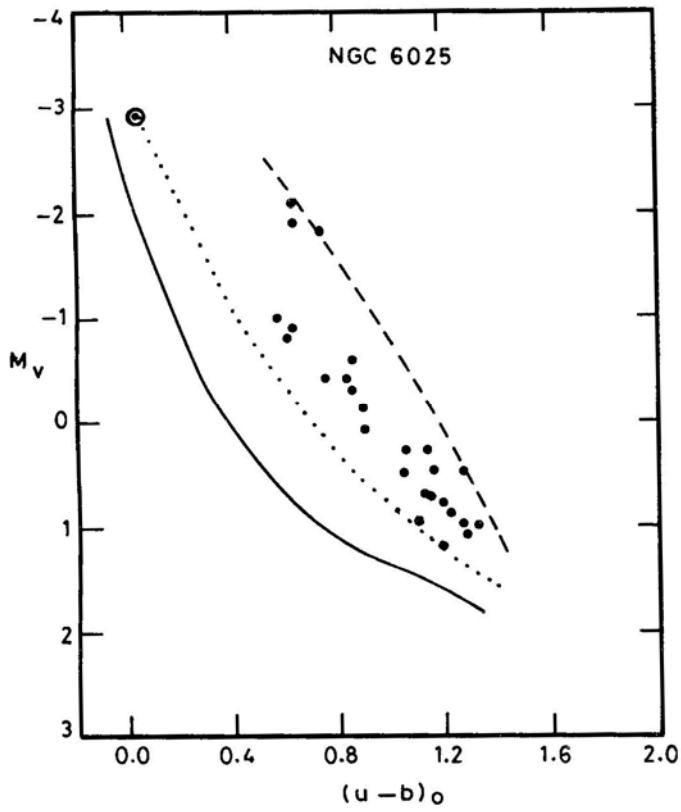

Figure 9. NGC 6025 in the M_V versus $(u-b)_0$ plane. Symbols are the same as in Fig. 6.

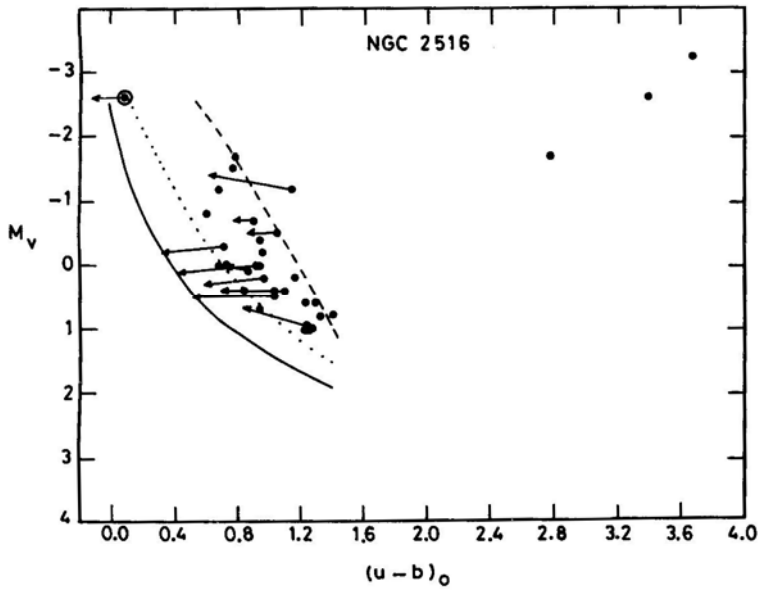

Figure 10. NGC 2516 in the M_V verses $(u-b)_0$ plane. Symbols are the same as in Fig. 6.

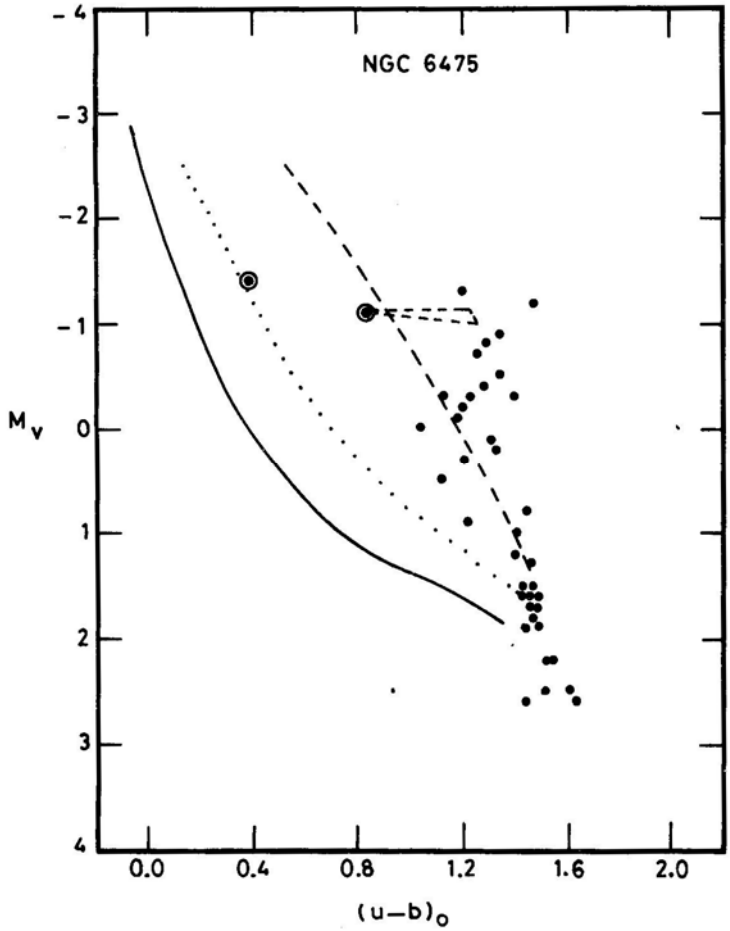

Figure 11. NGC 6475 in the M_v, versus $(u - b)_0$ plane. Symbols are the same as in Fig. 6. The triangle with one apex as the blue straggler (HD 162586) represents the correction for $\omega = 0.9$ for angles of inclination $i = 0°$ and $i = 90°$.

Table 4. List of the *B*-type blue stragglers.

S. no.	Cluster	Star no. HD(E)	Spectral type	$V \sin i$	Remarks
1.	NGC 6633	170054	B6IV	< 20	Constant Vr
2.	NGC 6475	162374	B5IVp	< 40	He weak, constant Vr
		162586	B6V	< 40	D 0″.5, 0^m.0
3.	NGC 2287	49333	B4p	100	He weak, probable non-member
4.	NGC 2516	66194	B2IVne	250	
5.	NGC 6025	143448	B3IVne		
6.	Pleiades	23630	B8IIIe	230	Alcyone
7.	NGC 2422	60855	B2IVe	320	D 5″.2, 6^m.8
8.	IC 2602	93030	B0IVp	195	SB1
9.	NGC 2439	DM31° 4911	B1.5Ib		

Table 5. Average change in indices for change in velocity of 100 km s^{-1}

$(u-b)_0$	ΔM_v	$\Delta(b-y)$	$\Delta(u-b)$
−0.058	−0.009	0.005	0.045
0.185	−0.019	0.006	0.059
0.436	−0.026	0.007	0.078
0.654	−0.034	0.007	0.103
0.830	−0.027	0.008	0.122
0.926	0.000	0.011	0.129
1.129	0.062	0.016	0.122
1.301	0.170	0.028	0.072
1.379	0.200	0.031	0.043
1.488	0.206	0.035	0.020

Table 6. References to cluster data for *B*-type stragglers.

S. no.	Cluster	Data	Reference	Distance modulus	$E(b-y)$
1.	IC 2602	*uvby*	Hill & Perry (1969)	5.92	0.021
2.	NGC 2422	*uvby*	Shobbrook (1984)	8.01	0.060
3.	Pleiades	*uvby*	Crawford & Perry (1976)	5.54	0.040
4.	NGC 6025	*uvby*	Kilambi (1975)	9.40	0.110
5.	NGC 2516	*uvby*	Snowden (1975)	8.01	0.088
6.	NGC 6475	*uvby*	Snowden (1976)	7.01	0.067

whatever be its true rotational velocity unless its helium weak nature can account for its large observed excess in the $(u-b)_0$ index. The ultraviolet excess may not be able to account for the observed $(u-b)_0$ index for HD 162374 unless it is also an intrinsic slow rotator while the other members of the cluster are fast rotators.

(g) *HD 170054 in NGC 6633*: This cluster has two blue stragglers in the A-type domain and one blue straggler in the B-domain. Fig. 5 in Section 2 shows that the position of the Am star (HD 170563) can easily be accounted for in terms of rotation effects. This star is a probable non-member. There are six red giants in the cluster, whose membership has been established from radial velocity measures by Mermilliod & Mayor (1989). The observed position of the giants in the colour-magnitude diagram of this cluster surely indicates that HD 169959 and HD 170054 are definite blue stragglers.

If some of the stragglers in the B0–B3 class are real, then they are probably produced by the mechanism of mass-exchange in binary stars proposed by McCrea (1964). Quasi-homogenous evolution proposed by Wheeler (1979b) appears ruled out as these few candidate stragglers, which are all in the early B-spectral range have a wide range in their observed $V \sin i$ distribution.

4. Conclusions

The effect of rotation on observed colours of stars was considered as a possible cause for the observed position of blue stragglers in star clusters. We find that the observed

blueness of the blue stragglers which are intrinsic slow rotators, in the B7–A2 type range can easily be accounted for by such effects. The reddening caused by rotation shifts the entire cluster main sequence away from the zero rotation main sequence leaving the slow rotators behind. The rotation effect in $(u - b)_0$ index reaches a maximum in the B7–A0 spectral type range where all the slowly rotating blue stragglers are also concentrated. It is also therefore not surprising that the majority of these A-type stragglers are found to be CP stars.

There are at least 6 blue stragglers which fall in the spectral type domain B0–B3 with the exception of the straggler in Pleiades. Amongst these objects, it is found that the dispersion in the $(u - b)_0$ index due to rotation can account for the blue stragglers in Pleiades and IC 2602. The position of the stragglers in NGC 6025 and NGC 2422 can probably be accounted for by a combination of rotation effects and the expected ultraviolet excess in Be stars. The position of two stragglers in NGC 6633, one in NGC 6475 and the NGC 2516 straggler cannot be accounted for by rotation effects alone.

References

Abt, H. A. 1979, *Astrophys. J*, **230,** 485.
Abt, H. A. 1985, *Astrophys. J.,* **294,** L103.
Abt, H. A., Clements, A. E., Doose, L. R., Harris, D. H. 1969, *Astr. J*., **74,** 1153.
Anderson, C. M., Stoeckly, R., Kraft, R. P. 1966, *Astrophys. J.,* **143,** 299.
Collins, G. W., II., Sonneborn, G. H. 1977, *Astrophys. J. Suppl.,* **34,** 41.
Collins, G. W., II., Smith, R. C. 1985, *M on. Not. R. astr. Soc,* **213,** 519.
Crawford, D. L, Barnes, J. V. 1969, *Astr. J.,* **74,** 818.
Crawford, D. L., Barnes, J. V. 1969, *Astr. J.,* **74,** 407.
Crawford, D. L., Perry, C. L. 1966, *Astr. J.,* **71,** 206.
Crawford, D. L., Perry, C. L. 1976, *Astr. J.,* **81,** 419.
Dworetsky, M. 1975, *Astr. J.,* **80,** 131.
Eggen, O. J. 1972, *Astrophys. J.,* **173,** 63.
Eggen, O. J. 1981, *Astrophys. J.,* **246,** 817.
Feinstem, A 1968, *Z. Astrophys.,* **68,** 29.
Feinstein, A., Forte, J. C. 1974, *Publ. astr. Soc. Pacific,* **86,** 284.
Hill, G., Perry, C. L. 1969, *Astr. J.,* **74,** 1011.
Hintzen, P., Scott, J. *Astrophys. J.,* **194,** 657.
Kawaler, S. D. 1987, *Publ. astr. Soc. Pacific,* **99,** 1322.
Kilambi, G. C. 1975, *Publ. astr. Soc. Pacific,* **87,** 975.
Levato, H. 1975, *Astrophys. J.,* **195,** 825.
Maeder, A. 1971, *Astr. Astrophys.,* **10,** 354.
Maeder, A. 1987, *Astr. Astrophys.,* **178,** 159.
Mathew, A., Rajamohan, R. 1990a, *J. Astrophys. Astr.,* **11,** 167.
Mathew, A., Rajamohan, R. 1990b, *Bull. astr. Soc. India,* **18,** 329.
Mathew, A., Rajamohan, R. 1991, *J. Astrophys. Astr.,* **13,** 61 (Paper 5).
Mathys, G., 1991, *Astr. Astrophys.* (Submitted).
McCrea, W. H. 1964, *Mon. Not. R. astr. Soc,* **128,** 147.
Mermilliod, J.-C. 1982, *Astr. Astrophys.,* **109,** 37.
Mermilliod, J.-C. Mayor, M. 1989, *Astr. Astrophys.,* **219,** 125.
Pendl, E. S., Seggewiss, W., 1975, in *IAU Coll. 32: Physics of Ap Stars,* Eds W. W. Weiss, H. Jenker & H. J. Wood, Universitäts Sternwarte, Wein, p. 357.
Pesch, P. 1961, *Astrophys. J.,* **134,** 602.
Rajamohan R. 1978, *Mon. Not. R. astr. Soc,* **184,** 743.
Rajamohan, R., Mathew, A. 1988, *J. Astrophys. Astr.,* **9,** 107.
Schmidt, E. G. 1976, *Publ. astr. Soc. Pacific,* **88,** 63.

Shobbrook, R. R. 1984, *Mon. Not. R. astr. Soc,* **211,** 659.
Snowden, M. S. 1975, *Publ. astr. Soc. Pacific,* **87**, 721.
Snowden, M. S. 1976, *Publ. astr. Soc. Pacific,* **88,** 174.
Stother R, Chin, C. W. 1979, *Astrophys. J.,* **233,** 267.
Strittmatter, P. A., Sargent, W. W. 1965, *Astrophys. J.,* **145,** 130.
Walborn, N. R. 1979, *Publ. astr. Soc. Pacific,* **91**,442.
Wheeler, J. C. 1979a, *Comments Astrphys.,* **8**, 133.
Wheeler, J. C. 1979b, *Astrophys. J.,* **234,** 569.
Williams, I. P. 1964a, *Mon. Not. R. astr. Soc.,* **128,** 389.
Williams, I. P. 1964b, *Ann. Astrophys.,* **27,** 198.

J. Astrophys. Astr. (1992) **13**, 129–144

Gain Calibration of CCD Systems at VBO

T.P. Prabhu,Y.D. Mayya[1] & G. C. Anupama[2] *Indian Institute of Astrophysics, Bangalore 560034*

Received 1991 November 4; accepted 1992 January 22

Abstract. The system gain of two CCD systems in regular use at the Vainu Bappu Observatory, Kavalur, is determined at a few gain settings. The procedure used for the determination of system gain and base-level noise is described in detail. The Photometrics CCD system at the 1-m reflector uses a Thomson-CSF TH 7882 CDA chip coated for increased ultraviolet sensitivity. The gain is programme-selected through the parameter 'cgain' varying between 0 and 4095 in steps of 1. The inverse system gain for this system varies almost linearly from 27.7 electrons DN^{-1} at cgain = 0 to 1.5 electrons DN^{-1} at cgain = 500. The readout noise is $\lesssim$ 11 electrons at cgain = 66. The Astromed CCD system at 2.3-m Vainu Bappu Telescope uses a GEC P8603 chip which is also coated for enhanced ultraviolet sensitivity. The amplifier gain is selected in discrete steps using switches in the controller. The inverse system gain is 4.15 electrons DN^{-1} at the gain setting of 9.2, and the readout noise ~ 8 electrons.

Key words: CCD photometry—CCD spectroscopy—system gain—readout noise

1. Introduction

The charge-coupled device (CCD) is increasingly favoured for astronomical observations in the optical and near-infrared domains because of its sensitivity, linearity and dynamic range. It is also a reuseable detector and hence can be calibrated accurately. Its applications are limited at present only by the small format in which the detector is available. A CCD is an analog device. The charge (q) accumulated in a CCD pixel is converted to voltage ($qA/C_0 = V_0$) where C_0 is the output node capacitance, and A the voltage gain of the amplifier. An analog-to-digital converter (ADC) digitizes the voltage such that a specific voltage V_m is converted to a specific number of bits. The full-well capacity of some CCD chips exceeds 500,000 electrons (McLean 1989). If one chooses to set the amplifier gain such that one electronic charge results in one count or 'data number' (DN), an ADC with 19 bits will be needed to realize the full-well capacity. It is easier to use an ADC with 14–16 bits, which, at 1 electron DN^{-1}, will utilize only 313 per cent of the dynamic range.

[1]Also Joint Astronomy Programme, Department of Physics, Indian Institute of Science, Bangalore 560 012.
[2]Present address: Inter-University Centre for Astronomy and Astrophysics, Post Bag 4, Ganeshkhind, Pune 411007.

The accuracy of detection of charge accumulated on the CCD is limited by the noise introduced in the process of measurement (the readout). The readout noise is in the range of 510 electrons for a majority of CCD chips currently used in astronomy (McLean 1989). There is no advantage in operating a CCD at gains much larger than one DN per readout noise. Most of the dynamic range of a typical CCD chip—defined as (full-well capacity)/(readout noise)—can be accommodated in 16 bits at one DN per readout noise. This setting is also optimal for the astronomical applications which range from background-noise-limited observations such as broad-band imaging where the sky background needs to be detected with significant accuracy (minimum detected signal » readout noise), and readout-noise-limited detection such as spectroscopy and speckle interferometry (minimum detected signal $\lesssim$ readout noise).

The system gain or transfer factor is defined as the value of DN per electronic charge detected. We denote this by the symbol G in the following. Often its inverse is also used in the units of electrons DN^{-1}, and we denote this value by Q. A count or DN is referred to in the literature also as an analog-to-digital unit (ADU) or an analog-to-digital count unit (ADCU). Q is sometimes referred as EPADU (electrons per ADU). The system gain needs to be calibrated for different values of amplifier gains so that an optimal setting may be determined. In addition, it is desirable to know its value for each observation, so that one can determine the scale factor between the observed counts and detected electrons. Simple procedures to do this will be useful in monitoring the long-term stability of the system. The information on the system gain and readout noise are necessary for estimating the total noise at any observed signal level, and are demanded by the standard software for reductions of CCD spectroscopy and photometry.

The system gain can be computed if the capacitance at the output node, the voltage gain of the amplifier, and the conversion factor at the ADC are known. On the other hand, it can easily be determined experimentally (*cf.,* Djorgovski 1984; Mackay 1986; Home 1988; McLean 1989; McCall, English & Shelton 1989). We have examined the experimental methods of calibrating the gain and readout noise of a CCD system, and tried to evolve a simple and accurate method using flats obtained routinely during spectroscopic observations. New commands have been added to the RESPECT software (Prabhu & Anupama 1991) for analysis of these spectroscopic flats.

Two CCD systems are available at VBO and each one is used both for imaging and spectroscopy. The 1-m Zeiss reflector is equipped with the CH210 camera head containing a Thomson CSF TH 7882 CDA chip coated for enhanced sensitivity in the ultraviolet, CE200 controller, and DIPS 1000 image acquisition and processing system, obtained from Photometrics Ltd., Tucson (USA) in 1988. The photometric calibration of this system has been performed by Sagar & Pati (1989) and Mayya (1991). The 2.3-m Vainu Bappu Telescope (VBT) is equipped with a CCD dewar and controller obtained from Astromed Inc., Cambridge (UK) in 1988 as CCD 2000 imaging system. It is equipped with a GEC P8603 CCD chip coated for enhanced ultraviolet sensitivity which replaced the original chip in 1991 January. A nearly identical system jointly belonging to TIFR, Bombay, and IUCAA, Pune (Bhat *et al.* 1990) is also available, and is used interchangeably. The data acquisition software currently in use was developed locally for this system using a personal computer (Ananth *et al.* 1991). We present new results on the calibration of these systems for system gain and readout noise in Section 3, after explaining the methodology in Section 2. The last section summarizes the conclusions.

2. The methodology

The gain calibration of a CCD system can be effected by studying its noise characteristics. In a unit integration period, N_e electrons are accumulated on a typical pixel as given by

$$N_e = b_e + d_e + fS_e,$$

where b_e is the DC offset ('bias') applied (in units of electronic charge) to avoid negative signal caused by fluctuations due to noise, d_e is the number of thermal electrons generated, and S_e is the number of electrons generated due to signal photons. The factor f varies from pixel to pixel, and denotes the relative quantum efficiency. If G denotes DN corresponding to one electron, the equation can be rewritten as

$$N_c = N_e G = b_c + d_c + fS_c,$$

where N_c, b_c ,d_c , and S_c are in units of DN. The mean and variance of observed counts for a uniform illumination can be written as

$$\langle N_c \rangle = b_c + d_c + \langle S_c \rangle, \tag{1}$$

and

$$\sigma^2 = G^2 B_e^2 + G(d_c + S_c) + \sigma_f^2 S_c^2, \tag{2}$$

where B_e is the base-level noise in electrons and equals the sum in quadrature of the readout noise (R_e) and noise from other signal-independent sources (Newberry 1991). In deriving Equation (2) we have assumed that the noise in electrons generated thermally as well as due to the signal is Poissonian. The noise in signal electrons equals $\sqrt{S_e}$ electrons (*cf,* Newberry 1991), and hence the noise in the signal counts is $G\sqrt{S_e} = \sqrt{GS_e}$ counts. We also assume that the mean value of f is unity (definition). In the following, we drop the angular brackets for simplicity. We will also assume that the mean thermal counts and bias have been subtracted from the data and the the rms thermal noise has been subtracted from the derived noise. Most CCD chips currently available have very low thermal charge, and hence also its variance, at liquid nitrogen temperatures. Equation (2) can thus be written as

$$\sigma^2 = G^2 B_e^2 + GS_c + \sigma_f^2 S_c^2. \tag{3}$$

It is clear from Equation (3) that it is possible to determine G and B_e using a set of observed, bias- and dark-subtracted, signal counts (S_c) and their rms scatter (σ), sometimes referred to as the variance diagram. A set of flat-field images obtained at a range of illumination levels (or equivalently exposure times) can be used to this end. A quadratic fit to the data yields all the constants in Equation (3). In practice, the the propagation of errors downwards, *i.e.,* $\varepsilon(\sigma_f^2 G^2) \ll \varepsilon(G) \ll \varepsilon(G^2 B_e^2)$. This problem can be alleviated by the procedures described below.

2.1 *Reducing the Magnitude of the Quadratic Term*

The accuracy of determination of G in Equation (3) can be enhanced by reducing the magnitude of the third term in the equation. The quadratic term arises due to pixel-to-pixel sensitivity variations as also the non-uniformity of illumination in the

flat-field. Its magnitude can hence be reduced by correcting for these effects. We consider below two methods of reducing the effect of the quadratic term.

2.1.1 *Correcting for the flatfield variations*

The most accurate way of reducing the flat-field variations is to correct for them by using an accurate flat-field frame. In practice, it is not possible to correct for pixel-to-pixel variations exactly but only to a desired accuracy. If one desires that the third term in Equation (3) should not be larger than the second term even at the largest values of S_c, one obtains the condition that $\sigma_f \lesssim [G/S_c(\max)]^{1/2} = S_e\ (\max)^{-1/2}$, where σ_f is the residual flat-field variation. For a signal reaching the full-well capacity of 10^5 electrons, this implies that the flat-field corrections should be carried out to an accuracy of 0.3 per cent in order to achieve 1 per cent accuracy in σ_f. Many flats need to be stacked to obtain a master flat accurate to this level. It should be noted that the individual images used for obtaining the master flat cannot be used to study the noise statistics since the master contains the memory of the noise in individual flats. The corrected flats would, in such a case, show a lower-than-real noise. An independent set of flats, corrected using the master flat, should be used to determine the noise statistics. A quadratic fit of Equation (3) would still be necessary for the determination of G, though the constant σ_f^2 would now be very small. An example of this procedure is given by Horne (1988).

2.1.2 *Division or subtraction of two flats*

An alternative method of reducing the effect of flat-field noise is dividing two flat-field images after subtracting bias and dark. Mackay (1986) suggests dividing two equally exposed flats. In general, for two unequal flat-field images with mean counts S_1 and S_2, the variance of the divided image is

$$\sigma^2(S_1/S_2) = [S_2^2\sigma^2(S_1) + S_1^2\sigma^2(S_2)]/S_2^4. \tag{4}$$

A relationship similar to Equation (3) can now be written as

$$\sigma'^2 = G^2B^2 + GS', \tag{5}$$

where

$$\sigma'^2 = \frac{S_2^4}{S_1^2 + S_2^2}\sigma^2\left(\frac{S_1}{S_2}\right),$$

and

$$S' = \frac{S_1S_2(S_1 + S_2)}{S_1^2 + S_2^2}.$$

The simplification for $S_1 = S_2$ is evident. Since the flat-field variations are not random, but affect both the frames the same way, the division does not contain the quadratic term ($\sigma_f(S_1/S_2) = 0$).

The propagation of errors due to normal flat-fielding operation is evident from Equation (5), since flat-fielding of image 1 involves division by image 2 such that $S_2 \gg S_1$. In practice, to restrict the relative error to e one requires $S_1/S_2 \ll \varepsilon^2$. On the other hand, Equation (5) is more general, and can be used for any ratio image.

The flat-field noise can also be eliminated by subtracting two equal flat-field images. If the two images are not exposed equally, it will become necessary to normalize

individual flats before subtraction. Denoting the normalized counts by s. The variance of the 'normalized difference image' can be expressed as

$$\sigma^2(s_1 - s_2) = \frac{\sigma^2(S_1)}{S_1^2} + \frac{\sigma^2(S_2)}{S_2^2}. \tag{6}$$

Equation (5) is valid in this case too, with

$$\sigma'^2 = \left(\frac{S_1^2 S_2^2}{S_1^2 + S_2^2}\right)\sigma^2(s_1 - s_2). \tag{7}$$

Again, the simplification for $S_1 = S_2$ is evident.

2.2 *Improving the Estimates of G and B*

The methods described in Section 2.1 reduced the magnitude of the quadratic term in Equation (3) and make it possible to determine the value of G accurately. However, the value of B determined by a least-squares polynomial fit would still be inaccurate since the linear term dominates. It is possible to improve the initial estimates of G and B obtained through usual least-squares analysis by iterative methods such as the Marquardt algorithm (*cf.*, Press *et al.* 1986). If the nonlinear term is small or absent, one can use a linear regression for initial estimates, and obtain the best fit by iteration.

The Marquardt algorithm is best suited for a minimization of χ^2 which requires an accurate model of the variance of the dependent variable. In the case of Equation (3), it is difficult to model the variance of σ^2, but its magnitude can be minimized by choosing a sufficiently large area to determine σ^2. We used Marquardt algorithm minimizing rms deviations, or equivalently, by assuming equal variance for all values of σ^2. Here again, it was seen that B cannot be determined accurately since the algorithm tries to fit larger values of σ^2 better. The problem can be alleviated, albeit rather arbitrarily, by obtaining the logarithm of Equation (3) and assigning equal weights to log σ^2 since now the weights get distributed more evenly. This representation has been in regular use (*cf.,* Horne 1988; McLean 1989). Though it does not have the rigour of a χ^2 fit, it yields a very good fit to the data.

2.3 *Analysis of Spectroscopic Flats*

Low-resolution spectroscopic flats often contain a range of signal levels due to the variation of instrumental response. Hence the division of two spectroscopic flats provides an easy way of constructing the variance diagram. We have set up a procedure to calibrate CCDs using low-resolution spectroscopic flats and the RESPECT software. The use of RESPCET software for spectroscopic data reduction has been described in detail by Prabhu & Anupama (1991). Here we describe the commands added more recently for gain calibration using the methods outlined above.

The command GSTAT determines the noise statistics based on two flats. The format of the command is

GSTAT flat l flat2 output.

The output contains mean counts and variances as (x, y) pairs. In the case of spectroscopic flats the programme automatically locates the spectrum, and evaluates the statistics using (10, 20) size boxes centred on the spectrum, spaced 10 pixels apart, The spectroscopic flats used here were about 40 pixels wide. The direction of dispersion (x direction) is assumed to be along columns. If it is along the rows, the information can be supplied through the qualifier/X = ROW. The box-size can be varied by the qualifier/BSIZE = (IX, IY). If one wishes to avoid some rows at the beginning and end of the spectrum, one can specify it as /XLIM = (X1, X2). The automatic centring of the boxes can be circumvented through explicit positioning by /YLIM = (Yl, Y2). If a mean bias value is to be subtracted from the data, one may do so with /MBIAS = const. Alternatively, one can input a bias frame as /BIAS = bias-frame. In this case, the mean value of bias is computed and subtracted. Further, the mean value is subtracted from the bias frame itself, boxes are centred on it at the same locations as on flats, and the mean and variance of these boxes are determined and added to the output file. These would help in fixing the readout noise better. It should be noted that the mean value of bias should actually be zero. Since this implies log $S = -\infty$, and it is not possible to plot it in the logarithmic representation of the variance diagram, the absolute value of (local mean – global mean) is used as the mean value of S with the value $S < 0.01$ being discarded. This is only a matter of convenience, and has no effect on the final results.

The noise and variance are computed as transformed by Equations (5) and (7), By default, the first frame is divided by the second, and Equation (5) is used. If subtraction is desired, one should add/MODE = SUB.

The system gain and the readout noise are determined through the command GFIT input curve.

The input is the output of GSTAT command. The resultant coefficients of the linear or quadratic fit and the standard errors are printed in the log file. The theoretical fit is computed over the entire range of values and stored for future display in the file ‘curve’. A linear relation transformed to the log-log domain is fitted by default. If a quadratic term is to be added, one uses/QUAD. A fit can also be obtained without using the logarithmic representation, with the qualifier/NOLOG.

3. Results

The two CCD systems in regular use at VBO were calibrated using the methods discussed above. The results are presented below.

3.1 *The Photometrics System*

The Photometrics CCD system at the 1-m reflector was calibrated in a greater detail compared to the Astromed system described in the following section. The system is in regular use since 1988. The noise statistics for the system were determined using the imaging flats at two different gain settings and spectroscopic flats at five different gain settings. No preflashing was employed in any of the observations.

The R band twilight sky flat images obtained during the imaging observations of 1991 April 16 and May 16 were used in the analysis. In addition to well-exposed flats

obtained routinely during observations, additional graded flats were obtained to uniformly cover lower signal levels. The gain setting 'cgain' = 0 was used in April, whereas a value of 33 was used in May. The first four rows and columns were trimmed since some of these showed abnormally low or high counts. The bias frames showed only faint strips which were not repeatable and hence only a mean bias value was subtracted from all the frames. A set of flats were stacked to obtain a master flat accurate to ~ 0.1 per cent. The remaining flats were corrected for pixel-to-pixel sensitivity variations, as also for the vignetting in the system, using the master flat. An area of the corrected flat enclosed by the rows (201, 500) and columns (101, 300) was used for determining the statistics, since this area was less affected by vignetting. The mean signal counts were determined from the flats before correction, in order to represent the signal accurately before the correction for vignetting. The rms noise was estimated over contiguous boxes of 5 × 5 pixels after rejection of deviants over three iterations.This procedure determines the local variance and should be relatively free of errors due to incomplete flat-field corrections. The EDRS subpackage of STARLINK software was used in all the reductions.

The spectroscopic flats were obtained during regular observing runs of 1991–92, using the Cassegrain UAG spectrograph and a 1501 mm^{-1} grating blazed at 8000 Å in the first order. Flat and bias frames at 'cgain' = 0 and 33 were obtained as a part of the observing programme, and a cgain = 66,100 and 500 were obtained specifically for calibration of the system. The closed shutters of the dome, illuminated by incandescent lamps, were used as the continuum source. The grating setting corresponded to the wavelength range of 4200–7400 Å on April 17 (cgain = 0) and May 12 (cgain = 33), and 6000–9200 Å on May 13 (cgain = 66). On 1992 January 7 flats were obtained at three different grating settings: 3800–7000 Å (cgain = 33), 4200–7400 Å (cgain = 33, 100, 500), and 6300–9500 Å (cgain = 33). In general two equal, well-exposed flats were used in obtaining the noise statistics, though on some occasions a low-exposure flat was also employed. The combined effect of the instrumental response and the colour of the radiation source made a range of signal levels available, which was particularly large for the blue setting. The range was further augmented by utilizing also the faint scattered light outside the slit area. Both the subtraction and division of flats gave similar statistics and the method of division was adopted. Statistics was obtained by division of two well-exposed flats, and by the division of the lower exposure flat with one of the well-exposed ones.

The initial estimates of G and B were obtained by a linear regression analysis, and were improved iteratively using the Marquardt algorithm. Equation (3) was fit both in the linear domain and in the logarithmic domain. In the case of spectroscopy flats, σ and S were transformed as given by Equation (5). Fits were attempted by including as well as neglecting the quadratic term. In general, the logarithmic fit was better as it passed through the bias values closely. It was noticed that whenever the quadratic term was negligible the fit tended to yield a negative value for the last coefficient. In such cases, as also whenever the value of the coefficient was less than its formal error, it was decided to use the fit that neglects the quadratic term.

The Statistical data and the adopted fits are shown in Figs 1–5, and the final results are presented in Table 1. The formal errors of G and B are < 1 per cent. The imaging flats yield a slightly higher value of G even when the quadratic term is included. It is apparent that even though flat-fielding is done to an accuracy of⩽ 1 per cent, the variance contains the effect of flat-field to the level of ~ 1 per cent. On the other

Table 1. System gain and readout noise.

Gain setting	Method	B electrons	G DN electron^{-1}	Q electron DN^{-1}
Photometrics:				
0	S	17.40	0.0361	27.71
		0.15	0.0002	0.17
	I	17.90	0·0367	27.26
		0.10	0.0001	0.09
33	S	12.26	0.0729	13.72
		0.10	0.0005	0.09
	I	11.85	0.0761	13.15
		0.10	0.0004	0.07
66	S	10.94	0.1105	9.05
		0.10	0.0010	0.08
100	S	11.52	0.1491	6.71
		0.06	0.0007	0.03
500	S	19.91	0.6469	1.55
		0.13	0.0043	0.01
Astromed:				
9.2	S	7.78	0.2410	4.15
		0.04	0.0011	0.02
	I	7.70	0.2517	3.97
		0.15	0.0043	0.07

Notes:
Formal errors of the fit appear below the values.
Method: S = spectroscopic flats: I = images flats.

hand, the spectroscopic data always yielded a satistically insignificant, slightly negative value for the quadratic term, exemplifying the advantage of using the more rigorous Equation (5).

In the case of zero cgain (Fig. 1), the variance shows appreciable departure from the standard curve at high signal levels. Such a behaviour is noticed in CCDs as the full-well saturation is approached, though the range of electron levels over which the effect is apparent varies (Mackay 1986). At 27.7 electrons DN^{-1}, the departure in the present case sets in at ~ 140,000 electrons and becomes pronounced at 250,000 electrons. The data beyond 5000 counts was hence not used in the analysis. On the other hand, Mayya (1991) finds using flats exposed to the level of 2.7–4.1 x 10^5 electrons per pixel, that the CCD is linear to an accuracy of 1 per cent over signal levels 8,200–300,000 electrons. The full-well capacity of the chip is expected to be 500,000 electrons (McCall, English & Shelton 1989).

The variance was generally found to be larger than predicted by the fit for $s \leqslant 5000$ electrons at all gain settings. The statistics at these signal levels was derived from the first 100 rows of the CCD frames. Mayya (1991) had found that stars recorded in this region showed appreciable departure form the standard magnitudes. A possible reason for these departures is the deferred charge nonlinearity, or the poor charge transfer efficiency (CTE) of the Thomson-CSF chip at low light levels (*cf.*, McLean 1989). The effect is more pronounced in the early rows, and vanishes after initial transfers leave back sufficient amount of charge in the pixel to overcome the inefficieny.

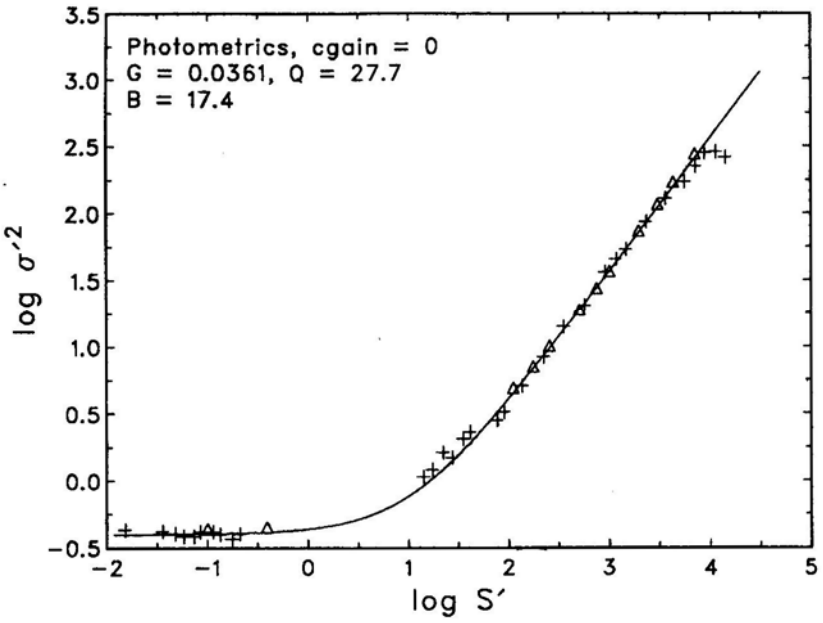

Figure 1. The logarithmic plot of variance versus signal together with the theoretical fit for the Photometrics CCD system at cgain = 0. The points based on spectroscopic flats (+) and imaging flats (Δ) are separately shown. Here, and in the subsequent plots, only selected points are shown for clarity, whereas a large number of points were used in deriving the fit; also the variance of bias counts is shown as log $S < 0$. The fits pass through the large S points better since the full data set used for the fit had a large number of points there. The fit is based on spectroscopic data in the range $150 \leqslant S \leqslant 5000$, and the bias statistics. The nonlinear behaviour of noise for $S > 5000$ counts is evident. Note that the noise is higher than expected at low signal values.

This nonlinearity can be overcome by preflashing. An alternative source of noise is the division by small numbers when two nearly equally exposed flats are used (McCall, English & Shelton 1989).

The base-level noise B includes, in addition to the readout noise R, truncation noise due to digitization of the analog data from the CCD chip and noise due to pick-up from external signals. The contribution to the base-level variance due to truncation is $T^2 = (Q^2 - 1)/12$ (Newberry 1991). The values listed in Table 1 decrease with increasing gain between 0 < cgain < 66, showing that such an effect is likely. The estimates of readout noise corrected using Newberry's prescription are 15.5, 11.6 and 10.6 electrons, respectively, for cgain = 0, 33 and 66. The values continue to decrease with increasing gain. The readout rate decreases with increasing cgain as described below and we ascribe the decrease in the readout noise from cgain = 0 to 66 to this fact.

The high value of B at cgain = 500 is due to external pickup. The pick-up appears as faint vertical strips at cgain = 0. As the gain is increased, the image data acquisition control increases the preamplifier gain and also reduces the readout rate. The strips become more pronounced, wider, and inclined. A pattern of spikes sometime becomes visible at cgain > 33. The pick-up was seen to be variable, and the source has since been identified and removed. In order to understand the nature of the pick-up, the following experiments were performed using the frames that showed significant pick-up.

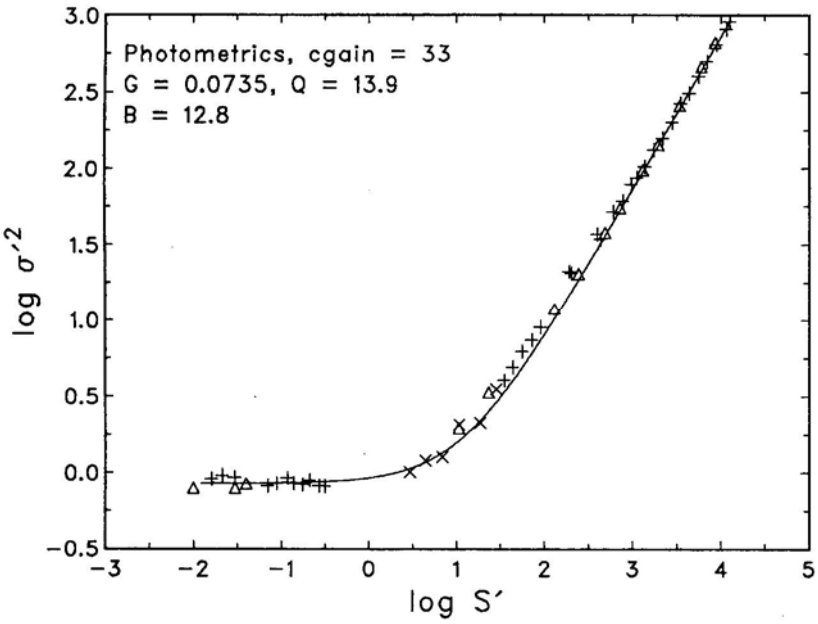

Figure 2. The logarithmic plot of variance versus signal together with the theoretical fit for the Photometrics CCD system and cgain = 33 based on the data obtained in 1992 January. The fit is based on spectroscopic data in the range $300 \leqslant S \leqslant 10000$, and the bias statistics. Other details are as in Fig. 1. Surprisingly, data from a different set (×) obtained on 1991 May 12, agrees with the theoretical fit even at low signal values.

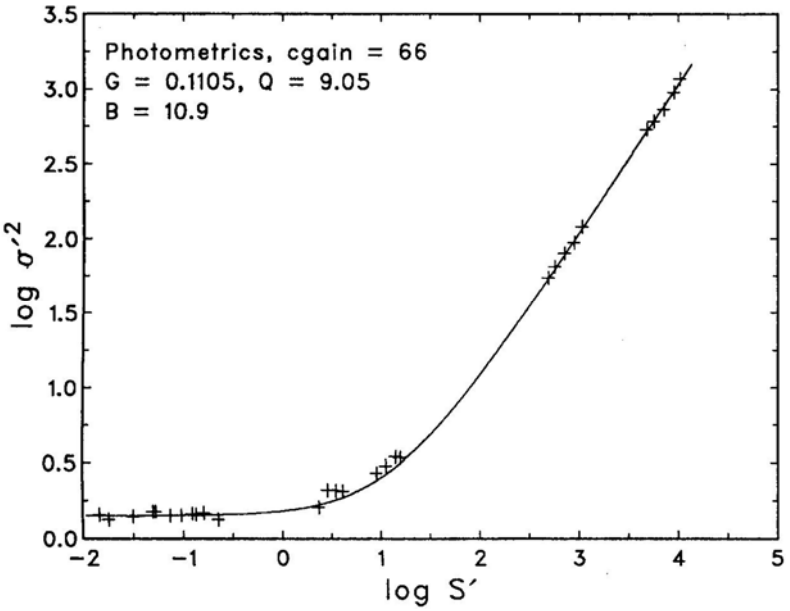

Figure 3. The logarithmic plot of variance versus signal together with the theoretical fit for the Photometrics CCD system and cgain = 66. The fit is based on data in the range $S > 500$, and the bias statistics. Other details are as in Fig. 1.

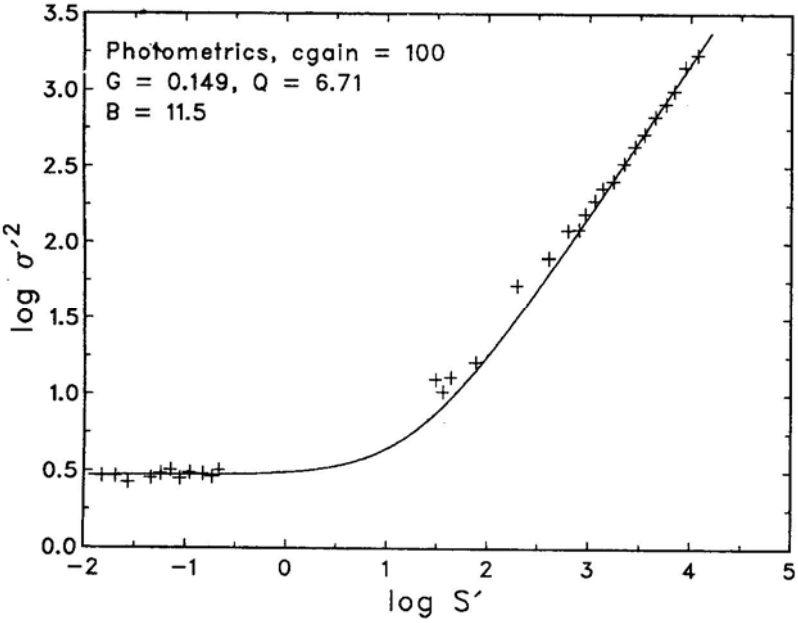

Figure 4. The logarithmic plot of variance versus signal together with the theoretical fit for the Photometrics CCD system and cgain = 100. The fit is based on data in the range $S > 600$, and the bias statistics. Other details are as in Fig. 1.

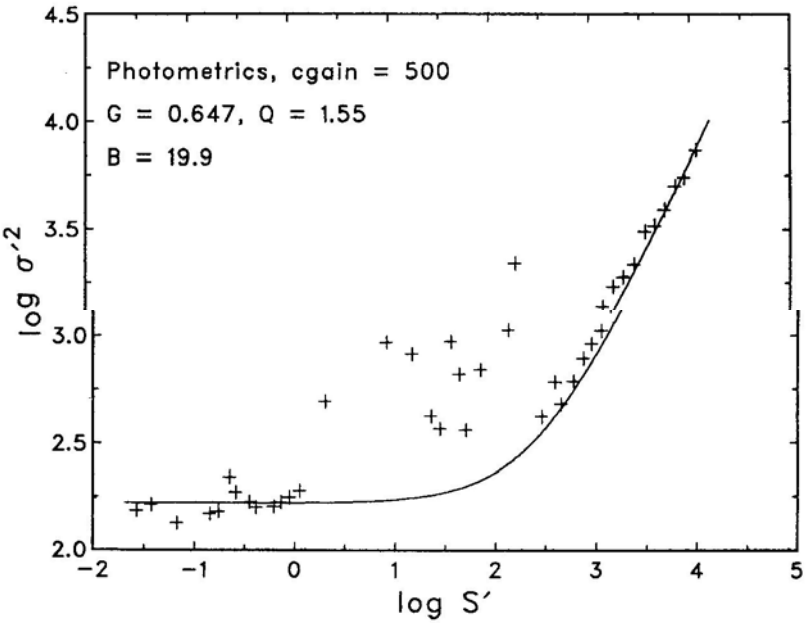

Figure 5. The logarithmic plot of variance versus signal together with the theoretical fit for the Photometrics CCD system and cgain = 500. The fit is based on data in the range $S > 3000$, and the bias statistics. Other details are as in Fig. 1. Note the discordant data for S = 1 – 100 counts (l – 150 electrons), which is probably due to the low-level charge transfer inefficiency (the 'deferred charge' problem).

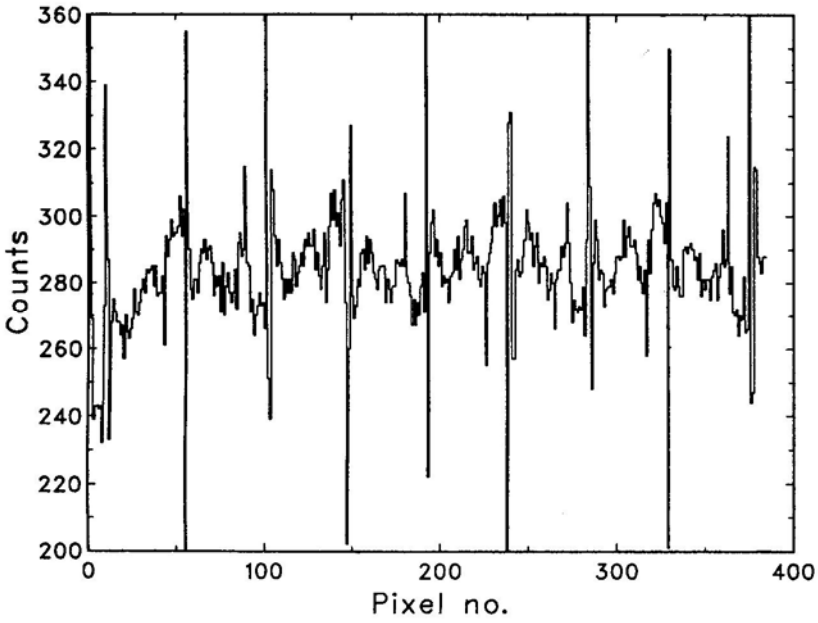

Figure 6. Data from row 101 of a bias frame obtained at cgain = 500 showing the modulation due to 50 Hz mains pick-up. The spikes often extend a little beyond the limits plotted.

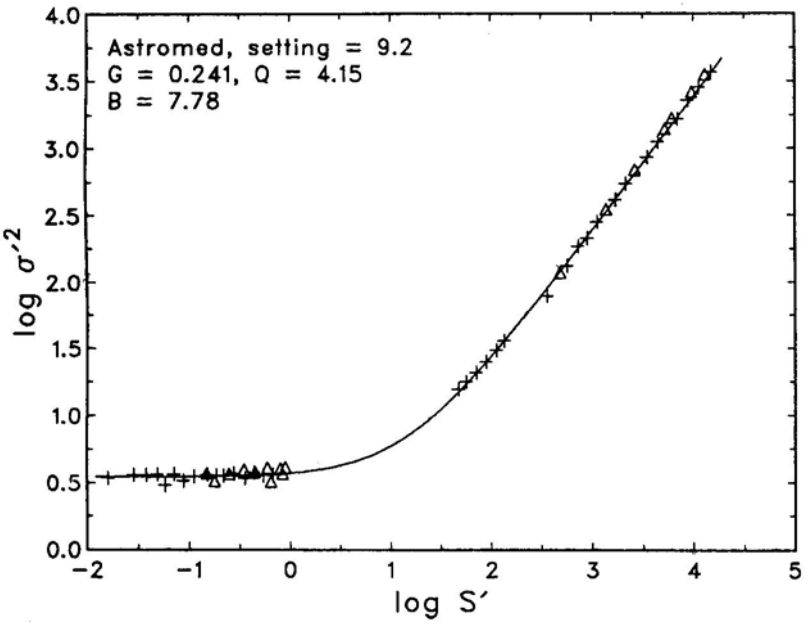

Figure 7. The logarithmic plot of variance versus signal and the corresponding theoretical fit for the Astromed CCD system at gain setting of 9.2. The symbols are as in Fig. 1.

First, the bias frame transfer times were measured to determine approximate readout rates. They were 4.9, 7.9, 10.9, 13.9, 49.4 and 94.0s, respectively, at cgain = 0, 33, 66, 100, 500 and 1000. These values fit a linear relation

$$\text{transfer time(s)} = (4.96 \pm .03) + (0.08901 \pm .00004)\text{cgain}, \quad (8)$$

with a correlation coefficient of 0.999999. Next, an 8192 point series of data was picked beginning from the first column of row 101. An examination of the data for cgain = 0 showed that spikes repeat with a period of 45 pixels (Fig. 6). However, alternate spikes have positive and negative deviations compared to the mean bias. There is also an almost sinusoidal pattern seen with 90 pixel periodicity, and 15 count amplitude. Superposed on this is a wave with a periodicity of about 18 pixels. The first three pixels of each row, which showed counts higher than average, were then replaced by mean counts and the power spectrum of the series was obtained for cgain = 33, 100 and 500. Two strong periods were seen at 18.1 and 90.7 pixels. Additional periodicities were also seen at 10.0,13.0 and 30.2 pixels. A similar pattern was evident at other values of cgain also, but with periods 3.66 and 6.49 times at cgain = 100 and 33, respectively. These factors are in a general agreement with the measurements of frame transfer times. The pick-up is hence due to the same source at all values of cgain; but the power in these periodicities falls quickly as the gain is reduced.

The manual for DIPS 1000 system informs that the readout rate is 50 kHz. If one assumes that this rate corresponds to the default value of cgain, the derived frequencies of pickup turn out to be close to 50 Hz and its harmonics. Assuming the 50 Hz mains to be the source, the derived readout rates are 29.4, 16.6 and 4.53 kHz at cgain = 33, 100 and 500, respectively. These results also follow a linear relationship which can be expressed as

$$\text{readout time per pixel } (\mu\text{s}) = (20.5 \pm 0.2) + (0.4003 \pm 0.0005)\text{cgain}. \quad (9)$$

For a format of 384 × 576 pixels, this agrees well with Equation (8). The exact mains frequency was not measured at the time of these experiments. It is known to vary between 48 and 51 Hz, though close to 50 Hz most often.

The amplitude of the spikes is about 60, 14, and 3 counts at cgain = 500,100 and 33, respectively. These can easily be rejected from the data, and were hence not considered while deriving the statistics. The underlying smooth variation at 50 Hz has an amplitude of 15 and 1 counts at cgain = 500 and 100, respectively, whereas it is hardly noticeable at cgain = 33. The pick-up increases the base-level noise significantly at cgain =100 and dominates at cgain = 500. Some effect could still be present at cgain = 66.

The system gain G listed in Table 1 appears to increase almost linearly with the parameter cgain. Since the parameter is software selectable and changes both the amplifier gain and the readout rate through internal programme, the relationship may not necessarily be linear. A polynomial fit to the data in Table 1 which serves as an interpolation formula is

$$G = (0.0358 \pm 0.0005) + (0.001111 \pm 0.000001)\ \text{cgain} + (2.2 \pm 0.1)\ 10^{-7}\ \text{cgain}^2 \quad (10)$$

with a standard error of 0·0005. An extrapolation to cgain = 4095 (which is certainly not justified) yields a value of G = 8.3 DN electron^{-1}, and a value of $G \simeq 1$ DN electron $^{-1}$ is reached for cgain ~ 750.

3.2 *The Astromed System*

The Astromed system was calibrated using the IIA CCD dewar and the TIFR controller. The amplifier gain was set to 9.2. Flats were obtained in 1991 March using a laboratory set-up to expose the CCD to diffuse daylight without using any filter. Altogether 21 graded flats were obtained with averge signal varying from 500 to 28300 counts above bias. The flats were interspersed by bias frames. Eleven best exposed flats were stacked to obtain the master flat; the remaining 10 were corrected using the master. The procedure for gain calibration was generally similar to the one with the imaging flats of Photometrics CCD system described earlier. The spectroscopic flats were obtained as a part of an observational programme on novae and galaxies on 1991 March 10 and 11. The Boller & Chivens spectrograph with a 3001 mm^{-1} grating and a 6-inch camera were used. The wavelength range covered was 4400–7000 Å. A whitened particle board fixed on the dome and illuminated by tungsten filament lamp was used as the source. The procedure of analysis was the same as for the Photometrics system described earlier. The results are presented in Table 1, and the fit is shown in Fig. 7. The data from scattered light in the range of 150–700 electrons also fit the theoretical curve well, indicating that the effect of the deferred-charge threshold is less important for this chip. The GEC chip is known to be good up to 25 electrons (McLean 1989). Mains pick-up was not evident in the bias frames, and the truncation noise is low at this gain. Hence the readout noise is likely to be close to 7.8 electrons.

Using a different chip available with TIFR unit in 1990, a value of $Q = 1.12$ was obtained for the amplifier setting of 34 (Bhat *et al.* 1991, in preparation). The preamplifier settings in the Astromed controller can be varied between 2 and 69 in a few discrete steps. The present results suggest that one obtains about 19 electron DN^{-1} at the gain setting of 2, and the total range of the ADC would then be about 624,000 electrons including the bias. At the gain of 69, on the other hand, one expects 0.5 electrons DN^{-1}. The optimal system gain would be at the setting of 4.9 giving 7.8 electrons DN^{-1}. The full-well capacity of the GEC chip is > 100,000 electrons, and typically 300,000 electrons. The saturation is reached within the limit of the ADC at the lowest gain setting.

4. Conclusions

The main conclusions of this work are listed below.

1. *The method of analysis*: The system gain, readout noise, and the threshold of a CCD can all be determined by studying the noise characteristics of a CCD image. The method of using graded flats, correcting for bias, dark if any, and flat-field response, is satisfactory. On the other hand, the method of using division of two flats, or substraction of two normalized flats, together with the signal and noise transformation of Equation (5), is more rigorous. The final fit giving base-level noise, system gain, and residual flat-field variation can be determined more accurately using the Marquardt alogorithm rather than the conventional regression fit. The RESPECT commands GSTAT and GFIT enable the evaluation of the statistics, and the computation of the fit, respectively, using a small number of low-resolution spectroscopic flats.

2. *The system gain*: The inverse system gain Q for the Photometrics system varies from 27.7 electrons DN^{-1} at cgain = 0 to 1.55 electrons DN^{-1} at cgain = 500. The value of 9.1 electrons DN^{-1} at cgain = 66 agrees with the determination of McCall, English & Shelton (1989) for a similar system. This gain setting is optimal for most of astronomical observations requiring good sensitivity as well as large dynamic range. The Astromed unit with the IIA data acquisition system at the VBT has Q = 4.15 electrons DN^{-1} at the gain setting of 9.2. The preamplifier gain may be reduced further by a factor of 2 for optimizing the system. On the other hand, the IIA Controller has been exhibiting 'binning bias' (Djorgovski 1984) in recent years, which has rendered the base-level noise higher by a factor of 2–3. Hence it is advisable to continue with this gain setting until the problem is rectified. The loss in dynamic range is not significant since the output has an extra bit available (maximum counts 32767).

3 *The readout noise:* The readout noise is estimated as $\leqslant$11 electrons for the Thomson-CSF 7882 CDA chip, and ~ 8 for the GEC P8603 chip. The models of noise in the data require the base-level noise which include, in addition to the readout noise, also the external source of noise. The readout noise itself increases with increasing readout rate. The base-level noise needs to be computed for each data set experimentally.

4. *Nonlinearity*: The Thomson-CSF chip shows nonlinearity in the variance diagram at signal levels below 10,000 electrons and above 150,000 electrons. Photometric studies have however shown the chip to be linear at least over the range of 8,000–300,000 electrons. Further investigations are needed to understand the behaviour at low and high signals. At the lowest signal levels ($\leqslant$ 150 electrons) the chip is affected by deferred-charge threshold. This can be alleviated by preflashing to the level of 100 electrons per pixel (*cf*., McCall, English & Shelton 1989). The effect of threshold was not detectable for the GEC chip which is known to be good above 25 electrons (McLean 1989).

Acknowledgments

We are grateful to K. R. Sivaraman for encouraging us to undertake this work. We thank A. K. Pati for introducing us to the Photometries CCD system, for its installation and maintenance, and for discussions. R. Srinivasan, A. V. Ananth and G. Srinivasulu rendered considerable help with the Astromed CCD system, and we have also benefited by discussions with them. We also wish to acknowledge the help rendered by the electronics group and the observational assistants at VBO. We thank William Tobin for detailed comments, especially for drawing our attention to the mains pick-up.

References

Ananth, A. V., Srinivasan, R., Srinivasulu, G., Chandramouli, S. S. 1991, *Indian J. Pure Appl. Phys.,* **29**, 529.

Bhat, P. N., Kembhavi, A. K., Patnaik, K., Patnaik, A. R., Prabhu, T. P. 1990, *Indian J. Pure Appl. Phys.,* **28**, 649.

Djorgovski, S. 1984, in *Proc. Workshop Improvements to Photometry,* Eds W. J. Borucki & A. Young, NASA CP-2350, p. 152.

Horne, K. 1988, in *New Directions in Spectrophotometry,* Eds. A. G. D. Philip D S Hayes & S. J. Adelman, L. Davis Press, Schenectady, p. 285.
Mackay, C. D. 1986, *A. Rev. Astr. Astrophys.,* **24**, 255.
Mayya, Y. D. 1991, *J. Astrophys. Astr,* **12,** 319.
McCall, M. L., English, J., Shelton, I. 1989, *J. R. astr. Soc. Canada,* **83**, 179.
McLean, I. S. 1989, *Electronics and Computer-aided Astronomy,* Ellis Horwood, Chichester.
Newberry, M. V. 1991, *Publ. astr. Soc. Pacific,* **103**, 122.
Prabhu, T. P., Anupama, G. C. 1991, *Bull. astr. Soc. India,* **19** (in press).
Press, W. H., Flannery, B. P., Teukolsky, S. A., Vetterling, W. T. 1986, *Numerical Recipes,* Cambridge Univ. Press.
Sagar, R., Pati, A. K. 1989, *Bull. astr. Soc. India,* **17**, 6.

Harlan J. Smith

1924–1991

Obituary

Harlan J. Smith
1924–1991

On October 17, 1991, some of the energy, enthusiasm and boldness departed astronomy; on that date, Professor Harlan J. Smith died in Austin, Texas, of complications related to cancer. Professor Smith was the Edward Randall, Jr., MD, Centennial Professor of Astronomy at The University of Texas at Austin. He had previously served as Director of the McDonald Observatory for twenty-six years and as Chairman of the Department of Astronomy for fifteen years. In 1991 he received the Distinguished Public Service Medal from NASA "for a lifetime of service to the astronomy and space communities." He was a member of the editorial board of this Journal since 1983. Harlan Smith was an enormously energetic and bold proponent of astronomy in all its breadth: research, teaching, the exploration of the solar system, and especially public education.

Harlan Smith was born in Wheeling, West Virginia, on August 25, 1924. At the age of 11 years he was given full access to a community telescope of 18-cm aperture, and a life-long interest in science was born. In 1942, his final year of public schooling, Smith was a national runner-up in the Westinghouse National Science Talent Search. From this he had several university scholarship opportunities, but the war intervened. Upon reaching the age of 18 that year, he enlisted in the U.S. Army Air Corps where he was assigned to the meteorological branch. There followed a year of training in physics and mathematics at Denison University in Ohio and a final three months at Harvard University learning new meteorological equipment. This encounter with Harvard was, in his own words, "a real eye-opener, and I determined to attend Harvard after the war." Smith spent his war years at various sites in the United States and the Pacific, being discharged in early 1946.

In the summer of 1946 he began his program of study at Harvard, which led to a B.A. in 1949, an M.A. in 1951, and his Ph.D. in 1955. In his Harvard Ph.D. dissertation Smith identified, and coined the name for the "dwarf Cepheid" variables as a class of pulsating star distinct from the RR Lyrae variables with which they had previously been classified. While he never really returned to research invariable stars, his experience with that field prepared him for a much more significant discovery later. During his years at Harvard, Harlan Smith developed friendships that he would nurture for many years; one such was with M. K. Vainu Bappu, the founding editor of this Journal, with whom Smith maintained a close personal friendship until Bappu's untimely death in 1982.

It was also at Harvard that Smith met Joan Swift Greene, a student at Radcliffe College, who became his wife in 1950. Joan Smith was born and raised in China as the daughter of a medical missionary, and she sparked his interest in that country.

Twenty five years later, as China emerged from the Cultural Revolution, Smith became an advocate for astronomical cooperation with China. He visited there several times to support astronomical development, and he hosted many Chinese astronomers and students in Texas. He delighted in telling the story of how he and a hotel clerk in Europe circumvented their language barrier by discovering that both spoke Mandarin! Harlan and Joan Smith raised four children who all survive him.

Prior to completing his dissertation, Smith received an Instructorship at Yale University and moved his family there in 1953. In the ten years that he spent in New Haven, he rose steadily through the professorial ranks; to Assistant Professor in 1957 and to Associate Professor in 1960. He extended his research interests to the new field of radio astronomy; became active in national astronomical affairs as co-Editor of the *Astronomical Journal* (1958–1963) and as Acting Secretary of the American Astronomical Society (1961–1962); established many of the professional relationships that would help him populate an astronomy department in remote Texas during the next decade; and he made his most important research contribution – discovery of the optical variability of Quasi–Stellar Objects.

In collaboration with Dorrit Hoffleit, Smith examined nearly eighty years of photographs from the Harvard plate collection in a search for variability of the newly discovered class of "radio stars." The first object studied (3C48) gave a negative result in 1961, but upon identification of the brighter QSO 3C273, a new search proved successful. Their discovery of the wholly unexpected and remarkable variability of 3C273 was announced at the April 1963 meeting of the American Astronomical Society, and the discovery paper appeared only two months later as Smith and Hoflleit, 1963, *Nature*, **198,** 650. While their demonstration of optical variability was an important observational contribution, their recognition that the time scale of variability required 3C273 to have solar system dimensions established the foundation of all theoretical interpretations of QSOs from that time forward. Twenty two years later, I listened to Harlan Smith talk about this discovery in his lecture accepting the Randall Professorship. His excitement and his delight were still palpable, yet tinged with a sense of wonderment that he had had the privilege to be involved in such a seminal contribution.

Later in 1963 Smith moved to Austin as the first University of Texas Director of the McDonald Observatory and as the new Chairman of a fledgling astronomy department. The department had been formed in Austin in 1958 as Texas prepared to take control of McDonald Observatory from the University of Chicago, which had overseen construction and operation of the observatory for thirty years. For the next twenty five years, Harlan Smith led a phenomenal expansion of this program.

When Smith took charge in Austin there were four faculty and a similar number of support staff. Under his direction the research programs in Austin expanded into radio astronomy, solar system programs, astronomical instrumentation, variable stars, and theory and expanded upon historically strong programs at McDonald Observatory in extragalactic astronomy and stellar spectroscopy. Today there are approximately sixty Ph.D. astronomers in the combined observatory and departmental staffs and a support staff of more than one hundred and twenty five people. The strength of the program Smith created is exemplified by the statistic that in the past decade Texas researchers have been awarded the Herschel Medal of the Royal Astronomical Society, the Gill Medal of the Astronomical Society of Southern Africa and, from the American Astronomical Society, the Russell Lectureship, the Heineman Prize, the Warner Prize,

the Pierce Prize (twice), and the Cannon Award. Another of Smith's legacies is that fourteen years after he yielded the Departmental Chairmanship to rotation among the faculty (in 1978), the separately administered Observatory and Department continue to work smoothly together.

As Director, Smith led a rejuvenation in McDonald Observatory facilities. He brought James Douglas from Yale to construct a large radio interferometer near Marfa, Texas, during the 1960s. In 1967, he augmented the radio program by moving a 5-m millimeter-wave radio dish to the Observatory. He convinced NASA, the National Science Foundation and the University of Texas to share the cost of a 2.7-m reflector, which was dedicated in 1969 as the third largest telescope in the world. A 76-cm telescope was installed in 1970. He welcomed the Apollo Laser Ranging Experiment onto the 2.7-m telescope, which led to international pre-eminence for McDonald Observatory laser ranging programs. A dormitory for visiting astronomers was constructed in 1969 and fifteen new staff residences were added to the mountain in 1974.

In 1978 Smith began planning for a 7·6-m telescope for McDonald Observatory. For the next seven years he devoted most of his effort to the technical and financial nurturing of that project. But with the fall in oil prices, the Texas economy crashed in 1985 and with it went the political and financial support for such a project. The failure of this project was perhaps his greatest professional disappointment. Characteristically, Smith wasted no time in finding another, equally bold undertaking. In 1986 he negotiated a collaboration with Pennsylvania State University to participate in their Spectroscopic Survey Telescope, an innovative 8.5-m telescope to be constructed at McDonald Observatory.

Harlan Smith loved what he called “public outreach,” the communication of astronomy to the public. He made it a requirement in his department that all faculty teach undergraduate students and that promotion be related to ability in that important undertaking. As a result, the University of Texas now teaches astronomy to approximately 6,000 undergraduate students per year. He instituted a newsletter on astronomy that distributes 100,000 issues annually, and he provided encouragement and start-up funds for what was to become the award-winning radio program Star Date, heard by ten million people per week throughout the world. His efforts not only to accommodate, but to welcome, visitors of McDonald Observatory led to the construction of a visitors’ center in 1980 which now serves 120,000 people per year. At his insistence, the 2.7-m telescope remains the largest telescope in the world open to the public for viewing one evening per month.

Throughout his career Smith actively served the larger astronomical community by participation in numerous national committees. A sampling of his contributions gives some indication of the breadth of his influence in U.S. astronomy: member of the National Academy of Science *ad hoc* committee on the Large Space Telescope, 1966–1970 (which eventually became the Hubble Space Telescope); Chairman of the Planetary Division of the American Astronomical Society (AAS), 1974–1975; Council member of the AAS, 1975–1978; Vice President of the AAS, 1977–1979; member of the Space Science Board of the National Research Council, 1977–1980; member of the Board of Directors of the Association of Universities for Research in Astronomy (AURA), 1972–1983; Chairman of the Board of AURA, 1980–1983; Chairman of the Management/Operations Working Group for Planetary Astronomy (NASA), 1988–1991.

Not only was Harlan Smith recognized by his colleagues through selection for such prestigious assignments, he also received other honors: honorary Doctorates from Nicolaus Copernicus University (1973) and from Denison University (1983), selected as the Edward Randall, Jr., MD, Centennial Professor of Astronomy (1984), and, most recently, received the Distinguished Public Service Medal from NASA (1991).

It is a dry summary of a man's life only to list his accomplishments and honors. There was so much more to Harlan Smith. He was bee keeper, whose gifts of honey were always welcome. He had incredible personal loyalty to people, standing by them, as he did for me on more than one occasion, when it may have been wiser not to do so. His steady, piercing gaze seemed almost to look into one's soul. He always had an aphorism to quote, with a twinkle in his eye, as justification for a course of action. When budgets argued against a purchase, he would smile and say, "Tom, God will provide," (Psalms 22:8). Upon laying the foundation for some distant goal, he would quote Lao-Tzu, "a journey of a thousand miles must begin with a single step."

Harlan Smith was a dreamer. He dreamed of a time when every person on the planet would look at the stars with awe and understanding; he dreamed of a McDonald Observatory pre-eminent among the world's astronomical centers; he dreamed of telescopes on the Moon; and he dreamed of colonists on the Moon and Mars, because it is in our nature to go there. So, I offer a quote from Goethe that I never heard Harlan say, but which seems to apply to the man so well: "What ever you can do, or dream you can, . . . begin it. Boldness has genius and power and magic in it." Harlan Smith dreamed boldly, and acted on those dreams to the betterment of all astronomy.

Thomas G. Barnes III

J. Astrophys. Astr. (1992) **13,** 151–165

Pulsar Observations at 34.5 MHz using the Gauribidanur Telescope: I

A. A. Deshpande* & V. Radhakrishnan *Raman Research Institute, Bangalore 560080*

Received 1991 September 25; accepted 1992 April 11

Abstract. The behaviour of pulsars at low radio-frequencies (below ~ 50 MHz) remains poorly understood mainly due to very limited observational data on pulsars at these frequencies. We report here our measurements of pulse profiles at 34.5 MHz of 8 pulsars using the Gauribidanur Radio Telescope. None of the 8 pulsars show any significant interpulse emission at this frequency which conflicts with an earlier claim from 25 MHz observations. With the exception of one pulsar (PSR 0943 + 10) all the observed pulsars show turnovers at frequencies above 35 MHz in their spectra. We also report our attempts to study the short and long term variations in the pulsar signals at this low frequency.

*Key words***:** pulsars—interstellar scattering—dispersion

1. Introduction

The mean pulse profile and the radiant flux density of a pulsar depend on frequency and therefore, these quantities need to be investigated over as wide a frequency range as possible. Most of the available data on pulsars, numbering now about 500, are from observations at high radio-frequencies. There is a considerable lack of observations towards lower radio-frequencies (below 50 MHz). This is due to various difficulties in observing pulsars at decametric wavelengths arising mainly from the effects of the propagation of pulsar signals through the interstellar medium. Two important effects in the interstellar medium, namely dispersion and scattering, cause considerable reduction in the apparent peak (pulsing) intensity of pulsars at low radio-frequencies. These propagation effects also cause smearing of the details in the pulse profile. As the sky background becomes brighter at lower frequencies, additional difficulties arise if the pulse energy decreases instead of increasing towards lower frequencies.

Some of the earliest observations at decametric wavelengths are due to Bash *et al.* (1970) at 38 MHz and Craft (1970) at 40 MHz. Successful detection of a few more pulsars by Bruck & Ustimenko (1973), in the frequency range of 10 to 25 MHz, confirmed the possibility of receiving pulsed signals from some pulsars at decametric wavelengths. Understandably, these were the pulsars with longer periods and lower dispersion. Through detailed studies of extensive data on a few pulsars at decametric wavelengths, Bruck and Ustimenko reported in a series of papers (1976,1977,1979), the

* Present address: Department of Physics, University of Tasmania, G.P.O. Box 252 C, Hobart, Tasmania, Australia 7001.

detection of interpulse emission not seen at higher frequencies. They also found evidence for emission away from the main pulse in some cases. The radio spectra down to 53 MHz for about a dozen pulsars were first studied by Comella (1972). The spectra in many cases were found to have low frequency turnovers. Observations at 80 and 160 MHz (Slee *et al.* 1986) of a larger sample of pulsars have shown that in general the spectra become less steep towards lower frequencies. Measurements of the spectra of five pulsars in the 17–1420 MHz range have been reported by Bruck *et al.* (1978). This study revealed turnovers in the spectra at low frequencies for all five pulsars, and that the maximum in the emission intensity lies at a frequency of 120 ± 60 MHz on the average. Measurements of the arrival times of the integrated pulses of PSR 0809 + 74 over a wide frequency range (Davies *et al.* 1984; Shitov & Malofeev 1985), have shown that the lower frequency signals arrive with delays longer than those expected from the known amount of dispersion.

The decametric observations described above have yielded very valuable information about the properties of the emission from pulsars (Bruck 1987). All of the five known decametric spectra indicate 'turnovers'. Therefore, the extension of the spectra towards lower radio-frequencies for other pulsars is naturally of great interest. This is especially so for those pulsars whose intensity is still increasing with decreasing frequency in the known part of their spectra. The possibility of interpulse emission appearing at lower frequencies also needs to be investigated in the case of more pulsars to establish general properties relating to the shape and size of the pulsar emission cones. The pulse profiles of many pulsars have been observed to change with frequency in the high frequency range (*e.g.* Manchester 1971; Kuzmin *et al.* 1986; Kardashev *et al.* 1986; Slee *et al.* 1987). The extension of these observations to low frequencies is extremely valuable. Moreover, the amount of interstellar scattering can be estimated at these wavelengths to test the present understanding (see Alurkar *et al.* 1986 and references therein) about the dependence of the amount of scattering on the dispersion measure and the wavelength of observation. We note that all the pulsars studied at decametric wavelengths so far have dispersion measures less than 13 cm^{-3} pc and are confined to the Northern hemisphere. More pulsars, therefore, may possibly be detected at decametric wavelengths if sufficiently sensitive observations can be made and if suitable schemes are employed to enable observation of highly dispersed pulsar signals.

Here, we report on our attempts to observe pulsar signals with high sensitivity and high time-resolution at a low radio-frequency. The Decameterwave Radio Telescope at Gauribidanur (GEETEE)*, India (Longitude: 77° 27′ 07″, Latitude: 13° 36' 12″ N), operating at 34.5 MHz (Deshpande, Shevgaonkar and Sastry 1989, DSS) was used for these observations. The observations and data processing procedure is described in detail. Our successful detections of 8 pulsars are reported. The results are discussed in the end.

2. Observations

The present observations made with the GEETEE used the new tracking facility to obtain more observing time per day. A detailed description of the tracking system is

*This telescope is jointly operated by the Indian Institute of Astrophysics, Bangalore and the Raman Research Institute, Bangalore.

given by DSS. The sensitivity improvement due to the new tracking facility made it feasible to attempt observations of a few strong pulsars having low dispersion measures (DM) with this telescope. As the signals from even the strongest of the pulsars will be well buried in the Galactic background noise it is impossible to detect individual pulses in our observations. However, with the use of the tracking facility a source can be observed over an interval of 42 × sec δ minutes. Thus, it is possible in one observing session to receive a large number of pulses, N (= 2520 sec δ/P), from a pulsar at declination δ and with a period P seconds. These pulses were averaged, using standard averaging techniques, to obtain $\sqrt{N}$ improvement in the signaltonoise ratio.

The present observations were made by using the existing single frequency channel correlation receiver, to correlate the outputs of the EW and S arms of the T array where we obtain both the in-phase (COS) and the quadrature (SIN) correlation outputs (see DSS for more details). A predetection bandwidth of 30kHz (optimum for low DM pulsars) was used. Post-detection time-constants in the range 10–30 milliseconds were employed. The EW arm was used in the tracking mode. In an ideal situation, the SIN correlation for a point source can be discarded as it does not contain the source contribution. However, in practice, due to beam pointing error and ionospheric refraction, the source contribution in the SIN correlation is generally non-zero. This also causes a corresponding reduction in the source contribution and consequent worsening of the signal-to-noise ratio in the COS correlation. In the Appendix we describe a procedure using both the correlations to partially recover such a loss in the signal-to-noise ratio. Both the correlations were recorded using a data logging system on to magnetic tapes at a rate of 3 milliseconds per sample. Thus, each of the two correlations is sampled at intervals of 6 milliseconds. The data recording is stopped for a short interval (~ 500 msec) every time the EW beam is switched to next position during the tracking to allow ample time for the settling of the tracking phase shifters.

The GEETEE accepts only ä single linear polarization. The observed output therefore depends on the source polarization, the observing frequency and the Faraday rotation in the intervening medium. Such a dependence can be ignored if the differential Faraday rotation across the pre-detection bandwidth is sufficiently large. However, with 30 kHz bandwidth the limited polarization sensitivity of the GEETEE may significantly affect observations of strong linearly polarized sources with rotation measures less than about 20 rad m^{-2}. To help reduce this effect to a large extent, different centre frequencies (in the range 34.4 to 34.6 MHz) were used during different observing sessions (4 to 10).

Using the above-mentioned procedure, observations were attempted on 20 known pulsars. These observations were made mostly at night to minimize possible interference due to terrestrial signals in the observing band. Most of these observations were made during 1984 (November)–1985 (March).

3. Data processing

The data processing procedure used here basically employs the standard ‘signal averaging technique’. Knowing the apparent period P, the number of output bins (N_B) is chosen, such that the bin-width (Δt_{bin}) is approximately the same as the sampling interval (Δt_s), and that $\Delta t_{bin}.N_B = N_p.P$, where N_p = no. of periods over which averaging is performed. In this kind of processing, the data averaging is customarily

performed only over a single period stretch i.e. N_p=1. However, here we use N_p = 2, i.e. perform averaging over a two-period stretch, for reasons that will be discussed a little later.

The data for the COS and SIN channels are processed separately using the following procedure. First, for each data block (obtained in one beam position during tracking; i.e. of duration 40 × sec δ seconds) a mean value is computed and subtracted from the corresponding samples. The standard deviation (σ_i) in each block is also estimated. Because of the asynchronous sampling (i.e. $\Delta t_{bin} = t_s$), the resultant profile would be smeared additionally by an amount equal to the bin-width if the samples are added to the nearest bin while averaging. Such smearing is avoided by using linear interpolation to add the sample value with suitable weights in both the bins which are on either side of the sample. We also keep an account of the effective number of samples added in each bin. The final average samples are obtained after appropriate normalization for the system gain. The estimate of the noise in such average profiles is computed using the standard deviations due to noise (σ_i) obtained for each data block.

In the course of this averaging process, if any absolute sample value is found to be greater than 5 times the standard deviation estimated for the data in the respective record, then that sample is rejected as possibly due to interference. However, the bin numbers corresponding to such samples are noted, so that the possibility of these high sample values being due to very strong pulses from the pulsar could still be considered, if the bins are found to be confined only to the pulse window in the average profiles. In this manner, the average profiles are obtained for both the SIN and COS channels separately.

As the data is averaged over a two-period stretch, each half of the stretch corresponds to the average of alternate pulses. These halves can be considered to be two independent sets of data obtained under the same observing conditions and to have, in general, the same average contribution from the pulsar signal. With this understanding, the data over two-period stretches are tested for a significant detection of two similar looking pulses separated exactly by the apparent period of the pulsar. The threshold for the significant detection is chosen to be three times the value of the standard deviation due to noise. This procedure increases the reliability of such detections as it can discriminate against any spurious detections due to interference. However, the signal-to-noise ratio in the two-period stretch is reduced by a factor of $\sqrt{2}$, compared to that in the case of averaging over a one-period stretch, making the detections difficult in the marginal cases. This disadvantage can be overcome by choosing a larger bin-width. It is required that at least one of the two correlation channels satisfies the detection criterion. It should be noted that, in any further processing, only the data with the original bin-size have been used. In the initial stages, as an additional check for the validity of our detections, the corresponding raw data were folded with wrong periodicities and were confirmed to fail in the detection test.

Using the above mentioned procedure, it has been possible to successfully detect signals from 8 pulsars. Their average profiles were obtained by combining the two halves of the two-period stretch for each channel. One such output obtained using the data in the direction of PSR 0834 + 06, is shown in Fig. 1

In the case of each successful detection, the average profiles over a one-period stretch were available for both of the COS and SIN channels. We have employed anew scheme (see Appendix) to combine the COS and SIN correlation channel outputs in an optimum way. We show that with this scheme the resulting average profile, in general,

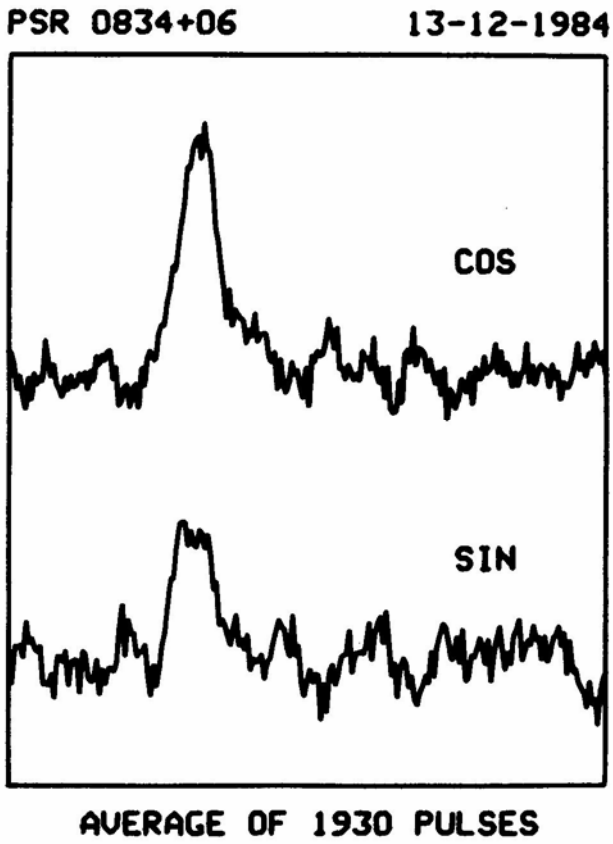

Figure 1. Typical average profiles obtained from data of the COS and SIN channels.

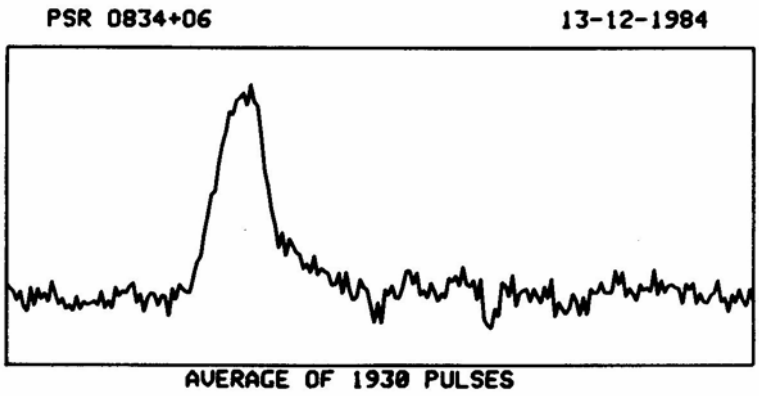

Figure 2. An average profile obtained after combining the COS and SIN channel outputs (shown in Fig. 1) in an optimum way.

will have better signal-to-noise ratio than that available in the individual channels. Fig. 2 shows one such average profile obtained for PSR0834 + 06.

3.1 *Flux Calibration*

To obtain appropriate flux calibrations, observations were made on suitable continuum point sources during every session of the pulsar observations. Sources with declinations close to those of the pulsars observed were selected for calibration. The assumed flux densities at 34.5 MHz for most of these calibrators were obtained by extrapolating from the 38 MHz values (Kellermann, Pauliny-Toth and Williams 1969). These values were used after applying the correction suggested by Baars *et al.* (1977). If such data were not available, the values at 80 and 160 MHz (Slee 1977) were used.

The recorded data during each calibration observation were used to obtain average deflections, D_c and D_s in the COS and SIN channels respectively. The deflection, D_0, corrected for collimation error was obtained as

$$D_0 = \frac{(D_c^2 + D_s^2)^{\ddagger}}{\operatorname{sinc}\left[\frac{1}{\pi}\tan^{-1}(D_s/D_c)\right]} \tag{1}$$

If S is the source strength in Janskys, then the calibration factor R_{cal}, in Janskys per count of deflection, is computed as $R_{\text{cal}} = S/(D_0K)$; where K is the system gain normalization factor. Such values of R_{cal} obtained from observation of 5–7 calibrators on each day, were used to obtain an average daily calibration $\langle R_{\text{cal}}\rangle$ (in Janskys per count), which was used in turn to obtain a calibrated profile, $a(t)$, as $a(t) = A_0(t)$. $\langle R_{\text{cal}}\rangle$ (Janskys).

3.2 *Estimation of the Average Pulse Energy and the Amount of Interstellar Scattering*

The calibrated average pulse profiles were used to estimate the average pulse energy and the amount of pulse broadening due to interstellar scattering. The calibrated profiles obtained on different days were combined together to improve the signal-to-noise ratios. For the purpose of estimating the average pulse energy, the data from different days were averaged with equal weights. The same input data were averaged

Table 1. Estimates of the Average Pulse Energy and the Scatter Broadening of the pulse at 34·5 MHz.

Pulsar	Average pulse energy‡ (10^{-29} Jm^{-2} Hz^{-1})	Scatter broadening§ (msec)
PSR 0628 − 28†	1750 ± 480	45 ± 15
PSR 0809 + 74	710 ± 320	3 ± 2
PSR 0834 + 06	2100 ± 100	16 ± 3
PSR 0942 − 13†	110 ± 60	—
PSR 0943 + 10†	960 ± 120	8 ± 3
PSR 0950 + 08	420 ± 60	9 ± 4
PSR 1133 + 16	900 ± 90	9 ± 3
PSR 1919 + 21	2560 ± 400	—

† New detections at decametric wavelengths
‡ Errors quoted are 5σ values
§ Errors quoted are 1σ values.

also with suitable weights (inverse noise power) to maximise the signal-to-noise ratio. This latter output was used to obtain the estimates of the amount of(interstellar) scatter broadening (τ_s). For this purpose, a best fit profile was obtained in each case. The nature of the function used to fit the observed profile is given by Equation A .5 (see Appendix). The estimate of the average pulse energy was obtained by integrating the observed pulse profile within the pulse window inferred from the best fit profile. The estimates obtained for 8 pulsars are listed in Table 1. Our estimates of τ_s may have larger errors than those quoted here, if our assumptions about the intrinsic pulse profiles ($i(t)$ in equation A.5) at 34.5 MHz do not hold good.

4. Results and discussion

a) Pulse profiles and energy spectra

Three pulsars, namely PSR 0628 – 28, PSR 0942 – 13 and PSR 0943 + 10, have been detected for the first time at decametre wavelengths. The average pulse profiles (Fig. 3) and the energy spectra (Fig. 4) are presented here for seven of the detected pulsars. The error bars correspond to five times the standard deviation due to noise.

i) PSR 0628 – 28 The profile shown in Fig. 3a is seriously affected by the dispersion smearing across 30 kHz. The spectrum of the pulse energy of this pulsar is found to be straight in the frequency range 61 to 1420 MHz (Kuzmin *et al*., 1978). However, an extension of the spectrum to frequencies below 60 MHz, using our estimate for the pulse energy, shows a turnover in the spectrum (Fig. 4a). The emission intensity appears to peak at frequencies close to 60 MHz.

ii) PSR 0809 + 74 This is the only pulsar that has been observed extensively down to a very low frequency of 10 MHz (Bruck & Ustimenko, 1973). Although this is one of the strongest pulsars at the frequency of our observation, the signal-to-noise ratio is rather poor. The telescope sensitivity in the direction of this pulsar is very much reduced due to its large zenith angle. However, the increased tracking time for this pulsar, by virtue of its high declination, has made integration of more number of pulses possible leading to a partial compensation in the signal-to-noise ratio. The pulse profile obtained by us is shown in Fig. 3g. The average pulse energy estimated using this profile is consistent with the turnover in the spectrum of Bruck *et al.* (1978). However, our estimate may have large calibration errors due to the lack of suitable calibration sources at nearby declinations. Fig. 4b shows the spectrum of the average pulse energy using our estimate along with other observations (Bruck *et al* 1978).

iii) PSR 0834+ 06 Observations on this pulsar were made on 11 days. After combining the data on all days, we are able to obtain a high signal-to-noise ratio for its average profile (Fig. 3b). Our estimate of the average energy per pulse in this case is in good agreement with the estimates at other frequencies (see Fig. 4c). The average profile (Fig. 3b) does not show any significant interpulse emission contrary to that reported at 25 MHz.

iv) PSR 0942 –13 Observations of this pulsar were made on two days. The final average profile is shown in Fig. 3c. Using our estimate for the pulse energy along with the value for the average flux at 400 MHz (Manchester & Taylor 1981), we estimate a spectral index of – 0.76 ± 0.28. Due to the large gap in the measured points on the

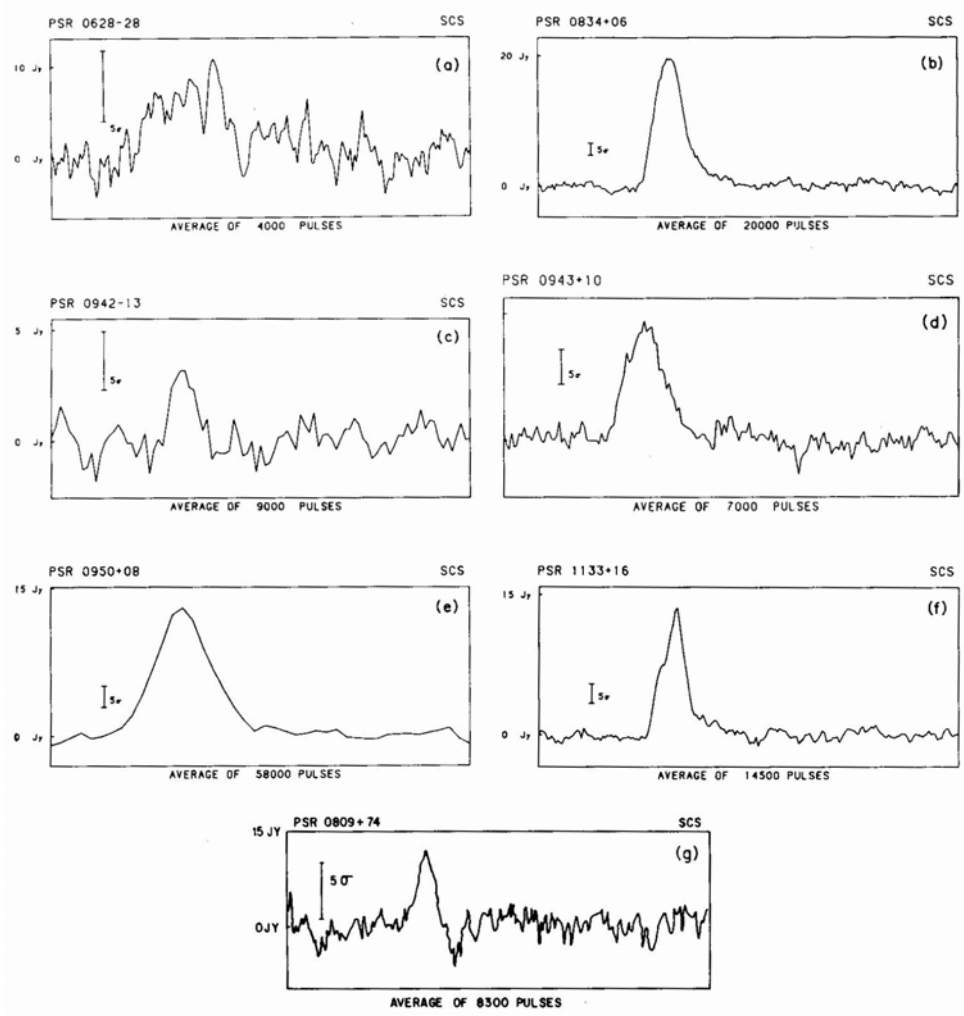

Figure 3. The average pulse profiles for (a): PSR 0628 – 28; (b): PSR 0834 + 06; (c): PSR 0942 – 13; (d): PSR 0943 + 10; (e): PSR 0950 + 08; (f): PSR 1133 + 16 and (g): PSR 0809 + 74 observed at 34.5 MHz. The error bars correspond to five times the r m.s. noise deviation.

spectrum, it is difficult to comment about the existence of a turnover in the spectrum in the frequency range of 35 to 400 MHz.

v) PSR0943 + 10 Suleimanova and Izvekova (1984) have reported mode changing for this pulsar at 62 and 102 MHz. The time-resolution in the profile obtained here (Fig. 3d) is not adequate to see any details in the pulse profile. Our estimate for the average pulse energy, when combined with similar estimates in the range 53 to 606 MHz by Comella (1972) and Slee *et al.* (1986), suggests that the spectrum is still rising even upto 34.5 MHz. This happens to be the first case to the best of our knowledge where the spectrum for a long period pulsar does not have a turnover above 34.5 MHz. Investigation of the spectrum at frequencies below 34.5 MHz would be important. The spectral index computed using our estimate with that at 400 MHz (Manchester & Taylor 1981) is about – 1.65.

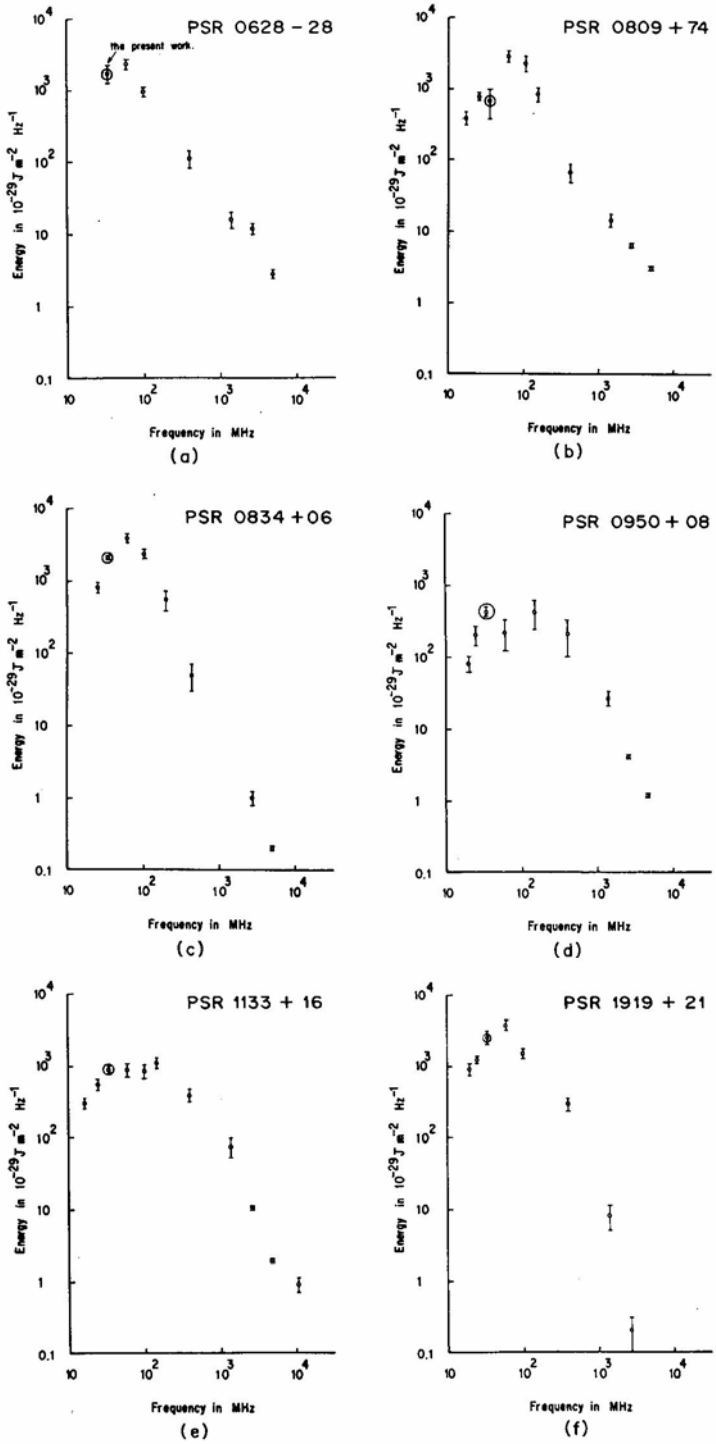

Figure 4. The average pulse energy spectra of (a): PSR 0628–28; (b): PSR 0809 + 74; (c): PSR 0834 + 06; (d): PSR 0950 + 08; (e): PSR 1133 + 16 and (f): PSR 1919 + 21 over the radio-frequency range. The points indicated by an extra circle correspond to the present measurements.

vi) PSR 0950 + 08 This has the smallest dispersion measure among known pulsars. Due to its short period, it was possible to average a large number of pulses leading to better sensitivity. Fig. 3e shows a profile averaged over 54000 pulses using the data obtained on six days. The longitude resolution in this case is not adequate to see finer details in the pulse. Our estimate of the average energy per pulse when compared with other observations (Bruck *et al.* 1978) appears to suggest that the estimate at 61 MHz (Kuzmin *et al.* 1978) may be in considerable error (see Fig. 4d).

vii) PSR 1133 + 16 Fig. 3f shows an average profile for PSR 1133+ 16 at 34.5 MHz. The observations were made on 8 days. The two components which have been observed at and above 61 MHz (e.g. Taylor and Huguenin 1971; Izvekova *et al.* 1979; Slee *et al.* 1986) are just distinguishable in this profile. However, a predicted profile (see equation A.5) assuming a single component in the intrinsic pulse could not give a good fit to the observed profile for the estimation of the scattering width. Therefore, the intrinsic pulse is assumed to have two components of width 12 msec each with a separation of 45 msec. The widths and the separation of the components at 61 MHz are used after $(\text{wavelength})^{0.25}$ scaling. With this assumption, it is possible to obtain a very good fit to the observed profile, provided a component intensity ratio of 0.6:1 is used. It should be pointed out that in the frequency range 80 to 102 MHz (Slee *et al.* 1987; Izvekova *et al.* 1979) this intensity ratio is about unity, and is greater than unity at 400 MHz (Manchester 1971). The energy spectrum is shown in Fig. 4e.

viii) PSR 1919 + 21 We estimate the average pulse energy to be $(2560 \pm 400) \times 10^{-29}$ Jm^{-2} Hz^{-1} . This estimate is obtained from observations made using a 16 frequency channel analog receiver (Deshpande, Sastry & Radhakrishnan 1984). Fig. 4f shows our estimate with those at other frequencies (Bruck *et al.* 1978) on an energy vs. frequency plot.

b) Decametric emission outside the main pulse window

One of the main motivations for the present observations was to look for low-frequency interpulse emission as reported by Bruck & Ustimenko (1976, 1977, 1979). None of the 8 pulsars show any significant interpulse emission at our frequency. Owing to the high signal-to-noise ratio in the case of 4 pulsars, we can obtain useful upper-limits for the emission, if any, outside the main-pulse window. The 3σ limits obtained are: 2% of the main pulse energy for PSR 0834 + 06, 6% for PSR 0950 + 08, 3.5% for PSR 1133 + 16 and 6% for PSR 0943 + 10 (Deshpande & Radhakrishnan 1990). Here we have assumed the width of any such feature outside the main-pulse window to be the same as that of the main pulse. Unless the spectrum of such emission is much steeper than that of the main pulse, these observations conflict with the results reported by Bruck and Ustimenko. Recent 25 MHz observations at Arecibo (Phillips & Wolszczan 1989) have also not detected any significant interpulse emission.

c) Short and long term variations

The prime objective of this work was to study average profiles for as many pulsars as possible and to estimate the above mentioned average parameters. However, it was also thought useful to study the fluctuation spectra and low-frequency variability of pulsar signals using the data obtained during these observations.

4.1 *Fluctuation Spectra*

The time-resolution obtainable in our case is adequate to attempt to study intrinsic subpülse and average profile fluctuations by obtaining suitable power spectra of the modulation function. Such fluctuation spectra can reveal the drifting nature of the subpulses and fluctuations of the pulse energy including the effects of pulse nulling (Drake & Craft 1968; Backer 1970). In general, the observed power spectra have contributions due to the fluctuations caused by the intervening medium. The observed spectrum is a convolution of the spectrum of the intensity modulations due to the invervening medium with the intrinsic modulation spectrum of the pulsar. Thus, any narrow spectral features due to the intrinsic modulation will in general be smeared due to the scintillation in the intervening medium. However, as the scintillations due to the interstellar medium have a very small decorrelation bandwidth at our frequency compared to the observing bandwidth, they will be effectively smoothed out. The interplanetary and the ionospheric scintillations, however, may affect the spectrum significantly.

The data obtained on some strong pulsars from the observations reported here were analysed using 'the longitude-resolved Fourier analysis' method first applied to the study of drifting subpulses by Backer (1970). In this method, the observed intensities as a function of time at each fixed longitude are Fourier transformed separately. We have chosen the width of the longitude bins, within which the data are averaged, to be about 2 per cent of the period. A sequence of samples for a fixed longitude is Fourier transformed in blocks of 256 samples and the amplitude spectra for many blocks are averaged. Such spectra suffer heavily from aliasing effects because at a given longitude only one sample per period can be available.

Fig. 5 shows the fluctuation spectra at different longitudes obtained for PSR 0834 + 06. The values at zero frequency as a function of longitude correspond to the average pulse profile. Such analyses were repeated for this pulsar on different days. At high radio frequencies, the fluctuation spectra for this pulsar show a narrow line feature indicating strong periodic modulation at about 0.46 cycles/period (Taylor & Huguenin 1971). However, our spectra for longitudes within the pulse window do not show any significant deviation from those for longitudes outside the pulse window. Our observations suggest that any periodic modulation which can result in a narrow line feature must be weak at 34.5 MHz and that the depth of modulation does not exceed 6 per cent, when it would have been seen above the noise. It is possible that there is strong

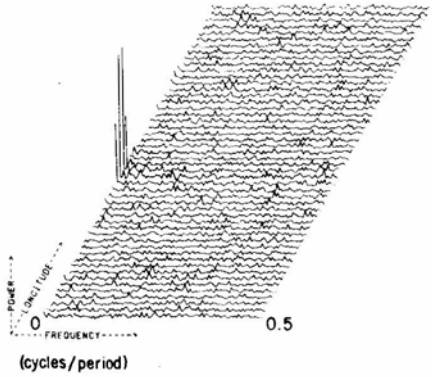

Figure 5. The fluctuation spectra at different longitudes for PSR 0834 + 06 at 34.5 MHz.

modulation, but then its contribution must be spread over a broad region in the spectrum

4.2 *Slow Variability*

Slow variability of the apparent intensity of pulsars has been extensively studied at high radio-frequencies (e.g. Huguenin, Taylor & Helfand 1973). These variations have time scales in a wide range. The slow variability is generally attributed to the refractive scintillations produced by large scale irregularities in the electron density in the interstellar medium (Goodman & Narayan 1985). No measurement of such variability at decametric wavelengths has been reported so far in the literature.

We have made some attempts to make such measurements using the observations discussed above. We have selected three strong pulsars (PSRs 0834 + 06,0950 + 08 and 1133 + 16) and have made observations over a span of about 80 days. The calibrated pulse energies obtained from these observations have been used to compute a modulation index, m, defined as

$$m = \frac{\left[\frac{1}{N_{\rm obs}} \sum^{N_{\rm obs}} (S_i - \bar{S})^2\right]^{\frac{1}{2}}}{\bar{S}} \qquad (2)$$

where $\bar{S}$ = average of S_i, S_i = the pulsar intensity in ith measurement, and $N_{\rm obs}$ = the total number of such measurements (about 10 in the present case). The computed modulation indices in two of the three cases did not indicate any modulation significantly above the standard deviations in calibration. Only in the case of PSR 0950 + 08 do we find significant modulation. The estimated value of m, in this case, is 0.34 ± 0.15. This value is in good agreement with similar estimates by Slee *et al.* (1986) at 80 and 160 MHz. The large error in the above estimate is mainly attributable to the calibration errors. The apparent non-detection of any significant variability in the other two cases may be understood as an effect of the short observing time (81 days) compared to the characteristic time scales of such intensity variations at our frequency (Deshpande & Nityananda 1990). Further observations over longer time spans can be undertaken for detailed investigation.

d) Scatter broadening

As can be seen from Table 1, our estimates of the scatter broadening at 34.5 MHz have large error bars. However, these estimates (within their errors) are in general agreement with similar estimates at higher frequencies (Alurkar *et al.* 1986). A more quantitative comparison of these estimates suggests that the wavelength dependence of the scatter broadening is steeper than $(\text{wavelength})^4$.

5. Summary

We have reported here our observations of 8 pulsars at a low frequency by employing the method described in this paper. The profiles obtained from the present observations are affected mainly by dispersion smearing over the 30 kHz band and fail to show the

pulse structure in detail. Subsequently, to obtain high resolution pulse profiles we have made observations employing the swept-frequency dedispersion method (Deshpande 1987; Deshpande & Radhakrishnan 1990). Details of these latter observations will be reported separately. Our estimates of the pulse energies in 5 cases do confirm the low frequency turnovers already known from other observations. Out of the 3 new detections by us at 34.5 MHz, only in one case (PSR 0943 + 10) does the spectrum not appear to have a turnover down to 34.5 MHz. Such a spectrum can be of great interest if this trend continues at even lower frequencies.

Regarding the interpulse emission, we notice no significant emission beyond the main pulse window in those cases where significant interpulse emission was reported at 25 MHz.

Our attempts to study fluctuation spectra and slow variability of pulsars have shown that such studies at decametric wavelengths are feasible and can be very valuable if pursued in future.

Acknowledgements

We thankfully acknowledge the help and cooperation from G. N. Rajasekhar and H. A. Ashwathappa during the observations. A.A.D. thanks Ch. V. Sastry for his constant encouragement and R. K. Shevgaonkar and R. Nityananda for many useful discussions. We also thank O. B. Slee and an anonymous referee for their suggestions which have helped to improve this paper.

APPENDIX

The procedure used for optimal combination of the pulse profiles from COS and the SIN correlation outputs.

In the present case, the COS and the SIN channel outputs ($A_c(t)$ and $A_s(t)$) can be written as

$$A_c(t) = gA_o(t)\cos\left(\frac{\pi\Delta\theta}{\theta_0}\right) \tag{A. 1a}$$

$$A_s(t) = gA_o(t)\sin\left(\frac{\pi\Delta\theta}{\theta_0}\right) \tag{A. 1b}$$

where g = the gain factor due to collimation error = $\mathrm{sinc}(\Delta\theta/\theta_0)$; θ_0 = separation between the peak and the first null of the S arm beam in N–S direction; $\Delta\theta$ = effective collimation error in N–S direction; and $A_0(t)$ = the COS channel output when $\Delta\theta = 0$.

$A_0(t)$, the main function of interest, can be obtained from $A_c(t)$ and $A_s(t)$ by using the equations (la, b) as

$$A_o(t) = \frac{1}{g}[A_c^2(t) + A_s^2(t)]^{\frac{1}{2}} \tag{A.2}$$

The factor g can be estimated using the value of $\Delta\theta$ obtainable as

$$\Delta\theta = \frac{1}{\pi}\tan^{-1}\left[\frac{A_s(t)}{A_c(t)}\right]\cdot\theta_0 \quad \text{for } A_o(t) \neq 0 \tag{A.3}$$

However, in a practical situation, i.e. in the presence of noise, the signal-to-noise ratio obtainable for $A_o(t)$ is worsened further, if the above procedure is used (Deshpande 1987). Hence, we have employed a new scheme to estimate $A_0\,(t)$ from the COS and SIN channel outputs in an optimum way.

In this scheme, the channel with better signal-to-noise ratio is selected first, As most of the times such a channel corresponds to the COS correlation, for further discussion, we will assume this channel to be the COS channel ($Ac(t)$ such that $0 \leqslant t < P$ where P is the pulsar period). A best fit pulse profile is obtained for this channel data. The best fit profile ($F_1(t)$) takes into account the intrinsic pulse width, dispersion smearing, the receiver time-constant and gives estimates for the pulse amplitude (Amp_1) and the amount of the interstellar scatter broadening(τ_s).The best fit profile can be written as

$$F_1\,(t) = \mathrm{Amp}_1 \cdot \mathrm{G}\,(t) \tag{A.4}$$

and

$$\mathrm{G}\,(\mathrm{t}) = i\,(t) * s\,(t) * d\,(t) * r(t) \tag{A.5}$$

where $i(t)$ = a Gaussian to represent the intrinsic pulse profile; $s(t)$ = a truncated exponential, with τ_s as the characteristic width representing the scattering in the interstellar medium; $d(t)$ = the receiver bandpass converted into time function by the dispersion law; $r(t)$ = the impulse response of the post-detection filter; and $*$ denotes convolution.

The equivalent width of the Gaussian pulse in $i(t)$ is obtained using the pulse width at 400 MHz (Manchester & Taylor 1981) and assuming that the pulse width is α (frequency)$^{-0.25}$. The best fit function, G(t), is then used to estimate the best-fit-pulse amplitude (Amp_2) for the other channel output $A_s(t)$ as,

$$\mathrm{Amp}_2 = \frac{\int A_s(t)\,\mathrm{d}t}{\int A_s(t) \cdot G(t)\,\mathrm{d}t} \tag{A.6}$$

The effective collimation error $\Delta\theta$ is then estimated as

$$\Delta\theta = [\tan^{-1}\,(\mathrm{Amp}_2/\mathrm{Amp}_1)] \cdot \theta_0/\pi \tag{A.7}$$

Now, it is possible to obtain two independent estimates (say $A_{o1}(t)$ and $A_{o2}(t)$) of $\mathrm{A}_o(t)$, as follows

and

$$\mathrm{A}_{o1}\,(t) = Y \cdot A_c\,(t)/\,\mathrm{Amp}_1 \tag{A.8a}$$

$$\mathrm{A}_{o2}\,(t) = Y \cdot A_s\,(t)/\,\mathrm{Amp}_2 \tag{A.8b}$$

where

$$Y = (\mathrm{Amp}_1^2 + \mathrm{Amp}_2)^{\frac{1}{2}}/\mathrm{g} \tag{A.9}$$

The r m.s. noise deviations (σ_1,σ_2) in the profiles $A_{o1}(t)$ and $A_{o2}(t)$ respectively are given by

$$\sigma_1 = \sigma Y/\mathrm{Amp}_1 \tag{A.10a}$$

$$\sigma_2 = \sigma Y/\mathrm{Amp}_2 \tag{A.10b}$$

where σ = r m.s. noise deviation in the profile $A_c(t)$, $A_s(t)$.

It should be noted that the errors in the determination of Amp_1 and Amp_2 are much smaller than σ and are therefore ignored here. The two independent estimates, $A_{o1}(t)$ and $A_{o2}(t)$, are combined with suitable weights, to obtain the best possible estimate of $A_o\,(t)$. The optimum weight is proportional to the inverse of the noise power in the estimate.

It can be shown that, the r m.s. of the noise, σ_o, for the profile A_o (t) is given by σ_o — σ/g and the corresponding signal-to-noise ratio is given by

$$\begin{aligned}(S/N)_{A_o} &= (S/N)_{A_c}[1 + (\mathrm{Amp}_2/\mathrm{Amp}_1)^2]^{\frac{1}{2}} \\ &= (S/N)_{A_s}[1 + (\mathrm{Amp}_1/\mathrm{Amp}_2)^2]^{\frac{1}{2}}\end{aligned} \tag{A.11}$$

where $(S/N)_i$ refers to the signal-to-noise ratio for the profile $A_i(t)$.

Thus, by using the above procedure, it is possible to partially recover the loss in signal-to-noise ratio in the COS channel due to collimation errors.

References

Alurkar, S. K., Slee, O. B., Bobra, A. D. 1986, *Austr. J. Phys.,* **39**, 433.

Baars, J. W. M., Genzel, R., Pauliny-Toth, I. I. K., Witzel, A. 1977, *Astr. Astrophys.,* **61,** 99.

Backer, D. C. 1970, *Nature,* **227**, 692.

Bash, F. N., Bozyan, F. A., Torrence, G. W. 1970, *Astrophys. Lett.,* **7,** 39.

Bruck, Yu. M. 1987, *Austr. J. Phys.,* **40,** 861.

Bruck, Yu. M., Davies, J. G., Kuz'min, A. D., Lyne, A. G., Malofeev, V. M., Rawson,B., Ustimenko, B. Yu., Shitov, Yu. P. 1978, *Soviet Astr.,* **22(5),** 588.

Bruck, Yu. M., Ustimenko, B. Yu. 1973, *Nature Phys. Sci.,* **242,** 58.

Bruck, Yu. M., Ustimenko, B. Yu. 1976, *Nature,* **260,** 766.

Bruck, Yu. M., Ustimenko, B. Yu. 1977, *Astrophys. Space Sci.,* **51,** 225.

Bruck, Yu. M., Ustimenko, B. Yu. 1979, *Astr. Astrophys.* **80,** 170.

Comella, J. M. 1972, *Ph. D. Thesis,* Cornell University.

Craft, H. D., Jr. 1970, *Ph. D. Thesis,* Cornell University.

Davies, J. G., Lyne, A. G., Smith, F. G.,Izvekova, V. A., Kuz'min, A. D., Shitov, Yu. P.1984, *Mon. Not. R. astr. Soc.,* **211,** 57.

Deshpande, A. A. 1987, *Ph. D. Thesis,* Indian Institute of Technology, Bombay.

Deshpande, A. A., Nityananda, R. 1990, *Astr. Astrophys.,* **231,** 199.

Deshpande, A. A., Radhakrishnan, V. 1990, Proc. of the IAU Colloquium 128 on "The Magnetospheric Structure and Emission Mechanisms of Radio Pulsars", Poland (to appear).

Deshpande, A. A., Sastry Ch. V., Radhakrishnan, V. 1984, Proc. of the "*Low Frequency Radio Astronomy". Workshop held at N RAO, Green Bank,* (eds W. C. Erickson and H. V. Cane).

Deshpande, A. A., Shevgaonkar, R. K., Sastry Ch. V. 1989, *Journal of IETE,* **35,** 342 (DSS)

Drake, F. D., Craft, H. D., Jr. 1968, *Nature,* **220,** 231.

Goodman, J., Narayan, R. 1985, *Mon. Not. R. astr. Soc.,* **214,** 519.

Huguenin, G. R., Taylor, J. H., Helfand, D. J. 1973, *Astrophys. J.,* **181,** L139.

Izvekova, V. A., Kuz'min, A. D., Malofeev, V. M., Shitov, Yu. P. 1979, *Soviet. Astr.* **23(2),** 179.

Kellermann, K. I., Pauliny-Toth, I.I. K., Williams, P. J. S. 1969, *Astrophys. J.,* **157,** 1.

Kardashev, N. S., Nikolaev, N. Ya., Novikov, A. Yu., Popov, M. V., Soglasnov, V. A., Kuz'min, A. D., Smirnova, T. V., Sieber, W., Wielebinski, R. 1986, *Astr. Astrophys.,* **163,** 114.

Kuz'min, A. D., Malofeev, V. M., Shitov, Yu. P., Davies, J. G., Lyne, A. G., Rowson, B. 1978, *Mon. Not. R. astr. Soc.,* **185,** 441.

Kuz'min, A. D., Malofeev, V. M., Izvekova, V. A., Sieber, W., Wielebinski, R. 1986, *Astr. Astrophys.,* **161,** 183.

Manchester, R. N. 1971, *Astrophys. J. Suppl.,* **23,** 283.

Manchester, R. N., Taylor, J. H. 1981, *Astr.* J., **86(12),** 1953.

Phillips, J. A., Wolszczan A. 1989, *Astrophys. J. Lett.* **344,** L69.

Shitov, Yu. P., Malofeev, V. M. 1985, *Soviet. Astr.,* **11(1),** 39.

Slee, O. B. 1977, *Astrophys. Suppl.,* **43,** 1.

Slee, O. B., Bobra, A. D., Alurkar, S. K. 1986, *Austr. J. Phys.,* **39,** 103.

Slee, O. B., Bobra, A. D., Alurkar, S. K. 1987, *Austr. J. Phys.,* **40,** 557.

Suleimanova, S. A., Izvekova, V. A. 1984, *Soviet Astr.,* **28(1),** 32.

Taylor, J. H., Huguenin, G. R. 1971, *Astrophys. J.,* **167,** 273.

J. Astrophys. Astr. (1992) **13,** 167–173

A Sweeping Local Oscillator System for Pulsar Observations

A. A. Deshpande* *Raman Research Institute, Bangalore 560080*

Received 1991 September 25; accepted 1992 April 11

Abstract. We discuss here the design details of an inexpensive programmable Sweeping Local Oscillator System (SLOS) built for use in a 'swept frequency dedispersion scheme' for pulsar observations. A useful extension of the basic Divide-and-Add algorithm for frequency synthesis is developed for this purpose. An SLOS based on this design has been built and used for high time-resolution observations of pulsars at low radio-frequencies.

Key words: pulsars—interstellar scattering—dispersion

1. Introduction

The dispersion smearing due to the interstellar medium poses serious difficulties in high time-resolution studies of distant pulsars at low radio-frequencies. High time-resolution, however, can be obtained by using some suitable scheme for dedispersion of the received pulsar signals. Many variations of the pre-detection and the post-detection dispersion removal techniques have been used at high radio-frequencies (e.g. Taylor & Huguenin 1971; Hankins 1971). One of these is the swept-frequency dedispersion procedure as used by Sutton *et al.* (1970) and McCulloch, Taylor & Weisberg (1979). In this method, the periodicity and the dispersed nature of the pulsar signals are used to advantage. It can be shown, that due to the dispersion, the intensity variations due to pulsar signals in time get mapped into the frequency domain (Fig. 1). Therefore, a pulse profile over one full period can be obtained, if the intensity as a function of frequency can be measured at any instant in time over a finite bandwidth

$$\Delta f \sim kPf_0^3/\mathrm{DM} \tag{1}$$

where k = a constant, f_0 = centre frequency of observation, DM = Dispersion Measure, and P = Period of the pulsar.

Such a spectral pattern, however, sweeps across the band at an approximate rate of $(-\Delta f/P)$. This pattern can be made to appear stationary by appropriately 'sweeping' the centre frequency of the receiver. Then the dispersed pulsar signal would result in a train of 'fixed' spectral features separated by Δf corresponding to the dedispersed pulse profiles. The pulse profiles can then be measured with high resolution using a suitable spectrometer. This requires that the centre frequency of observation is swept at a rate given by the dispersion relation, the sweep being reset at intervals of integral number of periods. The maximum time-resolution obtained in this way corresponds to the

* Present address: Department of Physics, University of Tasmania, G.P.O. Box 252 C, Hobart, Tasmania, Australia 7001.

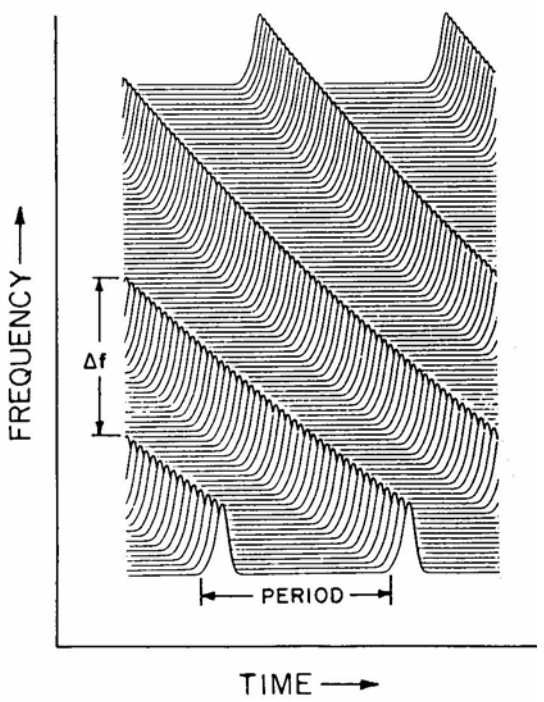

Figure 1. This figure shows typical intensity patterns in the time-frequency domain due to dispersed pulsar signals. The pulse profile over one period (P) can be equivalently obtained by measuring the intensity pattern in frequency over a finite bandwidth Δf at any instant. The spectral pattern drifts across the band with time at an approximate rate ($\Delta f/P$) and repeates after the period interval.

dispersion smearing over one spectral bin. The implementation of the above method requires a suitable sweeping local oscillator system.

In this paper, we describe a design of a suitable sweeping local oscillator system. The specifications are based on the requirements for pulsar observations at 34.5 MHz (Deshpande 1987, Deshpande & Radhakrishnan 1990) with the Gauribidanur Radio Telescope (GEETEE) (Deshpande, Shevgaonkar & Sastry 1989). However, the basic design concepts have wider applicability.

2. The Sweeping Local Oscillator System (SLOS)

We note from equation (1) that the bandwidth (Δf) to be swept by SLOS is a function of the dispersion measure (DM) and the period (P) of the pulsar. We have considered most of the pulsars detected at 102 MHz (Izvekova *et al.,* 1979), as possible candidates for detection at 34.5 MHz, and have indicated them on the Period vs DM plot (Fig. 2). The curves corresponding to different values of maximum bandwidth that can be swept by SLOS are indicated. For a given value of the maximum sweep width, the system can observe all pulsars below the corresponding straight line. The dotted curve shows the limit set by scattering in the interstellar medium and is obtained by extrapolating from the scattering width measurements at 160 and 80 MHz (Slee, Dulk & Otrupcek, 1980)

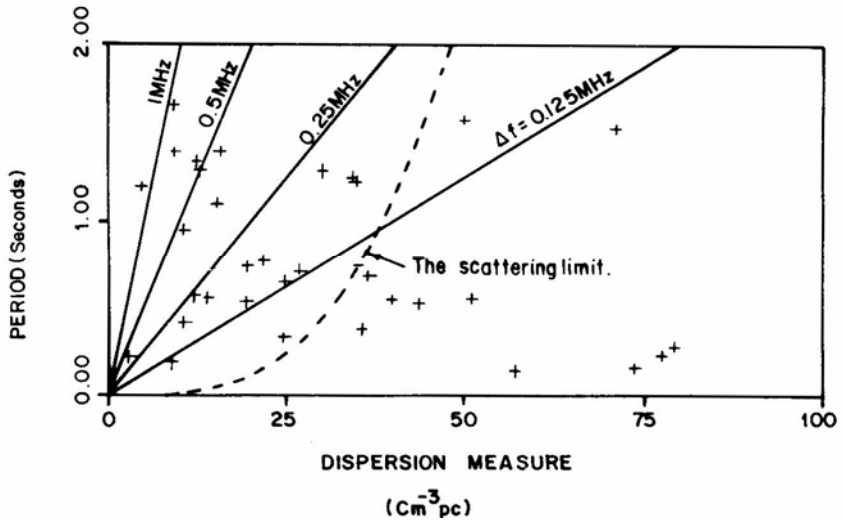

Figure 2. A plot of pulsar periods versus dispersion measures (see text for details).

assuming that $\tau_s \propto$ (wavelength)^4. For pulsars below this curve, the scatter broadening (τ_s) is expected to be larger than the pulsar period (P). A sweep bandwidth of 1 MHz (centred at 34.5 MHz) is sufficient for most of the pulsars indicated here. The pulsars, which need higher sweep bandwidths, have either very low DMs or longer periods and hence the effects of dispersion smearing are not so serious.

The next requirement is that the SLOS should produce the sweep as described by the dispersion relation with minimum possible error. The required frequency (f_r) in the range 34 to 35 MHZ can be computed as

$$f_r(t) = f_r(t') = f_{0s}\left[1 + \left(\frac{f_{0s}^2\, t'}{\mathrm{DM}.k'}\right)\right]^{-1/2} \tag{2}$$

where $t' = t - iP$; for i = 0,1,2,...; such that $0 < t' < P$, f_{0s} = the starting frequency of the sweep pattern, and k' = a constant.

The nonlinear sweep in frequency can be approximated by a "staircase" pattern with a uniform step width in time. In order to avoid any significant additional smearing of the pulse profile, the r m.s. error in the sweep frequency should be less than the resolution of the spectrometer (assumed > 400 Hz in the present case). For example, an r.m.s. error of 400 Hz results in an additional smearing of about 8 milliseconds for pulsars with a DM of 100 cm^{-3} pc.

We see from equation (2) that the sweep pattern can be considered as a fixed function of (t'/DM). This allows us to use a fixed staircase pattern for the sweep frequency, provided the step width (Δt, say) in the pattern is made proportional to DM. In the present case, we have chosen Δt to be DM/20 msec so that the step height is approximately 250 Hz. The number of such steps required to span 1 MHz is about 4000. It should be noted that any error in the value of DM used causes an effective error in the SLOS output frequencies. To keep the frequency error to less than 250 Hz we need to know the DM to an accuracy of ± 0.005 c m^{-3} pc. Fortunately, the DM values for most of the relevant pulsars are available to this accuracy.

We have used these criteria to design the SLOS shown in Fig. 3. We have assumed f_{0s}

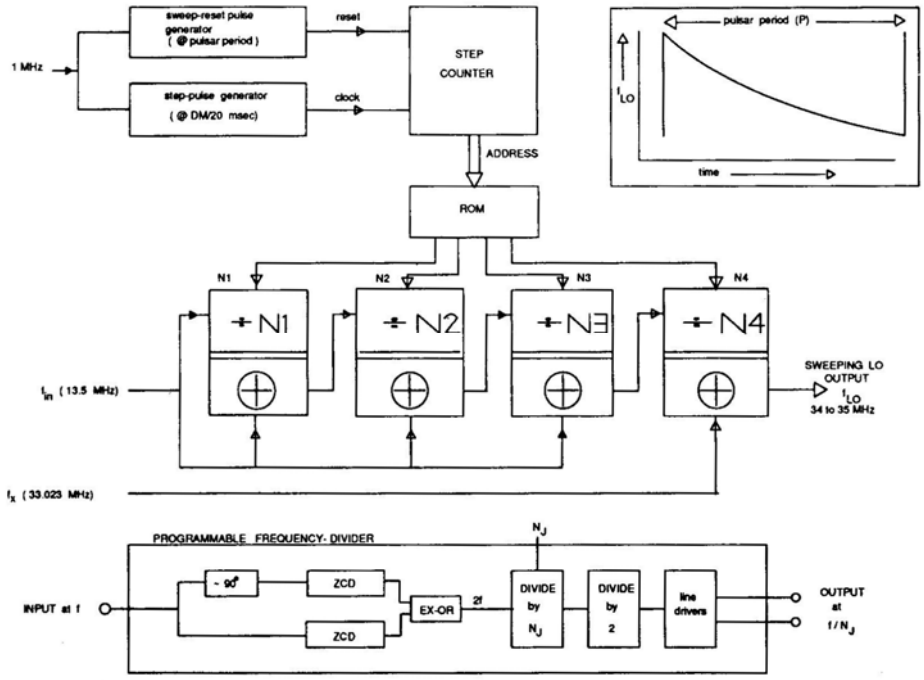

Figure 3. A simplified block diagram of the sweeping local oscillator system.

to be 35 MHz to determine a fixed staircase pattern for the sweep. A suitable section of this pattern can then be used to start the sweep from any desired starting frequency f_s such that $f_s < f_{0s}$ and the bandwidth to be swept is less than (f_s-34) MHz. The values of the starting frequency (f_s), dispersion measure (DM) and the period (P) of the pulsar are set on front panel switches. A 1 MHz reference frequency is used to derive the sweep-reset pulses at intervals of the pulsar period (P) and the sweep-step pulses at intervals of DM/20 msec. The step pulses increment a step-counter which is preset by the sweep-reset pulse to a starting step value ($\hat{n}_s$) depending on f_s. The step number $\hat{n}$ controls an oscillator to produce a predetermined frequency in the range 34 to 35 MHz.

The most attractive possibility for the controlled oscillator is a commercial fast-switching frequency synthesiser, which can be controlled digitally. We describe an inexpensive design that is suitable for the present purpose and is based on the Divide-and-Add algorithm for frequency synthesis. In this method, one input frequency is divided by an integer divisor and the resulting frequency is added to another or same input frequency. Different output frequencies are generated by varying the divisor value. Apart from the programmability, one of the main advantages of this method is that its performance is not sensitive to variations in voltage and temperature. If we consider a single stage of Divide-and-Add to meet the present requirements, the input frequency to the divider turns out to be larger than 4 GHz which makes the hardware realization very difficult. However, if several such divide-and-add stages are cascaded a much lower frequency can be used. Fig. 3 shows a simplified block diagram of the scheme employed by us using a 4-stage divide-and-add algorithm. The output

frequency, f_{out}, given by

$$f_{out} = f_{in}\left[\sum_{i=1}^{4} \frac{1}{\pi_{j=i}^{4} N_j}\right] + f_x \tag{3}$$

can be generated with suitable choices of fixed frequencies f_{in} and f_x and with appropriate N_j (j= 1 to 4) values in the range say $N_j = N_{min}$ to N_{max}. The smallest frequency f_{min} and the largest frequency f_{max} that can be generated, correspond to $N_j = N_{max}$ and N_{min} respectively. The range of the output frequencies, i.e. ($f_{max} - f_{min}$), is directly proportional to f_{in} . The choice of parameters in the above equation (3) is based on the following requirements.

i) The range ($f_{max} - f_{min}$) should be at least 1 MHz.
ii) Errors in the generated frequencies should be as small as possible.
iii) The frequency adder modules involve a mixer and a filter to pass the upper sideband, this filter should be easy to realize. Therefore, N_{max}, which determines the separation between the two side bands, should not be too large.
iv) The values of f_{in}, N_{max} and N_{min} are chosen so that the mixer outputs from the first 3 stages do not have any harmonic contributions in the range 34 to 35 MHz.

These constraints are satisfied if N_{max}= 15, N_{min} = 5, f_{in} = 13.5 MHz and f_x = 33.023 MHz.

The design of the programmable frequency-divider is also shown in Fig. 3. The input to the divider module is generally the analog output of the adder module. The input is converted to a digital signal using zero-cross detectors (ZCD) with differential inputs. In order to minimize harmonics in the output signal the divider circuits are arranged to provide a square-wave at the output frequency. For this purpose we generate a digital signal at twice the input frequency before the Divide-by-N counter. The frequency doubling is achieved by 'exclusive-or' ing the two ZCD outputs produced with about a quarter cycle phase difference. This signal is first divided by the programmable divide-by-N counter followed by a flipflop configured as divide-by-2 to produce a square wave at the required output frequency. The differential outputs of the line drivers isolate the analog and the digital grounds at the module level.

In the frequency-adder module, the two square wave inputs are AC coupled and low-pass filtered to obtain only the fundamentals. These signals are then mixed and the output is filtered to reject the lower side-band product. The output of the final adder module is passed through a ZCD and filtered to give + 10 dbm output level in the 34 to 35 MHz range.

Following the designs described above the SLOS was built successfully. Two readily available inexpensive synthesisers were used to provide the two inputs f_{in} and f_x. Spurious signals at the output were kept 30 dB below the main frequency output. Suitable values of N_j were made available as a function of the value of $\hat{n}$ (for $\hat{n}$ =0 to 4095) in a preprogrammed memory block. In order to obtain the 4096 'suitable' values of N_j, the frequencies corresponding to all the possible $((N_{max} - N_{min} + 1)^4)$ combinations were computed, sorted and scanned for suitability by comparing with a list of the desired frequencies. The distribution of the deviation of the final output frequency from the desired frequency is plotted in Fig. 4(A, B)· These deviations were measured by stepping through all values of $\hat{n}$ manually. The slight skew in the distribution of the deviations is real and results in a corresponding bias in the estimates

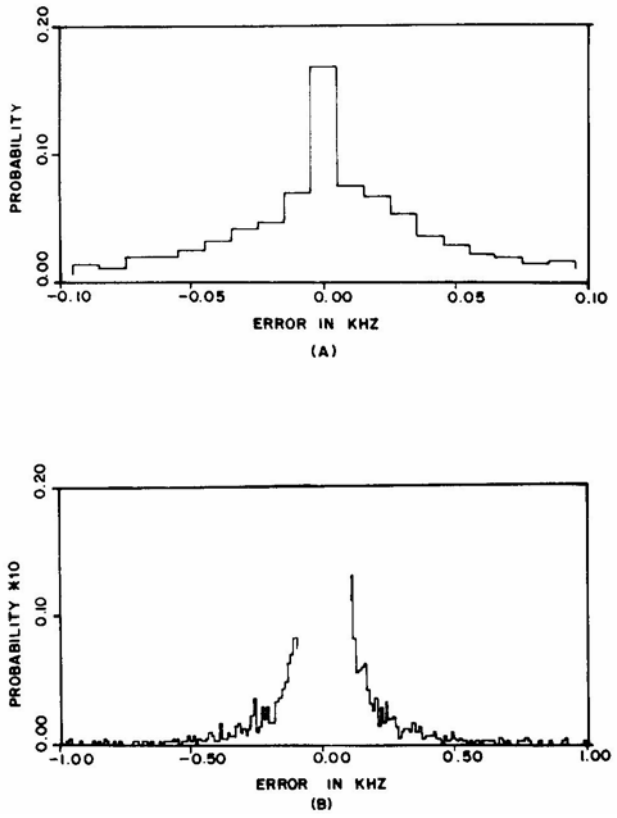

Figure 4. The distribution (probability density distribution with 10 Hz resolution bin) of the errors in the final output frequency of the SLOS.

of the time of arrival of pulsar signals. We expect this skew to depend on the starting sweep frequency and the band width swept.

3. Conclusion

In this paper, we have described a design of a programmable sweeping local oscillator system which was developed for pulsar observations at 34.5 MHz employing a swept-frequency dedispersion method. This design exploits the advantages of both analog and digital devices making the system inexpensive and reliable. Although the basic divide-and-add algorithm for frequency synthesis is well known, we have shown how the use of several such stages in cascade can reduce the frequency step-size without the need of a very high input frequency. This system together with a 128-channel digital autocorrelation receiver (Udaya Shankar & Ravishankar 1990) has been used successfully to study highly dispersed pulsar signals with high time resolution (Deshpande 1987, Deshpande & Radhakrishnan 1990). Fig. 5 shows a sample pulse-profile obtained for PSR 1919 + 21. The details of these observations will be discussed elsewhere (Deshpande & Radhakrishnan 1991).

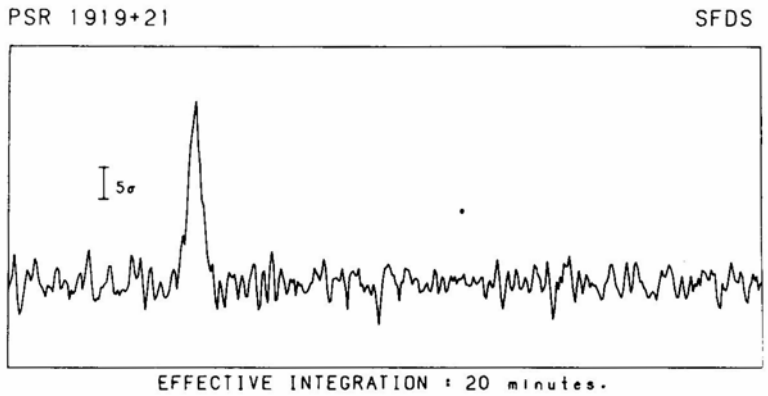

Figure 5. An average pulse profile for PSR 1919 + 21 at 34.5 MHz obtained from observations made using the sweeping local oscillator system.

Acknowledgements

The author thankfully acknowledges the invaluable help from T. S. Ravishankar & G. Jayakumar in the fabrication of the system described here. He also thanks N. Udayashankar, N. V. G. Sarma and V. Radhakrishnan for many useful discussions during the course of this work, P. M. McCulloch for critical reading of the manuscript and for suggestions to improve the manuscript and an anonymous referee for useful comments.

References

Deshpande, A. A. 1987, *Ph. D. Thesis,* Indian Institute of Technology, Bombay.
Deshpande, A. A., Radhakrishnan, V. 1990, in *I A U Coll. 128: The Magnetospheric Structure and Emission Mechanisms of Radio Pulsars,* Poland (to appear).
Deshpande, A. A., Radhakrishnan, V. 1992, *J. Astrophys. Astr.,* **13,** 151.
Deshpande, A. A., Shevgaonkar, R. K., Sastry Ch. V. 1989, *J. IETE,* **35,** 342.
Hankins, T. H. 1971, *Astrophys. J.,* **169,** 487.
Izvekova, V. A., Kuzmin, A. D., Malofeev, V. M., Shitov, Yu. P. 1979, *Soviet Astr.* **23(2),** 179.
McCulloch, P. M., Taylor, J. H., Weisberg, J. M. 1979, *Astrophys. J.,* **227,** LI33.
Slee, O. B., Dulk, G. A., Otrupcek, R. E. 1980, *Proc. Astr. Soc. Austr.,* **4,** 100.
Sutton, J. M., Staelin, D. H., Price, R. M., Weiner, R. 1970, *Astrophys. J.,* **159,** L89.
Taylor, J. H., Huguenin, G. R. 1971, *Astrophys. J.*, **167,** 273.
Udayashankar, N., Ravishankar, T. S. 1990, J, *Astrophys. Astr.* **11,** 297.

J. Astrophys. Astr. (1992) **13,** 175–194

Mid-Ultraviolet and Optical Photometry of Helium Stars

Gopal C. Kilambi & Praveen Nagar* *Center of Advanced Study in Astronomy, Osmania University, Hyderabad 500 007*
N. Kameswara Rao *Indian Institute of Astrophysics, Koramangala, Bangalore 560 034*

Received 1991 November 12; accepted 1992 April 11

Abstract. Mid-ultraviolet and optical photometric analysis of helium stars are presented. A linear relation exists between the effective temperature derived from model atmospheres and $(1965\text{-}V)_0$ index. The effective temperatures derived from $(1965\text{-}V)_0$ index are somewhat higher than that of MK spectral type estimates especially for late B-type helium objects.

Key words: Helium stars—photometry—effective temperature.

1. Introduction

Spectroscopic investigations of some B-type stars have shown anomalous helium abundances to that of normal B-type objects of similar temperatures. These anomalous objects are termed as 'Helium-stars' and are further subclassified into extreme, intermediate or rich or strong and weak-line stars based on HeI/H line intensity ratios. These stars have spectral types generally in the range B0–B9 III–V and effective temperatures of the order of 11000–30000 K. Except in the extreme helium stars, the helium peculiarity in these objects is believed to be confirmed to the atmospheric layers as a consequence of the complex interaction of diffusion processes, a weak stellar wind and a strong periodically varying magnetic field (Osmer and Peterson, 1974; Vauclair, 1975; Landstreet and Borra, 1978; Borra and Landstreet, 1979 and Michaud *et al.,* 1987). Recent reviews of these stars may be found in Hunger (1986) and Bohlender *et al.*, (1987). Walborn (1983) showed from the line strength measurements that the majority of helium-rich stars do not indicate any outstanding CNO or other metal anomalies compared to the stars of similar spectral types and has classified this subgroup members as Population I main-sequence objects with some exceptions.

So far, the classification of helium stars is being done mainly through spectroscopic investigations and no attempt has been made in identifying these subgroups through photometric investigations. In this analysis, an attempt has been made to identify these subgroups through photometric observations using both optical and mid-ultraviolet regions of the spectrum, as these stars are hot and emit a considerable amount of energy in the *UV* region and to estimate effective temperatures for a large sample, using calibrations based on the existing spectroscopic analysis of some of these stars.

*Now at Department of Physics and Astronomy, Lucknow University, Lucknow.

2. Observational data and reduction

Around 100 stars classified as 'Helium stars' and for which both optical and mid-ultraviolet measurements are available have been selected from the literature for this analysis. Some of these stars are classified as weak, strong or rich and extreme, and the rest have no subclassification and the latter group has been treated as 'unclassified' in this investigation. The m_1 and c_1 indices for these stars have been taken from the Catalogue compiled by Mermilliod and Hauck (1979). The *V, B–V, U–B* values and spectral types have been taken from the Photometric Catalogue compiled by Blanco *et al.* (1968) and Underhill *et al.* (1979). Table 1 gives the data for these stars. Though some other objects also have been classified as helium stars and for which *U B V* and *uvby* photometric indices are available in the literature, the non-availability of mid-uv measurements in Thomson *et al.'s* (1978) study restricts their inclusion in the present analysis. Thus, only three EHe stars have been found in the catalogue and are not further discussed in the present study. In addition, Table 1 also gives data for two O-type stars, one A-type star and two stars of luminosity class II which are all classified as helium stars and have both optical and mid-uv measurements, though these stars marginally deviate from the general definition of helium stars as 'B0–B9 III–V'.

The ultraviolet fluxes for all these stars at 2740 A (310 A), 2365 A (330 A), 1965 A (330 A) and 1565 A (330 A) have been taken from the Catalogue compiled by Thomson *et al.* (1978). These fluxes were recorded by the Sky Survey Telescope (S2/68) aboard the ESRO Satellite TD-1. The observed fluxes (F_λ) were converted to the visual magnitude scale through the absolute calibration formula given by Hayes and Latham (1975)

$$m(\lambda) = -2.5\ 1\log F_\lambda - 21.175.$$

Table 2 gives the details of the data and all columns are self explanatory.

In the following analysis, we have used the reddening relations mainly applicable for normal stars in order to estimate various intrinsic colours for helium stars as Groote and Hunger (1982) have demonstrated that helium enrichment in the temperature range and abundance range seen in these stars has little effect on their fluxes, at least in the optics region. This is justifiable because of the fact that the observed colours, luminosities, estimated radii of these stars are consistent with normal B-type Population I objects. (Greenstein and Wallerstein, 1958; Osmer and Peterson, 1974 and Walborn, 1983). In addition, the presence of several of these stars in very young clusters and associations and their coexistence with other normal B-type stars within a cluster or association and their location near the galactic plane definitely suggest that they are very young objects and of Population I inspite of their abnormal helium abundances (Odell, 1981; MacConnell *et al.,* 1970; Nissen, 1974, 1976). In addition, satellite observations show that the flux distributions in the ultraviolet of a majority of He-weak objects is normal for their *U B V* colours although a few He-weak stars are fainter in the ultraviolet than normal stars with the same *U B V* colours. Bernacca and Molar (1972) and Ciatti *et al.* (1978) had interpreted the flux deficiency in some of these stars to a possible line blocking by many spectral features.

The estimation of colour excess, *E(B – V),* for interstellar reddening correction to the observed magnitude has been made by using the following procedure:

i. In the case of stars for which reliable spectral types are available, the estimation of colour excesses has been made from the intrinsic colour-spectral type relation given

Table 1. Basic data.

HD No.	V	$B-V$	$U-B$	β	m_1	c_1	Sp. type	Remarks
5737	4.31	−0.16	−0.56	2.660	0.098	0.498	B7IIIp	Weak, HR 280
19400	5.53	−0.14	−0.51	2.709	0.111	0.512	B3V + A0IV	HR 939
21699	5.47	−0.10	−0.57	—	0.127	—	B8IIIp MN	HR 1063
22470	5.23	−0.13	−0.49	2.731	0.135	0.475	B9p	Weak, Var., HR 1100
22920	5.53	−0·15	−0.57	2.687	0.104	—	B9IIIp	HR 1121
23408	3.87	−0.07	−0.40	2.691	0.089	0.622	B8III	HR 1149
28843	5.81	−0.14	−0.54	2.718	0.103	0.409	B9III	Weak, HR 1441
30353	7.76	+0.46	−0.17	2.546	0.126	0.400	A1pe/A5p	Extreme
35298	7.89	−0.14	−0.62	2.709	0.091	0.369	B9V	
36046	8.07	−0.10	−0.55	2.721	0.088	0.414	B9	
36526	8.31	−0.11	−0.59	2.703	0.110	0.345	B8	
36540	8.11	+0.05	−0.49	—	0.066	0.393	B9	
36549	8.56	−0.08	−0.40	2.766	0.119	0.648	B9	
36629	7.68	−0.01	−0.65	—	—	—	B2V	
36668	8.06	−0.11	−0.45	2.730	0.124	0.594	B9	
36916	6.73	−0.05	−0.58	2.705	—	0.486	B9	
37017	6.56	−0.13	−0.77	—	—	—	B1.5V	Strong
37043	2.80	−0.24	−1.08	—	0.051	−0.105	O9III	HR 1899
37129	7.14	−0.15	−0.73	—	—	—	B2Vp	
37235	8.17	−0.10	−0.45	—	—	—	B9	
37321	7.09	−0.08	−0.55	—	—	—	B3V	
37776	6.98	−0.14	−0.86	2.632	0.108	0.058	B2V	Strong
44953	6.60	−0.15	−0.64	2.694	0.118	0.313	B8III	Weak, HR 2306
49333	6.08	−0.19	−0.62	—	—	—	B8	
49606	5.70	−0.13	−0.52	2.703	0.116	0.489	B7III	Weak, HR 2519
51688	6.30	−0.11	−0.47	2.705	0.110	0.519	B8III	HR 2605
57219	5.11	−0.16	−0.66	—	0.108	0.270	B2IVne	HR 2790
58260	6.73	−0.12	−0.74	2.614	0.086	0.134	B3III	Strong
60344	7.71	−0.17	−0.83	2.646	—	—	B5	Strong
61641	5.80	−0.16	−0.70	2.662	0.090	0.253	B2IV–V	Weak, HR 2954
62712	6.40	−0.16	−0.48	—	0.106	0.510	B9Vp	HR 3001
62714	7.30	−0.10	—	—	—	—	B9	

Table 1. Continued

HD No.	V	$B-V$	$U-B$	β	m_1	c_1	Sp. type	Remarks
64740	4.63	−0.23	−0.93	2.613	0.101	0.008	B1.5Vp	Strong, HR 3089
74196	5.61	−0.14	−0.50	—	0.104	0.515	B7Vn	HR 3448
79158	5.30	−0.14	−0.45	2.709	0.122	0.553	B0.5II	Weak, HR 3652
79447	3.97	−0.18	−0.67	2.661	0.100	0.299	B3III	HR 3663
82984	5.12	−0.12	−0.58	2.693	0.101	0.382	B4IV	Weak, HR 3817
84046	6.43	−0.09	−0.41	—	—	—	B8	
90264	4.99	−0.13	−0.51	2.717	0.114	0.427	B8V	Weak, HR 4089
96446	6.68	−0.15	−0.85	2.646	—	—	B2V	Strong
100340	10.19	−0.24	−0.94	—	0.088	−0.017	B9	
109026	3.87	−0.15	−0.62	2.692	0.110	0.346	B5V	Weak, HR 4773
120640	5.77	−0.16	+0.75	2.644	0.098	0.178	B2Vp	Strong, HR 5206
120709	4.32	−0.13	−0.60	—	0.096	0.251	B5IIIp	Weak, HR 5210
125823	4.42	−0.18	−0.75	2.664	0.089	0.204	B7IIIp	HR 5378
133518	6.39	−0.10	—	2.635	—	—	B3III	Strong
135038	8.50	—	—	2.692	—	—	B8	
135485	8.20	−0.07	—	2.703	0.106	0.406	B3	Strong
137509	7.00	(0.10)	—	—	0.183	0.411	B8	
142301	5.87	−0.06	−0.58	2.693	0.118	0.301	B8III	Weak, HR 5912
142884	6.79	+0.01	−0.48	2.737	0.092	0.383	B9	
142990	5.43	−0.09	−0.64	2.682	0.108	0.251	B5IV	Weak, HR 5942
143699	4.89	−0.14	−0.58	2.706	0.094	0.382	B6IV	Weak, HR 5967
144334	5.92	−0.08	−0.55	2.717	0.121	0.353	B8IIIp	Weak, HR 5988
144661	6.33	−0.06	−0.53	2.708	0.092	0.401	B7IIIp	Weak, HR 5998
144844	5.88	+0.02	−0.31	2.792	0.120	0.594	B9IVp	HR 6003
144941	10.11	+0.05	−0.70	2.748	—	—	B8	
146001	6.05	+0.04	−0.36	2.750	0.094	0.510	B7IV	Weak, HR 6054
151346	7.90	+0.41	−0.18	2.706	—	—	B8	
160641	9.84	—	—	—	—	—	O9	Extreme
162374	5.90	−0.10	−0.64	—	—	—	B8	
164769	9.90	(−0.80)	—	—	—	—	B3	Strong
165207	8.80	(−0.60)	—	—	—	—	B5	
168785	8.48	+0.06	−0.74	2.604	—	—	B	Strong

Table 1. Continued

HD No.	V	$B-V$	$U-B$	β	m_1	c_1	Sp. type	Remarks
169467	3.51	−0.17	−0.64	2.681	0.099	0.317	B3IV	HR 6897
172854	7.70	(−0.10)	—	2.644	—	—	B9	
175156	5.00	+0.17	—	2.626	0.029	0.472	B5II	HR 7119
175362	5.38	−0.14	−0.71	2.686	0.123	0.254	B8IV	HR 7129
176582	6.41	−0.17	−0.70	2.692	0.094	0.260	B5IV	HR 7185
177003	5.38	−0.18	−0.75	2.675	0.090	0.245	B2.5IV	HR 7210
178993	9.00	(+0.50)	—	—	—	—	A0	
181615	4.61	+0.10	−0.53	2.480	0.100	0.246	B2V + A2Ia	Extreme, HR 7342, υ Sgr
182568	4.97	−0.10	−0.71	2.667	0.071	0.237	B3IV	HR 7372
183339	6.60	−0.15	−0.56	2.706	0.088	—	B8IV	Weak, HR 7401
184927	7.46	−0.17	−0.82	2.659	—	—	B2	Strong
186205	8.53	+0.05	—	2.646	—	—	B2V	Strong
191980	8.10	(−0.30)	—	—	—	—	B5	
202671	5.40	−0.12	−0.49	2.683	0.098	0.552	B8III	Weak, HR 8137
207538	7.31	+0.33	−0.64	2.594	−0.042	−0.024	B0V	
208266	8.13	+0.26	−0.57	—	—	—	B5	
209339	6.66	+0.06	−0.82	2.595	−0.014	−0.022	B0IV	HR 8399
212454	6.16	−0.13	−0.55	2.694	0.098	0.416	B8	HR 8535
217833	6.50	−0.08	−0.55	2.691	0.100	0.365	B9III	Weak, HR 8770
224926	5.10	−0.12	−0.51	2.703	0.104	0.104	B7III–IV	HR 9087
+13°3224	—	—	—	—	0.069	—	—	Extreme

Table 2. Mid-ultraviolet data.

HD No.	$m(2740)$	$m(2365)$	$m(1965)$	$m(1565)$	$E(B-V)_{uv}$	$E(B-V)_{sp}$	$(2740-V)_0$	$(2365-V)_0$	$(1965-V)_0$	$(1565-V)_0$
5737	3.23	2.84	2.46	2.15	.00	.00	−1.08	−1.47	−1.85	−2.17
19400	4.53	4.15	3.76	3.46	.00	.06	−1.19	−1.71	−2.09	−2.37
21699	4.35	4.04	3.74	3.37	.01	.01	−1.15	−1.48	−1.78	−2.15
22470	4.27	4.01	3.59	3.33	.03	.00	−1.05	−1.38	−1.80	−2.05
22920	4.39	4.06	3.67	3.37	.01	.00	−1.17	−1.52	−1.91	−2.21
23408	3.25	3.03	2.58	2.14	.09	.04	−0.74	−1.06	−1.50	−1.93
28843	4.64	4.29	3.90	3.50	.02	.00	−1.23	−1.63	−2.02	−2.41
30353	8.72	—	8.94	9.85	—	.46	−1.06	—	−1.22	−0.22
35298	6.78	6.47	6.14	5.77	.02	.00	−1.17	−1.53	−1.86	−2.22
36046	7.04	6.61	6.34	6.03	.00	.00	−1.03	−1.46	−1.73	−2.04
36526	7.23	6.94	6.42	6.27	.02	.00	−1.14	−1.48	−2.00	−2.14
36540	7.30	—	—	—	—	.12	−1.18	—	—	—
36549	7.79	7.34	7.02	6.92	.00	.00	−0.77	−1.22	−1.54	−1.64
36629	6.50	6.38	5.70	4.98	.23	.23	−1.89	−2.55	−3.18	−3.87
36668	7.32	7.15	6.55	6.53	.06	.00	−0.93	−1.24	−1.83	−1.83
36916	5.67	5.35	5.00	4.77	.00	.02	−1.12	−1.49	−1.84	−2.06
37017	5.07	—	—	—	—	.12	−1.86	—	—	—
37043	0.66	−0.08	−0.56	−1.00	.00	.07	−2.36	−3.26	−3.73	−4.16
37129	5.58	5.10	4.65	4.09	.01	.09	−1.84	−2.53	−2.96	−3.51
37235	7.11	6.85	6.56	5.95	.08	.00	−1.31	−1.76	−2.03	−2.63
37321	5.95	5.59	5.13	4.58	.06	.12	−1.51	−2.15	−2.59	−3.12
37776	5.32	4.82	4.42	3.92	.00	.10	−1.97	−2.42	−3.08	−3.57
44953	5.44	5.16	4.78	4.41	.04	.00	−1.28	−1.66	−2.03	−2.39
49333	4.68	4.26	3.89	3.50	.00	.00	−1.40	−1.82	−2.19	−2.58
49606	4.89	4.51	4.16	3.78	.00	.00	−0.81	−1.19	−1.54	−1.92
51688	5.47	5.10	4.71	4.37	.00	.00	−0.83	−1.20	−1.59	−1.93
58260	5.23	4.77	4.41	3.88	.00	.08	−1.75	−2.40	−2.74	−3.26
60344	5.97	5.39	5.05	4.48	.00	.00	−1.74	−2.32	−2.66	−3.23
61641	4.27	3.71	3.27	2.68	.00	.08	−1.78	−2.53	−2.95	−3.53
62712	5.33	4.91	4.45	4.04	.01	.00	−1.10	−1.54	−2.00	−2.41
62714	6.38	5.98	5.61	5.17	.00	.00	−0.92	−1.32	−1.69	−2.13
64740	2.65	2.01	1.55	0.92	.00	.02	−2.04	−2.73	−3.19	−3.81

Table 2. Continued

HD No.	$m(2740)$	$m(2365)$	$m(1965)$	$m(1565)$	$E(B-V)_{ur}$	$E(B-V)_{sp}$	$(2740-V)_0$	$(2365-V)_0$	$(1965-V)_0$	$(1565-V)_0$
74196	4.69	—	—	—	—	.00	−0.92	—	—	—
79158	4.42	4.16	3.73	3.52	.00	.00	−0.88	−1.14	−1.57	−1.78
79447	2.50	1.98	1.57	1.12	.00	.02	−1.53	−2.10	−2.51	−2.95
82984	3.90	3.46	3.08	2.58	.00	.06	−1.41	−1.99	−2.35	−2.84
84046	5.67	5.51	4.98	4.84	.07	.02	−0.82	−1.03	−1.56	−1.69
90264	3.87	3.47	3.06	2.70	.00	.00	−1.12	−1.52	−1.93	−2.29
96446	5.09	4.58	4.20	3.59	.00	.05	−1.74	−2.37	−2.74	−3.34
100340	7.92	7.52	7.17	6.37	.07	.00	−2.49	−3.05	−3.39	−4.18
109026	2.55	2.09	1.67	1.18	.00	.02	−1.38	−1.89	−2.31	−2.79
120640	4.17	3.72	3.27	2.66	.03	.08	−1.85	−2.49	−2.92	−3.52
125823	2.75	2.21	1.79	1.27	.00	.00	−1.67	−2.21	−2.63	−3.15
133518	4.96	4.75	4.27	3.54	.16	.10	−1.74	−2.18	−2.65	−3.36
135038	8.03	7.71	6.85	7.03	.01	.11	−0.81	−1.39	−2.23	−2.03
135485	7.08	6.79	6.39	5.98	.05	.05	−1.27	−1.68	−2.07	−2.47
137509	6.23	6.15	5.60	5.55	.09	.01	−0.80	−0.90	−1.45	−1.50
142301	4.84	4.64	4.26	3.78	.09	.05	−1.18	−1.50	−1.87	−2.34
142884	6.03	5.98	5.57	5.12	.15	.08	−1.01	−1.25	−1.64	−2.08
142990	4.18	3.92	3.51	2.93	.09	.08	−1.50	−1.95	−2.34	−2.91
143699	3.65	3.22	2.83	2.37	.00	.01	−1.27	−1.72	−2.11	−2.57
144334	4.83	4.57	4.18	3.76	.06	.03	−1.18	−1.51	−1.90	−2.31
144661	5.43	5.28	4.84	4.34	.13	.07	−1.12	−1.43	−1.86	−2.34
144844	5.34	5.22	4.85	4.41	.11	.09	−0.82	−1.15	−1.50	−1.93
144941	—	10.63	8.28	7.71	—	.16	—	−0.35	−2.67	−3.21
146001	5.51	5.40	4.87	4.26	.18	.17	−1.07	−1.58	−2.07	−2.65
151346	8.57	9.11	8.12	8.22	.39	.52	−0.94	−1.53	−2.48	−2.31
160641	8.85	8.38	8.44	7.99	.00	—	−0.99	−1.46	−1.40	−1.85
165207	6.76	6.36	5.88	5.28	.06	.00	−2.23	−2.77	−3.24	−3.82
168785	7.34	7.20	6.77	5.95	.19	—	−1.73	−2.35	−2.74	−3.53
169467	2.03	1.46	1.02	0.49	.00	.03	−1.57	−2.21	−2.65	−3.17
172854	7.75	7.87	7.75	7.21	.18	.00	−0.51	−0.81	−0.90	−1.40
175156	4.91	5.12	5.08	4.61	.19	.33	−1.11	−1.67	−1.65	−2.06
175362	4.07	3.71	3.34	2.96	.01	.00	−1.34	−1.72	−2.09	−2.47

Table 2. Continued

HD No.	$m(2740)$	$m(2365)$	$m(1965)$	$m(1565)$	$E(B-V)_{uv}$	$E(B-V)_{sp}$	$(2740-V)_0$	$(2365-V)_0$	$(1965-V)_0$	$(1565-V)_0$
176582	5.00	4.57	4.18	3.75	.00	.00	−1.41	−1.84	−2.23	−2.66
177003	3.80	3.26	2.82	2.27	.00	.04	−1.70	−2.34	−2.77	−3.31
178993	9.90	9.67	9.45	9.79	.00	—	+0.90	+0.67	+0.45	+0.79
181615	4.67	5.19	5.27	5.14	.22	.34	−0.99	−1.24	−1.11	−1.20
182568	3.66	3.20	2.75	2.14	.03	.10	−1.62	−2.31	−2.75	−3.34
183339	5.46	5.00	4.59	4.17	.00	.00	−1.14	−1.60	−2.01	−2.43
184927	5.77	5.32	4.87	4.25	.03	.07	−1.91	−2.52	−2.96	−3.57
186205	7.71	7.77	7.15	6.52	.27	.29	−1.72	−2.33	−2.89	−3.49
191980	6.63	6.23	5.91	5.61	.00	.00	−1.47	−1.87	−2.19	−2.49
202671	4.47	4.10	3.75	3.36	.00	.00	−0.93	−1.30	−1.65	−2.04
207538	6.83	7.38	6.79	6.38	.42	.63	−2.43	−3.24	−3.76	−4.13
208266	7.60	7.48	6.99	6.76	.10	.43	−1.86	−2.95	−3.38	−3.55
209339	5.43	5.44	4.98	4.30	.23	.35	−2.31	−3.09	−3.50	−4.14
212454	5.09	4.74	4.37	3.99	.01	.00	−1.10	−1.47	−1.84	−2.22
217833	5.57	5.35	4.95	4.54	.07	.00	−1.15	−1.57	−1.95	−2.35
224926	4.09	3.70	3.29	2.87	.01	.01	−1.04	−1.45	−1.86	−2.28
+13°3224	8.64	8.20	7.95	7.67	.00	—	—	—	—	—

by FitzGerald (1970). The colour excess in $(U - B)$ has been estimated through the relation $E(U - B) = 0.70\ E(B - V)$

ii. The intermediate band indices, $(b — y)$, m_1 and c_1 have been corrected for the effects of reddening using the above estimated $E(B - V)$ and also through the standard relations given by Crawford (1973, 1975):

$$E(b - y) = 0.70\ E(B–V),$$
$$E(m_1) = -0.30E(b - y) \text{ and}$$
$$E(c_1) = 0.20E(b - y).$$

The apparent magnitude, V is corrected using the ratio of total to selective absorption value $R = 3.0$.

iii. The mid-ultraviolet magnitudes of each star have been corrected for reddening effects from the relation

$$A(\lambda) = \frac{A(\lambda)}{E(B - V)} E(B - V)$$

where the values of $A(\lambda)/E(B — V)$ have been given in Table 2 of Thomson's *et al.* Catalogue for each passband as a function of spectral type and reddening.

As a further check, $E(B— V)$ values have also been computed using the relation given in the same Catalogue for B-type stars: $E(B –V) = 0.40\ (m(1565) - m(2740)) - 0.60(m(1565) - m(2365))$. This relation is based on the UV colours alone without recourse to the spectral type and adequately represents the reddening.

As an independent check to our earlier estimate of colour excess, $E(B - V)$, we have computed the colour excesses for a sample of helium stars using the mean interstellar extinction (A_v) maps given by Neckel and Klare (1980) for a given 1, b and distance along the plane of the galaxy. In estimating these mean values, we have adopted an absolute magnitude, $M_v \sim -2.0$ based helium stars located in the OB associations (Drilling 1981) and also a value of $R = 3.0$. The mean colour excesses thus derived are: HD 60344 (0.06), HD 96446 (0.07 to 0.08), HD 133518 (0.14 to 0.15), HD 168785 (0.16) and HD 184927 (0.06 to 0.07). Inspite of different procedures used in the estimation of $E(B — V)$, in the majority of cases, the values obtained agree quite well. In the event of a large discrepancy between these values, more weight was given to the value obtained through spectral type – intrinsic colour relation. In a few cases where the derived $E(B — V)$ has a negative value, it is treated as zero. In Table 2, columns 6 and 7 show the colour excesses derived from the above procedures, and the rest of the columns give the reddening free parameters. Table 4 shows the data for normal B-type stars used for comparison in this analysis. All columns are self-explanatory.

3. Analysis

Figure 1 shows the position of helium stars on (β, c_0) plane, where c_0 is the c_1-index corrected for interstellar reddening. As we already know from Crawford's work (1975), β-index is an indicator of gravity and c_0 is a temperature parameter for B-type stars.

Table 3.

HD No.	Δ_1	Δ_2	Δ_3	Δ_4	log T_{eff}
5737	+ 0.01	+ 0.06	+ 0.77	0.70	4.21
19400	− 0.01	+ 0.09	0.77	0.69	4.24
21699	+ 0.03	− 0.07	0.63	0.67	4.20
22470	− 0.08	+ 0.15	0.74	0.67	4.20
22920	− 0.05	+ 0.09	0.73	0.69	4.22
23408	− 0.16	+ 0.02	0.74	0.88	4.15
28843	00.00	− 0.00	0.78	0.78	4.23
35298	+ 0.03	− 0.05	0.67	0.69	4.21
36046	+ 0.16	− 0.04	0.70	0.58	4.19
36526	− 0.19	+ 0.38	0.85	0.66	4.23
36549	+ 0.13	+ 0.22	0.77	0.42	4.16
36629	− 0.17	− 0.04	1.13	1.34	4.41
36668	− 0.29	+ 0.58	0.89	0.60	4.20
36916	+ 0.02	+ 0.13	0.72	0.57	4.21
37043	+ 0.43	+ 0.04	1.37	0.90	4.49
37129	+ 0.05	− 0.11	0.95	1.01	4.38
37235	+ 0.16	− 0.31	0.72	0.87	4.23
37321	− 0.05	− 0.08	0.87	1.00	4.32
37776	+ 0.15	− 0.09	0.95	0.89	4.39
44953	00.00	00.00	0.74	0.74	4.23
49333	+ 0.05	− 0.02	0.79	0.76	4.26
49606	+ 0.03	− 0.03	0.73	0.73	4.16
51688	− 0.02	+ 0.05	0.76	0.73	4.17
58260	+ 0.21	− 0.17	0.91	0.87	4.34
60344	+ 0.24	− 0.23	0.92	0.91	4.33
61641	+ 0.33	− 0.16	1.17	1.00	4.37
62712	− 0.03	+ 0.05	0.89	0.87	4.23
62714	+ 0.04	− 0.07	0.78	0.81	4.18
64740	+ 0.23	− 0.16	1.15	1.08	4.41
79158	− 0.17	+ 0.22	0.69	0.64	4.16
79447	+ 0.16	− 0.03	0.98	0.85	4.31
82924	+ 0.22	− 0.13	0.94	0.85	4.28
84046	− 0.35	+ 0.39	0.71	0.67	4.16
90264	− 0.01	− 0.05	0.81	0.77	4.22
96446	+ 0.26	− 0.23	1.00	0.97	4.34
100340	+ 0.22	− 0.45	0.90	1.13	4.44
109026	+ 0.06	− 0.07	0.90	0.91	4.28
120640	+ 0.21	− 0.17	1.07	1.03	4.37
125823	+ 0.12	− 0.10	0.96	0.94	4.33
133518	− 0.02	− 0.24	0.92	1.18	4.33
135038	− 0.30	+ 0.05	1.40	0.65	4.26
135485	+ 0.01	− 0.02	0.79	0.80	4.24
137509	+ 0.26	+ 0.51	0.82	0.57	4.15
142301	− 0.07	− 0.10	0.67	0.84	4.21
142884	− 0.15	− 0.05	0.63	0.83	4.17
142990	+ 0.02	− 0.17	0.82	0.97	4.28
143699	+ 0.04	− 0.07	0.82	0.85	4.25
144334	− 0.08	− 0.02	0.70	0.80	4.21
144661	− 0.14	− 0.02	0.72	0.88	4.21
144844	− 0.02	− 0.08	0.68	0.78	4.15
144941	—	+ 1.78	—	2.86	4.33
146001	+ 0.02	− 0.09	1.00	1.07	4.24
151346	− 0.36	+ 1.10	1.52	0.78	4.30

Table 3. Continued.

HD No.	Δ_1	Δ_2	Δ_3	Δ_4	log T_{eff}
160641	+0.53	−0.51	0.41	0.39	4.14
165207	+0.07	−0.11	1.01	1.05	4.42
168785	+0.21	−0.40	0.99	1.18	4.34
169467	+0.20	−0.08	1.08	0.96	4.33
172854	+0.21	−0.41	0.39	0.59	4.06
175156	+0.53	−0.55	0.49	0.51	4.18
175362	+0.92	−0.47	0.74	0.29	4.24
176582	+0.04	−0.04	0.82	0.82	4.26
177003	+0.21	−0.11	1.07	0.97	4.35
178993	+0.01	+0.56	0.45	−0.12	3.86
181615	−0.09	−0.21	−0.31	−0.01	4.09
182568	+0.25	−0.15	1.13	1.03	4.34
183339	+0.05	−0.01	0.87	0.83	4.23
184927	+0.17	−0.17	1.05	1.05	4.38
186205	−0.15	−0.02	1.01	1.18	4.37
191980	+0.08	+0.02	0.72	0.62	4.26
202671	+0.02	−0.04	0.72	0.74	4.18
207538	+0.21	+0.12	1.15	0.82	4.50
208266	+0.69	+0.25	1.51	0.57	4.44
209339	+0.53	−0.25	1.29	1.01	4.46
212454	+0.00	−0.01	0.74	0.75	4.21
217833	+0.04	−0.02	0.80	0.78	4.22
224926	00.00	−0.01	0.82	0.83	4.21
+13°3224	+0.19	−0.03	0.69	0.53	—

The observed positions of these stars on β, c_0 diagram suggest that these stars are not too different in nature when compared to the normal stars of similar spectral types and luminosity classes except the ones which are sub-classified as extreme. However it is likely that some stars are effected by variable $H\beta$ emission as seen in σ Ori E and HD 64740.

Figures 2a, b, c and d show the relation between $(m_{2740} - V)_0$, $(m_{2365} - V)_0$, $(m_{1965} - V)_0$ and $(m_{1565} - V)_0$ against c_0-index respectively for both helium stars and normal stars. The late-type helium stars lie considerably above the band drawn for normal stars indicating less flux in the *uv* bands relative to normal stars and show maximum deviation towards shorter wavelength region. These indices can thus be effectively used to distinguish the helium stars from normal stars.

Further, we have defined the following indices in order to see the nature of mid-ultraviolet fluxes of these stars:

$$\Delta_1 = m_0\,(2740 - 2365) - m_0\,(2365 - 1965)$$

$$\Delta_2 = m_0\,(2365 - 1965) - m_0\,(1965 - 1565)$$

$$\Delta_3 = m_0\,(2740 - 2365) + m_0\,(2365 - 1965)$$

and

$$\Delta_4 = m_0\,(2365 - 1965) + m_0\,(1965 - 1565)$$

The values of Δ_1, Δ_2, Δ_3 and Δ_4 are given in Table 3 for each of the stars and Table 4 gives these values for normal stars.

Table 4. Normal stars.

HR No.	Sp. type	$E(B-V)$	m_{2740}	m_{2365}	m_{1965}	m_{1565}	Δ_1	Δ_2	Δ_3	Δ_4
801	B3V	0.07	3.35	2.90	2.47	1.96	+0.19	−0.08	1.03	0.92
811	B7V	0.00	3.33	2.96	2.53	2.14	−0.06	+0.04	0.80	0.82
1144	B8V	0.04	4.98	4.70	4.25	3.84	−0.06	+0.04	0.82	0.84
1641	B3V	0.02	1.77	1.20	0.77	0.24	+0.20	−0.11	1.04	0.95
1861	B1V	0.07	3.40	2.83	2.38	1.77	0.33	−0.20	1.13	1.00
2056	B5V	0.01	3.64	3.19	2.75	2.25	0.03	−0.06	0.91	0.94
2845	B7V	0.04	2.31	1.97	1.62	1.30	0.10	+0.03	0.78	0.65
3454	B4V	0.02	2.70	2.13	1.71	3.67	0.20	+2.39	1.04	−1.55
3849	B5V	0.02	3.79	3.32	2.89	2.41	+0.09	−0.04	0.95	0.90
3856	B9V	0.00	4.05	3.72	3.31	3.04	−0.08	+0.14	0.74	0.68
3982	B7V	0.02	0.77	0.32	−0.05	−0.38	+0.13	+0.05	0.87	0.69
6165	B0V	0.05	0.73	−0.02	−0.57	−1.24	0.33	−0.13	1.41	1.21
39	B2IV	0.01	1.07	0.37	−0.04	−0.60	0.31	−0.15	1.13	0.97
153	B2IV	0.04	1.93	1.33	0.93	0.40	0.31	−0.13	−1.09	0.91
1956	B7IV	0.01	1.80	1.38	1.02	0.64	0.08	−0.02	0.80	0.74
2106	B2.5IV	0.04	2.95	2.46	2.07	1.59	0.21	−0.09	0.97	0.85
5953	B0.3IV	0.18	0.68	0.23	−0.26	−0.93	0.42	−0.20	1.32	1.10
6092	B5IV	0.02	2.68	2.20	1.79	1.33	0.12	−0.04	0.94	0.86
6588	B3IV	0.02	2.31	1.80	1.37	0.82	+0.14	−0.13	0.98	0.97
7906	B9IV	0.01	3.45	3.11	2.71	2.38	−0.04	+0.07	0.76	0.73
9076	B9IV	0.00	4.09	3.77	3.42	3.20	−0.03	+0.13	0.67	0.57
193	B5III	0.10	3.70	3.46	3.04	2.54	+0.09	−0.10	0.87	0.88
1552	B2III	0.08	2.06	1.56	1.29	0.73	+0.44	−0.30	0.94	0.80
7178	B9III	0.02	4.63	4.40	4.07	3.91	−0.05	+0.18	0.61	0.48
7446	B0.5IIIn	0.27	3.52	3.39	3.07	2.33	+0.38	−0.33	1.12	1.07
7447	B5III	0.09	3.50	3.24	2.77	2.30	+0.02	−0.01	0.92	0.91
8353	B8III	0.00	2.33	1.96	1.55	1.21	−0.04	+0.07	0.78	0.75
8781	B9.5III	0.00	2.55	2.32	1.95	1.87	−0.14	+0.29	0.60	0.45

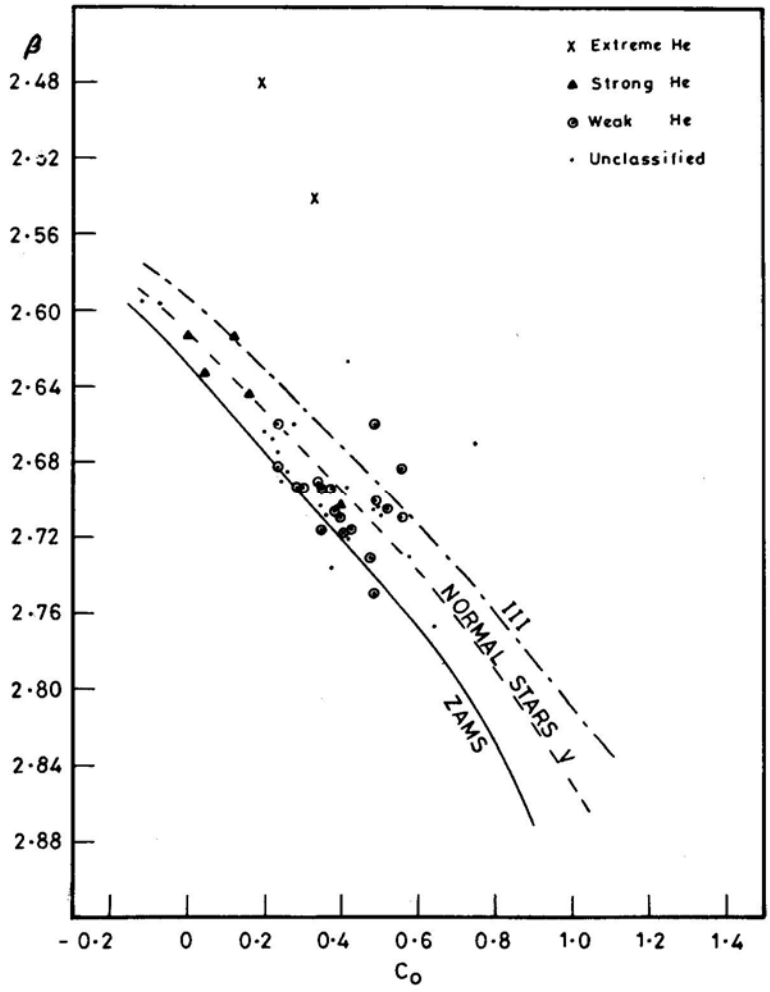

Figure 1. The relation between β-index and c_0.

Figure 3a shows the relation between Δ_1 and $(U - B)_0$ for all program and normal stars. Around 50 percent of the program stars lie above the band described for normal stars. In addition, both helium-weak and helium-strong stars are separated and the mean Δ_1 -index of these two groups differs by $0^m.2$.

Figure 3b shows the relation between Δ_3 and $(U - B)_0$. In this diagram, almost all program stars clearly lie above the band drawn for normal stars and thus enable one to distinguish the peculiar stars from the normal stars.

In the plots between Δ_1, Δ_2 and Δ_3, Δ_4 the helium stars lie within the band described by the normal stars.

3.1 *Effective Temperatures of Helium Stars*

Lesh (1977) found a linear correlation between Θ and the $(1910 - V)_0$ colour index using OAO-2 band at 1910 A and T_e values from Code *et al.* (1976) for stars earlier

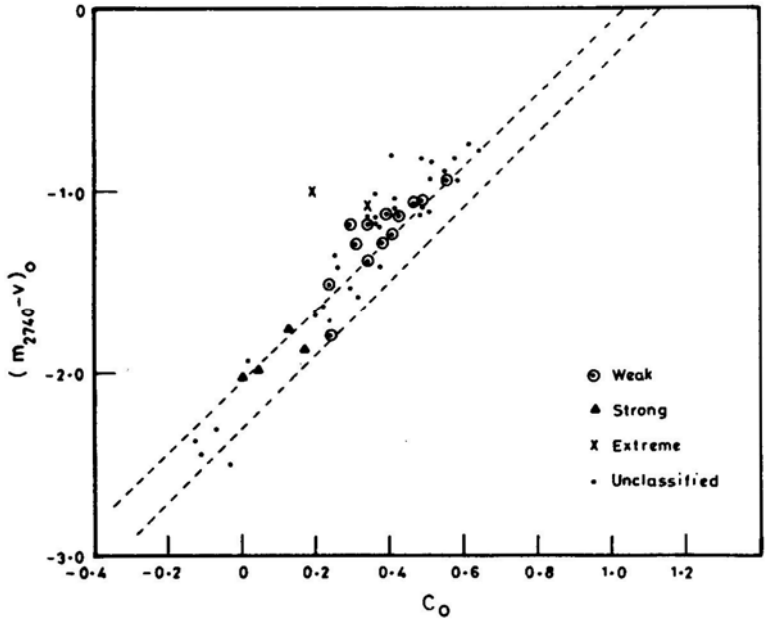

Figure 2a. The relation between $(m(2740) - V)_0$ and c_0 - index.

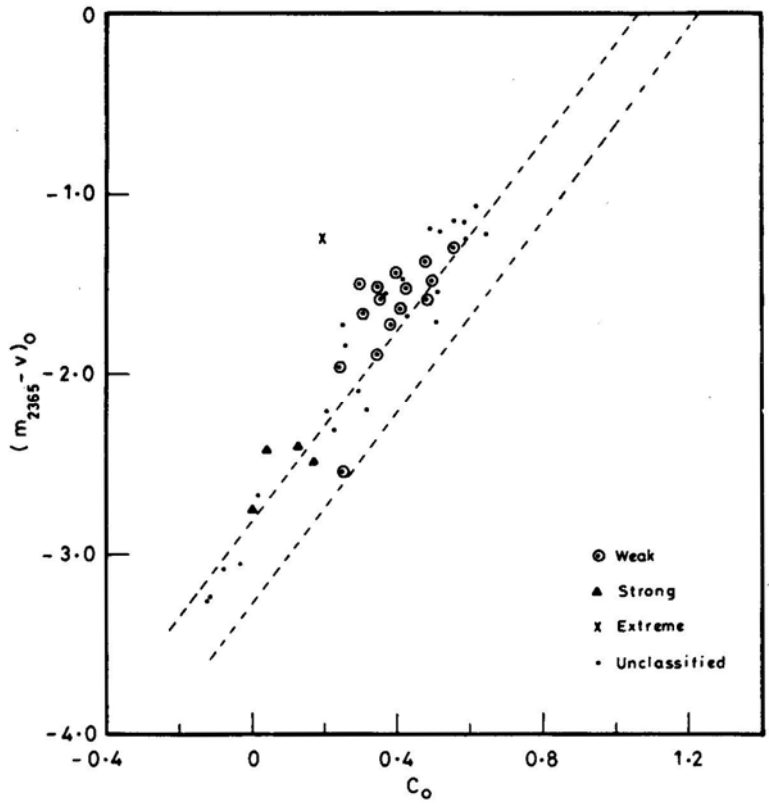

Figure 2b. The relation between $(m(2365) - V)_0$ and c_0 - index.

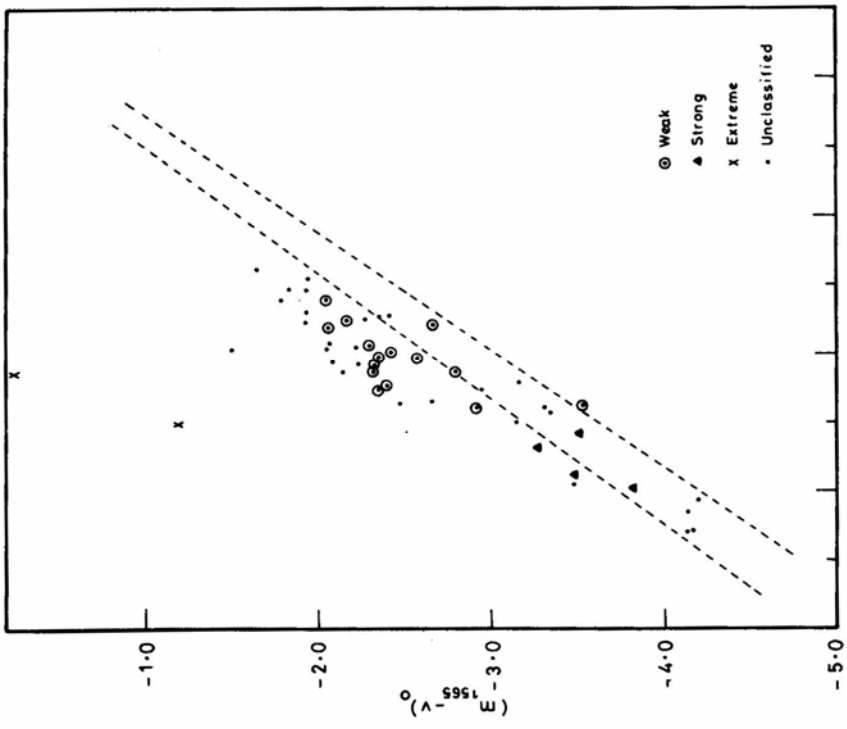

Figure 2d. The relation between $(m(1565)-V)_0$ and c_0-index.

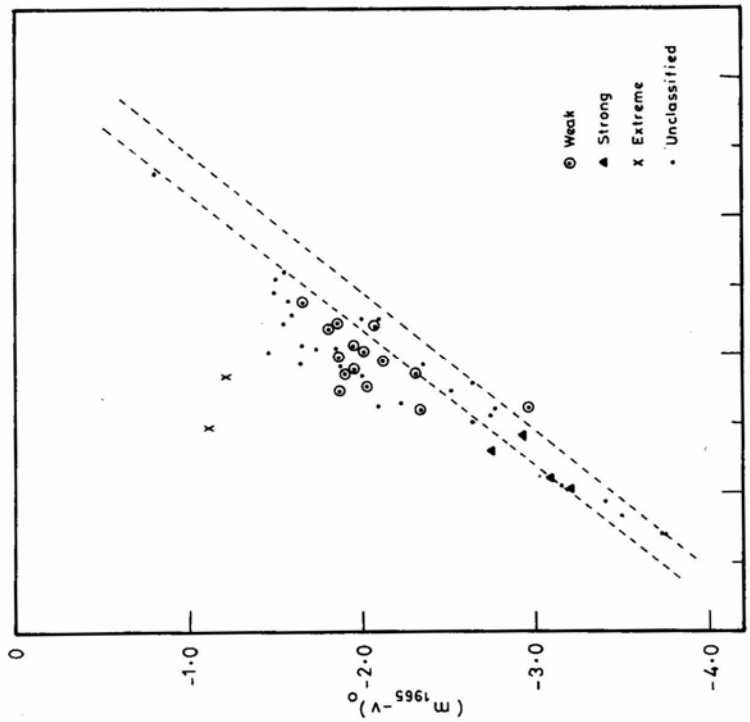

Figure 2c. The relation between $(m(1965)-V)_0$ and c_0-index.

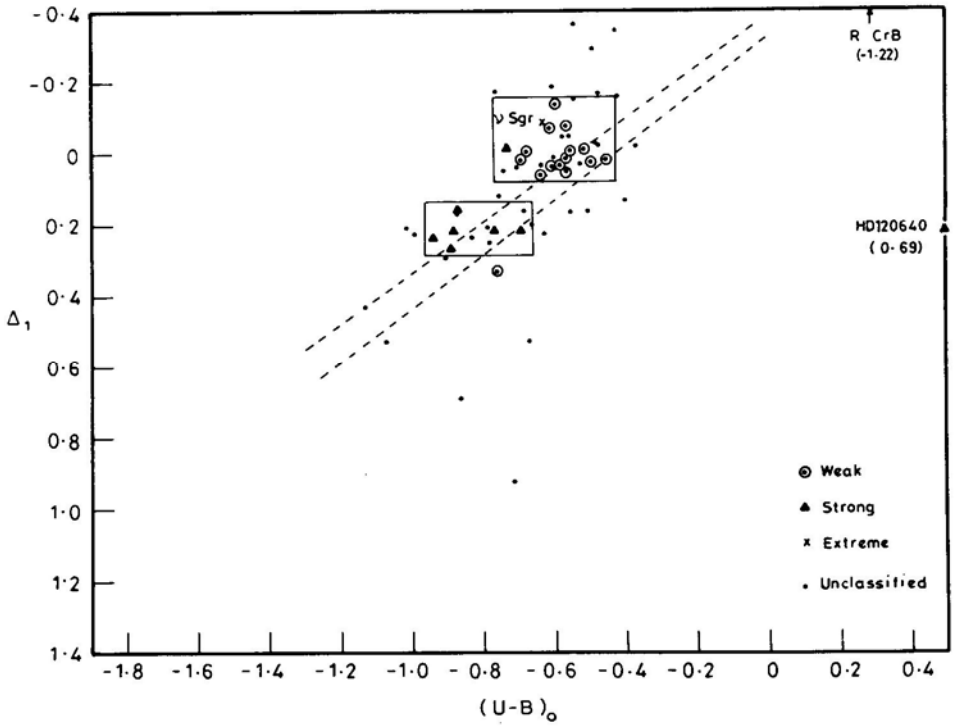

Figure 3a. The relation between Δ_1 and $(U-B)_0$.

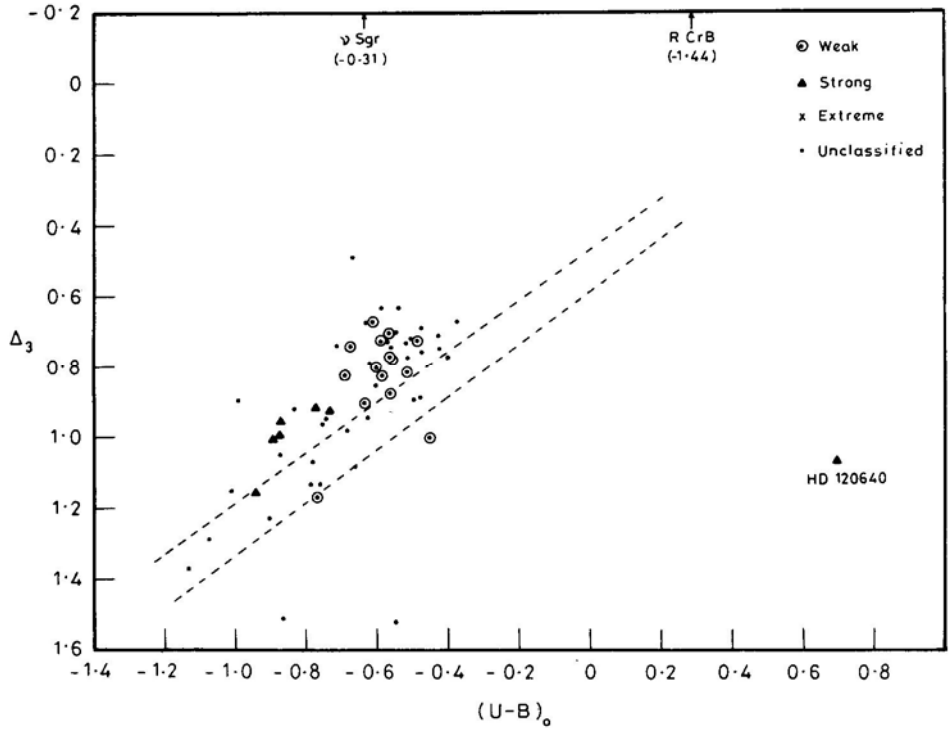

Figure 3b. The relation between Δ_3 and $(U-B)_0$.

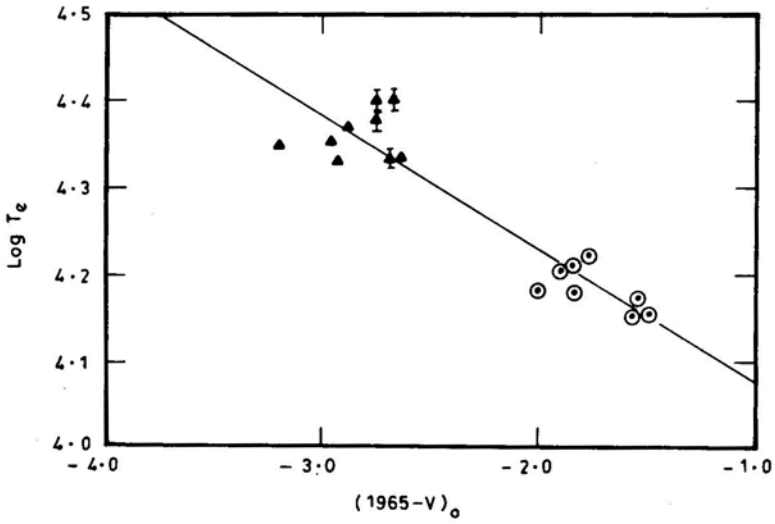

Figure 4. The relation between log T_e and (1965 — V)$_0$ index for Helium stars. The solid line represents the linear least-square relation.

than A2. Malagnini *et al.* (1984) had derived a quantity, R = log F(1965)/F(5445), proportional to a (U V– V) colour index, and found that to correlate with Θ_e for B5 to F non-supergiant stars. Since in the present analysis, one of the photometric passbands (1965 A) closely matches with that of OAO-2 passband (1910 A) and since the band 1965 A does not include any major spectral features which differ between normal and the peculiar stars, we tried to investigate whether the index (1965 – V)$_0$ refers to the effective temperature for all the B-stars, both peculiar or otherwise.

Figure 4 shows the relation between log $T_{\rm eff}$ and (1965 – V)$_0$ for helium stars, both strong-line and weak-line, irrespective of luminosity classification. The effective temperatures used are the estimated ones from model-atmosphere analysis. Table 5 gives the list of helium objects used for this calibration. A linear least-square relation,

$$\log T_{\rm eff} = (-0.1508 \pm 0.0165)(1965 - V)_0 + 3.9278 \pm 0.0376$$

is obtained for B-type helium stars. From this relation, we had derived the effective temperatures of other helium stars from their observed (1965 — V)$_0$ indices and are given in Table 3. Figure 5 shows the difference in the estimation of effective temperature, in the sense, $T_{\rm eff}$ (1965 – V)$_0$ – $T_{\rm eff}$ (spectral type) against the spectral type for all those stars for which spectral type and luminosity class are given. It is evident that the effective temperatures derived from (1965 – V)$_0$ index are somewhat higher than those of MK spectral type for a majority of helium stars. Besides, the difference increases as we progress towards the later spectral types reaching a value of around 4000–6000 K for B8 and B9 types of helium weak objects. For strong-line stars, an average difference of 1000 K–1500 K has been estimated. There are a few stars, HD 183339 (B8IV+ 9100 K) a helium weak object, HD 125823 (B7IIIp, + 8400K) an unclassified object which differ considerably from the mean differences mentioned above; HD 79158, a weak-line object, (B0.5II, – 10,400 K). Thus the $T_{\rm eff}$ estimated from spectral type alone can at best be only a lower limit.

From figure 5, it is also seen that a large dispersion exists in $T_{\rm eff}$ within any given spectral subclass and the dispersion seems to be much larger than the uncertainties

Table 5. Helium stars used for effective temperature calibration.

HD No.	Model atmosphere*	$(1965 - V)_0$ index**	Spectral type	Spectral class	Nature
5737	15300 K	16070 K	11930 K	B8III	Weak
21699	16600	15700	10780	B9III	Weak
23408	14000	14220	12750	B7III	Weak
49606	14800	14320	11930	B8III	Weak
60344	25000 ± 1000	21380	22820	B2V	Strong
64740	22400	25700	25720	B1.5V	Strong
79158	14000	14590	25000	B0.5II	Weak
96446	25250 ± 350	21980	22820	B2V	Strong
120640	21300	23390	22820	B2V	Strong
133518	21400	21280	18530	B3V	Strong
144334	16000	16370	11930	B8III	Weak
144941	21500 ± 500	21430	—	B8	Strong
168785	24000 ± 1000	21980	—	B3	Strong
183339	15300	17020	11900	B8IV	Weak
184927	22500	23710	22820	B2V	Strong
186205	23500	23170	22820	B2V	Strong
217833	16300	16670	10780	B9III	Weak

*From B stars with and without emission eds. A. Underhill and V. Doazan, NASA SP-456, p. 159 –163.
**From this analysis

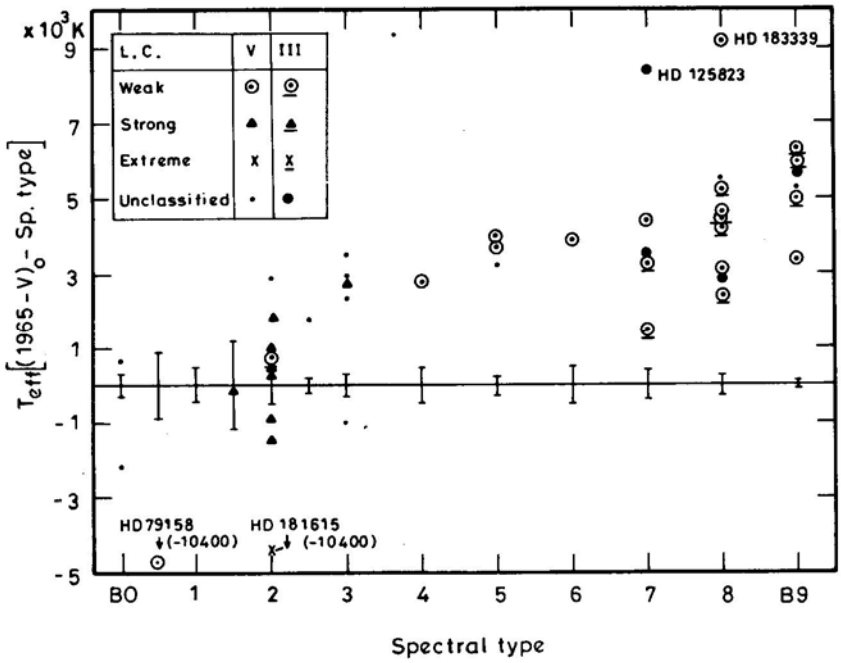

Figure 5. The relation between $\Delta T_e = T_e(1965- V)_0 - T_e$ (sp. type) and spectral type. The vertical bar corresponds to the mean difference in the effective temperatures between luminosity classes III and V.

associated with the individual $T_{\rm eff}$. Malagnini *et al.* (1984) have also noticed a similar kind of dispersion for B5 and later types while estimating the effective temperatures from *UV* index. For B5 stars, they had obtained extremes in $T_{\rm eff}$, around 2500 K apart and interpreted the observed dispersion in terms of the different behaviour of spectral energy distribution in the *U V* and visual regions and emphasized that the noticeable dispersion is not a result of the errors in $E(B - V)$. In the present analysis, we had estimated the colour excess, $E(B - V)$, for each star using two or three different techniques and in a majority of cases, the dispersion noticed in $E(B — V)$ is of marginal nature and thus, the differences in effective temperatures reflect the behaviour of energy distribution between *U V* and visual regions.

Finally, it is interesting to note the position of HD 61641 (B2IV–V), a weak-line star, in the figures 2 to 4. Kroll (1987) had inferred from the IRAS data that HD 61641 has a circumstellar dust shell on the basis of excess flux in the IRAS passbands.

4. Conclusions

The following conclusions could be drawn from the above investigation:

1. Regarding the attempts to segregate helium stars from normal B-type objects it is possible to separate these objects using with some care Δ_3 and $(U - B)_0$ plane and also $(2365 - V)_0$, $(1965 - V)_0$ with c_0.
2. A linear relation is obtained between $(1965 - V)_0$ index and the effective temperature derived from model atmosphere analysis.
3. The effective temperatures estimated from $(1965 - V)_0$ index are higher, especially for weak-line stars in the spectral range B6–B9, compared to the effective temperatures derived from spectral types.

Acknowledgements

The authors wish to thank Professor K. D. Abhyankar for the constant encouragement during the course of this investigation. We are very thankful to the referees for their critical comments in improving the quality of this analysis. Finally, we thank Mr. H. R. L. Narasimhan for drawing the figures.

References

Bernacca, P. L, Molnar, M. R. 1972, *Astrophys. J.,* **178,** 189.

Blanco, V. M., Demers, S., Douglas, G. G., FitzGerald, M. P. 1968, *Publ. U. S. nav. Obs.* 2nd Ser. no. 21.

Bohlender, D. A., Brown, D. N., Landstreet, J. D., Thomson, I. B. 1987, *Astrophys. J.,* **323,** 325.

Borra, E. F., Landstreet, J. D. 1979, *Astrophys. J.,* **228,** 809.

Ciatti, F., Bernacca, P. L., D'Innocenzo, A. 1978, *Astr. Astrophys.,* **69,** 171.

Code, A. D., Davis, J., Bless, R. C., Hanbury Brown, R. 1976, *Astrophys. J*., **203,** 417.

Crawford, D. L. 1973, in *Problems of Calibration of Absolute Magnitudes and Temperatures of Stars*, Eds. B. Hauck & B. E. Westerland, Dordrecht: Reidel, p. 93.

Crawford, D. L. 1975, in *Multicolor Photometry and the Theoretical H-R diagram,* Eds. A. G. Davis Philip & D. S. Hayes, Dudley Observatory Report no. 9, p. 17.

Drilling, J. S. 1981, *Astrophys. J*., **250,** 701.
FitzGerald, M. P. 1970, *Astr. Astrophys.,* **4,** 234.
Greenstein, J. L., Wallerstein, G. 1958, *Astrophys. J.,* **127,** 237.
Groote, D., Hunger, K.1982, *Astr. Astrophys.,* **116,** 64.
Hayes, D. S., Latham, D. W. 1975, *Astrophys. J.,* **197,** 593.
Hunger, K. 1986, in *Hydrogen Deficient Stars and Related Objects,* Eds. K. Hunger, D. Schonberner & N. K. Rao, Dordrecht: Reidel, p. 261.
Kroll, R. 1987, *Astr. Astrophys.,* **181,** 315.
Landstreet, J. D., Borra, E. F. 1978, *Astrophys. J.,* **224,** L5.
Lesh, J. R. 1977, in *B stars with and without emission lines,* Eds. A. B. Underbill & V.Doazan.,1983 NASA SP-456, p. 60.
MacConnell, D. J., Fyre, R. L, Bidelman, W. P. 1970, *Publ. astr. Soc. Pacific,* **82,** 730.
Malagnini, M. L., Morossi, C., Faraggiana, R.1984, in *MK Process and Stellar Classification,* Ed. R. F. Garrison, Toronto, p. 321.
Mermilliod, M., Hauck, B. 1979, *uvby and Hβ Photometric Catalogue.,* Geneva Obs.
Michaud, G., Dupuis, J., Fontaine, G., Montmerle, T. 1987, *Astrophys. J.,* **322,** 302.
Neckel, Th., Klare, G.1980, *Astr. Astrophys. Suppl,* **42,** 251.
Nissen, P. E. 1974, *Astr. Astrophys.,* **36,** 57.
Nissen, P. E. 1976, *Astr. Astrophys.,* **50,** 343.
Odell, A. P. 1981, in *Les Etoiles de Composition Chimique Anomale du Debut de la Sequence Principale.* Liege, Belgium: Universite de Liege, p. 439.
Osmer, P. S., Peterson, D. M. 1974, *Astrophys. J.,* **187,** 117.
Thomson, G. L, Nandy, K., Jamar, C, Monfils, A., Houziaux, L., Carnochan, D. J., Wilson, R., 1978, *Catalogue of Ultraviolet Fluxes,* UK: The Science Research Council.
Underhill, A. B., Divan, L., Prevot-Burnichon, M. L., Doazan, V. 1979, *Mon. Not. R. astr. Soc.,* **189,** 601.
Vauclair, S. 1975, *Astr. Astrophys.,* **45,** 233.
Walborn, N. R.1983, *Astrophys. J.,* **268,** 195.

J. Astrophys. Astr. (1992) **13,** 195–207

A High Speed Photometer in the Optical Region for Lunar Occultation Studies

T. Chandrasekhar, N. M. Ashok & Sam Ragland *Physical Research Laboratory Ahmedabad 380 009*

Received 1991 November 18; accepted 1992 April 11

Abstract. High speed photometry during the lunar occultation of a stellar system provides an effective means of achieving high angular resolution in one dimension at the sub arc second level which is well suited for resolving close binary projected separations in the range of 10–100 milliarc seconds. An optical fast photometer designed for such a purpose is described and some results from the initial observations taken with the system including the resolution of a projected separation of 55 milli arcsecond in one binary system are detailed.

Key words: lunar occultation—fast photometry—photomultiplier—binaries—angular resolution.

1. Introduction

High angular resolution is one of the most challenging goals for the next generation of large ground based telescopes. Over the last few years interferometric methods for high angular resolution have reached new heights of sophistication (Alloin, D. M. and Mariotti, J. M. (Eds.), 1989). While long base line optical interferometry achieves milliarcsecond angular resolutions the major impact of speckle interferometry has been in resolving close binaries in many stellar systems (McAlister, 1985). A favourable alternative to these sophisticated techniques for achieving high angular resolution in the optical and near infrared domains is offered by the relatively simpler technique of lunar occultation. The technique consists in recording the straight edge diffraction pattern of the star light produced by the sharp edge of the moon. As the moon moves to occult the source the diffraction pattern sweeps rapidly (~ 1 km/s) across the earth's surface and can be recorded by a fast photometer. The event is over, typically in about a hundred milliseconds—hence the need for a fast photometer. The limitations of the technique are that lunar occultations are fixed-time events occurring in the zodiacal belt. It is also a one-dimensional technique as high angular resolution is obtained only along the direction of occultation. The advantage is that milliarcsecond resolutions are achievable.

Apart from the more challenging task of determining stellar angular diameters for bright stars, lunar occultation high speed observations in the optical region can also readily resolve binary and multiple systems at the level of tens of milliarcsec. The first double star discovery from a photoelectric occultation trace was made as early as 1950 (O'Keefe, 1950) when the star 22B Aur was found to be double with a projected separation

of 53 milliarcsec and 0.5 mag brightness difference between components. Subsequently a triple star (BD + 27°943) was discovered by this technique which was not known to be a double (Beavers & Eitter, 1971). Single occultation measurement of a binary system provides only the vector separation between the components of the binary system and therefore multiple occultation measurements are required to get the plane of the sky separation. A discussion of discovery and measurement of occultation doubles is given by Nather and Evans (1971).

A program for observing lunar occultations in the visible and near infrared (1-5μ) region has been initiated at the 1.2 m telescope at Gurushikhar, Mt. Abu. In this paper a photomultiplier based fast photometer system which has been developed for high speed photometry for lunar occultation in the visible region is described. Some initial results pertaining to the binary nature of the occulted sources obtained with the instrument are also presented.

2. Instrumentation

2.1 *Optics*

Figure 1 shows the schematic diagram of the optical system of fast photometer designed and fabricated at PRL. The f/13 Cassegrain beam is brought to a focus at the aperture (A) where the scale size (for the 1.2 m Gurushikhar telescope) is 13 arcsec/mm. The aperture wheel has diaphragms of various sizes (Table 1) so that different fields of view on the sky can be selected as required. The filter wheel (F) has UBVRI Schott glass filters along with a clear glass filter through which initial adjustments of centring and focussing the object on the aperture can be made. Object acquisition is done through the flip mirror (M) and field eyepiece (E) arrangement. The post focal plane

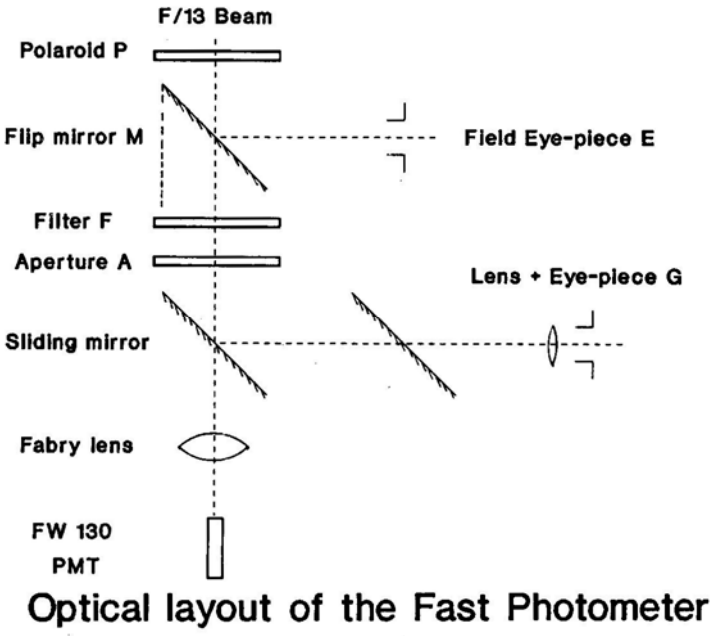

Figure 1. Schematic diagram (not to scale) of the fast photometer optics.

beam can be directed into a small lens-eyepiece assembly (G) to check on the centring of the object in the aperture whenever required. A fabry lens (focal length = 30 mm) images the telescope aperture on the sensitive surface of the photomultiplier. The optical parameters of the system are summarized in Table 1. A special requirement of the fast photometer used for lunar occultations is its ability to handle large light levels due to the scattered light from the moon. In occultation measurements what is of interest is not the absolute signal level but the changes in the signal level corresponding to fringe modulation especially during the last 50–100 millisec before the event (disappearance event) and corresponding time after the event in case of reappearance events. We have adopted a two-fold approach to tackle this problem. On the optical side a polariser – analyser assembly (P) is introduced at the entrance to the photometer to adjust the light level to be within the saturation limits of the detector electronics. The polariser approach of light attenuation is preferred over the step neutral density filter method as it offers a continuous smooth control of the light level during the crucial few minutes before an occultation. Electronic offset controls are used to further fine tune the signal level.

Use of narrow band filters like the Strömgren y filter along with smaller entrance apertures can also significantly reduce the sky background and improve S/N ratio. It is proposed to incorporate these changes in future.

2.2 *Detector*

The detector used for optical occultation measurements is an ITT FW130 (S20) photomultiplier tube. The details of the detector are given in Table 1.

In general, in the visible region, noise of the sky background from scattered moonlight dominates over the detector noise (at room temperature) even for occultation events occurring on the darklimb. Cooling the detector is therefore not necessary and the tube is operated at room temperature. Earlier a solid state stellar photometer employing a silicon PIN photodiode was used (SSP, Optec Inc.). Its time response was relatively poor for occultation measurements (~ 50ms), but it was nevertheless successful in recording the first diffraction fringe of the bright star α Leo during the occultation of 19 March 1989.

2.3 *Data Acquisition System* (*DAS*)

The data acquisition system has evolved over the years in our instrumentation starting from an 8 bit A/D used for the α Leo occultation of 1989. Presently two modes of data acquisition are being used.

a) An SR400 based system which has a large dynamic range but with a dead time of 2 millisec.
b) A frequency to voltage converter, offset controlled output system.

Mode a: The SR400 is a gated photon counter (Stanford Research Systems) and can be interfaced with a computer. It has two channels each of which can count up to a rate of 200 MHz. There are two independent gates which enable the counters and the gate width can be varied from 5 ns to 999.2 ms. The sampling intervals as well as the number of sampling can be predefined. Analog output of the digital input is available. In this

Table 1. Fast Photometer Specifications.

1. Detector			
Type		ITT FW130 16 stage Photomultiplier	
Effective photocathode size		2.5 mm (dia)	
Spectral response		S20	
Quantum efficiency		20% at 400 nm	
Photoelectron counting efficiency		> 80%	
Dark count		< 350 counts/sec at 23°C	
2. Apertures			
Aperture size (mm)		Field of view in arcsec. (1.2 m f/13 Cassegrain focus)	
0.50		06.5	
0.99		13.0	
1.57		20.6	
1.95		25.6	
2.90		38.0	
3. Filters			
Size		25 mm	
Thickness		7 mm	
Filter	Central wavelength nm	Bandwidth nm	Peak transmission %
U	370	30	30
B	440	90	62
V	540	80	75
R	660	200	80
I	880	230	90
4. Polaroid Attenuator			
Size		35 mm (diameter)	
Thickness		5 mm	
Max. Transmission (%) (in V Filter)		30	
Min Transmission (%) (when crossed in V Filter)		0.5	

mode of operation, the light level is controlled optically (by polaroids) without any electronic offset.

Mode b: In this mode, which has been more extensively used than Mode a, a pre-amplifier discriminator device (A-101 PAD, Amptek Inc.) is used with the photomultiplier for a pulse output. A Frequency to Voltage converter (100 KHz/10 V) converts the pulses to an analog form which is then fed to a signal conditioner. The signal conditioner has a variable gain (0–1) and a step gain of 10,100 and also an offset facility by which the voltage level corresponding to the large lunar background can be substracted. In practice the signal due to the star in the predetermined filter is taken long before the event under low background conditions. Then as the background light level builds up with the approach of the moon, the offset is continuously adjusted to keep the signal (star + sky) within saturation limits. The star is drifted in and out of the aperture periodically to ensure that it is being properly tracked and recorded. The use of F/V converter and subsequent A/D conversion has so far been necessitated by the absence of a pulse input module which could directly record the photomultiplier pulses. This improvement is to be effected shortly.

The output of either Mode a or Mode b is an analog signal which is fed to a Keithley (Micronics Inc.) 570 data Acquisition System. The System 570 is a Data acquisition and control system interfaced with an IBM like PC-AT. It can accommodate 32 channels of single ended or 16 channels of differential analog inputs and provides two channels of high speed analog outputs. The system has hardware selectable amplifier with gain steps of 1,10 and 100 and software controllable amplifier with gain steps of 1,2,5 and 10 for analog input signals. The system uses a 12 bit A/D converter for analog data acquisition and can be sampled as fast as 33 KHz. Presently data recording at 1 millisec sampling rate is for 30 sec. centred on the predicted time of the event. A change in signal in the monitoring scope signifies a successful run. The system 570 incorporates a powerful graphics program which enables any portion of the 30,000 samples acquired during a run to be displayed and studied. Presently the data acquisition routine is triggered manually. It is proposed to make it an automatic start at a predetermined time in the near future.

So far event time has been recorded only with about 1 second accuracy. Absolute time has not been recorded at the millisec level so far. The emphasis has been on accurate relative time samples at rates of ~ 1 KHz. Efforts are underway to record absolute time also with the accuracy of ~ 1 or 2 milliseconds. A few trials have been made to synchronise with NPL (National Physical Laboratory) time signal with appropriate propagation corrections. A time signal is to be derived from this synchronised quartz clock and recorded along with the data.

3. Observations

All the observations reported here were carried out at the 1.2 m telescope at Gurushikhar (72°47'E, 24°39'N). The details of the observations are given in Table 2.

Several difficulties such as sudden power failures, instrumental failures, detector saturation due to strong moon's background light and occasionally cloudy sky were encountered in occultation observations. In some cases the object was lost, at the crucial moments before the event and could not be centered due to the strong background

Table 2. Observational details of the occulted sources.

Source	SAO Number	Date	Time (IST) h	m	s	m_v	Sp type Class	Filter	FPA[1]	P.A.[2] Deg.	Alt Deg.	Instrument
αLeo	098967	19 Mar 89	21	10	42	1.30	B7 V	clear	6	111	62	SSP[3]
ZC1466	098876	15 April 89	23	58	36	5.26	B9 IV	clear	6	132	46	SSP
ZC0089	109369	31 Jan 90	21	17	09	6.50	F5	B	21	49	23	FP[4]
ZC0518	075999	03 Feb 90	23	41	34	5.90	A3 V	B	12	96	30	FP
ZC0701	076682	05 Feb 90	00	36	33	6.50	F0	B	12	62	34	FP
ZC0840	077295	05 Feb 90	21	01	46	6.50	K2	I	12	66	86	FP
ZC1549	118376	06 April 90	20	36	00	5.1	G8 I–III	V	12	55	61	FP
ZC1336	098247	27 Feb 91	01	43	16	5.20	A3	V	12	138	53	FP
ZC1015	078557	23 Mar 91	23	16	04	6.40	A2	V	12	43	35	FP
ZC1019	078572	23 Mar 91	23	32	27	6.70	A5	V	12	67	32	FP

[1]Focal Plane Aperture (arc sec) [2]Position Angle of occultation
[3]Solid State Photometer [4]Fast Photometer

light. So far the efficiency factor of observing an event successfully is only about 50% but it is likely to improve with system tuning and experience. Further, so far only disappearance events at the dark limb have been recorded. For reappearance events, the telescope tracking must be good enough for a star to remain in aperture of < 10 arcsec for ~ an hour. It is to be tried out in the near future, which will then double our observational capability.

Since the horizontal parallax of the moon is approximately 1°, occultation predictions have to be generated for particular observing sites. We generate our own occultation prediction for any object. These predictions agree very well with the predictions supplied by International Lunar Occultation Centre (ILOC, Tokyo) for bright stars ($m_v < 8$). As a precautionary measure we acquire data for 30 seconds at 1 KHz rate (1 millisec sampling) ±15 seconds centered on the event. The event is also visually observed at the finder telescope and analog output voltage fed to the data acquisition system is also monitored on a scope.

The occultation of α Leo on March 19, 1989 was one of our earliest attempts in recording a lunar occultation. A Solid State Photometer (SSP–I) was used without any filter. The detector used was a 0.5 mm Silicon PIN diode (OPTEC Inc.). The data was recorded with an 8 bit A/D converter. Inspite of these drawbacks the sytem did record the first diffraction maximum from α Leo (Fig. 2). The fringe patterns obtained with this relatively crude system provided the encouragement for building a more sophisticated system for occultation measurements in the visible region using a

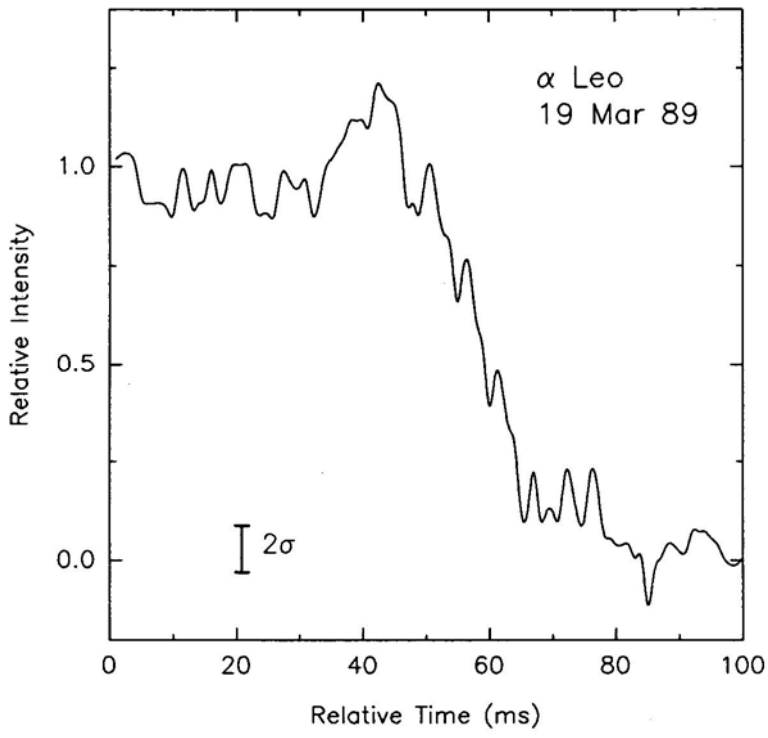

Figure 2. Occultation trace of α Leo observed on 19 March 1989. The large noise level is due to imperfect stellar image over filling the detector area. First fringe maximum can however be seen.

photomultiplier based system. Subsequently eight other optical lunar occultation events have been observed successfully, the details of which are given in Table 2.

4. Discussion

Observations of a single occultation event involving a multiple star produces a trace in which diffraction patterns of the components, separated in time, are added linearly. Analysis of the trace provides the difference in occultation times of the individual components and their relative brightness. From the geometry of occultation, knowing the velocity (V) of the lunar limb perpendicular to itself at the position occultation occurs, these time differences can be converted into angular separations. A single occultation provides only a projection ρ (in the direction perpendicular to the lunar limb) of the true separation ρ_0 (Fig. 3) such that $\rho_0 \cos(\theta - \theta') = \rho$ where θ' is the position angle defining the point of occultation and θ true position angle of the binary system (White, 1977). Observations of the same occultation from several sites provides a range of θ'. Repeated observations of occultations of a given star from a single site during many lunations or even during an 18.6 year nodal rotation period can provide a range of θ' and lead to true separation ρ_0 Details of the technique are discussed in Evans *et al.* (1977). However a large number of double stars measured by lunar occultation have been observed only once.

In the catalogue of photoelectric occultation observations prior to 1981 provided by Evans (1983) out of 3074 stars observed 224 (7%) were detected as double. For stars brighter than V= 6.7, 17% of the 342 stars were found to be double. The mean vector separation of double stars was 260 milliarcsec (mas) decreasing to 150 mas for stars brighter than V= 6.7. Internal errors were 13 mas.

The details of the optical occultation events observed successfully by us are as follows: Two of them (SAO 075999, SAO 076682) are multiple systems.

SAO 075999 is a triple star system with the fainter (10^{th} mag) third star well separated

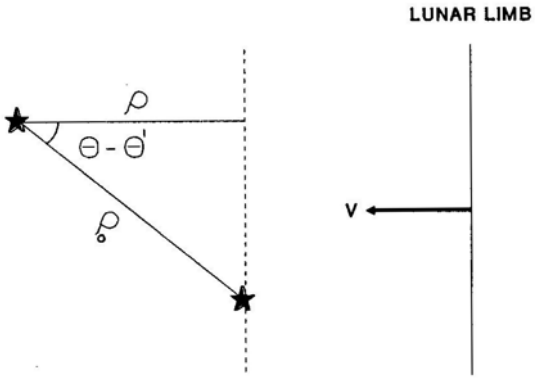

Figure 3. A simplified picture of a binary occultation. V is the velocity component of the moon perpendicular to the limb at the position angle (θ ') of occultation assumed the same for both components of the binary. Position angle of the binary system is denoted by θ. θ and θ' are measured from celestial North through East.

(22.4 arc sec) from the double stars. The bright stars are almost of equal brightness, m_1= 6.6, m_2 = 6.7, m_1+ m_2 = 5.9, $B - V$= 0.13. The absolute visual magnitude is M_V = 1.7, the spectral type is A3 V and the distance to the system is ~ 65 pc (spectroscopic parallax). Orbital elements of the binary system suggest a period of revolution of 568 years and a semi major axis of 650 milliarcsec in 1990. As the position angle of the binary system is very small presently (θ_3 = 3°) the observable separation by lunar occultation technique is a small fraction of the actual value. The star system had been observed earlier by Evans (1971) [Run no. 1226 on 17 Jan 1970]. The timing for the second star was recorded, the first having gone 1.5 sec sooner and failed to register.

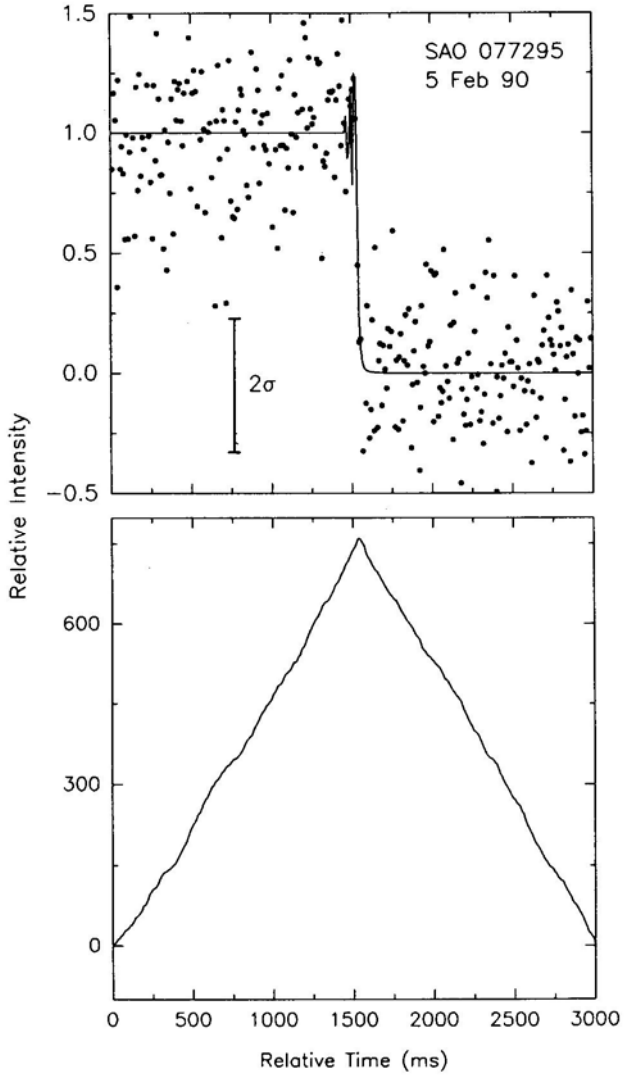

Figure 4a. Occultation data along with the integral curve are given for the observations of SAO 077295 (m_v = 6.5, K2). The source is not a binary as can be seen from the triangular shape of the integral curve. The main source of noise in the data is the sky photon noise due to the bright sky near the moon. 2σ error bar corresponding to this noise is shown.

A sensitive method of detecting binaries in occultation traces, in the presence of noise, involves computing the so called 'integral curve' (Dunham *et al.* (1973), Feirman (1987)). This curve is the running sum of deviations from a segment's mean raw data value ($\bar{I}$), plotted against time. A point $A(t)$ on the integral curve can be represented by

$$A(t) = \sum_{n=0}^{n=N} (I(t) - \bar{I})$$

where $t = t_0 + n\tau$ and τ is the sampling interval. The starting time t_0 is chosen to be typically several seconds before the occultation.

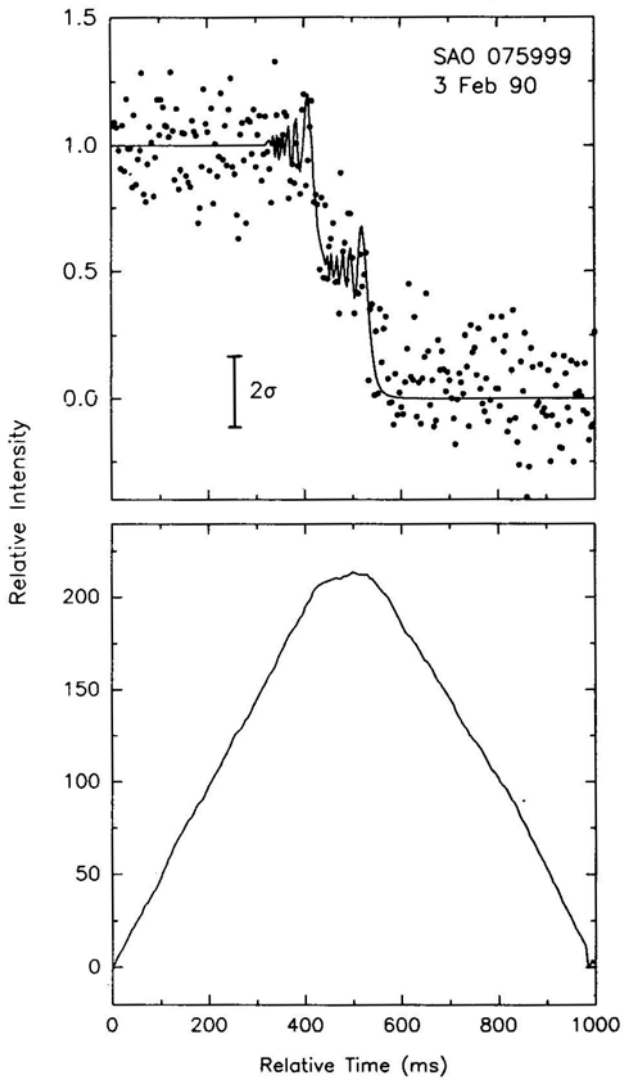

Figure 4b. Binary occultation of SAO 075999 (m_v =5.9, A3 V) observed on 3 Feb 1990 in the B filter. The component stars are of equal brightness and are seen clearly separated by 108 milliseconds corresponding to 55 milliarcsec. A composite point source diffraction pattern is fitted to the data.

The curve exhibits a positive slope before occultation which changes sharply to a negative slope after occultation in the absence of a binary. Fig (4a) depicting the occultation of SAO 077295 illustrates this case. For a binary system, the steeply rising curve before occultation flattens out before changing to negative slope. The extent of the flat portion is a measure of the projected binary separation in the direction of occultation. The integral curve is plotted as calculated and is not the result of any least square analysis. The error involved is unlikely to exceed a few milliseconds. From the integral curve of SAO 075999 (Fig. 4b) we find a binary separation of ~ 108 millisec corresponding to 55 milliarc sec. The observed values are consistent with the known

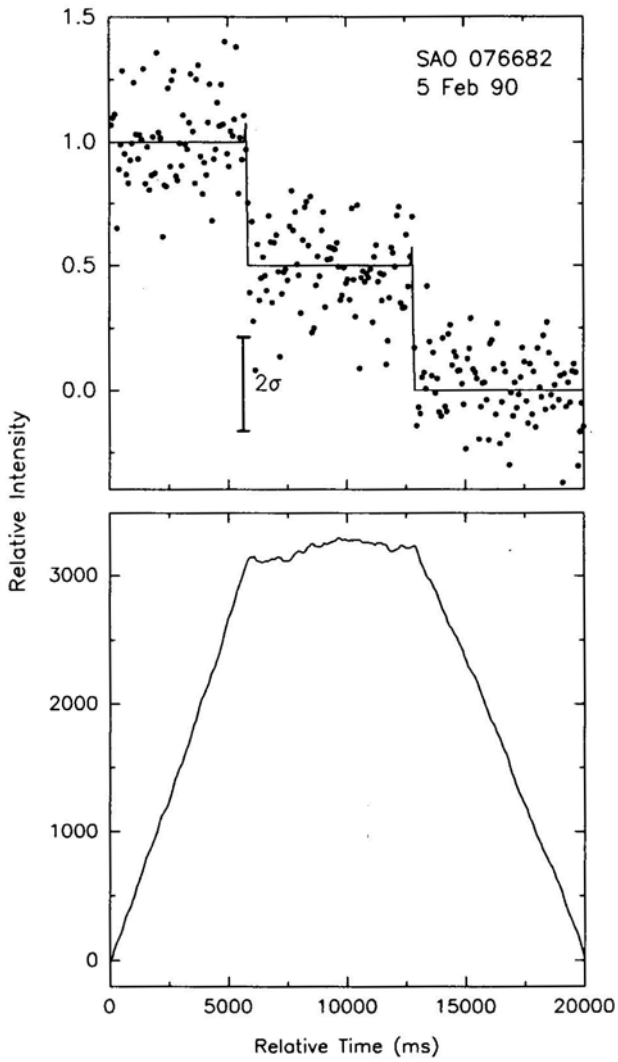

Figure 4c. Occultation data along with the integral curve are given for the observations of SAO 076682 (m_v = 6.5, F0). Integral curve clearly shows the binary with a separation of 4.4 arc seconds. The stars are of equal brightness. A composite point source diffraction pattern is fitted to the data, but the fringes are not evident in the figure as the time span covered is 20,000 milliseconds.

binary separation of 650 mas, position angle of the binary system of ~ 3° and a lunar slope of ~ – 2°.

SAO 076682 is a visual binary of visual magnitude 6.5 and of spectral type F0. The individual stars are of equal magnitude $m_1 = m_2 = 7.3$. From our observation (Fig. 4c) it is seen that the system has a binary separation of ~ 4.4 arc seconds. This binary system was earlier observed by Evans (1971).

Apart from SAO 075999 and SAO 076682 we find from the integral curves that the observed sources are not occultation binaries. SAO 118376 (m_v = 5.1, G8I–III) (Table 2) had been observed earlier (Eitter and Beavers (1974) and Evans (1971)). The lunar background noise in visible wavelengths through the 12 arc second focal plane aperture is large enough to mask the optical fringes except in bright sources like α Leo and hence the angular diameter information of the occulted optical objects could not be obtained. This minimum focal plane aperture size was necessitated by the optics of the Gurushikhar telescope. Presently the contrast factor in detecting binaries is not large due to the large focal plane aperture. Companions fainter than about magnitude $m_v \sim 8$ are unlikely to show up in the occultation traces. A significant improvement in S/N is likely when the telescope optics is improved sufficiently to allow us to see limited, smaller apertures of a few arcsec. It is also proposed to use the instrument at the 1 m telescope at Kavalur soon, to make use of its better optics. It is significant to note that even with the present limitation of the telescope optics we could obtain angular resolution of ~ 55 milliarc seconds in one multiple star system in the visible wavelength which is much below the seeing limit.

5. Conclusions

A high speed photometer has been developed for occultation measurements. Initial observations with this instrument have been encouraging and have led to the following results.

1. The projected observed angular separation between two close stars in the triple star system SAO 075999 is ~ 55 milliarc seconds and the slope at the point of occultation is ~ – 2°.
2. The projected observed angular separation between the visible binary system SAO 076682 is ~ 4.4 arc seconds.
3. The other occulted objects do not have companions brighter than about magnitude $m_v \sim 8$.

While the photometer has been primarily built for observations of lunar occultations of stellar systems in the optical region, the flexibility of the data acquisition system permits its use as a high speed photometer in other areas of astronomy. High time resolution studies of flare stars, millisec pulsars, some cataclysmic variables and optical counterparts of rapid varying X-ray sources are some of the other areas where the instrument will find use in the near future.

Acknowledgements

The authors are grateful to Mrs. S. K. Jani for computational help in generating the occultation predictions. This work was supported by the Department of Space,

Government of India. The authors would also like to thank the referees for their useful comments in improving the paper.

References

Alloin, D. M., Mariotti, J. M. 1989 (Eds.), *Diffraction-limited imaging with very large telescopes,* Kluwer Academic Publishers.
Beavers, W. I., Eitter, J. J. 1971, *Astr. J.,* **76,** 1131.
Dunham *et al.* 1973, *Astr. J.,* **78,** 482.
Eitter, J. J., Beavers, W. I. 1974, *Astrophys. J.,* **28,** 405.
Evans, D. S. 1971, *Astr. J.,* **76,** 1107.
Evans, D. S. 1983, in *Proc. 1AU Coll.* **62,** p. 63.
Evans, D. S., Africano, J. L., Fekel, F. C., Montemayor, T., Palm, C., Silverberg, E., Citters, W. V., Wiant, J. 1977, *Astr. J.,* **82,** 495.
Feirman, B. H. 1987, *I. A. P. P. P. communication* No. **28,** 1.
McAlister, H. A. 1985, *A. Rev. Astr. Astrophys.,* **23,** 59.
Nather, R. E., Evans, D. S. 1971, *Astrophys. Space Sci.,* **11,** 28.
O'Keefe, J. A. 1950, *Astrophys. J.,* **55,** 177.
White, N. M. 1977, *Revista Mexicana de Astronomia y Astrofisica*, **3,** 43.

J. Astrophys. Astr. (1992) **13,** 209–216

Spectroscopic Binaries near the North Galactic Pole Paper 22: HR 4793

R. F. Griffin *The Observatories, Madingley Road, Cambridge, England CB3 0HA*
J. J. Eitter *Erwin W. Fick Observatory, Iowa State University, Ames, Iowa 50011, USA*

Received 1992 February 8; accepted 1992 April 9

Abstract. Photoelectric radial-velocity observations, begun independently at Cambridge and at Ames by the respective authors and now including results from no fewer than six radial-velocity spectrometers, show that the K1 III star HR 4793 is a spectroscopic binary; it has a circular orbit with a period of 111 days and the quite modest amplitude of 7kms^{-1}

Key words: radial velocities—spectroscopic binaries—orbits—stars, individual—HR 4793

1. Introduction

HR 4793 (HD 109519; $\alpha = 12^h35^m8^s$, $\delta = +21°\ 5.3'$. (2000)) is a late-type giant star right in the centre of the constellation Coma Berenices; it is shown on the relevant map in *Norton's Star Atlas* (Norton 1943ff, Ridpath 1989), about three-quarters of a degree south of 23 Comae. It is an interesting coincidence that HR 4593,4693 and 4793 are all spectroscopic binaries in the North Galactic Pole field; the orbit of HR 4693 was given in Paper 19(Griffin 1991) of this series, but that of HR 4593 will have to wait along time yet because the period is tentatively estimated to be in the neighbourhood of 30 years.

The only photoelectric *UBV* photometry of HR 4793, as far as we are aware, is that of Haggkvist & Oja (1968) and of Guetter & Hewitt (1984). The former authors gave $V = 5^m.85$, $(B - V) = 1^m.222$, the latter $V = 5^m.88$, $(B - V) = 1^m.26$, $(U - B) = 1^m.33$; the agreement between them is far from good, the discrepancy in *B* amounting to nearly $0^m.07$, so there is a *prima facie* case for monitoring HR 4793 for photometric variability. The spectral type was classified as K0 in the *Henry Draper Catalogue* (Cannon & Pickering 1920), and as K1 III by Appenzeller (1967) on the basis of a slit spectrogram taken at 120 A mm^{-1} at the McDonald 82-inch Cassegrain.

2. Radial velocities

The radial velocity of HR 4793 was first measured by Shajn & Albitzky (1932), who used a Cassegrain prism spectrograph giving a reciprocal dispersion of 36 Åmm^{-1} at Hγ on the 40-inch Grubb reflector at the Simeis outstation of the Pulkova Observatory. Their four measurements are given in the above-cited publication only as a mean, of – 13.9 ± 2.9 kms^{-1} (the quoted 'probable error' has been converted here to a standard error), but shortly afterwards the same authors gave the dates and velocities for the

individual plates in a more extended account of their investigation (Albitzky & Shajn 1933). Christie & Wilson (1938) published without any details a mean of – 14.0 ± 1.2 km s^{-1} from three Mount Wilson plates; much later, Abt (1973) furnished the individual details together with the information that the dispersion used was 38 Å mm^{-1}. The discrepancies within each of the published data sets were evidently not great enough to arouse in the respective authors any suspicions of real variation of velocity, and the agreement of the mean values was excellent. Thus HR 4793 is one of the few late-type North Galactic Pole stars *not* to be considered a spectroscopic binary in the *Bright Star Catalogue* (Hoffleit 1982).

HR 4793 was naturally included in the Cambridge survey of radial velocities in the Galactic Pole field, and the first measurement of it with the original radial-velocity spectrometer (Griffin 1967) was made by R.F.G.'s student G.A. Radford in 1973. However, it was not until 1984 that the star was recognized in Cambridge as a spectroscopic binary and placed under routine surveillance. Meanwhile, it had been independently placed on the observing programme of the photoelectric spectrometer (Beavers & Eitter 1977) at the Erwin W. Fick Observatory at Ames, where the first observations of it were made in 1978 and a regular watch on it was instituted in 1985. Subsequently the observers at the two places learnt of one another's interest in the star and agreed to write up the orbit jointly.

The total number of photoelectric radial-velocity observations of HR 4793 now stands at 180, of which 68 have been made in the course of the Cambridge programme (all but two of them were made by R.F.G. personally, mostly at Cambridge but some with other instruments) and 112 by Fick observers. The first three Fick velocities have already been published by Beavers & Eitter (1986). The large number of measurements is mainly accounted for by a special effort made at the Fick Observatory throughout one orbital cycle in the spring of 1988 and another in the following spring.

All of the radial velocities, including the early photographic ones, are set out in Table 1. In an effort to maintain homogeneity of the velocity scale with that of the previous papers in this series, an adjustment of + 0.8km s^{-1} has been added to the Ames velocities and to those found in the literature. Such an adjustment represents the difference found in a direct comparison (Griffin & Herbig 1981) between R.F.G.'s velocities and those determined at Lick Observatory and forming the basis of the I.A.U. scale to which other velocities, including those made at Fick, are connected; it also represents well the zero-point discrepancy noticed in previous comparisons, *e.g.* Griffin & Beavers (1982), Griffin, Beavers & Eitter (1988), Griffin, Eitter & Reimers (1990), between Cambridge and Fick observatories, and indeed in *this* one.

Table 1. Radial-velocity measurements of HR 4793.

Date	MJD	Velocity km s^{-1}	Phase	(O – C) km s^{-1}	Source*
1931 Mar 25.92	26425.42	– 11.0	139.875	+ 2.5	Simeis
Apr 4.94	435.44	– 7.3	.965	+ 4.3	Simeis
6.89	437.39	– 21.0	.983	– 9.6	Simeis
18.88	449.38	– 12.8	138.091	– 0.5	Simeis
1935 Mar 16.37	27877.37	– 13.4	126.971	– 1.9	Mt. Wilson
18.37	879.37	– 11.0	.989	+ 0.4	Mt. Wilson
1936 Mar 9.37	28236.37	– 15.3	122.210	+ 1.2	Mt. Wilson
1973 Apr 26.01†	41798.01	– 25.7	0.576	– 1.4	Cambridge
1977 Mar 31.07	43233.07	– 23.8	13.525	+ 1.1	Cambridge

Table 1. Continued.

Date	MJD	Velocity km s^{-1}	Phase	(O − C) km s^{-1}	Source*
1978 Jan 31.46	43539.46	− 18.8	16.289	+ 1.1	Fick
Apr 5.26	603.26	− 12.9	.865	+ 0.8	Fick
May 18.20	646.20	− 18.3	17.252	0.0	Fick
1984 Apr 28.91	45818.91	− 13.7	36.856	+ 0.3	Cambridge
29.89	819.89	− 14.2	.865	− 0.5	Cambridge
May 11.89	831.89	− 10.6	.974	+ 0·9	Cambridge
June 9.90	860.90	− 17.9	37.235	− 0.3	Cambridge
July 11.91	892.91	− 24.3	.524	+ 0·6	Cambridge
Dec 21.22	46055.22	− 11.5	38.989	− 0·1	Cambridge
1985 Jan 12.28	46077.28	− 15.0	39.188	+ 0·6	Cambridge
26.43	091.43	− 20.9	.315	0.0	Fick
Feb 8.46	104.46	− 23.4	.433	+ 1.0	DAO
18.46	114.46	− 25.4	.523	− 0.5	DAO
27.34	123.34	− 23.5	.603	+ 0.1	Fick
Mar 15.02	139.02	− 19.0	.745	− 0.6	Cambridge
20.29	144.29	− 16.7	.792	− 0.3	Fick
Apr 16.23	171.23	− 10.8	40.035	+ 0.7	Fick
May 9.15	194.15	− 18.1	.242	− 0.2	Fick
29.96	214.96	− 24.7	.430	− 0.3	Cambridge
July 3.92	249.92	− 18.6	.745	− 0.2	Cambridge
1986 Jan 22.16	46452.16	− 24.6	42.570	− 0.2	Cambridge
Feb 10.42	471.42	− 17.6	.744	+ 0.9	Fick
27.10	488.10	− 13.3	.895	− 0.5	Cambridge
Mar 7.04	496.04	− 11.6	.966	− 0.1	Cambridge
22.27	511.27	− 15.5	43.104	− 2.7	Fick
Apr 5.06	525.06	− 17.4	.228	− 0.1	Coravel
22.16	542.16	− 24.2	.382	− 1.0	Fick
May 5.95	555.95	− 24.9	.507	+ 0.1	Cambridge
12.13	562.13	− 24.2	.562	+ 0.3	Fick
20.10	570.10	− 22.6	.634	+ 0.1	Fick
30.11	580.11	− 19.5	.725	− 0.2	Fick
June 4.91	585.91	− 17.1	.777	− 0.1	Cambridge
11.90	592.90	− 14.1	.840	+ 0.4	Cambridge
Aug 24.82	666.82	− 25.0	44.507	0.0	Coravel
Nov 24.56	758.56	− 22.0	45.335	− 0.3	Palomar
1987 Jan 6.21	46801.21	− 20.5	45.720	− 1.0	Cambridge
31.15	826.15	− 12.0	.945	− 0.2	Cambridge
Feb 21.10	847.10	− 12.5	46.134	+ 1.1	Cambridge
Mar 3.09	857.09	− 17.3	.224	− 0.2	Coravel
8.32	862.32	− 18.9	.271	+ 0.2	Fick
20.01	874.01	− 24.0	.377	− 0.9	Cambridge
31.33	885.33	− 25.0	.479	0.0	Fick
Apr 5.26	890.26	− 24.4	.523	+ 0.5	Fick
6.25	891.25	− 24.5	.532	+ 0.4	Fick
24.24	909.24	− 19.1	.694	+ 1.4	Fick
27.86	912.86	− 19.9	.727	− 0.7	Cambridge
May 1.20	916.20	− 17.2	.757	+ 0.7	Fick
7.21	922.21	− 17.2	.811	− 1.6	Fick
8.15	923.15	− 14.3	.820	+ 1.0	Fick
8.94	923.94	− 14.7	.827	+ 0.3	Cambridge
24.94‡	939.94	− 11.3	.971	+ 0.2	Cambridge
June 22.91	968.91	− 17.8	47.233	− 0.3	Cambridge
Dec 10.28	47139.28	− 17.5	48.770	− 0.2	Cambridge
22.23	151.23	− 12.8	.878	+ 0.5	Cambridge

Table 1. Continued.

Date	MJD	Velocity km s^{-1}	Phase	(O − C) km s^{-1}	Source*
1988 Jan 8.20	47168.20	− 11.5	49.031	0.0	Cambridge
23.48	183.48	− 14.7	.169	+ 0.2	DAO
Feb 1.43	192.43	− 18.1	.250	+ 0.1	DAO
18.40	209.40	− 23.6	.403	+ 0.2	Fick
19.38	210.38	− 24.2	.412	− 0.2	Fick
25.38	216.38	− 25.2	.466	− 0.3	Fick
26.36	217.36	− 25.5	.475	− 0.6	Fick
28.35	219.35	− 26.3	.493	− 1.3	Fick
Mar 6.35	226.35	− 24.4	.556	+ 0.2	Fick
10.34	230.34	− 24.4	.592	− 0.5	Fick
11.06	231.06	− 23.6	.598	+ 0.2	Coravel
11.33	231.33	− 23.8	.601	− 0.1	Fick
22.11	242.11	− 20.3	.698	+ 0.1	Cambridge
21.30	241.30	− 21.1	.691	− 0.4	Fick
22.29	242.29	− 19.6	.700	+ 0.7	Fick
27.28	247.28	− 17.8	.745	+ 0.6	Fick
30.27	250.27	− 16.8	.772	+ 0.5	Fick
31.27	251.27	− 16.2	.781	+ 0.7	Fick
Apr 7.26	258.26	− 14.8	.844	− 0.4	Fick
8.24	259.24	− 13.4	.852	+ 0.7	Fick
11.24	262.24	− 13.6	.880	− 0.4	Fick
12.92	263.92	− 12.8	.895	0.0	Cambridge
12.23	263.23	− 13.0	.888	0.0	Fick
13.24	264.24	− 12.6	.898	+ 0.1	Fick
15.23	266.23	− 12.0	.916	+ 0.3	Fick
16.22	267.22	− 12.7	.924	− 0.6	Fick
17.21	268.21	− 11.5	.933	+ 0.5	Fick
19.21	270.21	− 12.3	.951	− 0.6	Fick
28.18	279.18	− 11.5	50.032	0.0	Fick
29.19	280.19	− 12.0	.042	− 0.4	Fick
30.18	281.18	− 12.0	.050	− 0.3	Fick
May 1.17	282.17	− 11.6	.059	+ 0.2	Fick
4.17	285.17	− 12.6	.086	− 0.2	Fick
6.17	287.17	− 13.7	.104	− 0.9	Fick
6.91	287.91	− 12.7	.111	+ 0.3	Cambridge
11.15	292.15	− 15.1	.149	− 0.9	Fick
16.13	297.13	− 15.2	.194	+ 0.7	Fick
18.14	299.14	− 17.8	.212	− 1.2	Fick
19.13	300.13	− 17.4	.221	− 0.4	Fick
25.11	306.11	− 19.5	.275	− 0.2	Fick
26.11	307.11	− 19.4	.284	+ 0.3	Fick
27.88	308.88	− 20.4	.300	− 0.1	Cambridge
June 6.90	318.90	− 22.9	.391	+ 0.6	Cambridge
23.92	335.92	− 24.5	.544	+ 0.3	Cambridge
Nov 5.23	470.23	− 18.1	51.756	− 0.2	Coravel
Dec 21.54	516.54	− 14.7	52.174	+ 0.4	Fick
1989 Jan 13.47	47539.47	− 21.9	52.381	+ 1.3	Fick
18.18	544.18	− 24.7	.423	− 0.5	Cambridge
Feb 10.42	567.42	− 22.8	.633	0.0	Fick
11.14	568.14	− 22.6	.640	0.0	Cambridge
12.42	569.42	− 21.3	.651	+ 0.9	Fick
22.39	579.39	− 18.9	.741	− 0.3	Fick
24.24	581.24	− 18.1	.758	− 0.2	ESO
27.37	584.37	− 14.8	.786	+ 1.9	Fick

Table 1. Continued.

Date	MJD	Velocity km s^{-1}	Phase	(O − C) km s^{-1}	Source*
1989 Mar 10.35	47595.35	− 10.8	52.885	+ 2.3	Fick
17.32	602.32	− 11.2	.948	+ 0.5	Fick
18.04	603.04	− 12.8	.955	− 1.1	Cambridge
21.26	606.26	− 11.2	.984	+ 0.2	Fick
22.29	607.29	− 11.0	.993	+ 0.4	Fick
25.88	610.88	− 11.3	53.025	+ 0.2	Coravel
27.28	612.28	− 11.3	.038	+ 0.3	Fick
30.96	615.96	− 12.3	.071	− 0.3	Coravel
Apr 1.23	617.23	− 12.2	.083	+ 0.1	Fick
5.27	621.27	− 13.3	.119	− 0.1	Fick
16.21	632.21	− 16.7	.218	+ 0.1	Fick
19.21	635.21	− 17.6	.245	+ 0.4	Fick
20.20	636.20	− 18.6	.254	− 0.2	Fick
21.21	637.21	− 18.2	.263	+ 0.5	Fick
22.22	638.22	− 18.9	.272	+ 0.2	Fick
26.19	642.19	− 18.0	.308	+ 2.6	Fick
28.93	644.93	− 21.4	.333	+ 0.2	Coravel
May 2.20	648.20	− 22.7	.362	− 0.1	Fick
2.91	648.91	− 22.8	.368	0.0	Coravel
3.19	649.19	− 23.3	.371	− 0.4	Fick
7.14	653.14	− 24.7	.407	− 0.8	Fick
11.18	657.18	− 24.6	.443	0.0	Fick
13.14	659.14	− 24.8	.461	0.0	Fick
14.14	660.14	− 26.3	.470	− 1.4	Fick
15.15	661.15	− 24.5	.479	+ 0.5	Fick
16.14	662.14	− 24.9	.488	+ 0.1	Fick
19.91	665.91	− 25.0	.522	0.0	Cambridge
20.15	666.15	− 24.7	.524	+ 0.2	Fick
21.13	667.13	− 25.4	.533	− 0.5	Fick
23.15	669.15	− 25.1	.551	− 0.4	Fick
26.14	672.14	− 25.0	.578	− 0.8	Fick
27.12	673.12	− 24.0	.587	0.0	Fick
29.89	675.89	− 24.4	.612	− 1.0	Cambridge
June 4.11	681.11	− 23.0	.659	− 1.1	Fick
6.12	683.12	− 20.6	.677	+ 0.6	Fick
7.11	684.11	− 21.5	.686	− 0.6	Fick
10.11	687.11	− 19.6	.713	+ 0.2	Fick
17.11	694.11	− 18.1	.776	− 1.0	Fick
Oct 31.21	830.21	− 11.6	55.004	− 0.2	Coravel
1990 Jan 2.50	47893.50	− 24.2	55.575	+ 0.1	Fick
5.49	896.49	− 23.3	.602	+ 0.4	Fick
27.09	918.09	− 16.4	.797	− 0.2	Coravel
Feb 12.31	934.31	− 11.7	.944	+ 0.1	ESO
28.37	950.37	− 10.6	56.089	+ 1.8	Fick
Mar 13.45	963.45	− 16.3	.207	+ 0.1	DAO
18.31	968.31	− 18.7	.250	− 0.5	Fick
25.28	975.28	− 19.7	.313	+ 1.1	Fick
26.98	976.98	− 21.0	.329	+ 0.4	Cambridge
27.26	977.26	− 21.3	.331	+ 0.2	Fick
Apr 4.00	985.00	− 23.4	.401	+ 0.3	Cambridge
7.24	988.24	− 23.8	.430	+ 0.6	Fick
12.23	993.23	− 25.1	.475	− 0.2	Fick
16.21	997.21	− 24.9	.511	+ 0.1	Fick
22.19	48003.19	− 24.5	.565	0.0	Fick
25.19	006.19	− 23.8	.592	+ 0.1	Fick
29.03	010.03	− 22.6	.627	+ 0.4	Cambridge

Table 1. Continued.

Date			MJD	Velocity km s^{-1}	Phase	(O − C) km s^{-1}	Source*
1990	May	1.22	48012.22	− 21.7	56.647	+ 0.6	Fick
		5.16	016.16	− 21.6	.682	− 0.6	Fick
		6.14	017.14	− 20.4	.691	+ 0.3	Fick
		8.17	019.17	− 19.7	.709	+ 0.2	Fick
		13.14	024.14	− 18.5	.754	− 0·5	Fick
		26.90	037.90	− 13.8	.878	− 0.5	Cambridge
		30.14	041.14	− 12.6	.908	− 0.1	Fick
	June	6.10	048.10	− 11.5	.970	0.0	Fick
	Dec	27.21	252.21	− 15.5	58.812	+ 0.1	Cambridge
1991	Jan	29.12	48285.12	− 12.8	59.109	+ 0.1	Coravel
	Feb	6.13	293.13	− 15.4	.181	− 0.1	Coravel
	Apr	1.27	347.27	− 21.1	.670	+ 0.4	Fick
	May	2.94	378.94	− 12.4	.955	− 0.8	Cambridge
	June	12.92	419.92	− 21.9	60.325	− 0.6	Cambridge

* Sources of published radial velocities or descriptions of the instruments:
Photographic: Simeis: Albitzky & Shajn 1933
Mt. Wilson: Christie & Wilson 1938, Abt 1973
Photoelectric: Cambridge: Griffin 1967
Fick: Beavers & Eitter 1977, 1986
DAO (Dominion Astrophysical Observatory, Victoria): Fletcher *et al.* 1982
Coravel (Haute-Provence): Baranne, Mayor & Poncet 1979
Palomar: Griffin & Gunn 1974
ESO: Coravel on the Danish 1.54-m telescope
†Observed by G. A. Radford
‡Observed by R. I. J. Griffin

3. Orbit

Derivation of the orbit from the data in Table 1 was straightforward. The residuals of the 15 radial velocities measured with the Coravel spectrometers at Haute-Provence and ESO were so much smaller than the others that those measurements were treated as being twice as accurate as the rest, *i.e.* they were attributed weight 4 in the solution of the orbit. The Fick and Cambridge data have sufficiently similar residuals that they were both given unit weight; the number of observations from the other two sources is not great enough to warrant special treatment, so they too received weight 1. The question arises as to whether the old photographic observations should be included in the solution, since they greatly extend the time base even though they are less accurate than the photoelectric data. In practical terms the answer is no, as becomes clear when one sees where they fall on the radial-velocity curve (Fig. 1) computed from the photoelectric velocities alone. The Simeis measures are not only, confined to a total interval less than a quarter of an orbital period but show a very bad scatter, the r m.s. residual being 5.4km s^{-1}, nearly ten times that of the photoelectric work. The three Mount Wilson results have r.m.s. deviations of only 1.3 km s^{-1} from the photoelectric solution; since that is already less than one could really expect, it would be unwise—even if it were possible — to try adjust the orbit in order to reduce those residuals further. Moreover, the first two Mount Wilson measurements happen to fall close to

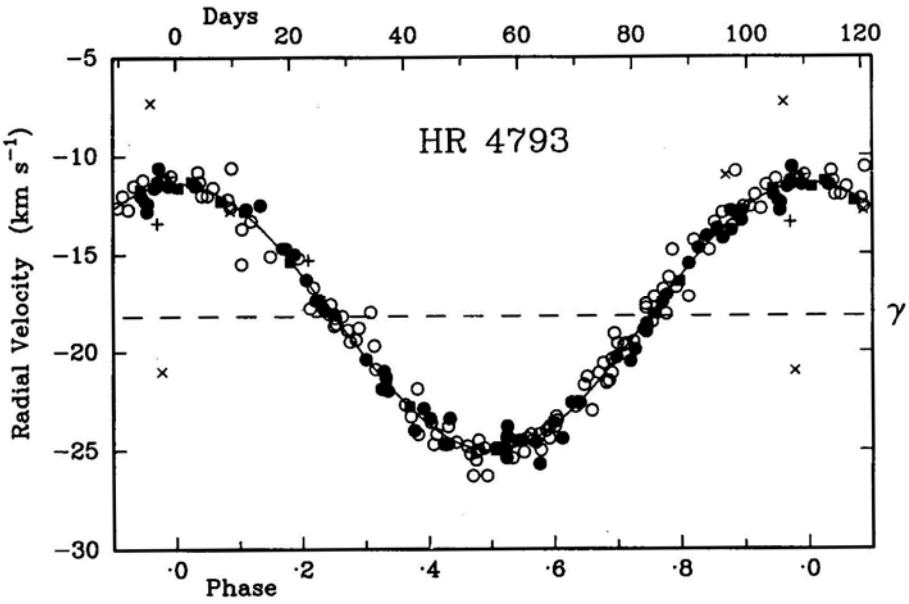

Figure 1. The computed radial-velocity curve of HR 4793, with the measured radial velocities plotted. Coravel observations (weight 4) are represented by filled squares; Cambridge, Victoria and Palomar (weight 1) by filled circles; Fick (weight 1) by open circles; Simeis (weight 0) by crosses; and Mount Wilson (weight 0) by plusses.

a node, where they have no leverage on the period, leaving only the third upon which to base any refinement of the period—and it already fits the orbit extraordinarily well, with a residual little more than 1km s^{-1} . We therefore have no hesitation in adopting the orbit computed just from our own observations. Its elements are:

P =110.829± 0.021 days	$(T_0)_{49}$ =MJD 47164.27 ± 0.16
$\gamma = -18.19 \pm 0.04$ km s^{-1}	$a_1 \sin i = 10.40 \pm 0.10$ Gm
$K = 6.82 \pm 0.06$ km s^{-1}	$f(m) = 0.00365 \pm 0.00010 M_\odot$
$e \equiv 0$	
ω is undefined	R m.s. residual (wt. 1) = 0.66 km s^{-1}

In that orbit the eccentricity has been held fixed at exactly zero. When the eccentricity is included as a free parameter in the solution its value turns out to be 0.012 ± 0.010, with ω = 248 ± 44 degrees, so there is hardly likely to be any significance in it, a conclusion reinforced by the fact that the sum of the squares of the deviations falls only from 78.29 to 77.69 (km s^{-1}) ^{2}.

4. Discussion

In a recent catalogue (Griffin 1990) of orbital elements for a considerable number of binary systems all of which include late-type giants, all orbits whose periods were less than a certain length were found to be circular. Owing to a gap in the period

distribution just at the relevant point, the critical length was not determined exactly, but it must have lain between 118 days, up to which all orbits were circular, and 260 days, the period of the shortest non-circular orbit. Since HR 4793 is a giant whose period is less than 118 days, it is not surprising to find that its orbit is circular, although exceptions to the 'rule' are known and one rather glaring one (HD 118234, thought to be about K1 III, $P \sim 59$ days, $e \sim 0.6$) has appeared in this series of papers (Griffin 1988). The expectation is that, up to some limiting orbital separation corresponding in the cases of giant stars of periods of 100–200 days, tidal effects will generally have circularized the orbits. It would be interesting to know the nature of the companion star that has raised so effectively the braking tides on HR 4793, but (as is so often the case, especially when the primary star is a giant) the companion is too faint relative to the primary to have been detected.

Acknowledgements

R.F.G. is very grateful to Dr. M. Mayor and the Observatoire de Geneve for observing time on the Haute-Provence Coravel, and to the Dominion Astrophysical Observatory, ESO and Palomar Observatory for guest-investigator privileges there, as well as to the UK Science & Engineering Research Council for travel grants. J.J.E. is pleased to acknowledge the assistance and support of Dr. W. I. Beavers, who initiated the Fick Observatory radial-velocity project and directed it until 1987, and of Dr. P. N. Appleton, who has directed the project since 1988. The project has been made possible by a series of grants from the U.S. National Science Foundation.

References

Abt, H. A. 1973, *Astrophys. J. Suppl.,* **26,** 365.
Albitzky, V. A., Shajn, G. A. 1933, *Poulkova Publ., Ser.* 2, **43,** 48.
Appenzeller, I. 1967, *Publ. astr. Soc. Pacific,* **79,** 102.
Baranne, A., Mayor, M., Poncet, J.-L. 1979, *Vistas Astr.,* **23,** 279.
Beavers, W. I., Eitter, J. J. 1977, *Publ. astr. Soc. Pacific,* **89,** 733.
Beavers, W. I., Eitter, J. J. 1986, *Astrophys. J. Suppl.,* **62,** 147.
Cannon, A. J., Pickering, E. C. 1920, *Ann. Harv. Coll. Obs.,* **95**, 62.
Christie, W. H., Wilson, O. C. 1938, *Astrophys. J.,* **88,** 34.
Fletcher, J. M., Harris, H. C., McClure, R. D., Scarfe, C.D. 1982, *Publ. astr. Soc. Pacific,* **94,** 1017.
Griffin, R. F. 1967, *Astrophys. J,,* **148,** 465.
Griffin, R. F. 1988, *J. Astrophys. Astr.,* **8,** 75.
Griffin, R. F. 1990, *J. Astrophys. Astr.,* **11,** 491.
Griffin, R. F. 1991, *J. Astrophys. Astr.,* **12,** 39.
Griffin, R. F., Beavers, W. I. 1982, *Publ. astr. Soc. Pacific,* **94,** 537.
Griffin, R. F., Beavers, W. I, Eitter, J. J. 1988, *Publ. astr. Soc. Pacific,* **100,** 358.
Griffin, R. F., Eitter, J. J., Reimers, D. 1990, *J. Astrophys. Astr.,* **11,** 255.
Griffin, R. F., Gunn, J. E. 1974, *Astrophys. J.,* **191,** 545.
Griffin, R. F., Herbig, G. H. 1981, *Mon. Not. R. astr. Soc.,* **196,** 33.
Guetter, H. H., Hewitt, A. V. 1984, *Publ. astr. Soc. Pacific,* **96,** 441.
Häggkvist, L, Oja, T. 1968, *Ark. Astr.,* **5,** 125.
Hoffleit, D. 1982, *The Bright Star Catalogue* (fourth edition), Yale Univ. Obs., New Haven.
Norton, A. P. 1943–1979, *Norton's Star Atlas and Reference Handbook,* Gall & Inglis, Edinburgh, editions 9–17.
Ridpath, I. (editor) 1989, *Norton's 2000.0,* Longman, Harlow.
Shajn, G., Albitzky, V. 1932, *Mon. Not. R. astr. Soc.,* **92,** 771.

J. Astrophys. Astr. (1992) **13,** 217–239

Kinematics of the Cometary Globules in the Gum Nebula*

T. K. Sridharan *Raman Research Institute, Bangalore 560 080 and*
Joint Astronomy Program, Indian Institute of Science, Bangalore 560 012

Received 1992 April 21; accepted 1992 July 4

Abstract. We report a study of the kinematics of the cometary globules in the Gum Nebula using the $J = 1 \rightarrow 0$ transition line of ^{12}CO. A morphological center for the system with which 60% of the globules are associated is identified. It is shown that the observed radial velocities of the heads of the globules are consistent with an expansion of the system. Systematic velocity gradients are present along some of the tails. The estimated *expansion age* and the *tail stretching age* are both ~ a few million years, suggesting a common origin for the expansion and the formation of the tails. The presence of young stars of similar ages in some of the globules points to star formation triggered by the same cause. Possible scenarios are briefly discussed.

Key words: Cometary globules—Gum Nebula—star formation

1. Introduction

It is now well established that many bright rimmed globules found in association with H II regions are sites of low mass star formation (Dibai 1963, Sugitani *et al.* 1989, Sugitani, Fukui and Ogura 1991, Cernicharo *et al.* 1991, Duvert *et al.* 1990). The earliest example of such star formation is the discovery of HH 46–47 in the cloud GDC 1 (ESO 210-6A) in the Gum Nebula discussed by Schwartz (1977) and Bok (1978). GDC 1 has characteristics similar to the Cometary Globules (CGs) found earlier by Hawarden & Brand (1976) and Sandqvist (1976) in the Gum-Vela region. Later, Zealey *et al.* (1983) and Reipurth (1983) found a total of 38 CGs in a survey of the SERC IIIa-J and ESO B plates of which 32 were in the Gum-Vela region. The Gum globules have the following characteristics:

- A compact dusty head.
- A long faintly-luminous tail extending from one side of the head; the other side has a sharp edge with narrow bright rims.
- The tails of these CGs point away from a general center.
- Sometimes the heads have embedded young stars in them.

It is now known that the CGs are not restricted to the Gum Nebula. The original list contains CGs in Orion and recently CGs have also been found in the Rosette Nebula

*In partial fulfillment of the requirements for the Degree of Doctor of Philosophy of the Indian Institute of Science.

(Block 1990). Carbon monoxide maps of molecular clouds in Orion show cometary structure with tails pointing away from the Ori OB1 Association (Bally *et al.* 1991). It is believed that the cometary globules are formed by the effects of UV radiation from young stars, stellar winds, and supernova shocks on nearby molecular clouds.

The globules in the Gum Nebula are in a complicated setting. This nebula is a large shell like structure (radius ~ 18°) seen in Hα(Gum 1952; 1955). The estimated distance of ~ 400 pc implies a radius of 125 pc (Brandt *et al.* 1971). In the general direction of the center of the nebula are the Vela SNR(age ~ 10^4yrs), the Pup A SNR(age ~3700 yrs), ζ Pup (O4f), the most luminous star in the southern sky, the Wolf-Rayet binary γ^2 Vel (WC8 + O9), and a possible B Association. These objects together represent a significant source of ionising radiation and stellar wind. Various models have been proposed for the Gum Nebula in which some of these objects play an important role (see for example Bruhweiler, 1983). Whether the Gum Nebula is expanding or not has been a point of controversy in the past but latest studies indicate expansion (Srinivasan *et al.* 1987). In the central region of the Gum Nebula the CGs are distributed non-uniformly over a rough *annulus* whose center is close to the place from which the tails point away. This center is offset from the center of the Gum Nebula by about 4°. The best fit circle to the distribution of CGs has a radius of ≈ 9.5°. There is firm evidence for star formation in some of the CGs as well as some of the other dark clouds in the Gum-Vela region (Schwartz 1977; Bok 1978; Reipurth 1983; Pettersson 1987, 1991; Graham 1986; Graham and Heyer 1989).

Soon after the discovery of HH 46–47, it was suggested that low mass star formation in the Gum Nebula may have been triggered by external events (Schwartz 1977), quite possibly the events responsible for the origin of the Gum Nebula itself (Brand *et al.* 1983). Stellar winds, SN shocks and shocks associated with the expansion of H II regions can compress small globules into gravitational instability leading to star formation. Numerical studies of such processes give credence to this idea (Woodward 1976; 1979). Reipurth (1983) has argued in favor of UV radiation from young stars being the cause for the origin of the CGs as well as star formation in them. There have also been studies of radiation driven implosion as a mechanism for star formation (Sandford, Whitaker & Klein 1982, Bertoldi & McKee 1990). Specifically Bertoldi & McKee (1990) have shown that clouds exposed to UV radiation will acquire a cometary structure.

The first systematic study of the CGs in the Gum Nebula was done by Zealey *et al.* (1983) (hereafter referred to as Z83). They made 4 cm formaldehyde absorption observations of 9 CGs with the Parkes 210 foot telescope. Only CGs big enough to have a good chance of detection with the 4.4′ beam were observed. Goss *et al.* (1980) had observed some of the CGs in an independent survey. Radial velocities for a total of 10 CGs were thus obtained. Z83 concluded from this data that the radial velocities were consistent with rotation of the system about an axis perpendicular to the galactic plane. They suggested that the orientation of this axis implied that the kinematics of the CGs is dominated by galactic rotation. In addition they found that in an *l–v* plot the CGs lined up on a straight line parallel to the HI data for the region, but offset in *l*. They took this to mean that the observed velocities of the CG complex are wholly due to large scale effects of the local spiral structure. Assuming that such a line represented galactic rotation effects they studied the deviations from the straight line fit to look for expansion or rotation. Their conclusion was that the CGs may be on a shell expanding up to 5kms^{-1}. [We find this surprising since the residuals (i.e. the deviations from

their straight line fit) were only ± 2 kms $^{-1}$]. In addition, from a study of the tails seen in optical photographs they identified two *centers* from where the maximum number of tails pointed away.

In this paper we wish to report ^{12}CO J=1→ 0 observations at 115.27 GHz of the system of cometary globules in the Gum Nebula using the 10.4 m millimeter-wave radio telescope at the Raman Research Institute, Bangalore (for a brief description of the telescope, see Patel 1990). The main objective was to make a more complete study of the kinematics of the system than was possible before. As was mentioned above, in previous attempts the velocity information was available only for 10 out of the more than 30 CGs. Since our beam size was 1′ we could detect even the smaller clouds that were not detected in the previous surveys. We also measured radial velocities along the tails of the CGs with a view to studying gas motions. The paper is organised as follows: In the next section the remeasured co-ordinates and the details pertaining to our observations are given. In section 3 we argue that there is a well defined *center* from where more than 60% of the tails point away. After a brief discussion of the distances to the CGs in section 4, in the following section we discuss the observed distribution of the radial velocities of the heads of the globules. In section 6 we show that these velocities are consistent with an expansion of the system from a common center with an expansion age of ~ 6 M yrs. The radial velocity measurements of the tails and their implications are given in section 7. The main results are discussed and summarised in section 8.

2. Observations

The CGs were observed in two separate runs in 1989 and 1990-91. The 1989 run using co-ordinates reported in literature detected only 18 out of the 29 CGs observed. Suspecting co-ordinate errors, the CG co-ordinates were remeasured from the ESO-SERC plates. The 1990-91 run using these new co-ordinates detected all the CGs except CGs 23 and 34. In addition to the heads, a few points along the tails were observed. An analysis of the statistics of detections and non-detections in the 1989 observations showed that the primary cause for non-detections during the 1989 run

Table 1. Co-ordinates of the Cometary Globules in the Gum Nebula.

	Co-ordinates (1950.0)													
	Head						Tail-end						Tail length (arc min)	Ref.
	RA			DEC			RA			DEC				
Source	h	m	s	°	′	″	h	m	s	°	′	″		
CG 01	7	17	49·7	−44	29	26.2	7	15	39.4	−44	29	2	23	M
CG 02	7	14	31.3	−43	52	43.8	7	12	49.3	−43	51	24.6	18	M
CG 03	7	37	45.9	−47	45	35.1	7	37	26	−47	47	51.4	4	M
CG 04	7	32	45.6	−46	50	8.9	7	30	40.5	−46	56	43.2	22	M
CG 05	7	39	15.8	−43	42	8.3	7	39	4.6	−43	41	55.1	2	M
CG 06	7	29	2.1	−46	37	14.5	7	28	18.9	−46	41	35	9	M

Table 1. Continued.

Source	Co-ordinates (1950.0) Head RA h	m	s	Head DEC °	′	″	Tail-end RA h	m	s	Tail-end DEC °	′	″	Tail length (arc min)	Ref.
CG 07	9	12	26.1	−42	16	54.4	9	13	14.2	−42	18	14.6	9	M
CG 08	7	41	1.3	−41	8	32.8	7	40	46.5	−41	8	23.2	3	M
CG 09	7	39	7.4	−41	20	4.4	7	38	52.6	−41	19	6.3	3	M
CG 10	7	40	55.2	−41	58	11.9	7	40	34.6	−41	59	48.4	4	M
CG 13	7	12	49.1	−48	23	16.4	7	10	17.6	−48	30	0.2	26	M
CG 14	7	37	16.2	−49	44	29.5	7	36	22.4	−49	52	51.8	12	M
CG 15	7	31	0.5	−50	39	20.2	7	29	55.2	−50	45	29.1	12	M
CG 16	7	26	19.4	−50	58	32.6	7	25	47	−51	1	48.7	6	M
CG 17	8	51	0	−51	41		8	51	6.5	−51	42	44.4	2	Z
CG 18	8	51	0	−50	29		8	51	2.6	−50	30	57.4	2	Z
CG 22 B1	8	26	48.0	−33	34	12.0	8	27	16.7	−33	14	12	21	S
CG 22 B2	8	27	16.7	−33	14	12.0	8	28	4.1	−32	46	11	30	S
CG 23	7	34	48	−50	6		7	34	14.6	−50	10	30	7	Z
CG 24	8	17	33.0	−42	44	58.4	8	17	14.5	−42	48	45.8	5	M
CG 25	7	35	56.0	−47	50	15.1	7	35	19.2	−47	54	47.5	8	M
CG 26	8	14	3.3	−33	40	52.8	8	14	12.9	−33	37	36.1	4	M
CG 27	8	10	28.4	−33	36	11.6	8	10	33	−33	33	53.6	2	M
CG 28	8	10	26.2	−33	46	32.4	8	10	25.8	−33	45	12	1	M
CG 29	8	10	27.9	−33	51	54.2	8	10	32.6	−33	49	36.1	3	M
CG 30	8	7	40	−35	56	2	8	7	13.4	−35	30	34.1	26	R
CG 31 A	8	7	10	−35	52	24	8	6	36.9	−35	26	53.2	26	R
CG 31 B	8	6	55	−35	54	14								R
CG 31 C	8	6	40	−35	50	44								R
CG 31 D	8	6	24	−35	52	58								R
CG 31 E	8	6	21	−35	55	18								R
CG 32 A	8	12	28.6	−34	21	8.4	8	12	10.8	−34	8	27.9	13	M
CG 32 B	8	12	22.4	−34	18	58.6	8	12	10.8	−34	8	27.9	11	M
CG 33	8	13	33.7	−33	55	19.4	8	13	40.3	−33	52	39	3	M
CG 34	7	27	54	−41	4		7	27	19	−40	57	24	9·4	Z
CG 36	8	35	22.7	−36	27	23.9	8	35	46.5	−36	22	47.1	7	M
CG 37	8	10	29.4	−32	56	21.7	8	10	30.8	−32	52	25.1	4	M
CG 38	8	7	47	−36	1	42								R
GDC 1	8	24	17	−50	52	5								R
GDC 2	8	25	10	−50	51	42								R
GDC 3	8	24	56	−50	41	13								R
GDC 4	8	25	2	−50	29	53								R
GDC 5	8	26	1	−51	0	2								R
GDC 6	8	30	30	−50	22	46								R
GDC 7	8	32	39	−50	8	21								R

References:
Z· Zealey *et al.,* 1983
R: Reipurth, 1983
S: Sahu *et al.*, 1988
M: Our measurements from ESO plates.
Notes:
1. For CGs 31B, C, D, E and 38 tail co-ordinates are not available.
2. The Gum Dark Clouds (GDCs) have been included for completeness.

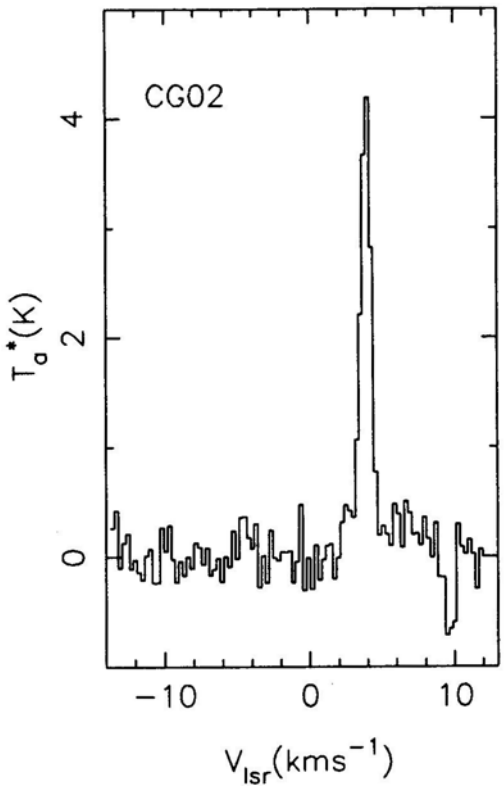

Figure 1. A sample spectrum from observations made during 1990–91. A fourth order polynomial has been subtracted to remove the baseline curvature due to frequency switching. The back-end was an AOS with 100 kHz resolution.

was the wrong co-ordinates used, combined with the small sizes of the heads of the CGs. The new measured co-ordinates of the heads and tail-ends along with the tail lengths are listed in Table 1.

Frequency switching by 15.25 MHz was used for all the observations. An ambient temperature chopper-wheel was used for calibration. The back-end was an acousto-optic spectrometer with 50 kHz resolution and 30 MHz coverage. The data was later bunched in frequency to get better S/N, giving spectra with 100 kHz resolution. Pointing was checked by beam switched continuum scans on Jupiter (See Patel 1990 for details). Fourth order polynomials were fitted to remove baseline curvature. A sample spectrum is shown in Fig. 1. Table 2 lists the noise levels, measured antenna temperatures and the LSR velocities found by fitting gaussians to the lines from the heads of the CGs.

3. The center of the distribution of the CGs

For any assumed center, the tail position angle θ_{TH} with respect to the line joining the head and the center can be calculated using spherical geometry. The center and the head of a CG can be joined by a great circle on the celestial sphere. The tail forms a part

Table 2 1990–91 observation

Source	T_a^* K	v_{LSR} kms^{-1}	v_{FWHM} kms^{-1}	rms K
CG 01	5.3	3.3	1.4	0.33
CG 02	4.2	4.1	0.9	0.22
GC 03	3.3	0.1	1	0.32
CG 04	1.2	1.7	1.2	0.25
CG 06	2.9	0.9	1.1	0.26
GC 07	5.2	− 1.1	0.6	0.54
GC 08	1.7	− 5.8	1	0.2
GC 09	3.9	− 4.2	1.3	0.59
CG 10	3.9	− 5.5	1.0	0.19
CG 13	3.7	3.7	0.8	0.41
GC 14	3.0	− 0.9	1	0.28
CG 15	3.6	− 0.8	0.6	0.57
CG 16	2.9	− 0.7	0.7	0.22
CG 17	0.8	3.7	0.8	0.33
CG 18	1.0	2.0	0.4	0.26
CG 22 B1	6.4	6.5	1.1	0.41
CG 22 B2	6.8	6.8	1.3	0.28
CG 22 B3	3.4	6.4	1.4	0.22
CG 24	2.9	− 12.5	1.2	0.2
CG 25	2.2	− 1.8	0.8	0.29
CG 26	3.5	2.0	1	0.51
CG 27	2.8	5.0	0.8	0.44
CG 28	2.9	5.2	1.1	0.54
CG 29	2.4	5.2	0.7	0.31
CG 30	3.8	5.8	2.2	0.25
CG 31 A	4.5	6.0	1.3	0.44
CG 31 B	4.2	6.0	1	0.36
CG 31 C	6.8	6.3	1.6	0.3
CG 31 D	1.5	6.9	1.6	0.29
CG 32 A	4.5	4.9	1.2	0.43
CG 32 B	4.7	4.8	1	0.38
CG 33	2.3	1.6	0.6	0.46
CG 36	1.4	− 8.5	0.7	0.39
CG 37	3.0	6.2	0.4	0.48
CG 38	1.7	7.0	1.2	0.23
GDC 1	5.6	5.3	1.3	0.36
GDC 2	5.1	6.0	1.4	0.36
GDC 3	1.9	5.9	1.0	0.43
GDC 4	3.1	4.9	1.3	0.52

of the great circle. θ_{TH} is angle between these two great circles.To identify a centre for the system of CGs we associate with every point in the central region a fraction *f*, defined as the fraction of CGs with θ_{TH} (calculated using the points as the centre) within ± 10°. We evaluated *f* over a 15° × 15° area in the central region with grid points separated 0.5° in both α and δ. Figure 2 shows a contour plot of *f* .Only these CGs have been used for which we have measured the co-ordinater. CGs 24 has not been included because of its anomalous tail direction. The CGs used in the analysis are shown as filled circles with tails and the unused CGs are shown as open circles with tails For clarity the tail length shown have been scaled up to 10 times.The counter spacing is 0.05 with

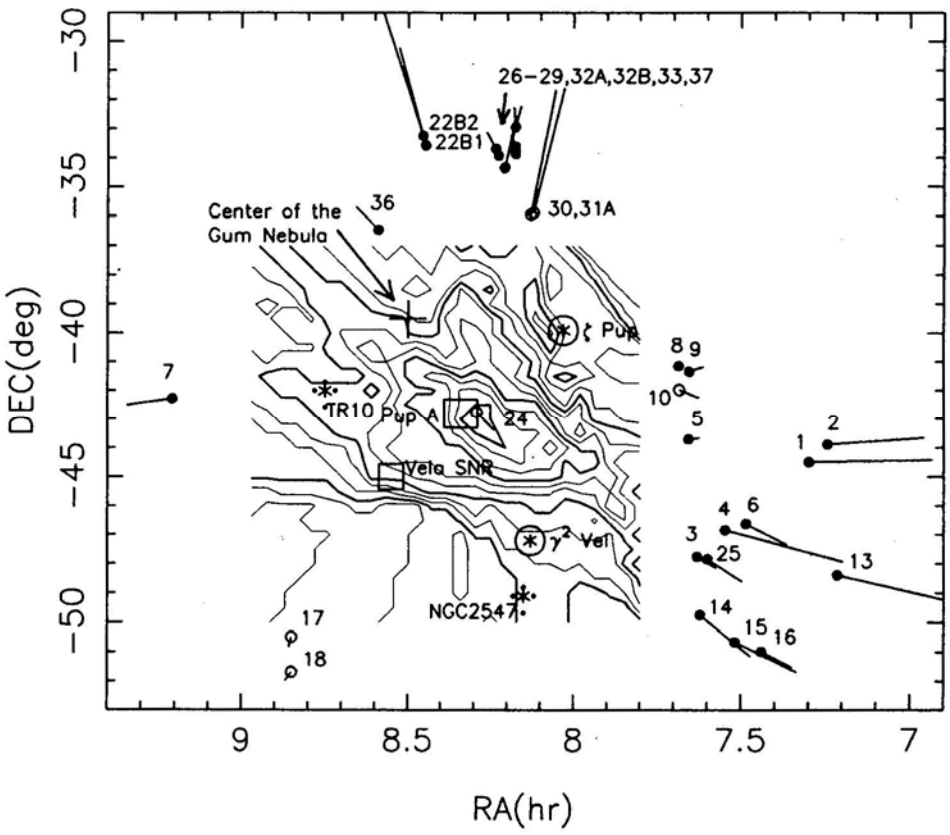

Figure 2. The figure shows contours of constant f where f is the fraction of the cometary globules with position angles of their tails $\leqslant 10°$. The position angles are measured with respect to the line joining the head of the globule and any particular point in the region. The inner most contour bounds the region where for at least 60% of the globules the position angles of the tails are$\leqslant 10°$. The contours are drawn in steps of 0.05 in f and were evaluated with a grid spacing of $0.5° \times 0.5°$. Every third contour is shown as a thick line. We designate the central maximum as the morphological center of the system. The globules used for evaluating the contours are shown as filled circles with tails and those not used as open circles with tails. For clarity, the tails have been scaled up 10 times. In addition the figure shows several other interesting objects such as the Pup A SNR, the Vela SNR, ζ Pup, γ_2 Vel and the open clusters TR 10 and NGC 2547.

every third contour drawn as a solid line. One can see that there is a central maximum with which 60% of the CGs are associated. The locations of the various interesting objects such as ζ Pup, γ^2 Vel, the Vela SNR etc. are marked in the figure. There are no strong local maxima associated with any of these objects. This indicates that most of the CGs are affected by a combination of objects rather than a particular object. The co-ordinates of the central maximum are $\alpha = 8^h\ 17^m$ and $\delta = -43°$. We will refer to this point as the *center* hereafter. The *center* deduced by us is 1.5° north of *center1* of Z83. Reducing the limiting θ_{TH} from ± 10° to ± 5° for calculating f merely results in increased noise on the contour plot. The apparently anomalous CG 24 tail can be understood by noticing that it is so close to *center* that even small errors in the location of *center* can make the tail direction look anomalous.

In view of the remarkable near coincidence of the deduced *center* with the SNR Pup A it is worth briefly discussing whether the two may be causally connected. Zarnecki *et al.* (1978) estimate a distance of 1 kpc for Pup A from X-ray absorption measurements. The Σ — D distance to Pup A is 2 – 2.5 kpc (Milne 1979, Casewell & Lerche 1979) although it should be emphasised that this method has been severely criticised in the literature (Srinivasan & Dwarakanath 1982; Green 1984). The latest estimate based on the kinematic distance to molecular clouds interacting wih Pup A gives 2.2 kpc (Dubner & Arnal 1988). We will therefore adopt a distance of 2 kpc to Pup A. At this distance it would be very difficult to detect the CGs, especially the ones close to the galactic plane. If the CGs are placed at the estimated distance to Pup A, then they will be ≈ 200 pc away from the SNR. From the size of the SNR it is clear that the SN shock has not reached the CGs. So the only way Pup A may be associated with the formation of the CGs is through the photon pulse at the time of the explosion or alternatively the UV radiation and stellar wind from its *progenitor.* The age of Pup A has been estimated to be ~ 3700 yrs (Winkler *et al.* 1988). From the measured electron density of ~ 100 cm^{-3} for the bright rim of CG30 (Pettersson 1984) we estimate a recombination lifetime $t_{\rm recomb} = (n_e \alpha)^{-1}$ ~ 1200 years. So it is difficult to see how the presently observed bright rims can be due to the initial excitation by the supernova flash. There is a further argument. Both the expansion age of the system of CGs and the age of the tails estimated in later sections are ~ a few million years, thus making a causal association between Pup A and the CGs very unlikely. We therefore conclude

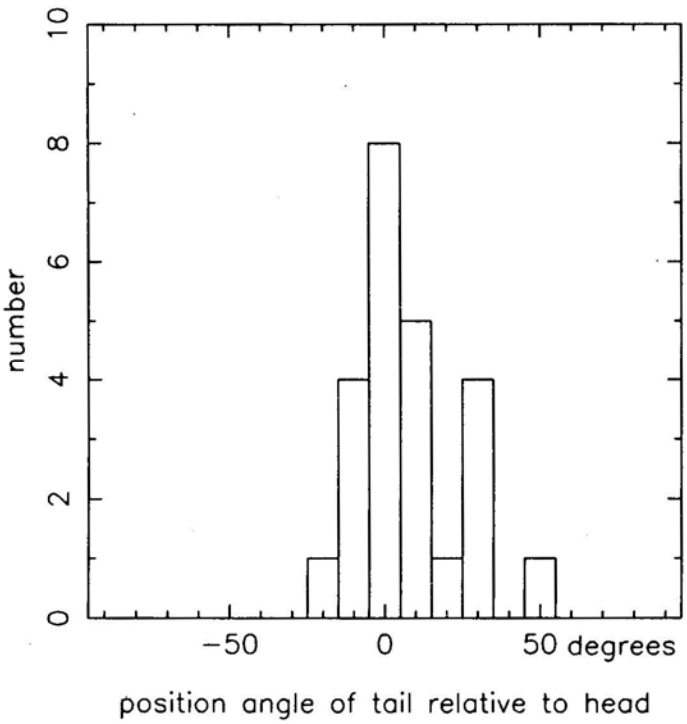

Figure 3. The distribution of the position angles θ_{TH} of the tails relative to the line joining the *center* and the respective heads for 24 CGs.

that the coincidence of Pup A and the *center* is a chance superposition. On similar grounds we rule out any role for Vela SNR in the formation of the CGs.

Figure 3 shows the distribution of θ_{IH} . We see that apart from the central peak there is a peak at 35° consisting of four globules, viz. CGs 26,27,29 and 33. Although the peak is not statistically significant, the directions of their tails suggest that they may be associated with ζ Pup alone. It is possible that they are closer to ζ Pup in the direction perpendicular to the plane of the sky. Even though we cannot associate a single object of any importance with the *center,* we will use it as the center of the distribution of the CGs for further analysis. The other objects in Fig. 2 are discussed in the next section.

4. Distance to the CGs

The most important objects in the region of the CGs from the point of view of momentum and energy are ζ Pup, γ^2 Vel, and the clusters NGC 2547 and TR 10. All these objects are at a distance of ~ 450 pc (Eggen 1980; Claria 1982). As seen in Fig. 4, a histogram of the distances of the early type stars towards the Gum Nebula used by Wallerstein, Silk & Jenkins (1980) to study gas in the nebula shows a peak at 450 pc. In an earlier study of the Gum Nebula, Brandt *et al.* (1971) had identified a possible B Association at 450 pc distance which has been later named Vela OB2. So it is clear that at a distance of 450 pc there exists a significant population of early type stars. The

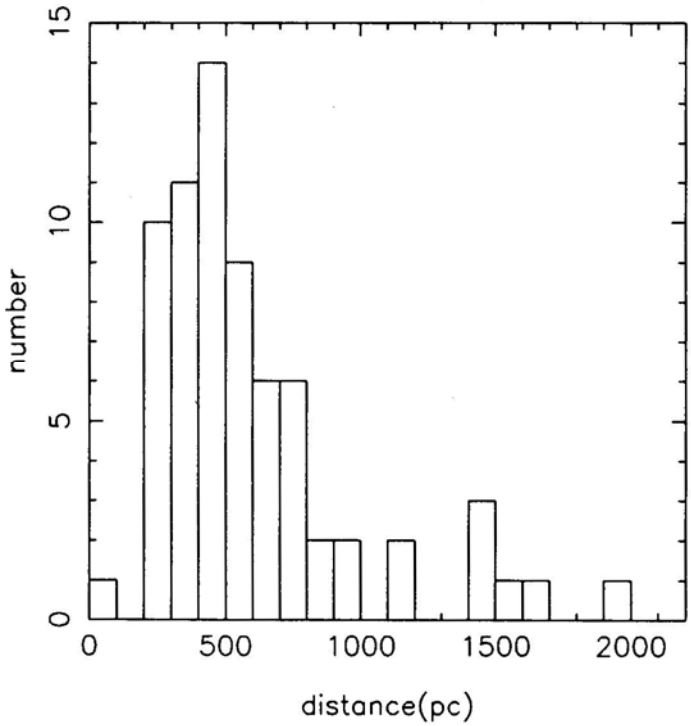

Figure 4. The distribution of the distances to the early type stars towards the Gum Nebula. The distances are from Wallerstein, Silk & Jenkins (1980).

location of some of these objects are shown in Fig. 2. The point to note is that these objects, some of which have to be necessarily invoked to explain the CGs, are at about the same distance and are centrally located with respect to the distribution of the CGs. So we assume that the CGs are at the same distance as these objects, viz. at ~ 450 pc. Further, Pettersson (1987) has estimated a lower limit for the distance to CG 30–31 complex to be 420 pc using a foreground star, and the distance to the young star in the head of CG 1 has been estimated to be ~ 500 pc (Brand *et al.* 1983). Adopting a distance of 450 pc would imply that the distribution of the CGs extends to about 150 pc perpendicular to the line of sight.

5. Radial velocities

From the observations described in section 2, we have radial velocities for all the CGs except CG 23 and CG 34 which were not detected. The radial velocities were obtained as the center velocity of the best fitting gaussian to the lines. As *CG* 10 and CG 30 show two components, we take the velocity of the stronger component.

The Columbia CO survey of the third galactic quadrant (May *et al.* 1988) covered a part of the region over which the CGs are distributed. Since this survey was done at 0.5° resolution we do not expect to see the small CGs because of beam dilution. But any larger scale distribution of CO along lines of sight to the CGs will show up. We can use these to check if our detections are contaminated by molecular gas not associated with the CGs. We see from the published survey data that CGs 1–6, 8–10, 13–16 and 25 are outside the region covered in the survey. This therefore leaves one with some uncertainty. But the CGs 1–4, 6, 13–16 and 25 have $b < -12$ and so their detections are unlikely to be confused by more widespread gas. CGs 5, 8, 9 and 10 have $b \sim -9$ and have nearby dark clouds distributed over larger spatial scales. These dark clouds show signs of being affected by ζ Pup and γ^2 Vel. These four CGs show more or less the same radial velocities. All the other CGs are in a region covered by the survey. The GDC complex of which GDCs 1 and 2 show CG features is extended consisting of 7 clouds and has been detected by the survey. The velocities are consistent. Similarly the CG 30–31 complex, which is extended with more dark clouds in the same region, and the largest globule CG 22, have been detected by the survey with velocities consistent with our values. All other CGs which are small and isolated have not been detected. So it is clear that the radial velocities we have obtained are reliable and do not suffer from contamination from other line-of-sight material. In addition, the fact that the 1989 observations using co-ordinates with errors resulted in a lower detection rate supports this conclusion. The survey detected strong CO emission from what is called the Vela Molecular Ridge (VMR), but it has been shown that this emission arises from GMCs at distances 800–2400 pc (Murphy 1985).

A comparison of our velocities with those of Z83 shows general agreement except for CG 17, for which we measure a velocity of +3.7 kms^{-1} as against the value of –6.5 kms^{-1} due to Z83. The radial velocity we measure for CG 18 ($\approx 1^o$ away from CG 17) is + 2.0 kms^{-1}. The velocities of the clouds in the GDC 1–7 complex which is nearby are again in the range + 5 to +6 kms^{-1} GDC 1 and GDC 2 have a windswept appearance with tail-like structures pointing in the same general direction as the other CGs and bright rims facing the center. The rough agreement between the velocities of CG 17, CG 18 and the GDCs suggests that the value reported by Z83 for CG 17 may be

in error. As they have not published their spectra, nor mentioned their S/N, we are not in a position to comment any further.

We now wish to discuss the implications of these radial velocities. First, we briefly touch upon the suggestion made by Z83, viz. that the velocity distribution can be understood in terms of the large scale galactic rotation effects. In Fig. 5 we have plotted the radial velocities against the position angles of the CGs measured with respect to the *center* with zero towards north and increasing through east. The sinusoid fitted by Z83 which led them to suggest a rotation of the system of CGs is also shown. Clearly, the fit is very poor. There are two reasons why the sinusoid is a poor fit to the new data: (i) the revised value of the radial velocity of CG 17, and (ii) velocities of the CGs not detected earlier. Our main conclusion from this figure is that the model of the system of CGs rotating about an axis perpendicular to the galactic plane is untenable. In Fig. 6 we have plotted the radial velocities against galactic longitude. Again, the new data does not permit a simple straight line fit as suggested earlier (Z83), and therefore an explanation based on galactic rotation effects is hard to reconcile. Nevertheless, the contribution due to galactic differential rotation will be present and should be removed before attempting to interpret the velocities.

Before one can correct for the galactic differential rotation one must assume a mean distance to the CGs. Based on the discussion given in section 4, we will adopt a distance of 450 pc. The dashed line in Fig. 6 represents the expected radial velocities for different

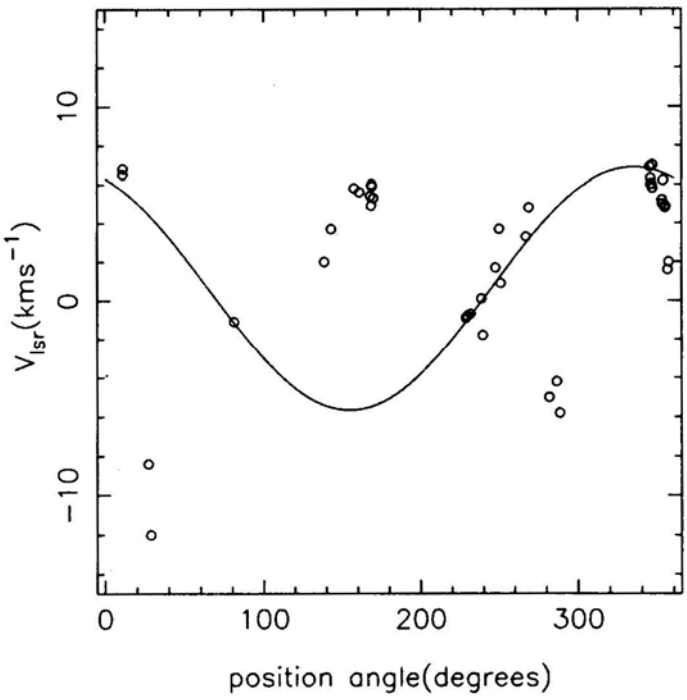

Figure 5. The velocities of the globules in the Gum Nebula with respect to the Local Standard of Rest. The horizontal axis is the position angle of the globules: zero is north and the position angle increases through east. The sinusoid shown is the fit made by Zealey *et al.* (1983) for their data.

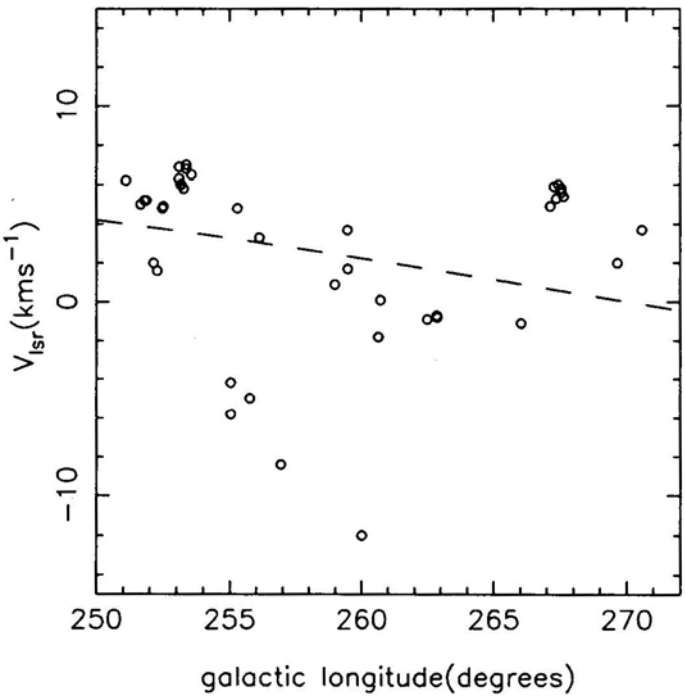

Figure 6. The velocities of the globules in the Gum Nebula with respect to the Local Standard of Rest versus the galactic longitude. The broken line shows expected velocities due to galactic differential rotation for an assumed heliocentric distance of 450 pc and $b = 0$.

galactic longitudes from the well known formula

$$v_r = A\, r \sin(2l)\cos^2 b \qquad (1)$$

with the heliocentric distance r=450 pc and $b = 0$. We have assumed a value of 14.5 kms $^{-1}$ kpc^{-1} for Oort's constant A (Kerr & Lynden-Bell 1986). The significant deviations of the observed radial velocities from the expected value given by the dashed line suggests local motions in the system of CGs. Fig. 7 shows the residuals after galactic rotation effects have been subtracted out using Equation 1. It should be remarked that the differences in the line-of-sight distances to the various globules (~ 150 pc) can only account for a scatter of — 1.4 kms^{-1}

6. Expansion of the globules

In this section we wish to argue that the velocity residuals can be easily understood in terms of an expansion of the system of globules from a common center. If the COs are distributed over a shell expanding with uniform velocity then, as can be seen from Fig. 8(a) the expected velocities are given by

$$v_{rad} = \pm v_{exp}(1 - \sin^2\theta/\sin^2\theta_{max})^{1/2} \qquad (2)$$

where v_{exp}, is the expansion velocity of the shell, v_{rad} is its line-of-sight component, and $\theta_{max.}$ is the angular distance of the farthest CG from the *center*. In this case one would

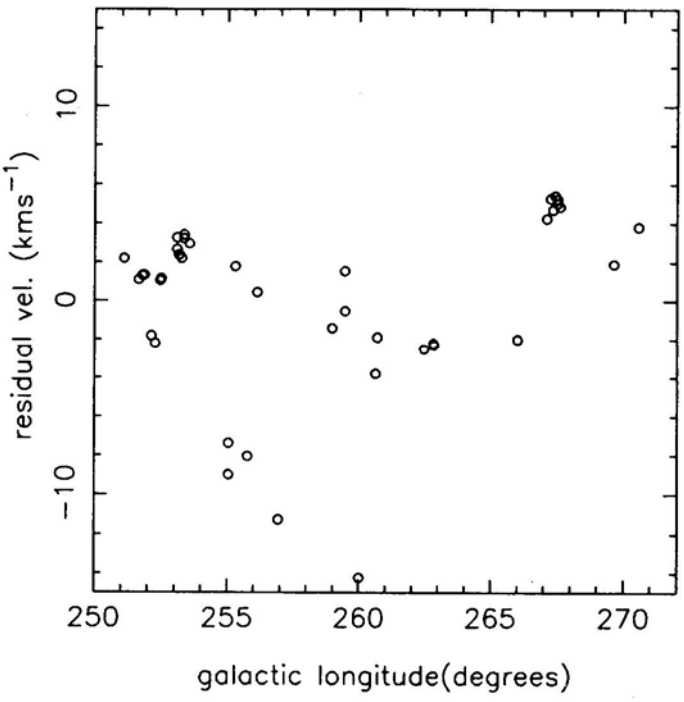

Figure 7. The residual velocities of the globules in the Gum Nebula after removing the contribution of the galactic differential rotation. A mean distance of 450 pc to the globules has been assumed.

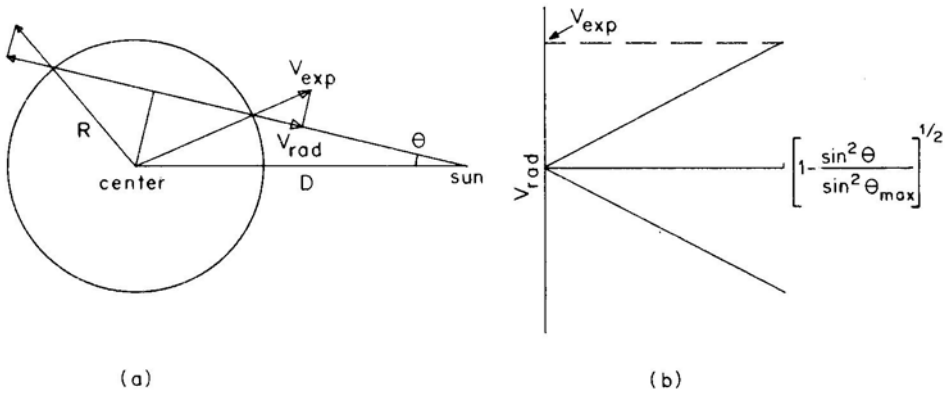

Figure 8. (a) Schematic diagram for deriving expected velocities from an expanding shell of objects. V_{exp} is the expansion velocity whose radial component is V_{rad} and θ is the angular distance to any point on the shell from the center of the shell, (b) The expected velocity plotted, against $(1 - \sin^2\theta/\sin^2\theta_{max})^{1/2}$.

expect the residual velocities, when plotted against $(1 - \sin^2\theta/\sin^2\theta_{max})^{1/2}$, to fall on two straight lines as shown in Fig. 8(b). If the CGs are not on a shell but distributed throughout the sphere, then the region between the lines will be filled up provided the inner CGs move slower than the outer CGs. If the distribution of the CGs within the sphere is not uniform one will find an incomplete filling of this region.

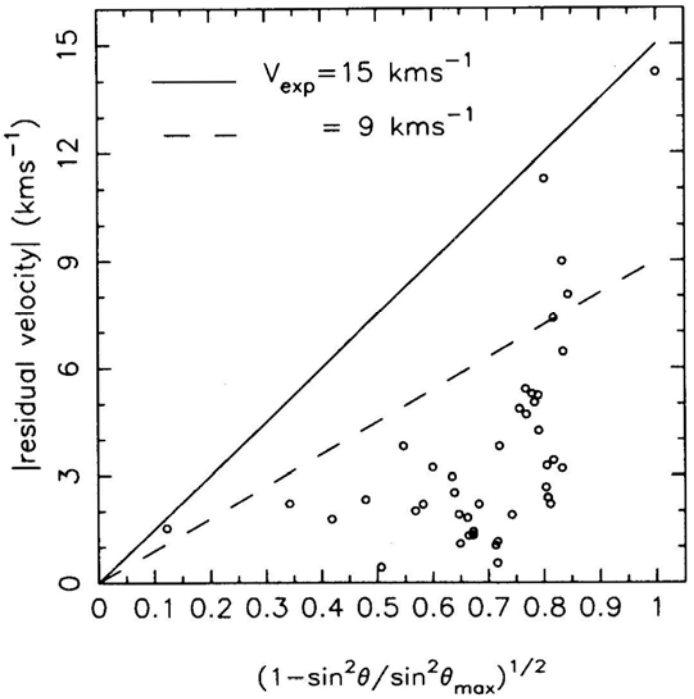

Figure 9. The absolute values of the residual velocities of the globules plotted against $(1 - \sin^2\theta / \sin^2\theta_{max.})^{1/2}$ where θ is the angular distance to the globule from the *center*. The line shown corresponds to a shell expanding at 12 kms^{-1}.

Figure 9 shows the absolute value of the residual velocities plotted against $(1 - \sin^2\theta/\sin^2\theta_{max})^{1/2}$ for all the CGs and the GDCs. We have taken θ_{max} to be 12.5°, corresponding to CG 13. It is clear that there is an upper limit to the velocities which increases as one goes closer to the center (abscissa = 1) implying an expansion of the system. A contraction of the system will also have the same signature, but is very unlikely. The two straight lines shown correspond to expansion velocities of 15 kms^{-1} and 9 kms^{-1}. We will adopt an expansion velocity of 12 kms^{-1}. The figure further shows that the CGs are distributed over a volume rather than in a shell, and that the distribution is not uniform. Finally, the inferred expansion velocity of 12 kms^{-1} implies an *expansion age* of ~ 6 M yrs.

7. Radial velocities along the tails

In addition to measuring the radial velocities of the heads of the cometary globules, we also measured the velocities along the tails. In this section we discuss these observations. The results of the observations of the tails are listed in Table 3. The velocities were obtained by fitting gaussians to the lines. We estimate the error on the velocities to be 0.15 kms^{-1} from several observations of the head of CG 22 spread over two months. We will regard this rms as the error on all radial velocity measurements.

Out of 21 CGs for which at least three points along the tails were observed, seven

Table 3. Observation of the tails.

Source	T_a^* K	v_{LSR} kms^{-1}	v_{FWHM} kms^{-1}	rms K	Distance from head in arcmin	Velocity gradient kms^{-1} arcmin^{-1}
CG 1 H	5.3	3.3	1.4	0.33	0.0	0.019
CG 1 T 2	4.0	3.7	1.1	0.55	14.2	(± 0.003)
CG 1 T 3	4.2	3.7	1.4	0.39	21.2	
CG 1 T 4	4.3	3.4	1.4	0.43	7.0	
CG 2 H	4.2	4.1	0.9	0.24	0.0	0.040
CG 2 T 1	1.0	5.1	0.6	0.19	25.3	(± 0.004)
CG 2 T 3	1.5	4.9	0.9	0.28	19.1	
CG 2 T 4	3.4	4.5	1.4	0.41	6.5	
CG 3 H	3.3	0.0	0.9	0.33	0.0	− 0.014
CG 3 T 2	2.0	0.1	0.9	0.32	2.1	(± 0.068)
CG 3 T 3	2.6	0.1	0.8	0.37	3.2	
CG 3 T 4	4.3	0.3	1.1	0.36	1.0	
CG 4 H	1.2	1.7	1.2	0.23	0.0	0.016
CG 4 T 1	4.9	1.9	1.2	0.49	17.4	(± 0.021)
CG 4 T 2	5.6	1.3	1.5	0.43	8.7	
CG 4 T 3	5.3	1.7	1.3	0.50	13.0	
CG 6 H	2.9	0.9	1.1	0.26	0.0	0.061
CG 6 T 1	1.7	1.6	1.5	0.22	10.9	(± 0.032)
CG 6 T 2	1.5	0.8	0.8	0.20	5.4	
CG 6 T 3	1.0	0.9	1.1	0.21	8.1	
CG 6 T 4	3.5	0.8	1.0	0.35	2.7	
CG 7 H	5.4	− 1.1	0.6	0.54	0.0	− 0.133
CG 7 T 2	4.1	− 1.3	0.7	0.51	1.0	(± 0.038)
CG 7 T 3	2.4	− 1.3	0.9	0.43	1.4	
CG 7 T 4	5.4	− 1.2	0.8	0.25	0.5	
CG 9 H	2.7	− 4.1	1.1	0.20	0.0	0.080
CG 9 T 2	4.1	− 4.1	1.0	0.45	1.6	(± 0.09)
CG 9 T 3	3.3	− 3.8	1.1	0.32	2.5	
CG 9 T 4	3.5	− 3.9	1.1	0.32	0.9	
CG 10 T 2	5.8	− 4.7	2.0	0.48	1.4	− 0.056
CG 10 T 3	5.9	− 4.5	1.9	0.36	2.0	(± 0.25)
CG 10 T 4	4.4	− 4.4	2.0	0.33	0.7	
CG 14 H	3.0	− 0.8	1.0	0.28	0.0	− 0.018
GC 14 T 2	1.5	− 0.9	1.0	0.44	7.4	(± 0.005)
CG 14 T 3	4.6	− 1.0	0.7	1.37	11.3	
CG 15 H	3.6	− 0.8	0.5	0.58	0.0	− 0.005
CG 15 T 2	3.6	− 0.8	0.8	0.52	8.1	(± 0.018)
CG 15 T 4	3.8	− 0.7	0.9	0.34	4.0	
CG 16 H	3.1	− 0.7	0.8	0.20	0.0	− 0.018
CG 16 T 1	1.3	− 0.8	1.0	0.17	6.6	(± 0.013)
CG 16 T 2	3.9	− 0.7	1.1	0.53	3.4	
CG 16 T 3	2.7	− 0.8	1.0	0.52	5.0	
CG 24 H	2.9	− 12.4	1.14	0.19	0.0	− 0.024
CG 24 T 1	0.3	− 12.4	2.14	0.15	4.2	(± 0.089)
CG 24 T 2	0.6	− 12.0	2.00	0.21	2.1	
CG 24 T 4	2.9	− 12.0	1.20	0.44	1.0	

Table 3. Continued.

Source	T_a^* K	v_{LSR} kms^{-1}	v_{FWHM} kms^{-1}	rms K	Distance from head in arcmin	Velocity gradient kms^{-1} arcmin^{-1}
CG 26 H	2.5	2.1	0.9	0.18	0.0	0.010
CG 26 T 1	1.7	2.2	1.0	0.24	3.5	(± 0.02)
CG 26 T 3	2.3	2.2	0.9	0.18	2.6	
CG 26 T 4	4.6	2.2	0.9	0.41	0.9	
CG 27 H	2.0	5.2	0.7	0.25	0.0	0.021
CG 27 T 2	4.2	5.1	0.7	0.40	1.2	(± 0.052)
CG 27 T 3	2.5	5.2	0.8	0.37	1.8	
CG 27 T 4	2.5	5.1	0.8	0.29	0.6	
CG 29 H	2.4	5.2	0.7	0.30	0.0	0.041
CG 29 T 1	2.6	5.3	0.7	0.24	2.5	(± 0.02)
CG 29 T 3	1.7	5.2	0.8	0.18	1.9	
CG 31 A	4.5	6.0	1.3	0.42	0.0	0.036
CG 31 AT 1	1.7	6.9	1.9	0.22	25.3	(± 0.006)
CG 31 AT 2	3.8	6.3	1.9	0.15	12.6	
CG 31 AT 3	3.5	6.6	1.8	0.14	19.0	
CG 32 AT 2	2.5	5.2	1.2	0.39	7.7	0.057
CG 32 AT 3	4.9	5.5	1.4	0.35	10.5	(± 0.007)
CG 32 AT 4	6.6	5.0	1.0	0.36	3.8	
CG 32 AH	4.5	4.9	1.2	0.43	0.0	
CG 32 BH	4.7	4.8	1.0	0.38	0.0	0.114
CG 32 BT 2	3.8	5.4	1.0	0.41	5.5	(± 0.043)
CG 32 BT 4	3.0	4.8	1.4	0.41	2.7	
CG 33 H	2.4	1.6	0.5	0.45	0.0	0.082
CG 33 T 1	1.6	1.9	0.5	0.35	3.0	(± 0.032)
CG 33 T 2	3.1	1.8	0.7	0.43	1.6	
CG 33 T 3	2.0	1.8	0.6	0.24	2.2	
CG 33 T 4	2.3	1.8	0.5	0.51	0.7	
CG 36 H	3.1	10.4	0.7	0.35	0.0	0.144
CG 36 T 2	2.8	10.7	0.9	0.35	2.4	(± 0.05)
CG 36 T 4	4.2	10.6	1.1	0.40	1.2	
CG 37 H	3.0	6.7	0.4	0.46	0.0	0.017
CG 37 T 3	1.0	6.8	0.6	0.22	2.9	(± 0.064)
CG 37 T 4	2.0	6.9	0.8	0.20	1.0	

Note: CG 33 H, for example, refers to the bead of the globule CG 33. Similarly, T refers to the tail. T4, T2, T3, T1 represent the sequence of points along the tails moving away from the head. The numbers in parenthesis are estimated errors in the velocity gradients (see text).

show very pronounced and systematic velocity shifts. In Fig. 10 the measured velocities are plotted against the distance from the head for some of these. The velocity gradients $\Delta\upsilon_m$ in kms^{-1} arcmin-^{1} were obtained by fitting straight lines which are also shown in the figure. These gradients are also listed in Table 3, along with the estimated errors in the gradients. In Fig. 11 the velocity difference between the head and the extreme end of

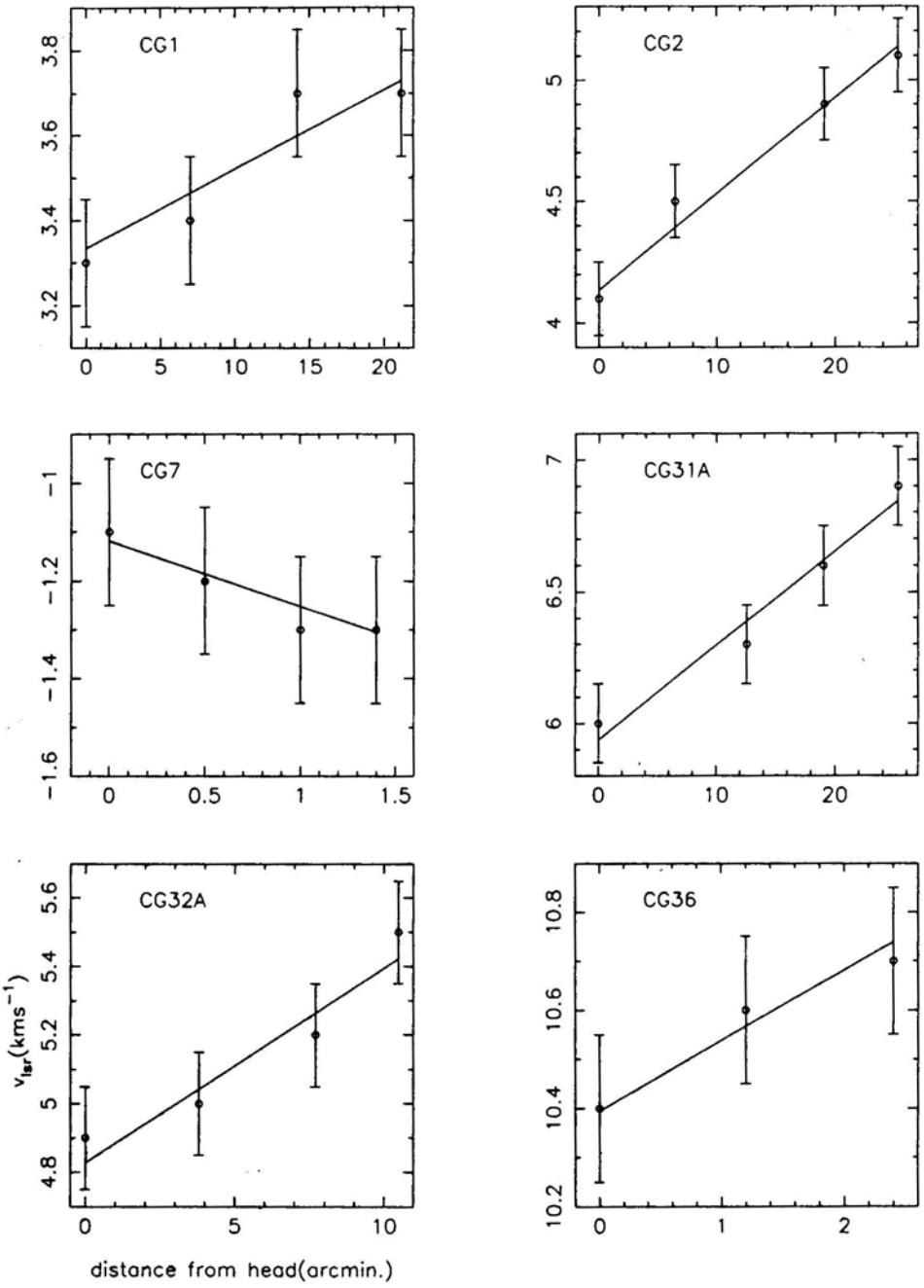

Figure 10. The velocity gradients along the tails for 6 out of 7 CGs which show pronounced gradients. The straight lines are least square fits to the data points.

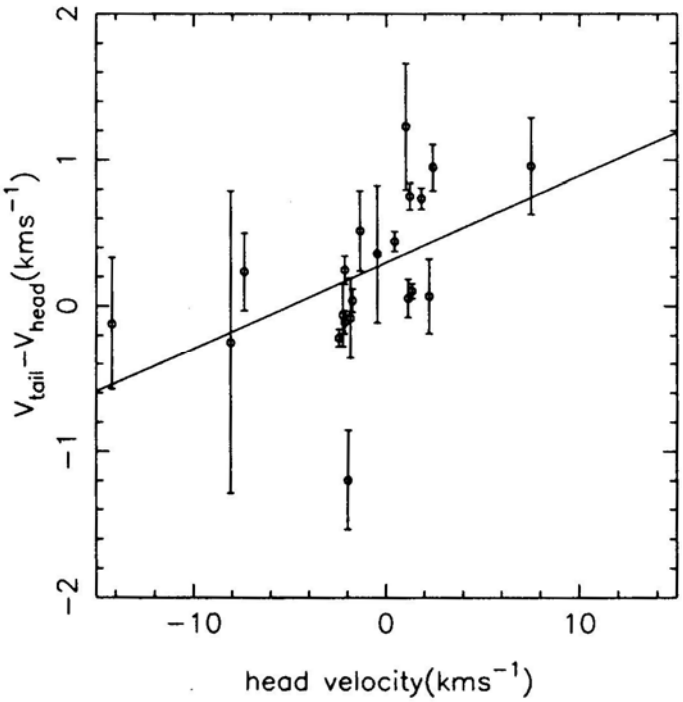

Figure 11. The difference in velocities between the ends of the *tails* and the respective *heads* plotted against velocities of the heads of the CGs.

the tail is plotted against the velocity of the head for all the 21 CGs. More precisely, the ordinate is calculated as the product of the velocity gradient along the tail and the tail length. The velocity differences so calculated are affected less by errors in the individual measurements. As may be seen, the data points fall approximately on a straight line passing close to the origin. This implies that the gas at the ends of the tails is moving faster than the heads and in the same direction as the heads.

If we assume that the tails are formed due to the stretching effect of these velocity differences over the course of time, one can calculate an age for the tails as the time taken for the presently observed velocity difference to result in an elongation equal to the measured tail length. Since we have only the *radial* component for the velocity differences and the *transverse* component of the tail lengths, the calculated ages suffer from projection effects. Figure 12 shows the distribution of the estimated apparent ages of the tails in millions of years; a distance of 450 pc has been assumed. The apparent age is related to the real age through the relation

$$t_{\text{apparent}} = t_{\text{real}} \times \tan\theta \tag{3}$$

where θ is the angle between the tail and the line of sight. Since most of the CGs are towards the periphery we believe that most CGs have $\theta > 45°$. So the apparent age represents an over estimate of the real age. We feel that ~ 3 M yrs is a reasonable estimate for the ages of the tails.

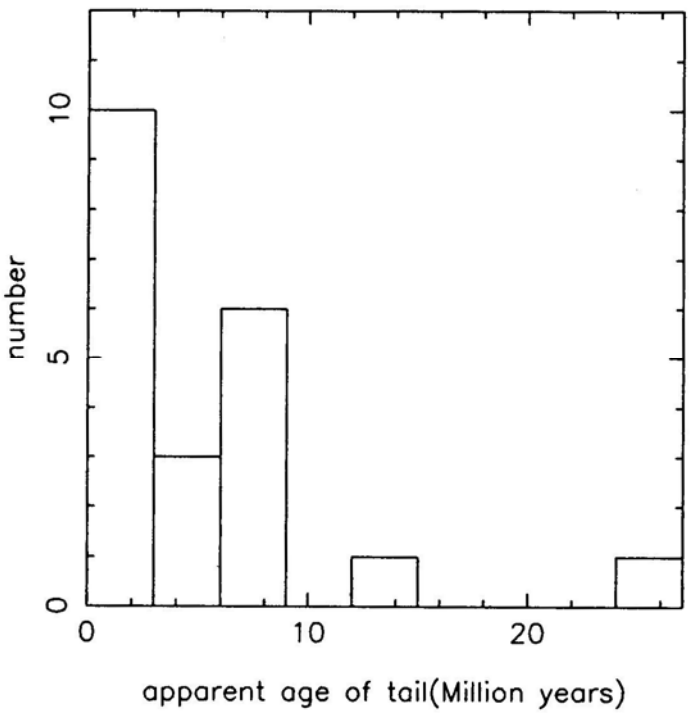

Figure 12. A histogram of the apparent *tail stretching ages* as the time required for the velocity difference between the heads and the tail-ends of the CGs to stretch the globules to their observed lengths.

8. Discussion and summary

The main results obtained in the previous two sections are the following:

(i) The system of cometary globules in the Gum Nebula appears to be expanding from a common center. The *expansion age* is ~ 6 M yr.
(ii) The observed velocity gradients along the tails of the globules suggest a *stretching age* for the tails of ~ 3Myr.

We now wish to discuss several scenarios that may have a bearing on the above two results. The rough agreement between the expansion age and the ages of the tails suggests that both the formation of the tails and the expansion of the globules may be due to a common cause. The presence of young stars in this region with estimated ages ranging from 10^5 to a few 10^6 years is an important clue. Some of these are embedded in the heads of the CGs, while others are isolated. CG 1 has an embedded star with age ~ 10^6 yrs (Brand *et al.* 1983, Reipurth 1983), and the embedded IR source CG 30IRS4 in CG 30 has an age ~ 10^6 yrs (Pettersson, 1984). The dynamical ages of the bipolar outflows associated with HH 46–47, HH 120 and HH 56–57 are ~10^5 yrs (Olberg *et al.* 1988). All these strongly point to the possibility that the processes responsible for the expansion of the globules as well as their cometary appearance have also triggered star

formation in some of them. The various possible mechanisms are (i) supernova explosion(s), (ii) radiation from massive stars found in the central region, and (iii) stellar wind from these massive stars. Before discussing each of these scenarios it would be useful to have an estimate of the kinetic energy of a typical globule and its momentum. Assuming a typical CG mass ~20$M_\odot$ (Harju *et al.* 1990; Sridharan 1992) and an expansion velocity of 12 kms^{-1} the kinetics energy is ~ 3 $\times 10^{46}$ ergs per globule and its momentum ~5 $\times 10^{40}$gm cms^{-1} We now proceed to make simple estimates for energy and momentum that can be imparted to globule from each of the processes mentioned above.

8.1 *Supernova Explosion*(*s*)

According to prevalent opinion the Gum Nebula is an old supernova remnant with an age ~ 10^6 yrs (Reynolds 1976; Leahy, Nousek & Garmire 1992). Therefore it is natural to ask if the original explosion that created the Gum Nebula could itself be responsible for the observed properties of the system of CGs. Assuming an ejected mass of $8M_\odot$, and an energy of explosion 5×10^{51} ergs and a typical CG size of 0.5 pc, we estimate that a typical CG has to be not more than a few pc from the explosion center in order to intercept sufficient momentum. This is a plausible scenario but it should be pointed out that the center of the Gum Nebula shell is 4.5° north of the *center* derived from the tail directions of the CGs. However, we would not like to over-stress this point because of the inherent difficulties in determining the center of explosion of such an old SNR. A more serious difficulty is the following: Although the original explosion could have caused the expansion of the system of CGs and the observed tail structures, the presently observed ionised bright rims cannot be attributed to it, as argued before in section 3 in a similar context.

8.2 *Radiation Pressure*

The most massive star in the region is ζ Pup (O4f) and therefore is the most significant source of photons for exerting radiation pressure. Its luminosity is 9×10^5 $L_\odot$ (Bohannan *et al.* 1986). The CG closest to ζ Pup is at a distance of 40 pc from it. For a typical CG size of 0.5 pc, we estimate that over 6 million years (the expansion age) the total kinetic energy and momentum acquired by a CG would be 3 $\times 10^{48}$ ergs and 10^{38} gmcms^{-1}, respectively. Even if we assume that the *CG* was much bigger to start with, and include the radiation from the other stars as well, the momentum imparted will fall short of the required 5 $\times 10^{40}$ gmcms^{-1}. In this estimate we have assumed 100% efficiency of momentum transfer from the photons to the CG. We therefore conclude that radiation pressure cannot be the sole cause for the expansion of the system.

8.3 *Stellar Wind*

Both Wolf-Rayet stars and O type giants are known to have strong stellar winds reaching terminal velocities upto 3000 kms^{-1} with mass loss, rates as high as 10^{-5}

$M_{\odot}yr^{-1}$. The stellar wind from ζ Pup has a velocity of 2600 kms^{-1} and the mass loss rate is 5×10^{-6} $M_{\odot}$ yr^{-1} (Bohannan *et al.* 1986). We estimate the energy and momentum intercepted to be 6×10^{47}ergs and 10^{38} gm cms^{-1}, respectively, over 6 million years. Stellar wind from γ^2 Vel will merely double these numbers and the momentum available will be less by an order of magnitude even given the assumed 100% efficiency of conversion of the stellar wind momentum to cloud momentum.

8.4 *Rocket Effect*

Finally, we consider the rocket effect resulting from the anisotropic expansion of the hot ionised gas from the bright rims first proposed by Oort and Spitzer (1955) for accelerating interstellar clouds. Reipurth (1983) has estimated that ζ Pup alone can easily account for observed ionisation level (n_e ~100 cm^{-3}) at the bright rims. Using mass loss rates derived by Reipurth (1983) and an expansion velocity of the hot gas of $10kms^{-1}$ (velocity of sound in the bright rim) we estimate the total momentum acquired by a typical globule due to the rocket effect operating for 6 million years to be ~ 10^{42} gm cms^{-1} the required momentum being ~5 $\times 10^{40}$ gm cms^{-1}. If we include γ^2 Vel and the other B stars, the clouds can be easily accelerated to the observed velocities even with larger initial masses. From the above discussion it appears that the only plausible mechanism which can explain both the bright rims and the expansion velocities is the heating caused by radiation (and possibly stellar wind) from the stars in the central region and the consequent rocket effect. In this paper we do not intend to go into the details of the energetics or the mechanism of formation of the tails. This we propose to do in a subsequent paper. We mention in passing that Bertoldi and McKee (1990) have shown that UV radiation and stellar wind can result in molecular clouds developing tail-like structures.

If one accepts this scenario, viz, that the expansion of the system and all the other features of the CGs are due to the luminous stars in the region, then one has to explain why there is a common *center of expansion.* This is because the sources causing the rocket effect are distributed around the *center.* This suggests that the center of expansion may be associated with event(s) which may have triggered the formation of the massive stars themselves.

9. Summary

We shall now summarize our main findings. Our objective was to study the kinematics of the system of cometary globules in the Gum Nebula.Towards this aim, we measured the radial velocities of 38 globules using the $J = 1 \rightarrow 0$ line of ^{12}CO. In addition we measured the radial velocities at a few points along the tails for 21 globules. This was done to study gas motions in the tails. As argued in section 5, our observations clearly show that the kinematics of the CGs cannot be interpreted in terms of a model where galactic rotation effects dominate, as was claimed by Z83 based on their study of a smaller sample of CGs. Our study points to two clear interpretations:

1. The distribution of the radial velocities of the heads of the cometary globules, after galactic differential rotation is subtracted, is best understood in terms of an

expansion of the system about a common *center*. The data is better fit by a model in which the globules are non-uniformly distributed throughout the interior of a sphere, rather than in a shell. The expansion velocity of the outermost globules is ~ 12 kms^{-1}. The implied *expansion age* of the system is ~ 6 M yr.

2. Some of the cometary tails show systematic velocity gradients. It is interesting that the estimated age for the formation of the tails inferred from these velocity gradients is about the same (~ 3 M yr) as the expansion age.

The presence of young stars with ages ~10^5–10^6yr embedded in the heads of some of the globules suggests that their formation was triggered by the same mechanism responsible for the expansion and the formation of the tails. Regarding the underlying mechanism, whereas the supernova explosion whose remnant is the Gum Nebula might have had an important influence on the dynamics of the system of globules, it is extremely unlikely that the bright ionized rims of the CGs can be understood in terms of an event that occurred ~ 10^6yr ago.In our opinion, the origin of the motions is due to a *rocket effect* resulting from an anisotropic evaporation of gas as envisaged a long time ago by Oort & Spitzer (1955). The most likely cause for this is the UV radiation from ζ Pup, γ^2 Vel and the other early type stars in the central region.

Acknowledgements

I wish to express my sincere thanks to the members of the Millimeter–wave Laboratory and the Observatory staff of the Raman Research Institute for their enthusiastic help and support over the years. It gives me great pleasure to thank B. Ramesh, V. Radhakrishnan and G. Srinivasan for encouragement and numerous discussions, as well as for critical comments which significantly improved the manuscript. My thanks are also due to C. S. Shukre and D. Bhattacharya for their comments on the manuscript. I am grateful to an anonymous referee for pointing out an error in equation 2 in an earlier version of the paper and for suggestions to shorten the paper.

References

Bally, J., Langer, W. D., Wilson, R. W., Stark, A. A., Pound, M. W. 1991, preprint.
Bertoldi, F., McKee, C.F.1990, *Astrophys. J*, **354**, 529.
Block,D.L.1990,*Nature,* **347**,452.
Bohannan, B.,Abbot, D.C,Voels, S. A.,Hummer, D.G.1986, *Astrophys. J*., **308**, 728.
Bok, B. 1978, *Publ. astr. Soc. Pacific*, **90**, 489.
Brand, P. W. J. L, Hawarden, T. G., Longmore, A. J., Williams, P. M., Caldwell, J. A. R. 1983, *Mon. Not. R. astr. Soc*.,**203**, 215.
Brandt, J. C, Stecher, T. P., Crawford, D. L, Maran, S. P. 1971, *Astrophys. J.* (*Letters*), **163**, L99.
Bruhweiler, F. C.1983,*Comments Astrophys*., **10**,1.
Caswell, J. L., Lerche, I.1979, *Mon. Not. R. astr. Soc*., **187**, 201.
Cernicharo, J., Bachiller, R., Duvert, G., Gonzalez-Alfonso, E., Gomez-Gonzalez, J. 1991, *Astr. Astrophys*., accepted.
Claria, J. J. 1982, *Astr. Astrophys. Suppl*., **47**, 323.
Dibai, E. A.1963, *Soviet Astr–A J*, **7**, 606.
Dubner, G. M., Arnal, E. M.1988, *Astr. Astrophys. Suppl*., **75, 363**.
Duvert, G., Cernicharo, J.¦ Bachiller, R., Gomez-Gonzalez, J.1990, *Astr. Astrophys*., **233**, 190.
Eggen, O. J. 1980, *Astrophys. J*., **238**, 627.

Goss, W. M., Manchester, R. N., Brooks, J. W., Sinclair, M. W., Mansfield, G. A., Danziger, I. J. 1980, *Mon. Not. R. astr. Soc*., **191**, 537.
Graham, J. A. 1986, *Astrophys. J*., **302**, 352.
Graham, J. A., Heyer, M. H. 1989, *Publ. astr. Soc. Pacific*, **101**, 573.
Green, D. A. 1984, *Mon. Not. R. astr. Soc*., **209**, 449.
Gum, C. S. 1952, *Observatory*, **72**, 151.
Gum, C. S.1955, *Mem. R. astr. Soc*., **47**,155.
Harju, J., Sahu, M., Henkel, C, Wilson, T. L., Sahu, K. C, Pottasch, S. R. 1990, *Astr. Astrophys.*, **233**, 197.
Hawarden, T. G., Brand, P. W. J. L. 1976, *Mon. Not. R. astr. Soc*., **175**, 19P.
Kerr, F. J., Lynden-Bell. D. 1986, *Mon. Not. R. astr. Soc*., **221**, 1023.
Leahy, D. A., Nousek, J., Garmire, G. 1992, *Astrophys. J*., **385**, 561.
May, J, Murphy, D. C, Thaddeus, P. 1988, *Astr. Astrophys. Suppl*.,**73**, 51.
Milne, D. K. 1979, *Austr. J. Phys*., **32**, 83.
Murphy, D. C. 1985, Ph.D. Thesis, Massachusetts Institute of Technology.
Olberg, M., Reipurth, B., Booth, R. S. 1988, in Symposium on Physics and Chemistry of *Interstellar Molecular Clouds: mm and Sub-mm Observations in Astrophysics.* Eds G. Winnewisser & J. T. Armstrong, (Heidelberg: Springer Verlag), p. 120.
Oort, J. H., Spitzer, L. 1955, *Astrophys. J*., **121**, 6.
Patel, N. A. 1990, Ph. D. Thesis, Indian Institute of Science, Bangalore.
Pettersson, B.1984, *Astr. Astrophys.*, **139**, 135.
Pettersson, B.1987, *Astr. Astrophys*.,**171**, 101.
Pettersson, B. 1991, in *Low Mass Star Formation in Southern Molecular Clouds*, Ed. B. Reipurth, ESO Scientific Report No. 11, p. 69.
Reipurth, B.1983, *Astr. Astrophys*., **117**, 183.
Reynolds, R. J. 1976, *Astrophys. J*., **206**, 679.
Sahu, M., Pottasch, S. R., Sahu, K. C, Wesselius, P. R., Desai, J. N. 1988, *Astr. Astrophys*., **195**, 269.
Sandford, M. T., Whitaker, R. W, Klein, R. I. 1982, *Ap. J.*, **260**, 183.
Sandqvist, Aa. 1976, *Mon. Not. R. astr. Soc.*,**177**,69P.
Schwartz, R. D. 1977, *Astrophys. J.* (*Letters*), **212**, L25.
Sridharan, T. K. 1992, in preparation.
Srinivasan, G., Dwarakanath, K. S. 1982, *J. Astrophys. Astr.* **3**, 351.
Srinivasan, M., Pottasch, S. R., Sahu, K. C, Pecker, J.-C. 1987, ESO Messenger, No. 51,11.
Sugitani, K., Fukui Y., Mizuno, A., Ohashi, N. 1989, *Astrophys. J.* (*Letters*), **342**, L87.
Sugitani, K., Fukui, Y., Ogura, K. 1991, *Astrophys. J. Suppl*, **77,** 59.
Wallerstein, G., Silk, J., Jenkins, E. B. 1980, *Astrophys. J*., **240**, 834.
Winkler, P. F., Tuttle, J. H., Kirshner, R. P., Irwin, M. J. 1988, in *Supernova Remnants and the Interstellar Medium*, Eds R. S. Roger & T. L. Landecker, (Cambridge: Cambridge University Press), p. 65.
Woodward, R. P. 1976, *Astrophys. J*., **207**, 484.
Woodward, R. P. 1979, in *Large Scale Characteristics of the Galaxy, IAU Symp.* **84**, Ed W. B. Burton, (Reidel, Dordrecht, Holland), p. **159**.
Zarnecki, J.C,Culhane, J.L,Toor, A., Seward, F. D.,Charles, P. A. 1978, *Astrophys. J.*(*Letters*), **219**, L17.
Zealey, W. J., Ninkov, Z., Rice, E., Hartley, M., Tritton, S. B. 1983, *Astrophys. Letters*, **23,**119. (Z83).

J. Astrophys. Astr. (1992) **13,** 241–265

SiO Maser Emission and the Intrinsic Properties of Mira Variables

Nimesh A. Patel[1,2], Antony Joseph & R. Ganesan *Raman Research Institute, Bangalore 560 080*

Received 1992 June 15; accepted 1992 August 17

Abstract. This paper presents observations of SiO maser emission from 161 Mira variables distributed over a wide range of intrinsic parameters like spectral type, bolometric magnitude and amplitude of pulsation. The observations were made at 86.243 GHz, using the 10·4 m millimeter-wave telescope of the Raman Research Institute at Bangalore, India. These are the first observations made using this telescope. From these observations, we have established that the maser emission is restricted to Miras having mean spectral types between M6 and M10. The infrared period-luminosity relation for Mira variables is used to calculate their distances and hence estimate their maser luminosities from the observed fluxes. The maser luminosity is found to be correlated with the bolometric magnitude of the Mira variable. On an H–R diagram, the masing Mira variables are shown to lie in a region distinct from that for the non-masing ones.

Key words: stars–SiO masers—stars–long period variables—star–slate type—masers–SiO—radio lines–molecular

1. Introduction

It is well known for more than a decade now, that many oxygen-rich Mira variables exhibit the SiO maser phenomenon. This emission has been observed in rotational transitions of excited vibrational states upto $v = 3$, (Alcolea, Bujarrabal & Gallego 1989; Jewell *et al.* 1985). One of the basic questions that has remained poorly investigated is that of the relationship between the maser emission and the intrinsic properties of the Mira variables. This question has a bearing on the understanding of both. So far, about 190 late-type stars have been observed by millimeter wave telescopes, and about 40 per cent of them have shown maser emission (Engels & Heske 1989). Preliminary attempts at studying the correlation of the maser power with spectral type were made by Cahn (1977) and Spencer *et* al. (1977).

Cahn (1977) reported a correlation between the absolute maser luminosity and the spectral type at maximum light and concluded that a Mira variable of any mean spectral type attains maximum value of maser power on approaching the zero phase of pulsation corresponding to the maximum light. Then, knowing the spectral type

[1] Also Joint Astronomy Programme, Indian Institute of Science Bangalore 560 012.

[2] Present Address: Five College Radio Astronomy Observatory, University of Massachusetts, Amherst 01033, Massachusetts, USA .

and the pulsational phase of the star, one can predict its maser power, and use its measured value to obtain the distance to the Mira variable. The range of spectral types covered by Cahn was from M6 to M10, and 15 sources were considered in his study. No negative detections were included. Subsequently, Dickinson *et al.* (1978), found seven new Mira variables to be masing, and noted that all of them had spectral types later than M4. Two of these, i.e. Y Cas and RT Aql, were observed at near zero phase and allowed easy confrontation with the above mentioned correlation. While Y Cas fitted with the correlation, RT Aql did not. The dependence of maser luminosity on spectral type earlier than M6, not considered by Cahn, remained unanswered due to lack of adequate observations.

Spencer *et al.* (1977) noted that at spectral types near M8, the probability for a Mira variable to show SiO maser emission is greater than 40 per cent. Their sample consisted of 81 stars with very few objects earlier than M6. Their detection limit was 30 Jy and their conclusions were based on fluxes, without taking distances into account.

In this paper, we report observations of 161 (mostly Mira) variables made at 86.243 GHz corresponding to the J:2→ 1, v=1 transition in SiO. One of the motivations of these observations was to study the dependence of the SiO maser luminosity on intrinsic properties of Mira variables. Therefore, we selected the sources to cover a wide range in spectral type. These observations are the first ones made using the Raman Research Institute (RRI) 10.4 m telescope at Bangalore, India. The method of observation and the instrumental characteristics are briefly described in section 2, (for more details see Patel 1990). In section 3, we present the list of sources we have observed, and the results of our observations. The integrated fluxes are converted to luminosities in section 4. The correlations between the maser luminosity and the intrinsic properties of Mira variables, that have emerged from our observations, are described in section 5. Finally, in section 6, we discuss these results and attempt their interpretation.

2. Observations and results

2.1 *Observations using the RRI 10.4 m Telescope*

The 10.4 m millimeter-wave telescope at the Raman Research Institute in Bangalore, is a Cassegrain type antenna on an altitude-azimuth mount, with the receiver at the Nasmyth focus. This telescope is located on campus, at a latitude = 13° 00′ 44.46″, longitude = 77° 34′ 59.67″, and at an elevation of 930 meters above mean sea level. The front-end receiver is a wave-guide mounted Schottky-barrier diode mixer followed by an IF Amplifier at 1.4 GHz, both cooled to about 20 K. The radiation is coupled by a lens to a quasi-optical diplexer which is closely attached to the dewar containing the mixer and the IF amplifier. The local oscillator is a Gunn-oscillator tunable from 85 to 120 GHz. The back-end used for the SiO observations consisted of a synchronous-detector for continuum measurements (for pointing and gain calibrations) and the following spectrometers: a 256 channel filter-bank having a resolution of 250 KHz (0.87 km/s at 86 GHz), and an acousto-optical spectrometer having an effective resolution of 210 KHz (0.71 km/s at 86 GHz), over a total bandwidth of 120 MHz.

The observations reported here were made during three seasons in 1988, 1989 and 1990. The typical values of double side-band system temperatures at zenith were

between 400 and 500 K. The observations were calibrated using a chopper-wheel positioned between the diplexer and the lens. The zenith optical depth $\tau_0(z)$, frequently monitored by taking dip scans on the sky, had typical values between 0.1 and 0.5. The r.m.s. pointing error was about 5 arcsec, as found from continuum scans of Jupiter and 5-point grids made on strong SiO sources. The aperture efficiency η_A, was calculated from continuum scans taken on Jupiter and Venus. The mean value of η_A was 0.45, during 1988 and 1989; for the 1990 data, η_A was found to be a function of elevation, due to a possible misalignment in the feed-horn inside the dewar. The value of η_A during this season was between 0.3 and 0·4. The measured fluxes of sources observed during this season, have been corrected for this effect. Furthermore, all observations made between IST 12 hrs to 18 hrs have been corrected for a drop in the gain of the telescope, due to the differential heating of the dish by the Sun. The reduction in the sensitivity of the telescope during daytime is about 20 per cent.

The variations in the detected power due to the inhomogeneous and varying atmosphere, and due to gain variations in the receiver, were cancelled by beam-switching which was achieved by tilting the tertiary mirror. The amount of beam thrown on the sky was about 80 arcsec (± 40 arcsec about the center of the beam).

Observations were made using a dual beam switching method. In this method two beam switched spectra are acquired, in which the respective reference positions straddle the source in azimuth. A residual ripple with a peak to peak antenna temperature of about 0.5 to 1K, which was present in each of these spectra, can be cancelled by averaging, leading to a very flat baseline as seen in Fig. 1.

2.2 *Selection of Sources*

The observed Mira variables were selected mostly from The General Catalogue of Variable Stars (Kholopov 1985, henceforth GCVS) and in a few cases from Gezari, Schmitz & Mead (1984). Since one of our aims was to check the hypothesis that SiO masers exist only in very late-type Mira variables (with mean spectral type greater than M6), we included a substantial number of objects at spectral types earlier than M6. We also attempted to select those objects which have been well studied at near infrared wavelengths, so that we can obtain information about the variation of spectral types during pulsation, and its relation to the maser emission. Thus, we had many objects which are common to the catalogue of Lockwood (1972). To avoid very long integrations, an attempt was made to exclude objects that are at a distance greater than 1 kpc from the Sun, by restricting the visual magnitude to lie below 15 magnitudes.

The list of selected objects along with their intrinsic properties is given in Table 1 in cols. 2–7. Among these, period was available for 143 objects. Fig. 2 shows their distribution in period. For 28 sources the spectral type was either unknown or not M. The distribution of the remaining 133 sources in the mean spectral type is shown in Fig. 3. The similarity of these histograms with the corresponding ones for the galactic Mira variables (Ikaunieks 1975), shows that the sample we have selected is unbiased.

The phases of pulsation (ϕ) and the visual amplitude of pulsation (Δm_v) for some of our sources were provided by the American Association of Variable Star Observers (AAVSO). These occur in cols. 8 and 17 of Table 1.

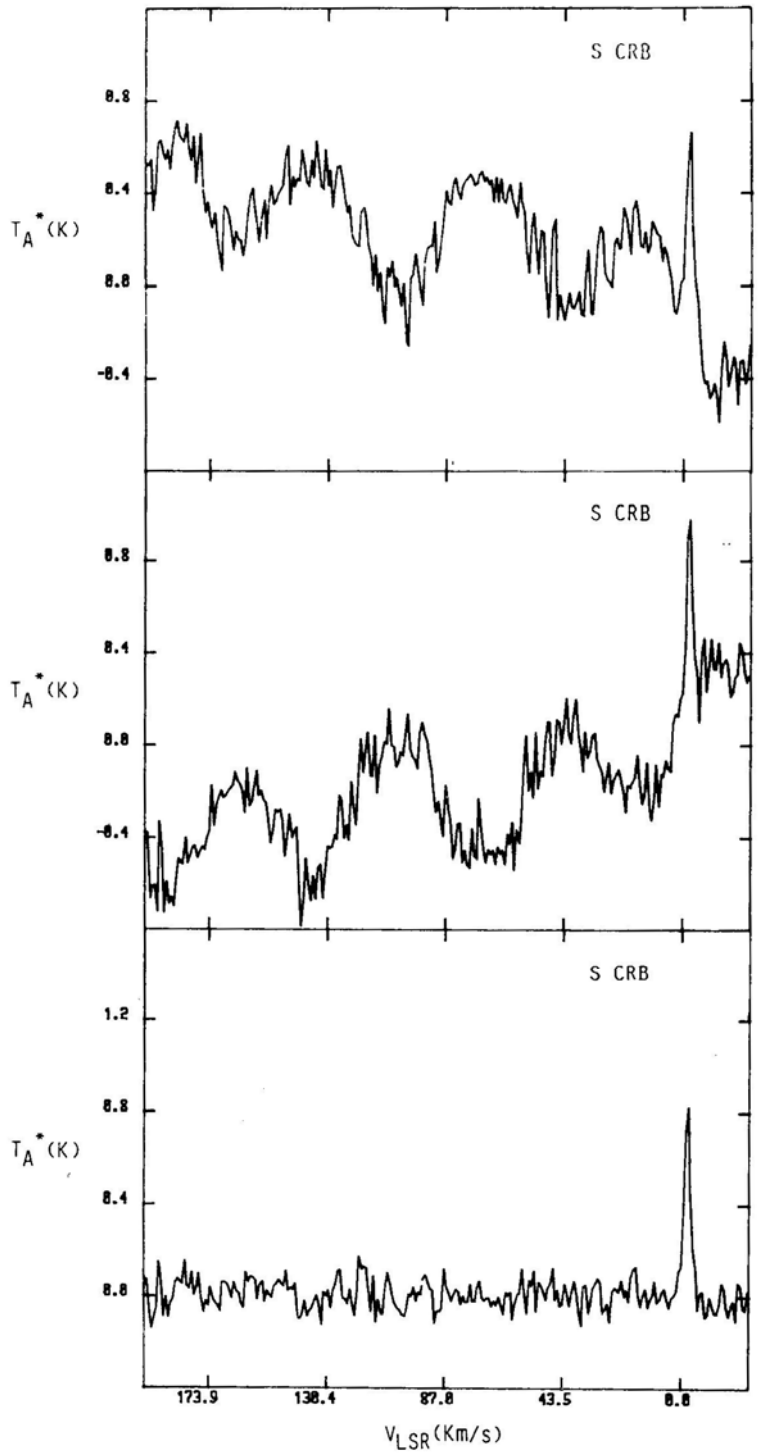

Figure 1. Beam-switched spectra acquired with offsets in azimuth, to one side (top panel), to the opposite side (middle panel) and their average (bottom panel).

Table 1: Catalogue of observed sources

No.	Source	α(1950)	δ(1950)	Variable type	Spectral type	Period (days)	ϕ	JD244—	Ta^* (K)	V km/s	ΔV km/s	σ	$\sigma(fit)$	Distance (pc)	SiO lum. phot./s	Δm_v AAVSO	Log. $T_{eff.}$
1	AFGL 3068	23 16 42.4	+16 55 10					7991				0.11					
2	AFGL1977	17 29 42	+17 47 36					7983				0.10					
3	And W	02 14 23.1	+44 04 30	M	S6.1E-S9.2E/M4-M10	396	0.54	7272				0.07				6.3	3.45
4	And Z	23 31 15.4	+48 32 32	ZAND	M2III+B1EQ			7260				0.05					3.55
5	Ant V	10 18 54.9	−34 32 44	M	M7IIIE	303	0.46	7229				0.06					3.45
6	Aqr R	23 41 14.1	−15 33 40	M	M5E-M8.5E+PEC	387	0.46	7229	0.54	−27.8	4.5	0.04	0.08	424	0.45	3.8	3.46
7	Aqr EP	21 43 56.8	−02 26 39	SRB	M8III	55		7991				0.096					3.39
8	Aql RT	19 35 36.0	+11 36 16	M	M6E-M8E(S)	327	0.95	7559				0.04		480	< 0.07	5.6	3.45
	Aql RT							7986				0.10		480	< 0.21		
9	Aql MU	19 39 52	+13 13 12	M	M4	142	0.10	7562				0.05					3.53
10	Aql V450	19 31 18	+05 21 24	SRB	M5III-M8III	64		7986				0.087		121	< 0.01		3.47
11	Ari R	02 13 16.0	+24.49 28	M	M3E-M6E	187	0.59	7233				0.05		1377	< 0.87	5.0	3.52
12	Ari U	03 08 16	+14 36 48	M	M4E-M9.5E	371	0.74	7560				0.06		698	< 0.21		3.46
13	Aur R	05 13 15	+53 31 57	M	M6.5E-M9.5E	457	0.11	7280				0.05		255	< 0.03	7.0	3.39
	Aur R							7986				0.14		255	< 0.07		3.57
14	Aur U	05 38 51.0	+32 00 46	M	M7E-M9E	408	0.84	7233				0.05		495	< 0.09	5.5	3.39
15	Aur UV	05 18 33.3	+32 27 51	M	C6,2-C8.2	394	0.68	7240				0.05		766	< 0.22		
16	Aur YY	06 00 35	+42 01 30	M	M5E	337	0.12	7548				0.05					3.51
17	Aur EY	04 49 39	+41 42 00	M	M6	270	0.96	7546				0.05					3.46
18	Aur NV	05 07 20	+52 48 48	M	M10	635		7988	0.34	3.5	2.3	0.08	0.09	1360	2.07		3.21
19	Boo R	14 34 59	+26 57 12	M	M3E-M8E	223		7988				0.10		667	< 0.44		3.50
20	Boo Z	14 04 04.2	+13 43 20	M	M5E-M6E	281	0.80	7235				0.05		1714	< 1.08	5.5	3.50
21	Boo RX	14 21 56.6	+25 55 47	SRB	M6.5E-M8IIIE	340	0.73	7229	0.20	−38.0	6.0	0.05	0.10	138	0.02	1.5	3.43
22	Cae R	04 38 43.9	−38 20 02	M	M6-M9*	391	0.65	7232	0.20	6.6	8.9	0.07	0.07	457	0.39	5.2	3.42
23	Cam W	06 19 05.0	+75 28 48	M	M7	284	0.43	7288				0.09					3.45
24	Cam TX	04 56 42	+56 06 42	M	M8-M10	557	0.40	7223	0.96	8.9	4.5	0.06	0.07	317	0.57		3.31
25	Cnc R	08 13 48.4	+11 52 51	M	M6E-M9E	362	0.27	7228	1.20	13.8	3.3	0.08	0.20	234	0.23	4.4	3.42
26	Cnc T	08 53 48.9	+20 02 28	SRB	C3.8-C5.5	482		7235	0.26	−3.5	1.8	0.09	0.09	655	0.20		
27	Cnc W	09 06 58	+25 27 06	M	M6.5E-M9E	393	0.33	7563				0.05		594	< 0.13		3.41
28	Cnc X	08 52 33.9	+17 25 21	M	C5.4(N3)	195	0.56	7250				0.05		262	< 0.03	1.3	
29	Cnc RR	08 08 05.0	+23 17 48	M	M3E	298	0.58	7249				0.04				5.5	3.54
30	Cnc RS	09 07 37.8	+31 10 05	SRC?	M6	120		7245				0.06		83	< 0.01	1.5	3.49

Table 1: Continued

No.	Source	α(1950)	δ(1950)	Variable type	Spectral type	Period (days)	ϕ	JD244—	T_a^* (K)	V km/s	ΔV km/s	σ	$\sigma(fit)$	Distance (pc)	SiO lum. phot./s	Δm_v AAVSO	Log. T_{eff}.
31	Cnc RT	08 55 33.0	+11 02 22	SRB	M5III	60		7249				0.04		124	< 0.01	1.3	3.51
32	CvN T	12 27 44	+31 46 46	M	M6.5E	290		7986				0.074		794	< 0.45		3.47
33	CvN V	13 17 17.1	+45 47 22	SRA	M4E-M6EIII	192	0.32	7255				0.04					3.51
34	CvN TX	12 42 18	+37 02 12	ZAND	M4			7553				0.06					3.53
35	CMa SY	07 08 23	−19 45 00	M	M4-6	220	0.69	7552				0.10					3.51
36	CMa VY	07 20 53.0	−25 40 24	?	M5EIBP(C6.3)			7560	1.30	10.0	33.0	0.05	0.10			0.5	3.51
37	CMa CY	07 20 59	−25 22 18	SRA	M6	117	0.74	7548				0.06		423	< 0.08		3.49
38	CMa DN	06 53 03	−16 44 00	M	M8			7547				0.05					3.39
39	CMi S	07 30 00	+08 25 34	M	M6E-M8E	333		7986				0.097		401	< 0.13		3.45
40	CMi U	07 38 38	+08 29 54	M	M4E	414	0.64	7553				0.06		1097	< 0.53		3.53
41	Cas R	23 55 53	+51 06 36	M	M6E-M10E	430	0.10	7545	0.80	26.1	3.5	0.06	0.06	164	0.08	6.0	3.39
42	Cas Y	00 00 45.0	+55 24 21	M	M6E-M8.5E	413	0.68	7270				0.05		586	< 0.16		3.43
43	Cen Y	14 28 01.6	−29 52 33	SRB?	M4E-M7	180		7217				0.04		181	< 0.01		3.50
44	Cen RT	13 45 25	−36 36 48	M	M6-M7.5e	255	0.40	7556				0.08		920	< 0.50		3.46
45	Cen RX	13 48 29.9	−36 41 57	M	M5E	328	0.60	7567				0.04		1078	< 0.34		3.51
46	Cen TU	14 31 02.0	−31 28 30	M	M4E-M7E	294	0.74	7249				0.06					3.50
47	Cen UU	13 18 52.0	−61 02 54	M	M8E	368	0.63	7216				0.20					3.39
48	Cen VX	13 47 48.3	−60 09 59	SR	S8.5E(M4-8)	308		7258				0.09		356	< 0.08		3.46
49	Cen V423	12 02 28	−40 56 00	M		325	0.82	7562				0.06					
50	Cen V744	13 36 53.5	−49 41 48	SRB	M8III	90	0.91	7258				0.07		142	< 0.01		3.39
51	Cep μ	21 41 58.5	+58 33 01	SRC	M2EIA	730		7984	0.60	−1.9	6.7	0.18	0.19	238	0.49		3.55
	Cep μ							*	1.10	−9.7	3.2						
52	Cep T	21 08 52.7	+68 17 13	M	M5.5E-M8.8E	388	0.85	7269				0.10		178	< 0.02	4.3	3.44
53	Cet o	02 16 49.0	−03 12 12	M	M5E-M9E	332	0.21	7241	8.00	45.6	7.8	0.10	0.30	112	0.81	5.5	3.45
54	Col W	06 26 13.0	−40 04 00	M	M6E	327	0.26	7214				0.07					3.49
55	Com R	12 01 41.6	+19 03 38	M	M5E-M8EP	363	0.23	7233				0.05		980	< 0.35	5.7	3.47
56	CrB S	15 19 22	+31 32 36	M	M6E-M8E	360	0.28	7237	0.66	−1.8	3.3	0.04	0.04	323	0.24	5.6	3.45
57	CrV R	12 17 02.3	−18 58 40	M	M4.5E-M9E	317	0.95	7234				0.05		750	< 0.21	6.3	3.46
58	Crt R	10 58 05.9	−18 03 20	SRB	M7	160		7231	0.39	6.5	5.8	0.04	0.04	121	0.03		3.45
59	Crt S	11 50 11.6	−07 19 04	SRB	M6E-M7E	155		7232				0.05		285	< 0.03		3.47
60	Cyg χ	19 48 38.0	+32 47 12	M	S6.2E-S10.4E	408	0.51	7276	2.00	9.7	4.9	0.10	0.20	762	5.92	8.2	

Table 1: Continued

No.	Source	α(1950)	δ(1950)	Variable type	Spectral type	Period (days)	ϕ	JD244—	Ta^* (K)	V km/s	ΔV km/s	σ	$\sigma(fit)$	Distance (pc)	SiO lum. phot./s	Δm_v AAVSO	Log. T_{eff}.
61	Cyg R	19 35 28.7	+50 05 12	M	S2.5,9E-S6,9E	426	0.12	7237				0.08		827	< 0.40	6.4	
62	Cyg U	20 18 03.4	+47 44 09	M	C7,2E-C9,2	463	0.84	7254				0.07		736	< 0.28	3.5	
63	Cyg Z	20 00 00.0	+49 54 06	M	M5E-M9E	264	0.15	7290				0.07		752	< 0.29	4.6	3.45
64	Cyg SX	20 13 36	+30 55 03	M	M7E	411		7986				0.10		753	< 0.56		3.45
65	Cyg UX	20 53 00.0	+30 13 24	M	M4E-M6.5E	565	0.89	7216				0.23		1078	< 1.96	7.5	3.51
66	Cyg KY	20 24 06	+38 11 16	LC	M3.5IA			7986				0.14					3.53
67	Cyg V407	21 00 26.0	+45 34 36	M+NB?	MEP	745	0.82	7256				0.09					
68	Dor R	04 36 10	−62 10 30	SRB	M8IIIE	338		7985	1.60	9.7	5.1	0.18	0.22	60	0.05		3.39
	Dor R							*	0.80	2.7	5.1						
69	Dra R	16 32 31	+66 51 30	M	M5E-M9EIII	246		7979				0.09		727	< 0.37		3.45
70	Eri V	04 02 01.5	−15 51 37	SRC	M6II	97		7248				0.06		114	< 0.01		3.49
71	Eri W	04 09 23.6	−25 16 04	M	M7E-M9	377	0.39	7233				0.05		814	< 0.30	5.2	3.39
72	Eri Z	02 45 32.0	−12 40 03	SRB	M4III	80		7215				0.06		157	< 0.01	1.4	3.53
73	Gem UZ	07 10 00	+17 44 24	M	M9	349	0.89	7547				0.05					3.31
74	Gem EE	06 36 30	+13 16 48	M	M6	289	0.08	7547				0.05					3.49
75	Her T	18 07 13	+31 00 42	M	M2.5E-M8E	165		7986				0.095		1414	< 1.86		3.51
76	Her U	16 23 35.0	+19 00 24	M	M6,5E-M9,5E	406	0.56	7256	1.40	−15.7	3.2	0.05	0.08	325	0.49	5.0	3.39
77	Her RU	16 08 05.7	+25 12 01	EA	M5.5-M9.2*	485	0.52	7560				0.06		512	< 0.12	5.7	3.43
78	Her V443	18 20 05	+23 25 23	ZAND	M3EP+O			7251				0.09				0.2	3.54
79	Hor R	02 52 12	−50 05 42	M	M5E-M8E	408	0.37	7239	0.33	33.7	3.8	0.07	0.07	575	0.54	7.0	3.47
80	Hya R	13 26 58.4	−23 01 23	M	M6E-M9E	389	0.38	7210	0.40	−9.8	6.5	0.06	0.10	119	0.05	3.5	3.42
81	Hya S	08 50 57.4	+03 15 29	M	M4E-M8E	257	0.28	7228				0.07		1037	< 0.55	4.9	3.49
82	Hya T	08 53 13.7	−08 56 56	M	M3E-M9:E	299	0.20	7285				0.05		881	< 0.28	4.8	3.49
83	Hya U	10 35 04.9	−13 07 24	SRB	C6.5,3(N2)	450		7248				0.04		293	< 0.03	1.0	
84	Hya V	10 49 11.3	−20 59 03	SRA	C6,3E-C7,5E(N6E)	531	0.75	7247				0.04		348	< 0.04	3.0	
85	Hya W	13 46 12.2	−28 07 05	SRA	M7.5E-M9EP	361	0.75	7560	5.30	34.9	3.4	0.10	0.40	92	0.52	4.0	3.37
86	Hya X	09 33 07	−14 28 02	M	M7E-M8.5E	301		7981				0.085		408	< 0.11		3.41
87	Hya Y	09 48 45.0	−22 46 56	M	C5.4(N3P)	303		7229				0.06		346	< 0.05	1.0	
88	Hya RR	09 42 42.0	−23 47 120	M	M3E-M8E	343	0.62	7231				0.03		1265	< 0.35		3.50
89	Hya RT	08 27 13.0	−06 09 00	SRB	M6E-M8E	290		7244				0.06		294	< 0.04	1.7	3.45
90	Hya RU	14 08 41.0	−28 39 00	M	M6E-M8.8E	331	0.23	7230	0.32	−4.95	2.07	0.083	0.053	671	0.31	5.6	3.43

Table 1: Continued

No.	Source	α(1950)	δ(1950)	Variable type	Spectral type	Period (days)	ϕ	JD244—	Ta^* (K)	V km/s	ΔV km/s	σ	$\sigma(fit)$	Distance (pc)	SiO lum. phot./s	Δm_v AAVSO	Log. T_{eff}.
91	Hya SW	13 00 37.0	−28 50 00	M	M2E	219	0.93	7244				0.05					3.55
92	Hya TU	08 55 43.0	−00 38 12	M	M5E	277	0.21	7243				0.06					3.51
93	IR 6	17 11 56	+08 59 12					7987				0.056					
94	IRC+60169	06 30 02.0	+60 58 54					7282	0.46	−23.8	6.3	0.10	0.10				
95	IRC+70066	05 41 16	+69 56 54					7987	0.38	−2.6	4.4	0.09	0.09				
96	IRC-10414	18 20 28	−13 44 06					7981	0.24	51.6	1.6	0.07	0.07				
97	IRC-10529	20 07 46	−06 24 42					7987				0.08					
98	Leo R	09 44 52.2	+11 39 40	M	M6E-M9.5IIIE	310	0.72	7224	0.72	2.6	3.2	0.10	0.10	108	0.25	4.2	3.41
99	Leo S	11 07 58.7	+06 27 01	M	M3E-M6E:	190	0.14	7229				0.06		3308	< 4.82	3.8	3.52
100	Leo VY	10 53 26	+06 27 12	LB:	M5.5III			7229				0.05					3.50
101	LMi R	09 42 34.6	+34 44 33	M	M6.5E-M9E(TC:)	372	0.65	7210	0.20	1.5	9.4	0.06	0.08	272	0.14	6.0	3.41
102	LMi RW	10 13 19	+30 49 07	SRA	C4.3EV	640		7979				0.063		778	< 0.35		
103	Lep R	04 57 19.7	−14 52 46	M	C7.6E(N6E)	427	0.89	7237				0.05		384	< 0.07	3.0	
104	Lep T	05 02 43	−21 58 18	M	M6E-M9E	368	0.64	7232				0.05		350	< 0.04	4.6	3.42
	Lep T							7986				0.14		350	< 0.14		
105	Lep RT	05 40 28	−23 43 00	M	M9E	399	0.55	7549				0.05					3.31
106	Lep SY	06 07 28	−13 06 18	M	M5E	307	0.44	7551				0.07					3.51
107	Lib RR	15 53 27.9	−18 09 54	M	M4E-M8E	277	0.36	7219				0.05		1062	< 0.41	5.6	3.49
108	Lib RU	15 30 28	−15 09 30	M	M5E-M6E	317		7986				0.12		902	< 0.88		3.50
109	Lib FS	15 57 37	−12 12 35	M	M8.1-M9	415	0.41	7230				0.04		1275	< 0.48		3.35
110	Lup R	15 50 13.1	−36 09 02	M	M5.5-M8*	236	0.26	7218				0.10		939	< 0.65	4.0	3.46
111	Lyr V	19 07 08	+29 34 00	M	M7E	373	0.55	7293				0.10		888	< 0.58	5.1	3.45
	Lyr V							7979				0.073		888	< 0.57		
112	Lyr RW	18 43 39.0	+43 34 54	M	M7E	504	0.67	7294				0.05		1019	< 0.38	4.3	3.45
113	Mic T	20 24 51.9	−28 25 41	SRB	M6E	347		7991				0.13					3.49
114	Mic V	21 20 35.5	−40 55 18	M	M3E-M6E	381	0.15	7248				0.09		1043	< 0.72		3.59
115	Mon U	07 28 24.2	−09 40 14	RVB	F8EVIB-K0PIB(M2)	91	0.26	7238				0.04		634	< 0.12	2.0	
116	Mon ER	06 55 35	−07 59 12	M	M9:	326	0.13	7547				0.08					3.31
117	Mon FX	06 42 21.4	+09 32 12	M	M1-M8	428	0.33	7264				0.06		875	< 0.34		3.52
118	Mon GN	06 23 19	+08 05 24	M	M9:			7547				0.05					3.31
119	Mon GX	06 49 59	+08 29 06	M	M9	527	0.89	7546	0.28	3.4	4.3	0.06	0.07	921	1.06		3.31
120	Oph RS	17 47 32	−06 41 49	NR	OB+M2EP			7566				0.10					3.55

Table 1: Continued

No.	Source	α(1950)	δ(1950)	Variable type	Spectral type	Period (days)	ϕ	JD244—	Ta^* (K)	V km/s	ΔV km/s	σ	$\sigma(fit)$	Distance (pc)	SiO lum. phot./s	Δm_* AAVSO	Log. T_{eff}.
121	Oph RT	17 54 11	+11 10 30	M	M7E(C)	426		7986				0.10		817	< 0.59	5.5	3.45
122	Oph RU	17 30 29.4	+09 27 23	M	M3E-M5E	202	0.61	7250				0.05		1680	< 1.03	4.5	3.53
123	Oph V1111	18 34 57.0	+10 22 27	M	M4III-M9			7246				0.05					3.47
124	Ori S	05 26 33	−04 43 54	M	M6.5E-M9.5E	414	0.92	7549				0.05		345	< 0.04		3.39
125	Ori U	05 52 50.9	+20 10 05	M	M6E-M9.5E	368	0.24	7213	0.51	−32.9	3.3	0.16	0.08	231	0.20	5.7	3.41
	Ori U							*	0.82	−38.0	2.3						
126	Ori V	05 03 25	+04 02 12	M	M3E-M8E	264	0.38	7246				0.06		1659	< 1.21	4.7	3.50
127	Ori W	05 02 48.5	+01 06 37	SRB	C5,4(N5)	212		7245				0.06		221	< 0.02	1.8	
128	Ori DT	06 00 38.0	+13 44 24		M10	429	0.71	7246				0.10		962	< 0.68		3.21
129	Ori EP	04 48 19	+03 03 42	M	M10E	358	0.28	7246				0.07					3.21
130	Ori EU	05 12 30	+03 26 00	M	M4	328	0.90	7552				0.07					3.53
131	Peg R	23 04 08.0	+10 16 22	M	M6E-M9E	378	0.92	7272	0.37	25.7	6.5	0.06	0.10	471	0.69	5.4	3.42
132	Per S	02 19 15.1	+58 21 34		M3IAE-M7	822	0.27	7219	0.96	9.3	3.3	0.06	0.06	761	1.91	2.0	3.51
133	Per AX	01 33 06	+54 00 18	ZAND	M3IIIEP+A0	682	0.94	7551				0.09					3.54
134	Pic S	05 09 37	−48 34 00	M	M6.5E-M8III-IIE	428	0.19	7245				0.09		548	< 0.25	5.7	3.43
	Pic S							7989				0.16		548	< 0.35		
135	PSc R	01 28 03	+02 37 30	M	M3E-M6E	344		7988				0.10		916	< 1.02		3.52
136	PSc WX	01 03 48	+12 19 42	M	M8	660		7978	0.50	8.1	3.1	0.07	0.07	1129	2.71		3.39
137	Pup Z	07 30 29	−20 32 49	M	M4E-M9E	509	0.76	7561	0.26	1.9	4.5	0.06	0.07	761	0.70	6.4	3.47
138	Pyx S	09 02 53.9	−24 52 49		M3-M5*	206	0.73	7217				0.08		1372	< 1.10	5.0	3.53
139	Pyx X	09 02 53.9	−24 52 49		ME	330	0.39	7559				0.07		2120	< 2.31		
140	Sge HM	19 39 41	+16 37 33					7256				0.10					
141	Sgr RR	19 52 49	−29 19 16	M	M4E-M9E	336	0.60	7290				0.06		472	< 0.10	6.4	3.47
	Sgr RR							7988				0.12		472	< 0.22		
142	Sgr VX	18 05 05.0	−22 14 00		M4EIA-M10EIA	732	0.12	7561	2.00	6.7	12.5	0.05	0.30	410	4.38	3.5	3.45
143	Sco RR	16 53 26	−30 30 06	M	M6II-IIIE-M9	281	0.59	7561				0.05		243	< 0.02	5.9	3.42
	Sco RR							7988				0.08		243	< 0.04		
144	Sco AH	17 08 01.9	−32 15 51		M4E-M5IA-IAB	714	0.53	7283	0.50	−13.7	5.5	0.08	0.10	533	0.81		3.52
145	Ser S	15 19 18.9	+14 29 33		M5E-M6E	372	0.90	7283				0.10		728	< 0.39	4.8	3.50
146	Ser WX	15 25 31.7	+19 44 20		M8E	425	0.64	7238				0.10		1197	< 1.05		3.39
147	Tau R	04 25 36.0	+10 03 30	M	M5E-M9E	321	0.21	7268				0.05		439	< 0.09	5.6	3.45
148	Tau NML	03 50 40.0	+11 15 00	M	M6E-M10E	470	0.63	7210	2.30	33.3	3.6	0.07	0.40	262	0.59	4.6	3.39
149	UMa R	10 41 08	+69 02 18	M	M3E-M9E	302		7983				0.093		313	< 0.07		3.49
150	UMa T	12 34 07	+59 45 42+59	M	M4IIIE-M7E	257		7979				0.09		1018	< 0.75		3.50

Table 1: Continued

No.	Source	α(1950)	δ(1950)	Variable type	Spectral type	Period (days)	ϕ	JD244—	Ta^* (K)	V km/s	ΔV km/s	σ	$\sigma(fit)$	Distance (pc)	SiO lum. phot./s	Δm_v AAVSO	Log. T_{eff}.
151	UMa ST	11 25 06.8	+45 27 38		M4-M5III	110		7256				0.04		214	< 0.01	1.1	3.52
152	UMi S	15 31 27	+78 48 08	M	M6E-M9E	331		7982				0.14		369	< 0.14		3.42
153	UMi RR	14 56 47	+66 07 54	SRB	M5III	43		7979				0.085		57	< 0.01		3.51
154	Vir R	12 35 58	+07 15 45	M	M3.5IIIE-M8.5E	146	0.17	7209				0.05		507	< 0.09	4.6	3.49
	Vir R							7982				0.092		507	< 0.22		
155	Vir S	13 30 24	−06 56 18	M	M6IIIE-M9.5E	375	0.63	7565				0.08		416	< 0.10	5.7	3.41
	Vir S							7987	0.28	9.3	3.3	0.08	0.08	416	0.21		
156	Vir RT	13 00 06	+05 27 18	SRB	M8III	155		7235	0.46	10.9	2.4	0.06	0.06	137	0.02		3.39
157	Vir RU	12 44 28.9	+04 25 49		C8,1E(R3EP)	433	0.55	7561				0.03		573	< 0.07	4.0	
158	Vir SS	12 22 46	+01 04 28	SRA	C6.3E(NE)	364	0.19	7249				0.05		463	< 0.10	2.1	
	Vir SS							7987				0.10		463	< 0.17		
159	Vir SW	13 11 29.7	−02 32 31		M7III	150	0.57	7244	0.31	−13.9	6.5	0.05	0.06	86	0.02	1.0	3.45
160	Vir BK	12 27 48.0	+04 41 33		M7III	150	0.48	7249				0.05		134	< 0.01		3.45
161	Vul R	21 02 09	+23 37 18	M	M3E-M7E	137		7988				0.073					3.51

Notes: Entries in cols. 2–7 are obtained from Kholopov (1985) and Gezari, Schmitz & Mead (1984).
Entries in cols. 8 and 17 are from the data provided by AAVSO (see text section 2.2).
For entries in cols. 15 and 16 see text section 3.
For entries in cols. 18 see text section 4.1.
*against JD denotes a second feature of the same observation.

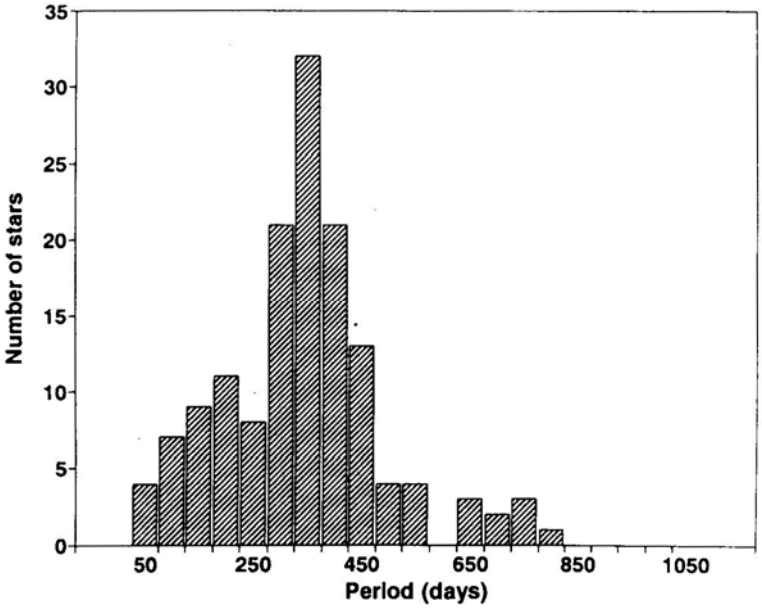

Figure 2. Distribution in pulsation period of the observed sources.

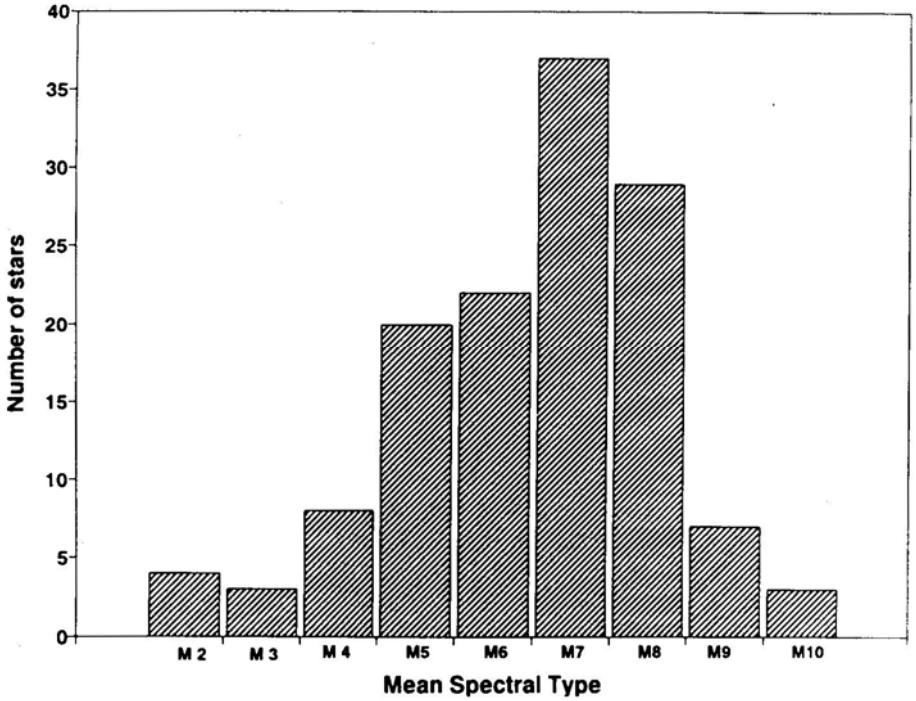

Figure 3. Distribution in mean spectral-types of the observed sources.

2.3 *Results*

The results of our observations are presented in cols. 10–14 of Table 1. Of the 161 sources observed, 37 showed SiO maser emission. The fluxes ranged from 0.2 to 11K (16 to 880 Jy) and the full width at half maximum from 1 to 10km/s. The 1σ noise level was 0.04 to 0.11 K (about 3 to 9 Jy).

Among the positive detections, the following seven sources are new detections at 86 GHz not found in the compilation of Engels (1979), or Engels & Heske (1989): R Cae, T Cnc, R Crt, R Hor, RU Hya, S Vir and SW Vir. Note that T Cnc is a C type star (Vardya 1989). In these stars the oxygen to carbon ratio is < 1 and one expects SiO to be a less dominant Silicon species compared to say SiS (Sahai 1987); thus the presence of SiO maser emission in T Cnc is surprising (see also Lloyd Evans 1990). The spectra of some new detections, and of one negative detection baseline are shown in Fig. 4(a) & (b). The parameters listed in cols. 9–14 of Table 1 are obtained by fitting gaussians to the line-profiles. In case of multiple peaks within the profile, we have fitted gaussians to the individual peaks, where we could discern the peaks to be separate. In blended features, we have not fitted more than one gaussian. To obtain upper limits on fluxes and luminosities for non-detections, we have used a mean value of 5 km/s for the line-width, and 3σ, for an upper limit in antenna temperature, where σ is the r.m.s. noise in the baseline.

3. Distances of the Mira variables

As a first step towards knowing the relationship between the maser phenomenon and the properties of the Mira variables, we convert the observed maser fluxes into luminosities.

To calculate the true maser luminosity, one needs to know or assume something about its isotropy. According to Alcock and Ross (1986), the maser emission is likely to be highly anisotropic. VLBI observations indicate emission from spots located around the star over a region of angular dimensions about 5 times the stellar radius (Moran *et al.* 1979; Lane 1984, McIntosh *et al.* 1989). It is likey that the emission is beamed and some of it is aimed towards us appearing as spots. However, at present there is not enough data (e.g., time-monitoring with VLBI), to conclude anything about the geometry of the total emission from the source. We can do no better than to assume that no matter from which direction one is looking at the Mira variable, one would see more-or-less the same fraction and that the filling factor is the same for all Miras. We have determined the distances to the Mira variables in our sample and obtained the maser luminosities from the observed integrated fluxes under the spectral lines by assuming isotropic emission.

Currently, the best available period-luminosity relation for Mira variables is in terms of the K-magnitudes, and is given by,

$$M_{\mathrm{K}} = 0.53 - 3.291 \log P \tag{1}$$

with r m.s. of about 0.1 magnitude (Feast 1984). We have used this relation to derive distances to Mira variables in our sample. Following Feast *et al.* (1982), we have corrected the apparent magnitudes for interstellar extinction, i.e.,

$$A_K = \frac{0.12}{\sin b}(1 - e^{-10r\sin b}), \tag{2}$$

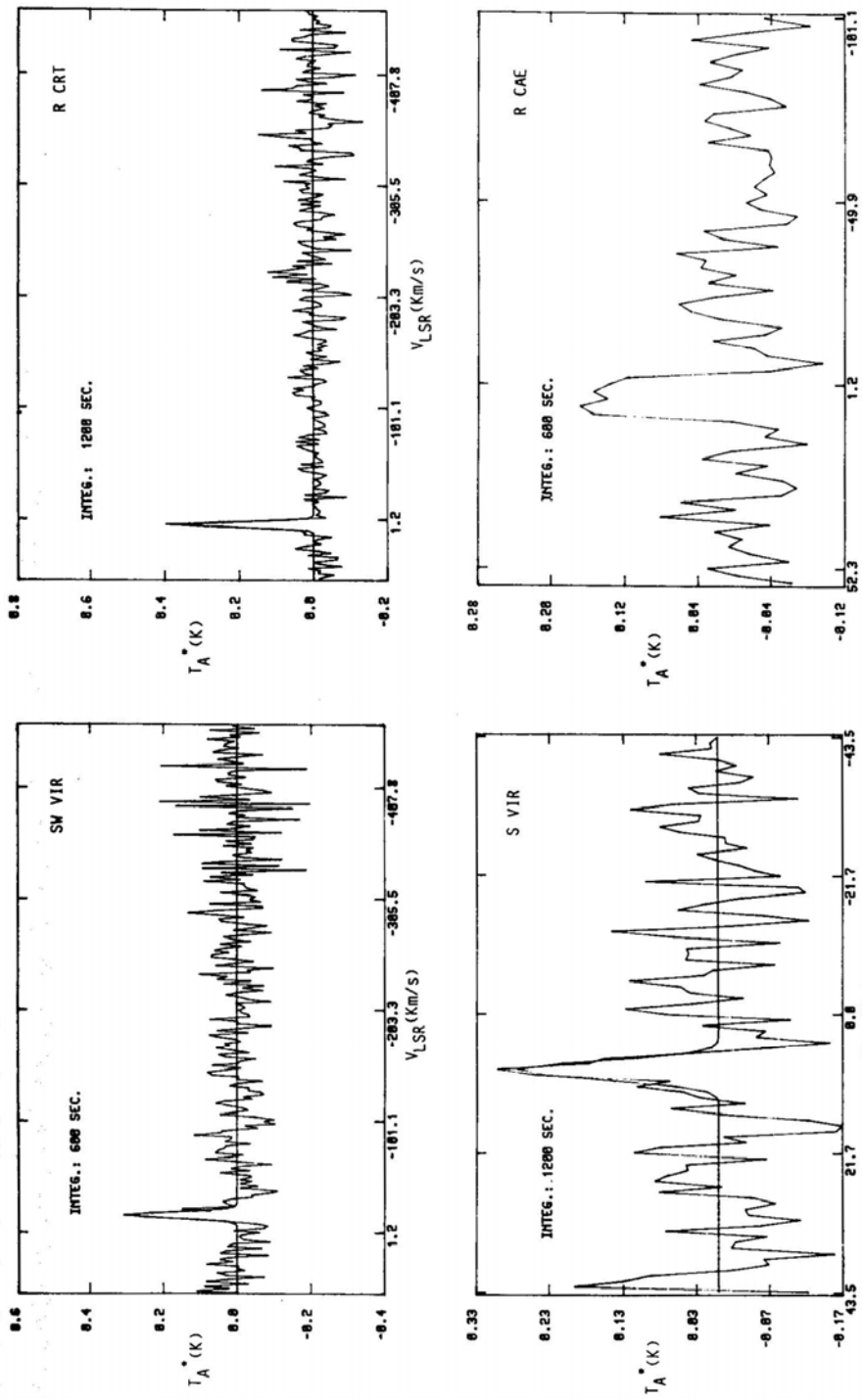

Figure 4(a). SiO $v = 1$, $J = 2 - 1$ maser emission spectra of our new detections.

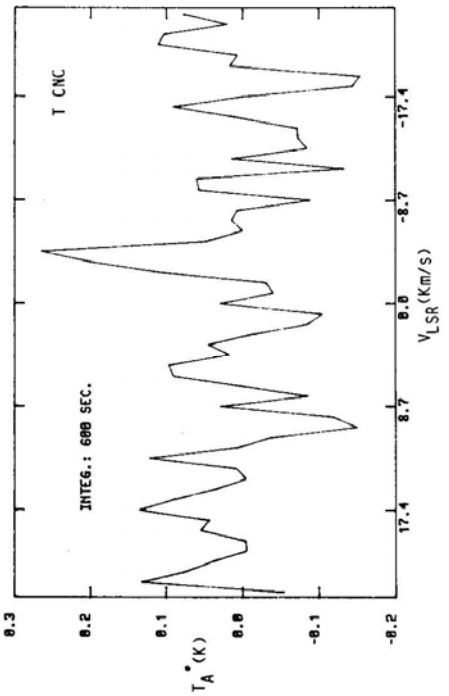

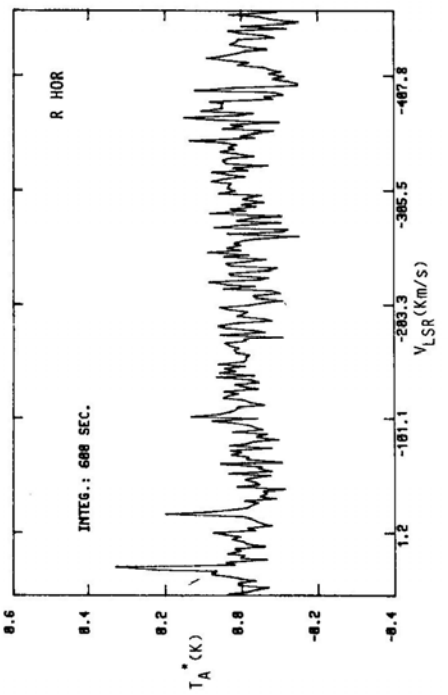

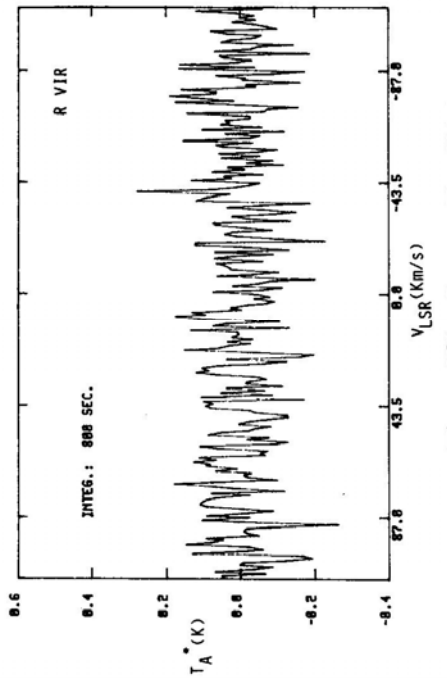

Figure 4(b). Same as Fig. 4(a) for two new detections and one negative detection baseline.

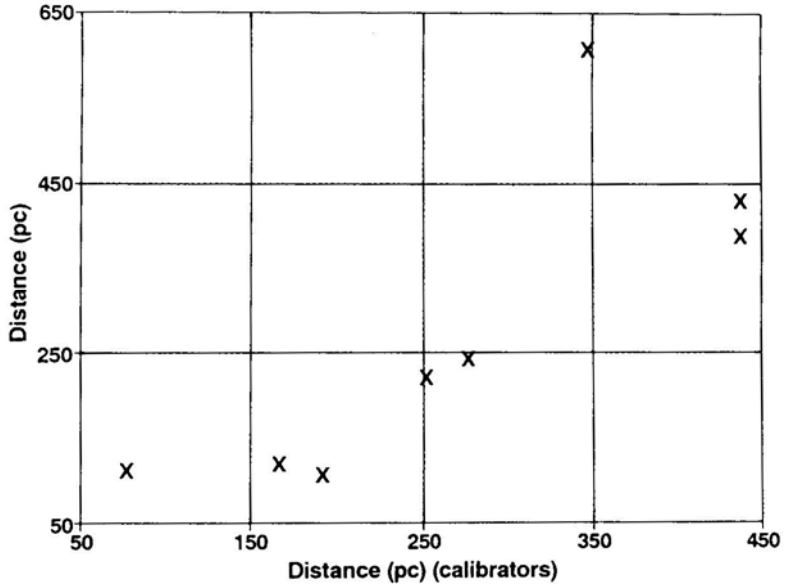

Figure 5. Comparison of our distances with the "Calibrator" distances (see text).

where r is the distance in kpc and b is the galactic latitude. The apparent K magnitudes were obtained from Catchpole *et al.* (1979) and from Gezari, Schmitz & Mead (1984). These derived distances, when plotted against the eight 'calibration' distances of Robertson & Feast (1981) in Fig. 5, are in good agreement. IR distances are reliable due to their relative insensitivity to extinction corrections and we have therefore adopted them. These calculated distances and luminosities of the observed sources are listed in cols. 15 and 16 of Table 1.

A correlation between distances and some intrinsic stellar property is not expected unless there is a hidden bias in our distance determination method. A check confirmed no correlation.

4. The SiO maser luminosity and intrinsic properties of Mira variables

4.1 *Determination of Effective Temperature*

The spectral type of a Mira varies during its pulsation. The spectral types listed in column 6 of Table 1, are from the General Catalogue of Variable Stars (Kholopov 1985), and represent the extreme values during the pulsation cycles. The spectral types for several Mira variables at optical maximum are given by Keenan, Garrison & Deutsch (1974), and throughout the pulsation period by Lockwood & Wing (1971). The calibration of the spectral type with effective temperature for the Mira variable is full of uncertainties (Bessell *et al.* 1989).

Dyck, Lockwood & Capps (1974) have obtained colour temperatures from black-body fits to their measured fluxes at 1.04 and 2.5 microns and have calibrated these colour temperatures with the effective temperatures of seven cool stars whose

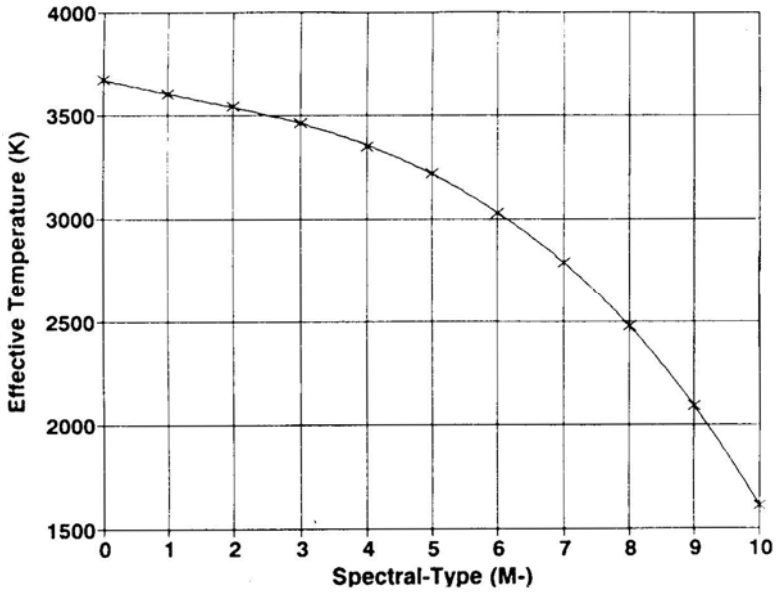

Figure 6. Dependence of effective temperature on the spectral-type of a Mira variable (from Dyck *et al.* 1974).

angular diameters have been measured. Their sample of stars contain Mira variables and IRC stars. The effective temperatures determined by this method, are shown in Fig. 6, which also shows a fitted polynomial. We have used this relation here. These temperatures appear in col. 18 of Table 1. One must note that the measured points are accurate to about half a division in spectral type. Since most of the energy is emitted at infrared wavelengths, it seems reasonable to adopt these temperatures which are obtained by measurements of fluxes and diameters at these wavelengths.

4.2 *The H–R Diagram for Mira Variables*

The absolute bolometric magnitudes from the P-L relation (Equation 1), and the effective temperatures obtained from spectral types as mentioned above, are used to plot an H–R diagram for the Mira variables in our sample. This is shown in Fig. 7. This figure may be compared with the H–R diagrams for Mira variables obtained previously by Keeley (1970), Scalo (1976) and Tsuji (1981). The H–R diagrams given by these authors are mainly for M-giant stars, including a very few Mira variables. As far as we know, Fig. 7 shows for the first time, the evolutionary status of the masing and non-masing Mira variables. From this we see that the masing sources lie in the region $M_{bol} \leqslant -4.8$ magnitude and $\mathrm{Log}(T_{eff}) \leqslant 3.47$. The four `#' symbols indicate supergiants, i.e. S Per, AH Sco, μ Cep, and VX Sgr. The three SiO maser sources with $M_{bol} \cong -4.2$ are R Crt, RT Vir and SW Vir whose variable types are SRB or unknown (i.e. not Mira). The SiO luminosities of these are ≈ 0.03 photons s^{-1} which are about 5 per cent of the typical values observed for Mira variables. The cutoffs in M_{bol} and T_{eff} mentioned above are only for Mira variables. A similar

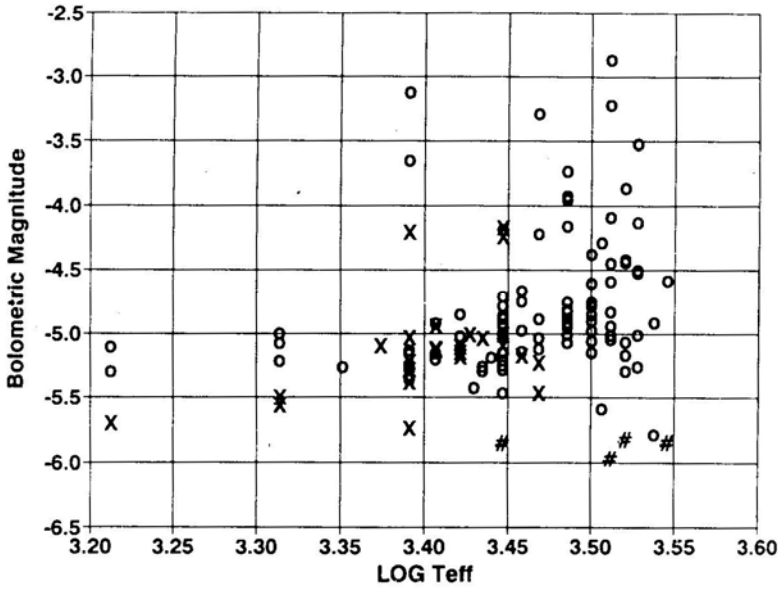

Figure 7. H–R diagram for the observed masing and non-masing sources. 'X' = maser, 'o' = non-maser and '#' = supergiant star.

conclusion for supergiants or variables of different types can be made only after more such stars are observed.

The limiting values of $M_{\rm bol}$ and $T_{\rm eff}$ may be indicating that a Mira variable has to attain a certain age before the onset of the SiO maser emission. On the other hand, using

$$M_{\rm bol} = 42.31 - 5\log\left(\frac{R}{R_\odot}\right) - 10\log T_{\rm eff}, \tag{3}$$

the limiting values of $M_{\rm bol}$ and $T_{\rm eff}$ imply a lower limit on the stellar radius of $\approx 300R_\odot$, below which the SiO maser emission is suppressed. A large value of radius may simply allow a larger path length for the gain of the maser, and hence a greater maser luminosity. It also implies the density of gas in the envelope to be low, a condition which is favourable for non-LTE.

4.3 *Correlation of Maser Luminosity with Spectral Type and Bolometric Magnitude*

In Figs. 8 and 9, we have plotted the maser photon luminosity, and the maser flux as a function of distance. These figures show that the maser sources are not equally luminous, and the variation in the luminosity is intrinsic to the source. Fig. 10 shows the SiO maser photon luminosity as a function of the mean spectral type (MST). The intrinsic properties of super-giants represented by '#' are expected to be different from those of the regular M-giant Mira variables. But for the three super-giants, all the masing Mira variables have MST later than M6. As a Mira variable approaches the maximum visual brightness during its pulsation (i.e. the zero phase), its spectral class

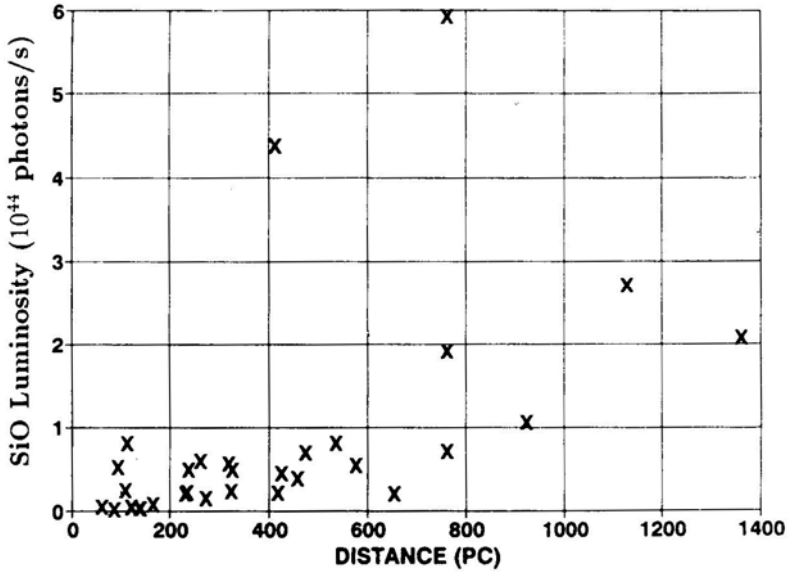

Figure 8. The SiO luminosity of maser sources versus their distances.

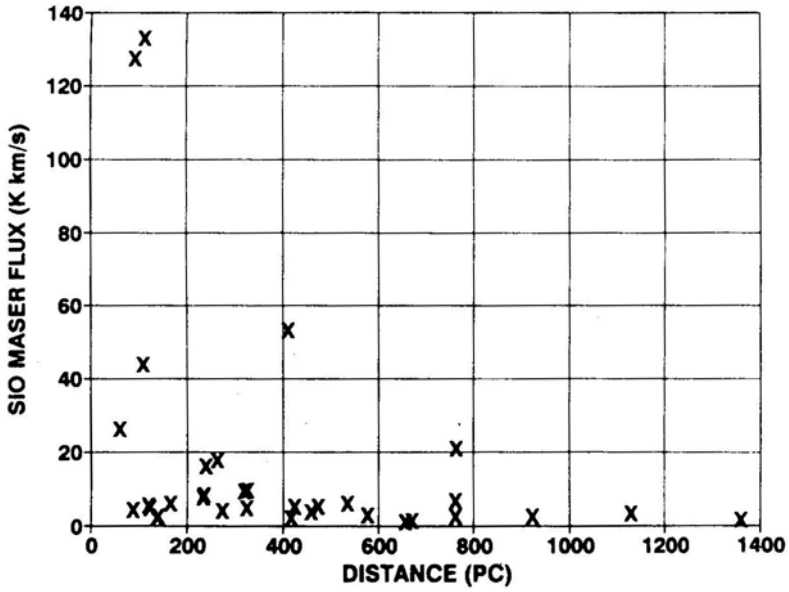

Figure 9. The SiO flux of maser sources versus their distances.

approaches an earlier type (corresponding to a hotter temperature). The limiting spectral type below which there is no maser emission is therefore expected to be even earlier in terms of the zero phase spectral type (ZPST) than the MST. In a plot similar to Fig. 10, instead of MST we used ZPST which was available for some sources from Keenan, Garrison & Deutsch (1974). The limiting value in terms of ZPST was found

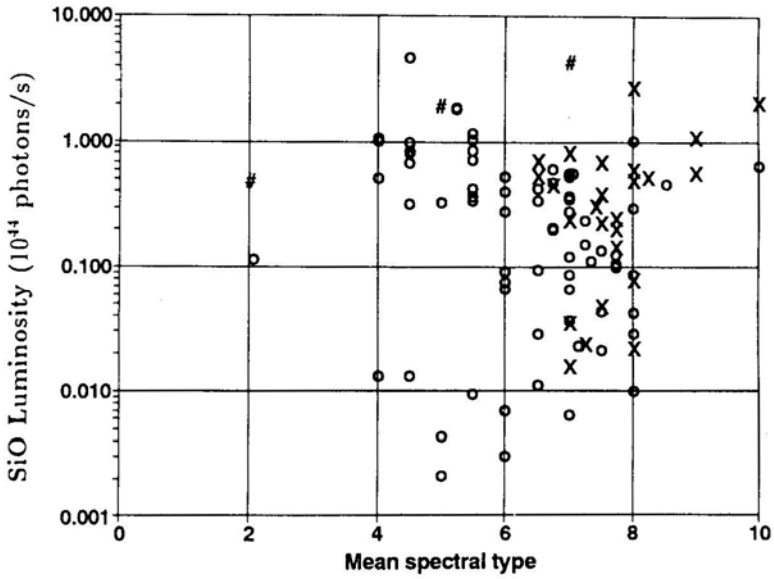

Figure 10. A plot of the SIO maser luminosity versus the mean spectral-type of the star. 'X' = maser, 'o' = non-maser and '#' = supergiant star.

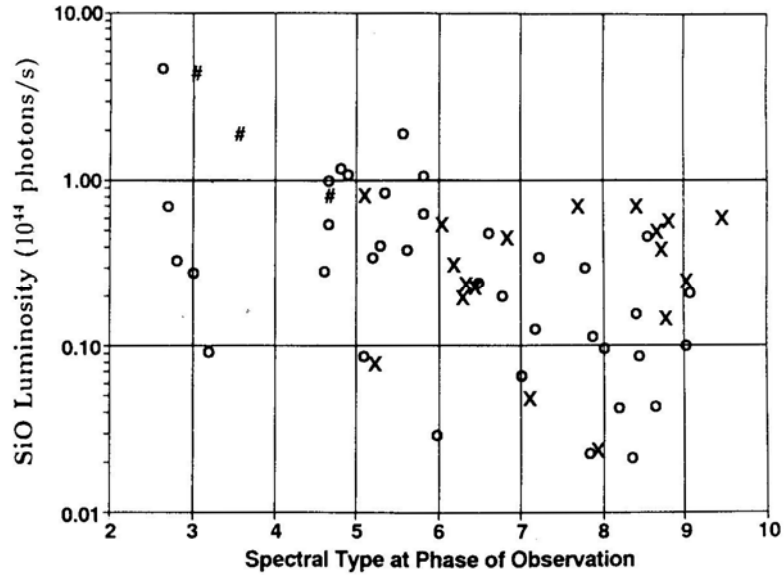

Figure 11. Same as Fig. 10 except the stellar spectral-type is the pulsation phase at he epoch of observation.

to be M5. Some of the sources for which we could find both, the distance as well as the phase of pulsation at the time of observation, are plotted in Fig. 11. Although this plot has a much smaller number of sources, we see that the masing Miras do not show a preferred value of spectral type in the range M6 –M10. The range of spectral types for which the maser emission occurs is thus not smaller than that for the MST.

There are a substantial number of non-masers even in the spectral range M6-M10, as listed in Table 2. To check if they are at phases which correspond to the minimum SiO luminosity, we have plotted their distribution with phase (see Fig. 12). Although the number of sources in this histogram is rather small, there is no indication of a preferred phase implying that being at the phase of minimum SiO emission cannot

Table 2: Non-detections among Mira variables with mean spectral-type > M6.

No.	Source	Variable type	Spectral type	M_{bol}	Δm_v AAVSO	Δm_v GCVS	Prev. Det.*	SiO lum. ($\times 10^{44}$)	Phase
1	Ant V	M	M7IIIE	−4.91			a,c		0.46
2	Aql RT	M	M6E-M8E(S)	−5.00	5.6	6.9	a,c	0.07	0.95
3	Ari U	M	M4E-M9.5E	−5.13		8.0	a,c	0.21	0.74
4	Aur R	M	M6.5E-M9.5E	−5.35	7.0	7.2	a,c	0.03	0.11
5	Aur U	M	M7E-M9E	−5.23	5.5	8.0	a,c	0.09	0.84
6	Cam W	M	M7	−4.85		3.7			0.43
7	Cnc W	M	M6.5E-M9E	−5.19		7.0	a,c	0.13	0.33
8	CvN T	M	M6.5E	−4.87		5.0		0.45	
9	CMa DN	M	M8						
10	CMi S	M	M6E-M8E	−5.01		6.6	a,c	0.13	
11	Cas Y	M	M6E-M8.5E	−5.24		6.6	a,b	0.16	0.68
12	Cen RT	M	M6-M7.5	−4.73		5.5		0.50	0.40
13	Cen UU	M	M8E.5	−5.12		4.0			0.63
14	Cep T	M	M5.5E-M8.8E	−5.18	4.3	6.1	a,b	0.02	0.85
15	Com R	M	M5E-M8EP	−5.11	5.7	7.5	a,b,c	0.35	0.23
16	CrV R	M	M4.5E-M9E	−4.96	6.3	7.7		0.21	0.95
17	Cyg Z	M	M5E-M9E	−4.77	4.6	7.6	a,c	0.29	0.15
18	Cyg SX	M	M7E	−5.24		7.0		0.56	
19	Dra R	M	M5E-M9EIII	−4.69		6.5		0.37	
20	Eri W	M	M7E-M9	−5.15	5.2	7.0	a,c	0.30	0.39
21	Gem UZ	M	M9	−5.06					0.89
22	Hya X	M	M7E-M8.5E	−4.91		6.4	a,c	0.11	
23	Lep T	M	M6E-M9E	−5.12	4.6	6.9	a,c	0.04	0.64
24	Lep RT	M	M9E	−5.21					0.55
25	Lib FS	M	M8.1-M9	−5.25				0.48	0.41
26	Lup R	M	M5.5-M8	−4.65	4.0	4.6		0.65	0.26
27	Lyr V	M	M7E	−5.13	5.1	7.5		0.58	0.55
28	Lyr RW	M	M7E	−5.45	4.3	6.2	b	0.38	0.67
29	Mon ER	M	M9:	−4.99					0.13
30	Mon GN	M	M9:						
31	Oph RT	M	M7E(C)	−5.27	5.5	6.9	a,b	0.59	
32	Oph V1111	M	M4III-M9			4.0			
33	Ori S	M	M6.5E-M9.5E	−5.24		6.8	a,b	0.04	0.92
34	Ori EP	M	M10E	−5.09		2.5			0.28
35	Pic S	M	M6.5E-M8III-IIE	−5.28	5.7	7.5		0.25	0.19
36	Sgr RR	M	M4E-M9E	−5.02	6.4	8.6	a,c	0.10	0.60
37	Sco RR	M	M6II-IIIE-M9	−4.84	5.9	7.4	b	0.02	0.59
38	Tau R	M	M5E-M9E	−4.98	5.6	8.2	a,c	0.09	0.21
39	Umi S	M	M6E-M9E	−5.01		>5.7	a,c	0.14	

Notes: a: Previous detection at 43 GHz.
b: Previous detection at 86 GHz.
c: Previous non-detection at 86 GHz.
*: Benson *et al.* (1990).

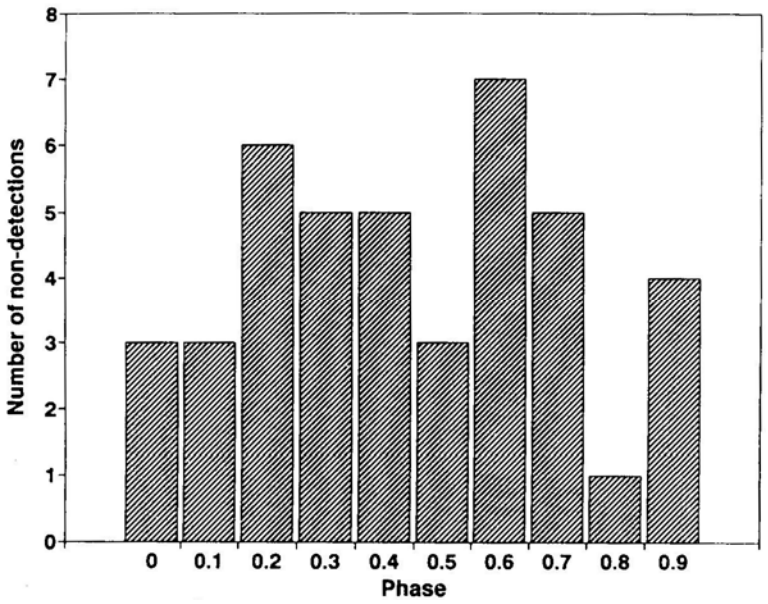

Figure 12. Distribution in the pulsation phase of Mira variables in which SiO maser emission was not detected.

be the sole cause behind their non-detection. Other possibilities are discussed in section 5.

Thus, spectral type later than M6 is a necessary but not a sufficient condition for masing. Fig. 13 shows that the masing Miras are brighter than – 4.2 in bolometric magnitude. Thus, another limiting factor is the bolometric magnitude. In fact, many of the non-masers in the spectral type range M6–M10 have bolometric magnitudes fainter than – 4.8*m*. Fig. 13 also shows a tendency for the maser luminosity to decrease with increasing bolometric magnitude; this is discussed in Patel & Shukre (1992).

4.4 *Dependence of Maser Luminosity on the Amplitude of Pulsation*

Another possible intrinsic property of Mira variables to which the SiO maser may be related, is the amplitude of pulsation. Mira variables show very large changes in the visual magnitude. The amplitudes of pulsation at infrared wavelengths on the other hand, are much smaller (about 1 magnitude at infrared, for an amplitude of about 5 magnitude at visual). This is expected due to variation in the temperature between 2000 K to 2500 K during pulsation, for a typical Mira variable. Apart from changes in temperature, the amplitude of pulsation will reflect changes in the diameter of the star; and since the SiO maser exists very close to the photosphere, we may expect a physical connection between the maser process and the amplitude of pulsation. To investigate this relation, we have plotted the SiO maser photon luminosity versus the pulsational visual amplitude Δm_v . Fig. 14 shows a tentative anti-correlation between the maser luminosity and Δm_v obtained from GCVS. In

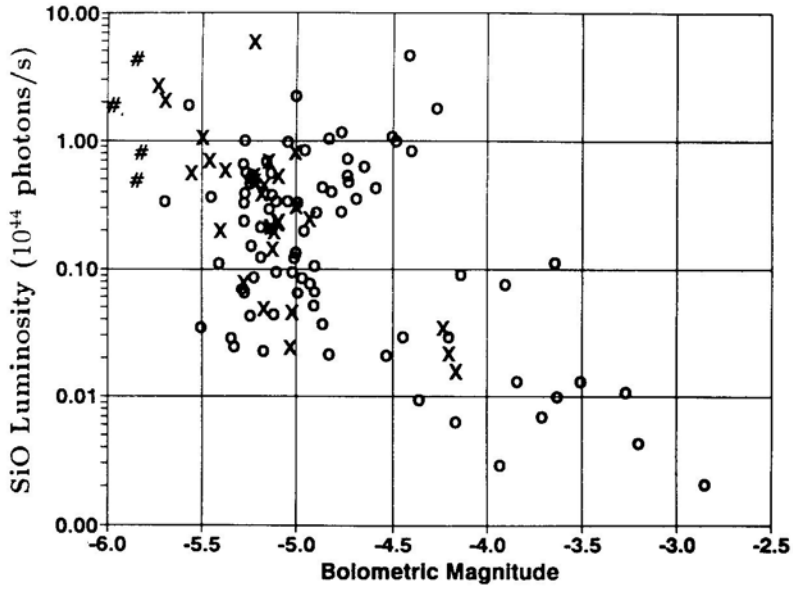

Figure 13. A plot of SiO maser luminosity versus the bolometric magnitude of the source, 'X' = maser, 'o' = non-maser and '#' = supergiant star.

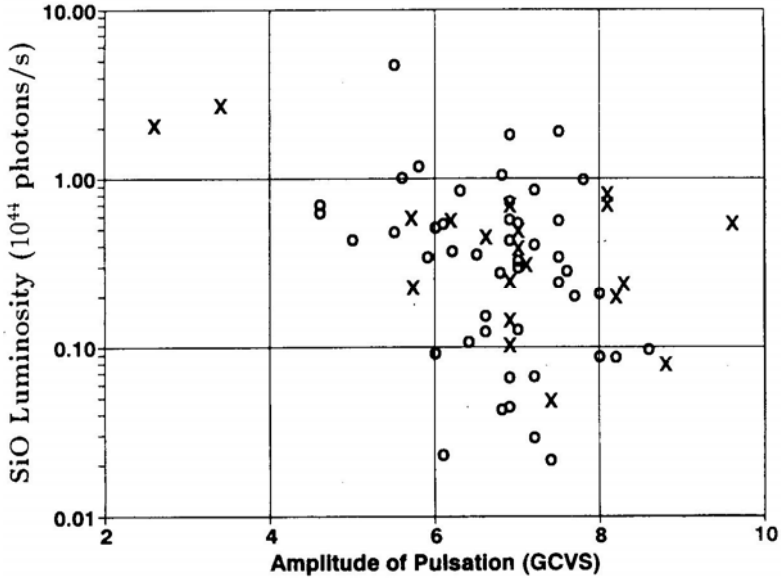

Figure 14. A plot of SiO maser luminosity of Mira variables versus their visual amplitude of the pulsation. The amplitude in magnitude units are from GCVS (Kholopov 1985. 'X' = maser and 'o' non-maser.

GCVS (Kholopov 1985) a value of Δm_v is available for almost all the sources in our list. These are recent values of Δm_v where as the AAVSO Δm_v (and the 'notes' in the third edition of GCVS) represent mean values which were not available for all the sources in Fig. 14.

This result needs to be confirmed by observing more sources and using the mean values of Δm_v. It may also be useful to check for this anti-correlation by plotting the ratio of SiO maser and thermal (v = 0) emission against Δm_v . We expect such a comparison to be free of distance uncertainties and independent of SiO abundance variation from source to source. Further, the visual amplitude has severe molecular blanketing effects (Lockwood & Wing 1971, Whitelock 1990); hence it is perhaps more reliable to use infrared amplitude where molecular absorption is minimal.

It is important to note that the correlations we have discussed are independent of each other. The bolometric magnitude, spectral type and amplitude of pulsation for stars in our sample, do not show any correlation with each other.

5. Interpretations

5.1 *Non-detections*

There are a large number of Mira variables with no detected SiO maser emission. In Table 2, we see that there are several Mira variables in the range of spectral types M6–M10, for which we only have upper-limits on the SiO maser luminosity. The limits for several of these are much below the luminosities for the masing sources detected in our sample. This raises the question— Why are these Mira variables such weak masers if they are masing at all? In Table 2, we find that there are many sources which have been detected previously, at 43 and 86 GHz. These sources are marked by 'a' and 'b' respectively, in column 7. Generally, the 43 GHz emission is expected to be about twice as strong as the 86 GHz (Snyder & Buhl 1975). Therefore, those sources which are already weak at 43 GHz should be even weaker at 86 GHz and thus will not be detectable with our sensitivity. On the other hand, there are many sources previously detected at 86 GHz, which we have failed to detect. We look at these and other non-detections in the light of the dependence of the maser power on intrinsic stellar properties discussed above.

For those sources for which data is insufficient, obviously, no statement can be made. Of the remaining, those which have $M_{\rm bol} > -4.8$ are expected to be weak masers.

The dependence on the phase of pulsation ϕ affects the maser emission in two ways. Because the spectral type varies with ϕ, for some stars (e.g. R Com, R Tau) the spectral type at the phase of our observation would have been earlier than M6, suppressing the maser emission. Secondly, the maser output is expected to vary with ϕ such that it will be low in the range $0.5 < \phi < 0.9$. This of course will be of more significance for those sources whose stellar parameters have values close to the cut-offs or are at a large distance (e.g., T Lep, RW Lyr).

The coordinates used for our observation of Y Cas were not precise. For some other sources (e.g., TCep, UUCen), the data is noisier than average ($\sigma \cong 0.10$K). In a few cases, just the large distance could push the flux level below our sensitivity limit, e.g., comparing W Cnc and R Hya we see that the flux for the former would be $\approx$ 1/30 of that for the latter.

The non-detection of the maser emission from sources in Table 2 can thus be understood in terms of the factors discussed above. It lends indirect support to the conclusions of previous sections. Only two sources (RT Aql and S Ori) cannot be

understood in these terms. It should be noted that at least a few of the sources are expected to show maser emission if observations are made with better sensitivity (e.g. W Cnc, W Eri) or at a proper phase (e.g. S CMi, X Hya).

5.2 *Dependence of Maser Power on Spectral Type*

The SiO maser power clearly must depend on the molecular abundance of SiO in the atmosphere of the Mira variable. As seen earlier, one of the main results that has emerged from our observations is that the masing Mira variables have spectral types later than M6. Indeed, this dependence of the maser power on the spectral type could simply be due to a lower abundance of SiO in stars having spectral types earlier than M6. Such an abundance variation was in fact predicted by Johnson, Beebe & Sneden (1975). Rinsland & Wing (1982)[1] observed the vibrational-rotational transitions in SiO, at 4 μm from several M-giants and a few Mira variables of various spectral types. They found that the equivalent width of the absorption band increased with the spectral type, showing that above a temperature of ~ 3000 K, there was a steep decline in the value of the equivalent width which could not be due to the dissociation of SiO. A similar effect is also expected for the abundance of water (Tsuji 1978). We therefore suggest that a reduction in the abundance of SiO in earlier spectral types is the cause for the observed dependence of the SiO maser power on effective temperature (spectral type). This can be tested by future observations of SiO in thermal rotational transitions from Mira variables covering a wide range of spectral types.

6. Conclusions

There seem to be two criteria which may inhibit a Mira variable from giving rise to SiO maser emission at 86 GHz: They are: (1) Spectral type earlier than M6 (or $\log T_{\rm eff} \geqslant 3.48$) and (2) Bolometric magnitude fainter than — 4.8 magnitudes.

7. Acknowledgement

This work would not have been possible without the continuous effort and enthusiasm of everyone at the millimeter-wave laboratory, electronics laboratory and the workshop of the Raman Research Institute. We are particularly grateful to P. G. Ananthasubramanian, K. Sukumaran, G. Rengarajan, R. Nandakumar, M. Selvamani, K. Chandrashekara and the telescope operators for their help in carrying out the observations; and to V. Radhakrishnan, N. V. G. Sarma, C. S. Shukre and R. Nityananda for their guidance and many helpful discussions. We also thank K. R. Anantharamaiah for helpful comments on the manuscript. It is a pleasure to thank Janet Mattei and the AAVSO for providing us the visual light-curves of most of the Mira variables in our sample. We are grateful to the referee for several useful comments.

[1]We are grateful to Dr. T. Tsuji for this reference.

References

Alcock, C, Ross, R. R. 1986, *Astrophys. J.*, **310,** 838.

Alcolea, J., Bujarrabal, V., Gallego, J. D. 1989, *Astr. Astrophys*., **211,** 187.

Benson, P. J., Little-Marenin, I. R., Woods, T. C, Attridge, J. M., Blaise, K. A., Rudolf, D. B., Rubiera, M. E., Keefe, H. L. 1990, *Astrophys. J. Suppl*., **74,** 911.

Bessell, M. S., Brett, J. M., Scholz, M., Wood, P. R. 1989, *Astr. Astrophys*., **213,** 209.

Cahn, J. 1977, *Astrophys. J. Lett*., **212,** L135.

Catchpole, R. M., Robertson, B. S. C, Lloyd-Evans, T., Feast, M. W. 1979, *South African Astronomical Observatory Circulars*, **1,** 61.

Dickinson, D. F., Snyder, L. E., Brown, L. W., Buhl, D. 1978, *Astr. J*., **83,** 36.

Dyck, H. M, Lockwood, G. W., Capps, R. W. 1974, *Astrophys. J*., **189,** 89.

Engels, D. 1979, *Astr. Astrophys. Suppl. Ser*., **36,** 337.

Engels, D., Heske, A. 1989, *Astr. Astrophys. Suppl. Ser*., **81,** 323.

Feast, M. W., Robertson, B. S. C, Catchpole, R., Lloyd-Evans, T., Glass, I. S., Carter, B. S. 1982, *Mon. Not. R. astr. Soc*., **201,** 439.

Feast, M. W. 1984, *Mon. Not. R. astr. Soc*., **211,** 51.

Gezari, D. Y., Schmitz, M., Mead, J. M. 1984, *Catalog of Infrared Observations,* NASA Ref. Publ. 1118.

Ikaunieks, J. 1975, in *Pulsating Stars* Ed. B. V. Kukarkin, John Wiley and Sons. p. 259.

Jewell, P. R., Walmsley, C. M., Wilson, T. L., Snyder L. E. 1985, *Astrophys. J*., **298,** L55.

Johnson, H. R., Beebe R. F., Sneden, C. 1975, *Astrophys. J. Suppl. Ser*., **29,** 123.

Keeley, D. A. 1970, *Astrophys. J*., **161,** 643.

Keenan, P. C., Garrison, R. F., Deutsch, A. J. 1974, *Astrophys. J. Suppl. Ser*., **28,** 271.

Kholopov, P. N. (Ed), 1985, General Catalogue of Variable Stars, Moscow Publishing House.

Lane, A. P. 1984, in IAU Symp. 110, *VLBI and compact radio sources,* Eds R. Fanti, K. Kellerman, & G. Setti, Reidel Publ. 1984 p. 329.

Lloyd Evans, T. 1990, *Mon. Not. R. astr. Soc*., **243,** 336.

Lockwood G. R., Wing R. F. 1971, *Ap. J*., **169,** 63.

Lockwood, G. R. 1972, *Ap. J. Suppl. Ser*., **24,** 373.

McIntosh, G. C, Predmore, C. R., Moran, J. M., Greenhill, L. J., Rogers, A. E. E., Barvainis, R. 1989, *Ap. J*., **337,** 934.

Moran, J. M., Ball, J. A., Predmore, C. R., Lane, A. P., Reid, M. J., Hansen, S. S. 1979, *Ap. J*., **231,** L 67.

Patel, N. A. 1990, *Ph.D. Thesis*, Indian Institute of Science, Bangalore.

Patel, N. A., Shukre C. S. 1992, submitted to *Astrophys. J.*

Rinsland, C. P., Wing, R. F. 1982, *Ap. J*., **262,** 201.

Robertson, B. S. C, Feast, M. W. 1981, *Mon. Not. R. astr. Soc*., **196,** 111.

Sahai, R. 1987, in I. A. U. Symposium 120. *Astrochemistry,* Eds M. S. Vardya & S. P. Tarafdar, D. Reidel Pub. Co., p 341.

Scalo, J. M. 1976, *Ap. J*., **206,** 474.

Snyder, L. E., Buhl, D. 1975, *Ap. J*., **197,** 329.

Spencer, J. H., Waak, J. A., Bologna, J. M., Schwarz, P. R. 1977, *Astron. J*., **82,** 706.

Tsuji, T. 1978, *Astron. Astrophys*., **62**, 29.

Tsuji, T. 1981, *Astron. Astrophys*., **99,** 48.

Vardya, M. S., 1989, in *Evolution of Peculiar Red Giants,* Eds H. R. Johnson, B. Zuckermann, Cambridge: Cambridge University Press, p. 349.

Whitelock, P. A. 1990 in *Confrontation between stellar pulsation and evolution*, EdC. Cacciari, Astron. Soc. Pacific Conference Series, to be published.

J. Astrophys. Astr. (1992) **13,** 267–277

Photopolarimetric Studies of Comet Austin

U. C. Joshi, A. K. Sen, M . R. Deshpande & J. S. Chauhan *Physical Research Laboratory, Ahmedabad 380 009*

Received 1991 September 20; accepted 1992 July 6

Abstract. Photopolarimetric observations of comet Austin with the IAU/IHW filter system were obtained on the 2.34 m Vainu Bappu Telescope (VBT) of the Indian Institute of Astrophysics, at Kavalur, India, during pre-perihelion phase on February 20,1990 and on the 1.2 m telescope of the Physical Research Laboratory at Gurusikhar, Mount Abu during post-perihelion phase on May 2 and 4, 1990. The comet appeared bluer than a solar analog during post-perihelion phase on May 2 and 4. The percent polarization shows a sharp increase towards the red on May 2 and 4. The dominant sizes of the dust particles appear to lie in a narrow range of 0.1 to 0.5 μm. Regarding the molecular band emission, CN and C_2 bands are quite strong; C_3 emission was also found to be strong though the observations on May 2 and 4 show significant variation as compared to C_2 emission. Molecular band polarization for CN, C_3, C_2 and H_2O^+ have been calculated. It has been found that emission polarization in CN, C_2 and C_3 is between 1–7% (phase angle between 107.4–109 degrees). For CN and C_2 the polarization values are close to the theoretically predicted values, but for C_3 the polarization value falls much below the theoretically predicted value. A similar result was found for comet Halley.

Key words: comet—polarization—molecules—dust

1. Introduction

Comets are generally known to have high degrees of polarization caused by two mechanisms: (1) scattering of sunlight by cometary particles and (2) fluorescence emission by cometary molecules. The molecular band polarization in comets is due to resonance fluorescence emission (Ohman 1941; Blackwell & Willstrop 1957; Bappu *et al.* 1967; Kharitonov & Rebristyi 1974; Bastein *et al.* 1986; Dobrovolsky *et al.* 1986; Le Borgene *et al.* 1987; Sen *et al.* 1988,1989) but our knowledge on this subject is very scanty. High precision photopolarimetric observations in continuum wavelengths and molecular bands are essential to compare observations with theoretically predicted values. Polarimetric observations in continuum and molecular bands were made in detail by various groups on comet Halley (Dollfus & Suchail 1987; Kikuchi *et al.* 1987; Le Borgene *et al.* 1987; Sen *et al.* 1988, 1989). Our observations (Sen *et al.* 1989) on comet P/Halley show that the polarization values for CN and C_2 agree with the theoretically predicted values, but for C_3 the polarization value falls much below the theoretically predicted value; emission from the ionic molecules: CO^+ and H_2O^+ show much higher polarization, though the errors were large (Sen *et al.* 1989). Comet Austin

has given us another opportunity to study the polarization behaviour of continuum and molecular bands. Comet Austin is perhaps a new comet (Sekanina 1990) in the Oort sense. If this is the case, we have an excellent opportunity to study and compare comet Austin with a dynamically older comet P/Halley. In the present paper we present results based on our photopolarimetric observations on comet Austin.

2. Observations and analysis

Observations during pre-perihelion phase were taken on the 2.34 m Vainu Bappu Telescope at Kavalur of the Indian Institute of Astrophysics, Bangalore and during post-perihelion phase observations were taken on the 1.2 m telescope at Gurusikhar, Mt. Abu, of the Physical Research Laboratory, Ahmedabad. Observations were taken with the IHW (International Halley Watch) filter system which contains three narrow band continuum filters (UC: 3650/80A; BC: 4845/65A; RC: 6840/90A) and five narrow band interference filters covering different molecular bands (CN: 3871/50; C_3: 4060/70A; CO^+: 4260/65A; C_2: 5140/90A; H_2O^+: 7000/175A). UC, BC, RC: represent ultraviolet, blue, and red continuum respectively and the numbers after the slash are FWHM for the filter bands. A photopolarimeter which is discussed elsewhere (Deshpande *et al.* 1985) was used for observations. Data reduction and analysis has been done in the same way as was done earlier by us for comet P/Halley (Sen *et al.* 1988, 1989). Instrumental polarization was determined by observing zero percent polarization stars. In the case of the 1.2 m telescope the instrumental polarization was negligible (less than 0.05% in all the bands) and, therefore, neglected. However, when observations were made on the 2.34 m telescope, the instrumental polarization was found to be 2.25% in ultraviolet decreasing to 0.50% in the reddest wavelength. The necessary corrections for instrumental polarization were made to the Polarimetric observations with the IHW filters. We present here observations made on February 20, 1990 (pre-perihelion phase) and May 2 and May 4, 1990 (post-perihelion phase). The comet coma was observed with an aperture of 60 arcsec on the 1.2 m telescope while on the 2.34 m telescope the aperture used was 24 arcsec. Polarimetrie data along with the error in the degree of polarization (E_p) are listed in Table 1. Error estimation is discussed in section 3.

The solar type stars HD29461 and HD 191854 were observed for photometric calibration. These stars have been chosen from a list of seven IHW solar analogs (given in IHW, Photometry and Polarimetry Net, Circular 8, November 1985). The observed magnitudes of comet were converted to the standard scale of IHW, using the method discussed in our earlier paper on comet Halley (Sen *et al.* 1989). These magnitudes were converted into flux by adopting the flux conversion formulae given in IHW Photometry and Polarimetry Net, circular 3 February, 1986. On February 20, observations could not be made in UC filter as the comet was quite faint in the ultraviolet continuum and also the altitude of the comet at the time of observation was very low.

Observed polarization in molecular bands is contaminated with continuum flux which has been estimated in the same way as discussed by us earlier (Sen *et al,* 1989) and polarization due to resonance fluorescence has been calculated.

Photopolarimetric data on comet Austin in continuum and emission bands are listed in Table 1 and Table 2. Results are discussed in section 4.

Table 1. Photopolarimetric data of comet Austin in the emission bands and the continuum bands (underlined). Observed degree of polarization (%P), error in polarization (%E_P), angle of polarization vector and magnitude are listed. Flux values for the continuum bands are also listed. Observations on February 20, 1990 are done on 2·34 m VBT; other two sets of observations are done on l·2 m telescope.

Date	UT (HHMM)	Filter wave-length	%P	%E_p	Angle (θ) (degree)	Magnitude (m)	Flux (ergs/ cm^2/sec/A)
	1422	4845	7·8	3·9	118	12·67	4·302E-14
	1416	5140	11·0	1·4	35	11·45	
	1409	6840	11·2	2·3	38	11·67	3·544E-14
	1404	7000	14·3	2·2	24	11·72	
May 2, 90	2341	3650	5·55	0·30	93	8·80	2·482E-12
	2333	3871	6·25	0·19	24	5·96	
	2328	4060	3·46	0·36	20	7·69	
	2324	4260	7·18	0·41	25	8·64	
	2319	4845	10·45	0·28	23	8·04	3·018E-12
	2315	5140	6·47	0·11	21	5·50	
	2310	6840	20·43	1·5	25	8·72	5·354E-13
	2304	7000	14·56	1·19	27	8·40	
May 4, 90	2331	3650	0·97	0·81	13	8·86	2·351E-12
	2334	3871	5·95	0·40	18	6·13	
	2336	4060	2·75	0·50	22	7·13	
	2327	4845	7·04	0·55	21	8·11	2·829E-12
	2323	5140	6·41	0·17	16	5·96	
	2319	6840	18·17	1·25	18	8·36	7·500E-13
	2316	7000	13·77	1·10	16	8·03	

3. Error analysis

3.1 *Error in Polarization Measurements*

The Polarimeter works on a rapid modulation principle, the sampling rate being 1 ms and the data are processed on line with an IBM–PC. The error in polarization measurement is estimated from photon statistics using a least square solution. The error in position angle is estimated by the relation given by Serkowski (1962):

$$E_\theta = 28.65^\circ \; E_p/P \text{ (for } E_p \ll P) \tag{1}$$

where E_θ and E_p are error in position angle (θ) and degree of polarization (P) respectively. Error in degree of polarization is listed in Table 1; E_θ may be computed using the above relation (1).

3.2 *Error in Flux Measurement*

The error in observed magnitude (including the error in extinction values and error in transformation to standard magnitude system) on May 2 and 4 is ~ 0.05 mag. At the time of observation, the comet was quite high in the sky (more than 30 degrees above the horizon). All continuum filters are free from cometary molecular emission except

Table 2. Flux in different emission bands due to molecular emission along with the background continuum contribution in the entire band in ergs/cm^2/sec is given for different dates. Estimated value of percent polarization due to molecular emission is listed for some molecules. P_{max} values (theoretically calculated) are also given.

Date		CN 3871/50	C_3 4060/65	CO^+ 4260/65	C_2 5140/90	H_2O^+ 7000/175
Feb 20, 90	P_o				11·0	14·3
	E_P				1·4	2·1
	θ_o				35	24
	E_θ				4	4
	F_c				6·145E-12	7·955E-12
	F_E				1·177E-12	
	P_E				10·0 ± 3·0	
May 2, 90	P_o	6·25	3·46	7·18	6·47	14·56
	E_p	0·20	0·6	0·14	0·5	1·9
	θ_o	24	20	25	21	27
	F_θ	1	3	1	1	2
	F_c	1·063E-10	5·055E-10	2·117E-10	3·435E-10	1·068E-11
	F_E	1·909E-09	7·075E-10		3·953E-09	4·919E-11
	P_E	6·0 ± 0·2	1·0 ± 0·6		6·0 ± 0·5	0·4 ± 1·9
	P_{max}	7·0	1·1		6·8	0·5
May 4, 90	P_o	5·95	2·75		6·41	13·77
	E_p	0·40	0·50		0·17	1·10
	θ_o	18	17		16	16
	E_θ	2	5		1	2
	F_c	1·005E-11	4·770E-10	1·993E-10	3·417E-10	1·545E-10
	F_E	1·628E-09	1·545E-09		2·474E-09	6·542E-11
	P_E	6·3 ± 0·6	2·6 ± 0·6		6·1 ± 0·3	1·1 ± 1·8
	P_{max}	6·8	2·9		6·7	1·2

the blue continuum filter which has a small contamination due to C_2 molecular emission. The blue continuum band (effective wave length: 4845 and half width: 65A) falls between the two C_2 bands at 4745A and 5165A. The effect of the tail of C_2 emission band starting at 5165A, on the continuum band at 4845A is of the order of 1%. The expression for estimating the corrected magnitude at λ=4845A is:

$$CM = m(4845) - 0.012\{m(5150) - m(4845)\} \quad (2)$$

where *CM* is corrected magnitude (refer IHW Photometry and Polarimetry Net circular No. 3, February 1986). Thus the total error, in flux measurement of the blue continuum, including the error in observed magnitude, is 7% and in other two continuum bands, which are nearly free of molecular emission, the error is 5%. The continuum flux at the molecular emission bands has been calculated using the expressions given in the IHW Photometry and Polarimetry Net, Circular 3,1986. The estimated error in flux in molecular bands is ~ 9%. For all practical purpose, we have considered the error in flux to be less than 10% in all the bands.

On February 20, the comet was very low at the time of observation (about 15 degrees above the horizon). The error in magnitudes due to errors in extinction and transformation to standard magnitude is found to be 0.15 mag. There are some other sources of error as discussed above. The total error in flux in continuum bands (BC and RC) and molecular bands (C_2 and H_2O+) is evaluated to be 20%.

4. Results and discussions

In the following we discuss the results on: (i) continuum energy distribution and polarization, (ii) molecular band emission and (iii) molecular band polarization.

4.1 *Continuum Energy Distribution and Polarization*

Table 1 lists the observed magnitudes and polarization values in the IHW filter system for comet Austin on February 20, May 2 and May 4, 1990. The error in polarization measurement is also given. Fluxes in three continuum filters have been calculated as discussed above and are given in Table 1. In Fig. 1, we have plotted the observed flux in the continuum bands normalized by a solar analog HD 191854 on May 2 and May 4. We have not plotted in Fig. 1 the flux values on February 20 since observations could not be made through the UC band and because the errors in observations in the other two continuum bands (BC and RC) are large (20%). Fig. 1 shows that on May 2 and May 4 the comet is bluer than the Sun. The error in flux measurement on May 2 and May 4 is less than 10% and the observed bluing is much higher (refer Fig. 1). The bluer color than a solar analog is not a common feature in comets; although bluing has been observed in the case of comet Ikeya-Seki (1967n) (Gebel 1970).

Figure 2a shows the wavelength dependence of the degree of polarization. There is a sharp increase in the degree of polarization towards the red wavelength in post-perihelion phase. Observations obtained on February 20 also show increase in the degree of polarization towards the red wavelength, though the rate of increase is

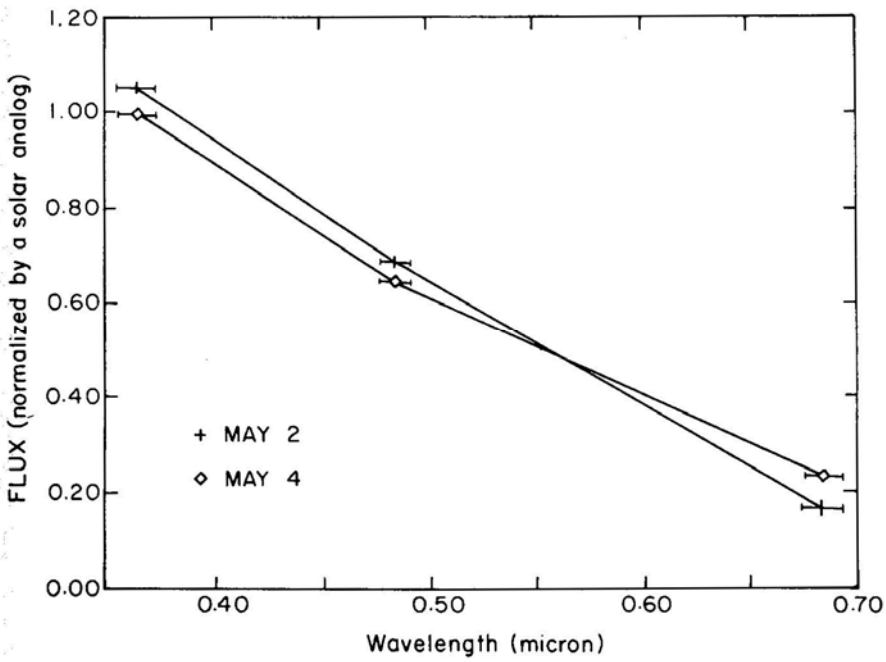

Figure 1. Plot of flux values (in unit of 10^{-12} ergs/cm^2/sec/A), normalized with respect to a solar analog HD 191854, in different continuum bands for comet Austin on May 2 and May 4.

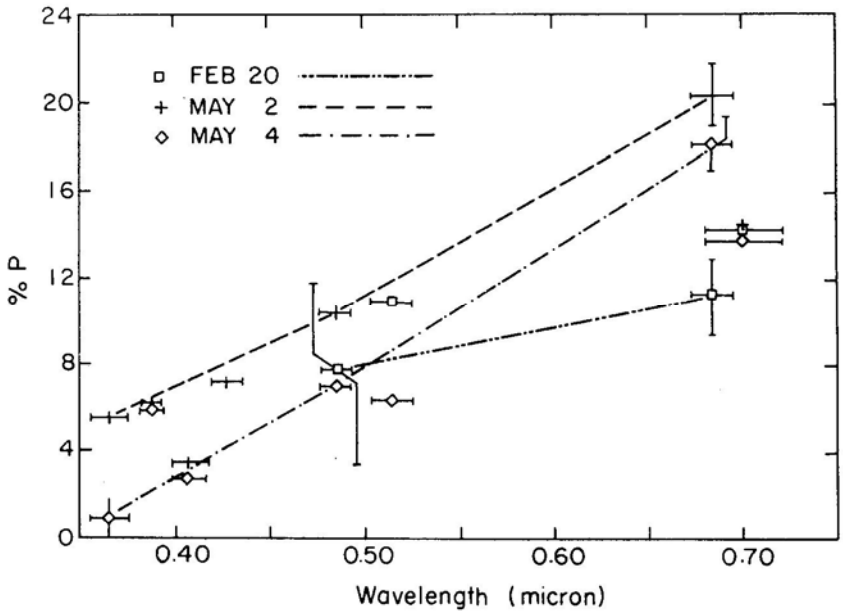

Figure 2a. Wavelength dependence of linear polarization for comet Austin as measured on different dates. Polarization values for continuum wavelengths are joined with different types of dashing. Observed values of polarization for molecular bands are also plotted for comparison. Error bars (two sigma) are also plotted.

relatively less compared to that on May 2 and May 4. The maximum polarization, P_{max} (polarization value at phase angle 90 degree) is related to the albedo A of the surface, by the classical so-called Umov approximate relationship $P_{max} \cdot A$ = const. (Dollfus 1989). The present observations on comet Austin have been made on May 2 and 4 when the phase angle is 109 and 107.4 degree respectively. Assuming that the observed polarization on May 2 and 4 is close to P_{max} (since the phase angle at the time of observation is not very much off from 90 degree), the above relation shows that for comet Austin the albedo in ultraviolet wavelength is 3 to 4 times higher than for the red wavelength which imply the brightness of comet Austin to be more in blue wavelength compared to that in red wavelength. This is consistent with the observations.

The steep rise of polarization towards longer wavelengths and bluing of the continuum flux in comet Austin indicate that the size of the dust particles in comet Austin lies in a narrow range and the imaginary part of the refractive index may be small i.e. close to zero (refer Greenberg 1978; Martin 1978). Comparison of the various curves for scattering efficiency and polarization due to dust particles, given by Greenberg (1978) and Martin (1978), with the present observations of flux and polarization help to put a limit on the sizes of the cometary dust particles; the sizes of the dominant dust particles appear to range between 0.1 μm to 0.5 μm. Calculations based on Mie scattering theory were carried out by us to match the observed polarization data in the B and R bands with the theoretical predictions and to find out the characteristics of the cometary dust. This analysis, published elsewhere (Sen *et al*. 1991) also shows that the relative abundance of smaller dust particles is more in comet Austin as compared to comet Halley and a large fraction of them are smaller than 0.62 μm.

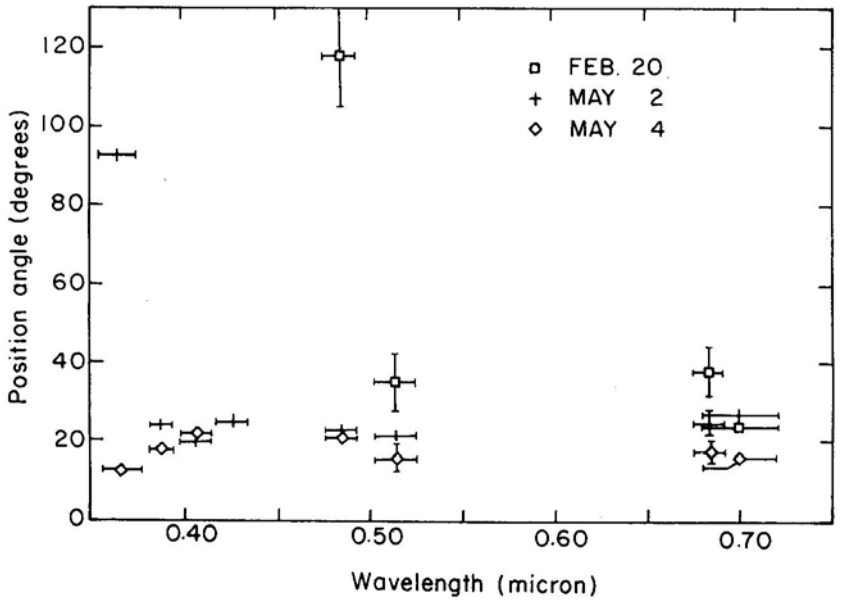

Figure 2b. Wavelength dependence of position angle as measured on different dates; error bars are plotted.

Figure 2b shows the wavelength dependence of position angle of the polarization. Within the errors of measurements, the polarization angle for continuum and molecular bands is constant (except for BC on February 20 and for UC on May 2) and is found to be perpendicular to the scattering plane. During pre-perihelion phase on February 20, the BC shows a flip of about 80 degrees in the position angle. Since observations could not be made on February 20 in other shorter wavelengths due to low flux level and high atmospheric attenuation as the comet was very low at the time of observations, it is difficult to infer whether the flip in position angle observed in BC extends to other shorter wavelengths. A flip of 90 degrees is possible for shorter wavelengths which again depends on the Sun-comet-Earth phase angle and characteristics of dust particles. The error in polarization measurement in BC on February 20 is large (refer Table 1) and expected error (one sigma) in position angle is also large ($E_\theta \sim 14$ degrees). Therefore, it is difficult to say whether the flip in position angle observed in BC corresponds to a 90 degree flip. The flip observed in UC on May 2 appears genuine as the error in polarization measurements are very low (refer Table 1). In general the flip in polarization angle has been noticed in most of the comets at low phase angle (phase angle < 22 degree) (Dollfus 1989). Weinberg & Beeson (1975, 1976) have made extensive polarization measurements on Ikeya-Seki (1965 VIII) for different scattering angles. The most interesting result of their observations is the change in polarization from positive to negative values for λ=0.53 μm as the scattering angle changes from 116 to 135 degrees. Polarization reversal is present in planetary atmospheres including the Earth's atmosphere and has been found in zodiacal light also (Wolstencroft & Rose 1967; Weinberg & Mann 1968; Frey *et al.* 1974). Of particular interest in the zodiacal light is the possibility of positive and negative polarization at small elongation in the vicinity of 0.43 μm (Weinberg & Mann 1968). The steep change in the degree of polarization and the large amount of negative

polarization are characteristics of a narrow range of small particles having a small imaginary part in their refractive index which is again consistent with the inference made earlier on the basis of continuum flux distribution and the wavelength dependence of the polarization.

The polarization reversal may arise as a result of (i) the segregation of different size grains in the tail of the comet due to the effect of radiation pressure; (ii) alignment of the non spherical grains in the cometary atmosphere (Swamy 1978; Kiselev & Chernova 1981). The second mechanism does not seem to fit the present observations of May 2 as both the positive and negative polarizations are present at different wavelengths. Segregation of the grains in the tail is one possibility or that comet Austin has a narrow range (0.1 to 0.5 μm) in the dust distribution in reality. Due to projection effects radiation from a larger area of the comet is reaching us on May 2 (phase angle 109.0 degree) as compared with May 4 (phase angle 107.4 degree). Therefore, segregation of the grains cannot be ruled out.

4.2 *Molecular Band Emission*

Flux in the emission bands of CN, C_3, CO^+, C_2, H_2O^+ are given along with the background solar continuum flux in Table 2. The data in Table 2 show that C_2 is always strongest whether it is pre- or post-perihelion phase. A similar trend has been observed in the case of comet Halley (Sen *et al.* 1989). The flux in C_3 relative to C_2 shows significant variation between May 2 and May 4. Regarding the emission from the ionic molecules: H_2O^+ is quite weak whereas CO^+ could not be detected.H_2O^+ has not been detected in our observation on February 20 (pre-perihelion time), while the observations made in the post-perihelion phase show the presence of ionic water molecule; the flux value shows an increase of about 30% on May 4 as compared to the flux on May 2. The increase in H_2O^+ flux is three times the estimated error and, therefore, it is significant. In comet Austin CO^+ is perhaps below our detection limit (lower than 1.0E-11 ergs/cm^2/sec) on all the observing dates; this molecule was found present in comet Halley on March 19, 1986 (Sen *et al.* 1989).

The present observations show that there is some correlation among the molecular emissions from the molecules: C_2, C_3, CN and H_2O^+. C_3 emission shows an enhancement (on absolute term) on May 4 by a factor of 2 as compared to the emission on May 2 and at the same time H_2O^+ is enhanced by about 30%. If we look at the emission flux from CN and C_2 on May 2 and 4, we find an anti-correlation with C_3 emission; C_3 emission decreases with the enhancement of CN and C_2 (refer Table 2). There are some ideas published in the literature on the production mechanism of C_3 molecule (Stief 1972) though the scenario is not clear. The present observations indicate that the enhancement of H_2O^+ is related with the enhancement of C_3. Perhaps one may explain the above observations as follows:

It is believed that most of the H_2O^+ is produced during an eruption. The higher mobility of the ionic water molecules causes them to travel farther out than the neutral molecules and can produce a halo around the comet nucleus which may prevent UV radiation from the Sun reaching inside the halo. This will reduce the dissociation rate of C_3 molecule and enhance C_3 emission. The possibility of sudden enhanced formation of C_3 molecule by chemical combination of some other carbon containing molecules,

released during eruption, cannot be ruled out. The formation mechanism of C_3 molecule is not well understood at present and its parent molecule is not known definitively.

4.3 *Molecular Band Polarization*

The observed degree of polarization and position angle in continuum filters and in the molecular bands are listed in Table 1. Flux in different emission bands are given along with the background continuum in Table 2. The polarization observations show that the polarization vector in the emission and continuum is in the same direction i.e. perpendicular to the scattering plane. The exception to this are the polarization vector in the B and U bands as observed on February 20 and May 2 respectively. However, the observed polarization vector for molecular bands redwards of the B-band on February 20 and of the U-band on May 2 are nearly perpendicular to the scattering plane. This means that the polarization vector due to the background continuum at the molecular band emission is also perpendicular to the scattering plane. This situation simplifies the procedure of separating the polarized flux due to the fluorescence emission from the observed molecular band polarization. In such a case the observed polarization flux in a molecular band is the scalar sum of emission and continuum polarization flux which can be expressed as:

$$P_o \cdot F_{\mathrm{Tot}} = P_E \cdot F_E + P_c \cdot F_c \tag{3}$$

where P_o is the observed degree of polarization and P_E and P_c are respectively the degree of polarization due to the molecular emission and continuum; F_{Tot} is the total flux and F_E and F_c are respectively the flux due to molecular emission and the continuum. In different emission bands, the contribution to the degree of polarization due to the background continuum has been found by interpolating the flux values between continuum values (using Fig. 2a). The continuum polarization at the position of molecular bands thus found is used to calculate the value of P_E using relation (3). The values of P_E are listed in Table 2.

The molecular band polarization values (Table 2) for C_2, C_3 , CN and $H_2\,O^+$ molecules measured on May 2 are close (within the error bars) to the values obtained on May 4. This is expected as the phase angle has not changed much during the observing run in May (phase angle at the time of observation on May 2 and 4 was respectively 109.0 and 107.4 degrees). We have theoretically calculated $P_{\max}$ (maximum polarization at phase angle 90°) as discussed by Sen *et aL* (1989) and the values thus obtained for May 2 and 4 are listed in Table 2. We have not calculated the value of $P_{\max}$ for February 20 as the error in flux measurement is relatively large. From the theoretical calculations by Ohman (1941) a value of 7.7% for $P_{\max}$ is expected for CN and C_2 molecules. The $P_{\max}$ values obtained for CN and C_2 in the present work are in agreement (within the error bar) with the theoretically expected values. The estimated value of C_3 band polarization on May 2 and 4 matches within the error bars. However, the $P_{\max}$ value (Table 2) is much below the theoretically expected value. In the case of comet Halley also (Sen *et al.* 1989) the polarization value was found to fall much below the theoretically predicted value based on the theoretical relation given by Ohman (1941). At present we have no satisfactory explanation.

The mean value of P_{max} for H_2O^+ emission in comet Austin on May 2 and May 4 is: $P_{H_2O} \sim 0.8 \pm 1.4\%$ (refer Table 2). In case of comet Halley the estimated polarization value of H_2O^+ is quite large ($P_{H_2O^+} \sim 29\%$) (Sen *et al.* 1989). However, in case of Halley the error was large (comparable to the observed polarization value) and therefore the estimated value of polarization for H_2O^+ molecule in Halley should be taken cautiously. The main reason for large errors in p/Halley is very low flux level for the ionic water molecule. In case of comet Austin the polarization of ionic water molecules has been found to be low. Future Polarimetric observations on ionic molecules in bright comets will be useful.

5. Conclusions

1 The flux distribution of comet Austin as observed through the three IAU/IHW continuum filters is bluer on May 2 and 4 compared with the solar flux distribution.
2 Wavelength dependence of polarization in comet Austin on May 2 and 4 shows that the polarization decreases sharply with decreasing wavelength. Polarization vectors in continuum and emission bands are perpendicular to the scattering plane. However, some measurements deviate significantly from it.
3. The steep wavelength dependence of the degree of polarization and the bluer flux distribution compared to a solar analog indicate that the dust size distribution lies in a narrow range and the sizes of the dominant particles are expected in the range of 0.1 μm to 0.5 μm.
4. Neutral molecular bands: C_2, CN and C_3 are strong. The flux values for C_3 molecule show (Table 2) significant variation on different dates; H_2O^+ was present on May 2 and 4 (post-perihelion phase).

Acknowledgements

We are thankful to Prof. R. K. Varma for encouraging this work and to Prof. J, C. Bhattacharya and Prof. N. K. Rao for allotting the telescope time on 2.34 m VBT. This work has been supported by the Department of Space, Govt. of India. We are also thank ful to the anonymous referees of this paper for their valuable comments.

References

Bappu, M. K. V., Sivaraman, K. R., Bhatnagar, A., Natrajan, V. 1967, *Mon. Not.R, astr. Soc.*, **136,**19

Bastein, P., Menard, F., Nadeau, R. 1986, *Mon. Not. R. astr. Soc.*, **223,** 827.

Blackwell, D. E., Willstrop, R. V. 1957, *Mon. Not. R. astr. Soc*., **117,** 590.

Deshpande, M. R, Joshi, U. C, Kulshrestha, A. K., Bansidhar, Vadher, N. M, Mazumdar, H. S., Pradhan, S. N., Shah, C. R. 1985, *Bull astr. Soc. India*, **13**, 157.

Dobrovolsky, O. V., Kiselev, N. N., Chernova, G. P. 1986, *Earth*, *Moon*, *Planets*, **34,** 189.

Dollfus, A., Suchail, J. -L. 1987, *Astr. Astrophys*., **187,** 669.

Dollfus, A. 1989, *Astr. Astrophys*., **213,** 469.

Frey, A., Hofmann, W., Lemke, D., Thum, C. 1974, *Astr. Astrophys*., **36** 447.

Gebel, W. L. 1970, *Astrophys. J*., **161**, 765.

Greenberg, J. M. 1978, in *Cosmic Dust*, Ed J. A. M. McDonnell, Interstellar Dust, p. 187.

Kharitonov, A. V, Rebristyi, V, T. 1974, *Sov. Astr*., **17,** 672.
Kikuchi, S., Mikami, Y., Mukai,.T., Mukai, S., Hough, J. H. 1987, *Astr. Astrophys*., **187,** 687.
Kiselev, N. N., Chernova, G. P. 1981, *ICARUS,* **48,** 473.
Le Borgene, J. F., Leroy, J. L., Arnaud, J. 1987, *Astr. Astrophys*., **173,** 180.
Martin, P. G. 1978, *Cosmic Dust*, Oxford University Press, p. 57.
Ohman, Y. 1941, *Stockholm Obs. Ann*., **13,** no. 11.
Sekanina, Z. 1990, *IAU Circular,* No. **4977**.
Sen, A. K .,Joshi, U. C,Deshpande, M. R., Kulshrestha, A. K.,Babu, G. S. D., Shylaja, B. S.1988, *Astr. Astrophys*., **204,** 317.
Sen, A. K., Joshi, U. C, Deshpande, M. R. 1989, *Astr. Astrophys*., **217,** 307.
Sen, A. K., Joshi, U. C, Deshpande, M. R. 1991, *Mon. Not. R. astr. Soc*., **253,** 738.
Serkowski, K. 1962, *Adv. Astr. Astrophys*., **1,** 1.
Swamy, K. S. K. 1978, *Astrophys. Space Sci*., **57,** 491.
Stief, L. S. 1972, *Nature* **237,** 29.
Weinberg, J. L., Beeson, D. E. 1975, *Photoelectric polarimetry of the tail of Comet Ikeya-Seki* (1965, VIII), in "The Study of Comets", Proc. IAU Colloq. No. 25.
Weinberg, J. L., Beeson, D. E. 1976, *Astr. Astrophys*., **48**, 151.
Weinberg, J. L., Mann, H. M. 1968, *Astrophys. J*., **152,** 665.
Wolstencroft, Rose 1967, *Astrophys. J*., **147**, 271.

J. Astrophys. Astr. (1992) **13,** 279–286

Photometric Analysis of the Chromospherically Active Giant Star HD 86005

Tania R. Scott, J. B. Hearnshaw, R. D. Watson†, P. M. Kilmartin & A. C. Gilmore *Mt John University Observatory, Department of Physics and Astronomy, University of Canterbury, Christchurch, New Zealand*

Received 1992 January 24; accepted 1992 August 3

Abstract. Photometric data, covering a span of two and a half years, have been analysed for the chromospherically active giant star HD 86005. It was found to undergo light variations and a photometric period of 89.0 ± 0.3 days was determined. Evidence suggests that these brightness variations are due to the rotation of unevenly distributed starspots.

Key words: chromospheric activity—late type giant—starspots—HD 86005

1. Introduction

HD 86005 has been observed at the Mt John University Observatory over a period of two and a half years as part of an extended photometric observation programme of possible active chromosphere stars. It was initially selected for observation due to the presence of several features characteristic of chromospheric activity, and was chosen for analysis because of the clear variability found in its photometric data.

The *Michigan Spectral Catalogue* (Houk 1975) lists it as spectral type K2 IIIp where the p indicates weak Ca II H and K line core emission. Bopp and Hearnshaw (1983) detected Hα emission above the continuum and Verma *et al.* (1983) measured a high infrared excess, which could partly be attributed to the presence of starspots. However, no radio emission was reported by Mutel & Lestrade (1985).

UBV photometric studies have been carried out by Grenier (1974) on one night, and by Bopp *et al.* (1986) over a period of nine nights. Udalski & Geyer (1984) conducted *UBV* $(RI)_C$ photometry over twelve nights, as did Cutispoto (1991) over fifteen nights. Bopp *et al*., Udalski and Geyer, and Cutispoto found no variation in light levels over the span of their observations, although their values are different, suggesting some sort of long-term variability.

2. Observations

Differential photometric observations were carried out at the Mt John University Observatory between 1988 November and 1991 April, during which time 79 sets of

†On sabbatical leave from Physics Department, University of Tasmania, Hobart, Australia.

BV(*RI*)*c* data points were obtained (Table 1). The comparison star used was HD 86034, while the check star was HD 85966.

Two telescopes were used for these observations, the 0.6 m Optical Craftsmen reflector (with an EMI9558B S20 photomultiplier tube) and the 0.6 m Boller & Chivens reflector (with an RCA C31034A GaAs photomultiplier tube). During each

Table 1. Mt John University Observatory photometric data for HD 86005.

HJD (2440000 +)	V	$(B-V)$	$(V-R)_C$	$(V-I)_C$	$V_{\text{checkstar}}$
7490.1056	7.305	1.301	0.696	1.271	7.448
7551.0722	7.298	1.312	0.728	1.252	7.434
7571.0453	7.301	1.298	0.713	1.290	7.452
7573.0480	7.284	1.312	0.736	1.301	7.438
7586.0112	7.344	1.294	0.697	1.272	7.449
7588.0892	7.332	1.297	0.700	1.278	7.450
7591.9843	7.351	1.291	0.703	1.282	7.447
7609.9278	7.345	1.295	0.730	1.317	7.452
7610.9265	7.343	1.310	0.730	1.315	7.443
7612.0509	7.332	1.301	0.728	1.312	7.441
7616.0363	7.339	1.284	0.709	1.291	7.449
7619.9413	7.326	1.289	0.714	1.265	7.439
7622.9755	7.326	1.285	0.706	1.280	7.451
7627.9659	7.296	1.300	0.723	1.296	7.434
7635.9537	7.306	1.292	0.697	1.274	7.435
7643.9646	7.313	1.286	0.712	1.267	7.447
7654.9936	7.294	1.287	0.701	1.263	7.436
7663.9182	7.305	1.305	0.703	1.266	7.440
7676.9469	7.318	1.318	0.732	1.307	7.455
7682.8899	7.336	1.302	0.729	1.316	7.441
7693.8552	7.354	1.302	0.705	1.300	7.446
7699.8888	7.328	1.310	0.725	1.306	7.442
7705.9132	7.321	1.302	0.740	1.316	7.451
7724.8597	7.332	1.290	0.710	1.294	7.441
7730.8272	7.316	1.300	0.699	1.283	7.448
7781.2273	7.391	1.301	0.713	1.321	7.449
7782.1500	7.358	1.317	0.688	1.290	7.427
7818.1102	7.312	1.301	0.707	1.277	7.448
7819.1078	7.315	1.298	0.707	1.284	7.425
7824.1581	7.307	1.301	0.688	1.279	7.453
7830.1069	7.301	1.303	0.693	1.273	7.441
7833.1254	7.301	1.295	0.696	1.275	7.460
7852.0633	7.331	1.326	0.700	1.284	7.428
7860.0660	7.366	1.302	0.726	1.320	7.470
7865.0782	7.363	1.303	0.712	1.296	7.444
7880.0711	7.322	1.303	0.699	1.290	7.439
7912.0348	7.306	1.281	0.708	1.288	7.449
7916.0733	7.285	1.288	0.695	1.271	7.437
7922.0688	7.299	1.277	0.702	1.281	7.459
7923.0696	7.280	1.284	0.698	1.260	7.445
7924.0682	7.277	1.302	0.695	1.266	7.447
7930.9573	7.287	1.298	0.698	1.276	7.448
7943.2069	7.337	1.299	0.712	1.300	

Table 1. Continued.

HJD (2440000 +)	V	$(B-V)$	$(V-R)_C$	$(V-I)_C$	$V_{\text{checkstar}}$
7943.9566	7.328	1.304	0.699	1.287	7.445
7949.9703	7.356	1.308	0.709	1.302	7.449
7955.9453	7.354	1.310	0.709	1.289	7.449
7964.9034	7.338	1.297	0.707	1.294	7.442
7968.9196	7.323	1.308	0.701	1.284	7.446
7971.9312	7.330	1.290	0.726	1.301	7.449
7986.0083	7.323	1.291	0.716	1.285	7.450
7989.9154	7.337	1.306	0.715	1.269	
7991.9217	7.318	1.293	0.709	1.284	7.447
7992.9300	7.318	1.293	0.701	1.294	7.444
7999.9352	7.313	1.289	0.706	1.281	7.445
8002.9409	7.307	1.283	0.705	1.288	7.446
8019.9506	7.306	1.292	0.705	1.284	7.443
8038.8698	7.359	1.302	0.702	1.304	7.447
8050.8907	7.318	1.320	0.733	1.298	7.424
8051.8869	7.329	1.299	0.718	1.291	7.465
8053.9093	7.370	1.293	0.752	1.326	7.434
8061.8853	7.314	1.292	0.722	1.310	7.452
8065.8725	7.328	1.303	0.701	1.297	7.447
8073.8546	7.342	1.298	0.706	1.320	7.461
8077.8790	7.350	1.297	0.720	1.307	7.461
8085.8205	7.341	1.292	0.717	1.289	7.449
8091.9205	7.314	1.314	0.693	1.296	7.459
8099.9075	7.317	1.269	0.694	1.301	7.464
8141.2183	7.342	1.294	0.688	1.285	7.447
8152.2213	7.320	1.307	0.706	1.290	7.457
8165.1956	7.309	1.278	0.715	1.301	7.412
8188.1345	7.303	1.293	0.707	1.278	7.459
8211.1200	7.326	1.283	0.670	1.242	7.420
8243.0471	7.294	1.258	0.697	1.283	7.431
8253.0733	7.300	1.292	0.709	1.271	7.453
8256.0223	7.313	1.275	0.716	1.288	7.462
8260.0539	7.308	1.290	0.708	1.281	7.451
8269.0386	7.304	1.290	0.704	1.287	7.452
8282.9907	7.295	1.293	0.696	1.280	7.476
8294.0253	7.275	1.291	0.689	1.256	7.446

observation, integrations lasting 5 or 20 seconds were repeated 3 or 2 times respectively, depending on the pass-band, with the integrations then being averaged. Two observations were obtained for each observing night and these were then averaged to give a nightly mean, which typically had a standard deviation error of $0^{m}.005$. The check star, however, had a standard deviation for all of the V data of $0^{m}.011$, so that one would expect the scatter in each data point of HD 86005 to be of this order.

It was found that the star exhibited variability over a time scale of around 100 days, with a peak-to-peak amplitude of approximately $0^{m}.07$ in V. This variability would not have been detected by the previous groups, assuming it was present during their observations, as their data spanned periods of two weeks or less.

3. Photometric period determination

Photometric periods in each pass-band were determined through the use of a FORTRAN program (Lawson 1990 *et al.)* based on the Lomb-Scargle method of applying a Fourier transformation to unevenly spaced data (Lomb 1976, Scargle 1982). The program produces a power spectrum in a specified frequency range, using a fixed frequency increment. Residual and phase data are also produced, as is a synthetic curve of the strongest frequency, and a facility is available to subtract this synthetic curve from the data so that a search for secondary frequencies can be made.

For HD 86005 significant power spectra peaks were identified for each of *B*, *V*,*R* and *I*, using the minimum possible frequency increment of 0.00001 cycles per day, and the results are given in Table 2. The average of these frequencies gives a photometric period for HD 86005 of 89.0 ± 0.3 days. Fig. 1 shows, as an example, the *V* data phased with its 89.6-day period, while Fig. 2 shows the power spectrum produced in *V*. Fig. 3 shows the power spectrum in *V* for the second harmonic (solid line), and the power spectrum in *V* after the second harmonic has been removed (dashed line).

Table 2. Fundamental and second harmonic frequencies for HD 86005, with, their phases and half-amplitudes.

Filter	Fundamental frequency	Phase	Half amplitude	First harmonic	Phase	Half amplitude
B	0.01119	4.68	0.029	0.02241	3.91	0.017
V	0.01116	4.57	0.023	0.02243	3.88	0.015
R	0.01126	4.68	0.017	0.02247	3.84	0.015
I	0.01132	4.54	0.012	0.02243	4.15	0.012
Average	0.011233	4.62		0.022435	3.95	
	± 0.000036	± 0.04		± 0.000013	± 0.07	
	(89.0 ± 0.3 days)			(44.57 ± 0.02 days)		

Phase, on a 0 to 2π basis, is the phase occurring on 1988 November 24 = HJD2447490.1056.

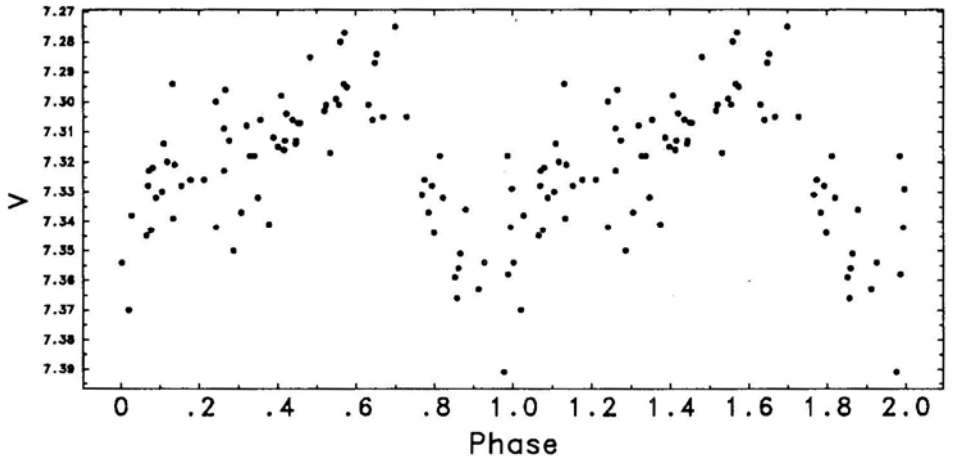

Figure 1. *V* data for HD 86005, phased with an 89.6-day period.

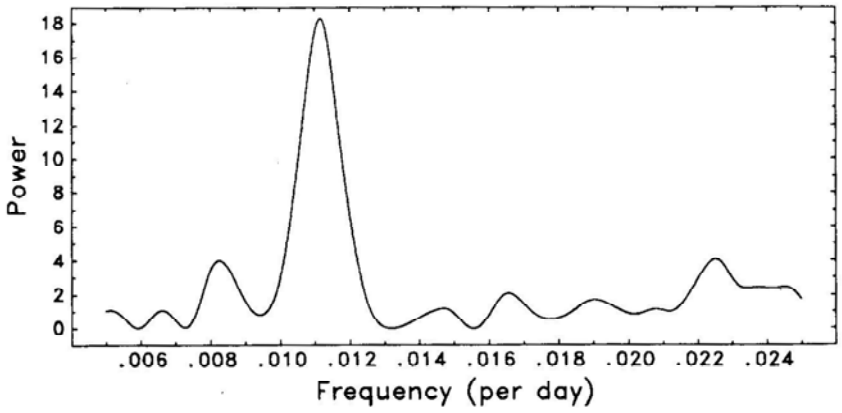

Figure 2. Power spectrum in *V* for HD 86005.

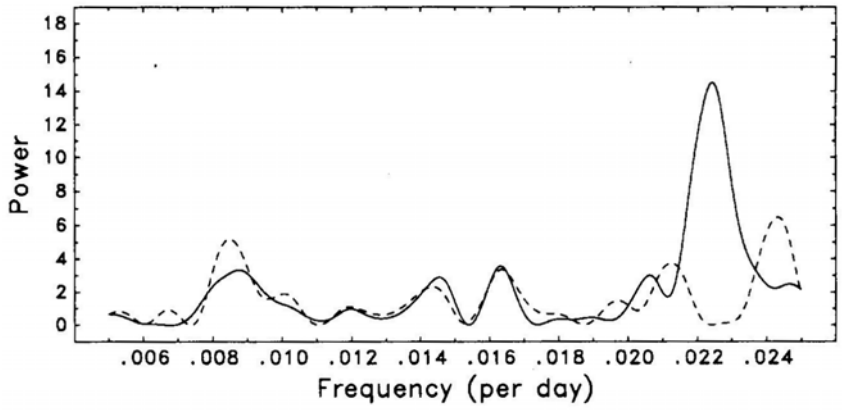

Figure 3. Power spectrum in *V* for HD 86005 obtained after the removal of the 89.6-day period (solid line), followed by removal of the second harmonic (dashed line).

The scatter in Fig. 1 has a standard deviation of $0^m.017$, which is larger than that expected from the observational errors. This is mainly due to the presence of a significant second harmonic. The residual in the data after the fundamental and second harmonic frequencies have been removed, has a standard deviation of $0^m.013$, which is much closer to the expected value. Additional scatter may be due to slight changes in period, amplitude or phase over the 9 cycles observed. Consideration of the first 36 data points in *V* resulted in a period of 87.3 days and a half-amplitude of $0^m.029$, while the final 43 points in *V* gave a period of 89.2 days and a half-amplitude of $0^m.020$. The mean *V* values were $7^m.325$ and $7^m.319$ respectively. It should be noted, however, that in each of the two cases the standard deviation of the scatter in the data was not significantly less than that resulting when all of the data was analysed together.

The peak-to-peak amplitudes of the light variations in each pass-band were measured from the synthetic curves composed of the fundamental and second harmonic sinusoids. The resulting amplitudes and error estimates are given in Table 3, along with the average values of *B, V, R* and *I* over the period of the Mt John observations.

Table 3. Average magnitudes of the Mt John data for HD 86005 and the amplitudes of the synthetic curves.

Filter	Average over observations	Peak to peak amplitude of synthetic curves
B	8.618	0.078 ± 0.005
V	7.322	0.066 ± 0.005
R	6·613	0.054 ± 0.005
I	6.033	0.043 ± 0.005

4. Discussion

The observed light variations of HD 86005 can be well explained by the application of a starspot model. If cool starspots were present on HD 86005 one would expect the amplitude of variation in the light curve to increase for shorter wavelengths, where the spots should radiate less light. This is indeed the case, as can be seen from Table 2. Furthermore, Fig. 4 shows a correlation between brightness and colour, with the star becoming bluer as it brightens.

The Mt John observations must have been carried out during a phase of high spot activity, such that at no time was an unspotted hemisphere facing Earth. This is supported by the fact that the light curve in Fig. 1 is not flat topped, as would be the case if no spots were visible over a time scale of several days. It is possible that the values obtained by Grenier (1974) and Bopp *et al.* (1986) correspond to the unspotted colour indices of the star, as their observations are the brightest of the five photometric studies, and their values agree remarkably well despite being obtained approximately 15 years apart. It is unfortunate that no $(V - R)$ or $(V - I)$ values are given by Grenier or Bopp *et al.,* since known unspotted colour indices for HD 86005 would have enabled a quantitative starspot model to be applied.

The results of Grenier (1974), Udalski & Geyer (1984), Bopp *et al.* (1986) and Cutispoto (1991) are all significantly brighter than any of the Mt John observations. It is thus clear that for this to be due to starspots a change in the number of spots, or a redistribution of spots, must have occurred at least in the couple of years prior to the Mt John observations, if not at other times. It may be that an activity cycle is present, such as that observed for other chromospherically active stars (Baliunas & Vaughan 1985).

Comparison between the colour indices obtained by the various groups reveals some anomalies. The colour indices are given in Table 4 and it can be seen that they are remarkably constant in colour as the star becomes fainter. Using a simplistic starspot model with no energy redistribution, one would expect a star to become redder as it becomes fainter if the area of the photosphere covered by starspots is increasing. This is not the case for HD 86005. Indeed, at the Mt John light maximum the $(B - V)$ colour index is bluer than that of Bopp *et al.* (1986), although this could lie within the error bars, as is the $(V - I)_c$ index for all of the Mt John observations. If a starspot model were applied at the Mt John light maximum, where ΔV between the Mt John value and the Bopp *et al.* value is marginally greater than ΔR, then hot spots would result.

In addition, there appears to be an excess of UV light. The $(B— V)$,$(V— R)_c$ and $(V–I)_c$ indices correspond roughly to a K3.5III star (Bessell 1979), whereas the

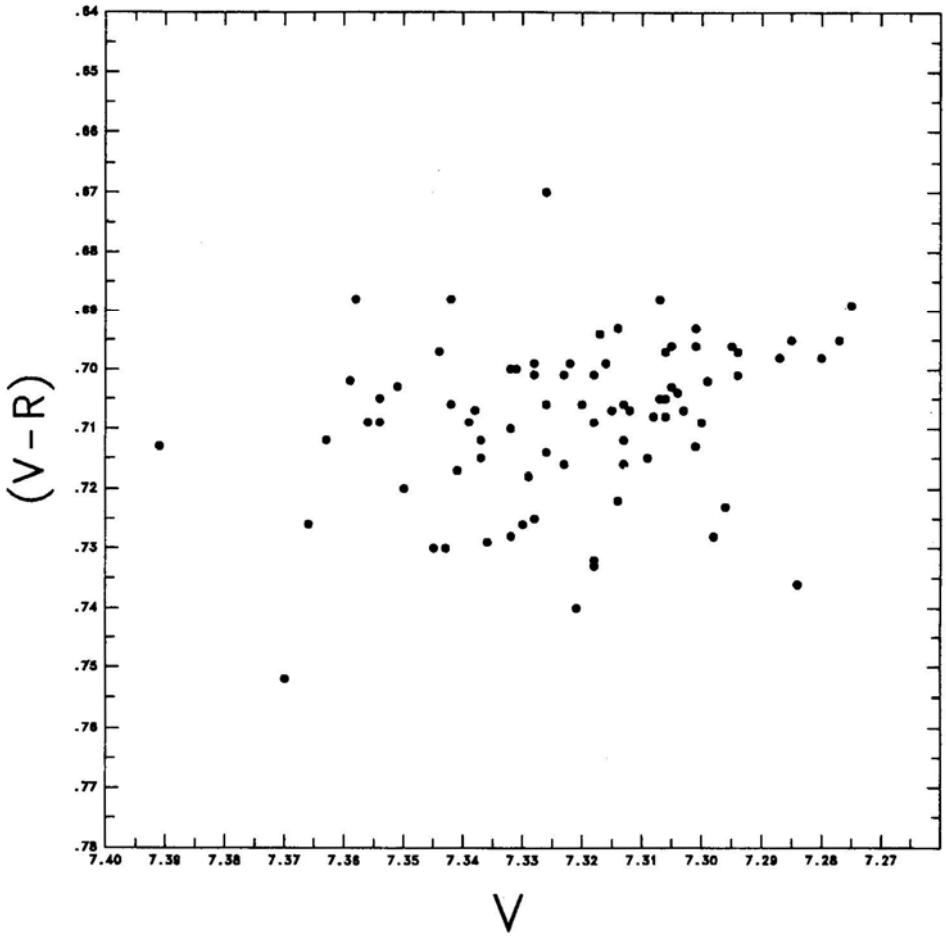

Figure 4. Colour correlation with brightness for HD 86005.

($U - B$) index is that for a K1 III star (Johnson 1966). As Cutispoto (1991) notes, this could be due to the presence of an early type companion, but in view of the fact that UV excess is a well known feature of chromospherically active stars (Hall 1976) this is probably not the only plausible explanation.

Chromospherically active stars with periods greater than that of HD 86005 have

Table 4. *UBV*(*RI*)*c* photometry of HD 86005.

	V	$(U-B)$	$(B-V)$	$(V-R)_C$	$(V-I)_C$
Grenier (1974)	7.18	1.09	1.30		
Bopp *et al.* (1986)	7.180	1.020	1.296		
Udalski & Geyer (1984)	7.230	1.026	1.307	0.711	1.347
Cutispoto (1991)	7.25	1.03	1.32	0.71	1.36
Mt John at maximum light	7.29		1.29	0·70	1.28
Mt John average	7.322		1.296	0.709	1.289
Mt John at minimum light	7.36		1.30	0.72	1.30

been observed (Fekel *et al.* 1986; Hall *et al.* 1990) but even so HD 86005 has an exceptionally slow rotation period compared to most other active chromosphere stars (Hartmann 1980; Baliunas & Vaughan 1985; Fekel *et al.* 1986). It may be that this is why only weak Ca II H and K core emission is present, and why the amplitude of light variation is at the lower end of that observed in other active chromosphere stars, where the amplitude can range up to $0^m.5$ in V (Hartmann 1980).

It is possible that HD 86005 may belong to the group of FK Comae stars, which are single late-type giants exhibiting strong chromospheric activity (Bopp & Stencel 1981). However in this case the star should be a rapid rotator, which is not observed for HD 86005. It seems that HD 86005 perhaps best belongs to the group, identified by Fekel *et al.* (1986), of medium to rapidly rotating single G8–K2 giants which exhibit moderate chromospheric activity.

5. Conclusion

The analysis of a two and a half year span of photometric $BV(RI)_c$ data has resulted in evidence that suggests that starspots are the cause of the observed 90-day light variations of HD 86005. The detection of this 90-day period demonstrates the desirability of long term photometric observations, as short term observations may result in a star being classified as non-variable when in fact that is not the case. The colour variations predicted by a starspot model were observed in the Mt John data. However, a simplistic starspot model is inadequate to explain the observed constancy of the colour indices of HD 86005 as the star brightens and modifications to the model would be required to explain this feature.

References

Baliunas, S. L., Vaughan, A. H. 1985, *A. Rev. Astr. Astrophys.,* **23,** 379.
Bessell, M. S. 1979, *Publ. astr. Soc. Pacific,* **91,** 589.
Bopp, B. W., Africano, J, Quigley, R. 1986, *Astr. J.,* **92,** 1409.
Bopp, B. W., Hearnshaw, J. B. 1983, *Astrophys. J.,* **267,** 653.
Bopp, B. W., Stencel, R. E. 1981, *Astrophys. J.*, **247,** L131.
Cutispoto, G. 1991, *Astr. Astrophys. Suppl. Ser.,* **89,** 435.
Fekel, F. C, Moffett, T. J., Henry, G. W. 1986, *Astrophys. J. Suppl. Ser.,* **60,** 551.
Grenier, S. 1974, *Astr. Astrophys. Suppl. Ser.,* **16,** 269.
Hartmann, L. 1980, in *NATO Advanced Study Institutes Series* **68:** *Solar Phenomena in Stars and Stellar Systems,* Eds R. M. Bonnet & A. K. Dupree, North Holland, Amsterdam, p. 487.
Hall, D. S. 1976, *I.A.U. Coll.,* **29,** 287.
Hall, D. S., Gessner, S. E., Lines, H. C, Lines, R. D. 1990, *Astr. J.,* **100,** 2017.
Houk, N. 1975, *Michigan Spectral Catalogue of Two Dimensional Spectral Types for the HD Stars,* **2,** University of Michigan.
Johnson, H. L. 1966, *A. Rev. Astr. Astrophys.,* **4,** 193.
Lawson, W. A., Cottrell, P. L, Kilmartin, P. M, Gilmore, A. C. 1990, *Mon. Not. R. astr. Soc,* **247,** 91.
Lomb, N. R. 1976, *Astrophys. Space Sci.,* **39,** 447.
Mutel, R. L., Lestrade, J. F. 1985, *Astr. J.,* **90,** 493.
Scargle, J. D. 1982, *Astrophys. J.,* **263,** 835.
Udalski, A., Geyer, E. H. 1984, *Inf. Bull. Var. Stars,* No. 2525.
Verma, R. P., Ghosh, S. K., Iyengar, R. V. K., Rengarajan, T. N., Tandon, S. N., Daniel, R. R., Sanwal, N. B. 1983, *Astrophys. Space Sci.,* **97,** 161.

J. Astrophys. Astr. (1992) **13,** 287–291

Globular Clusters as Gamma Ray Sources

V. B. Bhatia, S. Mishra & N. Panchapakesan *Department of Physics and Astrophysics, University of Delhi, Delhi 110 007*

Received 1992 March 18; accepted 1992 October 10

Abstract. There are indications now that globular clusters contain a large number of low magnetic field millisecond pulsars. Since millisecond pulsars are expected to emit γ-rays due to curvature radiation, it is likely that globular clusters will themselves be sources of γ-rays bright enough to be detectable by present day instruments. Using the expression derived by Scharlemann, Arons & Fawley (1978) of the energy acquired by the electrons moving along the open magnetic field lines of the pulsars we have calculated the likely luminosity of γ-rays from globular clusters. We discuss our results in the light of the calculations reported in the literature based on some of the other models.

Key words: globular clusters—pulsars—resurrected neutron stars—γ-rays

1. Introduction

In the last few years a new population of pulsars, namely the millisecond pulsars, has been discovered. The short period of rotation makes them good candidates for emitting γ-rays. Efforts are being made to detect high energy gamma rays from these pulsars and there are already hints that very high energy γ-rays from two of these pulsars have been observed (Chadwick *et al.* 1985, 1987).

These millisecond pulsars having typically magnetic fields of the order of 10^8 G, which is characteristic of slow-rotating old pulsars, are thought to be the spun-up neutron stars. The detection of binary companions of many of these pulsars has already been confirmed. This has supported the view that the old neutron stars are spun up by mass accretion from their respective companions over a long period of time. In this way an old neutron star with a low magnetic field (~ 10^8 G) gets spun up to a resurrected period given by the mass accretion relation (Radhakrishnan & Srinivasan 1981; Alpar *et al.* 1982)

$$p \sim B_8^{6/7}(\dot{M} \times 10^8/M_\odot/\mathrm{yr})^{-3/7}\mathrm{s}, \tag{1}$$

where $\dot{M}$ is the mass accretion rate and the maximum value of M is the Eddington rate given by $M_\odot/10^8$ per year.

It has been suggested that there may be of the order of a thousand millisecond pulsars in one globular cluster (Kulkarni 1990; Manchester *et al* 1991). Already 28 millisecond pulsars have been discovered in globular clusters (Chen 1991). Though the distribution of these millisecond pulsars with period is not exactly known yet a reasonable relation has been given by Chen, which is a power law distribution:

$$F(p) = (\alpha - 1)p_{\mathrm{min}}^{\alpha-1}\, p_{\mathrm{ms}}^{-\alpha}, \tag{2}$$

where period is in millisecond, $\alpha = 1.4$ for $p_{ms} > p_{min}$ and the minimum value of period p_{min} is 1.6 ms.

A globular cluster containing a large number of resurrected millisecond pulsars which emit gamma rays is likely to be itself a source of gamma rays. In this paper we discuss a model which gives an estimate of γ-luminosity of a globular cluster. In section 2, we present the model and an estimate of the luminosity of a globular cluster which contains the millisecond pulsars. In section 3 we compare our results with those derived on the basis of some other models.

2. Model and its prediction

The magnetic field far from the surface of a neutron star is basically due to the star's own dipole field. Field lines which originate very close to the polar caps of a pulsar do not close within the light cylinder and go across it. These field lines are called open field lines. According to the model of Goldreich & Julian (1969) there is an electric field $E_1 = \mathbf{E}\cdot\mathbf{B}/B$ parallel to the magnetic field B along these open lines. When charged particles move along these lines they get accelerated to very high energies. These accelerated charged particles emit γ-rays by curvature radiation and are subject to radiation reaction. It has been shown by Scharlemann *et al.* (1978) that radiation reaction is important when the period of the pulsar is given by the relation,

$$p < p_{rr} = 8{\cdot}108(B_8 R_6)^{3/7} \text{ ms.} \tag{3}$$

The radiation reaction limited Lorentz factor for the electrons is given by (Scharlemann *et al.* 1978)

$$\gamma_e \sim \gamma_{rr} = 1.8 \times 10^6 r^{1/8} R_6^{6/8} p_{ms}^{-3/8} B_8^{1/4} \tag{4}$$

where p_{ms} is the period of rotation in millisecond, R_6 is the radius of the star in units of 10^6cm, B_8 is the star's magnetic field in units of 10^8 G and r is the distance from the star's surface to the point where the radiation is emitted. It has been assumed, while arriving at the above result, that most of the work done in accelerating the charged particles is converted into γ-emission due to curvature radiation. In passing we note that if the period of the pulsar is longer than that given by Equation (3), the energy of the electron is given by (Scharlemann *et al.* 1978)

$$\gamma_e \approx 6 \times 10^8 B_8 R_6^3 p_{ms}^{-5/2} [10^{-3}(r/R_6)^{1/2} - 1]. \tag{5}$$

Data regarding the periods and magnetic fields of the spun-up millisecond pulsars is rather scanty. Periods and magnetic fields of four millisecond pulsars in the galactic disc (Bhattacharya & Srinivasan 1991) and a few millisecond pulsars in globular clusters (Chen 1991) are known. From this limited data we can reasonably assume that the millisecond pulsars of this variety have a minimum period of about 1.6 ms, which is the value we have used in Equation (2). For a magnetic field of the order of 10^8 G and a star of radius 10_6cm, Equation (3) gives us the limiting value of the period below which the energy gained by an electron will be limited by radiation reaction. The limiting value of the period is $p \approx 10$ ms. This is also the order of the period which any rotating neutron star with initial rotation period of 1.6 ms would acquire as a result of its slow down during the age of the galaxy (Bhattacharya & Srinivasan 1991).

The curvature photons will escape the pulsar magnetosphere without any absorption enroute (Scharlemann *et al.* 1978). The typical energy of a curvature photon is $(3/2)\ hcy_e^3\ \backslash R_c$, where $R_C \approx (cr/\Omega)^{1/2}$ is the radius of curvature of the field lines at a distance r from the star's surface and Ω is the angular frequency of rotation of the pulsar. For periods between 1.6 ms and 10 ms and γ_e given by Equation (4), the photon energies lie in the range 5×10^3 MeV to 2×10^2 MeV. The curvature radiation power is given by,

$$l = (2/3)(e^2 c\gamma_e^4/R_c^2). \tag{6}$$

The $E_{||}$ field causes the charged particles to flow away from the stellar surface. The density of the charged particles coming out of the polar cap is according to Goldreich & Julian (1969),

$$n = \Omega B/2ce. \tag{7}$$

If $\Delta s \approx \pi\,(\Omega R/c)R^2$ denotes the area of the polar cap then the net rate at which the particles are emitted by the neutron star is

$$\dot{N} \approx \Delta snc = \Omega^2 BR^3/2ce. \tag{8}$$

The total power radiated at a distance r from the star's surface is $\approx IN(r/c)$. Thus,

$$L(r) = e8\pi^3 BR^3\gamma_e^4/(3p^3c^2)\mathrm{erg\,s^{-1}}. \tag{9}$$

Using now the expression for γ_e from Equation (4) we get an expression for the luminosity at a distance r from the stellar surface as

$$L(r) = 4.2\times10^{31} B_8^2 R_6^6 p_{\mathrm{ms}}^{-9/2} r^{1/2}\,\mathrm{erg\,s^{-1}}. \tag{10}$$

Since r increases along the magnetic field lines, we assume that the dominant contribution to the total power comes from the vicinity of the light cylinder whose radius is given by $r \approx (c/\Omega)$. Since most of the curvature radiation is in the form of γ-rays, the luminosity $L(r)$ of a millisecond pulsar at the light cylinder can be written as L_γ and Equation (9) can be written as

$$L_\gamma = 9.2\times10^{34} B_8^2 R_6^6 p_{\mathrm{ms}}^{-4}\,\mathrm{erg\,s^{-1}}. \tag{11}$$

Since γ-emission forms a substantial fraction of the total spindown rate of a pulsar, we expect the γ-luminosity to be not much smaller than the spindown rate. This provides a reasonable basis for the present model. Equation (11) gives the γ-luminosity of individual millisecond pulsars. We now apply the above expression to find the luminosity of a globular cluster containing n_p millisecond pulsars. This is given by

$$L_\gamma^{gc} = \int F(p) L_\gamma n_p \mathrm{d}p. \tag{12}$$

Substituting Equation (11) and Equation (2) in Equation (12) we get

$$L_\gamma^{gc} = 9.1\times10^{34} n_p \int (\alpha-1) p_{\mathrm{min}}^{\alpha-1} p_{\mathrm{ms}}^{-\alpha} B_8^2 R_6^6 p_{\mathrm{ms}}^{-4}\mathrm{d}p. \tag{13}$$

The integration is to be performed with limits from p_{min} to p_{max}, that is, between 1.6 to 10 in our case. In view of Equation (1) and the data for millisecond pulsars given in Bhattacharya & Srinivasan (1991), it seems safe to assume that $p_{\mathrm{ms}} = kB_8^{6\backslash7}$ where k is of the order of unity. Substituting $p_{\mathrm{ms}} = B_8^{6\backslash7}$ in Equation (13) and integrating it, we arrive at the following result:

$$L_\gamma^{gc} = 3.8\times10^{36} n_{500}\,\mathrm{erg\,s^{-1}}, \tag{14}$$

where n_{500} is the number of millisecond pulsars in a globular cluster in units of five hundred. While carrying out the integration we have taken the stellar radius to be 10^6cm and in Equation (12), as is the practice, there should have been a beaming factor whose value varies between one and two. Here we have assumed it to be unity.

The assumption that $p_{\rm ms} \propto B^{6\backslash 7}$ amounts to the expectation that during spindown the pulsar stays close to the spin-up line. Alternatively, following Chen (1991), we could assume that $p_{\rm ms} \propto B$. In that case the luminosity of the globular cluster becomes

$$L_\gamma^{gc} = 2.9 \times 10^{36} n_{500}\, \mathrm{erg\,s^{-1}}, \tag{15}$$

which is not much different from the estimate of Equation (14). Therefore, it is reasonable to expect that on the basis of the present model the γ-luminosity of a globular cluster will be of the order of these estimates.

3. Discussion

It may be said that the millisecond pulsars in the globular clusters do not all have periods in the range 1.6 ms to 10 ms. However, the pulsars with periods in this range seem to be the most prolific emitters of γ-rays by the process discussed here. If the period of a pulsar is longer than that given by Equation (3) then the energy acquired by the electron after acceleration in the magnetosphere of the pulsar is given by Equation (5). To produce γ-rays with this energy by curvature radiation the magnetic field of the pulsar will have to be $> \sim 10^9$ G. If we assume this to be so, then its γ-luminosity can be shown to be proportional to $B_8^5 P_{\rm ms}^{-11}$. The rapid fall in luminosity with period of these pulsars makes them unimportant in comparison with the short period millisecond pulsars considered here. The globular clusters may also contain pulsars of the ordinary variety (which are not spun up). These may emit γ-rays by the Ruderman-Sutherland mechanism involving the polar gaps (Ruderman & Sutherland 1975). We have shown elsewhere (Bhatia, Chopra & Panchapakesan, 1987) that their γ-luminosity is much smaller than that given by the estimate in Equation (11). All in all, millisecond pulsars of periods between 1.6 ms and about 10 ms seem to be the dominant contributors to the γ-luminosity of globular clusters. There are indications (Manchester *et al.* 1991; Kulkarni 1990) that the globular clusters are very rich in millisecond pulsars, many of which are likely to have periods less than about 10 ms (all the eleven pulsars observed by Manchester *et al* (1991) have periods in this range). The case for the globular clusters as sources of γ-rays with estimated luminosities of the order of Equation (14) seems, therefore, well argued.

In addition to present calculation, there are two more models available in literature from which one could estimate γ-ray luminosity of a globular cluster which has. millisecond pulsars in it.

The first model is due to HTE (Harding, Tademaru & Esposito 1978). Though the model does not talk about pulsars having low magnetic fields ($\sim 10^8$G) yet an extrapolation has been made from high ($\sim 10^{12}$ G) to low magnetic fields. With this extrapolation the THE model predicts a luminosity given by

$$L_\gamma^{gc}(\mathrm{HTE}) = 9.65 \times 10^{34} n_{500}\, \mathrm{erg\,s^{-1}}. \tag{16}$$

This luminosity is much less than what we have obtained from our calculation and makes the globular clusters rather faint γ-ray sources. The second model is by

CHR (Cheng, Ho & Ruderman 1986) as adapted by Chen (1991). This also involves the extrapolation from high to low magnetic fields. Their resulting luminosity is not much different from ours. It must, though, remain a moot point whether the models developed for high magnetic field pulsars can be applied to pulsars with low magnetic fields since some of the physical processes possible in one regime may not be possible in a different regime. Our calculations do not, however, suffer from any such conjecture.

Our results show that globular clusters containing millisecond pulsars may be bright sources of γ-rays. They are well within the reach of modern γ-ray detectors and we hope that greater effort would be made to detect these sources. Their detection would serve as a support for our ideas.

4. Conclusions

We have shown that if globular clusters contain a large number of resurrected neutron stars of millisecond periods, of which there is some evidence, then the collective emission of all the pulsars will make globular clusters sources of γ-rays. The estimated luminosities are such that these sources may be within the range of detection of the present-day instruments. We hope that the observers will make an effort to detect γ-rays from globular clusters and measure the luminosities of these sources. This data will, hopefully, help refine theories.

References

Alpar, M. A., Cheng, A. F., Ruderrnan, M. A., Shahum, J. 1982, *Nature,* **300**,728.
Bhatia, V. B., Chopra, N., Panchapakesan, N. 1987, *Astrophys. Sp. Sci*., **129,** 271.
Bhattacharya, D., Srinivasan, G. 1991, *J. Astrophys. Astr.*, **12**, 17.
Chadwick, P. M., Dipper, N. A., Kirkman, I. W., McComb, T. J. L., Orford. K. J, Truvcr, K E., Truver, S. E. 1987, in *Very High Energy Gamma Ray Astronomy*, Ed K. E·. Truver, D Reidel, Dordrecht, p 159.
Chadwick, P. M., Dowthwaite, J. C., Harrison, A. B., Kirkman, I. W., McComb. T. J. L., Orford, K. J., Truver, K. E. 1985, *Nature,* **317,** 326.
Chen, K. 1991, *Nature,* **352,** 695.
Cheng, K. S., Ho, C, Ruderman, M. A. 1986, *Astrophys. J.*, **300,** 500, 522.
Goldreich, P., Julian, W. H. 1969, *Astrophys. J*., **157,** 869.
Harding, A. K., Tademaru, E., Esposito, L. W. 1978, *Astrophys. J.* **225**. 226
Kulkarni, S. R. 1990, *Bull. am. astr. Soc.*, **22,** 1308.
Manchester, R. N., Lyne, A. G., Robinson, C., D'Amico, N, 1991, *Nature.* **352,** 219.
Radhakrishnan, V., Srinivasan, G. 1981, *Proc. 2nd Asia-Pacific Regional Meeting of IAU,* Eds B. Hidayat & M. W. Feast, Tira Pustaka, Jakarta, p. 423.
Ruderman, M. A., Sutherland, P. G. 1975 *Astrophys. J*., **196,** 5.
Scharlemann, T. E., Arons, J., Fawley, M. W. 1978, *Astrophys. J.,* **222,** 297.

J. Astrophys. Astr. (1992) **13,** 293–305

VRI Photometry of M67 for CCD Standardization at 2.3m VBT

P. N. Bhat & K. P. Singh *Tata Institute of Fundamental Research, Bombay 400 005*
T. P. Prabhu *Indian Institute of Astrophysics, Bangalore 560 034*
A. K. Kembhavi *Inter University Centre for Astronomy & Astrophysics, Pune 410 007*

Received 1992 September 15; accepted 1992 November 16

Abstract. We present the results from CCD photometry in the *V, R* and *I* bands, of the 'Dipper Asterism' region of the open cluster M67 based on observations carried out at the prime focus of the 2.3 m Vainu Bappu Telescope of the Vainu Bappu Observatory, Kavalur. The CCD parameters like the system gain and the readout noise are measured using several flatfield frames taken through the standard *I* filter. The CCD chip is calibrated using the photometric standards in the field and linear colour transformation relations are derived. Also a few new *VRI* photometric measurements are reported for the members of the cluster.

Key words: Open clusters, M67—photometry—CCD calibration

1. Introduction

The use of a Charge Coupled Device (CCD) for optical photometry in astronomy allows a simultaneous definition of external variables such as the seeing, the sky brightness, and star positions on the detector along with the measurement of apparent intensities of an ensemble of stars. This involves the measurement of the photometric response of the detector which leads to a set of transformation equations to convert the Analog to Digital Units (ADU or sometimes called as Digital Numbers, DN) read from the CCD to apparent magnitudes. To calibrate the photometric response of a CCD, it is ideal to observe standard stars in a cluster having similar visual magnitudes and possessing as broad a spread in their colour indices as possible. M67 (NGC 2682) is an ideal open cluster for this purpose for the following reasons:

(i) In a small region covered by a single CCD frame it contains stars with a wide range of colours;
(ii) many of the stars are of similar brightness (V = 10 – 12), but very faint ($m_v \sim 20$) and very bright ($m_v \sim 9.7$) stars are also available in the same cluster;
(iii) the cluster is at a high galactic latitude (l = 216°, b = 32°) and the background stars do not interfere with the brightness measurements; and
(iv) it is an open cluster where individual stars can be easily resolved. The 'dipper asterism' region of the cluster is at $\alpha_{1950} = 8^h48^m36^s.6$ and $\delta_{1950} = +\ 11°57'33''$ which is easily accessible from the Vainu Bappu Observatory (VBO), Kavalur ($\lambda = +\ 12°34'.58$ and $l = -\ 78°49'.58$).

The exposures required on a 2.34 m Vainu Bappu Telescope (VBT), Kavalur, using

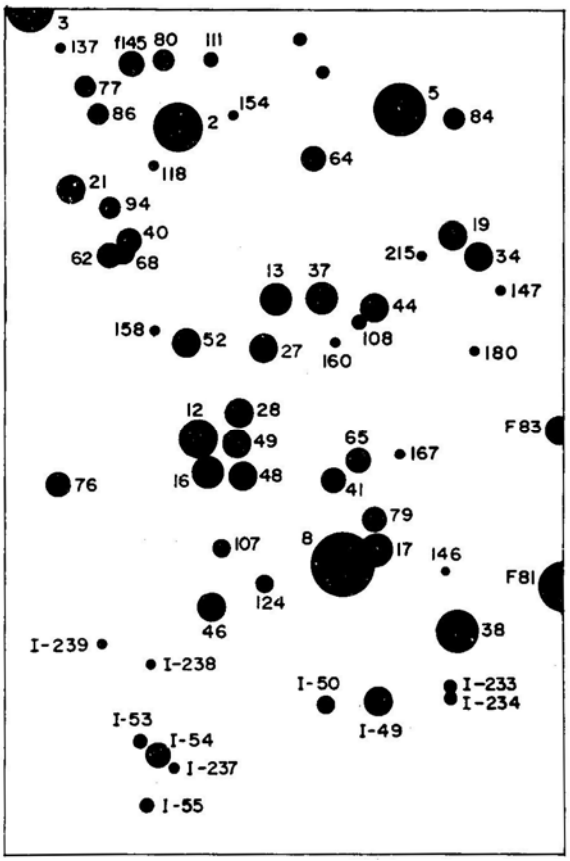

Figure 1. Finding chart of the CCD field of M67 centred around the 'dipper asterism'. The identifications follow Gilliland *et al.* (1991), Racine (1971) and Eggen & Sandage (1964). The whole field is about 6 arcmin × 4 arcmin. North is to the top and east is towards the left.

the CCD at its prime focus, were in the range 10–300s for *V, R* and *I* broadband filters. Fig. 1 is a finding chart of the region of M67 covered in our observations, centred around the 'dipper asterism' region. The stars are numbered following Gilliland *et al.* (1991) and Racine (1971). Previous photometric measurements of this cluster available in the literature are by Johnson & Sandage (1955); Eggen & Sandage (1964); Schild (1983, 1985) and more recently by Ram Sagar & Pati (1990); Joner & Taylor (1990); Chevalier & Ilovaisky (1991) and Mayya (1991). Time-resolved CCD photometry of the core region of M67 has recently been carried out by Gilliland *et al.* (1991)

In this paper we present the results from observations of M67 cluster using *VRI* broadband filters. The data from these observations are used to calibrate the CCD and also to obtain new photometric measurements. We have also used the flatfield images to derive CCD parameters like the readout noise, the system gain and the spatial noise component. The paper is organized as follows: In section 2 we describe the observations followed by data analysis and results in section 3. The conclusions are presented in section 4.

Table 1. Summary of filter characteristics.

Filter	Central wavelength (A)	Bandwidth (A)
I	8150	1700
R	6550	1300
V	5425	1050

Table 2. Summary of exposures through different broadband filters.

Date	Filter	Hour angle h m s	Air mass X	Sky brightness (mag/arcsec)	PSF FWHM (Pixels)	Exposure (*s*)
27.1.1990	*R*	0 53 44	1.024	20.13	6.5	10
27.1.1990	*R*	0 56 5	1.027		6.5	60
27.1.1990	*R*	1 0 31	1.035		6.5	300
28.1.1990	*V*	0 20 35	1.0034	21.87	6.0	20
28.1.1990	*V*	0 40 38	1.0147		5.8	120
28.1.1990	*I*	1 43 0	1.1004	19.16	5.8	10
28.1.1990	*I*	1 46 49	1.110		5.8	60
28.1.1990	*I*	1 50 50	1.124		5.6	300

2. Observations

The data acquisition system for the TIFR CCD is based on a GEC P8603/B (B-grade with a few bad columns) front illuminated chip which was commissioned sometime back (Bhat *et al.* 1990). The details of filters used for *VRI* photometry are summarized in Table 1. The observations were carried out during 1990 January 27–28, at the prime focus of VBT. The CCD consists of 576 × 385 pixels each of size 22 μm. This pixel size corresponds to a plate scale of 0.6 arcsec per pixel at the *F*/3.25 prime focus of VBT, at an image scale of 4.5 arcmin per cm. The total field of the CCD is 5.7 × 3.8 arcmin. Only one filter could be used per night since remote control of the filter wheel was not yet operational. A minimum of three frames of the dipper asterism were obtained with three different exposures in order to detect the faintest stars ($m_v \sim 20$) with a good statistical accuracy. The full width half maximum (FWHM) of the point spread function was $\simeq$ 3.0 arcsec. The sky brightness and the seeing were reasonably steady during these two observing nights. The cluster was close to the zenith during our observations. Several flatfields were taken using each filter. The details of the exposures are given in Table 2.

3. Data analysis and results

3.1 *Determination of the CCD Characteristics*

Two important characteristics of a CCD are its readout and spatial noise. The former determines the minimum detectable signal for situations with a small number of

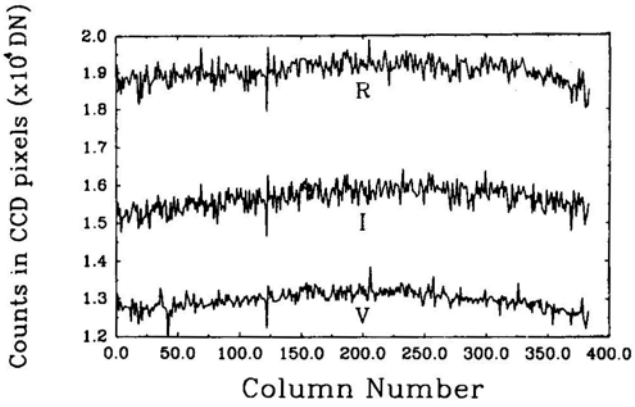

Figure 2. The typical variation of CCD pixels along a row in the centre of the chip through *V. R* and *I* filters. A bad pixel is seen at around column no. 123 showing a systematic dip in all the three filters. The rms variation in the flatfield counts along a row are less than 2% for each of the filters.

collected photons per pixel such as in spectroscopy and speckle interferometry, while the latter sets the limit for a large number of collected photons such as the detection of faint features superimposed on a night sky background. Although spatial noise can be corrected by dividing by a flatfield exposure, the variation in the quantum efficiency with wavelength from pixel to pixel is sufficiently large that differences between the spectrum of the signal and that of the flatfield become important at roughly the level of a few parts in 1000, for wavelengths near bright night sky lines (Gudehus & Hegyi 1985). Fig. 2 shows a typical variation of the counts in the CCD pixels along a central row for three different flatfields through the three filters. The root mean square fluctuations in the ADU along a typical row as shown are 1.9, 1.6 and 1.8% respectively for *V, R* and *I* flatfields.

The system gain, gain factor, or transfer factor of a CCD can be determined by studying the noise statistics of a uniform exposure or the flatfield (see e.g. Prabhu, Mayya & Anupama 1991). For a signal of N photons, the shot noise is $\sqrt{N_e}$. Since the electrons generated in a pixel are proportional to N through the scale factor of quantum efficiency of the pixel, it is generally assumed to a first degree of approximation that N_e electrons stored in a pixel have a noise component of $\sqrt{N_e}$. For a system gain of G DN/electron, the observed counts would be $S = GN_e$ and the corresponding noise $\sigma = \sqrt{N_e}$. One thus obtains $\sigma^2 = GS$, and G can be determined through the observables S and σ.

In practice the rms noise in counts is also affected by the readout noise R and the rms variations in the sensitivity of the pixels which is proportional to the signal itself. Any nonuniformity in the flatfield exposure also adds to the rms variation proportional to the signal. Thus the total variance of the counts is

$$\sigma_T^2 = G^2 R_e^2 + GS + f^2 S^2 \tag{1}$$

where f is the rms value of a normalized flatfield due to pixel-to-pixel variations and the nonuniformity of illumination of the CCD. It may appear that a least squares fit to the observed values of S and σ can yield estimates for G, R_e and f. However, since

the magnitudes of observables increase from the first term to the last term at the right hand side of Equation (1), the errors of conventional regression analysis propagate in the direction of $f_2 \rightarrow G \rightarrow G_2 R_e^2$. Horne (1988) suggests a recipe for the determination of G and R_e which was adapted here after some modifications. The following analysis were carried out using the PCVISTA software (Treffers & Richmond 1989).

Nine flatfleld images were obtained through the *I* band on January 29, 1990 with mean counts ranging from 2000 DN to 21,700 DN above bias. These were trimmed to remove the overscan area and also the first row and columns at either ends which generally showed high counts. A mean bias value was subtracted from trimmed images. The bias was estimated in three different ways:

(a) Mean of bias frames obtained before and after the series of flats;
(b) mean of row overscan region;
(c) mean of column overscan region. The difference in the different mean values was ~ 5%, and its effect on the final results is <1%.

The three flatfield exposures with highest counts were stacked to produce the master flatfield image. These images had together ~ 55000 DN per pixel implying that the field had an accuracy of ~0.4% at a system gain G ~ 1. The master flatfield was normalized to unity by dividing by the mean value over the frame. The remaining 6 flatfields were corrected using this master flatfield. A window of 100 × 200 was chosen on these frames in an area that was relatively free from defects. The remaining few defects were iteratively removed by comparing with adjacent pixels in a 5×5 window and rejecting pixels that deviated by > 3σ. The remnant rms noise was due to readout and photon statistics.

If two exposures are of similar DN, the ratios of the two will also be free of contribution to the rms by the variation due to flatfield and nonuniform illumination (Mackay 1988). One set of nearly equal flatfields was found among the six used in the above measurements, and another set was found in the three used for the master flatfield. The ratio images of these two sets were also used to obtain two more sets of estimates of noise.

3.2 *System Gain and Readout Noise*

The bias frames for this CCD used in our analyses had an rms value of 11.63 counts. Hence we added a value of variance 135 at zero signal to the set of (variance, signal) estimated from the flatfield, The resulting 9 Pairs of data were used to determine G and R using least-squares regression analysis. The SIXLIN routine developed by Isobe *et al*. (1990) was employed. The data has a regression coefficient of 0.9986.The mean of six different regression lines yields

$$\sigma^2 = (-106.85 \pm 199.14) + (0.9435 \pm 0.0267)S. \quad (2)$$

The Standard error of the fit is 337 counts. The negative value for the γ-intercept implies that there is a quadratic component still present in the data. The highest point in the data will be affected the most, particularly since the two flats used in arriving at the results were dissimilar at 10% level. Deleting this last point we obtain,

$$\sigma^2 = (142.70 \pm 132.67) + (0.8876 \pm 0.0159)S. \quad (3)$$

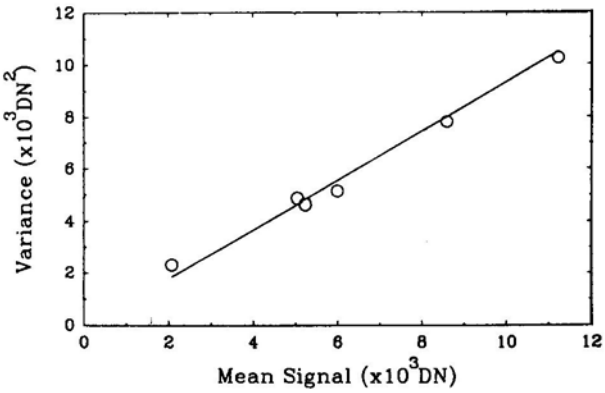

Figure 3. A plot of the total variance in units of square of ADUs as a function of the mean signal level. The data points have been computed from the flatfield frames taken with varied exposures using the *I* band filter. The straight line is a linear fit to the data points. The coefficients of the fit are used to derive the readout noise and the system gain.

The regression analysis also yields a correlation coefficient of 0.9984 and a standard error of fit 244 counts. The derived values are thus $G = 0.888 \pm 0.016$ DN per electron and $R_e = 13.5 \pm 13.0$ electrons. Fig. 3 shows a plot of σ^2 versus the mean and the regression fit to the data points.

The error on the derived value of R_e is rather high. This can be improved only by including a larger number of measurements with low values of *S*. On the other hand, the derived value is consistent with the mean value of 13.1 electrons derived from the rms of the bias frames. This value, in itself, is higher than the value specified by the manufacturers. On a closer inspection of the data, it was found that the last few bits of data had a significant probability of getting lost in the process of digitisation, possibly due to insufficient time delay between two successive data transfers. The rms of counts due to this fact had a value of 6 as seen from the flat frames. This does not have much effect at high count rates, but introduces extra noise at lower levels. Correcting the constant in the regression curve for this contribution, one obtains $R_e = 11.6$ electrons, which is only slightly higher than expected for the chip.

3.3 *Measurement of the Instrumental Magnitudes of Stars in M67*

A bias frame was subtracted from each of the observed frames. The analysis was carried out using the standard IRAF software package and the DAOPHOT (Stetson 1987) package on our SUN Sparc station. The star images were flatfielded using the twilight and the dawn sky flats. The cosmetic corrections and removal of the cosmic rays were done by applying a median filter with a 3×3 kernel. Since the CCD field is fairly crowded because of the poor seeing, we carried out the photometry of the stars in all our frames by simultaneous profile fitting using the DAOPHOT package. The relatively bright and isolated stars were used for getting the point spread function (psf) in the images. The psf radius was kept as 13 pixels and the fit radius was the

FWHM of the stars. The stars were identified using the 'daofind' program. The detection threshold was kept at 4σ counts above the sky. The sky values were determined from an annulus starting from a radius of 15 pixels and extending to a radius of 25 pixels. The measuring aperture was kept equal to FWHM of the psf (see Table 1). The minimum data value used for photometry was 3σ below the sky. The zero-point was kept equal to 23 mag for the *R* and *V* frames and 22 mag for the *I* frames. The final instrumental magnitudes r_i v_i and i_i were determined by carrying out the simultaneous psf-fitting to all the identified stars. The residual images after the removal of the simultaneously fitted stars were examined and results from badly fitted stars were ignored.

The instrumental magnitudes are then given by the following expressions.

$$v_i = -2.5\log(\mathrm{ADU}) + 23.0, \tag{4}$$

$$r_i = -2.5\log(\mathrm{ADU}) + 23.0, \tag{5}$$

$$i_i = -2.5\log(\mathrm{ADU}) + 22.0, \tag{6}$$

where ADU represents the integrated counts per sec in the psf of the star. Very bright stars that were close to saturating the CCD were ignored. An average of the magnitudes was taken where good multiple exposures were available in the same filter. These magnitudes were also used to derive the instrumental colours $(v - r)_i$ and $(r - i)_i$. The derived magnitudes and colours were then calibrated against the standard stars by carrying out regression analyses. The standard stars and their magnitudes and colours used for comparison and calibration of our CCD are listed in Table 3, and have been taken from the most recent CCD measurements by Gilliland *et al.* (1991) and Chevalier & Ilovaisky (1991). We used 15 stars with good measurements in all the three bands (and an additional one in the *V* and R only) as calibrators. Seven of these are in common with the ten calibrators used by Chevalier & Ilovaisky (1991). Three calibrators from their list had to be dropped because one (G8) was saturated, another (F81) was on the edge of the *R* frames, and third (G12) had a poor measurement. The list was, however, supplemented by additional stars from their list which had no previous record of any variability. The regression analyses were carried out for $V–v_i$ and $(v–r)_i$ as a function of *V–R* and for $(r - i)_i$, $R - r_i$ and $I–i_i$, as a function of *R–I* respectively. The standard magnitudes were taken from Chevalier & Ilovaisky (1991). The linear fit was performed by the task in the STSDAS package. The points were given weights according to their measurement errors (e.g. standard deviations for *V* listed in Table 3) while deriving the best fit linear relations.

One normally images the same star at various zenith angles so that one can use the data to compute the extinction correction on the estimated magnitudes due to the atmospheric absorption of light in a given waveband. The first order atmospheric extinction corrections for the site have been measured and given in Mayya (1991). Our observations were carried out very close to the zenith (see Table 2 for air-mass). We did not apply the air-mass correction explicitly and absorbed it in our zero point correction during the regression analysis. The correction due to differences in the air-mass for different exposures in the same filter were negligible compared to the Statistical errors.

Table 3. Standard stars used for calibration.

Star No.[a]	Gilliland *et al.* (1991) V_G	$(V-R)_G$	Chevalier & Ilovaisky (1991) V_{CI}	$(V-R)_{CI}$	$(R-I)_{CI}$	Present work V	sigma	$(V-R)$	$(R-I)$
5	10.31	0.65	10.301	0.641	0.570	10.310	0.010	0.596	...
13	12.14	0.27	12.124	0.283	0.273	12.123	0.007	0.268	0.240
16	12.27	0.32	12.247	0.347	0.326	12.265	0.008	0.361	0.315
19	12.67	0.29	12.671	0.293	0.304	12.628	0.006	0.240	0.327
27	12.78	0.32	12.765	0.329	0.320	12.758	0.006	0.311	0.348
28	12.91	0.26	12.884	0.275	0.279	12.873	0.007	0.257	0.272
34	12.83	0.32	12.820	0.329	0.322	12.801	0.006	0.305	0.312
37	12.63	0.46	12.636	0.461	0.431	12.615	0.004	0.441	0.445
41	12.73	0.31	12.724	0.336	0.349	12.734	0.008	0.346	0.322
44	13.09	0.32	13.077	0.329	0.313	13.065	0.006	0.301	0.341
46	13.10	0.33	13.096	0.356	0.347	13.135	0.012	0.388	0.369
48	13.16	0.32	13.147	0.337	0.317	13.151	0.010	0.334	0.320
49	13.20	0.34	13.174	0.343	0.332	13.215	0.009	0.358	0.334
64	13.70	0.34	13.670	0.339	0.353	13.711	0.007	0.343	0.320
79.	14.14	0.42	14.132	0.416	0.382	14.186	0.010	0.436	0.372
1–49[b]			13.458	0.355	0.343	13.458	0.010	0.353	0.353

[a] Refers to numbers by Gilliland *et al.* (1991)
[b] Identification number of Eggen & Sandage (1964).

3.4 *Photometric Performance and the Colour Equations*

The regression analysis of the measured magnitudes and colours of the standards resulted in the following linear transformation equations.

$$V - v_i = (0.253 \pm 0.026)(V - R) - (0.663 \pm 0.009), \tag{7}$$

$$(v - r)_i = (0.971 \pm 0.026)(V - R) + (0.576 \pm 0.009), \tag{8}$$

$$(r - i)_i = (0.790 \pm 0.050)(R - I) + (0.616 \pm 0.017), \tag{9}$$

$$R - r_i = (0.128 \pm 0.032)(R - I) - (0.064 \pm 0.011), \tag{10}$$

$$I - i_i = (0.089 \pm 0.070)(R - I) + (0.493 \pm 0.024). \tag{11}$$

Although normally the first three relations are sufficient for data obtained with the three filters, because the CCD frames with different filters did not cover the same set of stars we derived the last two relations also so as to be applicable when only the $(r - i)_i$ colours had been measured. The data points used for the regression analysis and the resultant linear fits are shown in Fig. 4. The deviations of the measured data points around the best fit linear relations are also shown in Fig. 5. The spread in the data points represents the accuracy of the magnitude estimations using the above transformation equations. The residual rms scatter of the data points is 0.022 mag for Equations (7) and (8), 0.017 mag for Equation (9), 0.013 for Equation (10), and 0.022 for Equation (11) for the standard stars in Table 3.

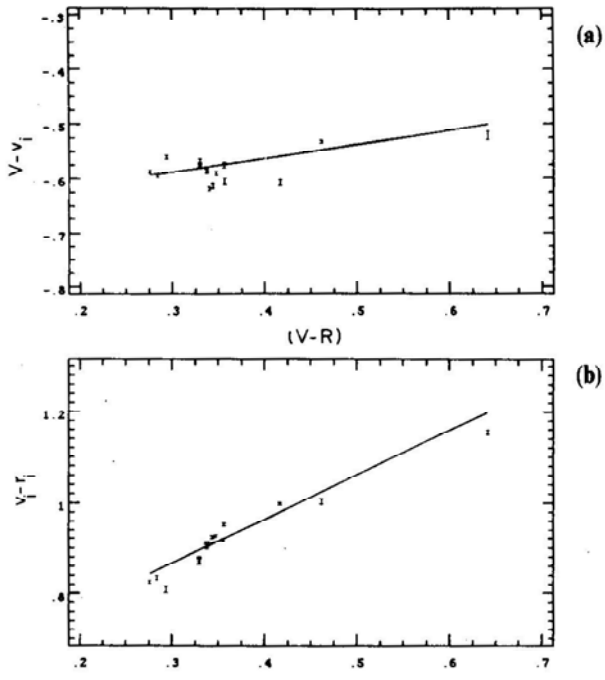

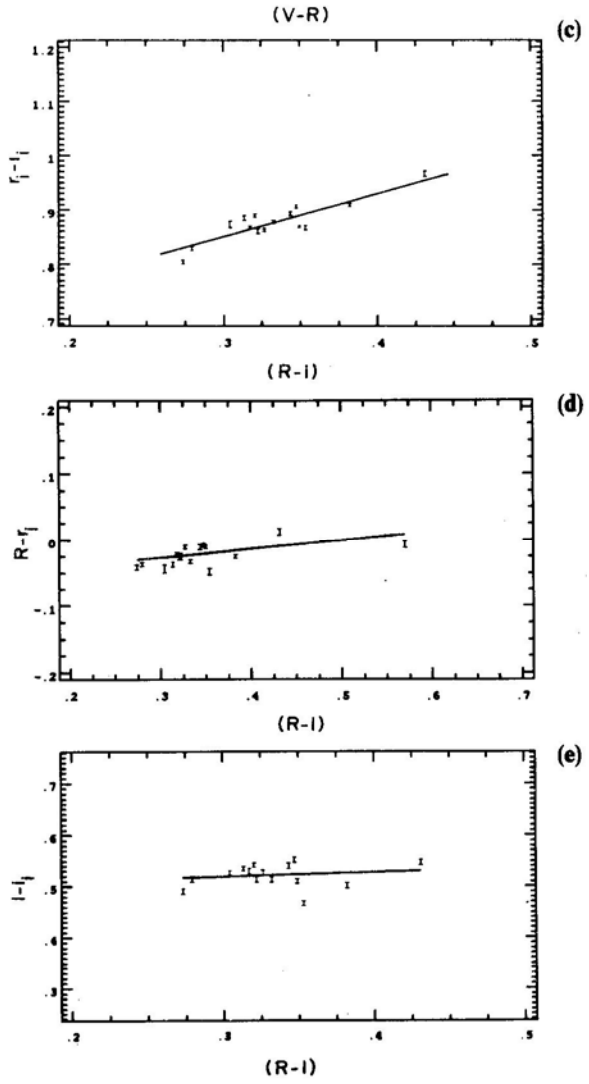

Figure 4(a–e). (**a**) Difference between the 'standard' V magnitudes published by Chevalier & Ilovaisky (1991) and our instrumental magnitudes v_i plotted as a function of the Standard colour index (V—R) for the 16 stars used as calibrators (see Table 3).The solid line represents the linear least-squares fit. Frames (**b**) through (**e**) show similar diagrams for $(v - r)_i$ and $(r - i)_i$ against (V—R) colours, and R—r_i and I — i_i against (R—I) colours, respectively.

In Table 4 we list the magnitudes and colours derived using these transformation equations for a few additional stars in M67 imaged in at least two contiguous filters. The I magnitudes have been derived using data from all three filters wherever available, else only the $(r–i)_i$ colours have been used. For comparison we also show previous measurements of these stars from the literature taken mostly from Gilliland *et al.* (1991). The stars G38 and G84 have significantly discrepant magnitudes. The V magnitude of star 38 is, however, consistent with the measurements by Racine (1971)

who also reported it to be a resolved double and somewhat blue in nature. It is probably a variable star. The *V* magnitude estimated by us for star 84 is consistent with the measurement of Chevalier & Ilovaisky (1991) who on the basis of its discrepancy with the value given by Gilliland *et al.* (1991) suspected it to be variable.

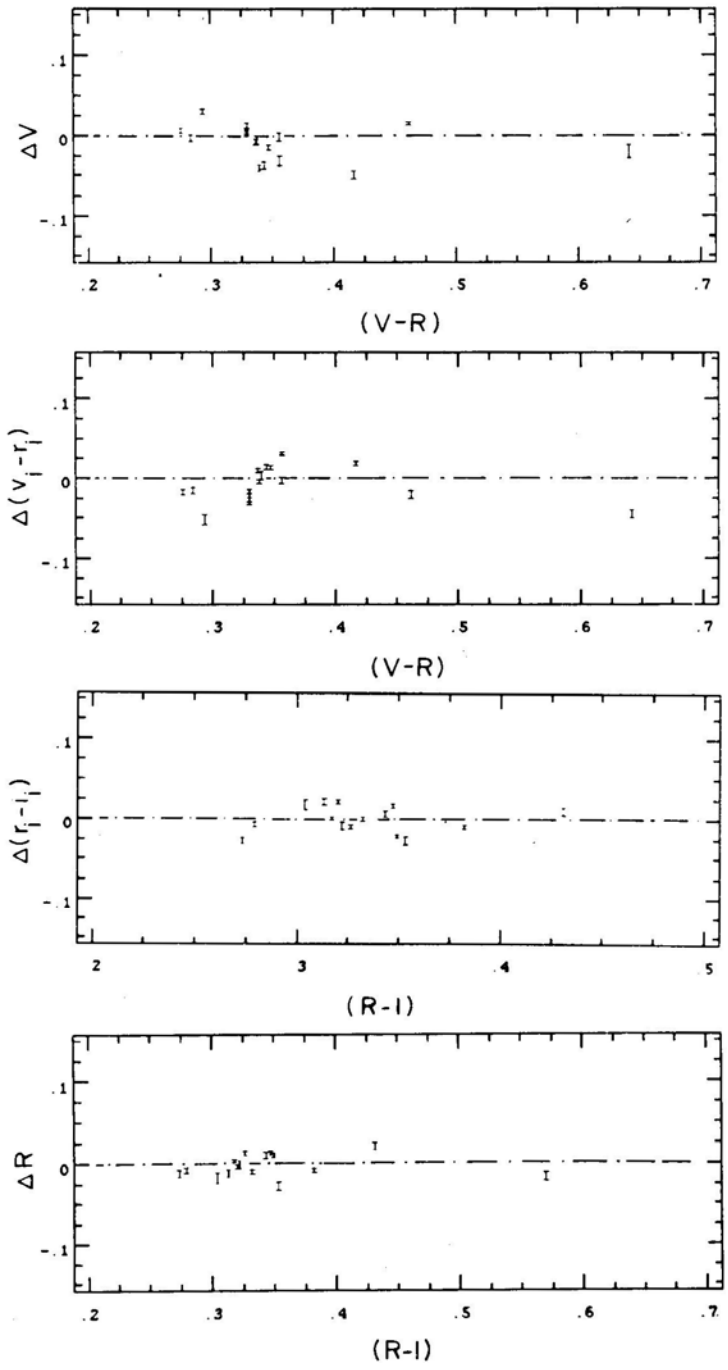

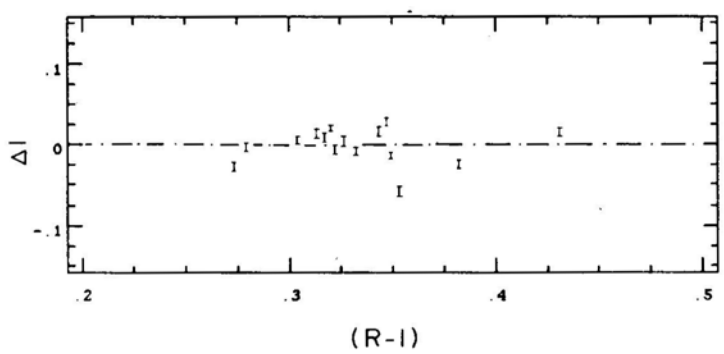

Figure 5. Residual differences between the fitted line and the data shown in Fig 4.

Table 4. Measurement parameters for stars in M67.

Star No.[a]	Previous measurement[a] V	$(V-R)$	$(R-I)$	Present work V	Sigma	$(V-R)$	$(R-I)$	R^b
17	12.40	0.42	0.441	12.408	0.008	0.448	0.359	11.96
21	12.57	0.34	0.341	...	...	...	0.315	12.20
38[c]	10.88	0.27	0.265	10.947	0.013	0.321	0.160	10.63
52	13.22	0.33	0.328	13.215	0.010	0.343	...	12.87
65	13.94	0.33	0.367	13.961	0.010	0.366	...	13.60
76	14.13	0.32	0.278	...	...	...	0.312	13.79
84	14.21	0.36	0.316	14.393	0.009	0.347	0.253	14.05

[a] Refers to numbers and measurements by Gilliland *et al.* (1991), except for *R–I* which are from Chevalier & Ilovaisky (1991).
[b] Using *R* and *I* data (See equations 10–11 in the text) where *V* data is not available.
[c] Cross-reference is *I*-242 (Joner & Taylor 1990).

4. Conclusion

CCD photometry of the stars in the 'dipper asterism' region of M67 has allowed us to obtain the colour transformation equations for the *VRI* standard bands. The typical residual rms scatter of measured quantities and therefore, the accuracy of the CCD photometry is $\simeq$ 0.02 mag for this particular CCD and filter combination used for observations in the 1990 season. The system gain is found to be 1.126 electrons per count and the readout noise is about 11.6 electrons. We conclude that stars G38 and G84 may be variable.

Acknowledgements

We would like to thank the Director of the Indian Institute of Astrophysics for allotting dark nights to us for our observations. We also appreciate the assistance rendered to us at various stages of these observations by the engineering and support the same institute.

References

Bhat, P. N., Kembhavi, A. K., Patnaik, K., Patnaik, A. R., Prabhu, T. P. 1990, *Indian J. Pure Appl. Phys.,* **28,** 649.
Chevalier, C, Ilovaisky, S. A. 1991, *Astr. Astrophys. Suppl.,* **90,** 225.
Eggen, O. J., Sandage, A. R. 1964, *Astr. J.,* **140,** 130.
Gilliland G. L., *et al.* 1991, *Astr. J.,* **101,** 541.
Gudehus D. H., Hegyi D. 1985, *Astr. J.,* **90,** 130.
Horne K. 1988, in New *Directions in Spectrophotometry,* Eds A. G. D. Phillip, D. Hayes, & S. Adelman, L. Davis Press, Schenectady, p. 285.
Howell, S. B. 1989, *Publ. astr. Soc. Pacific,* **101,** 616.
Isobe, T., Feigelson, E. D., Akritas, M. G., Babu, G. J. 1990, *Astrophys. J.*, **364,** 104.
Johnson, H. L., Sandage, A. R. 1955, *Astrophys. J.,* **121,** 616.
Joner, M. D., Taylor, B. J. 1990, *Publ. astr. Soc. Pacific,* **102,** 1004.
Mackay, C. D. 1988, *A. Rev. Astr. Astrophys.,* **24,** 255.
Mayya, Y. D. 1991, *J. Astrophys. Astr.,* **12,** 319.
Prabhu, T. P., Mayya, Y. D., Anupama, G. C. 1992, *J. Astrophys. Astr.* **13** 129.
Racine, R. 1971, *Astrophys. J.,* **168,** 393.
Ram Sagar, Pati A. K. 1990, *Bull. astr. Soc. India,* **17**, 6.
Schild R. E 1983, *Publ. astr. Soc. Pacific,* **95**, 1021.
Schild, R. E. 1985, *Publ. astr. Soc. Pacific,* **97**, 824.
Stetson, P. B. 1987, *Publ. astr. Soc. Pacific,* **99**, 191.
Treffers, R., Richmond, M. 1989, *Publ astr. Soc. Pacific,* **101,** 725.

J. Astrophys. Astr. (1992) **13,** 307–318

High Resolution Spectroscopy of the Semi-regular Variable LR Sco

Sunetra Giridhar & N. Kameswara Rao *Indian Institute of Astrophysics, Bangalore 560 034*
David L. Lambert* *Department of Astronomy, University of Texas, Austin, TX 78712 USA.*

Received 1992 September 4; accepted 1992 November 17

Abstract. A detailed spectroscopic investigation of LR Sco which was earlier misclassified as R CrB star is made. Atmospheric parameters and elemental abundances are determined using detailed depth-dependent model atmospheres and line synthesis technique. Most of the elements show near solar abundances.

The strength of circumstellar components seen in Na D lines are used to derive the mass loss rate. Another independent estimate of mass loss rate is made using the observed infrared flux from 1–100μm. These two approaches lead to nearly the same value of mass loss rate when M_v is assumed to be – 4.5 for this star.

Key words: Semi-regular variables—abundances—infrared flux—mass loss

1. Introduction

LR Sco has been listed as an SR variable in the *General Catalogue of Variable Stars* by Kukarkin *et al.* (1969). This classification is based on photometric observations of Shapley & Swope (1934) who estimated a period of 104.4 days using 202 observations covering 145 epochs. Stephenson (1978) examined a low dispersion (580 Å mm^{-1}) objective prism spectrum of this star in the blue spectral region and remarked that the spectrum resembled that of R CrB stars at light minimum. His remarks appear to have persuaded Bidelman (1979) to list this star with other R CrB stars.

Feast (1979) showed that the observed infrared excess of LR Sco is very similar to that of other R CrB stars i.e. the location of LR Sco in (J–H) vs (H–K), and (H–K) vs (K–L) diagrams is similar to that of other R CrB stars; J, H, K and L photometry of LR Sco was published by Carter, Roberts & Feast (1979). Later IRAS observations showed the infrared excess as prominent at 12, 25, 60 and 100 μm indicating that cold dust surrounds the star (Table 1). The infrared photometry lent further support to the classification of LR Sco as R CrB type star (Walker 1986). Drilling & Hill (1986) included this star in their list of cool hydrogen deficient stars. However, our high resolution spectra reveals that LR Sco is not a R CrB type star but a normal yellow supergiant of spectral type near G0Ib (Giridhar *et al.* 1991).

*Visiting Observer, Cerro-Tololo-Inter-American-Observatory, National Optical Astronomical Observatories, operated by the Association of Universities for Research in Astronomy, Inc., under cooperative agreement with U.S.A. National Science Foundation, La Serena, Chile.

Table 1. Basic observational data for LR Sco.

R.A. = 17:24:17	
Dec = −43:50.9	
Radial velocity $-12 \pm 3\,\mathrm{km\,s^{-1}}$	
V = 9.72(B − V) = 0.55	
Infrared magnitudes	
J	8.20
H	7.48
K	6.52
L	4.73
Infrared flux (Jy)	
12 μm	10.72
25 μm	7.75
60 μm	3.41
100 μm	7.06:

J, H, K, L magnitudes are from Carter *et al.* (1979)
The IRAS fluxes are from Walker (1986)
Radial velocity from Giridhar *et al.,* (1990)

2. Observation and data analysis

High resolution spectra with a GEC CCD detector were obtained using the cassegrain echelle spectrometer of the 4-m reflector of the Cerro-Tololo-Inter-American-Observatory. The spectral regions covered are 4200–4900 Å and 5450–6850 Å. The instrumental profile in the adopted configuration has a width (FWHM) of 0.34 Å in red and 0.32 Å in the blue spectral region. Three exposures were taken for each region to get better S/N ratio and identify cosmic ray hits. The exposure times were 20 minutes both in the red and in the blue. A xenon lamp was used for the flatfield images.

Our spectra were reduced using the spectroscopic data reduction package RESPECT (Prabhu, Anupama & Giridhar 1987) in its upgraded version (Prabhu & Anupama 1991). The extraction of the echelle spectrum follows the algorithm of Home (1986, 1988). The background level due to thermal noise and mean scattered light in the spectrograph is estimated using the counts in interorder rows after removing the effect of cosmic ray hits. Flatfielding was done using a normalized flatfield image. A Th + A hollow cathode lamp was used for wavelength calibration. The extracted spectrum orders were linearized in wavelength using a third degree polynomial for wavelength as a function of position. The standard error of the fit was around 0.02 Å. The pseudocontinuum for each order was determined using the highest points in spectrum known to be free of stellar lines. The spectra were then reduced to normalized continuum using spline interpolated values between these points. The accuracy of equivalent widths measured here are of the order of 10% for weak lines in equivalent width range 10–30 mÅ, 5–10% for lines in 50–200 mÅ range and 5% for lines in 200–350mÅ range. The S/N ratio was in the range of 60–80.

3. Description of the spectrum

LR Sco was observed alongwith 12 R CrB type stars and 5 Hdc stars during an observing run from 17–18 July, 1989, When the spectrum of LR Sco was compared

with well known R CrB stars like RY Sgr it was obvious that LR Sco did not belong to R CrB group (Giridhar, Rao & Lambert 1990). The CI lines that are a principal characteristic of R CrB stars are conspicuous by their absence. We could measure a few very weak CI lines at, for example, 4770 Å and 6587 Å, but these lines are seen at comparable strength in the spectra of normal F-G supergiants. Other differences were also striking. R CrB stars have numerous NI lines in 6400-6700 Å region but LR Sco spectra does not show them.

By contrast, the line spectrum of LR Sco is very similar to that of a normal supergiant of spectral type near G0. We have compared the equivalent widths of unblended FeI and FeII lines with those of μ Per (G0Ib) measured by Harris & Pilachowski (1984) and with δ C Ma (F8Ia) measured by Castley and Watson (1980). It is apparent from this comparison that LR Sco is slightly hotter than μ Per ($T_{\rm eff}$ 5500, log g = 1.5, as estimated by Luck 1982), but marginally cooler than δ C Ma ($T_{\rm eff}$ = 6250K, log g = 0.6, as estimated by Luck & Lambert 1985).

The observed (B–V) given in Table 1 corresponds to spectral type G0I (Fitzgerald 1970; Flower 1977). When this colour is compared with the colours computed from model atmospheres of Kurucz (1979) it indicates a $T_{\rm eff}$ = 6000K.

4. Abundance analysis

Since we had a large spectral coverage, we could measure equivalent widths for a large number of lines and therefore estimate abundances for several elements. We have calculated theoretical equivalent widths for lines of interest using model atmospheres based on the usual assumption of local thermodynamic equilibrium (LTE) in a plane parallel atmosphere in hydrostatic equilibrium. A model atmosphere grid calculated using the MARCS code (Gustafsson *et al.* 1975) was kindly supplied by R. E. Luck. Since the line spectrum is very similar to normal population I supergiants, we have used solar abundance models. The line equivalent widths are calculated using a program originally written by Sneden (1973) and revised by us. Details of our method of deriving abundances are described in Giridhar (1983). We have proceeded by first determining the atmospheric parameters $T_{\rm eff}$ (effective temperature), g (gravity) and V_t (microturbulence) using a set of iron lines comprising of 189 FeI and 26 FeII lines. The sample of FeI lines covering a range in excitation potential of (0.8–5.5 eV) and in equivalent widths of 20–450mÅ was used to determine $T_{\rm eff}$ and V_t. The comparison of FeI and FeII lines then gives the gravity. The atmospheric parameters could be estimated with an accuracy of 200 K in $T_{\rm eff,}$ 0.5 in log g, and 0.5 km s^{-1} in microturbulence velocity.

Oscillator strengths used in the present analysis were taken mostly from Führ, Martin & Wiese (1988) and Martin, Führ & Wiese (1988) for Fe-peak elements. For CI lines the gf values were taken from Luo & Pradhan(1989).

The gf values for the remaining elements were taken from the complilation of Luck (1991). We have used solar abundances tabulated by Grevesse (1984) to estimate relative abundances. The atmospheric parameters estimated for LR Sco are given below.

$$T_{eff} = 5500\text{K}$$

$$g = 10^{0.5}\ \text{cms}^{-2}$$

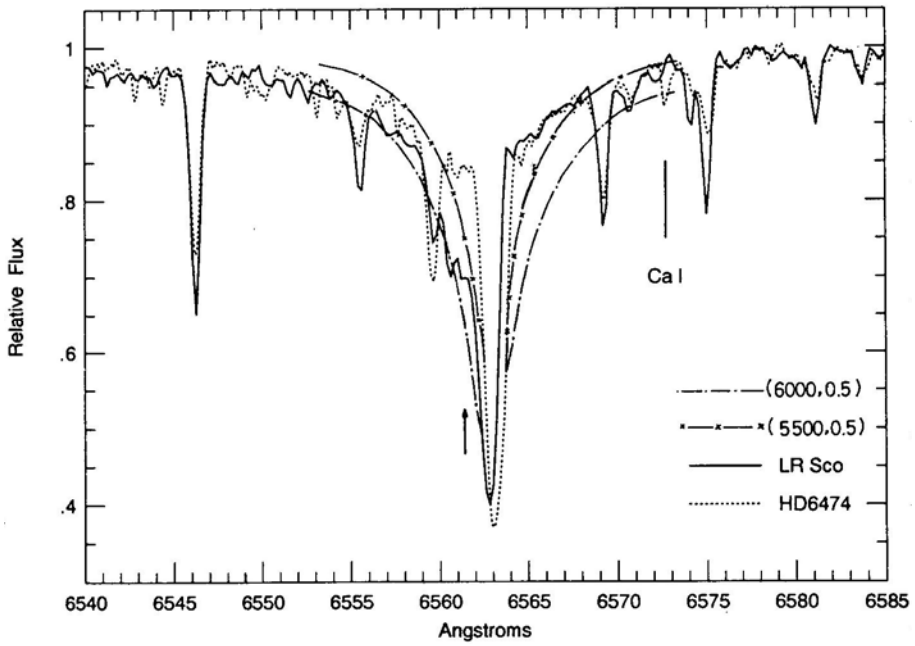

Figure 1. Hα line profile of LR Sco (shown by continuous line) with that of a G0 supergiant HD 6474 (shown by dotted line). The figure also contains Hα profiles calculated by Kurucz (1979) for model atmospheres with ($T_{\rm eff}$ = 5500K, log g = 0.5) and ($T_{\rm eff}$ = 6000K, log g = 0.5) shown by dash-cross and dash-dot pattern respectively.

$$V_t = 5.5 \text{ km s}^{-1}$$

The red wing of the observed Balmer alpha profile is consistent with the red wings of the profile computed by Kurucz (1979) for the model with $T_{\rm eff}$ = 5500K and *log* g = 0.5 as demonstrated in Fig. 1. The sensitivity of the abundances to the changes in the model parameters are as follows. A change of $T_{\rm eff}$ = 300 K results in a change of 0.3 in log (abundance) (eg. Fe), a change of V_t= 1 kms^{-1} results in a change of 0.3 in log (abundance) (effects the singly ionised metals), a change in log g of 0.5 results in a change of 0.15 in log (abundance).

4.1 *C, O Abundances*

Our abundances of light elements C, and O are based on very few lines. In the case of C, we could measure and use 5 lines and the gf values of Luo & Pradhan (1989) were used. All the five lines give a consistent value. In case of oxygen, the [OI] lines at 6300 Å and 6363 Å are weak and blended and therefore could not be used. We have used the OI line in the 6150 Å region, synthesized the 6152Å–6163Å region and compared with the observed spectrum (see Fig. 2). C and O are of approximately solar abundance. No convincing identification of NI could be made. Two possible candidates yield an upper limit [N/H] > 1.5, which exceeds the expected abundance of a supergiant.

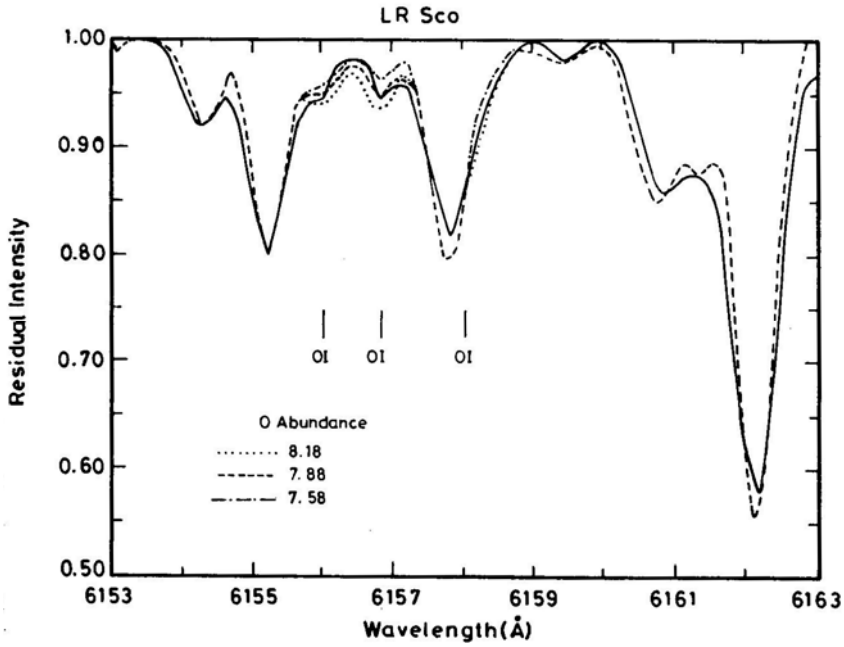

Figure 2. The agreement between the observed spectrum (continuous line) and the synthesized spectrum (dashed line) in 6153–6163 Å region that contains OI lines. The calculations are made for O abundance of 7.58, shown by dash dot line, 7.88 shown by dashed line and 8.18 shown by dotted line.

4.2 *Na–Ca Abundances*

Three NaI lines used in present analysis are of weak to moderate strength (NaI D lines were excluded), and the derived abundances are consistent (see Fig. 2 for comparison with synthetic spectrum).

The available Mg I lines were quite strong ($W_\lambda \cong$ 140–300 mÅ). Silicon is well represented by 13 neutral and 2 singly ionised lines. Although SiII lines are strong, they give an abundance value that is consistent with that estimated from the SiI lines. Sulphur is represented by 5 neutral lines of moderate strength and the scatter in the derived abundance is very small. We could measure 17 CaI lines and this element appears to be deficient compared to other elements (use of $T_{\rm eff} = 6000$ K would result in a solar abundance for CaI but this is inconsistent with FeI, FeII). Na, Mg and AI indicate mild deficiencies, whereas Si and S show a mild excess.

4.3 *Fe-peak Elements*

Scandium and Vanadium were represented by just a few lines of one ionisation state. We could measure a few TiI and TiII lines, but the TiII lines were very strong and the TiI lines weak and susceptible to blending effects. We had good coverage for CrI and CrII lines and the derived abundances are quite consistent. We could measure a large number of FeI and a reasonably good number of FeII lines and hence the

derived abundance are of better accuracy. A reasonably good number of neutral Mn and Ni lines were available and scatter in derived abundances is very small. All these Fe-peak elements show mild deficiency (by a factor of almost 2 relative to the Sun).

4.4 *s-process Elements*

We could estimate the abundances for Y and Ba. The YII and BaII lines show an underabundance of the same magnitude as shown by Fe-peak elements.

5. Sodium D lines

The strong sodium D lines show somewhat asymmetric profiles with long wavelength side being steeper indicating clearly the presence of blue-shifted components (Fig. 3). We have separated out these components by reflecting the longer wavelength part of each profile to the shortward side. The symmetrical profile generated this way was subtracted from the original line profile (point-by-point subtraction). We have plotted the separated D1, D2 components and the original D1 and D2 line in Fig. 3. We are interested in ascertaining the origin of these line components.

The central wavelengths for these components are found to be 5888.79 Å and 5894.72 Å indicating a radial velocity shift of – 47 kms^{-1} and – 50 kms^{-1} respectively with respect to the stellar lines. The corresponding equivalent widths are 177mÅ and

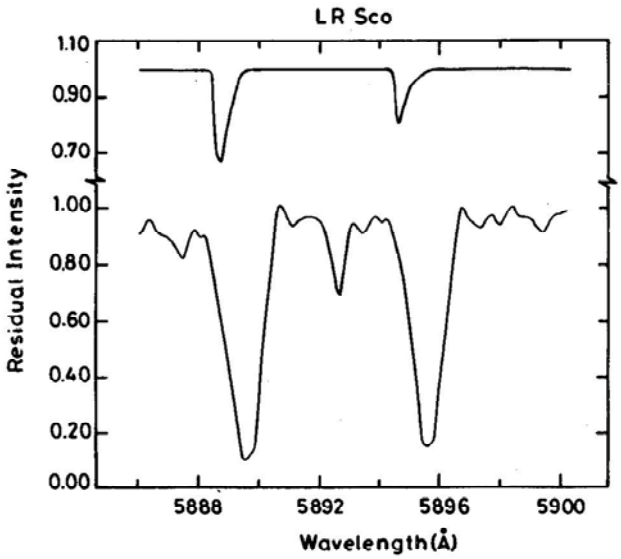

Figure 3. The lower portion of the figure shows observed profiles of NaI D1, D2 lines. The upper portion shows the circumstellar components extracted from the observed line profiles.

75mÅ for D1 and D2 respectively. The equivalent widths ratio is effectively 2:1 corresponding to the ratio of their gf values, and implies that the lines are optically thin. The column densities can then be estimated using the gf-value of 0.327 for D2- N(NaI) = 7.4×10^{11}cm^{-2}.

The question arises whether the observed line components are interstellar or of circumstellar origin. We believe they are of circumstellar origin for the following reasons. The radial velocity of the star $V_{LSR} = -17.4$kms^{-1} indicates a distance of around 2 kpc if it follows the galactic rotation (Pottasch 1984). If the cloud producing the NaI components is interstellar and also follows the galactic rotation then the cloud distance turns out to be about 6 kpc, hence the identification of the components as interstellar matter is unlikely. Further evidence comes from the fact that published 21 cm HI spectra taken closest to the location of LR Sco (l = 345°, b = – 3°; Sinha 1980) do not reveal any gas at the velocity of the NaI components. There might be interstellar components in the velocity range 10 to – 10 kms^{-1} which blend with the strong stellar line itself. Finally, there is a strong absorption component in the hydrogen alpha line profile which is blue shifted and corresponds to a velocity of – 60 kms $^{-1}$ (see Fig. 1 where the component is indicated by an arrow). The – 60 kms $^{-1}$ component is probably the deep absorption part of a P-Cygni profile. We, therefore, consider that the NaI absorption components are most likely of circumstellar origin.

We do not have sufficient information to estimate the degree of ionisation of Na in the circumstellar envelope. We assume that initially the physical situation in LR Sco is similar to that prevailing during the shell episode of ρ Cas studied by Sargent (1961) when the star (a F8Ib supergiant) showed shell lines including NaI D lines with an expansion velocity of about 40 kms^{-1} and emission in the Hα line. We use the parameter log(n_e/w) which is the ratio of the electron density and the dilution factor estimated for ρ Cas, and proceed to calculate the column density of N(Na) for LR Sco. We obtain N(Na) = 2×10^{17}cm^{-2}, and for a solar Na abundance derive the column density of hydrogen N(H) = 7×10^{22}cm^{-2}. Extending the analogy with ρ Cas further and assuming $M_v = -8$ for LR Sco, the stellar radius wiil be around 390$R_\odot$ Sargent (1961) estimated that the shell is situated at 2R from the star for ρ Cas. With this estimate we can calculate mass loss rate of the, star as given by $M = 4\pi\mu m_H N_H R_i V$, where μ is the mean molecular weight, m_H is the mass of the hydrogen atom, N_H is the hydrogen column density, R_t is the inner radius of the shell (assumed as $2R_*$) and V is the expansion velocity. We obtain $M = 7 \times 10^{-6}$ M$_\odot$ yr^{-1}. On the other hand, if LR Sco is like a Ib supergiant with $M_v = -4.5$ then the corresponding radius would be 81$R_\odot$ and $M = 1 \times 10^{-6}$M$_\odot$ yr^{-1}.

The Hα profile of LR Sco is rather complex. A comparison with another G0 Ia supergiant HD6474 (illustrated in Giridhar *et al.* 1991; see Fig. 1) shows that there is a P-Cygni kind of profile superposed on the normal absorption line. The deepest part of absorption seems to occur at –60kms^{-1} with respect to the neighbouring FeI lines. The emission is not very pronounced; the comparison star HD6474 may also have weak emission component. A comparison with the predicted Hα line profile (Kurucz 1979) brings out the P Cygni feature quite clearly (see Fig. 1). The absorption wings of Hα profile in LR Sco seem to extend more and are slightly deeper than those in HD6474 indicating a slightly hotter temperature for LR Sco.

6. The observed infrared excess

As mentioned earlier, LR Sco shows an infrared excess extending upto 100μm as illustrated in Fig. 4. The infrared flux shows a peak near 3.5 μm. The observed flux cannot be characterised by a single blackbody. One needs a combination of blackbodies at different temperatures (ranging from 1400 K to 100 K) to explain the observed flux distribution between 1 μm to 100 μm. The observed infrared excess between 1–100μm is 7×10^{-9} ergs $cm^{-2}s^{-1}$ and the infrared luminosity is $20d^2L_\odot$ where d is the distance in kpc. The observed (B–V) colour is quite consistent with the model atmosphere and does not indicate a significant reddening for the star. If we assume no reddening, then taking the bolometric correction from Kurucz (1979), the stellar luminosity comes out to be $120d^2L_\odot$ i.e. about 14 percent of stellar flux is radiated in the infrared.

Detailed modelling is necessary to be able to estimate the mass of the circumstellar dust. The photosphere is apparently oxygen–rich and hence the grains are probably silicates. An estimate of the dust mass can be made by assuming that the mean blackbody temperature of the dust is 830 K; this temperature corresponds to an infrared excess peak at 3.5μm. If we assume the dust shell to be optically thin, the dust mass following Barlow (1983) and Hildebrand (1983), is given by

$$M_d = \frac{4a\rho d^2 F_\nu}{3Q_\nu B_\nu(T_d)} \text{gm}$$

where ρ is the grain density (3.4gm cm^{-3} for silicates), F_ν is the observed flux at a given frequency, Q_ν is the absorption efficiency, a is the grain radius, and $B_\nu(T_d)$ is

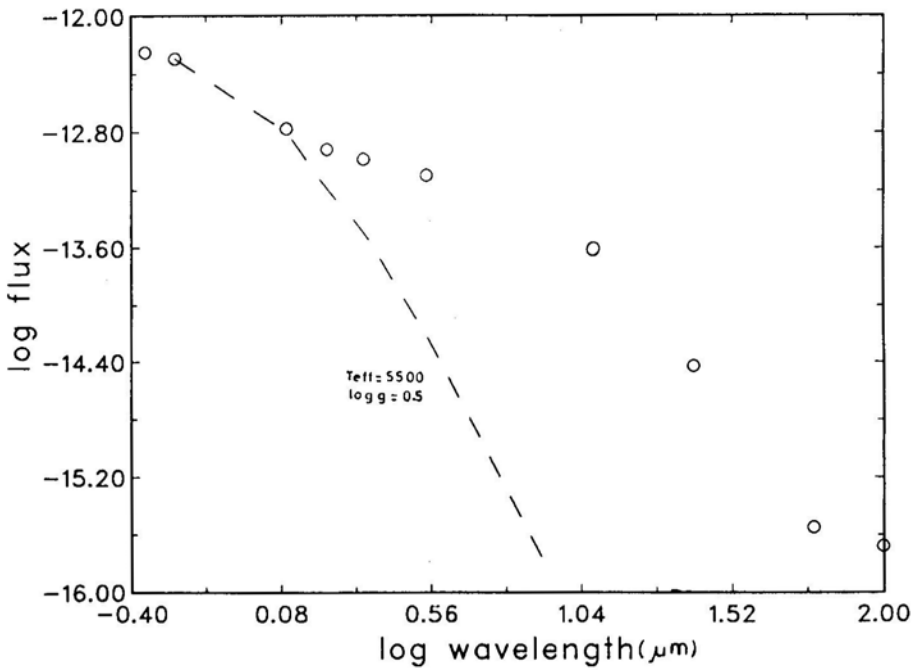

Figure 4. Observed infra red flux is plotted as a function of wavelength. The figure also shows theoretical fluxes for a stellar model atmosphere with T_{eff} =5500K, log g = 0.5 taken from Kurucz (1979).

the Planck Function for the dust temperature. We have taken the Q_v/a value from Draine (1981) for the astronomical silicates. The estimated dust mass is $4\times10^{24}d^2$gm where d is in kpc. If we assume a distance of around 2 kpc, the dust mass is about $7\times10^{-9}M_\odot$

Although the observed (BV) index is consistent with the intrinsic value for a star of this spectral type, it is conceivable that neutral extinction is present possibly caused by an optically thick dust envelope or due to the presence of larger grains in the envelope or both. The presence of neutral extinction is indicated from the following argument: the kinematical distance estimated from the radial velocity of the star is about 2 kpc. If LR Sco is considered as a Ia supergiant with $M_v = -8$, then the neutral extinction A_v turns out to be 6.2 mag. If M_v is assumed to be –4.5 (similar to Ib supergiant), then A_v is around 2.7 mag. Since $\tau_v/\tau_{3\cdot5\mu}$ is proportional to $Q_{absv}/Q_{abs3\,5\mu}$, the $\tau_{3\cdot5}$ is ~0.6 (see Draine 1981), and thus, even at 3.5 μ the dust might still be optically thick.

At the IRAS band of 12, 25, 60 and 100μ the dust is optically thin and leads to a more reliable estimate of mass loss (particularly at 60μ). Several methods of estimating the mass loss based on the modelling of circumstellar dust envelopes using IRAS band fluxes have been proposed for oxygen rich AGB stars with silicate dust. Herman *et al.* (1986) and Jura (1987) have obtained relations for mass loss rate based on 60μ IRAS flux densities (see also van der Veen & Olofsson (1990)). If we use the expression of Herman *et al.* (1986)

$$M = 0.66\mu V_{15} d^2 L_4^{-0\cdot47} F_v(60\mu)K_v \quad M_\odot\,\mathrm{yr}^{-1}$$

where μ is gas to dust mass ratio, V_{15} is the expansion velocity in terms of 15kms^{-1}, d is the distance in kpc, L_4 is the stellar luminosity in terms of $10^4\,L_\odot$, and $F_v(60)$ is the flux density in Jy. If we assume $\mu = 100$, V_{15} is around 3 (estimated from NaD line components) $d = 2$, and assuming that the $M_v = -4.5$, $L_4 = 0.5$, $F_v(60)$ observed is = 3.4 Jy and k_v = 240 cm2/gm leads to a mass loss rate $\sim4\times10^{-6}M_\odot$ yr^{-1}. If we use a similar expression given by Jura (1987), we obtain mass loss rate of $2\times10^{-6}M_\odot\mathrm{yr}^{-1}$.

Another expression for estimating the mass loss uses the ratio of flux densities at 12 and 25μm IRAS bands (van der Veen & Olofsson 1990). This expression is derived for circumstellar envelopes of oxygen rich AGB stars with continuous mass loss, assuming a radiation pressure driven wind with perfect coupling between the dust and the gas:

$$M = 1.3\times10^{-5}V_{15}^{-1}L4(F_v[25\mu\mathrm{m}]/F_v[12\mu\mathrm{m}])^{2\cdot9}\,M_\odot\,\mathrm{yr}^{-1}.$$

For LR Sco with the values mentioned. above the mass loss rate obtained is $1\times10^{-6}M_\odot\mathrm{yr}^{-1}$

Thus all these three relations using 12,25 μm and 60 μm flux densities give consistent value for the mass loss rate (i.e. gas + dust $\cong 2\times10^{-6}M_\odot$ yr^{-1}) for LR Sco from the dust which is in surprisingly good agreement with mass loss derived from the NaI D component lines (i.e. $1\times10^{-6}\,M_\odot$ when we assume $M_v = -4.5$).

7. Discussion

By luminosity and location, LR Sco appears to be a massive star. Luminous massive supergiants are known to be semi-regular variables with periods of the order of 100

days. Identification of LR Sco as a massive young star is not immediately supported by two observations: (i) the infrared excess, and (ii) the nonsolar values of certain elemental abundances ratios X/Fe.

Supergiants of spectral type earlier than about mid-G generally do not show an infrared excess (Stickland 1985; Jura & Kleinman 1990). We have argued that LR Sco is feeding a circumstellar shell that is presumably the site of the infrared emitting grains. Such mass loss and mass ejection is episodic; Jura & Kleinman argue that ρ Cas (spectral type F8 Ia) has recently developed an infrared excess as a result of mass shed during the star's deep minimum in 1946–1947.

The chemical composition of LR Sco is not exactly that of a massive supergiant. In Table 2, we show the expected abundance of a massive supergiant as derived from observations presented by Luck & Bond (1989) and adjusted to [Fe/H] = –0.3 by assuming [X/H] = 0. The most striking difference between LR Sco and the representative supergiant are seen for Ca and Sc which appear underabundant in LR Sco. Other large differences are seen for Si and Mn.

A competing identification of LR Sco would suppose it to be a post-AGB star. A pronounced infrared excess is a characteristic of post-AGB stars. Certainly LR Sco's composition resembles that of 89 Her, a well known high galactic latitude supergiant of (presumably) low mass (see Table 2). Note the similar Ca/Fe and Sc/Fe ratios of

Table 2. Elemental abundances for LR Sco and other supergiants.

	LR Sco			FG-Supergiants*			89 Her†		
Element	[A/H]	S.E.	N	[A/H]	S.E.	N	[A/H]	S.E.	N
CI	−0.05	0.17	5				−0.26	0.04	12
OI	−0.10		1				−0.27		1
NaI	−0.10	0.15	3	0.10	0.20		0.14	0.10	3
MgI	−0.35	0.20	3	−0.4			−0.02	0.43	9
AlI	−0.41		1	−0.1			−0.19		1
SiI	0.11	0.11	13	−0.2			0.01	0.32	16
SiII	0.29	0.29	2	−0.2					
SI	0.19	0.07	5				−0.26	0.03	2
CaI	−0.56	0.18	17	−0.2			−0.44	0.19	18
ScII	−0.94	0.82	4	−0.3			−0.89	0.18	2
TiI	−0.45	0.29	5	−0.1			0.19	0.92	58
TiII	−0.30	0.38	5	−0.2			−0.73	0.21	19
VI	−0.20	0.30	5	−0.1					
VII				−0.1			−0.36	0.06	2
CrI	−0.21	0.29	14	−0.2					
CrII	−0.20	0.23	7	−0.2			−0.03	0.12	12
MnI	−0.02	0.18	11	−0.5			−0.36	0.24	8
FeI	−0.27	0.20	181	−0.3			−0.38	0.28	245
FeII	−0.29	0.17	24	−0.3			−0.44	0.16	22
NiI	−0.23	0.23	37	−0.3			−0.29	0.23	32
ZnI	−0.55	0.05	2				−0.38	0.29	3
YII	−0.15		1	−0.1			−0.43	0.38	12
BaII	−0.19	0.16	3	−0.2			−0.79	0.26	2

*Mean abundances for 65 supergiants from Luck & Bond (1989)
† Abundances taken from Luck, Bond & Lambert (1990).

the two stars. A careful determination of the CNO abundances may provide the evidence to distinguish the competing identifications of LR Sco's evolutionary status.

Acknowledgement

D. L. Lambert thanks the U.S. National Science Foundation for its partial support of this research (grants AST 89–02835 and 91–15090 and a travel grant).

References

Barlow, M. 1983, in *Planetary Nebulae; Proceedings of I.A.U. Symp.* 103, Ed. D.R. Flower, (D. Reidel, Dordrecht), p. 105.
Bidelman,W.P. 1979, in *Mass loss and evolution of O type stars,* Eds P.S.Conti & C.W.H. deLoore, (D. Reidel; Dordrecht), p. 305.
Carter, B. S., Roberts, G., Feast, M. W. 1979, *Inf. Bull Var. Stars,* 1640.
Castley, J. C, Watson, R. D. 1980, *Astr. Astrophys. Suppl. Ser.,* **41,** 397.
Draine, B. T. 1981, *Ap. J.,* **245,** 880.
Drilling, J. S., Hill, P.W. 1986, in *Hydrogen Deficient stars and related objects,* Eds K. Hunger, D. Schönberner & N. Kameswara Rao, (D. Reidel, Dordrecht), p. 499.
Feast, M. W. 1979, in *Changing trends in variable star research, Proc. I.A.U. coll.* **46,** Ed. F. M. Bateson, (D. Reidel, Dordrecht), p.246.
Fitzgerald, P. M. 1970, *Astr. Astrophys.,* **4,** 234.
Flower, P. J. 1977, *Astr. Astrophys.,* **54,** 31.
Führ, J. R., Martin, G. A., Wiese, W. L. 1988, *J. Phys. Chem. ref. Data,* **17,** s.4, p. 1.
Giridhar, S. 1983, *J. Astrophys. Astr.* **4,** 75.
Giridhar, S., Rao, N. K., Lambert, D. L. 1990, *Observatory,* **110,** 120.
Grevesse, N. 1984, *Phys. Scripta T8,* p. 49.
Gustafsson, B., Bell, R. A., Eriksson, K., Nordlund, Å. 1975, *Astr. Astrophys.,* **42,** 407.
Harris, H. C, Pilachowski, C. A. 1984, *Ap. J.,* **282,** 655.
Herman, J., Burger, J. H., Penninx, W. 1986, *Astr. Astrophys.,* **167,** 247.
Hildebrand, R. H. 1983, *Q. J. R., astr. Soc,* **24,** 167.
Home, K. 1986, *Publ. astr. Soc. Pacific,* **98,** 609.
Horne, K. 1988, in *New directions in spectrophotometry,* Eds. A.G.D. Phillip, D. Hayes & S. Adelman, L. Davis Press, p. 145.
Jura, M. 1987, *Ap. J.,* **313,** 743.
Jura, M., Kleinman, S.G. 1990, *Ap. J.*,**351,** 583.
Kukarkin, B.V.,Kholopov, P. N.,Effremov, Yu. N., Kukarkina, N. P. KurochKurochkin, N. E., Medredeva, G.I., Perova, N. B.,Fedrovich, V. P., Frolov, M. S. 1969, General Catalogue of Variable stars, Moscow.
Kurucz, R. L. 1979, *Ap. J. Suppl. Ser.,* **40,** 1.
Luck, R. E. 1982, *Ap. J.,* **256,** 177.
Luck, R, E., Lambert, D. L. 1985, *Ap. J*, **298,** 782.
Luck, R. E., Bond, H. E. 1989, *Ap. J. Suppl. Ser.,* **71,** 559.
Luck, R. E., Bond, H E , Lambert, D. L. 1990, *Ap. J.,* **357,** 188.
Luck, R. E., 1991, Private communication.
Luo, D. Pradhan, A. K. 1989, *J. Phys.,* **B.22,** 3377.
Martin, G. A, Führ, J. R., Wiese, W. L. 1988, *J. Phys, Chem. Ref Data,* 17, Suppl. 3, 1.
Pottasch, S. R. 1984, in *Planetary Nebulae, Astrophys. Space Sci. Lib,***107,** (D. Reidel, Dordrecht), p. 29.
Prabhu, T. P., Anupama, G. C, Giridhar, S. 1987, *Bull. astr. Soc. India,* **15,** 98.
Prabhu, T. P., Anupama, G. C. 1991, *Bull astr. Soc. India,* **19,** 97.
Sargent, W. L. W. 1961, *Ap. J.,* **134,** 142.
Shapley, H., Swope, H. H. 1934, *Harvard Ann.,* **90,** No. 5.

Sinha, R. P. 1980, *Astr. Astrophys. Suppl. Ser.,* **37,** 403.
Sneden, C, 1973, Ph.D. Thesis, Univ. of Texas at Austin.
Stephenson, C. B. 1978, *Inf. Bull Var. Stars,* No. 1453.
Stickland, D. J. 1985, *The Observatory,* **105,** 229.
van der Veen, W., Olofsson, H. 1990, in *From Miras to planetary nebulae,* Eds M. O. Mennessier & A. Omont, Editions Frontiéres, Gif sur Yvette, p. 139.
Walker, H. J. 1986, in *Hydrogen deficient stars and related objects,* Eds K. Hunger, D. Schönberner & N. Kameswara Rao, (D. Reidel, Dordrecht), p. 407.

J. Astrophys. Astr. (1992) **13,** 319–326

Stochastic Stellar Orbits in a Pair of Interacting Galaxies

Ch. L. Vozikis & N. D. Caranicolas *Department of Physics, Section of Astrophysics, Astronomy and Mechanics, Aristoteleion University of Thessaloniki, 540 06 Thessaloniki, Greece*

Received 1992 April 27; accepted 1992 August 3

Abstract. A dynamical model composed of a disk galaxy with an elliptic companion, moving in a circular orbit, is used in order to study the stellar orbits in a binary galaxy. Using the Poincare surface of section we study the evolution of the stochastic regions in the primary galaxy considering the mass of the companion or the value of the Jacobi's integral as a parameter. Our numerical calculations suggest that the regions of stochasticity increase, as the mass of the companion or the value of the Jacobi's integral increase. An interesting observation is that only direct orbits become stochastic.

Key words: interacting galaxies—surface of section—stochastic orbits

1. Introduction

In many problems in stellar dynamics it is usual to consider galaxies without a nearby important companion. Schwarzschild (1981) calls these galaxies unperturbed galaxies. What in reality happens is that galaxies often appear in pairs, small groups or clusters. This galactic sociality suggests that they interact with their environment. Among these interactions gravitationally-induced collision and mergers of galaxies are possibly the dominant mechanism for their evolution (Schweizer 1986).

A well-known system of interacting galaxies is the Galaxy together with the Large and Small Magellanic Clouds. Information on the dynamical evolution of this triple system can be found in many interesting papers (see Kerr 1957; Avner & King 1967; Fujimoto & Sofue 1976 and references therein).

On the other hand it is worth mentioning the interesting work of Miller & Smith (1980) on the properties of individual encounters between pairs of interacting galaxies. Miller (1986) also discusses a spiral galaxy falling into a galaxy cluster and small galaxies in the potential field of larger galaxies.

Signs of galactic interactions come also from the study of elliptical galaxies with dust lanes. It is believed that the dust lanes are the result of a capture of a gas-rich system by the elliptical galaxy. This idea is strongly supported by recent observations (Bertola & Bettoni 1988) showing that the angular momenta of gaseous and stellar components are antiparallel. This fact supports the acquisition hypothesis and indicates that the dust lanes are a second event in the history of these galaxies.

In an earlier paper (Caranicolas & Vozikis 1988) we have studied the evolution of the families of periodic orbits in a pair of interacting galaxies. The main result of the above work was that the disappearance of the Lagrange points was followed by the

disappearance of the majority of the periodic orbits. This suggests that a change in the topology of the potential affects drastically the behaviour of the periodic orbits.

The purpose of the present paper is to study the regular and stochastic motion in the primary galaxy under the influence of the companion. In fact in the absence of the companion all orbits in the primary galaxy are quasi-periodic while, when the companion is present, stochastic regions appear in the Poincare surface of section. We shall try to connect the degree of stochasticity with the value of the mass of the companion or the value of the Jacobi's integral. Our model is described in section 2. The main results of this work are given in section 3 while a discussion and the conclusions of this research are presented in section 4.

2. Description of the model

The primary galaxy in our model is described by Bottlinger force law

$$F_g = \frac{-ar}{1+br^3}, \tag{1}$$

where r is the distance to the centre while a, b are adjustable parameters. The companion galaxy is described by a homogeneous spheroid with a potential law

$$V_c = -\frac{GM_c}{r_c}\left[1+\frac{1}{10}\left[\frac{\varepsilon}{r_c}\right]^2+\frac{9}{280}\left[\frac{\varepsilon}{r_c}\right]^4+\frac{5}{335}\left[\frac{\varepsilon}{r_c}\right]^6+\cdots\right], \tag{2}$$

where M_c is the mass of the companion, r_c is the distance to its centre while $\varepsilon^2 = \alpha^2 - \gamma^2$; α, γ are the two semiaxes of the spheroid. Further information on Bottlinger's model and homogeneous spheroids can be found in Perek (1962).

The companion galaxy moves in a circular orbit of radius R about the primary lying on the plane of the disk, with constant angular velocity $\Omega_p > 0$ given by

$$\Omega_p = \left[\frac{a}{1+bR^3}\right]^{1/2} \tag{3}$$

In our study we use a rotating system with the origin at the center of the primary galaxy which rotates clockwise at the angular velocity of the companion Ω_p. The position of the companion in this system is fixed at $x_c = R$, $y_c = 0$. The total potential V_T responsible for the motion of a star, with a mass $m = 1$, in the disk of the primary galaxy is

$$V_T = V_g(r) + V_c(s), \tag{4}$$

where

$$V_g = -\frac{\alpha}{b^{2/3}}\left[\frac{1}{6}\ln\left(1+\frac{3b^{1/3}r}{b^{2/3}r^2-b^{1/3}r+1}\right)+\frac{1}{\sqrt{3}}\arctan\left(\frac{\sqrt{3}}{2b^{1/3}r-1}\right)\right], \tag{5}$$

with

$$r^2 = x^2 + y^2,\ s^2 = (x-R)^2 + y^2\ .$$

The equations of motion are

$$\begin{aligned}\ddot{x} &= -2\Omega_p\dot{y} + \Omega_p^2 x + F_g x/r + F_c(x-R)/s\\ \ddot{y} &= 2\Omega_p\dot{x} + \Omega_p^2 y + F_g y/r + F_c y/s\end{aligned} \tag{6}$$

where $F_g = -\,dV_g/dr$, $F_c = -\,dV_c/ds$ and the dot indicates derivative with respect to the time. There is one exact integral of motion, the Jacobi's integral, given by the relation

$$J = \tfrac{1}{2}(\dot{x}^2 + \dot{y}^2) + V_T - \tfrac{1}{2}\Omega_p^2 r^2 = h, \tag{7}$$

where h is the numerical value of J, The units of length, mass and time are 20 kpc, $1.8 \times 10^{11}\, M_\odot$ and 0.99×10^8 yr respectively. In this system of units the velocity unit is equal to 197 km/sec while the constant of gravity G is equal to unity.

For large values of r the force given by equation (1) must be that of a point mass. This gives the mass of the primary galaxy as a function of a, b which is

$$M_g = \frac{a}{Gb}. \tag{8}$$

For all the numerical experiments, in the adopted system of units, we take a = 9.1, b = 5.14 so that M_g= 1.77 = 3.2 × $10^{11} M_\odot$. The values of α, γ are 0.15 and 0.075 respectively so that ε = 0.06495. Furthermore, from the series in equation (2) we take only the first four terms.

3. Regular and stochastic orbits

Figure 1 shows the contours of constant effective potential $V_{\text{eff}} = h$, where

$$V_{\text{eff}} = V_T - \tfrac{1}{2}\Omega_p^2 r^2. \tag{9}$$

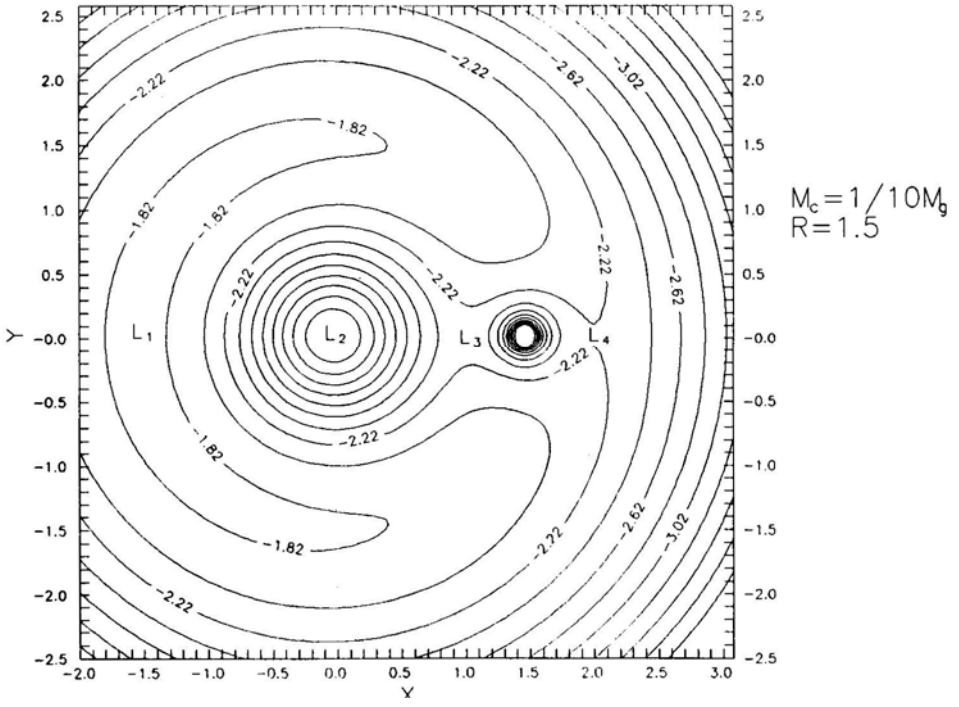

Figure 1. Contours of constant effective potential V_{eff} when M_c = 0.1 M_g, R= 1.5.

The values of M_c, R are 0.1 M_g, and 1.5 respectively. The four points L_1, L_2, L_3, L_4 are the Lagrange equilibrium points at which both $\partial V_{eff}/\partial x$, $\partial V_{eff}/\partial y$ vanish. L_1 is a maximum, L_2 is a minimum while L_3, L_4 are saddle points of V_{eff}. The curves in Fig. 1 are often called the zero velocity curves.

In order to study the regular and stochastic motion we use the (x, x) (y = 0, y> 0) Poincare surface of section. In the absence of the companion all orbits in the primary galaxy are regular. Of course this is natural for an integrable system, where all orbits are quasi-periodic. Fig. 2 shows the x, x phase space portrait when R = 1.5, M_c = 0.1 M_g, h = – 3. As one can see there are only well-defined invariant curves and the motion is regular. The two stable invariants points D and R represent the direct (i.e. in the same direction as the rotation) and retrograde 1:1 periodic orbits respectively. The outermost curve is the limiting curve defined by $J(x, x) = h$.

In the phase space portrait shown in Fig. 3 the values of M_c, R are the same as in Fig. 2 but the value of h is now equal to – 2.3. We can see that the two periodic points D and R are still stable while two new stable periodic points P, Q have appeared. These belong to a stable periodic orbit shown in Fig. 4 together with the direct and retrograde 1:1 periodic orbits. But the most important characteristic is that almost half of the surface of section appears stochastic. It is interesting to notice that all stochastic orbits are direct orbits. This can be easily found if we compare Fig. 3 with Fig. 5, where the shaded area represents the region of starting positions, on the surface of section, of all orbits that are direct.

In order to see whether the companion affects the retrograde orbits we began gradually increasing the value of the mass of the companion up, to 0.5 M_g, taking the appropriate value of the Jacobi's integral so that the corresponding zero velocity curves

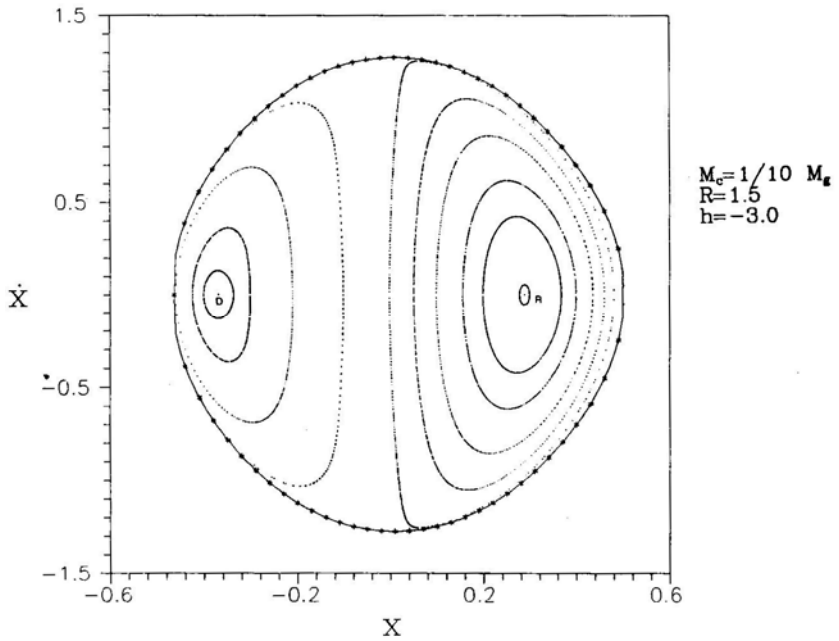

Figure 2. The x–x surface of section when $M_c = 0.1\ M_g$, $R = 1.5$, $h = -3.0$.

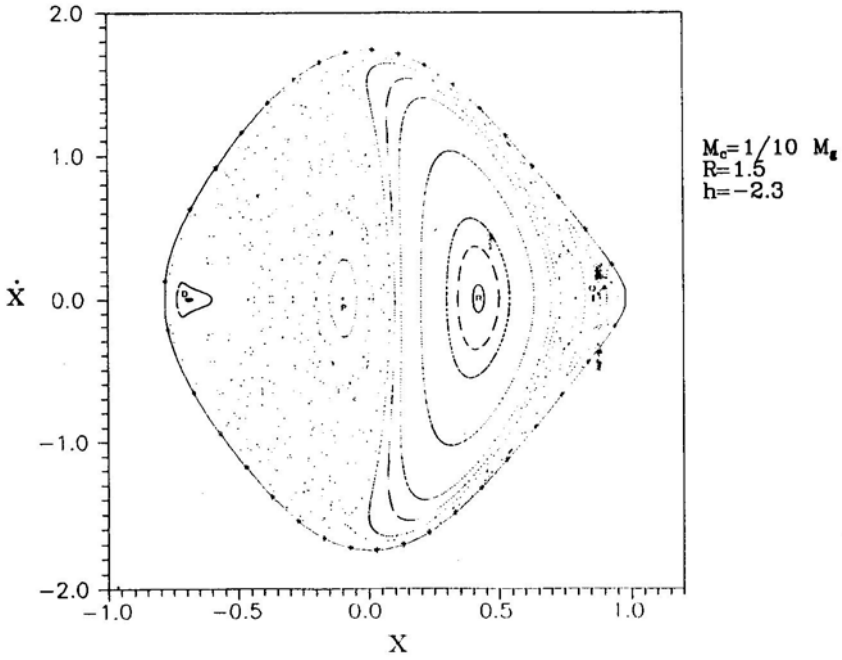

Figure 3. Same as Fig. 2 when $h = -2.3$.

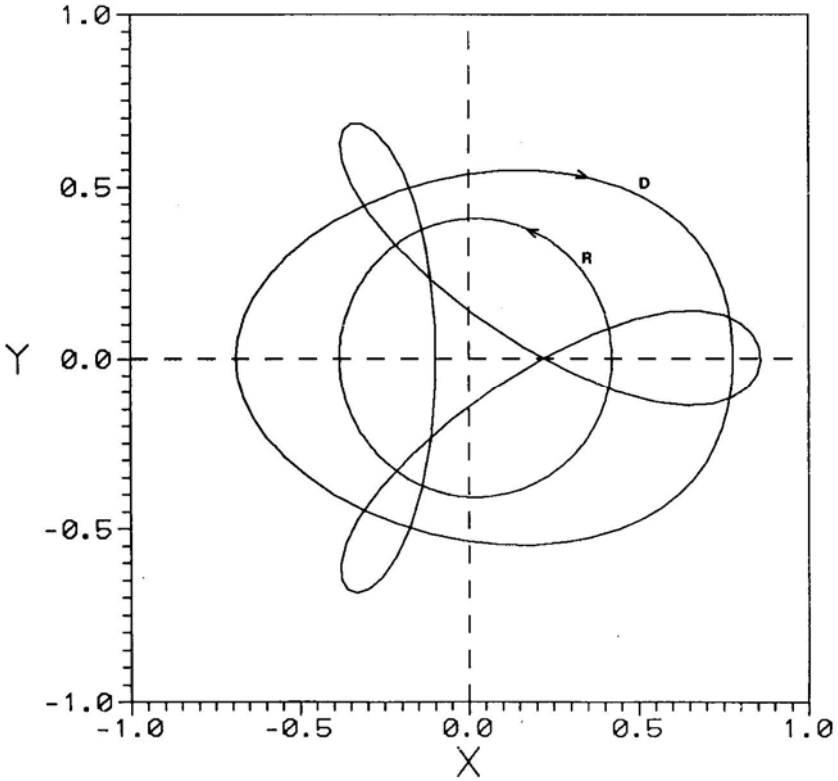

Figure 4. The direct and retrograde 1:1 periodic orbits together with a loop orbit. The values of the parameters are those of Fig. 3 while further details are given in the text.

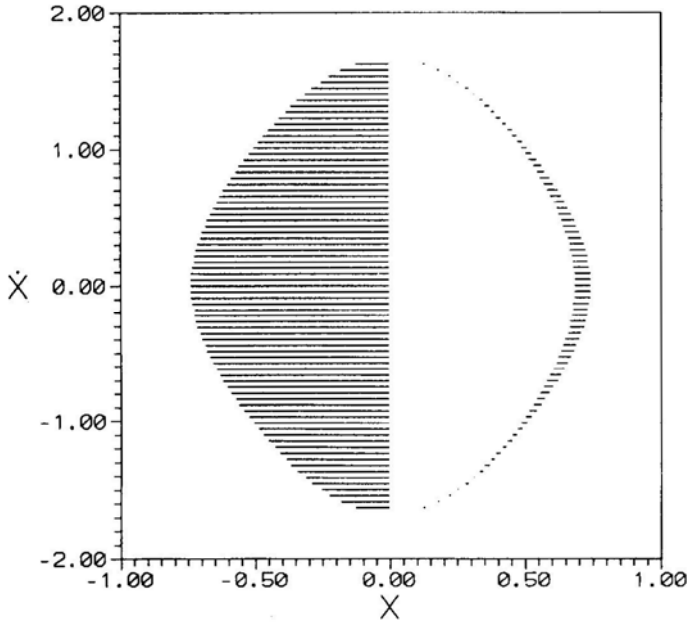

Figure 5. Area of direct orbits when $M_c = 0.1\ M_g$, $R = 1.5$, $h = -2.3$.

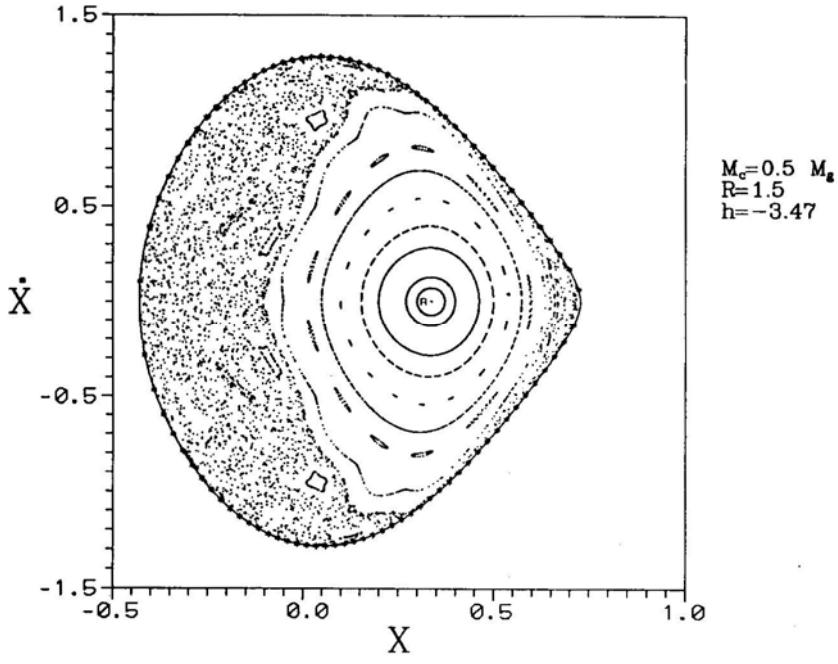

Figure 6. The x -x surface of section when $M_c = 0.5\ M_g$, $R=1.5$,$h = -3.47$

be closed and computing the corresponding surface of section. Our numerical experiments always showed that the corresponding retrograde motion is regular. Fig. 6 shows a surface of section when $M_c = 0.5M_g$, $R = 1.5$, $h = -3.47$. One can see that almost all the direct orbits are stochastic while the retrograde orbits are regular. We did not feel it was necessary to go to larger masses for the companion, because then, due to the shape of the zero velocity curves, the majority of the orbits would escape. Thus, our numerical calculations strongly suggests that, in the case of stochastic motion induced by a companion galaxy, this motion is present only in the direct orbits.

4. Discussion

The present work was devoted to the study of regular and stochastic orbits in the primary galaxy of a binary system. It is evident that, for a companion of a given mass, the motion in the primary galaxy is regular when the value h of the Jacobi's integral is small. As the value of the Jacobi's integral increases part of the orbits become stochastic. Our numerical calculations show that only direct orbits become stochastic.

In order to check this we computed a large number of surfaces of section using the mass of the companion as a parameter which was increased up to $0.5M_g$. For all these numerical experiments the value of h was chosen properly so that the test particle would be able to cover nearly all the galaxy while the corresponding curve of zero velocity was closed. The results of this experiment showed that, even when nearly all direct orbits were stochastic, the retrograde orbits were still regular!

It is natural then to ask: why do only the direct orbits become stochastic? To answer this question we could say that, as the star in the direct orbits rotate at the same direction as that of the companion, it suffers a greater perturbation, because it is closer to the companion during its motion. Therefore, it seems reasonable to expect these orbits to display stochastic behaviour, rather than the retrograde ones, where the star spends only a small amount of time near the companion.

Furthermore, it is well known that, the interaction of a companion with the direct orbits produces spiral structure (see for instance Sundelius *et al.* 1987; Noguchi 1988). In order to relate the spiral structure with the stochasticity found in the present work, one needs a self-consistent model. Since our model is not self-consistent, it is not possible to make such a comparison.

All numerical calculations were made by means of a Bulirch-Stoer method in double precision while the accuracy of the calculations was checked by the constancy of the Jacobi's integral which was conserved up to the fifteenth significant figure. The time scale for the calculation of each orbit on the surface of section was between $0.6 - 1 \times 10^{10}$yr.

Acknowledgement

This paper is part of the first author's (Ch. L. Vozikis) Ph.D. thesis work. The authors would like to thank Professors B. Barbanis and J. Hadjedemetriou for their constant interest during this research.

References

Avner, E, King, I. 1967, *Astr. J.,* **72,** 650.
Bertola, F., Bettoni, D. 1988, *Astrophys. J.,* **329,** 102.
Caranicolas, N., Vozikis, Ch. 1988, in *Long-Term Dynamical Behaviour of Natural and Artificial N-Body Systems,* Ed A. E. Roy, Kluwer Academic Publishers, p. 297.
Fujimoto, M., Sofue, Y. 1976, *Astr. Astrophys.,* **47,** 263.
Kerr, F. G., 1957, *Astr. J.,* **62,** 93.
Miller, R. H. 1986, *Astr. Astrophys.,* **167,** 41.
Miller, R. H., Smith, B. F. 1980, *Astrophys. J.,* **235,** 421.
Noguchi, M. 1988, *Astr. Astrophys.,* **203,** 259.
Perek, L. 1962, in *Advances in Astronomy and Astrophysics,* Ed Z. Kopal, Academic Press, p. 165.
Schwarzschild, M. 1981, in *The Structure and Evolution of Normal Galaxies,* Eds S. M. Fall & D. Lynden-Bell, Cambridge University, London, p. 43.
Schweizer, F. 1986, *Science,* **231,** 227.
Sundelius, B., Thomasson, M., Valtonen, M., Byrd, G. 1987, *Astr. Astrophys.,* **174,** 67.

J. Astrophys. Astr. (1992) **13,** 327–347

Physical Identification of Static and Axially-Symmetric Vacuum Metric Tensors

N. Spyrou & D. Papadopoulos *Astronomy Department, University of Thessaloniki, 540 06 Thessaloniki, Macedonia, Greece*

Received 1992 June 1; accepted 1992 September 29

Abstract. We present a method of a possible physical identification of the static and axially symmetric Weyl-type vacuum γ and $n\gamma$ metrics. This method, in which no interior solutions of any kind are involved, is based on the comparison of the far-field forms of the γ and $n\gamma$ metrics, and of the far-field form of the metric tensor due to a bounded gravitating perfect-fluid source given correctly to post-Newtonian accuracy. The parameters of the vacuum solutions are expressed in terms of physical parameters of a prolate fluid source, namely total mass-energy, semiaxes and eccentricity, defined consistently to post-Newtonian accuracy. The results, based on the otherwise arbitrary fluid source, appear physically general. Possible astrophysical candidates for the far-field γ and $n\gamma$ metrics are proposed, based on the conditions imposed on them by the identification method. The advantages and deficiencies of the identification method are briefly discussed.

Keywords: Weyl metrics—perfect fluid sources—far field metrics—identification

1. Introduction and motivation

A large class of vacuum solutions of the general-relativistic field equations comprises the asymptotically flat, static and axially symmetric solutions (for a general account see Carmeli 1982). Two members of this class have attracted interest. The first one, the so-called γ *solution* (known also as the Vorhees or the Zipoy-Vorhees solution), is a two-parametric solution known since long ago (Weyl 1917, 1919; Winicour, Janis & Newman 1968; see also Papadopoulos, Stewart & Witten 1981) below for the long history of the γ metric and its name). The other one, the so-called $n\gamma$ *solution,* is a triparametric solution (Papadopoulos & Witten 1982). Several mathematical properties of the above solutions have been studied, especially those related to the existence and structure of multipole directional singularities (Papadopoulos & Witten 1982; Janis & Newman 1965; van den Burg 1968; Szekeres 1968; Papadopoulos, Stewart & Witten 1981). In contrast, not much information is available concerning the physical properties of the above solutions, especially the probable gravitating source producing the gravitational field described by these vacuum sources (see e.g. Clarke & Sciama 1971; Esposito & Witten 1975), the properties of the motion of test particles in it (Krisch 1983) and more generally the physical identification of these solutions.

Usually the term *physical identification* of a vacuum solution means to find an interior solution of the non-vacuum field equations, matching smoothly with the vacuum (exterior) one on the surface of the gravitating source considered. As already noted (Szekeres 1968), this is exactly the difficult question to be answered, namely whether the singularities can or cannot be covered with a realistic mass-energy distribution. Towards the answering of this difficult and interesting question, in the case of the γ-solution some efforts have been made, but the interior γ solutions determined are not always characterised by astrophysically interesting properties. Thus, they are expected to be dynamically unstable under adiabatic perturbations of the gravitating source's material content, or the matter's density in the source's interior is not always, everywhere in the source, a non-increasing function of the distance from its centre, or even the source does not always correspond to a pure fluid (Stewart *et al* 1982). Therefore the physical identification of the γ solution is still an interesting and open problem, and to the extent of our knowledge the available relevant data concerning the $n\gamma$ solution is even poorer, if existent at all.

But in trying to physically identify a vacuum solution, it is possible to follow a different and indirect method. More specifically, instead of determining (if possible at all) an interior solution and matching it smoothly on the source's surface with the known vacuum solution, it is possible to try to identify the far-field metric of the vacuum solution with the far-field metric of a known gravitating source. As such a source, we shall consider here a bounded perfect-fluid gravitating source. This choice is not quite unjustified, because on the one hand the perfect fluid has been studied extensively in both the Newtonian and the relativistic levels, and on the other hand the interior of many astrophysical systems can be approximated to a (degenerate or non degenerate) perfect fluid, quite satisfactorily. As it has already been emphasised (Spyrou 1981a; 1981b; 1984), with the aid of this method of physical identification it is possible to give a very precise and astrophysically useful physical meaning on the one hand to the vacuum solution's free parameters in terms of the perfect-fluid's internal physical characteristics, and on the other hand to the system of coordinates in which the vacuum solution has been expressed. In view of the above, the problem we posed (Spyrou & Papadopoulos 1990) is the following: Is it possible that the γ metric's and the $n\gamma$-metric's (and more generally any static and axisymmetric metric's) components, properly evaluated at large spatial distances, be written, to the extent it is required, in exactly the same functional form as the corresponding components of the metric tensor of a bounded perfect-fluid source, properly evaluated at spatial distances large compared with the perfect-fluid source's linear dimensions? If this can be achieved to the extent it appears to be necessary, then by simple comparison of the corresponding components of the two metric tensors, and also by properly using the integrals of the motion of test-particles (and gyroscopes) dictated by the spacetimes' symmetries, it is possible to identify **i)** the origins of the two systems of coordinates in which the vacuum (γ- or $n\gamma$-) solution and the perfect-fluid solution have been expressed, and **ii)** the parameters of the vacuum solutions with physical parameters of the fluid source, known to relativistic accuracy as volume integrals over the perfect-fluid source's three-dimensional volume. In this way the far-field metric of the vacuum solution from a dynamical and astrophysical point of view can be considered as equivalent to that of the perfect-fluid source.

An outline of the papers' content is as follows: In section 2 we derive the far-field metric tensor due to a bounded gravitating perfect-fluid source, correctly to

post-Newtonian accuracy. In section 3 we describe the Weyl-type γ- and *n*γ vacuum solutions, and derive the latters' form in properly generalized spherical polar coordinates. In section 4 we discuss the notion of the mass-energy, associated with the *γ* and *nγ* solution, and its possible interpretation. In section 5 we present the vacuum metric's multipole expansion, based on earlier work. In section 6 we describe the physical identification of the far-field expressions of the *γ* and *nγ* metrics with the perfect-fluid's far-field metric, and describe briefly some astrophysical properties of the corresponding fluid sources. Finally in section 7 the advantages, deficiencies and some open problems related to the identification method are exposed, and possible astrophysical fluid candidates for the far-field vacuum metrics are proposed, based on the conditions imposed on them by the physical identification. In an Appendix at the end some auxiliary formulae have been included concerning the far-field forms of the *γ* and *nγ* metrics, their multipole expansion, and some properties of the Newtonian gravitational potential of a prolate perfect-fluid source.

2. The far-field metric of a perfect-fluid source

The metric tensor due to a bounded gravitating perfect-fluid source to post-Newtonian (pN) accuracy of general relativity has been given long ago (see e.g. Chandrasekhar 1965). In order to derive the far-field expression of the above metric correctly to pN accuracy, in the gauge of (Chandrasekhar 1965) and in the standard pN notation, the following six steps are enough:

i). Express the metric's components in terms in the fluid's *inertial-mass* or *total mass-energy density* (Spyrou 1977)

$$f^* = \rho^* \left[1 + \frac{1}{c^2}\left(\frac{v^2}{2} - \frac{1}{2}U + \Pi \right) + O\left(\frac{\varepsilon^4}{c^4} \right) \right]$$

where, in the standard notation,

$$\rho^* = \rho \left[1 + \frac{1}{c^2}\left(\frac{v^2}{2} + 3U \right) + O\left(\frac{\varepsilon^4}{c^4} \right) \right]$$

is the rest-mass density, and

$$\varepsilon^2 = \max\left(v^2, U, \Pi, \frac{p}{\rho} \right) \ll c^2, \quad \nabla^2 U = -4\pi G\rho$$

ii). Taylor expands the metric's components in power series of $|\vec{x}'|/|\vec{x}| << 1$, where $\vec{x}$ and $\vec{x}'$ are the Cartesian three-vectors to the field and source-point respectively, the latter being confined in the source's three-dimensional volume *V*.

iii): Express the above expansion in the *center-of inertial-mass* (*cim*) *frame,* uniformly moving to pN accuracy (Contopoulos & Spyrou 1976), so that both the source's dipole moment $\vec{S}$ and linear momentum $\vec{P}$ defined by

$$\vec{S} = \int_V f^*(\vec{x}, t)\vec{x}\, \mathrm{d}^3 x \qquad \text{(Dipole moment)}$$

$$\vec{P} = \frac{\mathrm{d}\vec{S}}{\mathrm{d}t} \qquad \text{(Linear momentum)}$$

vanish.

iv). Assume secularly stationary conditions for the source in the form of the *virial theorem* (in its Newtonian form (Chandrasekhar 1969)

$$\left\langle \int_V f^* \left(v^2 - \frac{1}{2}U + \frac{3p}{f^*} \right) \mathrm{d}^3 x \right\rangle = O\left(\frac{\varepsilon^2}{c^2} \right)$$

v). Assume axially symmetric and time-independent distributions of mass-energy and internal velocities.

vi). Transform the metric tensor's components from the Cartesian coordinates to the usual spherical polar coordinates R, Θ, ϕ

Then one can easily prove that the mixed components $g_{0\alpha}(\alpha = 1,2,3)$ in Cartesian coordinates are of an order enough to be neglected, namely

$$g_{0\alpha}^{(f)} = O\left(\frac{\varepsilon^3}{c^3} \frac{L^2}{D^2} \right)$$

where $L(\sim |\vec{x}|)$ and $D(\sim |\vec{x}'| \gg L)$, measured in the cim frame, denote in orders of magnitude the linear dimensions of the fluid source and the distance to the field-point. Thus the metric tensor becomes diagonal to the approximation considered and we find

$$g_{00}^{(f)} = 1 - \frac{2m_f}{R} + 2\left(\frac{m_f}{R} \right)^2 - \frac{q_f}{R^3} + O_4 + O\left(\frac{\varepsilon^6}{c^6} \right) \tag{1}$$

$$g_{RR}^{(f)} = -\left[1 + \frac{2m_f}{R} + \frac{q_f}{R^3} + O_4 + O\left(\frac{\varepsilon^4}{c^4} \right) \right] \tag{2}$$

$$g_{\Theta\Theta}^{(f)} = R^2 g_{RR}^{(f)} \tag{3}$$

$$g_{\Phi\Phi}^{(f)} = R^2 \sin^2\theta\, g_{RR}^{(f)} \tag{4}$$

with

$$m_f := \frac{GM}{c^2}, \quad q_f := \frac{GQ}{c^2} \tag{5}$$

where

$$M := \int_V f^* \mathrm{d}^3 x = \text{Total mass-energy (inertial mass) of the source} \tag{6}$$

$$Q := 3n^\alpha n^\beta J_{\alpha\beta} - J_\rho^\rho = \text{Generalized quadrupole moment of the source} \tag{7}$$

$$\vec{n} := \frac{\vec{x}}{|\vec{x}|} = \text{Unit vector along the field point's direction} \tag{8}$$

$$J_{\alpha\beta} := \int_V f^* \left[1 + \frac{1}{c^2}\left(v^2 - \frac{1}{2}U + \frac{3p}{f^*} \right) + O\left(\frac{\varepsilon^4}{c^4} \right) \right] x^\alpha x^\beta \mathrm{d}^3 x$$

$$= \text{Generalized moment of inertia of the source} \tag{9}$$

The above results will be specialized to a homogeneous prolate fluid spheroid (of semiaxes $\alpha_1 = \alpha_2 << \alpha_3 := \alpha$) and eccentricity $[e := (1 - \alpha_1^2/\alpha_3^2)^{1/2}]$ close to unity $(e \leq 1)$.

For such a homogeneous source we shall assume that f^* can be treated as a constant throughout the spheroid, whence, in view of the virial theorem, the virial density itself (v^2 — (1/2)U + (3/2)p/f^*) is not expected to differ very much from zero. Then in $J^{\alpha\beta}$ the coefficient of $1/c^2$ can be omitted, so that finally we obtain

$$Q = \frac{2}{5} M\alpha^2 P_2(\cos\Theta_3) + \text{Terms proportional to } 1 - e^2 \text{ or } (1-e^2)^{1/2} \tag{10}$$

where α and e are related to the pN invariant M via

$$\alpha^3 (1 - e^2) = 3M/4\pi f^*$$

and cos Θ_3 is the direction cosine with respect to the large semiaxis α.

3. The γ and nγ Weyl-type vacuum solutions

The general form of the line element for the Weyl-type vacuum solutions, in the Weyl canonical coordinates $x^0 (= ct)$, ρ, φ, z, is

$$ds^2 = e^{2\lambda}(dx^0)^2 - e^{-2\lambda}[e^{2\mu}(d\rho^2 + dz^2) + \rho^2 d\varphi^2] \tag{11}$$

where $\lambda(\rho, z)$ and $\mu(\rho, z)$ satisfy the Einstein vaccum field equation (a comma denotes partial spatial derivative)

$$\lambda_{,\rho\rho} + \frac{\lambda_{,\rho}}{\rho} + \lambda_{,zz} = 0$$

$$\mu_{,\rho} = \rho(\lambda_{,\rho}^2 - \lambda_{,z}^2)$$

$$\mu_{,z} = 2\rho\lambda_{,\rho}\lambda_{,z}$$

We recall here (Carmeli 1982; Kramer *et al* 1980) that p, z are related to the *prolate spheroidal coordinates* (known also as *elliptical coordinates*), denoted by x and y, through the relations

$$\rho^2 = \sigma^2(x^2 - 1)(1 - y^2), \qquad 2\sigma x = r_+ + r_-$$

$$z = \sigma xy, \qquad 2\sigma y = r_+ - r_-$$

$$\sigma = \text{const.}, \qquad r_\pm^2 = \rho^2 + (z \pm \sigma)^2 \tag{12}$$

and also that the surfaces x = const, are ellipsoids, the surfaces y = const, are hyperboloid, and they are mutually orthogonal families.

In many cases the line element (11) is reexpressed in spherical polar coordinates x^0, r, θ, φ satisfying

$$\rho = \left(1 - \frac{2\sigma}{r}\right)^{1/2} \pi \sin\theta$$

$$z = \left(1 - \frac{\sigma}{r}\right) r\cos\theta \tag{13}$$

from which and equation (12) we see that

$$x = \frac{r}{\sigma} - 1$$

$$y = r\cos\theta \tag{14}$$

and also that the surfaces of constant r are biaxial *prolate* ellipsoids of semiaxes

$$\alpha_\rho = r\left(1-\frac{2\sigma}{r}\right)^{1/2}, \quad \alpha_z = r\left(1-\frac{\sigma}{r}\right) > \alpha_\rho$$

In the spherical polar coordinates the line element for the two-parametric γ solution, with parameters m and $\gamma \neq 1$, takes the form (for $\sigma = m - n^{-1}$ in equation (13))

$$ds^2 = g_{00}^{(\gamma)}(dx^0)^2 + g_{rr}^{(\gamma)}dr^2 + g_{\theta\theta}^{(\gamma)}d\theta^2 + g_{\varphi\varphi}^{(\gamma)}d\varphi^2 \tag{15}$$

where

$$\begin{aligned} g_{00}^{(\gamma)} &= e^{2\lambda} \\ g_{rr}^{(\gamma)} &= -e^{2\mu(1/\gamma^2-1)-2\lambda} \\ g_{\theta\theta}^{(\gamma)} &= -r^2 e^{2\lambda(1/\gamma-1)+2\mu(1-1/\gamma^2)} \\ g_{\varphi\varphi}^{(\gamma)} &= -r^2\sin^2\theta\, e^{2\lambda(1/\gamma-1)} \end{aligned} \tag{16}$$

with

$$\begin{aligned} e^{2\lambda} &= \left(1-\frac{2m}{r}\right)^{\gamma} \\ e^{2\mu} &= \left(\frac{1-\frac{2m}{r}}{1-\frac{2m}{r}+\frac{m^2}{r^2}\sin^2\theta}\right)^{\gamma 2} \end{aligned} \tag{17}$$

It is obvious that as $\gamma \to 1$ the γ solution tends to the exterior Schwarzschild solution of total mass-energy m.

Moreover the line element for the three-parametric $n\gamma$ solution, with parameters m, $\gamma \neq 1$, and $n \neq \infty$ as given in Papadopoulos & Witten 1982, takes the form (for $\sigma = m$)

$$ds^2 = g_{00}^{(n\gamma)}(dx^0)^2 + g_{rr}^{(n\gamma)}dr^2 + g_{\theta\theta}^{(n\gamma)}d\theta^2 + g_{\varphi\varphi}^{(n\gamma)}d\varphi^2 \tag{18}$$

where

$$\begin{aligned} g_{00}^{(n\gamma)} &= e^{2\lambda} \\ g_{rr}^{(n\gamma)} &= -e^{2(\mu-\lambda)}\left[1-\frac{2m}{r}+\frac{2}{nr}+\left(\frac{m}{r}-\frac{1}{nr}\right)^2\sin^2\theta\right]\left(1-\frac{2m}{r}+\frac{2}{nr}\right)^{-1} \\ g_{\theta\theta}^{(n\gamma)} &= -r^2 e^{2(\mu-\lambda)}\left[1-\frac{2m}{r}+\frac{2}{nr}+\left(\frac{m}{r}-\frac{1}{nr}\right)^2\sin^2\theta\right] \\ g_{\varphi\varphi}^{(n\gamma)} &= -r^2\sin^2\theta\, e^{-2\lambda}\left(1-\frac{2m}{r}+\frac{2}{nr}\right) \end{aligned} \tag{19}$$

with

$$e^{2\lambda} = \left[\frac{(R_1+R_2-2m)(\bar{R}_1+\bar{R}_2-2m)}{(R_1+R_2+2m)(\bar{R}_1+\bar{R}_2+2m)}\right]^{\gamma/2} \tag{20}$$

$$e^{2\mu} = \left\{[R_1+R_2-2m+2(i/n)][\bar{R}_1+\bar{R}_2-2m-2(i/n)]\right. \\ \left.\times\frac{[R_1+R_2+2m-2(i/n)][\bar{R}_1+\bar{R}_2+2m+2(i/n)]}{16\,R_1\bar{R}_1R_2\bar{R}_2}\right.$$

$$\times \frac{(R_1+R_2-2m)(\bar{R}_1+\bar{R}_2-2m)(R_1+R_2+2m)(\bar{R}_1+\bar{R}_2+2m)}{[(R_1+\bar{R}_1)^2+4n^{-2}][(R_2+\bar{R}_2)^2+4n^{-2}]}\Bigg\}^{\gamma^2/4} \tag{21}$$

and

$$R_1^2=\rho^2+[(i/n)-(z-m)]^2$$
$$R_2^2=\rho^2+[(i/n)-(z+m)]^2 \tag{22}$$

It is obvious that as $n\to\infty$ the $n\gamma$ metric tends to the γ metric, and as $n\to\infty$, $\gamma\to 1$ it tends to the exterior Schwarzschild metric of total mass-energy m. As far as we know the form of the $n\gamma$. metric described by equations (18) and (19) is given here for the first time.

4. The mass-energy of the γ and $n\gamma$ solutions

It is well-known (Weyl 1917; 1919; Szekeres 1968) that in the Weyl coordinates the exterior Schwarzschild metric can be thought of as being generated by a constant linear mass-energy density 1/2 (in geometrized units, or $c^2/2G$ in conventional units, G being the universal constant of gravitation), distributed symmetrically along the z-axis for a *length* $2m$ (in geometrized units, or $2GM/c^2$ in conventional units with $m = GM/c^2$, M being the total massenergy in conventional units), so that

$$\text{Linear density } 1/2 \times \text{Length } 2m = m = \text{Total mass-energy of the Schwarzschild metric} \tag{23}$$

More generally the vacuum γ metric can be thought of as being generated by a constant linear mass-energy density $\gamma/2$ (in geometrized units) distributed symmetrically along the z-axis for a *length 2m,* so that

$$\text{Linear density } \gamma/2 \times \text{Length } 2m = \gamma m = \text{Total mass-energy of the } \gamma \text{ metric} \tag{24}$$

This last result (24) can be independently verified by proving that, as is the case for other exterior metric tensors (e.g. Schwarzschild, Kerr, Kerr-Newman), the third Kepler's law holds for the circular (radius r) equatorial time-like geodesics of the γ metric in the form $(d\varphi/dt)^2 r^3 = \gamma m$, implying that γm is the mass-energy associated with the γ solution.

Furthermore, for understanding the origin of the directional singularities of the γ and $n\gamma$ solutions, it has been assumed (Papadopoulos & Witten 1982) that the $n\gamma$ metric can be thought of as being generated by the linear mass-energy density

$$f(z)=\frac{\gamma}{2r}[\arctan(nz+nm)-\arctan(nz-nm)] \tag{25}$$

distributed symmetrically along the entire z-axis. Although with such a choice of the density the directional singularities are no longer present, other problems arise, either mathematical or physical. The most important of the latter is the fact that, as it can be readily verified,

$$\int_{z=-\infty}^{z=+\infty} f(z)\,dz=\gamma m \tag{26}$$

Hence the hypothetical source of the $n\gamma$ metric characterized by a density of the form (25), has total mass-energy equal to γm, *only if its linear dimension along the*

z-axis is infinite. But this is a least acceptable astrophysical property of the source because: **i**) An astrophysical source would appear as of infinite dimension and **ii**) As it will be proved in section 5 below, in a proper multipole expansion of the $n\gamma$ (and (γ) metrics, appropriate for static and axisymmetric vacuum metrics, the monopole term, describing the active gravitational mass-energy of the source, is exactly equal to γm for both the γ and $n\gamma$ solutions.

So, as one is led to the conclusion that the $n\gamma$ metric cannot have a bounded source like the above, one can ask the question: Under what conditions, namely for what values of γ, m and n could the source be approximated to one having total mass-energy γm and also finite linear dimension? In trying to answer this question we first define M_z via

$$M_z := \int_{-z}^{z} f(z)\mathrm{d}z \tag{27}$$

Then M_m is the hypothetical source's mass-energy contained in the region between $z = -m$ and $z = m$ (which in the case of the γ metric is thought to be the total linear dimension of the hypothetical linear source of constant density $\gamma/2$). Moreover we readily verify that

$$M_z = \frac{\gamma}{\pi n}\left\{(nz+nm)\arctan(nz+nm) - (nz-nm)\arctan(nz-nm) - \frac{1}{2}\ln\left[\frac{1+(nz+nm)^2}{1+(nz-nm)^2}\right]\right\} \tag{28}$$

and hence

$$M_m = \frac{\gamma m}{\pi}\left\{2\arctan(2nm) - \frac{1}{2nm}\ln[1+(2nm)^2]\right\} \tag{29}$$

According to equation (29) M_m can be equal to γm only for $2mn=\infty$, meaning, for $m \neq 0$, that $1/n = 0$, namely only when the $n\gamma$ solution is degenerated to the γ solution.

One, however, notices that

$$\text{a) If } 2nm \gg 1, \text{ then } \lim_{2nm\to\infty} M_m = \gamma m \tag{30}$$

$$\text{b) If } 2nm \ll 1, \text{ then: } \lim_{2nm\to 0} M_m = 0 \tag{31}$$

Thus, although the exact equality $M_m = \gamma m$ is not possible for $n^{-1} \neq 0$, from equation (30) it becomes transparent that, if

$$2nm \gg 1 \tag{32}$$

the mass-energy in the region $(-m,m)$ could by approximated to the total mass-energy γm. In section 6 below (see equations (71)–(73)) the physical meaning of the condition (32) will be explained in detail. For the present we simply notice that the combination $2nm$ will be related to the linear dimension of the spheroidal fluid source perpendicular to the semimajor axis, namely to the semiminor axis $\alpha_1 = \alpha(1 - e^2)^{1/2}$, and hence to the spheroid's eccentricity (for a given α).

5. The vacuum metric's multipole expansion

It has been recently proved (Quevedo 1986, 1989) see also (Manko 1989; Hoenselaers & Perjes 1990; Quevedo & Mashhoon 1990) that the functions λ and μ in the metric (11) can be written in the multipole expansion forms

$$\lambda = \sum_{i=0}^{\infty} (-1)^{i-1} q_i Q_i(x) P_i(y)$$

$$\mu = \sum_{i,k=0}^{\infty} (-1)^{i+k} q_i q_k \Gamma^{(ik)} \tag{33}$$

where q_i are unknown constants, x and y are the prolate coordinates [see equations (12) and 14)], P_i and Q_i are, respectively, the Legendre polynomials and associated Legendre functions of the second and of the corresponding arguments, and $\Gamma^{(ik)}$ are known functions of x, y, P_i as well as Q_i, and dQ_i/dx defined through equation (44) of Quevedo (1986, 1989). Also in Quevedo (1986, 1989) it was proved, using the coordinate-invariant Ehlers (Ehlers 1981) definition of the Newtonian moments, that the parameters q_i determine, modulo a constant factor, the *Newtonian* multipole moments N_i of a static axisymmetric mass distribution, whose exterior gravitational Field is described by the above multipole-expansion-form vacuum solution (33). Specifically if U is the Newtonian gravitational potential (satisfying the Poisson field-equation $\nabla^2 U = -4\pi(Gp)$ and if

$$U(r,\theta) = \sum_{i=0}^{\infty} N_i \frac{P_i(\cos\theta)}{r^{i+1}}$$

then

$$N_i = (-1)^i \frac{i!}{(2i+1)!!} q_i m^{i+1} \tag{34}$$

where m is the source's mass in geometrized units.

Furthermore, the *relativistic* multipole moments G_i of static (and more generally axisymmetric) vaccum solutions are evaluated with the aid of the original method of Geroch (1970a, b) and Hansen (1974) (see also Thorne 1980; Gursel 1983), and are essentially the derivatives of the conformally transformed Ernst (Ernst 1968) potential, as it is described in the Appendix of Quevedo (1986, 1989). In the case of static and axisymmetric vacuum solutions,

$$G_i = N_i + R_i \ (i = 0, 1, 2, \ldots) \tag{35}$$

where R_i can be expressed in terms of N_i as

$$R_0 = R_1 = R_2 = 0,\ R_3 = -(2/3) m^2 N_1 \ldots \tag{36}$$

Especially for the γ metric equations (34) imply

$$N_0 = q_0 m,\ N_1 = (1/3) q_1 m^2,\ N_2 = (2/15)\, q_2 m^3 \ldots \tag{37}$$

Furthermore according to the Geroch-Hansen method and after some algebraic calculations performed with the aid of the 1986 version of the μ-tensor computer language for a computer Model IBM 80-11l/PS/2 we find

$$G_0 = \gamma m$$

$$G_1=0$$

$$G_2=-(1/3)\gamma(\gamma^2-1)m^3 \tag{38}$$

Simple comparison of equations (35) supplied by equations (37) and (38) yields the following values of the first few constants q_i

$$q_0=\gamma, q_1=0, q_2=(5/2)(\gamma-\gamma^3) \tag{39}$$

the knowledge of which enables us to evaluate λ and μ through equations (33) and furthermore g_{ik} by appropriate Taylor expansion through equations (16).

As described in the Appendix at the end, the result is

$$g_{00}^{(\gamma)}=1-\frac{2\gamma m}{\mathscr{R}}+2\left(\frac{\gamma m}{\mathscr{R}}\right)^2+\frac{2}{3}\left(1-\frac{1}{\gamma^2}\right)P_2\left(\frac{\gamma m}{\mathscr{R}}\right)^3+O_4 \tag{40}$$

$$-g_{\mathscr{R}\mathscr{R}}^{(\gamma)}=1+2\left(\frac{\gamma m}{\mathscr{R}}\right)+\frac{2}{3}\left(1-\frac{1}{\gamma^2}\right)P_2\left(\frac{\gamma m}{\mathscr{R}}\right)^2+O_3 \tag{41}$$

$$-g_{\theta\theta}^{(\gamma)}=\mathscr{R}^2\left[1+\frac{2\gamma m}{\mathscr{R}}+\frac{4}{3}\left(1-\frac{1}{\gamma^2}\right)\left(\frac{\gamma m}{\mathscr{R}}\right)^2+\frac{2}{3}\left(1-\frac{1}{\gamma^2}\right)P_2\left(\frac{\gamma m}{\mathscr{R}}\right)^2+O_3\right] \tag{42}$$

$$-g_{\varphi\varphi}^{(\gamma)}=\mathscr{R}^2\sin^2\theta\left[1+\frac{2\gamma m}{\mathscr{R}}+\frac{2}{3}\left(5-\frac{1}{2\gamma^2}\right)\left(\frac{\gamma m}{\mathscr{R}}\right)^2+O_3\right] \tag{43}$$

where $\mathcal{R}$ is defined by equation (A3) in the Appendix, and the symbol 0_1 denotes terms of order l in $\gamma m/\mathcal{R}$.

6. A physical identification of the γ and *n*γ metrics

In deciding in which way the identification of the γ and the fluid far-field metrics will be accomplished, we notice that for the static and axially symmetric solutions **i**) the purely temporal components of the two metrics must be equal,

$$g_{00}^{(\gamma)}=g_{00}^{(f)} \tag{44}$$

because g_{00} is the squared norm of the time-like Killing vector, and **ii**) the purely azimuthal components of the two metrics must be equal,

$$g_{\varphi\varphi}^{(\gamma)}=g_{\Phi\Phi}^{(f)} \tag{45}$$

because $g_{\varphi\varphi}$ is the squared norm of the space-like Killing vector

Noticing now that in view of equations (1) and (40) $g_{00}^{(\gamma)}$ and $g_{00}^{(f)}$, and in their respective coordinates, are of the same functional form, they dictate the following three steps of physical identification:

i). Identify the origin of the γ metric-coordinate system with the fluid's cim.
ii). Identify the γ metric's radial coordinate with the fluid's radial coordinate R (measured from its cim).

Then equation (44) reduces to an identically vanishing third-order polynomial in

$1/\mathcal{R}$ (or $1/R$), yielding

$$\gamma m = m_f \tag{46}$$

$$\frac{2}{3}\left(\frac{1}{\gamma^2}-1\right)(\gamma m)^3 P_2(\cos\theta) = q_f \tag{47}$$

Recalling now [see equation (10)] that for a prolate spheroid q_f is proportional to $P_2(\cos\Theta_3)$,

iii). Identify the γ metric's polar angle θ with the fluid metric's polar angle Θ (and both with Θ_3). Then equations (46) and (47) reduce to

$$\gamma m = \frac{GM}{c^2} = m_f \tag{48}$$

$$1-\frac{1}{\gamma^2} = -\frac{3}{5}\left(\frac{\alpha}{GM/c^2}\right)^2 < 0; \quad \gamma^2 < 1 \tag{49}$$

and so

$$m^2 = \left(\frac{GM}{c^2}\right)^2 + \frac{3}{5}\alpha^2 \tag{50}$$

Through equations (48)–(50) the parameters γ and m are expressed in terms of the fluid's parameters, and this completes the identification.

We remark that practically the identification has been based on the fact that only the two components $g_{00}^{(\gamma)}$ and $g_{00}^{(f)}$ have been put in the same functional form (this is not independent of the fact, that (Clarke & Sciama 1971) in the underlying method and especially Geroch's (1970a, b) method, only the purely temporal component g_{00} was used to define multipoles). As a consequence the condition (45) was not used. However, this is not necessary, because to the approximation equations (4) and (43) have been given, the condition (45) is *trivially* satisfied. In this case, this does not cause any problems in the identification procedure, because the condition (44) provides us with two conditions, (46) and (47), sufficient for determining m, γ in terms of M, α.

According to the interpretation of the mass-energy of the γ solution in section 4, the combination γm is identified with the fluid's total mass-energy. Furthermore these two mass-energies ought to be included in linear regions of dimensions $2m$ and 2α. If, in this sense, these two linear dimensions are assumed of the same order of magnitude

$$m = \alpha \tag{51}$$

then equations (48)–(50) reduce to

$$\alpha = \left(\frac{5}{2}\right)^{1/2}\frac{GM}{c^2}; \quad 2\alpha = 0.15\left(\frac{M}{10^{15}M_\odot}\right)\text{kpc} \tag{52}$$

$$\gamma = \frac{GM}{2c^2} = \left(\frac{2}{5}\right)^{1/2} \sim 0.63 \tag{53}$$

and, for the source's linear mass-energy density along α, to

$$l_\alpha := \frac{M}{2\alpha} = \frac{c^2}{2G}\gamma = \left(\frac{2}{5}\right)^{1/2}\frac{c^2}{2G} \sim 1{\cdot}0775 \times 10^{27}\frac{\text{gr}}{\text{cm}} \tag{54}$$

Table 1. Astrophysical linear mass-energy densities.

Astrophysical system	M/2α(gr/cm)
Milky Way	1.0743×10^{22}
Core of giant prolate galaxy	1.6115×10^{26}
γ-source (hypothetical)	$(=(2/5)^{1/2}c^2/2G \approx) 1.0775 \times 10^{27}$
Schwarzschild source	$(=c^2/2G \approx) 3.3670 \times 10^{27}$
Kerr-Newman source	$(c^2/4G \approx) 6.7341 \times 10^{27}$
nγ-source (hypothetical)	3.3724×10^{28}

These results, although only indicative due to the arbitrariness of the condition (51), impose certain restrictions on the properties of the possible astrophysical source. In view of the content of Table 1, these sources are relativistically active (see also section 7 below).

Applying in the case of the $n\gamma$-metric the same procedure, we find

$$q_0 = \gamma,\ q_1 = 0,\ -\frac{2}{15}q_2 = \frac{1}{3}(\gamma^3 - \gamma) + \frac{\gamma}{m^2 n^2} \tag{55}$$

and furthermore, by using equations (A2) and (A3) in the Appendix at the end,

$$g_{00}^{(n\gamma)} = 1 - \frac{2\gamma m}{\mathcal{R}} + 2\left(\frac{\gamma m}{\mathcal{R}}\right)^2 + \frac{2}{3}\left(1 - \frac{1}{\gamma^2} + \frac{3}{\gamma^2 m^2 n^2}\right)P_2\left(\frac{\gamma m}{\mathcal{R}}\right)^3 + O_4 \tag{56}$$

which differs from equation (40) by the appearance of only the additional term $3/\gamma^2 m^2 n^2$ proportional to $P_2(\cos\theta)$.

Thus following the same steps of identification we find the following generalizations of equations (48)–(50)

$$\gamma m = \frac{GM}{c^2} \tag{57}$$

and

$$1 - \frac{1}{\gamma^2}\left(1 - \frac{3}{m^2 n^2}\right) = -\frac{3}{5}\left(\frac{\alpha}{GM/c^2}\right)^2, \left(\gamma^2 + \frac{3}{m^2 n^2} < 1\right) \tag{58}$$

or, equivalently

$$m^2 - \frac{3}{n^2} = \left(\frac{GM}{c^2}\right)^2 + \frac{3}{5}\alpha^2 > 0 \tag{59}$$

The two equations (57) and (59) contain the maximum information for the three parameters m, γ, n as functions of the fluid's parameters. So we need one further condition to complete the identification. As such we could use the condition (45) and so we should evaluate also the rest of $g_{ik}^{(n\gamma)}$ (beyond $g_{00}^{(n\gamma)}$. However, unless we calculated $g_{\varphi\varphi}^{(n\gamma)}$ correctly up to and included terms of order $(\gamma m/\mathcal{R})_3$, the use of condition (45) would not provide any further information concerning the relation of m, γ, n to the fluid's parameters, because it would be trivially satisfied. But, furthermore, even if such an extended form of $g_{\varphi\varphi}^{(n\gamma)}$ was obtained, it would be of little physical significance, because in this way the three parameters m, γ, n would finally be related to only two and the same fluid parameters, namely M and α, something that would obviously

imply that one of γ, *m, n* can be expressed in terms of the other two, its probable astrophysical importance being severely restricted.

Furthermore we notice that the assumption-choice (51; $m = \alpha$) used in the γ metric implies

$$\gamma = GM/c^2\alpha \tag{60}$$

$$\gamma^2 + (3/m^2n^2) = 2/5 \tag{61}$$

$$3/n^2 = (2/5)\alpha^2 - (GM/c^2)$$

the last of which can be valid provided that

$$2\alpha \geqslant 0.15(\mathrm{M}/10^{15}\mathrm{M}_{\odot})\mathrm{kpc} \tag{62}$$

Equations (61) and (62) look reasonable and the assumption (60) seem to avoid the difficulty of the infinite dimensions (along *z*) of the possible *n*γ-solutions source. However, a simple inspection of equations (60) and (61) reveals that again through them the parameter *n* as well (beyond the parameters *m,* γ)is related to the two parameters (*M* , α) only of the fluid source.

The physical identification of the γ solution so far was made possible by considering only the linear dimension along *z*, which implies that the fluid source is considered as strictly linear, corresponding to a degenerate spheroid with $e = 1$. Furthermore the identification was also complete, because the two parameters m, γ were expressed in terms of the fluid's two parameters *M*. and α. In the case of the triparametric *n*γ-solution we have to consider a third characteristic of the probable fluid source. Quite naturally we shall use as such a characteristic the divergence of the fluid-source's shape from the strict linear one. So beyond demanding satisfaction of the condition (32), so that γ*m* (which is equal to m_f) can be approximated to the mass-energy M_m, we shall relate *m* to the semiminor axis α_1 of the (elongated, $e \lesssim 1$) fluid source. Thus putting in equation (59)

$$m = k\alpha_1,\ k > 0 \tag{63}$$

we obtain

$$\frac{3}{n^2} = k^2(1-e^2) - \frac{3}{5} - \left(\frac{GM}{c^2\alpha}\right)^2 \geqslant 0 \tag{64}$$

which can hold provided that

$$\alpha \geqslant \left[k^2(1-e^2) - \frac{3}{5}\right]^{-1/2} \frac{GM}{c^2} \tag{65}$$

with obviously

$$e < e_{\max},\quad e_{\max} = \left(1 - \frac{3}{5k^2}\right)^{1/2},\quad k^2 > \frac{3}{5} \tag{66}$$

It is interesting that through equations (64)–(66) for any permitted value of *k* (and α_1, of course), upper limits can be determined for the fluid source's eccentricity (and hence semimajor axis) and linear mass-energy density along a,

$$l_{\alpha} \leqslant \left[k^2(1-e^2) - \frac{3}{5}\right]^{-1/2} \frac{c^2}{2G} \tag{67}$$

Also, for $k \lesssim 1$, the maximal permitted value of the eccentricity ($e_{\max} \sim 0.63$) does not exceed the values of the observed eccentricities of the elliptical galaxies $e \lesssim 0.95$ [derived from the observed oblatenesses $\omega < 0.7$; (see e.g. Taylor 1978)] which correspond to $k \sim 3.609$.

In what follows we shall prove that the above results can also guarantee the validity of the conditions $2nm \gg 1$ and $M_m \sim \gamma m$. Thus, from the definition of $f(z)$ [equation (25)] we readily obtain

$$\left.\frac{df(z)}{dz}\right|_{z=0} = 0 \tag{68}$$

$$\left.\frac{d^2 f(z)}{d^2 z}\right|_{z=0} = -\frac{\gamma}{\pi}\frac{2n^2}{(nm)^3} < 0 \quad \text{for } \gamma > 0, mn > 0 \tag{69}$$

Hence

$$f_{\max} = f(z=0) = \frac{\gamma}{\pi}\arctan(nm) \tag{70}$$

On the other hand, the homogeneous fluid's maximal linear mass-energy density is, for obvious reasons, along the semiminor axis α_1,

$$(l_{\alpha_1})_{\max} = \frac{M}{2\alpha_1} \tag{71}$$

Consequently, as the required third condition for independently determining m, γ and n in terms of the fluid's parameters, we shall use the equality of the two maximal values (70) and (71), namely

$$\frac{c^2}{2G} f_{\max} = (l_{\alpha_1})_{\max} \tag{72}$$

which in view of equations (57) and (63) can be written as

$$2nm = 2\tan\left(\frac{k\pi}{2}\right) > 5.141 \tag{73}$$

implying that $k \leqslant 1$ for $nm > 0$. Some representative values of k (and hence $e_{\max}$), $2nm$ and $M_m/\gamma m$, for $e = 0.63$ are shown in Table 2, from the content of which we conclude that $2nm$ is always larger than unity and increases indefinitely as $m \to \alpha_1$, while at the same time $M_m \to \gamma m$. Of course, the value $k=1$ (for which $m = \alpha_1$ and $M_m = \gamma m$) is not attainable, because then $2mn$ and hence, for $m > 0$, n are infinite, and the $n\gamma$ solution is degenerated to the γ solution. For e.g. $k = 0.9999$ (and $e = 0.63$), $2mn$ is of the order of 10^4 and M_m comprises more than 99.95% of γm. Hence M_m is an excellent representation of γm. For the same value of k, and for $e \sim 0.6$,

$$l_\alpha \leqslant 3.3724 \times 10^{28}\,\mathrm{gr/cm}$$

$$\alpha > 5.008\,GM/c^2;\ (GM/\alpha c^2)^{1/2} < 0.4469$$

$$\alpha_1 = 0.800\,\alpha > 4.0064\frac{GM}{c^2};\ \left(\frac{GM}{\alpha_1 c^2}\right)^{1/2} < 0.4996$$

$$m = k\alpha_1 = 0.9999\,\alpha_1 = 0.7499\,\alpha > 4.0060\frac{GM}{c^2}$$

Table 2. Representative values of $k, e_{\max}$ $2nm$, $M_m/\gamma m$ for $e = 0.63$.

k	$e_{\max}$	$2nm$	$M_m/\gamma m$
0.7750	0.000	5.4212	0.6834
0.8000	0.250	6.1554	0.7082
0.8500	0.4117	8.3306	0.7614
0.9000	0.509	12.6275	0.82169
0.9900	0.623	127.3135	0.9708
0.9990	0.632	1273.2386	0.9959
0.9999	0.632	12732.428	0.9995

$$l_{\alpha_1} < 1.6808 \times 10^{27}\,\mathrm{gr/cm}$$

$$\frac{1}{n} = \frac{2m}{12{,}732.428} = 1.5706 \times 10^{-4}\alpha_1$$

$$= 1.2565 \times 10^{-4}\alpha > 6.2926 \times 10^{-4}\frac{GM}{c^2} \tag{74}$$

Comparison of these results with the content of Table 1 implies that the probable $n\gamma$ source should be a relativistically active perfect-fluid.

We notice that, in case we had assumed $m=\alpha$ (instead of $m=\alpha_1$), the condition (72) would read

$$2nm = 2\tan\left[\frac{r}{2}(1-e^2)^{-1/2}\right] < 0 \tag{75}$$

contrary to the assumption [see equation (69)] that mn (and γ) are positive.

We shall complete this section by noticing that for the relativistically active perfect-fluid sources described by the above results, the basic condition of the post-Newtonian theory is valid, namely

$$\frac{U}{c^2} \ll 1 \tag{76}$$

The proof, given in the Appendix at the end, is based on the fact that for a homogeneous prolate spheroid the surface gravitational potential on the two axes is smaller than GM/α.

7. Discussion and outlook

We presented a possible method for physically identifying the vacuum γ and $n\gamma$ metrics with the metric of a fluid mass. We based our identification scheme on the assumption that the total mass-energy of the vacuum solutions, which is finite, should also be included in a finite region of space. Hence we used the quantity M_m which is a known function of the parameters m, γ,n only, since the argument of using any M_z with $|z| \gtrsim$ m does not seem to be of any practical interest and use here, because it doesn't solve any problem.

Although the physical identification is entirely independent of any interior γ and *n*γ-solutions, however the solution's parameters (*m*, *γ, n*) are directly related to physical quantities known as integrals of the fluid source's internal characteristics over its three-dimensional volume. The far-field expression of the perfect-fluid metric has been given consistently and correctly to pN accuracy, to which the source's parameters are also evaluated. So the γ and *n*γ metrics' identification is valid not simply to Newtonian theory but to the pN approximation. By identifying the origins of the system (s) of coordinates used in the γ and the *n*γ-solutions with the fluid's cim, we explored the relation of the corresponding coordinates to those measured from the cim. The importance of this relation is obvious, since the cim is moving uniformly, not simply to the Newtonian theory, but to the pN approximation. The physical properties of the fluid sources, appropriate for the description of the two vacuum solutions, dictated by the latters' mathematical properties, are not unreasonable. So they raise the question on the possibility of the existence and of the nature of such objects. In our opinion the most probable astrophysical candidates are the highly eccentric relativistically active nuclei of the giant elliptical galaxies. The theoretical framework of the relativistic galactic dynamics for the study of such systems is known (Spyrou & Varvoglis 1982), and it allows for the fluid-source's internal physical characteristics to be taken into account as sources of the observed motions of their stars (test particles). In the special case of the giant prolate elliptical galaxies, this influence of the relativistically active prolate nucleus is very interesting (Spyrou & Varvoglis 1987; Spyrou 1988). Actually, a fast-rotating and possibly expanding or contracting nucleus affects the distribution of the box-type orbits near the (observed) surface of the galaxy. Hence the study of the post-Newtonian effects, and the consequent modifications of the corresponding non-relativistic results, could in principle provide useful information concerning the kinematical and dynamical characteristics of the nuclei of elliptical galaxies. It is important that the above theoretical framework provides an explanation (of at least the post-Newtonian part) of the flattening of the elliptical galaxies. The study of the above subjects is based on the use of the relativistic nucleus' far-field metric tensor evaluated at the surface of the galaxy. On the other hand in our physical identification the far-field metrics have been used. Therefore, studies of the observed motions of the stars on the galaxy's surface could in principle permit an observationally-based determination of the parameters γ, *m*, *n,* provided, of course, that the identification is accepted and the above galactic nuclei really exist on both observational and theoretical grounds.

In spite of all the above we have to particularly emphasize that our proposed method of identification is only approximate, and it refers only to two classes of static and axisymmetric vacuum solutions, since it relies heavily on the multipole expansion valid only for such vacuum solutions. Possible extensions of our results to perfect-fluid sources, either prolate or oblate, endowed with further physical properties like e.g. a magnetic field, could present some interest. But of great interest could surely be the extension to stationary vacuum solutions. It seems, however, that for the latter we shall have to wait until the corresponding gravitational field's multipole expansion will be available. Furthermore the vacuum metric's identification has been related practically to prolate perfect-fluid sources. The latter although general and possibly astrophysically interesting surely are not the only sources to be considered, because additionally, as it is known (Florides 1972, 1973, 1975), the possible spheroidal source of vacuum axisymmetric metrics (Kerr metric) cannot consist of a rigidly rotating and homogeneous perfect fluid. Also we point out that in the

identification we essentially considered a strictly linear fluid source of the γ-metric, and so the third parameter n of the $n\gamma$-metric was related to divergences of the corresponding prolate fluid source from linearity. Obviously this by no means implies that the γ metric's probable source is necessarily linear, and that one of the $n\gamma$-metric's is not, and furthermore such a relation does not contradict the omission in equation (10) of terms proportional to $(1 - e^2)$ and $(1- e^2)^{1/2}$. Moreover the identification procedure didn't rely on the use of moments beyond the quadrupole. The reason for this is threefold: **i).** The calculation of the octopole-moment term, at least, in the expansion of the γ- and especially the $n\gamma$-metric proved quite laborious, **ii).** The dependence of the octopole-moment term on the eccentricity, in the fluid-metrics expansion, is rather complicated, something that could perplex the moments, in view mainly of the consistent omission of the eccentricity-dependent terms of the quadrupole term, **iii**). Retaining, on the other hand, the eccentricity-independent terms of the octopole-moment terms, in the case of the γ-metric would result in a non-necessary third relation between m, γ and M, α [beyond Equations (48) and (50)]; similarly, in the case of the $n\gamma$-metric it would result in a third relation [beyond Equations (57) and (59)] between m, γ, n and M, α, with the aid of which, however, one of the parameters m, γ, n would be expressed in terms of the other two, thus reducing the $n\gamma$ solution to a two-parametric one. In view of the above reasons, and in order to take into account the eccentricity of the fluid source, *in the simplest possible way,* we related the parameter n to the divergence of the source's shape from the strict linear one, through the physical condition (73) in which the eccentricity does appear explicity.

All the previous advantages and mainly deficiencies of the proposed identification emphasize the interest in the question of the physical identification of the axisymmetric vacuum solutions, and simply indicate that this is still far from being answered satisfactorily. We believe that this first approach to the problem of the physical identification of the far-field metric tensors of the static and axisymmetric γ and $n\gamma$ vacuum solutions with the far-field metric tensor of a bounded perfect-fluid gravitating source, is characterized by a completeness, pN accuracy and consistency, and simplicity, that do not seem to have been attempted before.

Acknowledgements

We thank warmly Jürgen Ehlers, Petros Florides, and Louis Witten for reading an earlier version of the manuscript as well as for their constructive criticism and useful comments and suggestions.

APPENDIX

In the Appendix we give the final expression for the far-field form of the γ and $n\gamma$ metric tensors in the $x^0 = ct$, r, θ, φ coordinates. This form is

$$g_{ik} = A_{ik} + B_{ik}P_2, \quad i,k = x^0, r, \theta, \varphi \tag{A1}$$

where

$$A_{00}^{(\gamma)} = 1 - \frac{2\gamma m}{r} + 2\left(1 - \frac{1}{\gamma}\right)\left(\frac{\gamma m}{r}\right)^2 + \frac{4}{3}\left(\frac{1}{\gamma} - 1\right)\left(1 - \frac{2}{\gamma}\right)\left(\frac{\gamma m}{r}\right)^3 + O_4$$

$$B_{00}^{(\gamma)} = \frac{2}{3}\left(1-\frac{1}{\gamma^2}\right)\left(\frac{\gamma m}{r}\right)^3 + O_4$$

$$-A_{rr}^{(\gamma)} = 1 + \frac{2\gamma m}{r} + \frac{2}{3}\left(1+\frac{1}{\gamma}\right)\left(2+\frac{1}{\gamma}\right)\left(\frac{\gamma m}{r}\right)^2 + \frac{4}{3\gamma}\left(1+\frac{1}{\gamma}\right)\left(2+\frac{1}{\gamma}\right)\left(\frac{\gamma m}{r}\right)^3 + O_4$$

$$-B_{rr}^{(\gamma)} = \frac{2}{3}\left(1-\frac{1}{\gamma^2}\right)\left(\frac{\gamma m}{r}\right)^2 + \frac{2}{3}\left(1-\frac{1}{\gamma^2}\right)\left(1+\frac{2}{\gamma}\right)\left(\frac{\gamma m}{r}\right)^3 + O_4$$

$$-A_{\theta\theta}^{(\gamma)} = r^2\left[1 + 2\left(1-\frac{1}{\gamma}\right)\frac{\gamma m}{r} + \frac{2}{3}\left(1-\frac{1}{\gamma}\right)\left(2-\frac{1}{\gamma}\right)\left(\frac{\gamma m}{r}\right)^2 + O_3\right]$$

$$-B_{\theta\theta}^{(\gamma)} = r^2\left[\frac{2}{3}\left(1-\frac{1}{\gamma^2}\right)\left(\frac{\gamma m}{r}\right)^2 + \frac{2}{3}\left(1-\frac{1}{\gamma^2}\right)\left(1+\frac{1}{\gamma}\right)\left(\frac{\gamma m}{r}\right)^3 + O_4\right]$$

$$-A_{\varphi\varphi}^{(\gamma)} = r^2\sin^2\theta\left[1 + 2\left(1-\frac{1}{\gamma}\right)\frac{\gamma m}{r} + 2\left(1-\frac{1}{\gamma}\right)\left(\frac{\gamma m}{r}\right)^2 + \frac{4}{3}\left(1-\frac{1}{\gamma}\right)\left(1+\frac{1}{\gamma}\right)\left(\frac{\gamma m}{r}\right)^3 + O_4\right]$$

$$-B_{\varphi\varphi}^{(\gamma)} = r^2\sin^2\theta\left[-\frac{2}{3}\left(1-\frac{1}{\gamma}\right)\left(1-\frac{1}{\gamma^2}\right)\left(\frac{\gamma m}{r}\right)^3 + O_4\right]$$

Also

$$g_{00}^{(n\gamma)} = 1 - \frac{2\gamma m}{r} + 2\left(1-\frac{1}{\gamma}\right)\left(\frac{\gamma m}{r}\right)^2 + \left[-\frac{4}{3}\left(1-\frac{1}{\gamma}\right)\left(1-\frac{2}{\gamma}\right) + \frac{2}{3}\left(1-\frac{1}{\gamma^2}+\frac{3}{\gamma^2 m^2 n^2}\right)P_2\right]\left(\frac{\gamma m}{r}\right)^3 + O_4 \tag{A2}$$

Using the transformation, for *both* the γ and $n\gamma$ metric,

$$r = \mathscr{R}\left[1 + \frac{m}{\mathscr{R}} + \frac{2}{3}\left(1+\frac{1}{2\gamma^2}\right)\left(\frac{\gamma m}{\mathscr{R}}\right)^2 + O_3\right] \tag{A3}$$

we obtain equations (56) in the text

Furthermore from equations (44) of Quevedo (1986, 1989) and equations (14) (for $\sigma = m$) we find

$$\Gamma^{(00)} = \frac{1}{3}(P_2 - 1)\frac{1}{x^2} + O(x^{-4}) = \frac{1}{3}(P_2-1)\frac{m^2}{r^2} - \frac{2}{3}(P_2-1)\left(\frac{m}{r}\right)^3 + O(r^{-4})$$

$$\Gamma^{(02)} + \Gamma^{(20)} = O(x^{-4})$$

$$\Gamma^{(22)} = O(x^{-4}) \tag{A4}$$

whence equations (33) imply

$$\mu = \frac{1}{3}(q_0)^2(P_2-1)\frac{1}{x^2} + O(x^{-4})$$

$$= \frac{1}{3}(P_2 - 1)\left(\frac{q_0 m}{r}\right)^2 + \frac{2}{3}(P_2 - 1)q_0^2 \frac{m^3}{r^3} + O(r^{-4}) \tag{A5}$$

$$\lambda = -\frac{q_0}{x} + \left(-q_0 + \frac{1}{3}q_1 P_1\right)\frac{1}{x^3} + O(x^{-4})$$

$$= -\frac{q_0 m}{r} + \left(-q_0 + \frac{1}{3}q_1 P_1\right)\left(\frac{m}{r}\right)^2$$

$$+ \left(-\frac{4}{3}q_0 + \frac{2}{3}q_1 P_1 - \frac{2}{15}q_2 P_2\right)\left(\frac{m}{r}\right)^3 + O(r^{-4}) \tag{A6}$$

direct consequence of which are equations (40) and (56) in the text.

Finally we prove that in the context of the physical identification described in the text, the basic assumption of the post-Newtonian expansion is valid, namely

$$U(r, z) \ll c^2 \tag{A7}$$

Actually for a prolate spheroid the surface gravitational potential satisfies (Chandrasekhar 1969)

$$U(\alpha_1, 0) = U(0, \alpha)\frac{1}{2}\left[1 + \frac{A_3}{(1 - e^2)A_1}\right] \tag{A8}$$

$$U(0, \alpha) = \frac{3GM}{2\alpha}A_1, \quad 2A_1 + A_3 = 2 \tag{A9}$$

But, as it can be easily verified, for every $0 < e \lesssim 0{\cdot}63$ (we consider the above upper bound of e, using $\kappa = 0{\cdot}999$)

$$\frac{2}{3} < A_1 \lesssim 0{\cdot}73 \tag{A10}$$

Moreover, in equations (A8) the coefficient of $U(r = 0, z = \alpha)$ is smaller than unity, because the condition

$$A_3 \ll (1 - e^2)A_1 \tag{A11}$$

is equivalent to

$$A_1 \gg 2/(3 - e^2) \tag{A12}$$

Since, however, for $0 < e \lesssim 0{\cdot}63$

$$0{\cdot}768 > \frac{2}{3 - e^2} > \frac{2}{3} \tag{A13}$$

the condition (A12) can be satisfied, it $A > 2/3$, namely if $e > 0{\cdot}1$. The latter requirement is obviously satisfied for systems diverging from spherical symmetry, as is the case here.

Hence equations (A8) and (A9) reduce to

$$\frac{U(\alpha_1, 0)}{c^2} < \frac{U(0, \alpha_3)}{c^2} \lesssim \frac{GM}{c^2 \alpha} \tag{A14}$$

On the other hand the positivity of n^2 implies [see equation (65)]

$$\frac{GM}{c^2 \alpha} \lesssim \left[k^2(1 - e^2) - \frac{3}{5}\right]^{1/2} \tag{A15}$$

whence, for typical values ($k = 0{\cdot}999$, $e = 0{\cdot}63$) we find

$$\frac{GM}{c^2\alpha} < 0{\cdot}0435 \tag{A16}$$

In view of equations (A 14) and (A 16) the basic post-Newtonian condition (A7) is satisfied. In other words the condition $n^2 \geqslant 0$ guarantees the validity of the post-Newtonian condition.

References

Carmeli, M. 1982, *Classical Fields: General Relativity and Gauge Theory* (John Wiley and Sons, New York).

Chandrasekhar, S. 1965, *Astrophys. J.,* **142,** 1488.

Chandrasekhar, S. 1969, *Ellipsoidal Figures of Equilibrium,* (Yale University Press, New Haven).

Clarke, C. J. S., Sciama, D. W. 1971, *Gen. Rel. Grav.,* **2,** 331.

Contopoulos, G., Spyrou, N. 1976, *Astrophys. J.,* **205,** 592.

Ehlers, J. 1981, in *Grunglagenprobleme der modernen Physik.* Eds J. Nitsch, J. Pfarr, & E. W. Stachov, B. I. Verlag, Mannheim.

Ernst, F. J. 1968, *Phys. Rev.,* **168,** 1415.

Esposito, F. P., Witten, L. 1975, *Phys. Rev. Lett.,* **B58,** 357.

Florides, P. S. 1972, *II Nuovo Cimento,* **13B,** 1.

Florides, P. S. 1973, *II Nuovo Cimento,* **14B,** 157.

Florides, P. S. 1975, *II Nuovo Cimento,* **25B,** 251.

Geroch, R. 1970a, J. *Math. Phys.,* **11,** 1955.

Geroch, R. 1970b *J. Math. Phys.,* **11,** 2580.

Gursel, Y. 1983, *Gen. Rel. Grav.,* **12,** 1003.

Hansen, R. O. 1974, *J. Math. Phys.,* **15,** 46.

Hoenselaers, C, Perjes, Z. 1990, *Class. Quantum Grav.,* **7,** 1819.

Janis, A. I., Newman, E. T. 1965, *J. math. Phys.,* **6,** 902.

Kramer, D., Stephani, H., Herlt, E., MacCallum, M. 1980, *Exact Solutions of Einstein's Field Equations,* (Deutcher Verlag der Wissenschaften, Berlin).

Krisch, J. P. 1983, *Phys. Rev.,* **D27,** 2305.

Manko, V. S. 1989, *Gen. Rel. Grav.,* **21,** 1193.

Papadopoulos, D., Stewart, B., Witten, L. 1981, *Phys. Rev.,* **D24,** 320.

Papadopoulos, D., Witten, L. 1982, *Phys. Rev.,* **D25,** 1465.

Quevedo, H. 1986, *Phys. Rev.,* **D33,** 324.

Quevedo, H. 1989, *Phys. Rev.,* **D39,** 2904.

Quevedo, H., Mashhoon, B. 1990, *Phys. Rev. Lett. A.,* **148,** 149.

Spyrou, N. 1977, *Gen. Rel. Grav.,* **8,** 463.

Spyrou, N. 1981a, *Gen. Rel. Grav.,* **13,** 551.

Spyrou, N. 1981b, *Gen. Rel. Grav.,* **13,** 771.

Spyrou, N. 1984, *Gen. Rel. Grav.,* **16,** 411.

Spyrou, N. 1988, *Newtonian and Relativistic Aspects of the Elliptical Spheroidal Galaxies*, in special volume *In Memoriam D. Kotsakis*, Eds G. Contopoulos, B. Barbanis & P. G. Laskarides, Athens.

Spyrou, N., Papadopoulos, D. 1990, Talk given at the Greek National Workshop *Recent Developments in Gravitation-IV,* June 25–29, 1990, Thessaloniki, Greece.

Spyrou, N., Varvoglis, H. 1982, *Astrophys. J.,* **255,** 674.

Spyrou, N., Varvoglis, H. 1987, *J. Astrophys. Astr.,* **8,** 1.

Stewart, B. W., Papadopoulos, D., Witten, L., Berezdivin, R., Herrera, L. 1982, *Gen. Rel. Grav.* **14,** 97.

Szekeres, P. 1968, *Phys. Rev.,* **176,** 1446.
Tayler, R. J. 1978, *Galaxies: Structure and Evolution,* (Wykeham Publications, London).
Thorne, K. S. 1980, *Rev. Mod. Phys.,* **52**, 299.
van den Burg, M. G. J. 1968, *Proc. R. Soc.,* **4303,** 37.
Weyl, H. 1917, *Ann. Physik,* **54**, 117.
Weyl, H. 1919, *Ann. Physik,* **59**, 185.
Winicour, J., Janis, A. I., Newman, E. T. 1968, *Phys. Rev.,* **176,** 1057.